The Dissertation Committee for Eric David Kelly
Certifies that this is the approved version of the following dissertation:

UNRECOGNIZED COMPLEXITIES OF METAMORPHISM: CRYSTALLIZATION KINETICS, REACTION AFFINITY, AND GEOCHRONOLOGY

Committee:

William D. Carlson, Co-Supervisor

Richard A. Ketcham, Co-Supervisor

James E. Gardner

Mark Cloos

David R. M. Pattison

John R. Farver

UNRECOGNIZED COMPLEXITIES OF METAMORPHISM: CRYSTALLIZATION KINETICS, REACTION AFFINITY, AND GEOCHRONOLOGY

by

Eric David Kelly, B.A.; M.S.

Dissertation
Presented to the Faculty of the Graduate School of
The University of Texas at Austin
in Partial Fulfillment
of the Requirements
for the Degree of

Doctor of Philosophy

The University of Texas at Austin
December 2011

ACKNOWLEDGEMENTS

I am grateful to several funding sources for making this research possible: the National Science Foundation, the Jackson School of Geosciences, the Geological Society of America, the Thomas R. Banks Memorial Scholarship, the Glen and Martha Vargas Endowed Presidential Scholarship, and the Robert H. Cuyler Endowed Presidential Scholarship.

I thank my advisors for including me in this fundamental research and for their hard work in supervising these projects. I especially thank Bill for being perpetually enthusiastic, creative, and enlightening as a mentor in research and teaching, and I thank Rich for thorough analyses that persuaded me to look more closely at many aspects of my work.

My gratitude goes to Jim Connelly for the opportunity to work with his samples, for his personalized training in the laboratory, and for candid discussions on a variety of topics. Todd Housh was a great mentor in all aspects of isotope geology. I appreciate the time and effort of my committee members, and I especially thank them for their thoughtfulness and critical comments that spurred my thinking to greater depths.

In the past six years, the members of the Carlson research group have contributed to my deeper understanding of metamorphism during individual conversations and discussions during group meetings. I look forward to working with these colleagues throughout my career.

I thank my parents for giving me the freedom to choose a career that excites me and for setting examples of what one can achieve with enough effort and commitment. My most heartfelt gratitude goes to Kristine for her hard work, patience, and support.

UNRECOGNIZED COMPLEXITIES OF METAMORPHISM: CRYSTALLIZATION KINETICS, REACTION AFFINITY, AND GEOCHRONOLOGY

Eric David Kelly, Ph.D.
The University of Texas at Austin, 2011

Supervisors: William D. Carlson and Richard A. Ketcham

Unrecognized metamorphic complexities can produce erroneous interpretations when using equilibrium thermodynamics and isotope geochronology. Universally employed methods for determining pressure-temperature conditions during regional metamorphism are based on the assumption of chemical equilibrium, and geochronology in metamorphic rocks can suffer from cryptic redistribution of isotopes. In this research, the scales of disequilibrium in regionally metamorphosed rocks and the effects of garnet resorption on Lu-Hf garnet ages were examined through numerical simulations of these processes.

Concerning scales of disequilibrium, thirteen porphyroblastic datasets, previously measured using X-ray computed tomography, were examined by numerically simulating diffusion-controlled nucleation and growth of garnet while tracking chemical potential gradients to determine reaction affinity A_r ($-\Delta_r G$). Maximum nucleation rates are $10^{-13.6}$-$10^{-9.8}$ nuclei cm^{-3} s^{-1}, interfacial energies are 0.004-0.14 J m^{-2} assuming shape factors of 0.1-1.0, and Al intergranular diffusion (Q_D = 140 kJ mol^{-1}) is $10^{-14.4}$-$10^{-11.1}$ m^2 s^{-1} at 600 °C. Limitations in determining crystallization kinetics arise from difficulties in constraining rock-specific properties (e.g., porosity and Al solubility). A_r at the time and location of nucleation is 0.4-5.9 kJ mol^{-1} of 12-oxygen garnet (ΔT = 4.0-62.0 °C) for the earliest nuclei, and 5.3-29.0 kJ mol^{-1} (ΔT = 50-125 °C) for nucleation at maximum A_r. The results demonstrate potential for delayed nucleation and metastability that can generate spurious interpretations.

The timing of metamorphic events is also critical for understanding geologic history. In the Makhavinekh Lake Pluton aureole, Labrador, garnet resorption caused redistribution of Lu and loss of Hf from consumed rims, creating spuriously young ages. Garnet-ilmenite Lu-Hf geochronology using bulk separates yields apparent ages that young toward the contact from 1876 ± 21 Ma (4025 m) to 1396 ± 8 Ma (450 m). Toward the contact, garnet crystals are progressively more resorbed. Numerical modeling was used to test retention of Lu and loss of Hf during resorption as the dominant control on age. More resorption and Lu retention produce younger apparent ages (false ages). Application of the model to the aureole yields model ages from 1850 Ma to 1374 Ma, younging toward the contact. Thus, Lu-Hf geochronology applied to resorbed garnets requires careful examination of Lu zoning.

TABLE OF CONTENTS

LIST OF TABLES

LIST OF FIGURES

INTRODUCTION

Metamorphic rocks can provide valuable information about the pressure, temperature, and chemical conditions deep in the Earth's crust, as well as the timing of those conditions. Despite great progress in our ability to extract information used to reconstruct geologic history from metamorphic rocks, the complexities of metamorphism continue to hinder our ability to recognize and interpret the precise conditions and timing of metamorphic events. Therefore, studies of metamorphism remain vulnerable to flawed interpretations. This research investigates previously unaddressed complexities and corresponding sources of potential errors of interpretation in both petrological and geochronological applications. Part A explores the kinetics of nucleation and intergranular diffusion and their effects on departures from chemical equilibrium during crystallization. Part B examines the intricacies of interpreting Lu-Hf ages based on their behavior in partially resorbed garnet crystals. Separate introductions are given for parts A and B.

PART A: CRYSTALLIZATION KINETICS AND DEPARTURES FROM EQUILIBRIUM

CHAPTER 1: INTRODUCTION

SIGNIFICANCE

Universally employed methods for examining metamorphic processes include pressure-temperature-time (*P-T-t*) path construction, geothermobarometry, and pseudo-section analysis, all of which are based on the assumption of chemical equilibrium. This assumption is customarily predicated on the long timescales of crystallization during regional metamorphism, but evidence of disequilibrium crystallization in these settings invalidates that assumption (Chernoff & Carlson, 1997, 1999; O'Brien, 1999; Hirsch *et al.*, 2003; Meth & Carlson, 2005; Wilbur & Ague, 2006; Hetenyi *et al.*, 2007; Padron-Navarta *et al.*, 2008). Disequilibrium crystallization can produce metastable mineral assemblages and unreasonable *P-T* estimates leading to erroneous reconstructions of geologic histories (Pattison *et al.*, in press). However, the magnitude of disequilibrium during crystallization of regionally metamorphosed rocks has rarely been quantified (Hetenyi *et al.*, 2007; Padron-Navarta *et al.*, 2008), and thus the extent of its impact on equilibrium-based methods of analysis remains unclear. Evidence of disequilibrium can be cryptic, but the locations and sizes of porphyroblastic crystals can be used to identify the presence of disequilibrium and further reveal the rates and processes that produced the disequilibrium conditions.

DIFFUSION-CONTROLLED NUCLEATION AND GROWTH OF PORPHYROBLASTS

Several processes must occur to grow a porphyroblast: dissolution of reactant phases, nucleation of product phases, nutrient transport between reactants and products, and addition of the nutrients to the growing product crystals (Kretz, 1966; Walther & Wood, 1984; Carlson, 1989). Dissolution of reactant phases increases the concentrations of components in the intergranular fluid. Upon nucleation of product crystals, the components are consumed at the nucleation sites, and concentration gradients are established between the nucleation sites and the surrounding reactant phases. Differences in concentration result in differences in chemical potentials that are the driving forces for transport of components to the growing crystal. The transport rate may be slower or faster than the rate of attachment to the crystal surface, resulting in dominance of either diffusion-controlled nucleation and growth (DCNG) or interface-controlled nucleation and growth, respectively.

Under diffusion-controlled conditions, concentration gradients around a product crystal extend into the surrounding matrix, and for components incorporated into the growing crystal, chemical potentials near the crystal are decreased. The sum over all components of the chemical-potential differences between the reactant and the product crystals defines the Gibbs free energy change of the reaction ($\Delta_r G$), and reaction affinity (A_r) is defined as the negative of $\Delta_r G$. Therefore, lower concentrations of components decrease the reaction affinity near the product crystal (Fig. 1-1a).

Nucleation kinetics depend strongly on reaction affinity, and as a result the reduction in reaction affinity around a growing crystal decreases the nucleation probability near it. This creates a tendency toward spatial ordering of crystal centers in homogeneous portions of a rock, because new crystals have a lower probability of nucleating next to existing crystals and a higher probability of nucleating in isolation. In contrast, if crystallization is dominated by interface-controlled nucleation and growth (Fig. 1-1b), new crystals have an equal probability of nucleating next to or far from existing crystals, so the distribution of crystals is more nearly random.

In addition to spatial ordering of crystals, DCNG creates competition between crystals, in which nutrient-depletion zones impinge (Fig. 1-2), resulting in a tendency toward smaller sizes for neighboring porphyroblasts and larger sizes for those that grow in isolation. Porphyroblastic textures in metamorphic rocks commonly show a statistically ordered (non-random) spatial disposition of crystals and crystal sizes, which is interpreted as a result of suppressed nucleation and growth near existing porphyroblasts due to sluggish intergranular diffusion of Al (Carlson, 1989). The relative rates of nucleation and diffusion are fundamental to controlling the distribution and size of crystals

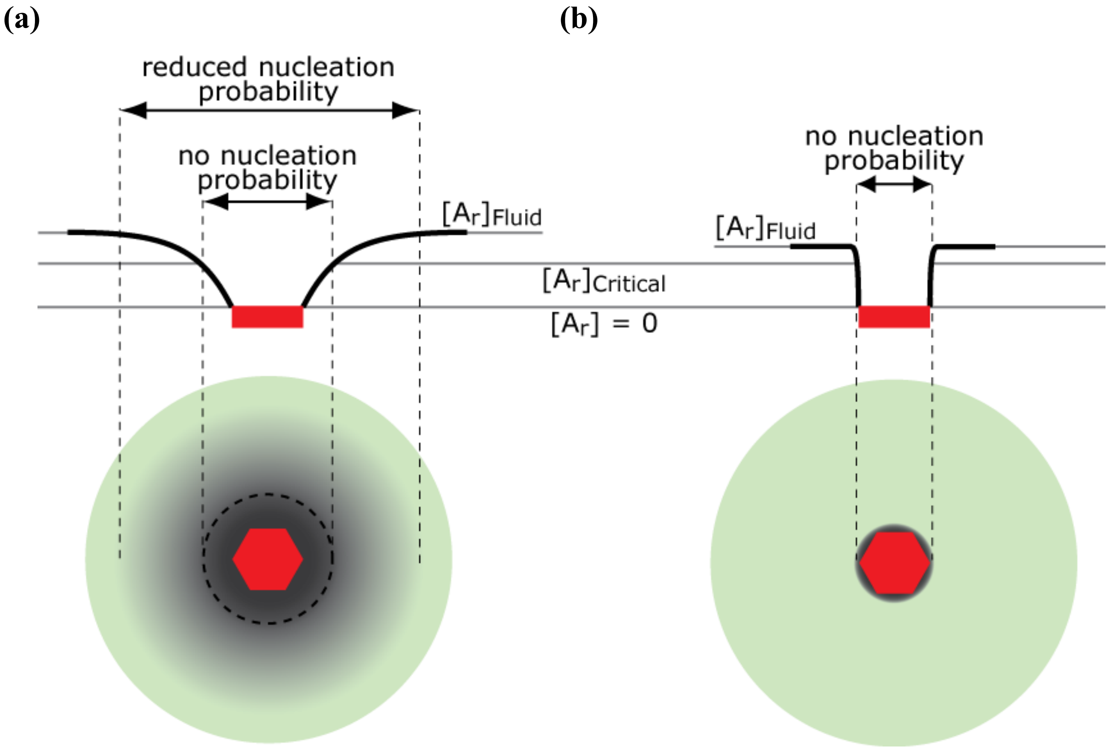

Figure 1-1. Schematic diagram of reduction in reaction affinity due to nutrient depletion around growing porphyroblasts. The upper part of the figure shows the magnitudes of reaction affinity (A_r) for the drawings of porphyroblasts (red hexagons) surrounded by reactants (green) in the lower part of the figure. (a) In diffusion-controlled nucleation and growth, a zone of reduced A_r hinders nucleation near growing porphyroblasts and produces an ordered porphyroblastic texture, in which porphyroblast locations depart from randomness. Below a critical value of A_r, nucleation is not possible. (b) In conditions of high diffusive flux, A_r is not reduced appreciably by growing porphyroblasts, allowing nucleation close to existing crystals, so that the porphyroblast locations approach randomness. After Hirsch et al. (2000).

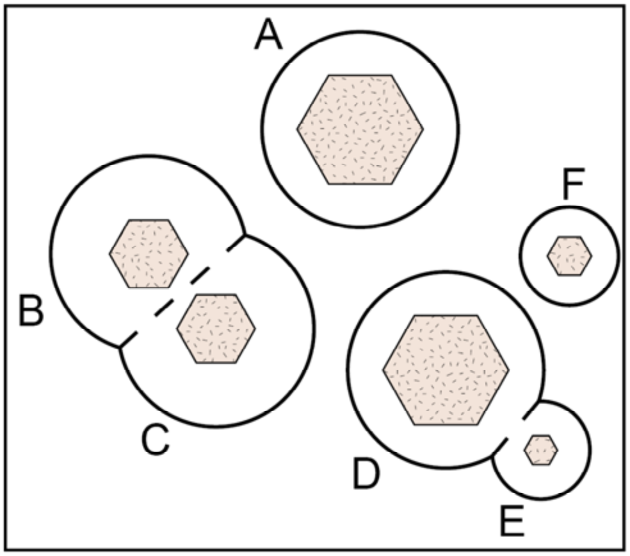

Figure 1-2. Schematic illustration of nutrient competition between crystals under DCNG. The hexagons are garnet crystals in a uniform matrix and their nutrient depletion zones are shown by the black circles. Crystals A, B, and C nucleated at the same time; however, crystals B and C grew less due to competition for nutrients (illustrated by impinging nutrient depletion zones). Crystal A grew in isolation and achieved a larger size. Crystals E and F nucleated later. Crystal E had a small effect on the growth of crystal D, although its own growth was appreciably reduced; crystal F is larger than crystal E because it grew in isolation. From Hirsch et al. (2000).

in metamorphic rocks, and by modeling these textures, key parameters that govern nucleation rates and intergranular diffusivity can be determined (Kretz, 1973; Carlson, 1989). In addition, the magnitude of disequilibrium can be measured from simulated concentration gradients and expressed in terms of the reaction affinity.

DEPARTURES FROM EQUILIBRIUM

The importance of determining kinetic parameters is in better characterizing metamorphic processes and estimating the scales of reaction affinity. Barriers to nucleation and slow rates of diffusion can prevent equilibrium from being established during crystallization (e.g., Waters & Lovegrove, 2002; Pattison & Tinkham, 2009), which can produce problematic mineral assemblages and compositions that lead to erroneous interpretations. In fact, crystallization can be delayed by energetic barriers to nucleation of the product crystals, as shown in an example from Waters and Lovegrove (2002) in a contact metamorphic setting. In the aureole of the Bushveld Complex, textural relationships indicate the reaction sequence but equilibrium calculations of the stable mineral assemblages along the prograde path indicate a very different sequence (Fig. 1-3). In Fig. 1-3a, for example, the first mineral assemblage to appear at the low temperature is Cld + Chl (+Ms). With increasing temperature, the assemblage becomes Cld + Chl + And. In contrast, Figure 1-3b shows that although the first mineral assemblage observed in the natural samples at low temperature is indeed Cld + Chl (+Ms), with increasing temperature, the next assemblage formed is Cld + Chl + St. This example suggests that andalusite nucleation was delayed due to large activation energy for nucleation. The appearance of several phases near the same temperature also suggests that some reactions may have been metastable. The mismatch between the equilibrium sequence and the observed sequence is a strong demonstration that equilibrium calculations can be misleading (and confusing) if mineral assemblages that grew under disequilibrium conditions are used to estimate *P*-*T* conditions. This example demonstrates the need to quantify the magnitudes of nucleation barriers. As described above, slow

(a) Equilibrium

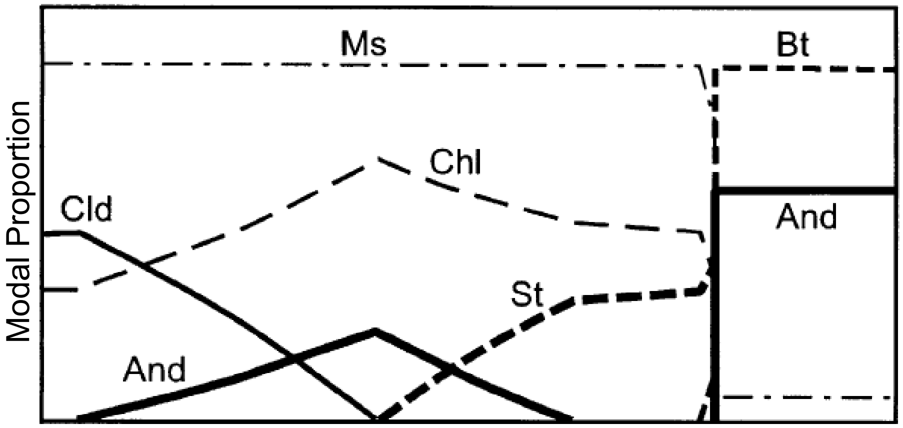

(b) Observed

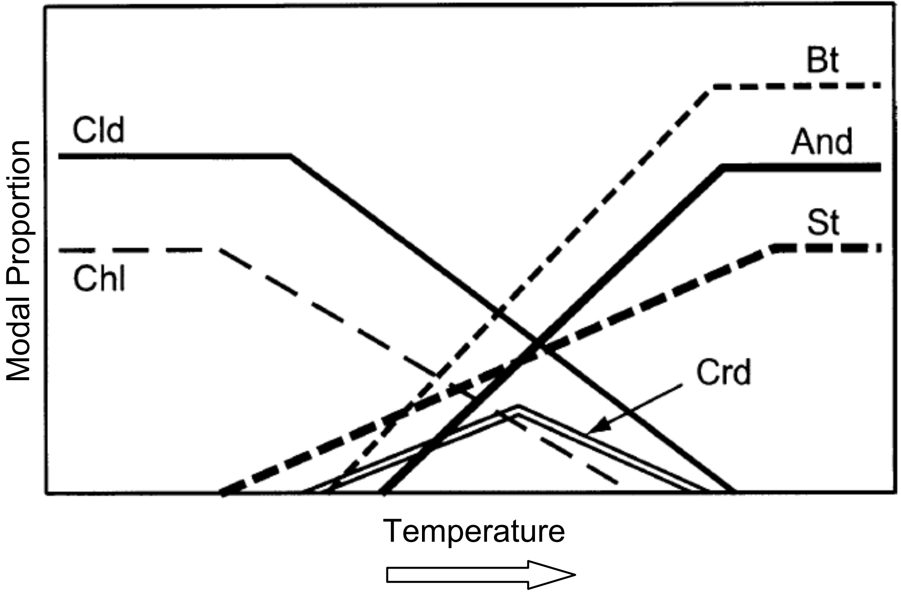

Figure 1-3. Example of departure from equilibrium. Disequilibrium is expressed in the appearance and disappearance of minerals along a metamorphic field gradient in the aureole of the Bushveld Complex (Waters & Lovegrove, 2002). (a) Relative modal abundance of each phase with increasing temperature as calculated from phase equilibria. (b) Actual modal abundance with increasing temperature as observed from textural relationships in the natural samples. And = andalusite, Bt = biotite, Chl = chlorite, Cld = chloritoid, Crd = cordierite, Ms = muscovite, St = staurolite. All assemblages include muscovite and quartz.

diffusivity can reduce chemical potential and decrease nucleation probability, and thus determinations of diffusion rates are also critical in understanding disequilibrium crystallization.

PREVIOUS DETERMINATIONS OF KINETIC PARAMETERS

Nucleation

Although experimental studies have attempted to determine nucleation rates in metamorphic rocks, the difficulty of properly replicating in the laboratory the mechanisms operating in nature have prevented useful determination of nucleation rates relevant to regional metamorphism (Carlson, 2011). Attempts to glean information on nucleation rates and processes directly from natural samples also face difficulties: the nucleation site is rarely preserved as the new mineral overgrows the site and the surrounding matrix. Therefore, nucleation rates have been estimated only from numerical models of crystallization (Carlson *et al.*, 1995; Hirsch & Carlson, 2006), but even these estimates are flawed.

In Carlson et al. (1995), limitations in computational power and the lack of determinations of the critical components of the classical nucleation theory required simplification of the expression for the nucleation rate. A form of the nucleation rate equation was employed in which the nucleation rate increased exponentially without limit and required unrealistically large activation energies for nucleation to reproduce the crystal-size distributions of natural samples. The resulting nucleation rates from models of diffusion-controlled nucleation and growth of garnet porphyroblasts range from 10^{-14} to 10^{-12} nuclei cm^{-3} s^{-1}. Although these values seem reasonable because they produce the correct number of crystals for the rock over reasonable crystallization duration, the large activation energies suggest that the formulation is flawed and the rates cannot be reliably used. The same model was used to simulate nucleation and growth of biotite porphyroblasts (Hirsch & Carlson, 2006), but the same conclusion, that the nucleation rates are not reliable, was drawn.

Diffusion

Diffusion of particles (atoms or molecules) in a solid or fluid phase occurs as random thermal motions that allow the particles to spread from high concentrations to low concentrations. The temperature dependence of the diffusion coefficient D that relates the material flux to the gradient in concentration is commonly expressed in terms of the Arrhenius relation as

$$D = D_\infty \exp\left(\frac{-Q_D}{RT}\right) \tag{1-1}$$

in which D_∞ is the diffusivity at the conceptual infinite temperature ($1/T = 0$), Q_D is the activation energy for diffusion, R is the universal gas constant, and T is absolute temperature. In metamorphic rocks, the fluid in which particles diffuse is located along interconnected pore spaces at the intersections of three-grain boundaries and, therefore, the paths of particles are restricted to the volume of the interconnected pore spaces (porosity ϕ) and conform to the geometry of the three-grain boundaries (tortuosity τ, commonly defined as L/L_a, in which the straight-line distance is L and the actual path length is L_a). Therefore, diffusivity in metamorphic rocks must be described by an effective diffusivity D_{eff}:

$$D_{eff} = D_\infty \exp\left(\frac{-Q_D}{RT}\right)\phi\tau\,. \tag{1-2}$$

The quantities ϕ and τ are dimensionless constants that range between 0 and 1 and effectively reduce diffusivity. The diffusive flux J of a particle through the intergranular fluid is given by Fick's First Law:

$$J = -D_{eff}\nabla c\,, \tag{1-3}$$

in which ∇c is the concentration gradient that drives diffusion and is variable throughout a reaction volume in diffusion-controlled conditions. To a first order, ∇c scales with the solubility of the component. To the extent that ϕ, τ, and solubility can describe the properties of the interconnected porosity and the amount of the component dissolved in it, the intrinsic properties of diffusion, D_∞ and Q_D, can be determined. Therefore, to determine D_∞ and Q_D for a reaction component, the properties unique to the rock must be isolated. Once this has been done, the diffusivity becomes D, which only depends on T, so D_∞ and Q_D can be determined from the Arrhenius relationship, commonly expressed on a plot of $\log_{10}(D)$ against inverse T (Shewmon, 1969), in which the slope of the line equates to ($-Q_D/R$) and the intercept is $\log_{10}(D_\infty)$. The diffusivities are best constrained at the temperatures of crystallization for each sample, so a characteristic temperature T_c is used to represent diffusivity over a range of temperatures and to determine Q_D: T_c is defined as the temperature at which the diffusivity over the duration of the event is equal to the integrated diffusivity at each temperature throughout the event:

$$D(T_c) = \int_0^t D[T(t)]dt, \tag{1-4}$$

(e.g., Carlson, 2006).

Only a limited number of studies have estimated intergranular diffusivity in metamorphic rocks. In an isotopic study that determined garnet growth rates and intergranular diffusion, Vance and O'Nions (1990) dated cores and rims of large (~12 mm diameter) garnet porphyroblasts by Sm-Nd geochronology (and Rb-Sr geochronology as a check) to determine growth rate and diffusivity. They used a derivation of growth rate in terms of garnet radius r per unit time t described by Nielsen (1959). Starting with Fick's First Law (Equation 1-3), multiplying through by the molar volume of garnet ($\bar{V}$), and recognizing that transport of elements to the growing garnet is subject to the porosity and tortuosity of the rock, the rate of radial crystal precipitation was expressed as:

$$\frac{dr}{dt} = D_{eff}\,\overline{V}\,\frac{dc}{dx}. \tag{1-5}$$

Using an estimate of the concentration gradient of Mg between the intergranular fluid and the garnet surface, Vance and O'Nions (1990) solved this expression and calculated Mg effective intergranular diffusion rates to be $10^{-17.4}$ to $10^{-16.2}$ $m^2 s^{-1}$ at 500 °C.

Carlson et al. (1995) determined D_∞ from D_{eff} by assigning a value to Q_D (84 $kJ \cdot mol^{-1}$) and numerically modeling DCNG of garnet porphyroblasts, comparing the simulated textures to those of the natural samples determined from high-resolution X-ray computed tomography (HRXCT). Their model treated diffusion of Al as a simple problem of determining the characteristic length scale of diffusion integrated over time ($D_{T(t)}$) to estimate the radius (r_d) of the depleted volume surrounding a garnet porphyroblast:

$$r_d(t) = \left(\int_{t_0}^{t} D_{T(t)} dt \right)^{1/2}, \tag{1-6}$$

in which

$$D_{T(t)} = D_{\infty} \exp\left(\frac{-Q_D}{RT(t)} \right) \tag{1-7}$$

The diffusivity from their work ($D_{T(t)}$) incorporates the composite effects of porosity, tortuosity, and Al solubility on diffusion of Al to the porphyroblast, so it is an effective diffusivity that includes the influence of solubility and here it is referred to as the composite diffusivity D_{com}. The diffusivities from their work range from $10^{-19.5}$ to $10^{-18.6}$ m^2 s^{-1} at 600 °C.

One of the goals of the current study is to determine the intrinsic properties of intergranular diffusivity in metamorphic rocks. Toward that goal, this work seeks to separate ϕ, τ, and Al solubility from other factors in an attempt to estimate D_{∞} and Q_D through a numerical-modeling approach.

NUMERICAL MODELING OF PORPHYROBLAST CRYSTALLIZATION

This research quantifies the scales of disequilibrium and the kinetics of metamorphic processes in regionally metamorphosed rocks by numerical modeling of porphyroblast crystallization. The numerical models are created by CRYSTALLIZE3D, a program that simulates DCNG by calculating intergranular diffusive fluxes of a rate-limiting component (RLC) from a reactant assemblage (e.g., chlorite + quartz) through the intergranular fluid to the growing product assemblage (e.g., garnet) (Ketcham & Carlson, in review). Natural textures can be compared with simulations to elucidate the mechanisms controlling such crystallization, and this is done using crystal sizes and locations within natural samples determined by HRXCT (Carlson & Denison, 1992;

Denison *et al.*, 1997; Ketcham, 2005a; Ketcham *et al.*, 2005) and extracted by specialized processing software (BLOB3D) (Ketcham, 2005a). In this research, CRYSTALLIZE3D is applied to porphyroblastic textural datasets derived from a broad sample suite to extract values of kinetic parameters and reaction affinity.

CHAPTER 2: CRYSTALLIZE3D

ABSTRACT

Numerical simulations of diffusion-controlled nucleation and growth can be used to determine nucleation kinetics and the intrinsic properties of intergranular diffusion when compared with natural samples. From these determinations, the magnitudes of disequilibrium (values of reaction affinity) can be quantified. The program CRYSTALLIZE3D simulates diffusion-controlled nucleation and growth of porphyroblasts by modeling the diffusive fluxes of a rate-limiting component (RLC) between reactants and products in a 3-D volume. The program tracks concentrations of the RLC and calculates nucleation probabilities following classical nucleation theory, and growth rates of porphyroblasts based on the flux of the RLC. Nucleation rates are controlled by adjusting a parameter for the maximum steady-state nucleation rate, and a parameter for nucleation acceleration that incorporates the effects of interfacial energy on atomic-cluster formation. Diffusive fluxes are controlled by adjusting parameters for intergranular diffusivity, activation energy of intergranular diffusion, and solubility of the RLC. The resulting porphyroblastic textures tend to be ordered in crystal locations and sizes, reflecting the effects of diffusion-controlled nucleation and growth. To the extent that external constraints, like intergranular porosity and Al solubility, can be precisely specified, modeled crystallization kinetics can be used to determine nucleation rates, intergranular diffusivity, and the departures from equilibrium in the natural samples.

INTRODUCTION

Abundant information on geologic history is recorded in regionally metamorphosed rocks, and interpretation of that information has relied heavily on equilibrium-based methods of analysis. However, the ability to make reliable interpretations depends on our understanding of the departures from equilibrium that characterize most regionally metamorphosed rocks (Carlson, 1989). The consistency with which the metamorphic facies concept applies to regionally metamorphic rocks has been thought to imply that departures from equilibrium might be a secondary effect (Pattison *et al.*, in press), but as long as the magnitudes of disequilibrium remain unknown, their effects cannot be fully assessed. A complete understanding of disequilibrium includes estimates of the rates of nucleation and intergranular diffusion that can cause departures from equilibrium.

Slow diffusive fluxes can lead to reduced nucleation and growth rates of porphyroblastic crystals, producing disequilibrium crystallization manifested in delayed nucleation and metastable mineral growth. Therefore, porphyroblastic textures that result from diffusion-controlled nucleation and growth (DCNG) and that demonstrate ordering of crystal locations and sizes can be measured in natural samples and simulated through numerical models to understand scales of disequilibrium. To the extent that numerical models capture the essential characteristics of DCNG, the kinetics of crystallization and the departures from equilibrium can be determined. As context for understanding the methods and limitations of the application of the model used in this study, this chapter describes the previous models that lead to the current generation, CRYSTALLIZE3D.

PREVIOUS MODELS

Early studies of the spatial dispositions and sizes of porphyroblasts in metamorphic rocks reached the conclusion that random nucleation occurred in the samples studied (Kretz, 1966, 1969), implying that interface control was the dominant influence on porphyroblast microstructures in those samples. However, in that work, too few garnets were measured (24 in one sample and 107 in another) to permit statistically significant conclusions to be drawn from the simple statistical tests, as shown by Denison et al. (1997), who conducted a sensitivity analysis on the effects of the number of crystals used in the statistical tests and concluded that roughly 1000 crystals must be included for accurate results using the techniques in use at that time. Carlson (1989), in a study of 11 regionally metamorphosed rocks with several hundred measured garnets in most samples, used the same tests plus an additional, more sophisticated test that examines the degree of impingement of nutrient depletion zones of neighboring porphyroblasts that tends to reduce the randomness of crystal nucleation sites; that work showed that the crystal dispositions were spatially ordered. From these results he inferred that diffusion control is most commonly the principal constraint on the sizes and dispositions of porphyroblasts in metamorphic rocks. Carlson (1989) then applied a 2-D DCNG model (CRYSTALLIZE) to the same samples and produced simulations whose textures corroborated the inference that DCNG operated in the natural samples.

The first generation of CRYSTALLIZE (Carlson, 1989) was an empirical model of DCNG , intended to compare a modeled texture with the texture of a natural sample. The model simulated growth of garnet porphyroblasts using an exponentially increasing nucleation rate with nucleation probabilities approximated by step functions that extended from the nucleation site to a radius determined by the diffusional length scale. It used a diffusion-limited radial growth rate for all garnets that was dependent on the time since nucleation. With these approximations of nucleation probability and growth rate, the model greatly simplified the effects of reduced nucleation probability on the disposition of crystal centers and also ignored the effects of nutrient competition on growth rate.

Subsequently, Carlson (1991) added volume elements (voxels) to the 2-D model, which added thickness and the ability to track the volume of the diffusional domain surrounding a porphyroblast and assign that volume to the crystal. Although the calculations remained 2-D, as a garnet grew, the diffusional domain of each crystal was limited by the number of voxels encountered during growth, explicitly accounting for nutrient competition between neighboring porphyroblasts, and making it possible to examine the correlations between size and isolation of neighboring crystals. The nucleation probability remained a step function, approximating ordering of crystal centers.

These previous models created simulations in 2-D space and used dimensionless time, but the next generation (Carlson *et al.*, 1995) expanded to truly 3-D space, due to the availability of 3-D datasets generated from high-resolution X-ray computed tomography (HRXCT). The model used more realistic thermally-accelerated intergranular diffusion and incorporated time explicitly, allowing input of absolute rates and temperatures for crystallization. The importance of explicit time was in the ability to test modeled textures against external constraints, such as field relations, thermochronology, and thermobarometry. This generation of the model included a term in the nucleation rate law that specified a spatial variation of potential nucleation sites to examine clustering and the effects of layering in natural samples.

The model, however, remained limited in several ways: it used constant heating rates, a step function to approximate nucleation probability surrounding porphyroblasts, an approximation to diffusive transport that corresponded to a fixed and uniform concentration gradient, and it allowed only homogeneous initial reactant distributions. In addition, as discussed by Hirsch and Carlson (2006, p. 775), the formulation of the nucleation rate law allowed the nucleation rate to increase exponentially without limit, and tended to produce a large number of nuclei at high temperature; this required a very large range of activation energies for nucleation (including values that were unrealistically large) to fit the crystal-size distributions of the natural samples.

CURRENT MODEL: CRYSTALLIZE3D

In this research, CRYSTALLIZE3D is applied to a variety of porphyroblastic textural datasets to extract kinetic parameters and reaction affinity. As necessary background to the modeling, the program is briefly described in this chapter following the more detailed description in Ketcham and Carlson (in review). The theoretical formulation and program implementation is the work of Ketcham and Carlson, whereas the application of the model is the work of this study, primarily described in Chapters 3-5.

CRYSTALLIZE3D is more firmly grounded in the physical processes that control nucleation and growth than were its predecessors. Instead of using spatially averaged values for the intergranular medium, individual calculations are made of reactant dissolution, fluid concentration, nucleation probability, diffusional fluxes, and product growth for each volume element (voxel) in the simulation. This also provides a means for specifying a variety of reactant distributions (e.g., layers, ellipsoids, and blocks) that mimic reactant-poor and reactant-rich layers that may be present in natural protoliths.

A time-temperature-(-$\Delta_r G$) path is specified to accommodate any *P*-*T*-*t* path and model reaction. Local equilibrium is now maintained between the rate-limiting component (RLC) in the intergranular fluid and either the reactant assemblage or the product assemblage in contact with it. This allows the concentration of the RLC to be buffered to high concentrations where reactants are present and depleted to low concentrations where products have formed, creating concentration gradients that drive diffusive fluxes and produce lower nucleation probability near existing crystals. Nucleation rates now vary in space and time according to temperature (*T*) and the RLC concentration of each voxel. This generation of the model simulates diffusive flux more comprehensively by incorporating the porosity (volume) and tortuosity (geometry) of the intergranular medium and the solubility of the RLC in the intergranular fluid.

Reaction affinity

The principal features of the model are demonstrated in Figure 2-1, using a simple reaction in which chlorite is the principal reactant, garnet is the product, and Al is the RLC. As temperature rises, the free-energy change of the reaction increases and the reactants are progressively dissolved. The concentration of the RLC rises in the intergranular fluid, which increases the reaction affinity. Nucleation occurs in portions of the model with high reaction affinity and the concentration of the RLC is depleted near the growing crystals. The resulting gradients in concentration between reactant and product assemblages drive diffusion of the RLC toward product crystals. Concentration gradients determine the rate of intergranular diffusion and the scale of the local reaction affinity, which in turn governs the rate of nucleation.

The model can simulate any reaction, but for the following description, the simple reaction in Figure 2-1 will be used to illustrate the pertinent aspects of crystallization. In this reaction, Fe-Al chlorite is the Al-bearing reactant and garnet is the Al-bearing product:

$$2\,(\mathrm{Fe}_{4.5}\mathrm{Al}_{1.5})(\mathrm{Al}_{1.5}\mathrm{Si}_{2.5})\mathrm{O}_{10}(\mathrm{OH})_8 + 4\,\mathrm{SiO}_2 \leftrightarrow 3\,\mathrm{Fe}_3\mathrm{Al}_2\mathrm{Si}_3\mathrm{O}_{12} + 8\,\mathrm{H}_2\mathrm{O} \qquad (2\text{-}1)$$

chlorite + quartz = garnet + fluid

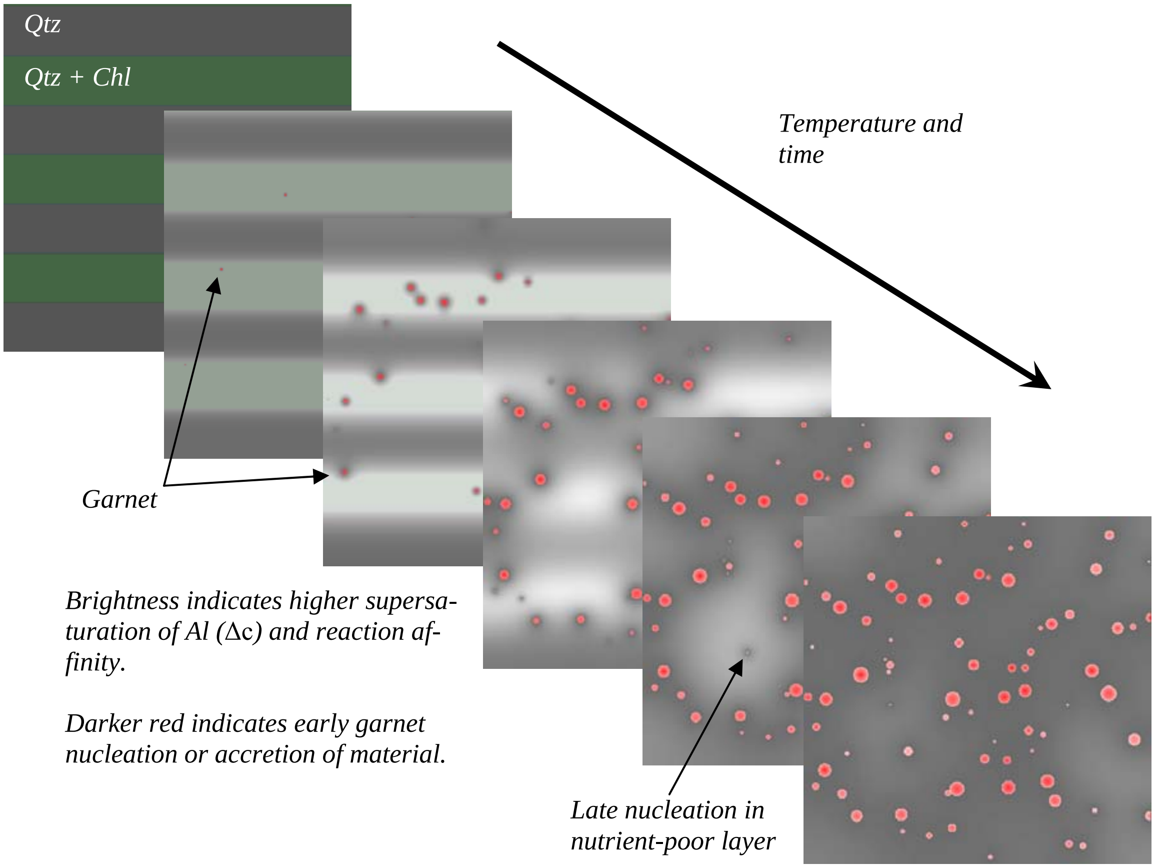

Figure 2-1. Illustration of modeled nucleation and crystal growth through time and temperature using CRYSTALLIZE3D. The upper left image shows the layered model before nucleation where chlorite + quartz is indicated by the green-shaded layers and quartz is indicated by the dark gray layers. Brightness indicates the degree of Al supersaturation in the intergranular fluid (Δc), which increases with increasing T and solubility of reactants; green tint shows regions in which reactants persist; red color in porphyroblasts indicates time of accretion of material. The second image shows the increase in Δc and the first nuclei (red dots) and the remaining images show the model stepping through time. The crystals deplete the intergranular medium of nutrients, creating depletion halos. As diffusive flux increases with increasing T, nutrients can diffuse into the nutrient-poor layers, allowing late nucleation to occur there. The largest crystals are generally isolated and found along the nutrient-rich layers.

The sum of the differences in chemical potentials of the components ($\Delta\mu_i$) between reactants and products describes the Gibbs free energy change for reaction ($\Delta_r G$). In the case of the reaction above, the sum is given by

$$\Delta_r G = \Delta\mu_{Si} + \Delta\mu_{Al} + \Delta\mu_{Fe} + \Delta\mu_{H_2O} . \tag{2-2}$$

Garnet crystallization in metapelitic rocks commonly occurs with (1) Si and Fe in chemical equilibrium ($\Delta\mu_{Si} = \Delta\mu_{Fe} = 0$), because Si is normally abundant in metapelitic rocks due to the presence of quartz and other silicate phases that are soluble at the temperatures and pressures of garnet crystallization, and because the intergranular diffusivity of Fe is relatively fast compared with the other components (Carlson, 2002); (2) the intergranular medium saturated with hydrous fluid ($\Delta\mu_{H_2O} = 0$) from the breakdown of hydrous minerals with increasing temperature; and (3) relatively slow Al intergranular diffusivity, which is attributed to its high charge and low solubility. In the case of large Si and Fe diffusive fluxes and smaller Al diffusive fluxes, gradients between reactants and products will be established ($\Delta\mu_{Al} \neq 0$). Following Equation 2-2, $\Delta_r G$ is dependent only on $\Delta\mu_{Al}$, and garnet crystallizes under partial chemical disequilibrium, limited by the rate of Al transport. Therefore, determinations of Al concentration gradients during crystallization provide a method for estimating the reaction affinity during crystallization.

The model calculates the supersaturation of Al from the garnet-forming reaction at all points in space and time in the intergranular fluid, and because Al is the RLC, the expression for $\Delta_r G$ (Equation 2-2) reduces to the difference in the chemical potential of Al in the fluid in equilibrium with products ($\mu_{Al}^{Fl_{Grt}}$) and the chemical potential of Al in the fluid in equilibrium with reactants ($\mu_{Al}^{Fl_{Chl}}$):

$$\Delta_r G = \Delta\mu_{Al} = \mu_{Al}^{Fl_{Grt}} - \mu_{Al}^{Fl_{Chl}} \tag{2-3}$$

where

$$\begin{aligned} \mu_{Al}^{Fl_{Grt}} &= \mu_{Al}^{\circ} + RT \ln c_{Al}^{Fl_{Grt}} \\ \mu_{Al}^{Fl_{Chl}} &= \mu_{Al}^{\circ} + RT \ln c_{Al}^{Fl_{Chl}} \end{aligned} \tag{2-4}$$

and $\mu^{\circ}_{\mathrm{Al}}$ is the chemical potential for Al at a reference state (*P*-*T* of equilibrium), *R* is the ideal gas constant, *T* is absolute temperature, and *c* is concentration of Al in the fluid in equilibrium with chlorite (Chl) or garnet (Grt). Substitution and cancellation of like terms yields the expression:

$$\Delta_{\mathrm{r}}\mathrm{G} = \mathrm{RT}\ln\left(\frac{\mathrm{c}_{\mathrm{Al}}^{\mathrm{Fl}_{\mathrm{Grt}}}}{\mathrm{c}_{\mathrm{Al}}^{\mathrm{Fl}_{\mathrm{Chl}}}}\right). \tag{2-5}$$

Therefore the ratio in concentration between products $\left(c_{\mathrm{Al}}^{\mathrm{Fl}_{\mathrm{Grt}}}\right)$ and reactants $\left(c_{\mathrm{Al}}^{\mathrm{Fl}_{\mathrm{Chl}}}\right)$ is the physical manifestation of $\Delta_{\mathrm{r}}G$. Thus the reaction affinity (equivalently, $-\Delta_{\mathrm{r}}G$), can be quantified from modeled porphyroblastic textures in regionally metamorphosed rocks as a function of time and space during a reaction.

Nucleation

The nucleation rate is based on classical nucleation theory, which balances the energetics of interface-creation versus phase transformation. The following description follows Porter and Easterling (1992). Homogeneous nucleation occurs when the atoms (or molecules) in a supersaturated fluid precipitate to form a solid cluster, treated for the moment as spherical with radius *r* (Fig. 2-2a). The free energy change of the transformation of components dissolved in the fluid into a cluster can be expressed by

$$\Delta \mathrm{G} = \frac{4}{3}\pi \mathrm{r}^3 \Delta \mathrm{G}_{\mathrm{V}} + 4\pi \mathrm{r}^2\gamma, \tag{2-6}$$

in which the first term accounts for the difference in Gibbs free energy per unit volume of the fluid and the solid cluster of the same volume and composition (ΔG_{V}), and the second term accounts for the interfacial energy (γ) per unit area between the surface of the cluster and the fluid. The interfacial free energy is approximately the excess free energy not used in bonding the atoms along the boundary between the two phases, due to misfit between atoms in adjacent phases, plus the energy associated with the interfacial entropy (excess atomic vibrations due to fewer bonds). Figure 2-3 illustrates ΔG as a function of *r* (Equation 2-6). To exceed the activation energy for nucleation (ΔG^*), the volume of the cluster must be large relative to the surface area between the cluster

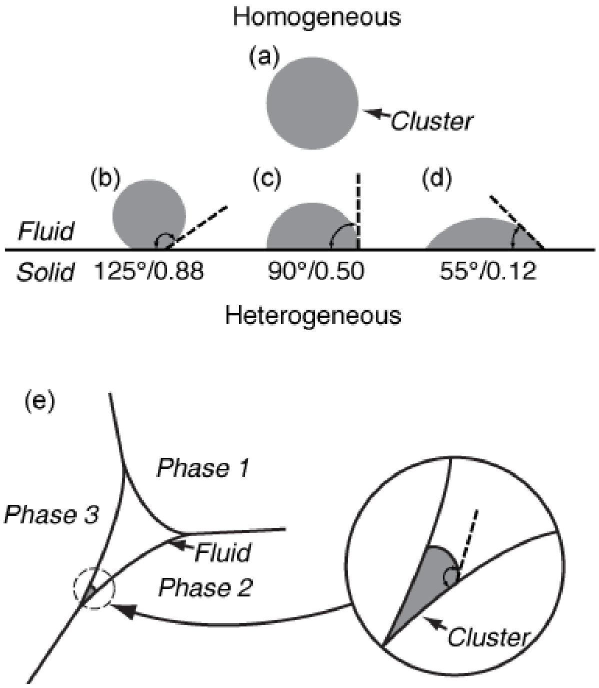

Figure 2-2. Examples of homogeneous and heterogeneous nucleation. Gray shading indicates a cluster of atoms or molecules. (a) Homogeneous nucleation involves only two phases, here a solid cluster within a fluid. (b-d) Heterogeneous nucleation involves a third phase and generally occurs when a cluster of atoms precipitates onto a solid substrate. The cluster in (c) is half of the volume of (a), and each of the clusters in (b-d) is equal in volume. Heterogeneous nucleation is energetically more favorable than homogeneous nucleation because the surface area of the cluster is reduced relative to its volume. The angles between the solid surface and the surface of the cluster θ are given below each example with their corresponding shape factors *s* (θ/s). (e) Nucleation in metamorphic rocks is likely to occur in three-grain junctions because the surface area between the cluster and the fluid is even smaller than on a flat surface. After Porter and Easterling (1992) and Shewman (1969).

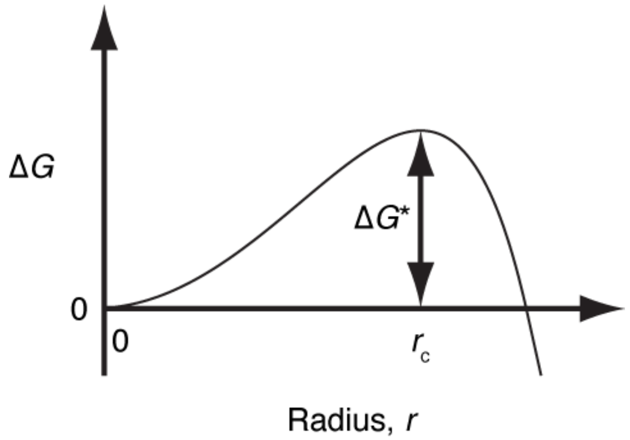

Figure 2-3. Schematic illustration of the free energy of cluster formation Δ*G* as a function of the cluster radius *r*. Δ*G** is the activation energy for nucleation and r_c is the critical radius that must be exceeded to overcome Δ*G** and grow into a crystal nucleus. After Porter and Easterling (1992).

and the fluid: if the cluster is supercritical, such that its radius exceeds a critical radius ($r > r_c$), the first term in Equation 2-6 will dominate and additional growth will produce a decrease in the free energy of the cluster so the cluster will grow into a crystal, but if the cluster is subcritical ($r < r_c$), dissolution of the atoms (or molecules) decreases the free energy of the cluster and the cluster will shrink.

A smaller surface area relative to volume can be accomplished by heterogeneous nucleation involving a third phase: a solid substrate on which the atomic cluster can precipitate. In Figure 2-2, examples of heterogeneous nucleation on a flat substrate are given in (b-d). The shape of the cluster varies with the sum of the interfacial energies of the three phases, and for clusters of the type shown (spherical caps), the effects of heterogeneous nucleation can be expressed by a shape factor *s* that is dependent on the wetting angle θ between the substrate and the cluster, which takes on values between 0 and 1:

$$s = \frac{1}{4}(2 + \cos\theta)(1 - \cos\theta)^2. \tag{2-7}$$

By incorporating *s* into Equation 2-6, an expression for ΔG for heterogeneous nucleation can be written:

$$\Delta G = \left(-\frac{4}{3}\pi r^3 \Delta G_V + 4\pi r^2 \gamma \right) s. \tag{2-8}$$

Nucleation in cracks and grain-boundary intersections may be even more energetically favorable because surface area between the cluster and the fluid can be reduced greatly (Fig. 2-2e).

Following classical nucleation theory (e.g., Shewmon, 1969; Porter & Easterling, 1992), nucleation rate can be expressed as

$$\frac{dN_V}{dt} = \nu C_N \exp\left(\frac{-s\gamma_{SF}^3}{k_B T (\Delta G_V)^2} \right) \tag{2-9}$$

in which N_V is the number of crystals nucleated per unit volume, ν is the frequency with which atoms or molecules are added to a cluster, C_N is the concentration of clusters, and the exponential term describes the fraction of the clusters that are of critical size (r_c).

Within the exponential, *s* describes the effect on the overall interfacial energies of the shape of a cluster (Equation 2-7), k_B is Boltzman's constant, *T* is absolute temperature, and

$$\Delta G_V = \frac{\Delta G}{\overline{V}_{\mathrm{Grt}}\, n_{\mathrm{Grt}}}. \tag{2-10}$$

ΔG is the difference in Gibbs free energy between a supersaturated fluid and a solid cluster within a saturated fluid, which has a maximum value of $\Delta_r G$ in portions of the model in which the RLC is buffered by reactants, $\bar{V}_{\mathrm{Grt}}$ is the molar volume of garnet, and n_{Grt} is the number of moles of garnet produced by the reaction. The model uses the concentration of the RLC to determine the reaction affinity along concentration gradients, but to calculate ΔG for each step in the model is computationally inefficient, so a conversion from ΔG to Δc is made using

$$(\Delta c)^n = k_0\,(\Delta G)^2 \tag{2-11}$$

in which k_0 and *n* are fitting constants, and k_0 has units of $(\mathrm{mol\ cm^{-3}})^n\ \mathrm{kJ^{-2}}$. Normalizing factors, T_{eq} and $\left(c_{\mathrm{Al}}^{\mathrm{FlGrt}}\right)^n$, are used to ensure that the exponent of the nucleation rate equation is dimensionless, and substituting all terms gives

$$\frac{dN_V}{dt} = \nu C_N \exp\left(-\frac{s\gamma^3 k_0 \overline{V}_P^2 n_P^2}{k_B T_{eq} (c_{\mathrm{Al}}^{\mathrm{Fl}_{\mathrm{Grt}}})^n} \frac{T_{eq}}{T} \frac{(c_{\mathrm{Al}}^{\mathrm{Fl}_{\mathrm{Grt}}})^n}{(\Delta c)^n} \right). \tag{2-12}$$

The equation is simplified by combining the constants into parameters k_1 and k_2 giving

$$\frac{dN_V}{dt} = k_1 \exp\left(-k_2 \frac{T_{eq}}{T} \frac{(c_{\mathrm{Al}}^{\mathrm{Fl}_{\mathrm{Grt}}})^n}{(\Delta c)^n} \right). \tag{2-13}$$

The units for the nucleation rate are nuclei $\mathrm{cm^{-3}\ s^{-1}}$. Adjustments to the parameters k_1 and k_2 are used to fit the simulated textures to the rock textures. The nucleation rate is weakly dependent on *T* but strongly dependent on the supersaturation of the diffusing element (Δc). With increasing *T*, Δc rises, increasing the probability of nucleation (Fig. 2-4). Upon nucleation, the concentration of Al surrounding the nucleus of the new crystal decreases to equilibrium with the product assemblage, and Al diffuses toward the

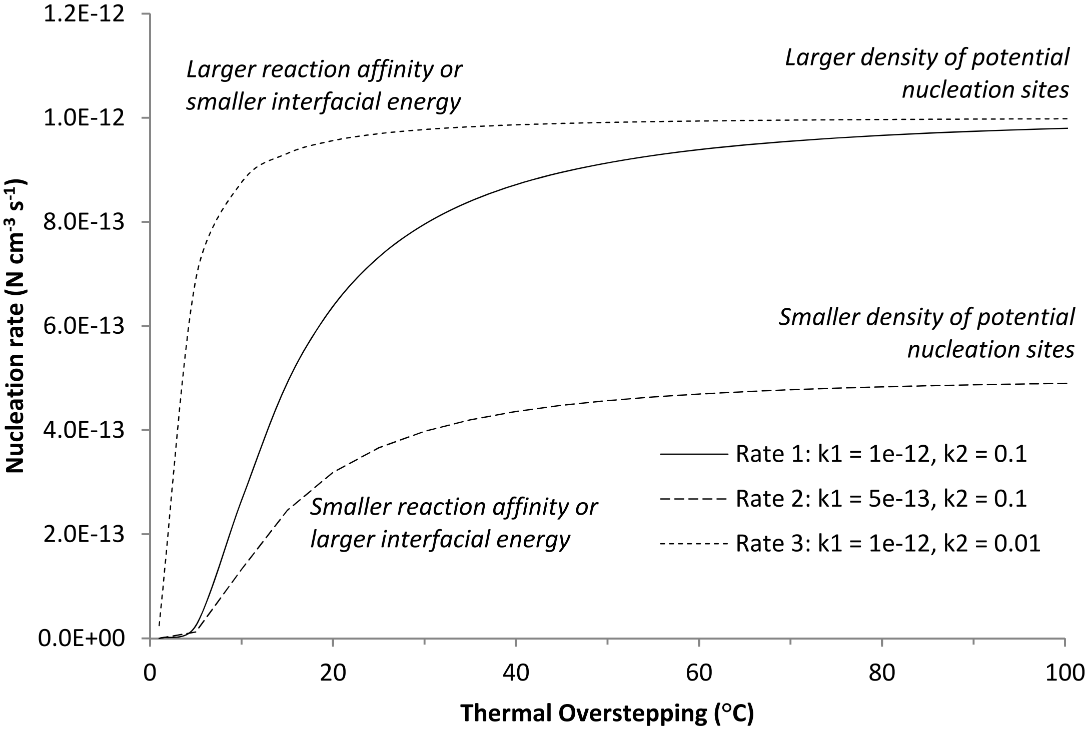

Figure 2-4. Nucleation rate in regions of maximum reaction affinity as a function of thermal overstepping of the equilibrium temperature of the reaction. The nucleation rate is primarily controlled by the factors k_1 and k_2, which are the steady-state nucleation rate and an acceleration factor. The steady-state rate is a function of the density of potential nucleation sites, and the acceleration factor is partly a function of the interfacial energy of the cluster of atoms that can potentially grow into a nucleus. As the nucleation rate rises with thermal overstepping, it approaches k_1 at a rate controlled by k_2.

growing crystal, reducing the probability for nucleation near the crystal (e.g., Figs. 1-1a & 1-2).

Diffusive flux

Dissolution of reactant phases raises the concentrations of the chemical components in the intergranular fluid within pore spaces near the reactants. The interconnected pore spaces along three-grain junctions are pathways that allow transport of the components through the rock at a rate described by the diffusivity *D* of the component and a magnitude dependent on the difference in concentration over a distance (d*c*/d*x*). The flux of a component in one dimension is therefore given by Fick's First Law:

$$J = -D\frac{dc}{dx} \tag{2-14}$$

In metamorphic rocks, the interconnected porosity ϕ describes the volume fraction of the interconnected pathways, which are not straight lines, so the diffusive length is scaled by tortuosity τ, which is commonly defined as L/L_a, in which the straight-line distance is L and the actual path length is L_a. Both ϕ and τ are factors that reduce the diffusive flux and have values between 0 and 1. Incorporating these factors into *J* gives a variant of Fick's First Law that governs the diffusive flux in a metamorphic rock:

$$J = -D\nabla c\ \phi\ \tau. \tag{2-15}$$

∇c is the concentration gradient in three dimensions surrounding a product crystal and extending into the matrix over a radial distance *r*.

$$\nabla c = \frac{\Delta c}{\Delta r} = \frac{c_{Al}^{Fl_{Grt}} - c_{Al}^{Fl_{Chl}}}{\Delta r} \tag{2-16}$$

Solving Equation 2-5 for $c_{Al}^{Fl_{Chl}}$ and substituting into Equation 2-16 yields the full expression for ∇c

$$\nabla c = \frac{c_{\mathrm{Al}}^{\mathrm{Fl_{Grt}}}\left[\exp\left(\frac{-\Delta_r G}{RT}\right) - 1\right]}{\Delta r}, \tag{2-17}$$

which demonstrates that the diffusive flux scales with the Al solubility $c_{\mathrm{Al}}^{\mathrm{Fl_{Grt}}}$. The diffusivity *D* is given by

$$D = D_{\infty} \exp\left(\frac{-Q_D}{RT}\right) \tag{2-18}$$

in which D_{∞} is the diffusivity in the direction of infinite thermal overstepping, and Q_D is the activation energy for intergranular diffusion. The diffusive flux can then be expressed as

$$J = D_{\infty} \exp\left(\frac{-Q_D}{RT}\right) \nabla c \; \phi \tau, \tag{2-19}$$

and by grouping the constants, D_{∞}, ϕ, and τ into a new constant k_3, *J* becomes

$$J = k_3 \exp\left(\frac{-Q_D}{RT}\right) \nabla c. \tag{2-20}$$

The diffusive flux in the model can be adjusted by changing the values of k_3, Q_D, and $c_{\mathrm{Al}}^{\mathrm{Fl_{Grt}}}$. As reactants dissolve, $c_{\mathrm{Al}}^{\mathrm{Fl_{Chl}}}$ rises and gradients between reactants and products are established, creating a dynamically changing reaction space with reactants and products separated by Al-free phases and the intergranular fluid, as described next.

Reaction space

For the samples in this study, the model is used to simulate the growth of garnet porphyroblasts and the RLC is Al. In order to describe reactions that may involve multiple product and reactant phases, the distribution of Al in the system is specified in terms of a composite aluminous reactant (CAR) and composite aluminous product

(CAP), which can be thought of as the respective bulk compositions of assemblages comprised of the reactant and product minerals taking part in the reaction. Figure 2-5 shows a 2-D illustration of the reaction space. Each simulation begins with voxels that contain reactants (Al-bearing and Al-absent phases, e.g., chlorite and quartz). As temperature and reaction affinity increase, reactants progressively dissolve and release Al into the intergranular fluid. Nucleation of porphyroblasts begins when the reaction affinity is large enough to exceed the activation energy for nucleation, and the new crystals act as sinks for Al that create zones of depletion and drive diffusion of Al toward the product assemblage (from interface *R* to interface *P*). When the aluminous reactants are completely consumed, the aluminous products take up whatever Al remains dissolved in the intergranular fluid, at rates still limited by the computed diffusive fluxes, and the reaction is complete. For reactions with multiple Al-bearing products (e.g., garnet and biotite), the proportion of the CAP volume that is garnet is allotted to a garnet crystal aligned with the center of the volume.

MODEL IMPLEMENTATION

The changes in reaction affinity that drive dissolution, nucleation, and intergranular diffusion can be used to simulate the textures of natural samples and quantify a variety of characteristics of DCNG. To do this, a variety of parameters need to be specified. Table 2-1 summarizes many of the parameters in this study and organizes them into four categories to distinguish those that are known, externally constrained, extracted from the simulations, and derived from the modeling results. The known parameters are those that are measured in the samples using HRXCT (e.g., crystal number density). The externally constrained parameters are estimated from calculations in this study or from the literature (e.g., garnet rim temperature). The parameters that are extracted from model fits are those that are determined from iteratively fitting each porphyroblastic texture (e.g., steady-state nucleation rate). The derived parameters are calculated from the modeling results (e.g., reaction affinity).

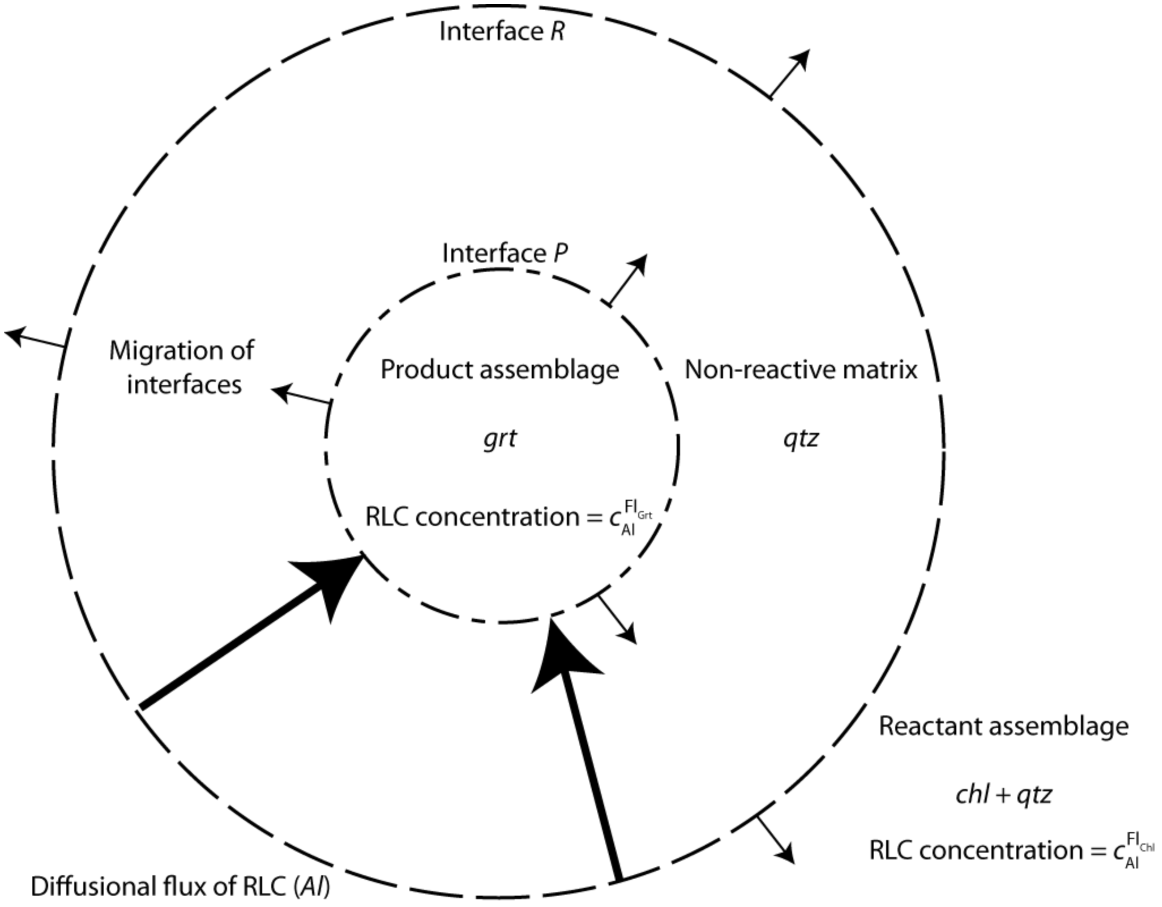

Figure 2-5. Two-dimensional illustration of the reaction space in the CRYSTALLIZE3D model. The reaction space is divided into three types of volumes, those with the reactant assemblage, those with the product assemblage, and those between that are depleted in RLC-bearing reactants but do not include RLC-bearing products. At interface *R*, the RLC in the intergranular fluid is in equilibrium with the reactant assemblage (e.g., Chl + Qtz) and at interface *P*, the RLC in the intergranular fluid is in equilibrium with the product assemblage (e.g., Grt). The concentration of RLC in the intergranular fluid decreases from *R* to *P* and defines diffusional gradients. Both interfaces migrate outward, away from the nucleation site. Modified from Ketcham and Carlson (in review).

Table 2-1. Model parameters.

Parameter	Symbol	Units
Known rock characteristics for comparison with simulations		
Number of crystals (nuclei)	N	(unitless)
Crystal number density		Crystals cm^{-3}
Mode		Volume %
Radius, minimum	r_{min}	cm
Radius, mean	r_{mean}	cm
Radius, maximum	r_{max}	cm
Externally constrained inputs		
Porosity	ϕ	(unitless)
Tortuosity	τ	(unitless)
Concentration of Al in the fluid in equilibrium with the product assemblage	$c_{\mathrm{Al}}^{\mathrm{Fl_{CAP}}}$	mol cm^{-3}
Equilibrium temperature of reaction (units are K for calculations)	T_{eq}	°C
Equilibrium pressure of reaction	P_{eq}	GPa
Garnet rim temperature (units are K for calculations)	T_{rim}	°C
Garnet rim pressure	P_{rim}	GPa
Gibbs free energy change of reaction (per mole of 12-oxygen garnet)	$\Delta_{\mathrm{r}}G$	kJ mol^{-1}
Extracted from best-fit simulations		
Steady-state nucleation rate	k_1	N cm^{-3} s^{-1}
Maximum nucleation rate	$(\mathrm{d}N/\mathrm{d}t)_{\mathrm{max}}$	N cm^{-3} s^{-1}
Nucleation acceleration	k_2	(unitless)
Diffusive flux constant	k_3	m^2 s^{-1}
Derived from extracted parameters		
Pre-exponential constant for intergranular diffusion of Al	D_{∞}	m^2 s^{-1}
Activation energy for intergranular diffusion of Al	Q_{D}	kJ mol^{-1}
Intergranular diffusion of Al	D	m^2 s^{-1}
Reaction affinity (per mole of 12 oxygen garnet)	A_{r}	kJ mol^{-1}

In addition, a model reaction is determined for each sample, and the change in free energy along the P-T path over time is specified as a t-T-Δ_rG path. The model calculates the amount of Al released from the dissolving reactants using the t-T-Δ_rG path as T rises above the T_{eq} of the reaction (thermal overstepping). Nucleation kinetics are adjusted by changing k_1 and k_2, and the diffusive flux of Al between the CAR and CAP through the intergranular fluid is adjusted by specifying values for k_3, Q_D, and $c_{Al}^{Fl_{CAP}}$.

The parameters for the model are either directly input or they are generated from constrained values described below and incorporated into other parameters that are directly input into the model. For example, the reaction affinity ($-\Delta_rG$) during crystallization is generated from a model reaction and P-T constraints from the natural sample, but the input for the model is in the form of t-T-Δ_rG triples, in which pressure is inherent to the value of Δ_rG. Table 2-2 is an example of a parameters file listing parameters that are directly input into the program.

Evaluation of porphyroblastic textures

The model is capable of reproducing a wide variety of porphyroblastic textures in natural samples that exhibit an ordered pattern in the size and degree of isolation of the crystals, reflecting DCNG conditions. These capabilities are discussed here.

Effects of nucleation rate and diffusive flux

To simulate porphyroblastic textures, the model parameters are adjusted until the simulated texture matches the natural specimen as closely as possible. Measurements used to judge the match will be described in more detail below. Adjustments to k_1 and k_2 change the steady-state nucleation rate and the rate at which the steady-state rate is approached, respectively (Fig. 2-4). Figure 2-6 illustrates some of the diverse textures and growth conditions that can be produced from the model. Panel (a) shows a typical porphyroblastic texture with a range of crystal sizes. In panel (b), an increased diffusive flux (resulting from a larger value of k_3) allowed the crystals to deplete the intergranular medium of Al more rapidly. With less Al available in the intergranular medium and shorter crystallization duration, there were fewer nucleation events and

Table 2-2. Example of model parameters used for simulations.

Model parameter	Value
Interconnected porosity ϕ (0-1):	3.00E+01*
Tortuosity τ (0-1):	1.0
Activation energy for diffusion Q_{D} (kJ/mol):	140
D_{∞} (cm^2/s):	5.00E-06*
Al concentration in fluid in equilibrium with CAP $c_{\mathrm{Al}}^{\mathrm{FlGrt}}$(moles/$cm^3$):	5.00E-07
Nucleation rate at infinite overstepping k_1 (nuclei/s/cm^3):	2.70E-12
Nucleation acceleration k_2 (dimensionless):	1.0
Al content of CAR (moles Al/moles CAR):	2.25
Molar mass of CAR (g CAR / mol CAR):	634.7072
Al content of CAP (moles Al/moles CAP):	2.25
Molar mass of CAP (g CAP / mol CAP):	625.7249
Density of CAP (g/cm^3):	4.07
Voxel edge length (cm):	0.012
Time step (yr):	200
Number of voxels in X:	115
Number of voxels in Y:	115
Number of voxels in Z:	115
CAR amount (g/cm^3 rock):	2.2
FD approximation source/sink parameter F (dimensionless):	200
Subvoxel growth acceleration factor (dimensionless):	2.8284
Volume fraction of porphyroblast in CAP assemblage (0-1):	0.7490
Number of moles of porphyroblast in reaction equation (mol):	1.0
Concentration to ΔG conversion power-law factor n:	1.4165
Equilibrium temperature used for ΔG-Δc conversion (°C):	528
Number of Time-Temp-$\Delta_r G$ triplets:	3
t-T-$\Delta_r G$ path (Myr after start, °C, kJ/mol):	(0.0,435.0,-0.0001) (10.0,535.0,-19.0582) (30.0,535.0,-20.1369)

*Porosity is enhanced to allow a lower value to be used for D_{∞} and maintain numerical stability with large time steps; see text.

k_3 is a value used for discussion and is not a direct input into the program. Instead, the individual components of k_3 are specified: ϕ, τ, and D_{∞}.

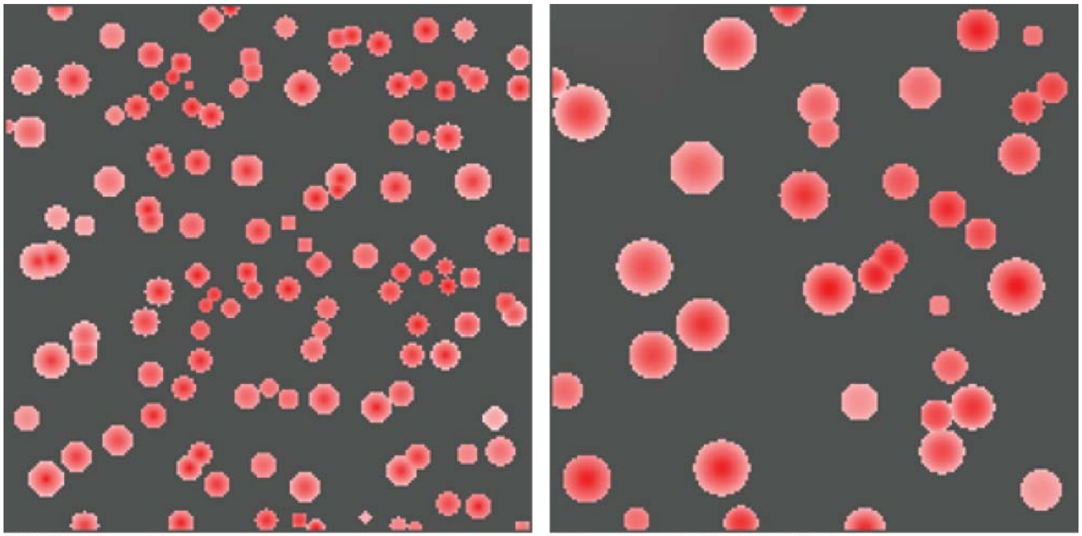

(a) "Benchmark"
T range = 448-554 ºC
Δt = 16.6 Myr

(b) Increased effective diffusion
T range = 448-486 ºC
Δt = 7.0 Myr

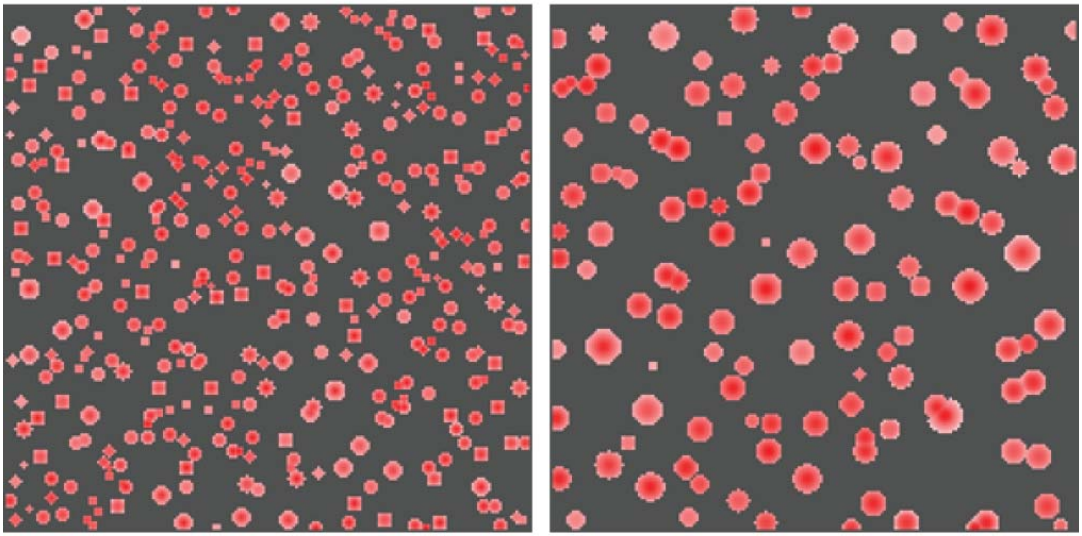

(c) Increased nucleation rate
T range = 446-537 ºC
Δt = 13.0 Myr

(d) Increased nucleation rate and effective diffusion
T range = 446-486 ºC
Δt = 6.2 Myr

Figure 2-6. Two-dimensional illustrations of the diversity of porphyroblastic textures that can be produced by Crystallize3D. The red shading indicates nucleation time and accretion of material, and the temperature range and duration of crystallization for each model are given below each texture. (a) A typical porphyroblastic texture. (b) With increased intergranular diffusivity of Al (by increasing k_3), fewer but larger crystals have grown and the duration of the event is shorter than in (a). (c) With increased nucleation rate (by increasing k_1), more numerous but smaller crystals have grown and the duration of the event is shorter than in (a). (d) Increases in both k_1 and k_3 have effects that combine to produce the same texture but over an even shorter duration. Independent constraints from thermal histories of natural samples help to produce both the texture of the sample and the durations of temperature and time that bracket nucleation rate and diffusive flux.

there was less time to nucleate crystals. The result is a shorter crystallization event and a crystal-size distribution (CSD) that has only relatively few large crystals. In panel (c), an increased nucleation rate (resulting from a larger value of k_1) allowed more crystals to nucleate early in the crystallization interval, and again, the crystallization duration is less than in the original model shown in panel (a). In panel (d), increases in both k_1 and k_3 have shortened the crystallization duration (as might be required to account for independent constraints on the thermal history of a rock) yet the texture is equivalent to that in panel (a). To be clear, however, the peak temperature of metamorphism is given by the rim temperature of garnet in all of the simulations in this study (from thermometry and phase equilibria), and all of the heating paths end with an isothermal segment, as would be expected near the end of a metamorphic event, so the duration of crystallization calculated for each of the current rocks is only a broad goal in the modeling and not a strict constraint on the duration of crystallization.

Criteria used to determine a statistically precise agreement between the modeled texture and the natural one include the crystal number density, the CSD, the degree of crystal center ordering, and the correlation between crystal size and isolation. The CSD is examined visually through histograms of the crystal radii (Fig. 2-7). The remaining two criteria are assessed using a Pair Correlation Function (PCF) and a Mark Correlation Function (MCF) (Hirsch *et al.*, 2000; Ketcham *et al.*, 2005), both of which are implemented in a program written to analyze natural and simulated porphyroblastic textures (Hirsch, 2011). The PCF tests for ordering of crystal centers by comparing the center-to-center distances of crystals to test for a departure from randomness (ordering of crystal centers). The MCF uses the same data but also incorporates crystal volume and evaluates the correlation between crystal volume and center-to-center distances to test for growth suppression due to competition between neighboring crystals. The correlation functions are applied to a 3-D porphyroblastic data set and the results are plotted with a null-hypothesis envelope derived from simulated crystal arrays of nearly random placement (Fig. 2-8). The mean nearest-neighbor distance between crystals is the scale at which DCNG influences crystallization perceptibly, so this test distance (±1σ)

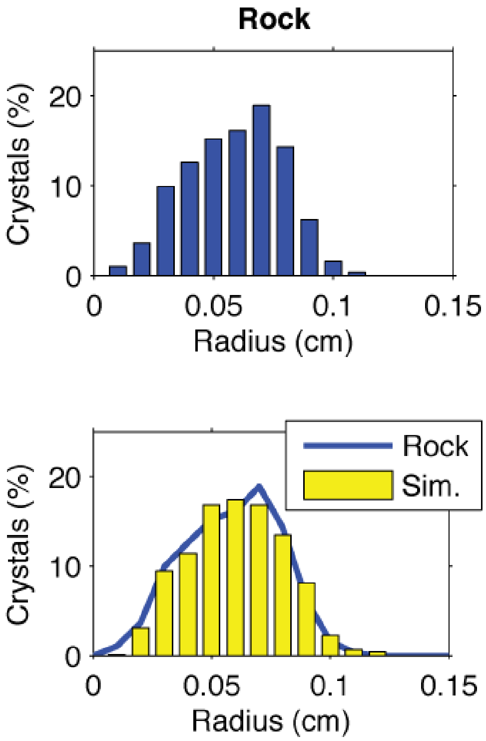

Figure 2-7. Comparison of crystal-size distributions for a rock and a simulation.

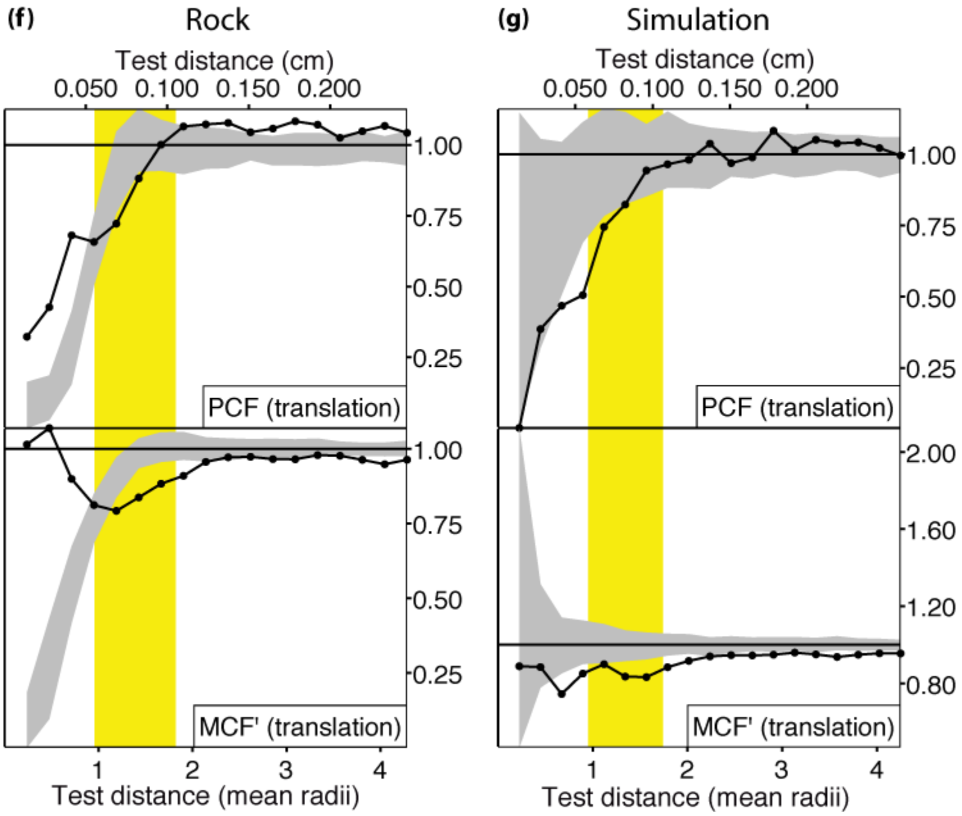

Figure 2-8. Example plots of the Pair-Correlation Function and the Mark-Correlation Function. The left column shows the analysis for a natural sample (PM1) and the right column shows the analysis of a simulation of PM1. The correlation values are given by the black points. The gray area shows a null-hypothesis envelope determined at 95% confidence for a population of crystals with the same characteristics of the rock or simulation (e.g., crystal number density, CSD, etc.) but are nearly randomly distributed. The vertical yellow bar is the mean nearest-neighbor distance between crystals (width is 2σ) that highlights the approximate length scale of diffusion. At values above the mean nearest-neighbor distance (outside the yellow bar), the effects of DCNG rapidly become insignificant. For the PCF, data that plot above the envelope indicate clustering, and those that plot below indicate ordering. For the MCF, data below the envelope indicate a correlation between crystal size and isolation as would result from growth suppression.

is highlighted in the plots. The null-hypothesis envelope is determined using a Monte Carlo method, in which one hundred crystal arrays are constructed that match the observed CSD but lack trends of ordering and clustering (nearly random placement of crystals). The most extreme 5% of these values are discarded to produce a 95% confidence envelope. For the PCF, values that plot above the envelope indicate clustering and values that plot below indicate ordering at the length scale indicated by the test distance. For the MCF, values that lie below the envelope suggest that there is a correlation between crystal size and isolation and thus nutrient competition between crystals at the test distance. Despite differences in the absolute correlation values between the rock and the simulation, the interpretation of the measurements (nucleation and growth suppression at the mean nearest neighbor distance) is the same for the natural sample and the simulation in Figure 2-8.

Effects of reactant distribution

The model accommodates a wide range of initial reactant distributions, and the effect on the CSD is significant. Initially homogeneous reactant distributions invariably produce CSDs with negative skewness (e.g., Fig. 2-9a). Increasing inhomogeneity (e.g., Fig. 2-9a-d) will produce progressively more positively skewed and wider CSDs. In the simulations described here, the CSD from an inhomogeneous model is a composite of two or more component CSDs that arise in subvolumes that are locally homogeneous in reactant concentration (Fig. 2-10). Although each of the component CSDs has negative skewness, summing them can produce whole-rock CSDs with variability as great as the initial inhomogeneity.

Although the effects of reactant inhomogeneity are complex and difficult to quantify, it is useful to understand some basic aspects of the effects. (1) The length scale of the diffusive flux may be greater than or less than the length scale of the inhomogeneity structure (e.g., the thickness of the smallest dimension of a layer). If the thickness of a structure is smaller than the length scale of the flux, the structure will have a minor effect on the CSD because the flux will transport material away from the high concentration structure and smooth any differences in concentration between

Figure 2-9. Effect of reactant distribution on simulated crystal-size distributions. Histograms of porphyroblast radii show the crystal-size distributions (CSDs) for several modeled porphyroblastic textures. The insets show initial reactant distribution for each model as a two-dimensional slice through the three-dimensional model. Brighter green of the reactants indicates higher concentration. (a) A homogeneous distribution of reactants invariably produces negative skewness in the CSD. (b) Addition of layering to the model produces a non-negatively skewed CSD that is wider than the homogeneous model. The reason for the increased width in the CSD is that the higher concentration layers produce larger crystals and the lower concentration layers produce smaller crystals. (c) If the layers are thinner and the diffusive length scales remain smaller than the thickness of the layers, a very similar CSD to the one in (b) can result. (d) More contrast in layer concentrations will widen the CSD more so, and the skewness can also change. The change in skewness is due to the small and large crystal peaks emerging as the CSD is deconvolved (Figure 2-10). (e) This CSD also has positive skewness and a similar width as the one in (d) demonstrating that reactant distributions are not unique. If the number and scales of concentration gradients are the same from two different reactant distributions, a similar texture can result within the limitations of other externally constrained parameters.

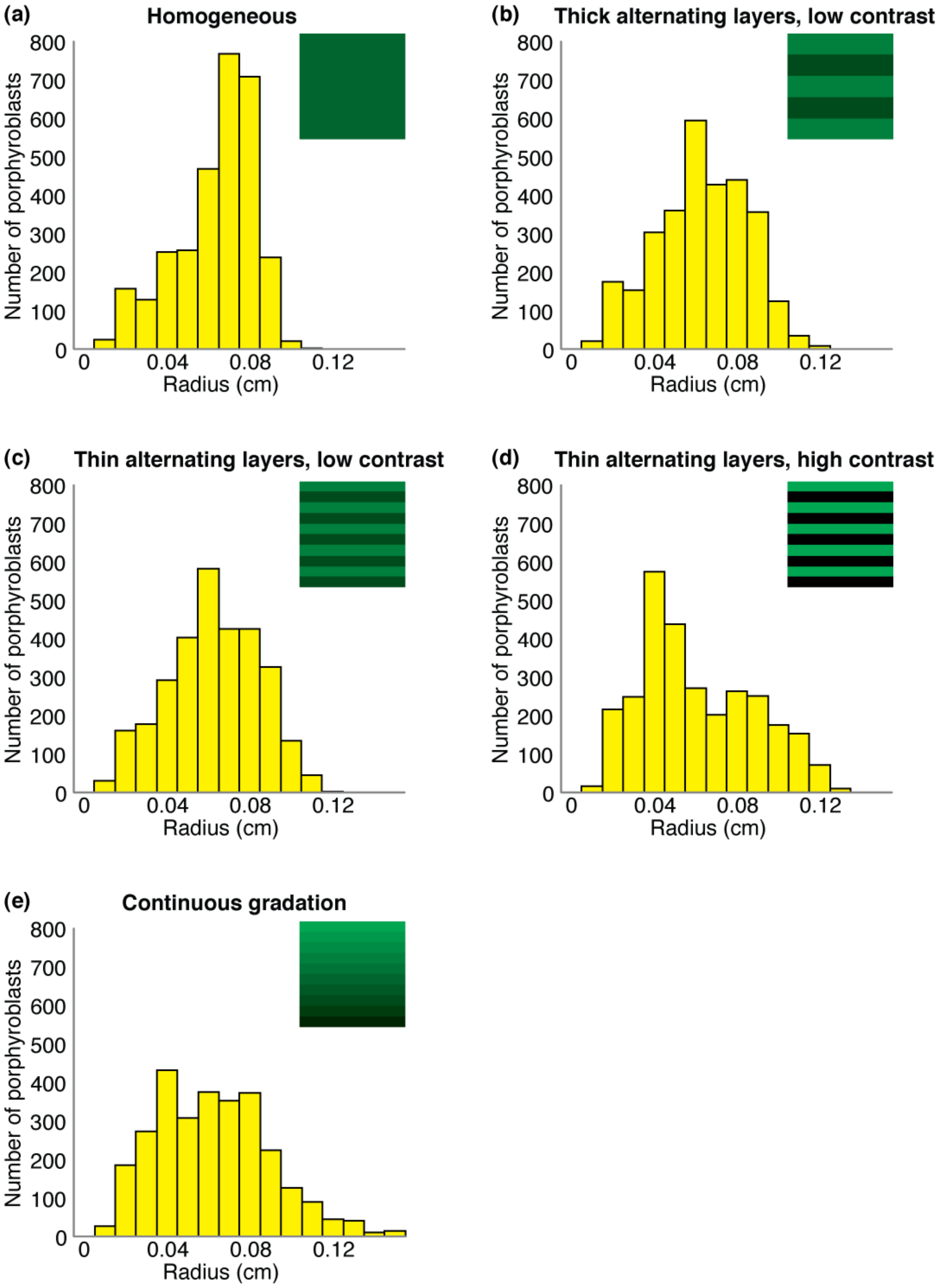
(a)
Homogeneous
(b)
Thick alternating layers, low contrast
(c)
Thin alternating layers, low contrast
(d)
Thin alternating layers, high contrast
(e)
Continuous gradation
Number of porphyroblasts
0
100
200
300
400
500
600
700
800
Radius (cm)
0
0.04
0.08
0.12

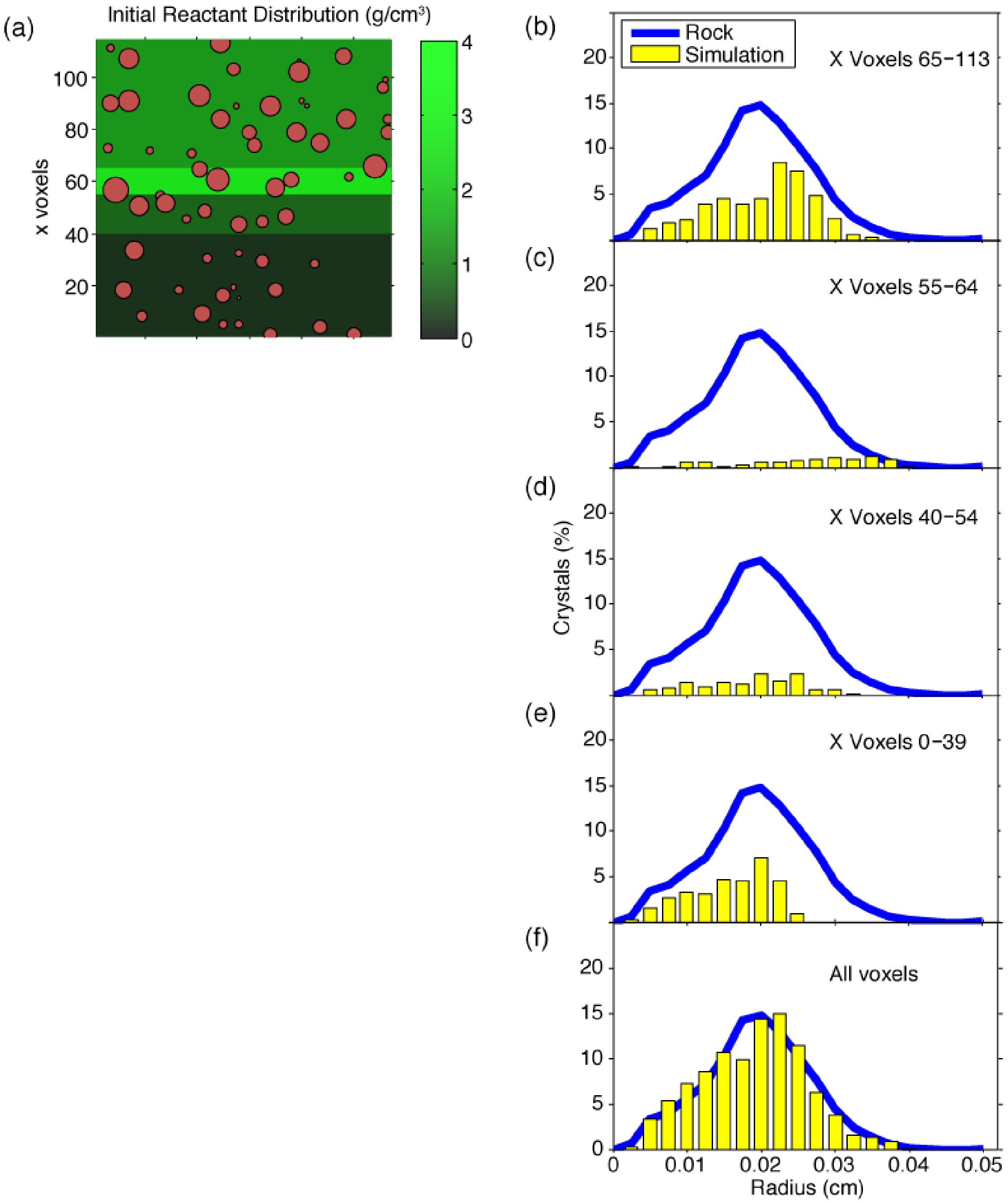

Figure 2-10. Effect of initial reactant distribution on CSD. (a) A 2-D slice through a 3-D model showing four reactant layers with different concentrations. Red circles with black outlines show the diameters of garnets that nucleated near this slice in the simulation. Notice that larger crystals are generally found in or near high concentration layers. (b-e) CSDs for individual layers. (f) CSD for all crystals from all layers. Each layer is locally homogeneous in reactant concentration and produces a negatively skewed CSD. A non-negatively skewed CSD is created by the sum of the CSDs in the individual layers.

structures. The resulting concentration gradients will thus approach those of a model with a homogeneous reactant distribution (Figs. 2-11 and 2-12). (2) Greater differences in concentration between structures (higher contrast in concentrations) produce larger crystals in the high concentration structures, due to larger diffusional fluxes, and smaller crystals in the low concentration structures resulting in a wider CSD (Fig. 2-9c,d). (3) An increase in the volume of a structure (e.g., thicker layer) will increase the number of crystals in it, because there is more space to nucleate crystals, but the CSD will retain the same width and skewness. (4) If high-concentration structures are divided into smaller structures, and the volume of the structures is held constant, there will be more gaps between the structures with low reactant concentrations and the resulting whole rock CSD will have more crystals of medium and small sizes, and fewer crystals of large size. Notice that in Figure 2-12, with increasing numbers of blocks, the number of small crystals rises (small peak at left) and the number of large crystals falls (number of maximum crystal radii decrease and shift left).

Obstacles and limitations

The model is well suited for simulating crystallization in regionally metamorphosed rocks and can provide valuable insight into the mechanisms controlling nucleation and growth of porphyroblasts. However, some obstacles and limitations remain.

As with any model, CRYSTALLIZE3D requires independent constraints on parameters that influence the diffusional fluxes and the duration and temperatures of crystallization. In determining the diffusional fluxes, the Al solubility or the diffusivity parameter k_3 can be co-varied along with the nucleation parameters in such a way that the model will produce equivalent textures that differ in their crystallization durations or temperatures of crystallization (e.g., Figs. 2-6a and 2-6d). Because the diffusive flux is a function of both diffusivity and solubility, uncertainty in solubility will affect the determination of k_3. Likewise, to the extent that k_3 can be determined, D_∞ can be estimated. However, k_3 is the product of D_∞, ϕ, and τ, and without precise determinations of ϕ, which can vary by roughly two orders of magnitude (10^{-6}-10^{-4}, Bickle & Baker, 1990; Ferry & Dipple, 1991; Farver & Yund, 1992), or τ, constraints on D_∞ can vary by

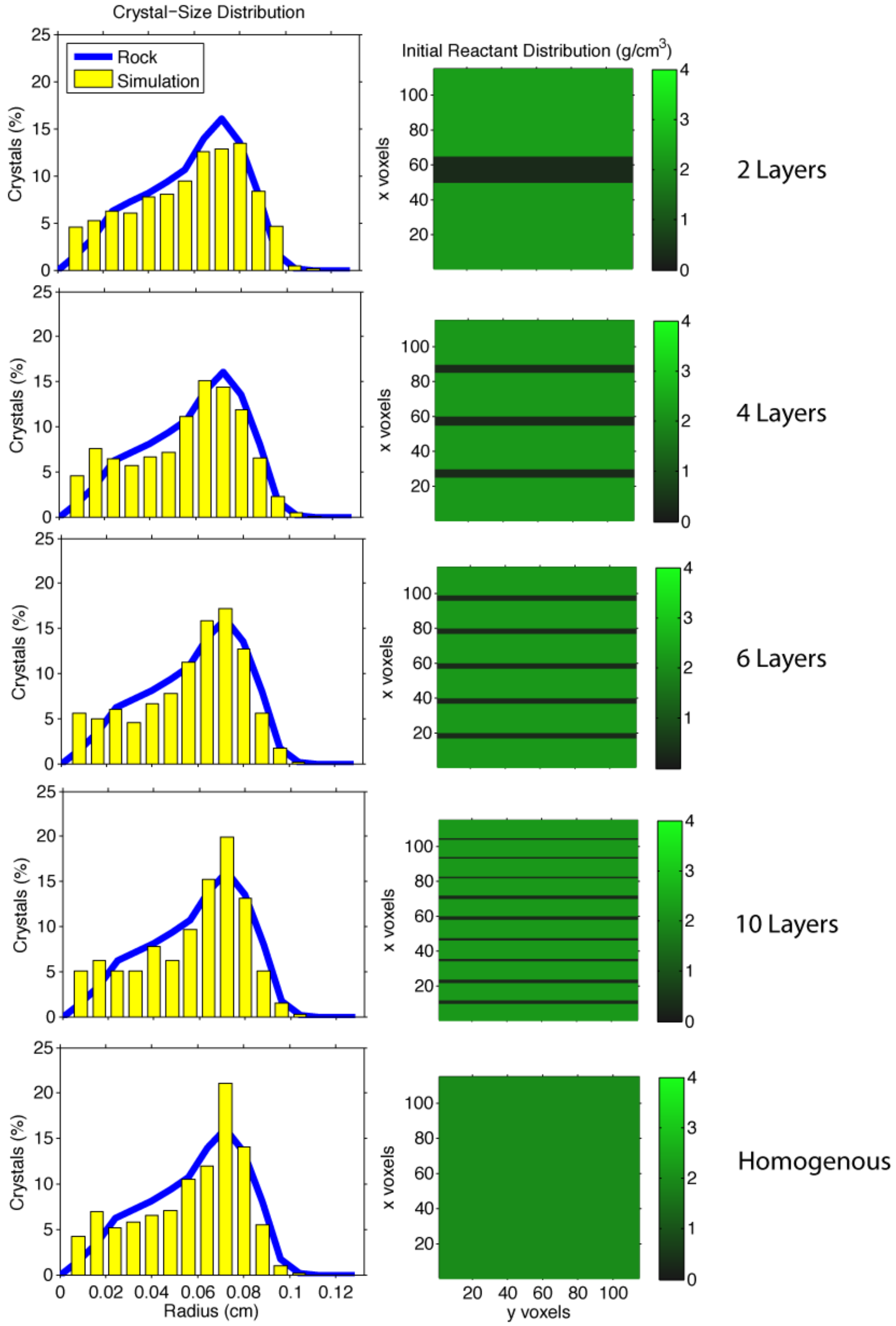

Figure 2-11. Effect of layering on CSD. An increase in layering approaches a homogeneous distribution of reactants and produces and a more negatively skewed CSD. In this example, the mode of the sample was held constant by maintaining the number of voxels with Al-bearing reactants of a fixed concentration and this results in layers that are slightly different thicknesses and gaps between the layers that might vary slightly in thickness as well (e.g., the 10-layer model).

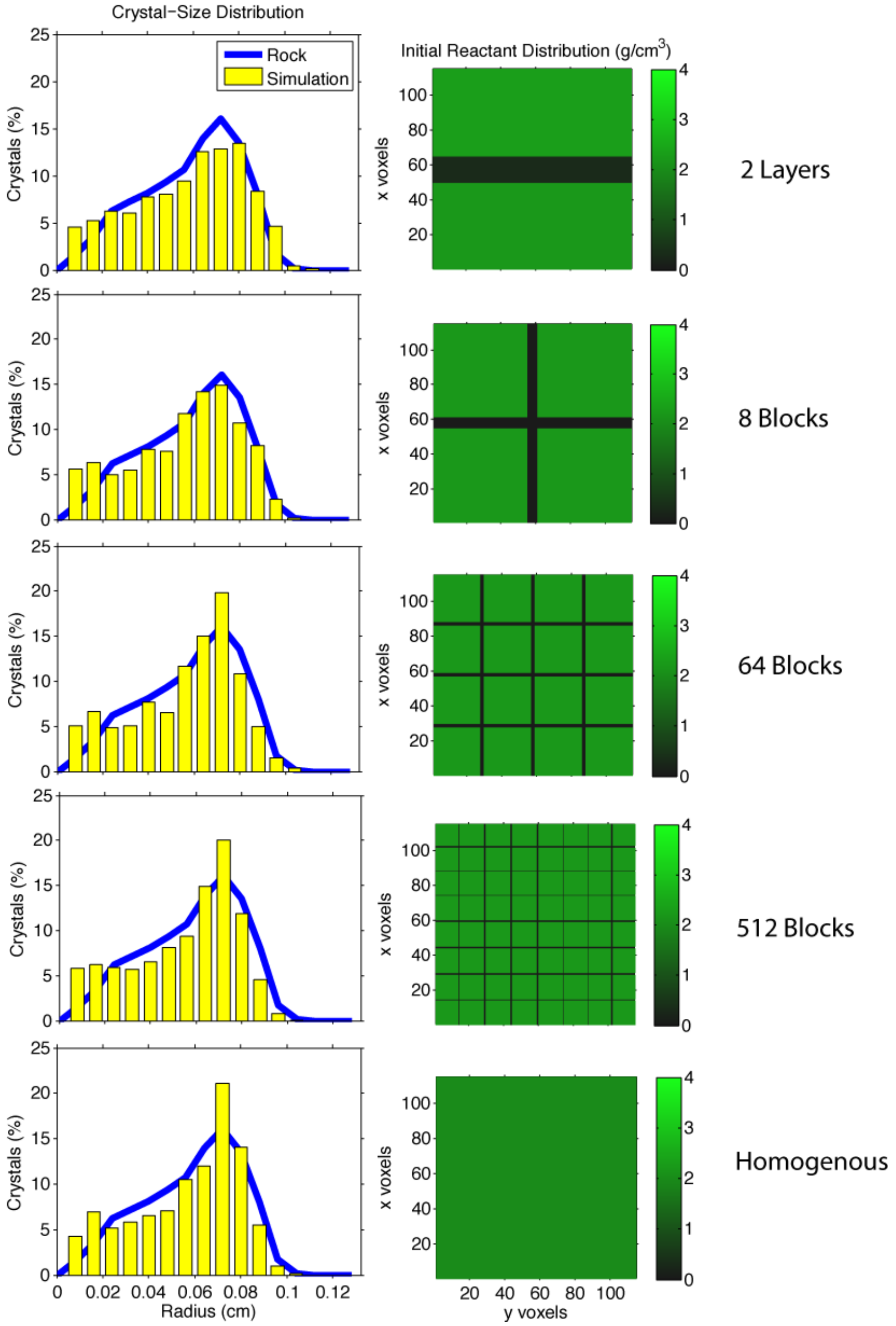

Figure 2-12. Effect of blocks on CSD. An increase in the number of blocks approaches a homogeneous distribution of reactants and produces a more negatively skewed CSD. As in the previous example, the mode of the sample was held constant by maintaining the number of voxels with Al-bearing reactants of a fixed concentration and this results in blocks that are slightly different sizes and gaps between the blocks that might vary slightly in thickness as well (e.g., the 512-block model).

roughly two orders of magnitude. Similarly, without precise determination of D_∞, estimates of Q_D made using D_∞ will contain a propagated uncertainty. In terms of timing and temperatures of crystallization, the model must be constrained by heating rate and temperatures of crystallization. Heating rate commonly must be inferred in the absence of independent information on the heating path, and the equilibrium temperature of the reaction is commonly estimated from equilibrium thermodynamics applied to samples that have experienced disequilibrium crystallization. Despite the limitations from externally constrained parameters, the modeling results demonstrate good determinations for most of the derived values. These topics will be explored further in the next chapter.

Another potential limitation is the simplification of the porphyroblast-forming reaction. The model approximates natural reactions, which are continuous multivariant garnet-forming reactions, using discontinuous reactions that are univariant. In other words, rather than garnet crystallization with changing *P*-*T* across a divariant stability field in which the mineral compositions change to maintain stability, the model simulates a univariant reaction curve in which the mineral compositions do not change with changing *P*-*T* conditions. However, this simplification should not have an appreciable effect on the results of the model. In the modeling, it is assumed that all components except the RLC have negligible chemical-potential gradients due to large diffusive fluxes relative to the RLC. In this case, Al is the RLC, and the stoichiometry of Al in the minerals modeled in this study does not change in amounts sufficient to affect the results appreciably; consequently, to the extent that the reaction affinity is indeed entirely due to the gradient in Al concentration, the reaction in nature and in the model is effectively univariant.

CONCLUSIONS

In comparison with previous efforts to numerically simulate crystallization of garnet porphyroblasts, CRYSTALLIZE3D more accurately captures the rates and processes of natural metamorphic crystallization. It is capable of simulating the most pertinent characteristics of natural porphyroblastic rocks to assess our understanding of

DCNG mechanisms and processes. The model is sensitive to the key parameters of nucleation rate, interfacial energy, and intergranular diffusivity, and it allows a wide range of initial reactant distributions to simulate natural inhomogeneities of reactant materials. The main limitations of the application of the model are in the independently constrained parameters, like ϕ and Al solubility, which can introduce uncertainties that affect the precision of the extracted and derived parameters (k_1, k_2, D_∞, and Q_D).

CHAPTER 3: APPLICATION OF CRYSTALLIZE3D TO REGIONAL METAMORPHIC ROCKS

ABSTRACT

Numerical modeling of diffusion-controlled nucleation and growth (DCNG) of garnet porphyroblastic textures is a powerful method for quantifying crystallization kinetics and quantifying disequilibrium (reaction affinity) in regionally metamorphosed rocks. The model CRYSTALLIZE3D was used to simulate DCNG in a large sample suite extending from pelitic to mafic compositions, temperatures and pressures ranging from 375-650 °C and 0.35 to 2.0 GPa, and a variety of tectonic settings that encompass a broad range of metamorphic environments. Input parameters play a significant role in constraining output so determinations of crystallization conditions, including temperature, pressure, heating rate, garnet-forming reaction, Al solubility, and porosity, were carefully considered for each sample. An exploratory sensitivity analysis conducted on one of the samples shows that the steady-state nucleation rate k_1 varies by only 1.4 $\log_{10}$ units (nuclei $\mathrm{cm}^{-3}\ \mathrm{s}^{-1}$), the nucleation acceleration k_2 ranges by only 1.0 $\log_{10}$ unit, and the diffusivity constant k_3 ranges over 0.7 $\log_{10}$ units ($\mathrm{m}^2\ \mathrm{s}^{-1}$). Considering the near-absence of prior determinations of such values, these ranges are small and demonstrate that the modeling can produce reasonably precise determinations of the extracted parameters. Nevertheless, the rock-specific properties (especially porosities and Al concentrations) can be difficult to obtain and uncertainties in them influence the values derived from the modeling. Therefore, the derived values (kinetics of nucleation and diffusion) will be precisely determined only to the extent that the input parameters can be accurately specified.

INTRODUCTION

The purpose of this research is to simulate the processes that underlie diffusion-controlled nucleation and growth (DCNG) in regionally metamorphosed rocks, to gain a quantitative measure of crystallization kinetics, and to further constrain the scales of disequilibrium during crystallization. In Chapter 2, CRYSTALLIZE3D was described in terms of its theoretical foundation and its practical implementation. In this chapter, the model is applied to garnet crystallization in a suite of natural rocks to build a database of kinetic parameters and scales of reaction affinities with which to evaluate metamorphic processes.

Thirteen datasets from rocks collected at six localities (Table 3-1) were compiled from previous studies (Carlson *et al.*, 1995; Denison & Carlson, 1997; Barnett, 1999; Schneider, 1999; Meth & Carlson, 2005; Hirsch, 2008). Textural characteristics of garnet porphyroblasts in the rocks were measured by high-resolution X-ray computed tomography (HRXCT) and processed using techniques developed for extracting crystal sizes and locations from HRXCT data (Denison & Carlson, 1997; Ketcham, 2005a; Ketcham *et al.*, 2005).

Although some of the data have been analyzed previously through numerical modeling (Carlson *et al.*, 1995), the current study applies a more sophisticated formulation of a numerical model that simulates DCNG and more rigorously constrains the key parameters of crystallization kinetics, and the compendium of data is expanded from three localities to six, and from four datasets to thirteen.

PREVIOUS WORK

Carlson et al. (1995) expanded the efforts of Carlson (1989, 1991), partly by utilizing 3-D datasets made available by the advent of HRXCT. They applied a numerical model to garnet crystallization in four natural samples to extract values of previously undetermined kinetic parameters for nucleation and diffusion. The samples are pelitic and mafic in bulk composition and represent a range of *P*-*T* conditions. The results of that work, re-evaluated in Carlson (2010), produced the first determinations of intergranular diffusivities of Al in regionally metamorphosed rocks. The diffusivities range from $10^{-19.9}$ to $10^{-18.6}$ $m^2 s^{-1}$ at 600 °C and correspond with an activation energy for intergranular diffusion of Al of 136 ± 35 kJ mol^{-1}. As noted in Chapter 1, these are '

Table 3-1. Sample localities.

Sample Numbers	Rock Unit	Locality
PM1, PM2, PM3	Rinconada Formation	Picuris Mountains, New Mexico
160A, 191A, 711A	Waterville Formation	South-Central Maine
AG4	Orange Gneiss	Passo del Sole, central Swiss Alps
MD	Lower pelite unit, Mica Creek assemblage	Mica Creek, British Columbia
HE-1	Franciscan Complex	Healdsburg, California
Jen-2-80	Franciscan Complex	Jenner, California
WR1bt, WR1tp, WR3m	Valley Spring Domain, Llano uplift	Whitt Ranch, Texas

composite' diffusivities, in the sense that they incorporate the effects of porosity, tortuosity, and of Al solubility.

Four of the samples in the current study are those used by Carlson et al. (1995): a sample from the Picuris Mountains (PM1), one from Mica Dam (MD), and two from Whitt Ranch (WR1bt and WR3m) in the Llano Uplift. The current model incorporates aspects of interface creation, phase transformation, and geometric factors of diffusional transport that better describe the parameters that control nucleation and intergranular diffusion, providing a more comprehensive framework in which to estimate and evaluate kinetic parameters.

MODELING PARAMETERS

Given the comprehensive formulation of the model, a wide variety of parameters must be determined to simulate crystallization and compare the results with natural samples (cf. Table 2-1). These are organized into three categories, which are based on the ability to measure the parameter directly, to estimate the parameter from independent constraints, or to calculate an appropriate parameter that balances computational limitations with the need to approach natural characteristics of DCNG in regional metamorphism.

Known rock characteristics for comparison with simulations

The primary method for determining the success of the simulation is in comparing the simulated texture with the texture of the natural sample. Techniques used to extract textural information from porphyroblastic samples have evolved to a state of high precision due to the development of HRXCT data collection and the corresponding processing methods (Denison *et al.*, 1997; Ketcham, 2005a; Ketcham *et al.*, 2005). Pertinent measurements of porphyroblasts include location, size, mode, number density, and size distribution. Some of these measurements are given in Table 3-2 and Figure 3-1. The simulated textures produced from the model are compared with the measured textures, and further evaluations are made using correlation functions to examine the degree of ordering, clustering, and competition of the crystal populations.

Table 3-2. Rock characteristics from measurements and estimates

Sample	Rock Type	Number of Crystals	Rock Volume (cm^3)	Crystal Number Density (N cm^{-3})	Mode (%)	Min *r* (cm)	Mean *r* (cm)	Max *r* (cm)	Matrix grain diameter (μm)	Estimated Porosity[a]	Estimated Al Solubility[b] (mol cm^{-3})
PM1	pelitic quartzite	1362	3.56	382	37.4	0.006	0.058	0.104	20-200	1.00E-05	5.60E-07
PM2	pelitic quartzite	1528	13.7	112	8.3	0.008	0.047	0.108	10-100	1.00E-05	5.60E-07
PM4	pelitic quartzite	1248	28.2	44	6.2	0.01	0.063	0.13	10-200	1.00E-05	5.60E-07
160A	metapelite	4795	0.75	6413	15.1	0.003	0.017	0.035	50-200	5.00E-05	5.00E-07
191A	metapelite	1052	0.033	31946	9.5	0.002	0.009	0.015	10-100	5.00E-05	7.66E-07
711A	metapelite	5260	1.7	3103	12.4	0.003	0.019	0.05	50-200	5.00E-05	8.80E-07
AG4	metapelite	1348	48	28	9	0.012	0.074	0.271	100-400	1.00E-05	1.80E-06
MD	metapelite	1604	222	7	8.8	0.035	0.121	0.388	400-4000	1.00E-05	5.80E-06
Jen-2-80	mafic eclogite	655	2.74	239	28.1	0.006	0.046	0.15	unknown	1.00E-05	1.60E-06
HE-1	mafic eclogite	1851	7.03	263	29.2	0.008	0.059	0.113	unknown	1.00E-05	5.50E-06
WR1bt	mafic eclogite	656	3.4	193	48.3	0.017	0.077	0.172	unknown	1.00E-06	1.20E-05
WR1tp	mafic eclogite	304	4.79	64	39.3	0.012	0.102	0.197	unknown	1.00E-06	1.20E-05
WR3m	mafic eclogite	726	1.85	393	23.1	0.006	0.041	0.123	unknown	1.00E-06	1.20E-05

[a] For rocks with unknown matrix grain size, porosity is based on temperature assuming that grain size increases with temperature.

[b] Based on an extrapolation from Tropper and Manning (2007) and Newton and Manning (2008) (Fig. 3-9).

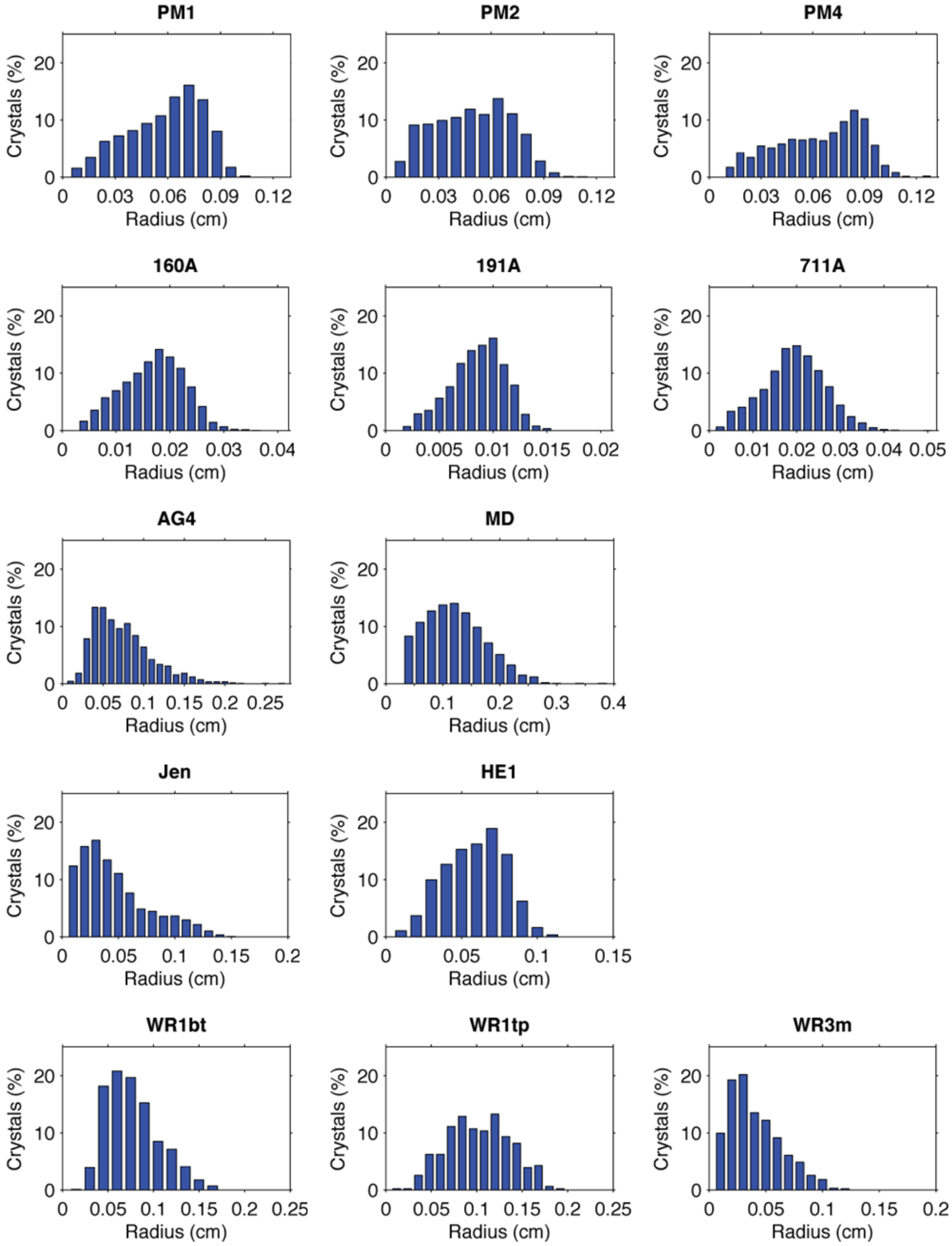

Figure 3-1. Crystal-size distributions of the natural samples.

Externally constrained inputs

Other modeling parameters that describe the conditions of crystallization are estimated from a variety of common techniques or constrained by values reported in the literature. The discussion starts with considerations that apply to most of the samples and then is organized by locality to explain the specific choices unique to each metamorphic event. A compilation of these inputs is given in Tables 3-2 and 3-3.

Temperature, pressure, heating rate, and model reactions

Estimates of the equilibrium temperature T_{eq} and pressure P_{eq} for the onset of garnet stability are difficult to constrain because the phases that were present when garnet nucleated are typically no longer in the rock, or their compositions have evolved with changing temperature and pressure. Many of the T_{eq} and P_{eq} estimates are derived from isochemical phase diagrams that describe P-T conditions for mineral assemblages and compositions specific to the rock bulk composition. The P-T conditions of the end of crystallization (P_{rim} and T_{rim}) are mostly constrained by garnet rim thermometry and barometry, which represent the best estimate of the peak conditions in all of the samples.

Heating rates and garnet-crystallization durations are not available for all samples but some constraints can be placed on them from determinations in other studies. Thermal models of orogenic events suggest heating rates should be approximately 5-20 °C Myr^{-1} (England & Thompson, 1984). Estimates of heating rates in orogenic settings from other techniques generally fall within this range. Using geochronology combined with a variety of P-T constraints (thermometry, isochemical phase diagrams, etc.), various studies estimate heating rates of 12.8 +13.6/-4.4 °C Myr^{-1} (Vance & O'Nions, 1992), ~2-5 °C Myr^{-1} (Foster *et al.*, 2004), and 8-15 °C Myr^{-1} (Janots *et al.*, 2009). In the absence of locally determined heating rates, values of 5-20 °C Myr^{-1} were used in this study as noted below.

Table 3-3. Model Reactions

Chlorite + Muscovite + Quartz ↔ Garnet + Biotite + H_2O (1)

$$(3/4)Fe_5Al_2Si_3O_{10}(OH)_8 + (1/4)KAl_3Si_3O_{10}(OH)_2 + (3/4)SiO_2$$
$$\leftrightarrow Fe_3Al_2Si_3O_{12} + (1/4)KFe_3AlSi_3O_{10}(OH)_2 + 3H_2O$$

Chlorite + Muscovite + Plagioclase ↔ Garnet + Biotite + Margarite + H_2O (2)

$$(0.6)Fe_5Al_2Si_3O_{10}(OH)_8 + (0.2)KAl_3Si_3O_{10}(OH)_2 + CaAl_2Si_2O_8$$
$$\leftrightarrow [Fe_3Al_2Si_3O_{12} + (0.2)Ca_3Al_2Si_3O_{12}] + (0.2)KFe_3AlSi_3O_{10}(OH)_2 + (0.4)CaAl_4Si_2O_{10}(OH)_2 + 3H_2O$$

Chloritoid + Chlorite + Muscovite + Quartz ↔ Garnet + Biotite + Kyanite + H_2O (3)

$$FeAl_2SiO_5(OH)_2 + Fe_5Al_2Si_3O_{10}(OH)_8 + KAl_3Si_3O_{10}(OH)_2 + SiO_2$$
$$\leftrightarrow Fe_3Al_2Si_3O_{12} + KFe_3AlSi_3O_{10}(OH)_2 + 2Al_2SiO_5 + 5H_2O$$

Amphibole + Epidote + Quartz + Albite ↔ Garnet + Omphacitic-pyroxene + H_2O (4)

$$[(1/6)Na_2Fe_3Al_2Si_8O_{22}(OH)_2 + (1/3)NaCa_2Mg_4Al_3Si_6O_{22}(OH)_2] + (2/3)Ca_2FeAl_2Si_2O_{12}(OH) + (1/3)SiO_2 + (1/6)NaAlSi_3O_8$$
$$\leftrightarrow [(7/18)Fe_3Al_2Si_3O_{12} + (5/18)Mg_3Al_2Si_3O_{12} + (1/3)Ca_3Al_2Si_3O_{12}] + [(5/6)NaAlSi_2O_6 + CaSiO_3 + (1/4)Mg_2Si_2O_6] +$$
$$(5/6)H_2O$$

All of the samples have constraints on T_{eq} and T_{rim}, some have constraints on heating rate, and none have constraints on crystallization duration. Estimates of garnet-crystallization durations can range from ~3-40 Myr (e.g., Vance & O'Nions, 1992; Hoisch *et al.*, 2008; Skora *et al.*, 2009; Pollington & Baxter, 2010) or possibly longer, so without specific information about the samples in this study, duration can only be estimated from heating rates and temperatures of garnet growth. For samples with unknown heating rates, durations were estimated using arbitrarily chosen heating rates, within the range stated above.

Model reactions for all samples are given in Table 3-3. Although crystallization in some samples can be simulated using a relatively simple model reaction that dissolves reactants within one assemblage and grows garnet within another assemblage, more complex garnet growth occurs when garnet passes through several stability fields before crystallization is complete. Sample MD provides an example of a more complex garnet growth history that includes changes in the reactant and product assemblage during garnet crystallization, and the isochemical phase diagram of Tinkham and Ghent (2005) provides an illustration of the changes (Fig. 3-2).

Along the *P*-*T* path in Figure 3-2, the isochemical diagram shows that garnet stability crosses through several fields that define a variety of mineral assemblages, including the gain and loss of staurolite. The net effect of the changes in mineralogy is ideally the sum of the differences in free energy across all of the reactions along the path (the lines crossed by the *P*-*T* path shown in Figure 3-2), which is the same as the difference in free energy between the starting and ending mineral assemblages associated with garnet core and rim growth. The assemblage before garnet nucleated in MD was chloritoid + chlorite + muscovite + quartz, and the final assemblage after garnet crystallization is garnet + biotite + quartz + kyanite + muscovite + plagioclase. These assemblages can be used as the reactant and product assemblages, respectively, as a simplified model of the complex reaction history. This approach also was taken in the Franciscan and the Whitt Ranch samples as described below.

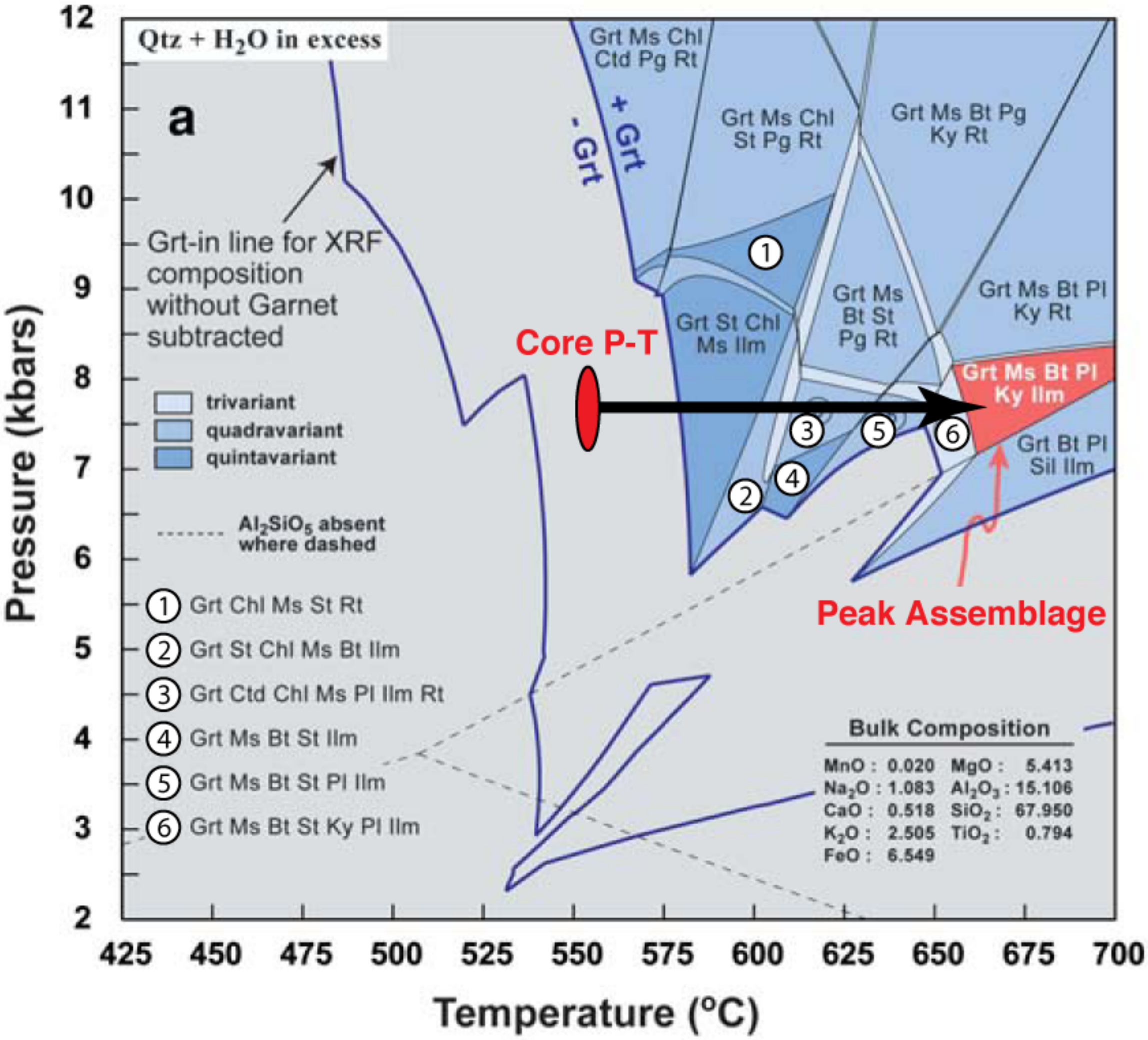

Figure 3-2. Isochemical phase diagram for sample MD. Several mineral assemblages are shown along the *P-T* path taken by MD, suggesting that the garnet growth history involved a series of reactions rather than one garnet-forming reaction. Modified from Tinkham and Ghent (2005)

The changes in *P*, *T*, Gibbs free energy change of the reaction ($\Delta_r G$), and heating rate constrained in this section were input to the model by calculating $\Delta_r G$ at *P*-*T* conditions along a free-energy path input as *t*-*T*-$\Delta_r G$ triplets. The values are given in rows in Table 3-4, in which each row contains the endpoints of the segments along the *t*-*T*-$\Delta_r G$ path as well as the model reaction used to determine $\Delta_r G$ at each *P*-*T*.

Picuris Mountains. Samples PM1, PM2, and PM4 were collected in the Picuris Mountains of New Mexico (Carlson, 1989) where Barrovian metamorphism crystallized garnet at conditions near the aluminum-silicate triple point during a 1450-1400 Ma orogenic event (Holdaway, 1978; Daniel & Pyle, 2006). The samples are garnet-biotite quartzites with minor muscovite, plagioclase, and graphite. A typical protolith of this assemblage is a muscovite-chlorite-quartz rock (Spear, 1995), therefore a suitable model reaction for these samples is chlorite + quartz + muscovite = garnet + biotite + H_2O.

A minimum estimate of T_{eq} for the PM samples is provided by experimental phase equilibria that place a lower temperature limit of 414 ± 5 °C (at 0.3 GPa) on the stability of Mn-bearing garnet from a chlorite + quartz + H_2O starting material (Hsu, 1968). Considering the simple mineralogy of the PM samples, the precursor was likely to be a chlorite + quartz (+ muscovite) rock. The triple-point conditions of the locality suggest pressures near 0.4-0.5 GPa (Pattison, 1992; Daniel & Pyle, 2006), so the experimental results of Hsu (1968) were extrapolated to this pressure range, giving T_{eq} of ~435 °C.

Garnet-biotite thermometry (Holdaway, 2000) was calculated from rim compositions of these samples assuming values of Fe^{3+}/Fe^{total} of 3% for garnet and 11.6% for biotite based on the presence of graphite (Holdaway *et al.*, 1997). Two garnets in each of three samples from the current study were combined with average biotite analyses in each sample to determine garnet rim temperatures of 530, 535, and 540 ± 25 °C. Other determinations fall within this same range (Carlson, 1989, p. 18; Daniel & Pyle, 2006), therefore an average temperature of 535 °C is taken as T_{rim} for these samples.

A clockwise *P*-*T* path proposed for the Picuris Mountains (Fig. 3-3, Daniel & Pyle, 2006) is partly based on the aluminum-silicate textural relationships that show the

Table 3-4. Constrained values

Locality/Sample	t (Myr)	P (GPa)	T (°C)	Δ_rG[a]	Heating Rate[b] (°C Myr^{-1})	Reaction
Picuris Mountains	0	0.40	435	0	10	1
	10	0.50	535	-19.1	0	
	30	0.40	535	-20.1	0	
Maine: 160A	0	0.35	485	0	5	2
	10	0.35	535	-5.6	0	
	40	0.35	535	-5.6	0	
Maine: 191A	0	0.35	485	0	~12	2
	7	0.35	570	-9.5	0	
	30	0.35	570	-9.5	0	
Maine: 711A	0	0.35	485	0	23	2
	5	0.35	600	-12.9	5	
	30	0.35	600	-12.9	0	
Passo del Sole	0	0.40	540	0	15	2
	4	0.50	600	-6.3	0	
	30	0.50	600	-6.3	0	
Mica Dam	0	0.75	555	0	5	3
	20	0.75	655	-31.1	0	
	30	0.75	655	-31.1	0	
Franciscan: Jenner	0	0.80	375	0	100	4
	1.25	1.30	500	-7.6	0	
	30	1.30	500	-7.6	0	
Franciscan: Healdsburg	0	1.50	450	0	100	4
	1	2.00	550	-7.5	0	
	30	2.00	550	-7.5	0	
Whitt Ranch	0	0.90	575	0	10	4
	7.5	1.40	650	-7.3	0	
	30	1.40	650	-7.3	0	

Each row contains values used to make the endpoints of each segment along the t-T-Δ_rG path (see text).

[a] Δ_rG is in units of kJ per mole of 12-oxygen garnet.

[b] Heating rate for a segment is specified at the beginning of the segment.

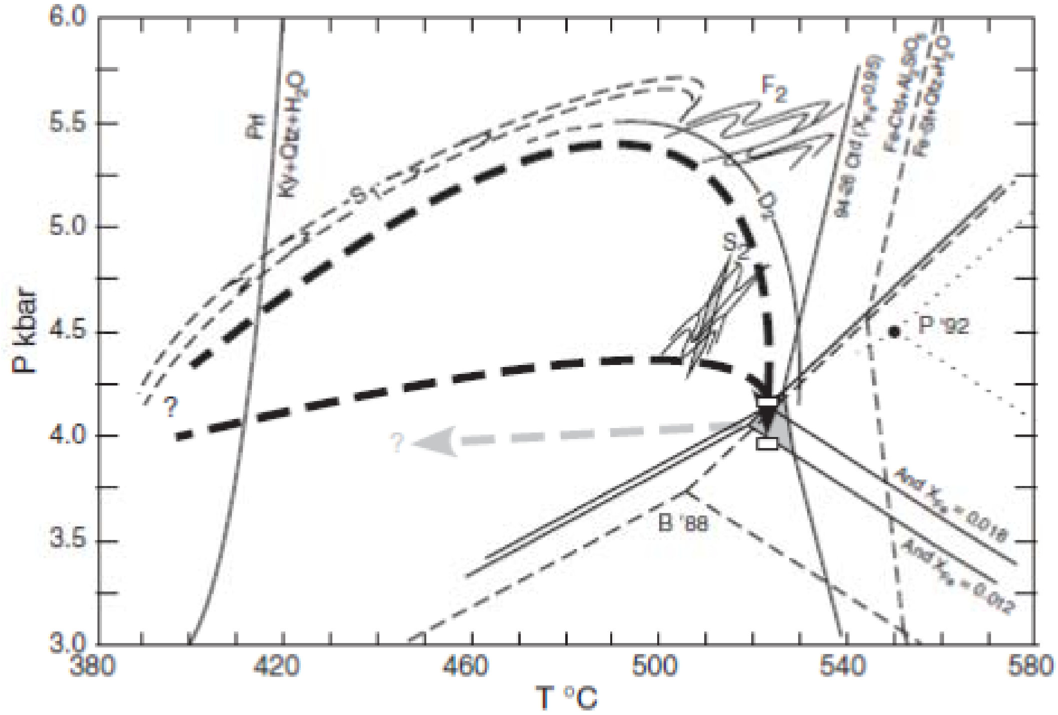

Figure 3-3. Pressure-temperature paths for the Picuris Mountains proposed by Daniel and Pyle (2006). The upper-grade portion of the path is better constrained than the lower-grade portion so two paths (heavy dashed arrows) could be suitable for crystallization of garnet in these samples. A path that lies between these two paths, rising in pressure from 4 to 5 kbar, was chosen for this study.

order of crystallization as kyanite-sillimanite-andalusite, respectively, and partly based on Gibbs-method modeling from garnet chemical zoning. However, the lower grade portion of the path is not well constrained, hence two paths are proposed by Daniel and Pyle (2006) that could represent the path of the rocks: either isobaric heating or heating with a small increase in pressure from roughly 0.4 to 0.55 GPa. Considering that contours of garnet mode have steep slopes in P-T space at these pressures for metapelitic compositions (Spear, 1995), pressure has only a small influence on $\Delta_r G$ for the model reaction, so either P-T path is sufficient for modeling. For modeling garnet growth in these samples, P_{eq} is 0.4 GPa for core growth, pressure rises to 0.5 GPa, and then falls to 0.4 GPa during rim growth.

Without additional constraints of the rate of heating, a rate of 10 °C Myr^{-1} was arbitrarily chosen for these samples. Given the heating rate and the temperature constraints, the duration of garnet growth for modeling purposes should be on the order of 5 Myr or more.

Maine. Samples 711A, 191A, and 160A are metapelitic rocks from the Waterville Formation in central Maine, provided by John Ferry and previously analyzed by Hirsch (2008). The samples experienced Buchan metamorphism in the Devonian during the Acadian Orogeny (Osberg, 1971; Dallmeyer, 1979; Ferry, 1981). Near the end of Buchan metamorphism, the area was intruded by possibly synmetamorphic quartz monzonite stocks at 0.35 ± 0.03 GPa that raised temperatures beyond those of the deformational event, and garnet growth occurred in these later stages of slow, regional heating (Ferry, 1978; Dallmeyer, 1979; Ferry, 1980; de Yoreo *et al.*, 1989). Isograds, which are nearly parallel to the intrusive contact (Fig. 3-4), and post-deformational garnet growth textures support the notion that garnet growth was influenced by the intrusive heating. Sample 711A is located near the contact with the intrusion, sample 191A is farther from the contact, and 160A is farthest from the contact, just above the garnet isograd indicating that heating there was just sufficient to produce garnet crystallization, as suggested by Hirsch (2008). Regional thermal models by de Yoreo et al. (1989), used to investigate the evolution of the geothermal gradient in central Maine by

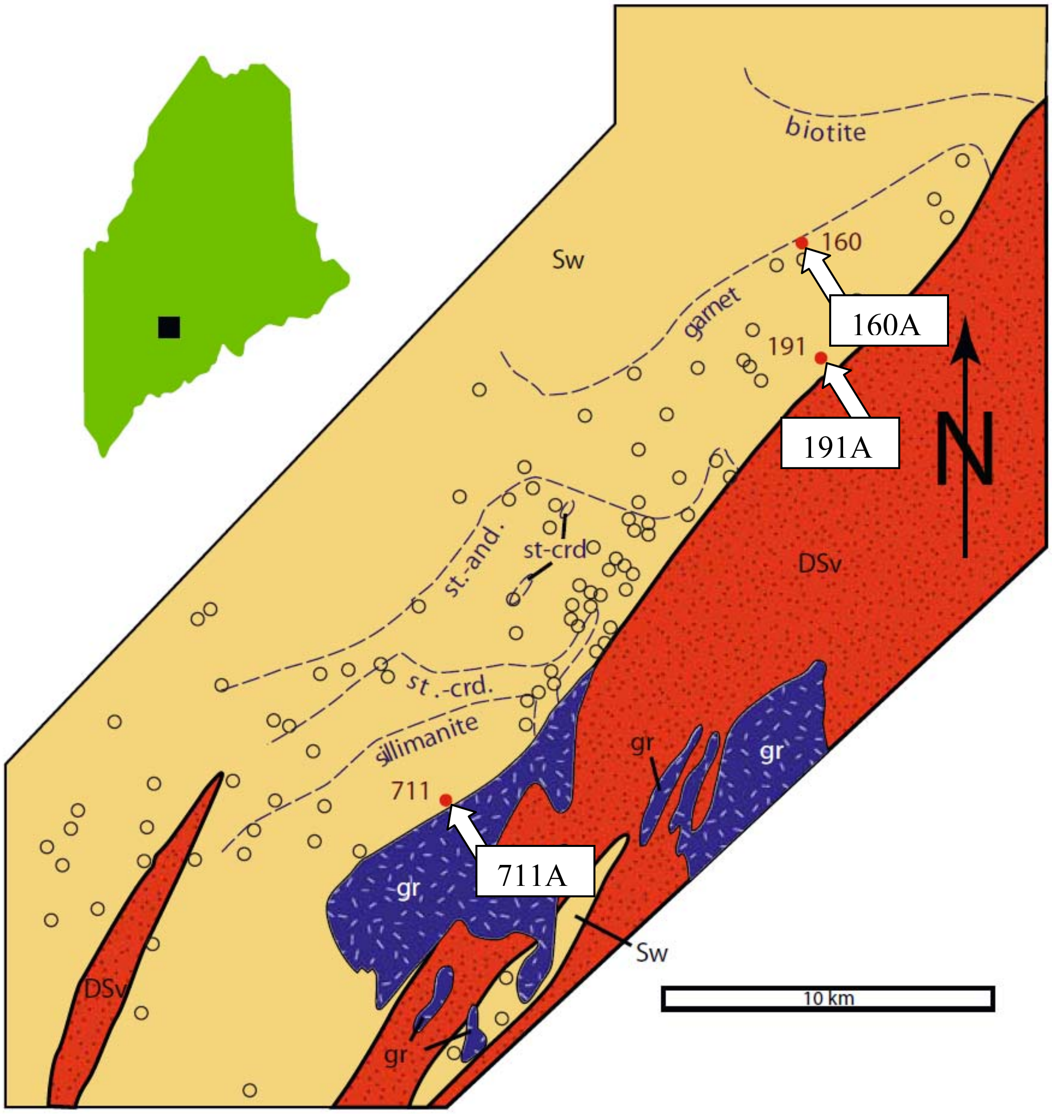

Figure 3-4. Simplified geological map of sample locations in south-central Maine. The samples (indicated with arrows) were collected in the Silurian Waterville formation (Sw). Other units are the Hallowell granite (gr) and the Devonian-Silurian carbonate Vassalboro formation (DSv). Dashed lines are isograds as labeled. Compiled by Hirsch (2008) after Barker (1961) and Ferry (1980).

simulating heating from sheet-like plutons dipping to the northeast, suggest that prograde metamorphism to sillimanite conditions required additional heating from the intrusions beyond the "normal mantle heat flow and crustal radiogenic heat production" (de Yoreo *et al.*, 1989, p. 186).

The thermal modelling of de Yoreo et al. (1989) provides a context in which to determine heating rates (Their Fig. 11), and estimates made in this study give minimum and maximum heating rates for the depth of burial of these samples of 5-15 °C Myr^{-1}, which bracket the estimate of 10 °C Myr^{-1} determined by Hirsch (2008) using the same model results. However, Hirsch (2008) used this rate for sample 711A, closest to the pluton, and estimated rates of 6.6 and 2 °C Myr^{-1} for samples 191A and 160A, respectively, assuming a decreasing heating rate with distance from the pluton. Progressively decreasing heating rates are also supported by the progressively decreasing rim temperatures with distance from the intrusion given below. Following Hirsch's example but using slightly higher rates, considering that 711A is adjacent to the pluton and probably experienced heating rates that were faster than for the average geothermal gradient in the area, rates of 23, 12, and 5 °C Myr^{-1} were used for 711A, 191A, and 160A, respectively.

The rocks contain quartz, plagioclase, garnet, biotite, and a variety of accessory phases. Two samples (160A and 191A) contain muscovite and carbonate minerals (probably from post-garnet fluids), and two samples (711A and 191A) contain graphite (including graphite sector zoning in garnet in 711A). All three samples should have crystallized garnet from the same bulk composition given that they were collected from the same geologic unit and they have similar, though not identical, garnet core compositions. But the presence of carbonates in samples 160A and 191A, and problematic isochemical modeling of these two samples led Hirsch (2008) to suggest that metasomatic fluids may have altered the bulk compositions of the two samples after garnet crystallization. Due to these difficulties, Hirsch (2008) estimated T_{eq} for garnet crystallization in the two samples from a Monte Carlo analysis that varied the bulk compositions to find suitable ones that produced the measured garnet core compositions on mineral assemblage diagrams. Those results, combined with traditional isochemical phase equilibria modeling for 711A, yielded temperatures of 485, 477, and 481 °C at 0.35 GPa for T_{eq} of 711A, 191A, and 160A, respectively. Therefore, conditions of 485 °C and 0.35 GPa were used for T_{eq} and P_{eq} in the current study.

Estimates of T_{rim} are from Hirsch (2008) and calculations in this study. Hirsch (2008) determined rim temperatures of <650, 570, and 535 °C for 711A, 191A, and 160A, respectively, using the Holdaway (2000) garnet-biotite thermometer. Additional determinations were made in the current study using the same thermometer to understand the high, poorly constrained temperature determined for 711A (<650 °C). The same Fe^{3+} proportions as in the PM rocks above were used for sample 711A, due to graphite sector zoning in garnet, and the results indicate a T_{rim} of 594 ± 25 °C. This temperature and the reported temperatures of 570 ± 25 °C for 191A and 535 ± 25 °C for 160A from Hirsch (2008) were used in the modeling.

The minerals that provide evidence of the garnet-forming reaction are those that were present prior to infiltration of metasomatic fluids, namely plagioclase, garnet, and biotite. Garnet and biotite are typically formed from the breakdown of chlorite, quartz, and muscovite. Plagioclase also played a role in the reaction, and therefore anorthite was included to exchange Ca with a grossular component of garnet and a margarite component of muscovite.

Passo del Sole. Sample AG4 was collected in the central Swiss Alps on the northern edge of the Lucomagno nappe; it was provided by John Rosenfeld and previously studied by Meth & Carlson (2005) and by Berg (2007). Estimated *P*-*T* conditions in the region are 500-600 °C and 0.4-0.5 GPa (Adams *et al.*, 1975; Todd & Engi, 1997). The area experienced three episodes of deformation: the first two involved large-scale thrusting and folding, and the third is signified by small-scale folding and amphibolite-facies metamorphism (Frey *et al.*, 1980), which crystallized garnet in the metapelitic Orange Gneiss unit in Passo del Sole. Garnets are as large as 10 mm in diameter and contain sigmoidal inclusion trails due to heterogeneous syn-metamorphic shearing. Other minerals in the rock include quartz, plagioclase, muscovite, biotite, minor staurolite and rare kyanite.

The T_{eq} used for modeling is taken from garnet-core isopleth intersections on isochemical phase diagrams for sample AG4, which indicate a temperature of 540 °C (Fig. 3-5, Berg, 2007). The P_{eq} is taken from the low end of the pressure estimates for the area (0.4 GPa) because the isopleths of Berg (2007) act essentially as thermometers and do not constrain pressure precisely; nonetheless Berg's estimated P_{eq} is quite similar at about 0.45 GPa. The thermal history of Berg (2007) further provides an estimate of T_{rim} (~600 °C) and the upper end of the pressure estimates for the region (0.5 GPa) was taken as P_{rim}.

Heating rates determined in the northern Lepontine dome using allanite and monazite geochronology are estimated at 8-15 °C Myr^{-1} during ~31-19 Ma Barrovian metamorphism spanning the temperature range ~430-580 °C (Janots *et al.*, 2009). A heating rate of 12.8 +13.6/-4.4 °C Myr^{-1} was estimated from U-Pb ages of garnet cores and rims in the western Lepontine dome, about 50 km to the southwest of Passo del Sole, and the ages of these garnets are in the range 32-25 Ma and temperatures in the cores and rims span ~520-575 °C (Vance & O'Nions, 1992). Two garnet separates of AG4 give a garnet-rutile Lu-Hf age of 25.43 ± 0.44 Ma (Berg, 2007). Considering the similar ages and temperatures of metamorphism to the other studies in the northern Lepontine dome, a similar heating rate is appropriate for sample AG4, so a rate of 15 °C Myr^{-1} was used in the modeling.

Considering the major minerals in this rock (not including minor staurolite and rare kyanite) and the amphibolite-facies conditions of metamorphism, the same chlorite-muscovite consuming reaction used for the Maine samples was used to approximate the garnet-forming reaction in AG4.

Mica Dam. Sample MD is a metapelite collected in the Mica Creek area in British Columbia within the Selkirk-Monashee-Cariboo complex in the hinterland of the Canadian Cordillera. Thermobarometry in the region near Mica Creek from various studies (summarized by Crowley *et al.*, 2000) yields *P-T* conditions of 540-700 °C and

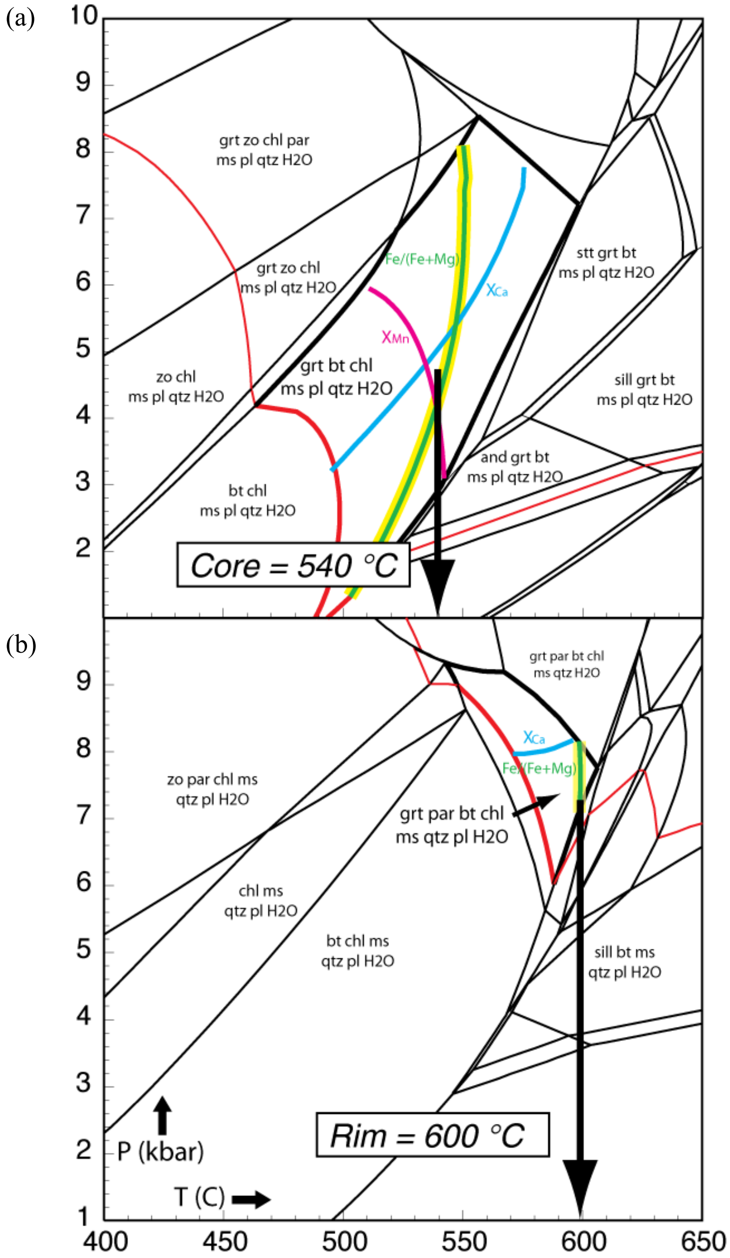

Figure 3-5. Isochemical phase diagrams for sample AG4. (a) Compositional isopleths and Fe# from garnet core intersect at about 540 °C indicating the *P-T* conditions of garnet stability. (b) Nearly vertical Fe# curve indicates the temperature of the garnet rim at about 600 °C. Modified from (Berg, 2007).

0.58-0.72 GPa. Metamorphism, including garnet growth, likely occurred at ~100-60 Ma, and two fabrics are prominent in the sample: an internal foliation defined by sigmoidal inclusion trails in garnet that are oblique to a foliation that wraps around garnet (S_{1+2}) (Crowley *et al.*, 2000). An additional crenulation (S_3), defined by kinked and folded biotite, garnet, staurolite, kyanite, and sillimanite, is superimposed on S_{1+2} and is found in some rocks in the Mica Creek area (Simony *et al.*, 1980). In the sample used in this study, S_3 is evident from kinked biotite grains. Garnets are elongate and their long axes are aligned (Ketcham, 2005b). Chemical zoning of Mn in garnet is ellipsoidal and subparallel to inclusion trails (Tinkham & Ghent, 2005). Other major minerals in the sample include biotite, quartz, kyanite, muscovite, and plagioclase.

The orientations of the internal and external foliations suggest that garnet growth was pre- to syn-kinematic to S_{1+2} and pre-kinematic to S_3. Ketcham (2005b) proposed that the Mn zoning and the lack of temperatures sufficient to cause plastic deformation of garnet suggests that early garnet growth may have been ellipsoidal, although other mechanisms cannot be ruled out, and he further suggests that alignment of garnet porphyroblasts may have been caused by development of S_3, and therefore the crystals may have moved since nucleation.

P-T information specific to the locality from which this sample was collected is given by the *P-T* path constructed by Tinkham and Ghent (2005) based on isochemical phase diagram modeling (Fig. 3-2). They used intersecting garnet-core isopleths to determine the equilibrium *P-T* conditions and estimated the rim *P-T* conditions from the rock mineral assemblage. Their interpretation is an isobaric path (~0.75 GPa) starting at 555 °C and ending at 680 ± 47 °C. Their results provide the *P-T* conditions used in this study: 0.75 GPa for P_{eq} and P_{rim}, 555 °C for T_{eq}, and ~655 °C for T_{rim}.

About 40 km to the south of Mica Creek is the Monashee complex, which is structurally below the Selkirk-Monashee-Cariboo complex, where metamorphic events overlap in age and *P-T* conditions with those in the Mica Creek area (Gibson *et al.*, 1999; Foster *et al.*, 2004). Prograde *P-T-t* paths were constructed by Foster et al. (2004) from garnet-monazite thermometry, monazite-xenotime thermobarometry, and in situ monazite U-Pb geochronology. Textural relationships and monazite growth zones, delimited by Y zoning, allowed them to determine ages and *P-T* conditions during prograde metamorphism in the Monashee complex between 75 and 55 Ma. They derived a heating rate of 5 ± 2 °C Myr^{-1}, and considering that garnet in sample MD grew between 100 and 60 Ma, MD most likely experienced a similar heating rate during garnet growth. Therefore, a heating rate of 5 °C Myr^{-1} was used to model garnet growth in MD. This rate suggests crystallization duration of 20 Myr for garnet in this sample.

As described above, the assemblage before garnet nucleated and the final assemblage after garnet crystallization were taken as reactants and products to approximate a model reaction: chloritoid + chlorite + muscovite + quartz = garnet + biotite + kyanite.

Franciscan. Samples collected in California near Jenner (Jen-2-80) and Healdsburg (HE-1) are from eclogitic blocks within the low-grade matrix of the Franciscan Complex; these samples were provided by Mark Cloos. These blocks were metamorphosed in the late Jurassic (Krogh *et al.*, 1994; Page *et al.*, 2007) during subduction of the Farallon Plate beneath the North American Plate. Given that the blocks are mafic, they are probably pieces of the oceanic plate (Cloos, 1985) that were metamorphosed at the onset of subduction when the hot upper plate was initially in contact with the subducting slab. They were later entrained in the mélange wedge and experienced retrograde metamorphism during transport to the surface (e.g., Cloos, 1982). Although garnet is subidioblastic to idioblastic, the matrix has been retrogressed and no longer contains the complete eclogitic assemblage.

In a compilation of *P-T* estimates used to decipher the complex prograde and retrograde metamorphic history of the Jenner eclogite blocks, Krogh et al. (1994) suggest that garnet core growth occurred at 350-400 °C and >0.8-0.9 GPa, partly based on garnet-clinopyroxene Fe-Mg exchange thermometry (Krogh, 1988), and that garnet crystallization ended at about 440-520 °C and 1.3 GPa. A study by Krogh Ravna and Terry (2004) reported new *P-T* determinations, but those results appear to be erroneous (Page *et al.*, 2007). For modeling of sample Jen-2-80, equilibrium *P-T* conditions are 375 °C and 0.8 GPa, and rim conditions are 500 °C and 1.3 GPa.

Garnet-pyroxene thermometry and garnet-phengite barometry yield *P-T* conditions for the cores of the Healdsburg garnets of 400-500 °C and 1.3-1.7 GPa (Page *et al.*, 2007). The peak *P-T* conditions during eclogitization are difficult to constrain, but Page et al. (2007) suggest a peak of ~550 °C and 1.8-2.2 GPa based on a compilation of garnet-pyroxene-phengite thermobarometry from the literature and their own calculations. For modeling of sample HE-1, values of 450 °C and 1.5 GPa are used for the equilibrium *P-T* conditions, and 550 °C and 2.0 GPa are used for the rim conditions.

Although rates of subduction are well established, the heating rate of a single block during subduction is a highly complex problem. The Franciscan eclogites are high-grade blocks that were likely metamorphosed near the onset of subduction before the upper plate cooled significantly. Pieces of the mafic oceanic plate were broken off and entrained in the incipient mélange wedge and could have descended or stalled in the subduction zone during eclogite metamorphism. In addition, the isotherms through this dynamic system evolve as heat transfers from the hot upper plate to the cold lower plate (Fig. 3-6). At the initiation of subduction, the isotherms in the upper plate are nearly horizontal, and as the mélange wedge evolves, the isotherms are drawn down to deeper levels in the wedge. A rock that is entrained at the early stages of subduction may undergo a heating path similar to the hypothetical path shown for early subduction in the *P-T* diagram in Figure 3-6b ($t \approx t_0$).

Despite the potentially complex prograde history of the eclogite blocks, some constraints on the heating rate can be estimated from the age of the Coast Range Ophiolite and from cooling ages determined for phengite within the eclogites. The Coast Range Ophiolite was emplaced at the onset of subduction when the oceanic crust was relatively hot and buoyant (Wakabayashi, 1990). The age of ophiolite emplacement at Healdsburg is estimated from U-Pb dating of zircon in plagiogranite that yields 163 ± 2 Ma (Hopson *et al.*, 2008). Phengite ^{40}Ar/^{39}Ar ages (cooling through ~400 °C) are

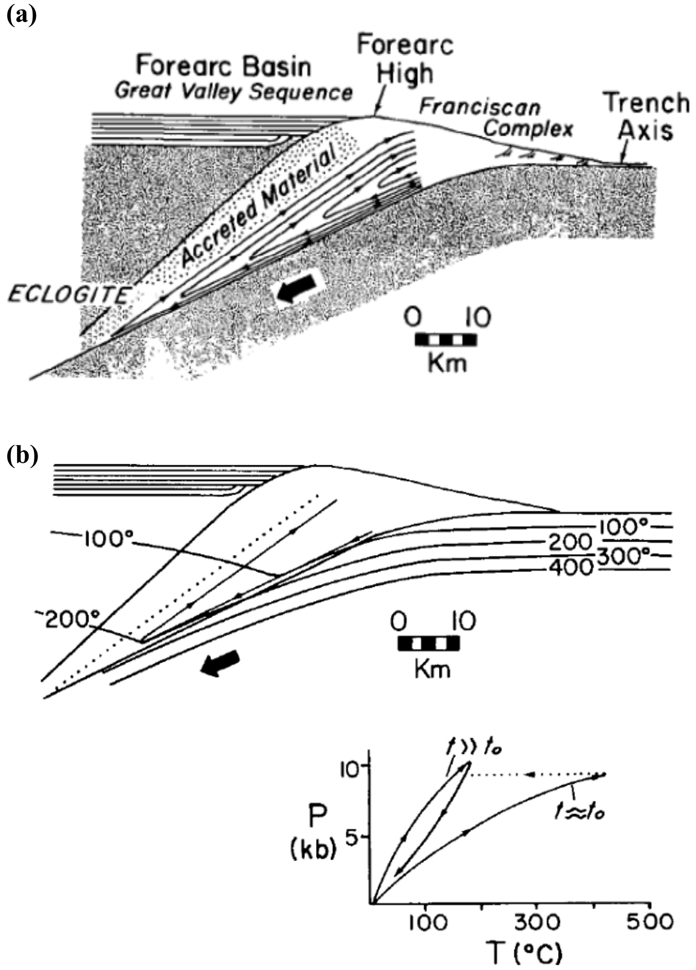

Figure 3-6. Mélange wedge laminar flow model of Cloos (1982). (a) Conceptual cross section of the mature (late Mesozoic) Franciscan mélange wedge showing flow paths of particles (blocks) in a low-angle corner model. (b) Schematic isotherms through the upper plate, mélange wedge, and subducting slab in the mature mélange wedge model. The near horizontal isotherms at the onset of subduction should evolve toward the model shown here. The *P-T* diagram illustrates hypothetical paths experienced by descending particles at the onset of subduction ($t \approx t_0$) and during the mature stages of subduction ($t \gg t_0$).

154.0 ±1.6 Ma from a sample near Healdsburg (Ward Creek, Wakabayashi & Dumitru, 2007) and between 150 and 160 Ma from a sample ~100 km to the southeast (Tiburon, Catlos & Sorensen, 2003), showing that heating of the eclogites ceased before 154 Ma. These ages provide an approximate heating and cooling cycle that spans about 10 Myr. Taking half of this cycle (5 Myr) as the heating duration and 500 °C as the approximate temperature of garnet growth, the heating rate is 100 °C Myr^{-1}. Using this heating rate, crystallization durations for garnet growth over the temperature interval of 100-125 °C gives an estimate of crystallization duration of around one million year.

Krogh et al. (1994) describe a series of reactions to account for the textural features and inclusions within the Jenner block, and Page et al. (2007) provide mineral assemblages for the Healdsburg samples. The mineral assemblage before garnet growth was likely epidote + Na-amphibole ± omphacite, and the eclogitic assemblage was garnet + omphacite ± phengite ± Na-amphibole. The simplified garnet-forming reaction used for both of the Franciscan eclogite samples in the model is Na-amphibole + epidote + quartz + albite = pyropic garnet + omphacitic pyroxene + H_2O.

Whitt Ranch. Samples WR1 and WR3 are retrogressed mafic eclogites (Carlson *et al.*, 2007) that formed during continental collision at the southern margin of Laurentia at 1150-1120 Ma (Mosher, 1998; Mosher *et al.*, 2008). The matrices of these eclogites are nearly completely retrogressed to amphibolite-facies assemblages, leaving only garnet and inclusions within garnet as evidence of the eclogite and pre-eclogite mineral suites. The inclusions within the cores of the garnet include quartz, andesine, epidote, tschermakitic amphibole, and ilmenite. The rims also host quartz, but contain no plagioclase or ilmenite, contain fewer inclusions of epidote and amphibole (pargasitic in the rim), and host rutile and omphacite (one instance identified).

Temperatures at the onset of garnet growth cannot be determined directly from thermometry but can be inferred from phase diagrams reported for amphibolite and eclogite rocks in the literature. In experimental determinations of the amphibolite-eclogite transformation in basaltic rocks, Poli (1993) shows the stability of garnet and omphacite at conditions of 550-650 °C and 1.3-1.4 GPa, consistent with the *P-T* conditions of the rims of the Whitt Ranch garnets, and the first appearance of garnet in their experiments is ~550-650 °C and 0.8-1.0 GPa (Fig. 3-7). Therefore the equilibrium *P-T* conditions used in this study for modeling are 575 °C and 0.9 GPa.

Garnet-amphibole and garnet-clinopyroxene inclusion thermometry in the rims of garnet yield ~610-690 °C as a minimum estimate of eclogite conditions, and considering that chemical zoning of the major cations in garnet is preserved, intracrystalline diffusivities were limited and suggest T_{rim} was probably ~650 °C (Carlson *et al.*, 2007). GRIPS inclusion barometry in regions approaching the garnet rims gives a pressure of 1.4 ± 0.1 GPa (Carlson *et al.*, 2007).

Without constraints on heating rate for these samples, an arbitrary rate of 10 °C Myr^{-1} was used for these samples. This rate, combined with the estimated T_{eq} and T_{rim}, suggests garnet crystallization duration of 7.5 Myr.

Based on the inclusion suites in the core and rim of the garnet, the reaction that grew garnet started with a mineral assemblage typical of an amphibolite and produced eclogite. Considering the compositions of the inclusions, the model reaction used to simulate crystallization in this sample is the same as in the Franciscan eclogites: Na-amphibole + epidote + quartz + albite = pyropic garnet + omphacitic pyroxene + H_2O.

Time-temperature-(free-energy difference) paths

In creating a t-T-$\Delta_r G$ path, the goal is to approximate the magnitude of the difference in free energy between the product assemblage and the reactant assemblage that persists metastably as pressure and temperature rise above the equilibrium *P-T* conditions of the reaction. The magnitude of $\Delta_r G$ is strongly dependent on the thermal overstepping and the entropy change for the reaction, which is larger in reactions that yield more extensive dehydration of hydrous phases (Fig. 3-8). This obviates the need to construct detailed model reactions that match the thermodynamic behavior of the minerals in the rock: as long as appropriate mineral phases are represented in the reaction, the choice of endmember compositions or particular solid solutions will not affect the magnitude of $\Delta_r G$ significantly (e.g., Fig. 3-8).

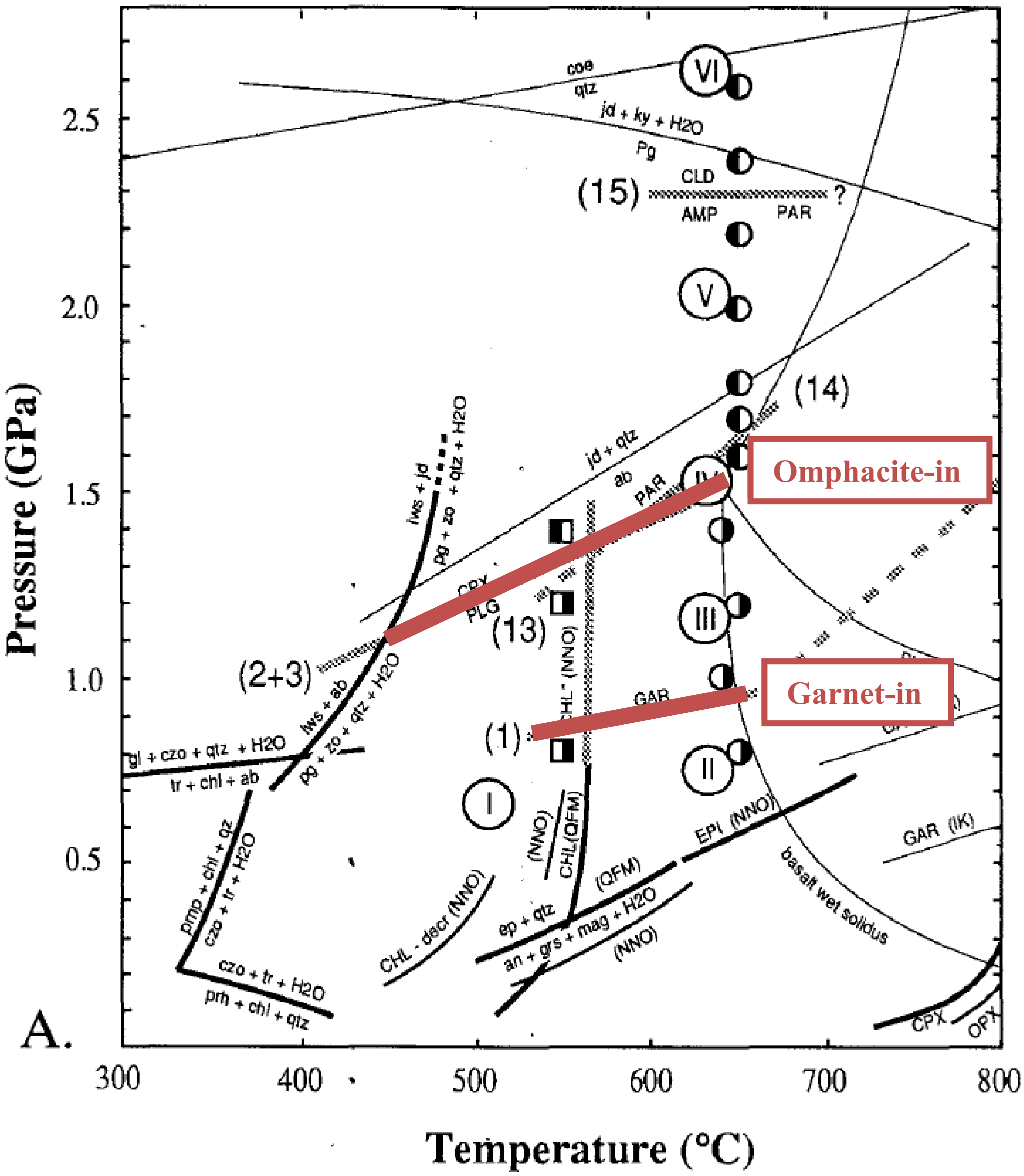

Figure 3-7. Phase diagram for mafic rocks. The garnet-in line and the appearance of omphacitic pyroxene are shown, and these provide estimates of the *P*-*T* conditions of garnet growth in the Whitt Ranch samples. Modified from Poli (1993).

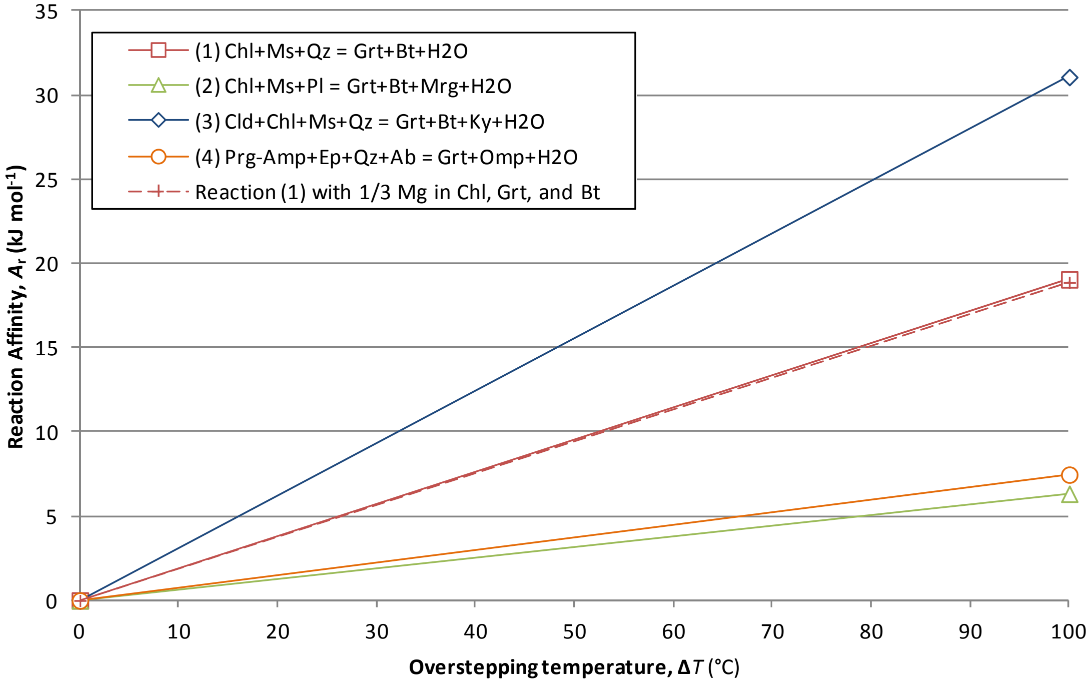

Figure 3-8. Reaction affinity ($-\Delta_r G$) as a function of thermal overstepping of the garnet-forming reaction (ΔT) for several reactions. Reactions that liberate larger proportions of H_2O have steeper slopes, reflecting the larger reaction entropies associated with more hydrous reactions as shown by Pattison and Tinkham (2009). Reaction (1) uses Fe end members. The dashed line was constructed from Reaction (1) using solid solutions of chlorite, garnet, and biotite that contain Mg/Fe in mole proportions of 1:2, which easily extends beyond the range of Fe/Mg of garnet in the rocks in which this reaction was applied. Addition of some Mg to the Fe end-member reaction increases the reaction affinity, at 100 °C of thermal overstepping, by only 0.2 kJ mol^{-1}. The reactions demonstrate that the correct choice of phases used in the reaction to represent the magnitude of reaction affinity for CRYSTALLIZE3D modeling outweighs the choice of solid solutions.

Dissolution of reactant phases in the model is dependent on $\Delta_r G$ at each step along the *P-T-t* path. The *P-T* path for each simulation was constructed from the pressure and temperature constraints discussed above. For all of the natural samples, the end of the heating path was determined by T_{rim} of garnet, mostly from thermometry. Without additional evidence to suggest that the heating path continued to higher temperatures, the heating paths all end by becoming isothermal at the temperature of T_{rim} (e.g., Fig. 3-3).

The values of $\Delta_r G$ for each model reaction were calculated along the *P-T-t* path using thermodynamic data from the Holland and Powell (1998) dataset with supplemental data from Holland and Powell (1990) as described in Appendix B. By minimizing the free energy of the simplified model phases ($\Delta_r G = 0$), a pressure and temperature of equilibrium for the model reaction was found. However, the simplified compositions of the model phases produce equilibrium *P-T* conditions that do not necessarily correspond with the equilibrium *P-T* conditions determined from the natural samples. Then again, $\Delta_r G$ depends primarily on the magnitude of the *P-T* overstepping of a reaction, which is well-approximated by the model reactions used here, so $\Delta_r G$ along the *P-T-t* path was determined using the magnitudes of the temperature and pressure changes from the natural samples applied to the model reaction. The full model reactions and the corresponding *t-T*-$\Delta_r G$ paths are given in Tables 3-2 and 3-3.

Parameters related to intergranular diffusive fluxes

Aluminum solubility. The solubility of Al in metamorphic fluids depends on pressure, temperature, and the fluid's pH and chemistry. The pH of a fluid has a strong effect on Al solubility, but in the case of a metamorphic fluid in the presence of feldspars and white mica, the pH of the fluid is expected to remain close to neutral and have a minor effect on the Al solubility (Beitter *et al.*, 2008). Using the experimental results of Marshall and Franck (1981), Beitter et al. (2008) calculated a pH of 4.4 for pure H_2O under amphibolite-facies conditions (500 °C and 0.5 GPa). At this pH, Al solubility is enhanced only slightly in a KOH fluid (~10^{-8} mol cm^{-3} at 500°C and 0.5

GPa) (Wohlers & Manning, 2009), and the more dominant control on Al solubility is the presence of NaCl (~10^{-6} mol cm^{-3} at 500°C and 0.5 GPa) (Beitter *et al.*, 2008; Newton & Manning, 2008).

In this study, the experimental results of Tropper and Manning (2007) and Newton and Manning (2008) were used to estimate the Al solubility in each sample. Tropper and Manning (2007) used a piston-cylinder apparatus and weight-loss methods to derive an empirical model for corundum solubility in pure H_2O over a range of *P-T* conditions (700-1100 °C and 0.5-2.0 GPa). In order to extend this work toward more realistic metamorphic fluid compositions, Newton and Manning (2008) examined corundum solubility in $NaCl$-SiO_2-H_2O fluid at 800 °C and 1.0 GPa over varying X_{NaCl} fluid conditions. In metamorphic fluids at these conditions, X_{NaCl} is expected to be approximately 0.1, and should produce Al concentrations of about 4 x 10^{-5} mol cm^{-3} (Newton & Manning, 2008), which is 1.2 orders of magnitude higher than the Al solubility given by the Tropper and Manning (2007) model in the case of pure H_2O at 800 °C and 1.0 GPa. By increasing the values from the pure H_2O model by 1.2 orders of magnitude, estimates of Al solubility were made for the *P-T* conditions of the rocks in the current study (Fig. 3-9, Table 3-2). The estimates were made using the *P-T* conditions midway through garnet growth.

Confirmation of the validity of this approach comes from a geochemical modeling study to determine the Al solubility associated with quartz-kyanite veins that formed during amphibolite-facies metamorphism in metapelitic host rocks, in which Beitter et al. (2008) estimated Al solubility at 500-600 °C and 0.5 GPa. Their determinations are less than a factor of two larger than those made in this study (Fig. 3-9).

Diffusion constant k_3. The intergranular diffusivity constant k_3 is the mathematical product of the pre-exponential constant for intergranular diffusivity D_∞, the interconnected porosity ϕ, and the tortuosity τ. It is the value of k_3 that is determined in the model fits, but if ϕ and τ can be adequately constrained, a value for D_∞ can be estimated.

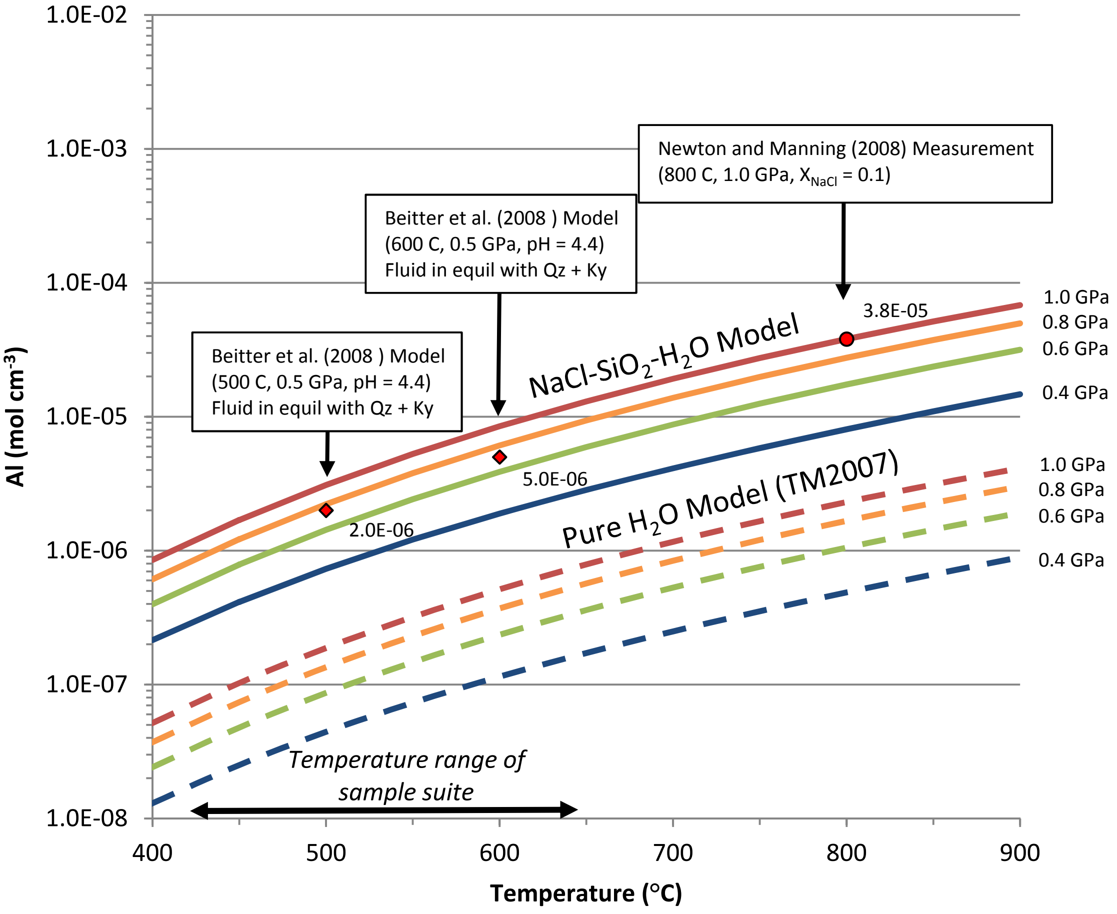

Figure 3-9. Aluminum solubility extrapolated from Tropper and Manning (2007) and Newton and Manning (2008). Tropper and Manning (2007) [dashed lines] determined corundum solubility in pure H_2O fluid, and Newton and Manning (2008) [solid lines] determined corundum solubility for NaCl-SiO_2-H_2O fluids; their estimates at 0.1 X_{NaCl} were used in this study to extrapolate the pure H_2O model. Estimates of Al concentration shown from Beitter et al. (2008) for pressure of 0.5 GPa are derived from geochemical modeling of vein fluids that appear to have been associated with amphibolite-facies metamorphism of metapelitic assemblages including garnet and staurolite.

Estimates of ϕ in metamorphic rocks are 10^{-6}-10^{-4} (Bickle & Baker, 1990; Ferry & Dipple, 1991; Farver & Yund, 1992) and scale with the inverse square of grain diameter (Carlson & Gordon, 2004). At a magnitude of 10^{-4}, fluid transport is along cracks rather than interconnected porosity (Bickle & Baker, 1990), so values of 10^{-6}-10^{-5} are more reasonable for metamorphic rocks. Because the eclogite samples (Franciscan and Whitt Ranch) have recrystallized matrices, grain size could not be measured but was inferred assuming larger grain size with increasing *T*. The inverse square of average matrix grain sizes in these samples (Table 3-2) ranges by three orders of magnitude, which is larger than the expected range of ϕ. Therefore, samples in this study were assigned a ϕ in the range 10^{-6}-10^{-5} based roughly on the trend of matrix grain sizes (Table 3-2).

Tortuosity τ is defined as L/L_a where L is the linear distance between two points, and L_a is the actual path distance of the diffusing species along interconnected grain boundaries, which depends on grain size and shape (Bear, 1988). Reported values of τ in porous materials fall in the range 0.5-0.8 (Bear, 1988, p. 111; Lindquist *et al.*, 1996), and because the values are close to 1.0, they will only decrease diffusive fluxes slightly (Brady, 1983). Therefore, the uncertainties for other parameters (e.g., ϕ) are much larger than for τ, so a value of 1.0 was used in the modeling.

Activation energy for intergranular diffusion. The initial estimate of Q_D for Al comes from Carlson et al. (1995), who used a similar model with a different formulation for nucleation rate to simulate crystallization and match porphyroblastic textures to natural samples. The estimate was revised by Carlson (2010), who reported a value of 136 ± 35 kJ mol^{-1}. Cations with similar size and charge should share a similar Q_D (Farver & Yund, 1995, p. 353), and thus an estimate of Q_D of Al can also be made from values determined for Si (e.g., Carlson, 2002, p. 195). Experimental work by Farver and Yund (2000) on Si intergranular diffusivity in a quartz aggregate under hydrothermal conditions constrained Q_D of Si to 137 ± 18 kJ mol^{-1}. For simplicity, these prior estimates were rounded up to produce a provisional value of 140 kJ mol^{-1} for the initial modeling.

Evidence for nearly simultaneous nucleation at Passo del Sole

Nucleation in sample AG4 was nearly simultaneous for all crystals, as described by Meth and Carlson (2005), who demonstrated that in AG4, chemical zoning patterns are nearly the same in garnets of all sizes. They showed that a major Ca spike correlates with the location of sigmoidal inclusion trails in all garnets, demonstrating that a single event in time (assuming deformation was pervasive) is correlated with the chemical zoning regardless of garnet size. They further demonstrated that average garnet composition at several Ca spikes along the radius of the garnets correlates rock wide. The rapid and limited nucleation in this sample can be explained by saturation of a limited number of nucleation sites.

The evidence from this sample suggests that the nucleation window was short, and estimates of the volume of garnet for the last crystals to nucleate (those that are missing a small portion of the zoning pattern) suggest that nucleation had finished when 6-15% of the garnet mode had grown. To account for this in the numerical simulations, the number of nucleation events in the simulation was capped at a value that would produce 6-15% of the garnet mode when the last crystal nucleated.

Additional input parameters related to numerical-simulation procedures

To reduce bias and artifacts from the model while considering computational limitations, additional parameters need to be determined. To maintain robust statistical measures of nucleation and growth suppression, the number of crystals in a model is ideally on the order of 1000, but the modeling volumes needed to produce this many crystals tend to require considerable numbers of calculations at each time step, which slows the processing time of the simulation. In general, ~1000 crystals in a model volume will produce more precise results and allow crystals near the boundaries of the model to be removed to avoid boundary effects, without affecting precision. Considering that each natural rock contains a different crystal number density, and that each model will require a unique volume to contain 1000 crystals, the volume of each model space was calculated by dividing 1000 crystals by the crystal number density of the natural sample to yield volume. When the crystal number density of the simulation matches that of the natural sample, the simulation will contain roughly 1000 crystals.

Once the volume of the model is determined, the number of voxels and the size of each voxel needed to create this volume also must be determined. If a substantial number (e.g., $>10^6$) of small voxels is used (fine grid spacing), the number of calculations at each time step can result in long calculation times. Crystals nucleate at the center of a voxel, so if the number of voxels is small and the size of each voxel is large (coarse grid spacing), the voxels can induce artificial ordering of crystal centers that becomes convolved with the effects of ordering controlled by concentration gradients surrounding crystals (Fig. 1-2). Therefore, the edge length of a voxel was chosen to be smaller than the radius of the smallest crystal in the natural sample (excluding outliers), and the number of voxels necessary to create the volume described above was calculated from the voxel size.

An additional effect of the discretization of the model is that k_3 could be poorly constrained if the amount of Al in the fluid rises too high. Computational instability is possible if either D or the size of the time step is too large compared to the voxel edge length. If Al travels over distances ($\sqrt{D\Delta t}$) that exceed the distance across a voxel (Δx) in one time step, then some voxels can be skipped and deficits in Al concentration can build up. To avoid this, a Courant condition is monitored:

$$\frac{D\Delta t}{(\Delta x)^2} \leq 1, \qquad (3\text{-}1)$$

and $D\Delta t$ is kept near or below a maximum equal to $(\Delta x)^2$. To speed up model runs while avoiding instability, large time steps can be used in exploratory runs if values of k_3 (the mathematical product of D_∞, ϕ, and τ) are constructed by using low values for D_∞, which keep D low, compensated by (unrealistically) large values of ϕ. However, this causes large amounts of Al to be stored in the intergranular fluid, which affects the textural evolution. More Al in the intergranular fluid increases nucleation probability near existing crystals and thus raises nucleation rates slightly. Through experience with the model, it was found that the amount of Al in the intergranular fluid must be kept below 10-20% of the total Al in the system. If this was maintained, preliminary runs with large time steps carried out to estimate k_1 and k_3 values that are close to the final values, yielded final runs with smaller time steps in which no adjustment to k_1 and k_3 was needed, demonstrating that the parameters converge on realistic values with smaller time steps.

MODEL SENSITIVITY

By modeling DCNG to produce porphyroblastic textures that fit the textures measured in the natural samples, the kinetic parameters used to adjust the model (k_1, k_2, and k_3) can be determined. This section describes an initial exploration of the sensitivity of the model to these parameters to give estimates of their uncertainties, and then describes an optimal fitting procedure that is needed to achieve the uncertainties described.

One of the goals in this work is to determine values characterizing the kinetics of nucleation and diffusion that are difficult or impossible to measure at laboratory time scales, namely interfacial energy (γ), the activation energy for intergranular diffusion of Al (Q_D), and the pre-exponential constant for intergranular diffusion of Al (D_∞). However, an important discovery from this work is that other parameters must be understood and quantified to a greater extent than they are now in order to put tight brackets on the kinetic values. The parameter k_3 is the mathematical product of D_∞, porosity, and tortuosity, and is used to adjust diffusive flux, which also depends on Al solubility. As described above, our knowledge of porosity has a range of 2-3 orders of magnitude, which directly contributes to the uncertainty of D_∞. Likewise, Al solubility was extrapolated from experimental work in ideal systems, and may contribute to a large uncertainty in an estimate of D_∞. These concepts will be discussed further below.

Exploratory sensitivity analysis

The purpose of modeling DCNG of regionally metamorphosed rocks is partly to extract unknown parameters of nucleation and growth kinetics. Toward this end, an estimate of the uncertainty in the extracted values must be made, and in a model with several unknown parameters, an efficient method is to perform a sensitivity analysis. However, in a model with as many parameters as this one — and in which many parameters are strongly cross-correlated with one another — proper sensitivity analysis is a complex problem. A complete analysis lies beyond the present scope of this study, but an exploratory analysis provides some broad constraints on the uncertainties in estimates of the various kinetic parameters.

Considering that more than one model can produce an acceptable fit to the texture of a natural sample, one approach to estimating uncertainties in derived parameters is to vary the model inputs to determine how far they can be adjusted and still produce an equivalent model within the existing constraints. To do this, a model is fit to the natural texture and then one parameter is changed by progressively greater amounts while holding the others constant. After each change, a second parameter is adjusted in an attempt to create an equally satisfying fit to the natural texture. When changes made to the first parameter become so large that they cannot be compensated by adjustments to the second parameter, it is concluded that the first parameter is at the limit of its acceptable range of values. This procedure has been performed on the heating rate (dT/dt), the activation energy for intergranular diffusion of Al (Q_D), and the unknown parameters (k_1, k_2, and k_3) that are used to fit the simulated texture to the natural texture.

Sample PM1 was used to perform the analysis because it is a rock that has undergone a relatively simple crystallization history in a simple bulk composition, and therefore the effects of additional uncertainties on the analysis are small.

Co-variation of k_1 and k_3

The steady-state nucleation rate (k_1) is the rate at infinite thermal overstepping and maximum reaction affinity. With increasing temperature and supersaturation of Al, the nucleation rate increases toward the steady-state value, producing a higher crystal number density. At higher crystal number densities, the distance between crystals is smaller, and growth competition between neighboring crystals is more intense, producing smaller crystal sizes. Higher crystal number density also reduces the crystallization duration, because Al travels over a shorter distance and therefore the amount of time needed to transport Al between reactants and products is smaller.

Modifications to the porphyroblastic texture from changes in k_1 can be balanced by adjustments to k_3, which affects the magnitude of the diffusivity, and therefore the diffusivity of Al between the reactants and products. Larger values of k_3 produce longer length scales of diffusion and wider concentration gradients that reach farther into the surrounding matrix (Fig. 3-10). The supersaturation of Al in the intergranular fluid at a given distance from a porphyroblast will decrease if the length scale of diffusion is increased, so the probability of nucleation in a larger portion of the simulation volume is decreased and fewer crystals nucleate. Because each crystal has access to a larger volume of reactant material through longer length scales of diffusion, the crystals grow larger. In addition, more rapid Al transport increases the rate of growth, so the duration of crystallization decreases. Concomitant increases in k_1 and k_3, therefore, can produce similar porphyroblastic textures, but over different time scales.

Although the model is capable of producing crystallization durations as short as 1-2 Myr (large k_1 and k_3) or as long as 40 or more Myr (small k_1 and k_3), both durations are probably outside the limits for the samples in this study considering that garnet growth has been estimated on the scale of ~3-40 Myr in several localities (e.g., Vance & O'Nions, 1992; Hoisch *et al.*, 2008; Skora *et al.*, 2009; Pollington & Baxter, 2010) and durations outside of this range are likely to be rare. Unfortunately, crystallization durations in these samples are determined from rough estimates of heating rates, so the durations are not a constraint on the modeling, except perhaps as a measure of consistency in employing the estimated heating rates over the temperature ranges given by core and rim garnet temperatures. For example, if the heating rate is 10 °C Myr^{-1} and the temperature difference between core and rim of garnet is 100 °C, then the simulation should finish after roughly 10 Myr or more.

The resulting simulations from the sensitivity analysis for k_1 and k_3 are shown in Figures 3-11 to 3-13. Correlations among crystal size and isolation (described in the previous chapter) do not vary significantly between the simulations, demonstrating that

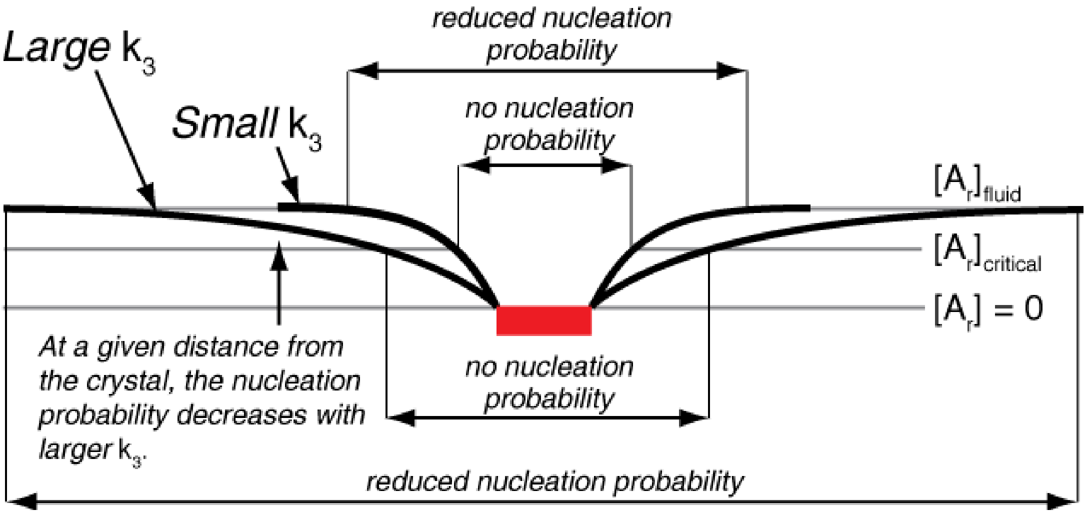

Figure 3-10. Effect of diffusivity on nucleation probability surrounding an existing porphyroblast. The magnitude of diffusivity is adjusted by changing k_3. Larger k_3 produces longer length scales of diffusion that deplete more of the surrounding matrix of Al. Reaction affinity (A_r), and therefore nucleation probability, between the reactants and products scales with the magnitude of the Al concentration, so larger k_3 creates larger volumes surrounding existing crystals with a lower probability of nucleation. Nucleation rate, therefore, decreases when k_3 increases, so increases in the crystal number density produced by increases in the steady-state nucleation rate k_1 can be offset with increases in k_3. Modified from Carlson (1989).

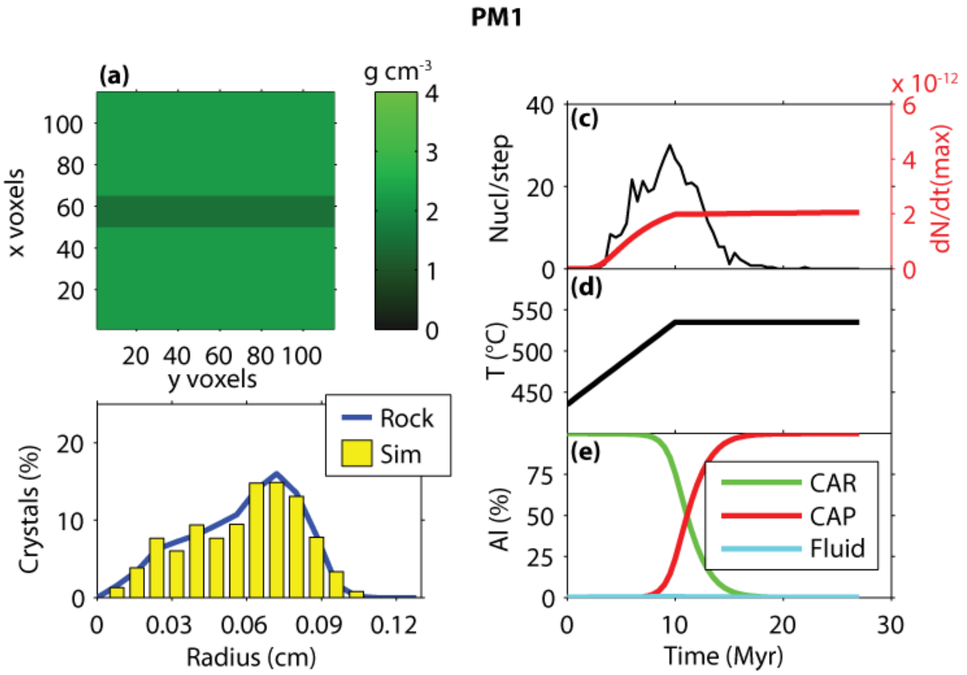

Selected model parameters			
Steady-state nucleation rate	k_1	2.7E-12	nuclei cm^{-3} s^{-1}
Nucleation acceleration	k_2	1.0	
Diffusive flux constant	k_3	1.5E-8	m^2 s^{-1}
Activation energy	Q_D	140	kJ mol^{-1}

Figure 3-11. Results from the sensitivity analysis of the co-variation of k_1 and k_3. (a) Initial distribution of the reactants. In this model, two layers of Al-bearing reactants were used with a layer of Al-poor reactants between. (b) Comparison of the crystal-size distribution between the rock and simulation. (c) Number of nuclei per time step (black curve, nuclei per 0.5 Myr per cm^3) and the maximum nucleation rate (red curve, nuclei cm^{-3} s^{-1}). (d) Extent of the prescribed heating path attained in the simulation. (e) Percentage of Al in the system (mole %) for the reactant assemblage (CAR), the product assemblage (CAP), and the intergranular fluid. The amount of Al in the CAP serves as a proxy for the duration of crystallization when viewing these figures.

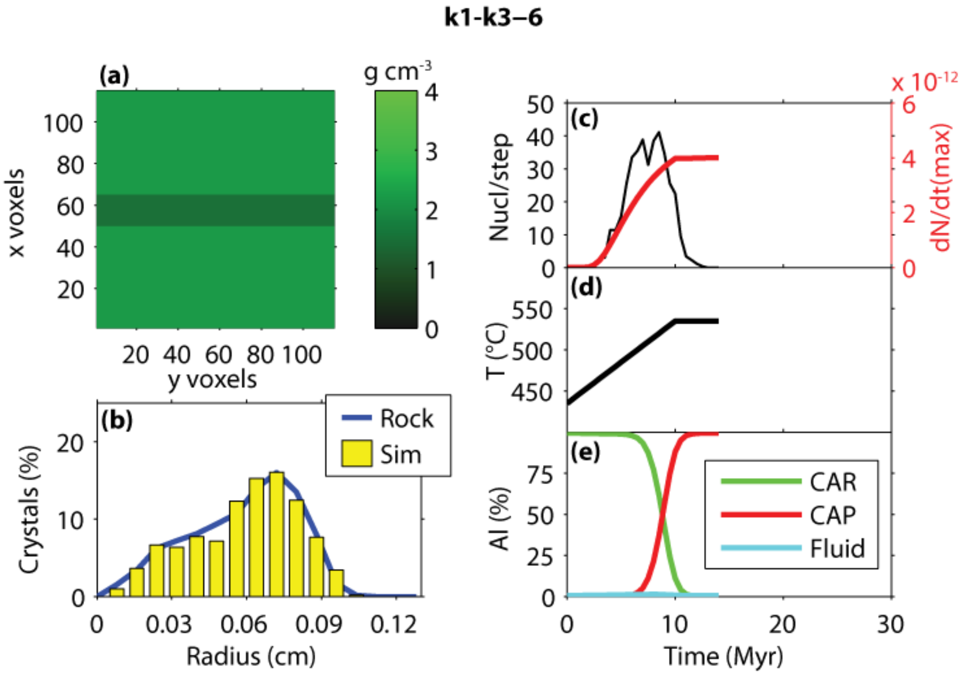

Selected model parameters			
Steady-state nucleation rate	k_1	5.4E-12	nuclei cm^{-3} s^{-1}
Nucleation acceleration	k_2	1.0	
Diffusive flux constant	k_3	4.0E-8	m^2 s^{-1}
Activation energy	Q_D	140	kJ mol^{-1}

Figure 3-12. Results from the sensitivity analysis of the co-variation of k_1 and k_3. (a) Initial distribution of the reactants. In this model, two layers of Al-bearing reactants were used with a layer of Al-poor reactants between. (b) Comparison of the crystal-size distribution between the rock and simulation. (c) Number of nuclei per time step (black curve, nuclei per 0.5 Myr per cm^3) and the maximum nucleation rate (red curve, nuclei cm^{-3} s^{-1}). (d) Extent of the prescribed heating path attained in the simulation. (e) Percentage of Al in the system (mole %) for the reactant assemblage (CAR), the product assemblage (CAP), and the intergranular fluid. The amount of Al in the CAP serves as a proxy for the duration of crystallization when viewing these figures.

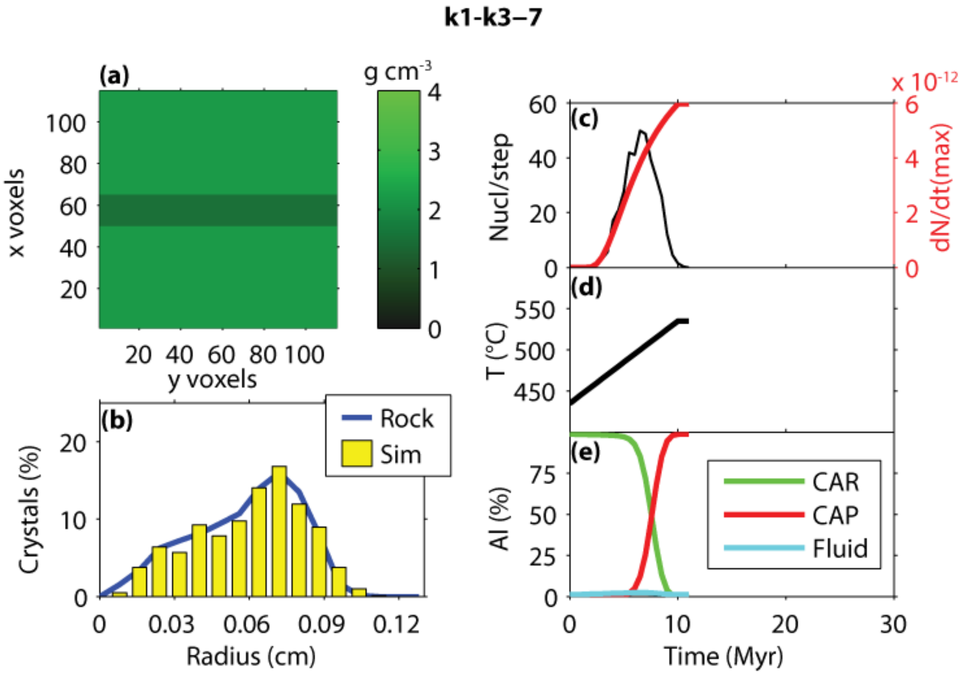

Selected model parameters			
Steady-state nucleation rate	k_1	8.1E-12	nuclei cm^{-3} s^{-1}
Nucleation acceleration	k_2	1.0	
Diffusive flux constant	k_3	8.0E-8	m^2 s^{-1}
Activation energy	Q_D	140	kJ mol^{-1}

Figure 3-13. Results from the sensitivity analysis of the co-variation of k_1 and k_3. (a) Initial distribution of the reactants. In this model, two layers of Al-bearing reactants were used with a layer of Al-poor reactants between. (b) Comparison of the crystal-size distribution between the rock and simulation. (c) Number of nuclei per time step (black curve, nuclei per 0.5 Myr per cm^3) and the maximum nucleation rate (red curve, nuclei cm^{-3} s^{-1}). (d) Extent of the prescribed heating path attained in the simulation. (e) Percentage of Al in the system (mole %) for the reactant assemblage (CAR), the product assemblage (CAP), and the intergranular fluid. The amount of Al in the CAP serves as a proxy for the duration of crystallization when viewing these figures.

other characteristics are more sensitive to the magnitudes of adjustments in k_1 and k_3, so the other characteristics are examined here. In each of the simulations, the nucleation density was matched to the natural sample, but other characteristics depart from those of the natural sample. With increasing k_1 and k_3, the duration decreases, in this case from 12 to 6.5 Myr. Although duration is not a firm constraint on the simulation, another consequence of increased k_1 and k_3 related to duration is that the final temperature of the crystallization simulation can decrease below the accepted temperature of the garnet rim. As duration decreases, the final temperature of crystallization tends to decrease because the crystallization event does not extend as far along the heating path. In the example shown here, the shorter duration is not enough to end crystallization before the simulation achieves the isothermal portion of the T-t path so there is no decrease in T_{rim}.

The sensitivity analysis for the co-variation of k_1 and k_3 on models for sample PM1 demonstrates the potential uncertainty of these values. An increase in k_1 by a factor of three will require a concomitant increase in k_3 by a factor of about five to maintain the nucleation density of the simulation (Fig. 3-14). Further constraints from well-determined modeling parameters, like heating rates and crystallization durations, would improve upon the uncertainty in k_1 and k_3. Alternatively, improved estimates of Al solubility and porosity would decrease uncertainty in k_1 and k_3, and these values could provide estimates of heating rates and durations.

Co-variation of k_2 and k_1

The nucleation acceleration factor k_2 (Equation 2-13) controls the rate at which the nucleation rate rises toward the steady-state (Fig. 2-4). The value of k_2 reflects the energetic barriers to creating a nucleus and depends, in part, on the shape and interfacial energy of a critically sized cluster of atoms (or molecules). Adjustments to k_2 are meant to account for the differences between nucleation sites in rocks with different mineralogy and fluid compositions that may aid or impede nucleation. If k_2 is large, nucleation is difficult and the nucleation rate increases slowly with increasing temperature.

Because k_2 can increase or decrease the rapidity with which the maximum rate is achieved in the model, a complementary parameter used to counteract the effects of k_2

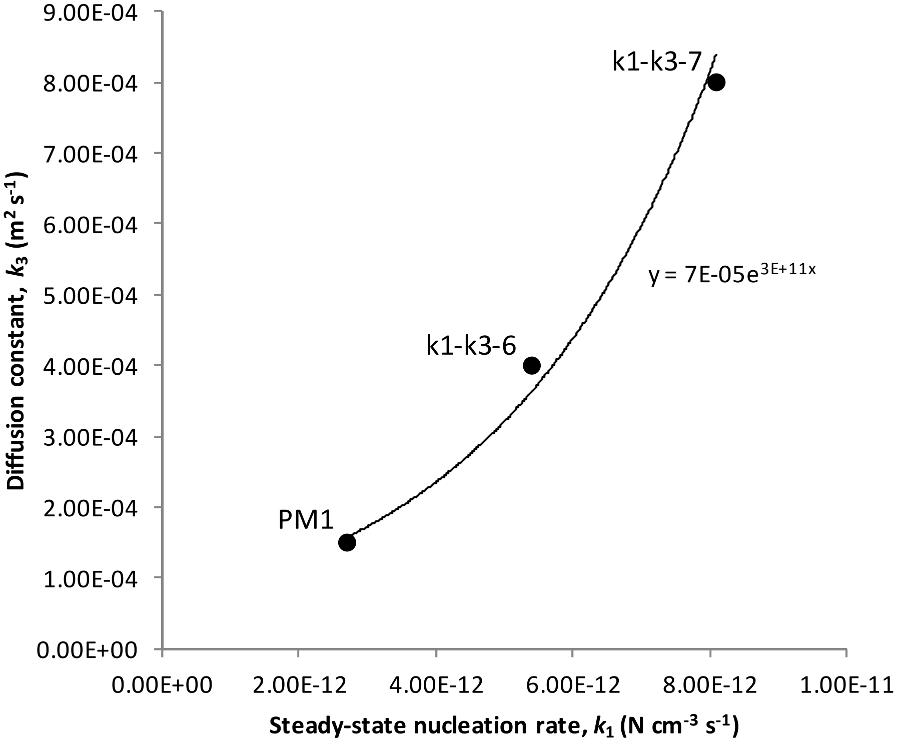

Figure 3-14. Summary of the co-variation of k_1 and k_3. The curve represents constant nucleation density. An increase in k_1 by a factor of three requires an increase in k_3 by a factor of approximately five to maintain the nucleation density.

is k_1. Larger values of k_2 cause later nucleation at higher temperatures when the diffusive flux is larger (commonly maximized) and the length scales of the concentration gradients are long (Fig. 3-10). Therefore, overall nucleation probabilities are reduced because a larger portion of the simulation volume has a supersaturation that is less than the maximum. To reduce this effect (small crystal number density), k_1 is increased (larger crystal number density). Adjustments to both k_2 and k_1 can produce similar textures (Figs. 3-15 to 3-20).

The effects of adjustments to k_2 are manifested in the magnitude of thermal overstepping, the CSD, and the degree of crystal ordering. Thermal overstepping is the magnitude of the temperature interval between the equilibrium temperature of the reaction and the temperature of nucleation of a crystal. For large values of k_2, nucleation is less favorable energetically, and the first few crystals to nucleate do so at higher temperatures, producing larger values of thermal overstepping. Comparing simulations k1-k2-3 and k1-k2-7, the first few crystals nucleate, respectively, at about 436 °C, corresponding with one degree of thermal overstepping, and 497 °C, corresponding with 62 degrees of thermal overstepping. Therefore smaller values of k_2 result in smaller overstepping values.

Patterns of late nucleation are also noticeably affected by k_2. Again, simulations k1-k2-3 and k1-k2-7 (Figures 3-15 and 3-20) serve as examples for this discussion. The last crystals to nucleate in a simulation (or a rock) are generally those that grow to the smallest sizes (the left side of a CSD). If k_2 is large (slow acceleration shown in red nucleation rate curve), crystals nucleate later along the heating path at higher temperatures and diffusive fluxes, as shown by the number of nuclei per time step given by the black curve in the nucleation rate plots. For small k_2 (Simulation k1-k2-3), crystals nucleate immediately and nucleation continues until the latest stages of crystallization. In simulation k1-k2-7, nucleation begins at higher temperature and occurs over a more restricted interval because higher temperatures create greater reaction affinities that increase nucleation probability. Therefore, with larger k_2 values (less rapid acceleration) the last crystals to nucleate actually appear earlier in the crystallization interval than in

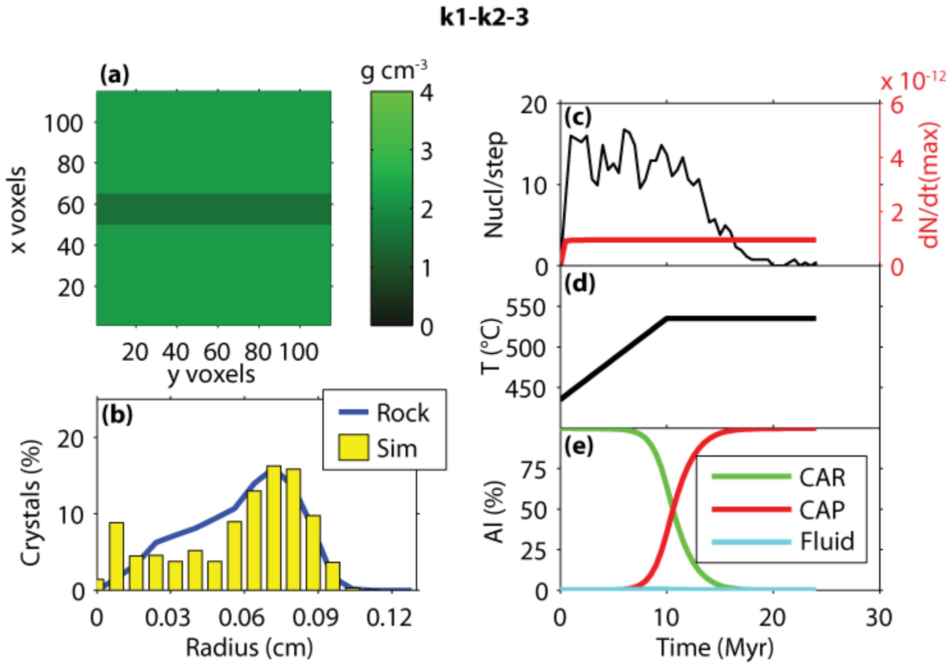

Selected model parameters

Steady-state nucleation rate	k_1	9.5E-13	nuclei cm^{-3} s^{-1}
Nucleation acceleration	k_2	0.001	
Diffusive flux constant	k_3	1.5E-8	m^2 s^{-1}
Activation energy	Q_D	140	kJ mol^{-1}

Figure 3-15. Results from the sensitivity analysis of the co-variation of k_2 and k_1. (a) Initial distribution of the reactants. In this model, two layers of Al-bearing reactants were used with a layer of Al-poor reactants between. (b) Comparison of the crystal-size distribution between the rock and simulation. (c) Number of nuclei per time step (black curve, nuclei per 0.5 Myr per cm^3) and the maximum nucleation rate (red curve, nuclei cm^{-3} s^{-1}). (d) Extent of the prescribed heating path attained in the simulation. (e) Percentage of Al in the system (mole %) for the reactant assemblage (CAR), the product assemblage (CAP), and the intergranular fluid. The amount of Al in the CAP serves as a proxy for the duration of crystallization when viewing these figures.

k1-k2-4

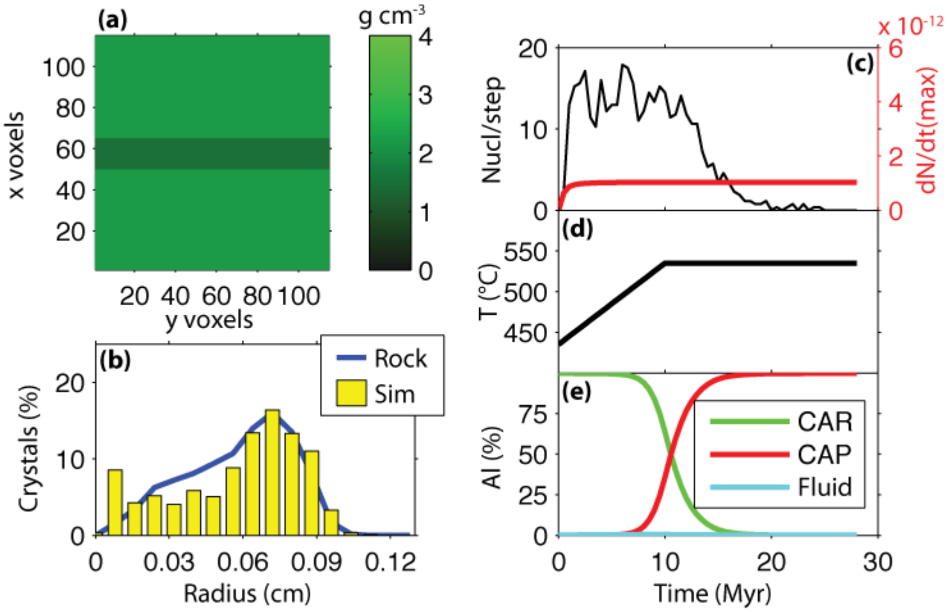

Selected model parameters			
Steady-state nucleation rate	k_1	1.03E-12	nuclei cm^{-3} s^{-1}
Nucleation acceleration	k_2	0.01	
Diffusive flux constant	k_3	1.5E-8	m^2 s^{-1}
Activation energy	Q_D	140	kJ mol^{-1}

Figure 3-16. Results from the sensitivity analysis of the co-variation of k_2 and k_1. (a) Initial distribution of the reactants. In this model, two layers of Al-bearing reactants were used with a layer of Al-poor reactants between. (b) Comparison of the crystal-size distribution between the rock and simulation. (c) Number of nuclei per time step (black curve, nuclei per 0.5 Myr per cm^3) and the maximum nucleation rate (red curve, nuclei cm^{-3} s^{-1}). (d) Extent of the prescribed heating path attained in the simulation. (e) Percentage of Al in the system (mole %) for the reactant assemblage (CAR), the product assemblage (CAP), and the intergranular fluid. The amount of Al in the CAP serves as a proxy for the duration of crystallization when viewing these figures.

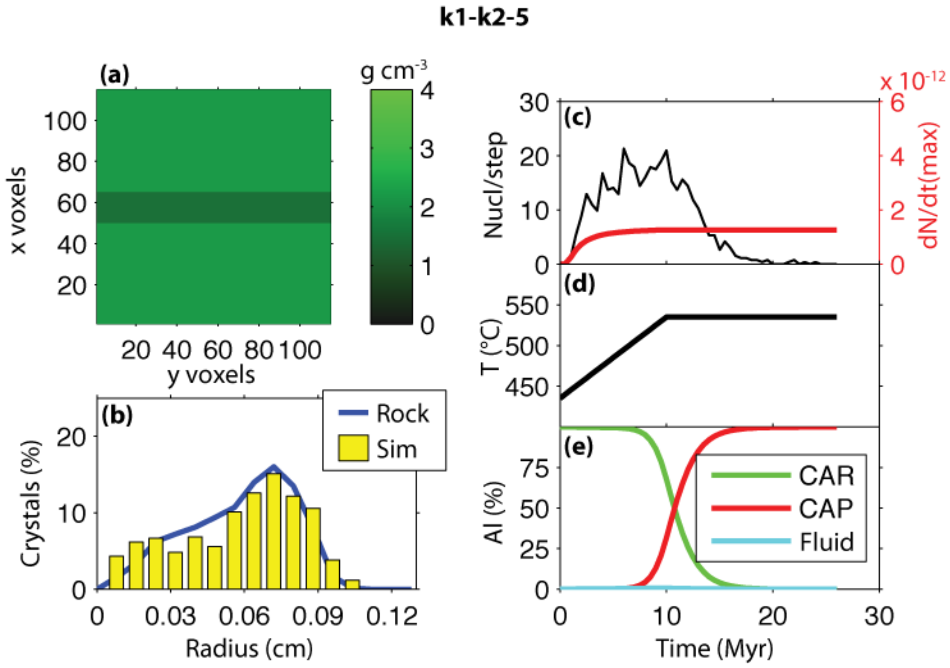

Selected model parameters

Steady-state nucleation rate	k_1	1.3E-12	nuclei cm^{-3} s^{-1}
Nucleation acceleration	k_2	0.1	
Diffusive flux constant	k_3	1.5E-8	m^2 s^{-1}
Activation energy	Q_D	140	kJ mol^{-1}

Figure 3-17. Results from the sensitivity analysis of the co-variation of k_2 and k_1. (a) Initial distribution of the reactants. In this model, two layers of Al-bearing reactants were used with a layer of Al-poor reactants between. (b) Comparison of the crystal-size distribution between the rock and simulation. (c) Number of nuclei per time step (black curve, nuclei per 0.5 Myr per cm^3) and the maximum nucleation rate (red curve, nuclei cm^{-3} s^{-1}). (d) Extent of the prescribed heating path attained in the simulation. (e) Percentage of Al in the system (mole %) for the reactant assemblage (CAR), the product assemblage (CAP), and the intergranular fluid. The amount of Al in the CAP serves as a proxy for the duration of crystallization when viewing these figures.

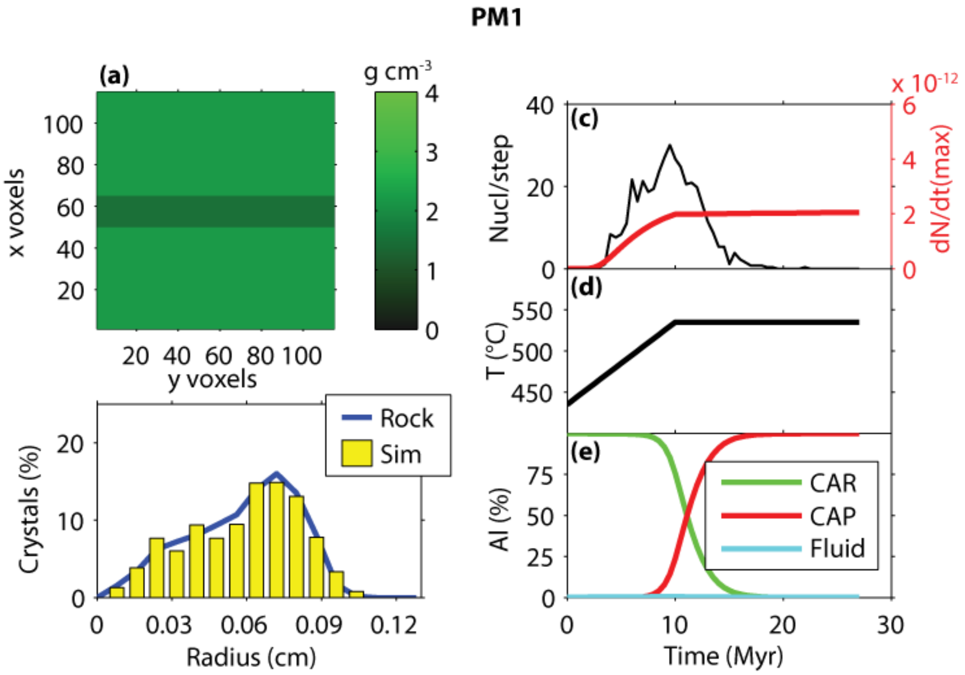

Selected model parameters

Steady-state nucleation rate	k_1	2.7E-12	nuclei cm^{-3} s^{-1}
Nucleation acceleration	k_2	1.0	
Diffusive flux constant	k_3	1.5E-8	m^2 s^{-1}
Activation energy	Q_D	140	kJ mol^{-1}

Figure 3-18. Results from the sensitivity analysis of the co-variation of k_1 and k_3. (a) Initial distribution of the reactants. In this model, two layers of Al-bearing reactants were used with a layer of Al-poor reactants between. (b) Comparison of the crystal-size distribution between the rock and simulation. (c) Number of nuclei per time step (black curve, nuclei per 0.5 Myr per cm^3) and the maximum nucleation rate (red curve, nuclei cm^{-3} s^{-1}). (d) Extent of the prescribed heating path attained in the simulation. (e) Percentage of Al in the system (mole %) for the reactant assemblage (CAR), the product assemblage (CAP), and the intergranular fluid. The amount of Al in the CAP serves as a proxy for the duration of crystallization when viewing these figures.

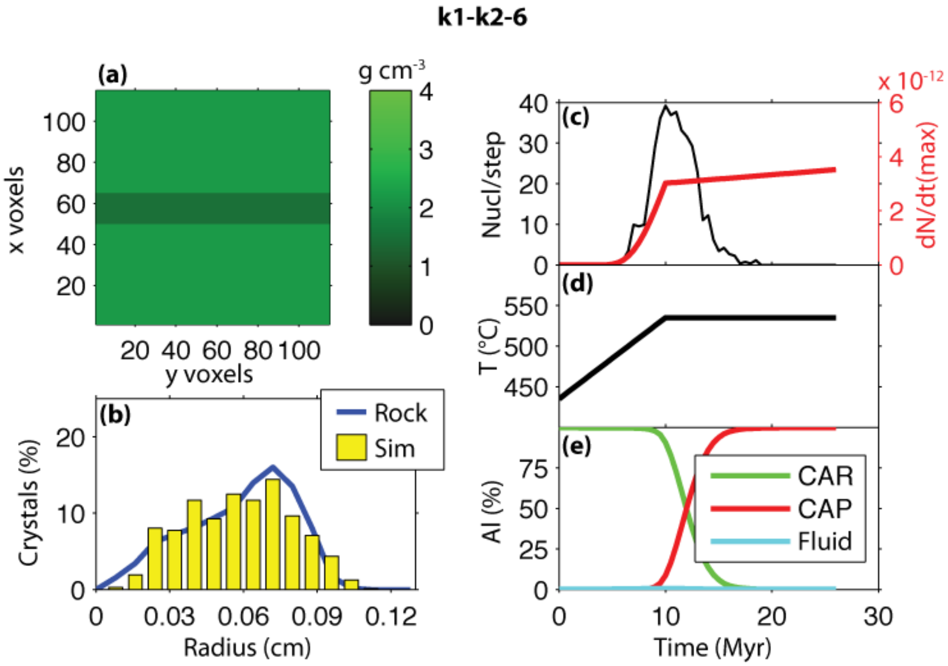

Selected model parameters			
Steady-state nucleation rate	k_1	1.4E-11	nuclei cm^{-3} s^{-1}
Nucleation acceleration	k_2	5	
Diffusive flux constant	k_3	1.5E-8	m^2 s^{-1}
Activation energy	Q_D	140	kJ mol^{-1}

Figure 3-19. Results from the sensitivity analysis of the co-variation of k_2 and k_1. (a) Initial distribution of the reactants. In this model, two layers of Al-bearing reactants were used with a layer of Al-poor reactants between. (b) Comparison of the crystal-size distribution between the rock and simulation. (c) Number of nuclei per time step (black curve, nuclei per 0.5 Myr per cm^3) and the maximum nucleation rate (red curve, nuclei cm^{-3} s^{-1}). (d) Extent of the prescribed heating path attained in the simulation. (e) Percentage of Al in the system (mole %) for the reactant assemblage (CAR), the product assemblage (CAP), and the intergranular fluid. The amount of Al in the CAP serves as a proxy for the duration of crystallization when viewing these figures.

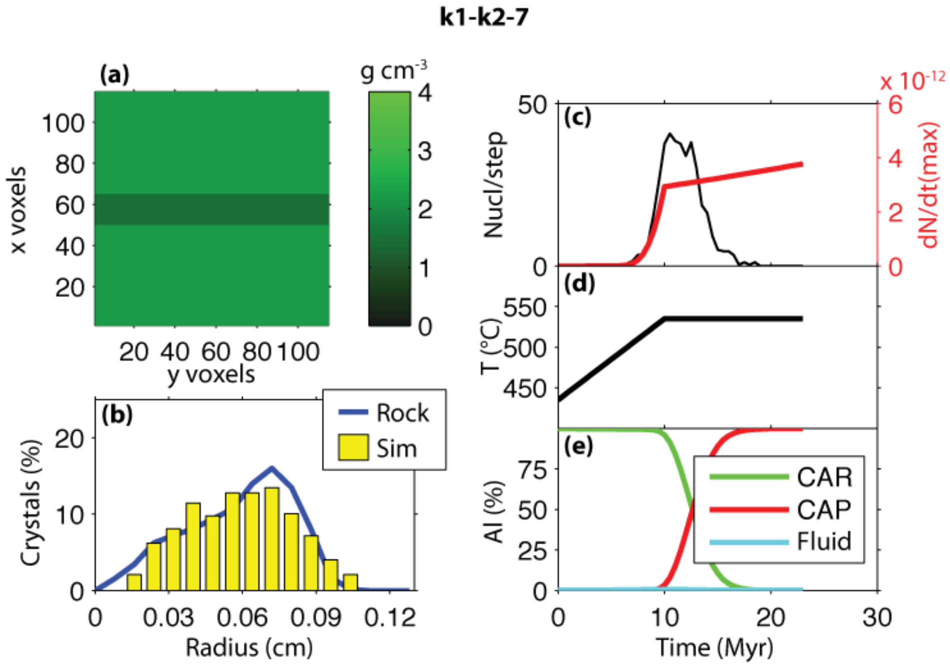

Selected model parameters			
Steady-state nucleation rate	k_1	6.3E-11	nuclei cm^{-3} s^{-1}
Nucleation acceleration	k_2	10	
Diffusive flux constant	k_3	1.5E-8	m^2 s^{-1}
Activation energy	Q_D	140	kJ mol^{-1}

Figure 3-20. Results from the sensitivity analysis of the co-variation of k_2 and k_1. (a) Initial distribution of the reactants. In this model, two layers of Al-bearing reactants were used with a layer of Al-poor reactants between. (b) Comparison of the crystal-size distribution between the rock and simulation. (c) Number of nuclei per time step (black curve, nuclei per 0.5 Myr per cm^3) and the maximum nucleation rate (red curve, nuclei cm^{-3} s^{-1}). (d) Extent of the prescribed heating path attained in the simulation. (e) Percentage of Al in the system (mole %) for the reactant assemblage (CAR), the product assemblage (CAP), and the intergranular fluid. The amount of Al in the CAP serves as a proxy for the duration of crystallization when viewing these figures.

the case of smaller *k*$_2$, and they are able to grow larger. The effect of small values of *k*$_2$ can be seen in the small crystals in the CSDs, where simulation k1-k2-3 has a noticeable small-radius peak and simulation k1-k2-7 lacks the peak.

It may be expected that an influence on crystal ordering comes from increased diffusive fluxes and longer length scales of diffusion from nucleation at higher temperatures. However, with higher temperature comes larger reaction affinity and increased nucleation probability, so the effects of ordering should be somewhat negated. The lack of trends in ordering in the models used in the sensitivity analysis suggests that either the effects are negated or the correlation functions are not especially sensitive to the ordering signals over the range of values tested.

For the simulations that lack the small-radius peak in the CSD (PM1, k1-k2-6, and k1-k2-7), and which fit closely the texture of the natural sample (the small-radius peaks in simulations k1-k2-3 through k1-k2-5 are not considered a good fit), the range of *k*$_2$ is about one order of magnitude (Fig. 3-21). The range of *k*$_1$ used to compensate for *k*$_2$ is also about one order of magnitude. In addition to this uncertainty estimate for *k*$_2$, another important result is that values less than one have virtually no effect on the texture of the simulations for sample PM1 (Fig. 3-21), placing a lower boundary on the effectiveness of *k*$_2$ for this sample. This occurs because *k*$_2$ is a factor in the exponent of the nucleation rate equation (Equation 2-13) and smaller values of *k*$_2$ (combined with low Al supersaturation (Δc) on the order of 10^{-7}-10^{-5}) take the exponent asymptotically toward zero and, thus, toward a nucleation rate equal to *k*$_1$. From experience with the model, simulations of other samples show a lower limit for *k*$_2$ between 0.001 and 0.01.

Co-variation of heating rate and k$_1$, k$_2$, *or* k$_3$

The rate at which temperature increases in the simulations primarily influences the duration of the crystallization event, but the heating rate also affects thermal overstepping determined from the simulations due to discretization effects. The co-variation of heating rate with *k*$_1$ is shown in Figures 3-22 through 3-26.

A slow heating rate allows more opportunities for nucleation at temperatures that can be less than the maximum *T* of the simulation (e.g., Fig. 3-22c, d). The

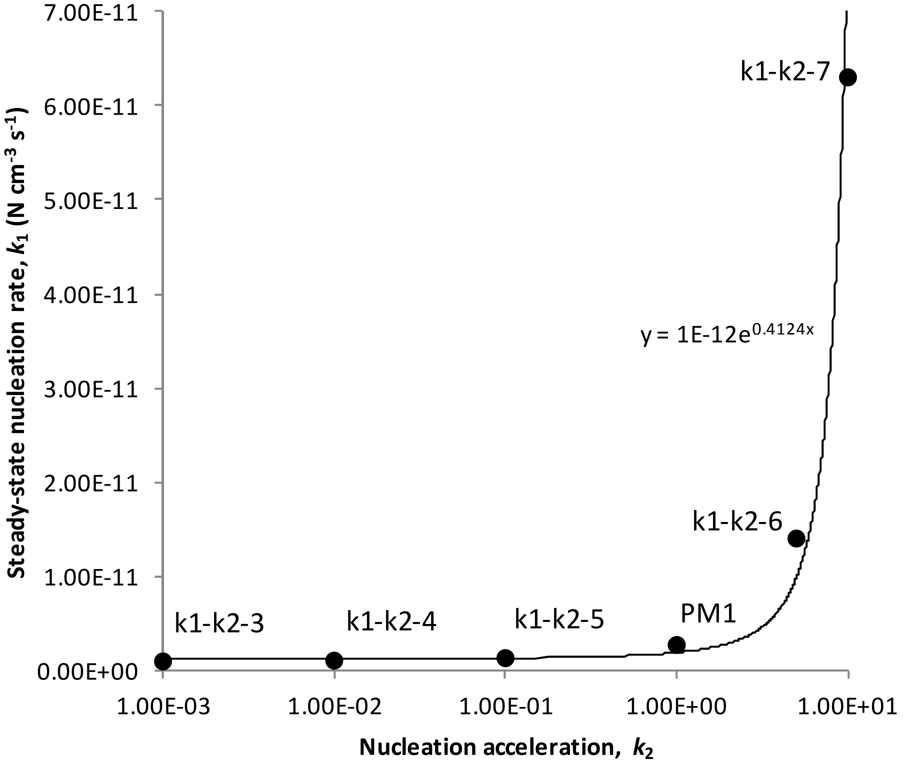

Figure 3-21. Summary of the co-variation of k_2 and k_1. The curve represents constant nucleation density. The model is not sensitive to changes in k_2 less than about 1, but above 1, an increase in k_2 of one order of magnitude requires an increase in k_1 of about one order of magnitude.

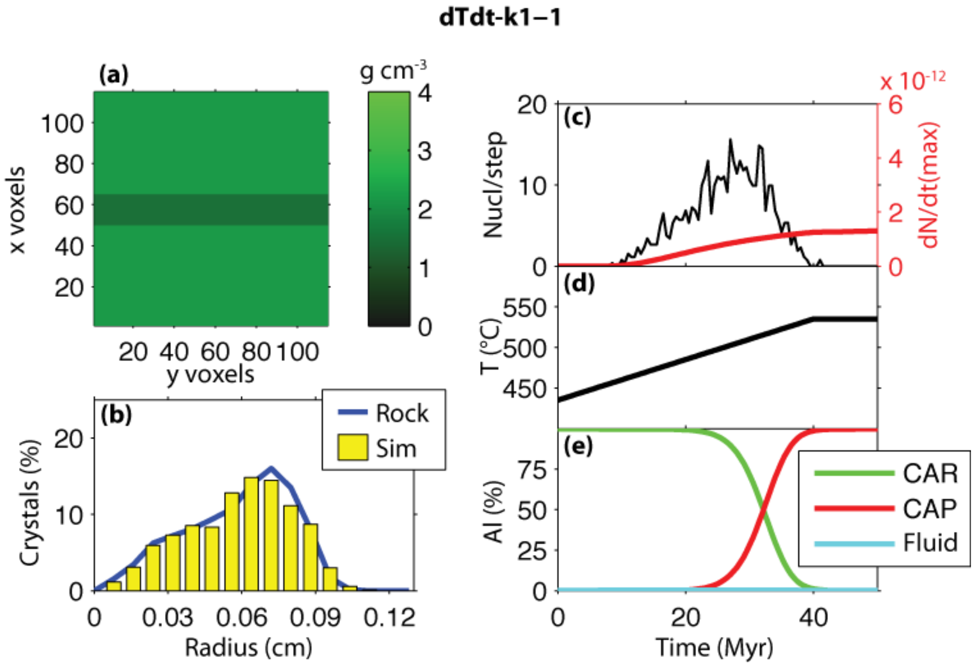

Selected model parameters			
Steady-state nucleation rate	k_1	1.7E-12	nuclei cm^{-3} s^{-1}
Nucleation acceleration	k_2	1.0	
Diffusive flux constant	k_3	1.5E-8	m^2 s^{-1}
Activation energy	Q_D	140	kJ mol^{-1}

Figure 3-22. Results from the sensitivity analysis of the co-variation of dT/dt and k_1. (a) Initial distribution of the reactants. In this model, two layers of Al-bearing reactants were used with a layer of Al-poor reactants between. (b) Comparison of the crystal-size distribution between the rock and simulation. (c) Number of nuclei per time step (black curve, nuclei per 0.5 Myr per cm^3) and the maximum nucleation rate (red curve, nuclei cm^{-3} s^{-1}). (d) Extent of the prescribed heating path attained in the simulation. (e) Percentage of Al in the system (mole %) for the reactant assemblage (CAR), the product assemblage (CAP), and the intergranular fluid. The amount of Al in the CAP serves as a proxy for the duration of crystallization when viewing these figures.

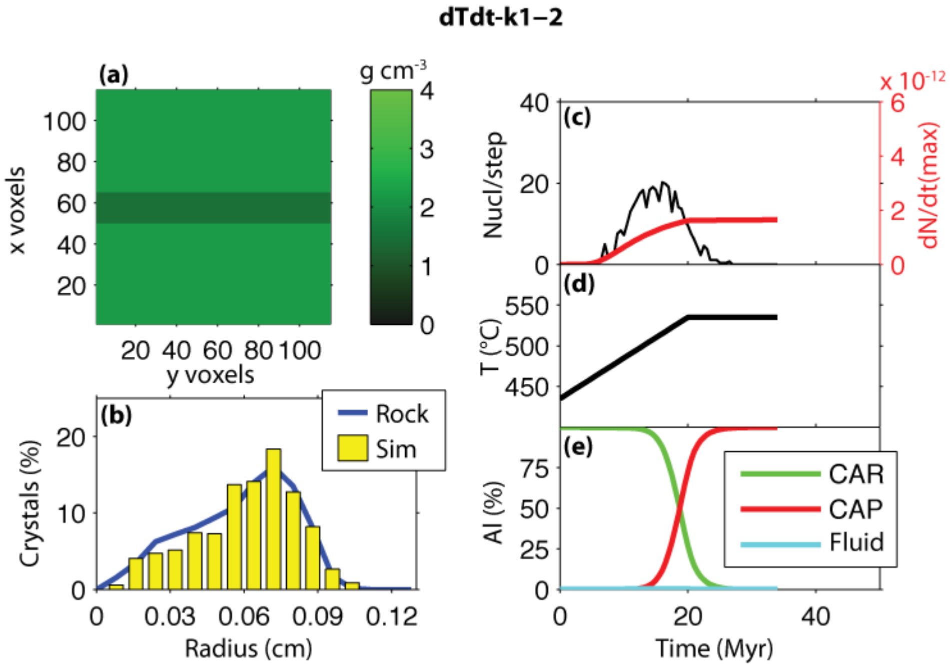

Selected model parameters			
Steady-state nucleation rate	k_1	2.2E-12	nuclei cm^{-3} s^{-1}
Nucleation acceleration	k_2	1.0	
Diffusive flux constant	k_3	1.5E-8	m^2 s^{-1}
Activation energy	Q_D	140	kJ mol^{-1}

Figure 3-23. Results from the sensitivity analysis of the co-variation of d*T*/d*t* and k_1. (a) Initial distribution of the reactants. In this model, two layers of Al-bearing reactants were used with a layer of Al-poor reactants between. (b) Comparison of the crystal-size distribution between the rock and simulation. (c) Number of nuclei per time step (black curve, nuclei per 0.5 Myr per cm^3) and the maximum nucleation rate (red curve, nuclei cm^{-3} s^{-1}). (d) Extent of the prescribed heating path attained in the simulation. (e) Percentage of Al in the system (mole %) for the reactant assemblage (CAR), the product assemblage (CAP), and the intergranular fluid. The amount of Al in the CAP serves as a proxy for the duration of crystallization when viewing these figures.

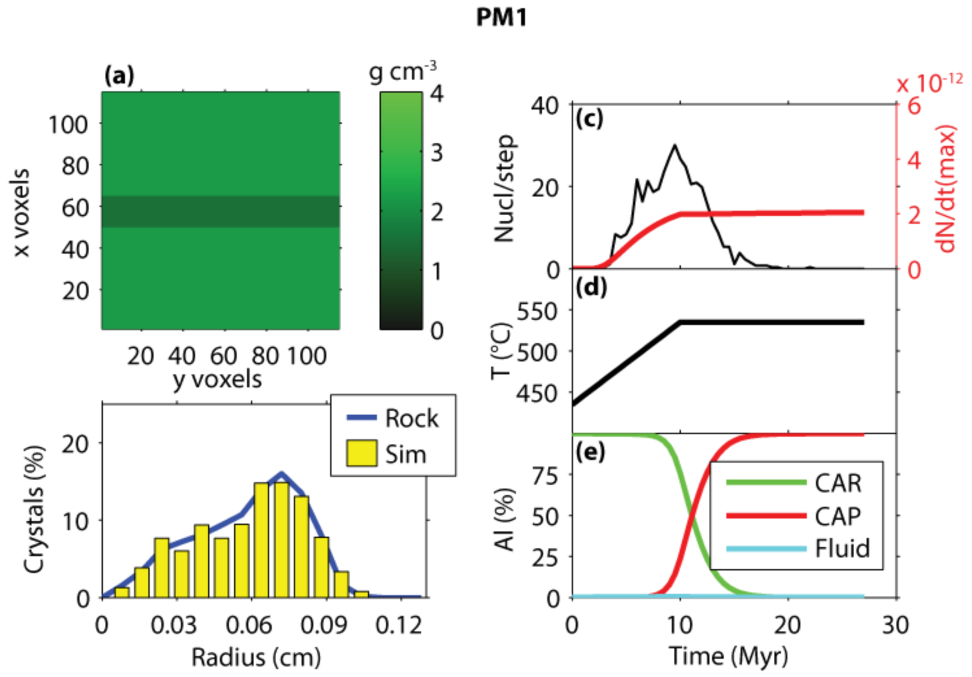

Selected model parameters			
Steady-state nucleation rate	k_1	2.7E-12	nuclei cm^{-3} s^{-1}
Nucleation acceleration	k_2	1.0	
Diffusive flux constant	k_3	1.5E-8	m^2 s^{-1}
Activation energy	Q_D	140	kJ mol^{-1}

Figure 3-24. Results from the sensitivity analysis of the co-variation of d*T*/d*t* and k_1. (a) Initial distribution of the reactants. In this model, two layers of Al-bearing reactants were used with a layer of Al-poor reactants between. (b) Comparison of the crystal-size distribution between the rock and simulation. (c) Number of nuclei per time step (black curve, nuclei per 0.5 Myr per cm^3) and the maximum nucleation rate (red curve, nuclei cm^{-3} s^{-1}). (d) Extent of the prescribed heating path attained in the simulation. (e) Percentage of Al in the system (mole %) for the reactant assemblage (CAR), the product assemblage (CAP), and the intergranular fluid. The amount of Al in the CAP serves as a proxy for the duration of crystallization when viewing these figures.

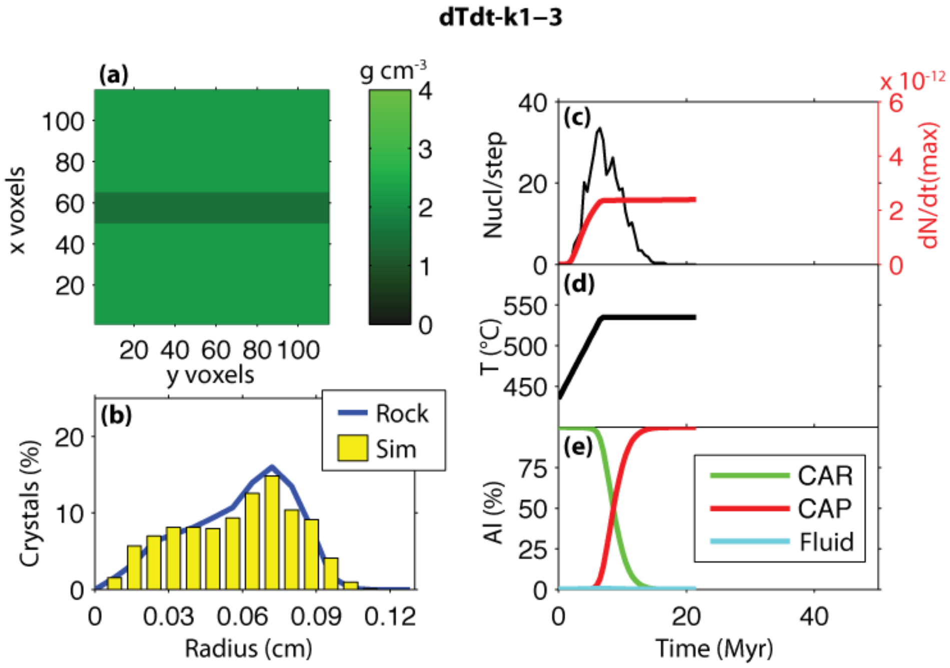

Selected model parameters			
Steady-state nucleation rate	k_1	3.2E-12	nuclei cm^{-3} s^{-1}
Nucleation acceleration	k_2	1.0	
Diffusive flux constant	k_3	1.5E-8	m^2 s^{-1}
Activation energy	Q_D	140	kJ mol^{-1}

Figure 3-25. Results from the sensitivity analysis of the co-variation of dT/dt and k_1. (a) Initial distribution of the reactants. In this model, two layers of Al-bearing reactants were used with a layer of Al-poor reactants between. (b) Comparison of the crystal-size distribution between the rock and simulation. (c) Number of nuclei per time step (black curve, nuclei per 0.5 Myr per cm^3) and the maximum nucleation rate (red curve, nuclei cm^{-3} s^{-1}). (d) Extent of the prescribed heating path attained in the simulation. (e) Percentage of Al in the system (mole %) for the reactant assemblage (CAR), the product assemblage (CAP), and the intergranular fluid. The amount of Al in the CAP serves as a proxy for the duration of crystallization when viewing these figures.

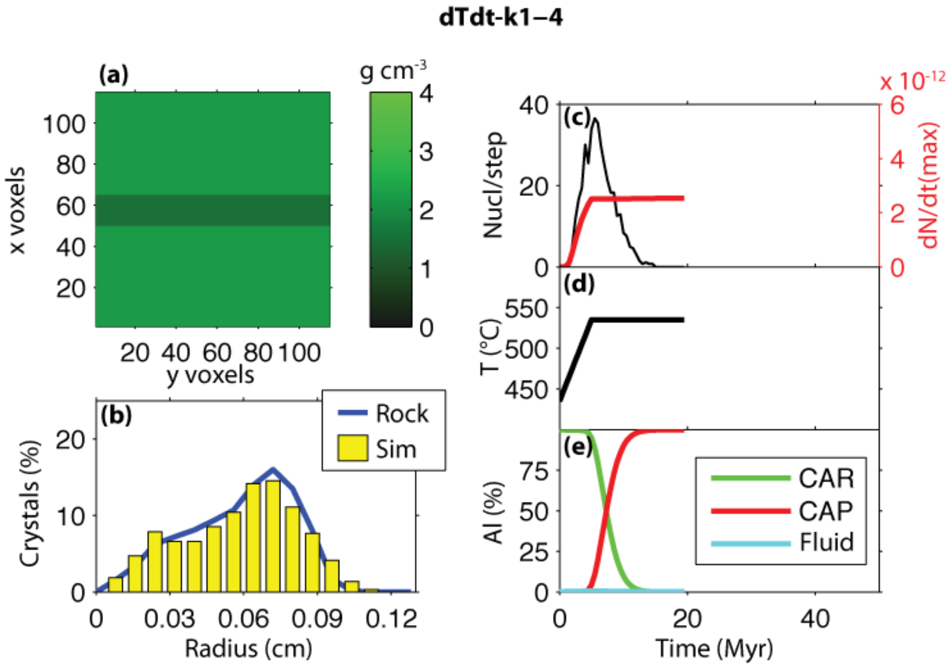

Selected model parameters			
Steady-state nucleation rate	k_1	3.4E-12	nuclei cm^{-3} s^{-1}
Nucleation acceleration	k_2	1.0	
Diffusive flux constant	k_3	1.5E-8	m^2 s^{-1}
Activation energy	Q_D	140	kJ mol^{-1}

Figure 3-26. Results from the sensitivity analysis of the co-variation of dT/dt and k_1. (a) Initial distribution of the reactants. In this model, two layers of Al-bearing reactants were used with a layer of Al-poor reactants between. (b) Comparison of the crystal-size distribution between the rock and simulation. (c) Number of nuclei per time step (black curve, nuclei per 0.5 Myr per cm^3) and the maximum nucleation rate (red curve, nuclei cm^{-3} s^{-1}). (d) Extent of the prescribed heating path attained in the simulation. (e) Percentage of Al in the system (mole %) for the reactant assemblage (CAR), the product assemblage (CAP), and the intergranular fluid. The amount of Al in the CAP serves as a proxy for the duration of crystallization when viewing these figures.

nucleation events happen during smaller reaction affinities causing slower rates of nucleation and diffusion that slows the progress of the reaction. Slower reaction kinetics can produce longer crystallization durations. Conversely, if the heating rate is rapid, more nucleation events can happen at the maximum *T* of the simulation when kinetics are more rapid (e.g., Fig. 3-26c, d), and the crystallization duration can be shorter.

Nucleation overstepping is not dependent on heating rate, and this is expressed in the nucleation rate equation (2-13), which has no dependence on heating rate. However, discretization in the model has an influence on nucleation overstepping. Small time steps allow more opportunities for nucleation than larger time steps, so slower heating rates produce thermal overstepping values that tend to be a few degrees smaller. In the case of PM1, the difference in thermal overstepping between the slowest heating rate and the fastest heating rate is nine degrees.

Changes in the heating rate primarily affect crystallization duration, and thus the parameters that can compensate are the steady-state nucleation rate (k_1), the nucleation acceleration factor (k_2), and the pre-exponential constant for Al intergranular diffusion (k_3). The heating rate was varied for PM1 between 2.5 and 20 °C Myr^{-1}, and each parameter was adjusted to match the nucleation density of the simulation to the rock.

An increase in k_1 produce shorter durations because more nucleation events happen at each time step and the Al in the fluid is drawn down faster, speeding the reaction. Comparison of the heating rate and nucleation curves in Figures 3-22 and 3-26 demonstrates that the majority of nucleation occurs at temperatures less than T_{rim} for shorter heating rates but at T_{rim} for faster heating rates. The range of k_1 used to compensate for the heating rate is $10^{-11.8}$-$10^{-11.5}$ nuclei cm^{-3} s^{-1} or a factor of 2.0.

An increase in the nucleation acceleration (decrease in k_2) causes a faster rise in the nucleation rate toward the steady-state rate (Fig. 2-4), maintaining the nucleation density of the simulation. The results (Figs. 3-27 through 3-31) are similar to those for the analysis of k_1 immediately above. The range of k_2 used to compensate for the heating rate is 0.65-1.6 or a factor of 2.5.

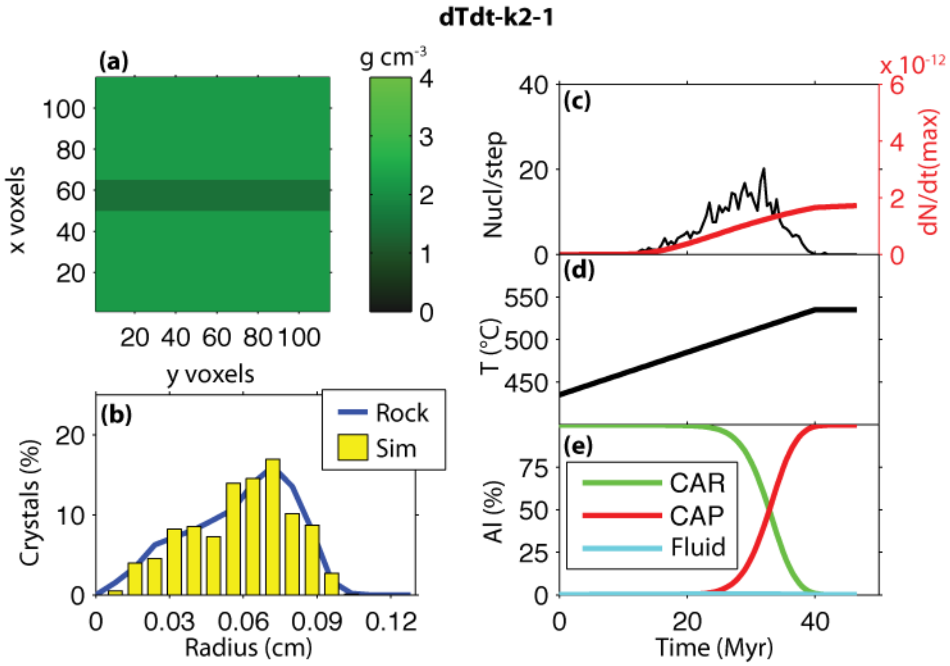

Selected model parameters			
Steady-state nucleation rate	k_1	2.7E-12	nuclei cm^{-3} s^{-1}
Nucleation acceleration	k_2	1.6	
Diffusive flux constant	k_3	1.5E-8	m^2 s^{-1}
Activation energy	Q_D	140	kJ mol^{-1}

Figure 3-27. Results from the sensitivity analysis of the co-variation of d*T*/d*t* and k_2. (a) Initial distribution of the reactants. In this model, two layers of Al-bearing reactants were used with a layer of Al-poor reactants between. (b) Comparison of the crystal-size distribution between the rock and simulation. (c) Number of nuclei per time step (black curve, nuclei per 0.5 Myr per cm^3) and the maximum nucleation rate (red curve, nuclei cm^{-3} s^{-1}). (d) Extent of the prescribed heating path attained in the simulation. (e) Percentage of Al in the system (mole %) for the reactant assemblage (CAR), the product assemblage (CAP), and the intergranular fluid. The amount of Al in the CAP serves as a proxy for the duration of crystallization when viewing these figures.

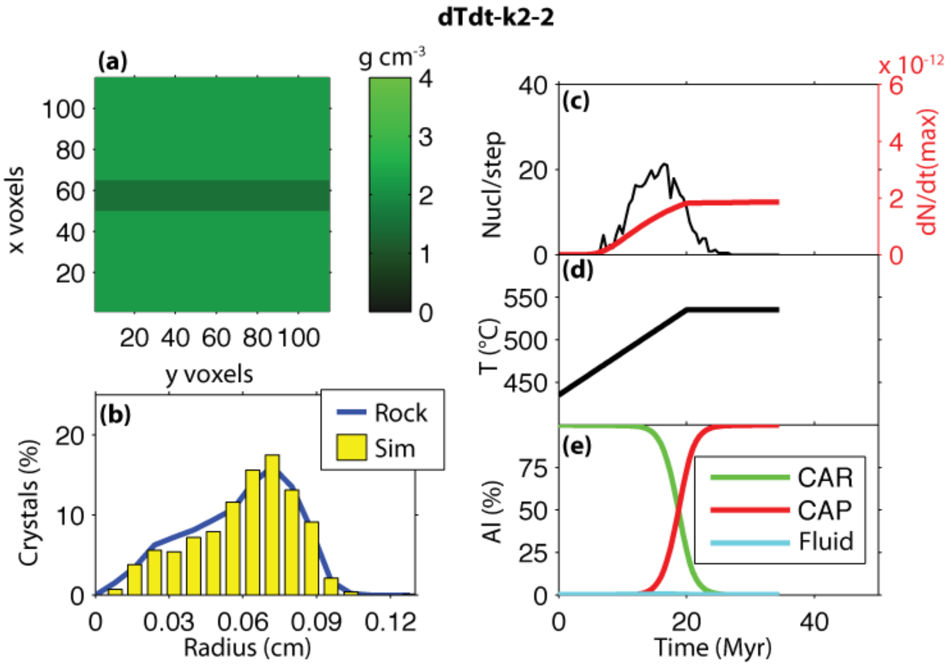

Selected model parameters

Steady-state nucleation rate	k_1	2.7E-12	nuclei cm^{-3} s^{-1}
Nucleation acceleration	k_2	1.3	
Diffusive flux constant	k_3	1.5E-8	m^2 s^{-1}
Activation energy	Q_D	140	kJ mol^{-1}

Figure 3-28. Results from the sensitivity analysis of the co-variation of d*T*/d*t* and k_2. (a) Initial distribution of the reactants. In this model, two layers of Al-bearing reactants were used with a layer of Al-poor reactants between. (b) Comparison of the crystal-size distribution between the rock and simulation. (c) Number of nuclei per time step (black curve, nuclei per 0.5 Myr per cm^3) and the maximum nucleation rate (red curve, nuclei cm^{-3} s^{-1}). (d) Extent of the prescribed heating path attained in the simulation. (e) Percentage of Al in the system (mole %) for the reactant assemblage (CAR), the product assemblage (CAP), and the intergranular fluid. The amount of Al in the CAP serves as a proxy for the duration of crystallization when viewing these figures.

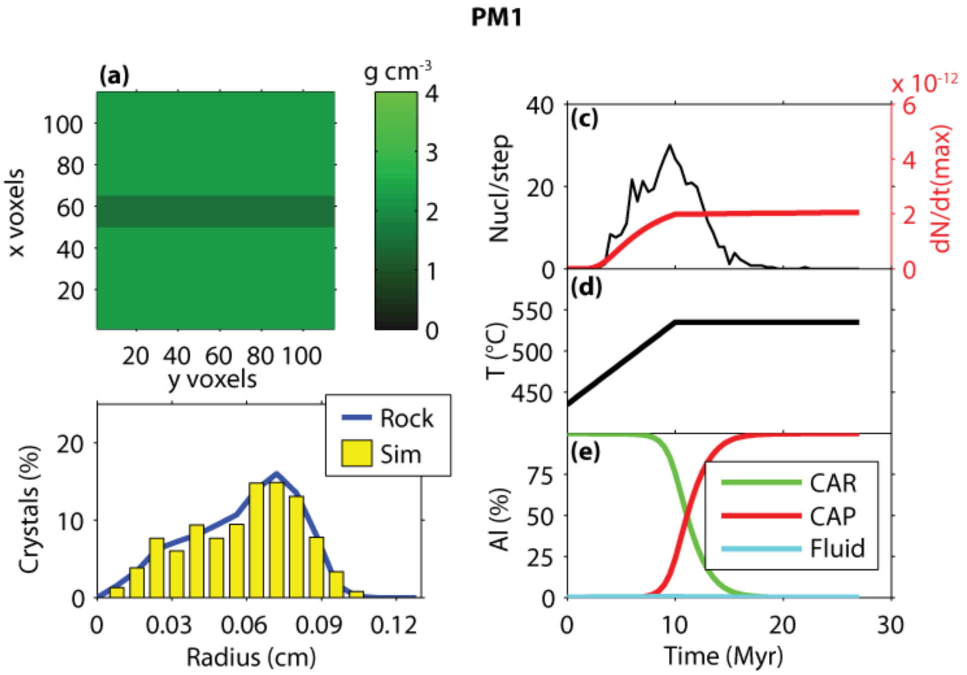

Selected model parameters			
Steady-state nucleation rate	k_1	2.7E-12	nuclei cm^{-3} s^{-1}
Nucleation acceleration	k_2	1.0	
Diffusive flux constant	k_3	1.5E-8	m^2 s^{-1}
Activation energy	Q_D	140	kJ mol^{-1}

Figure 3-29. Results from the sensitivity analysis of the co-variation of d*T*/d*t* and k_2. (a) Initial distribution of the reactants. In this model, two layers of Al-bearing reactants were used with a layer of Al-poor reactants between. (b) Comparison of the crystal-size distribution between the rock and simulation. (c) Number of nuclei per time step (black curve, nuclei per 0.5 Myr per cm^3) and the maximum nucleation rate (red curve, nuclei cm^{-3} s^{-1}). (d) Extent of the prescribed heating path attained in the simulation. (e) Percentage of Al in the system (mole %) for the reactant assemblage (CAR), the product assemblage (CAP), and the intergranular fluid. The amount of Al in the CAP serves as a proxy for the duration of crystallization when viewing these figures.

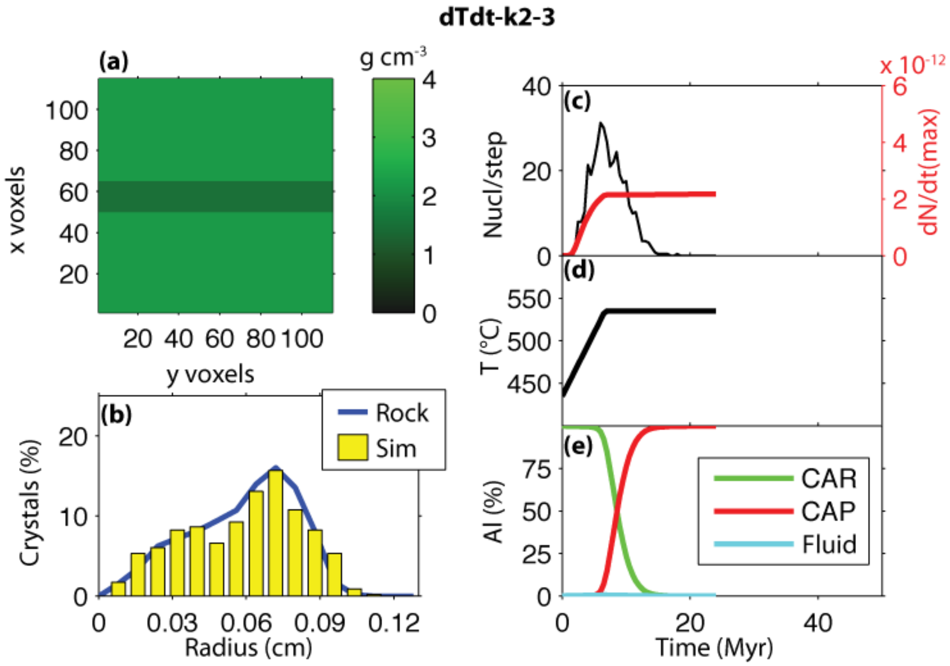

Selected model parameters			
Steady-state nucleation rate	k_1	2.7E-12	nuclei cm^{-3} s^{-1}
Nucleation acceleration	k_2	0.75	
Diffusive flux constant	k_3	1.5E-8	m^2 s^{-1}
Activation energy	Q_D	140	kJ mol^{-1}

Figure 3-30. Results from the sensitivity analysis of the co-variation of d*T*/d*t* and k_2. (a) Initial distribution of the reactants. In this model, two layers of Al-bearing reactants were used with a layer of Al-poor reactants between. (b) Comparison of the crystal-size distribution between the rock and simulation. (c) Number of nuclei per time step (black curve, nuclei per 0.5 Myr per cm^3) and the maximum nucleation rate (red curve, nuclei cm^{-3} s^{-1}). (d) Extent of the prescribed heating path attained in the simulation. (e) Percentage of Al in the system (mole %) for the reactant assemblage (CAR), the product assemblage (CAP), and the intergranular fluid. The amount of Al in the CAP serves as a proxy for the duration of crystallization when viewing these figures.

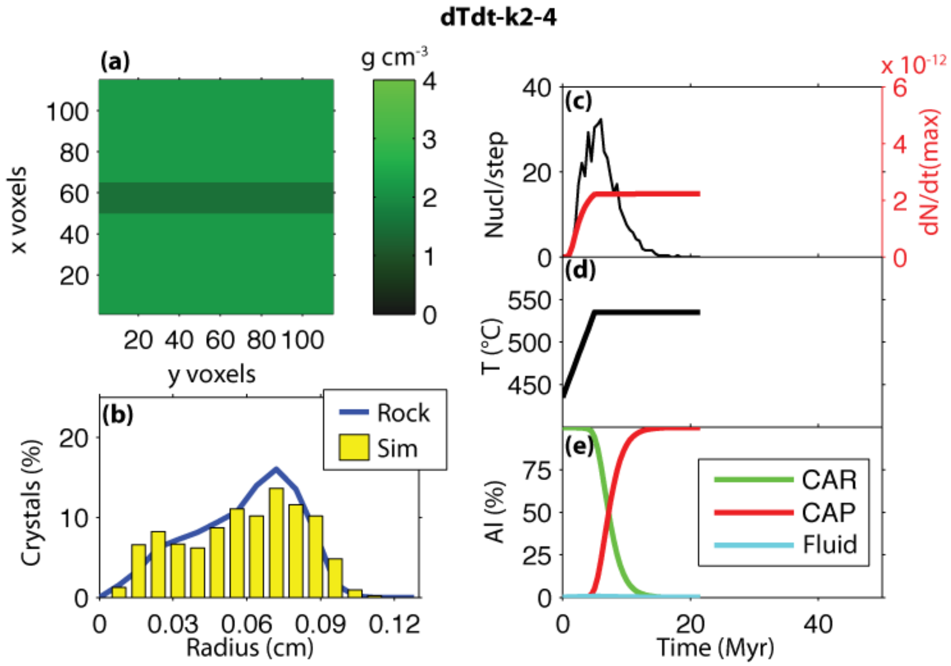

Selected model parameters			
Steady-state nucleation rate	k_1	2.7E-12	nuclei cm^{-3} s^{-1}
Nucleation acceleration	k_2	0.65	
Diffusive flux constant	k_3	1.5E-8	m^2 s^{-1}
Activation energy	Q_D	140	kJ mol^{-1}

Figure 3-31. Results from the sensitivity analysis of the co-variation of dT/dt and k_2. (a) Initial distribution of the reactants. In this model, two layers of Al-bearing reactants were used with a layer of Al-poor reactants between. (b) Comparison of the crystal-size distribution between the rock and simulation. (c) Number of nuclei per time step (black curve, nuclei per 0.5 Myr per cm^3) and the maximum nucleation rate (red curve, nuclei cm^{-3} s^{-1}). (d) Extent of the prescribed heating path attained in the simulation. (e) Percentage of Al in the system (mole %) for the reactant assemblage (CAR), the product assemblage (CAP), and the intergranular fluid. The amount of Al in the CAP serves as a proxy for the duration of crystallization when viewing these figures.

As described in Figure 3-10, an increase in k_3 reduces the overall nucleation rate and prolongs crystallization. Therefore a decrease in k_3 will counteract the effects of faster heating rates and maintain the crystal number density of the simulation (Figs. 3-32 through 3-36). The range of k_3 needed to compensate for heating rate is $10^{-7.9}$-$10^{-7.5}$ m^2 s^{-1} or a factor of 2.5.

A summary of the sensitivity analysis for changes in the heating rate is given in Figure 3-37. For a change in heating rate of approximately one order of magnitude (2.5-20 °C Myr^{-1}), the nucleation density of the model can be maintained by adjusting the steady-state nucleation rate (k_1) by a factor of 2.0, or by adjusting the nucleation acceleration (k_2) by a factor of 2.5, or by adjusting the pre-exponential constant for Al intergranular diffusion (k_3) by a factor of 2.5.

Co-variation of Q_D *and* k_3

The diffusional flux for Al (Equation 2-20) is dependent on the pre-exponential constant for intergranular diffusion (k_3) and the activation energy for intergranular diffusion (Q_D). In general, a larger Q_D will increase the crystal number density of a simulation, and k_3 can be increased to compensate for the effect. This effect can be visualized using an Arrhenius diagram in which the intercept is the natural log of k_3 and the slope is $-Q_D/R$ (Fig. 3-38). The flux, integrated over the heating interval, can be held constant if Q_D and k_3 are both increased or both decreased.

The texture of the simulation should be affected by changes in Q_D because the flux can be lower or higher early or late in the crystallization event. For example, Figure 3-38 contains two lines, one with a shallow slope and the other with a steep slope. The simulation corresponding with the steep slope should experience lower fluxes early in crystallization and higher fluxes late in crystallization. The effect on the simulation would be smaller length scales of diffusion early during crystallization, which would reduce the ordering of crystal centers, and larger length scales of diffusion late in crystallization, which would increase growth competition.

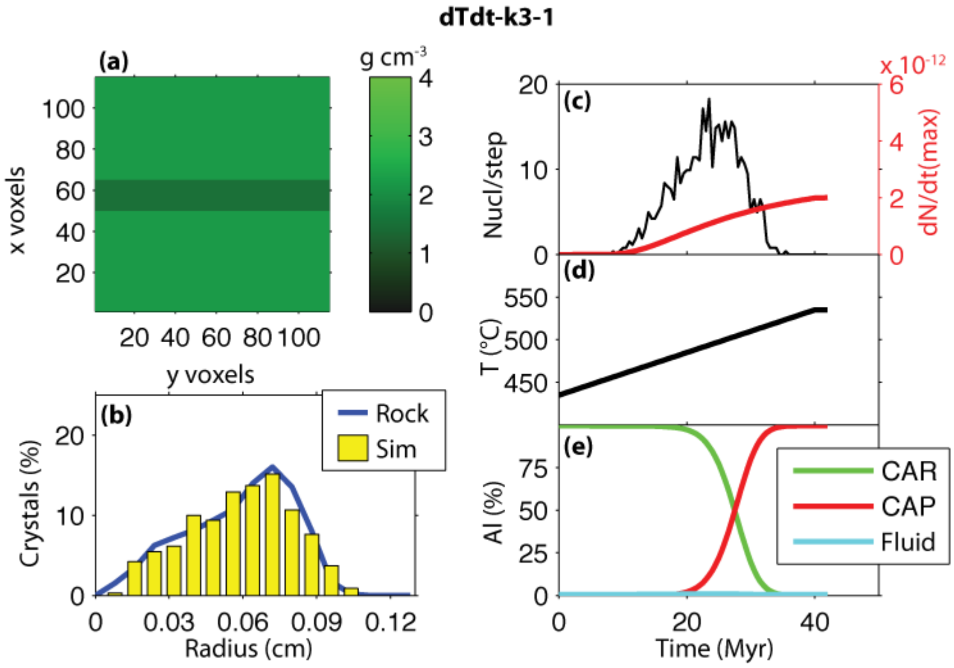

Selected model parameters			
Steady-state nucleation rate	k_1	2.7E-12	nuclei cm^{-3} s^{-1}
Nucleation acceleration	k_2	1.0	
Diffusive flux constant	k_3	3.0E-8	m^2 s^{-1}
Activation energy	Q_D	140	kJ mol^{-1}

Figure 3-32. Results from the sensitivity analysis of the co-variation of dT/dt and k_3. (a) Initial distribution of the reactants. In this model, two layers of Al-bearing reactants were used with a layer of Al-poor reactants between. (b) Comparison of the crystal-size distribution between the rock and simulation. (c) Number of nuclei per time step (black curve, nuclei per 0.5 Myr per cm^3) and the maximum nucleation rate (red curve, nuclei cm^{-3} s^{-1}). (d) Extent of the prescribed heating path attained in the simulation. (e) Percentage of Al in the system (mole %) for the reactant assemblage (CAR), the product assemblage (CAP), and the intergranular fluid. The amount of Al in the CAP serves as a proxy for the duration of crystallization when viewing these figures.

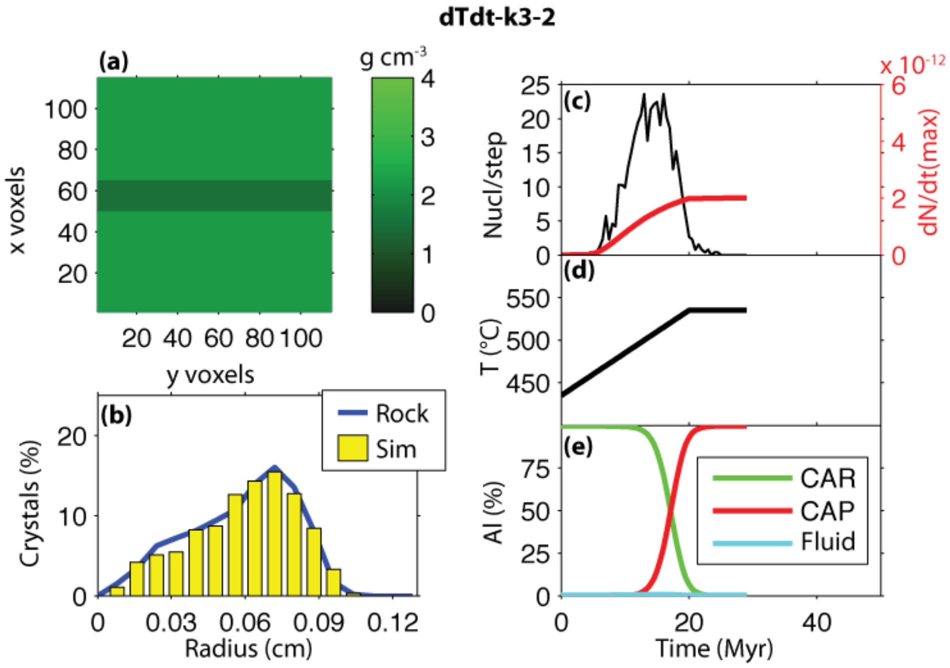

Selected model parameters			
Steady-state nucleation rate	k_1	2.7E-12	nuclei cm^{-3} s^{-1}
Nucleation acceleration	k_2	1.0	
Diffusive flux constant	k_3	2.2E-8	m^2 s^{-1}
Activation energy	Q_D	140	kJ mol^{-1}

Figure 3-33. Results from the sensitivity analysis of the co-variation of d*T*/d*t* and k_3. (a) Initial distribution of the reactants. In this model, two layers of Al-bearing reactants were used with a layer of Al-poor reactants between. (b) Comparison of the crystal-size distribution between the rock and simulation. (c) Number of nuclei per time step (black curve, nuclei per 0.5 Myr per cm^3) and the maximum nucleation rate (red curve, nuclei cm^{-3} s^{-1}). (d) Extent of the prescribed heating path attained in the simulation. (e) Percentage of Al in the system (mole %) for the reactant assemblage (CAR), the product assemblage (CAP), and the intergranular fluid. The amount of Al in the CAP serves as a proxy for the duration of crystallization when viewing these figures.

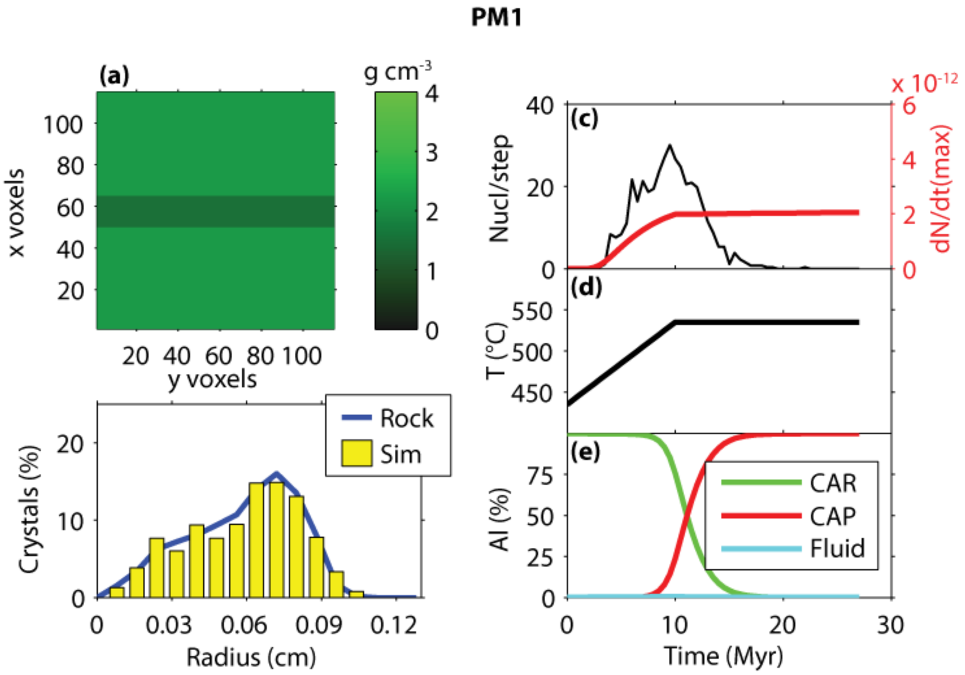

Selected model parameters

Steady-state nucleation rate	k_1	2.7E-12	nuclei cm^{-3} s^{-1}
Nucleation acceleration	k_2	1.0	
Diffusive flux constant	k_3	1.5E-8	m^2 s^{-1}
Activation energy	Q_D	140	kJ mol^{-1}

Figure 3-34. Results from the sensitivity analysis of the co-variation of dT/dt and k_3. (a) Initial distribution of the reactants. In this model, two layers of Al-bearing reactants were used with a layer of Al-poor reactants between. (b) Comparison of the crystal-size distribution between the rock and simulation. (c) Number of nuclei per time step (black curve, nuclei per 0.5 Myr per cm^3) and the maximum nucleation rate (red curve, nuclei cm^{-3} s^{-1}). (d) Extent of the prescribed heating path attained in the simulation. (e) Percentage of Al in the system (mole %) for the reactant assemblage (CAR), the product assemblage (CAP), and the intergranular fluid. The amount of Al in the CAP serves as a proxy for the duration of crystallization when viewing these figures.

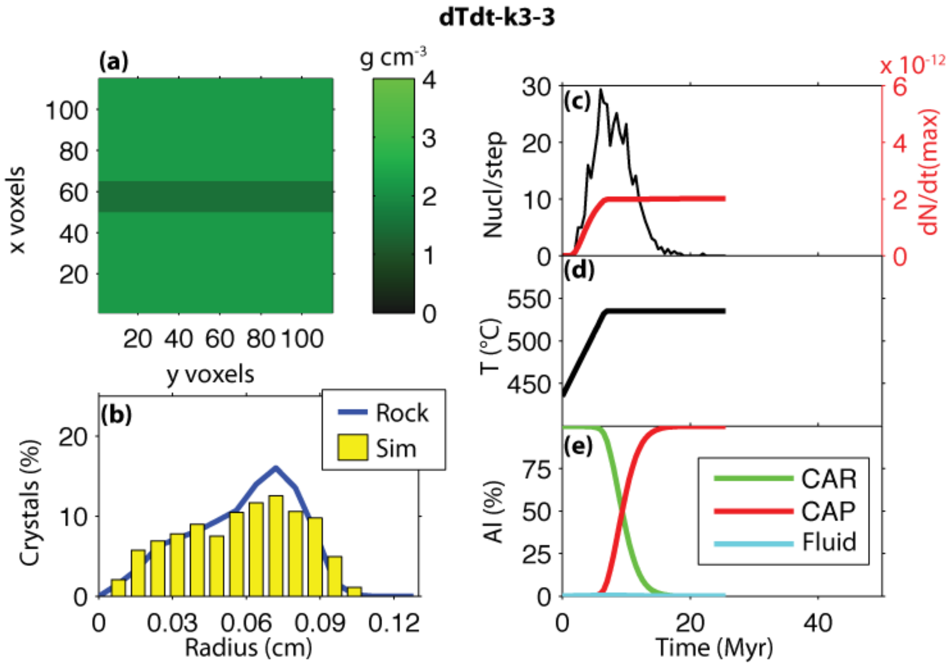

Selected model parameters			
Steady-state nucleation rate	k_1	2.7E-12	nuclei cm^{-3} s^{-1}
Nucleation acceleration	k_2	1.0	
Diffusive flux constant	k_3	1.25E-8	m^2 s^{-1}
Activation energy	Q_D	140	kJ mol^{-1}

Figure 3-35. Results from the sensitivity analysis of the co-variation of d*T*/d*t* and k_3. (a) Initial distribution of the reactants. In this model, two layers of Al-bearing reactants were used with a layer of Al-poor reactants between. (b) Comparison of the crystal-size distribution between the rock and simulation. (c) Number of nuclei per time step (black curve, nuclei per 0.5 Myr per cm^3) and the maximum nucleation rate (red curve, nuclei cm^{-3} s^{-1}). (d) Extent of the prescribed heating path attained in the simulation. (e) Percentage of Al in the system (mole %) for the reactant assemblage (CAR), the product assemblage (CAP), and the intergranular fluid. The amount of Al in the CAP serves as a proxy for the duration of crystallization when viewing these figures.

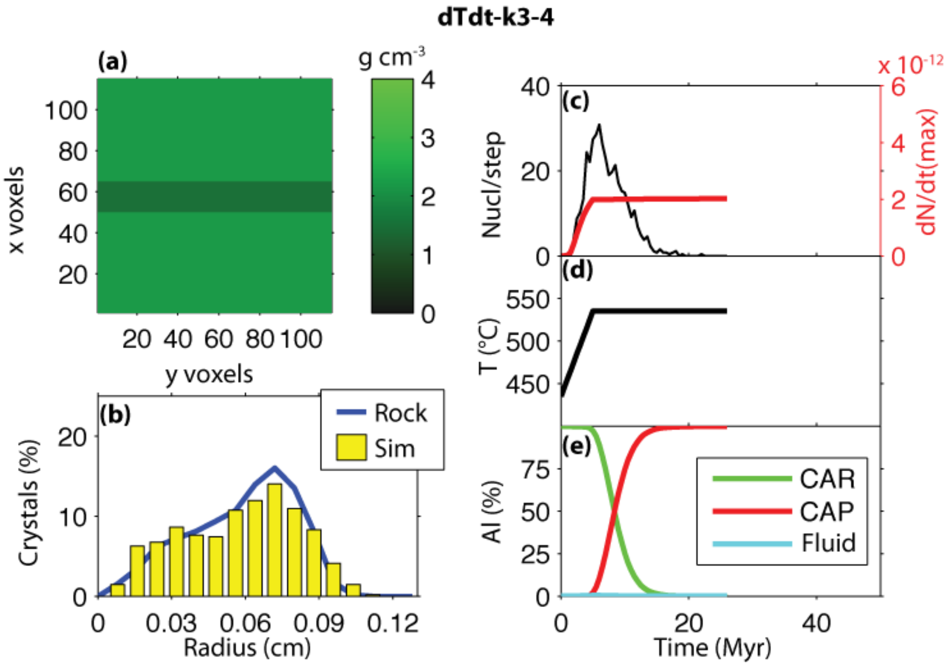

Selected model parameters			
Steady-state nucleation rate	k_1	2.7E-12	nuclei cm^{-3} s^{-1}
Nucleation acceleration	k_2	1.0	
Diffusive flux constant	k_3	1.2E-8	m^2 s^{-1}
Activation energy	Q_D	140	kJ mol^{-1}

Figure 3-36. Results from the sensitivity analysis of the co-variation of d*T*/d*t* and k_3. (a) Initial distribution of the reactants. In this model, two layers of Al-bearing reactants were used with a layer of Al-poor reactants between. (b) Comparison of the crystal-size distribution between the rock and simulation. (c) Number of nuclei per time step (black curve, nuclei per 0.5 Myr per cm^3) and the maximum nucleation rate (red curve, nuclei cm^{-3} s^{-1}). (d) Extent of the prescribed heating path attained in the simulation. (e) Percentage of Al in the system (mole %) for the reactant assemblage (CAR), the product assemblage (CAP), and the intergranular fluid. The amount of Al in the CAP serves as a proxy for the duration of crystallization when viewing these figures.

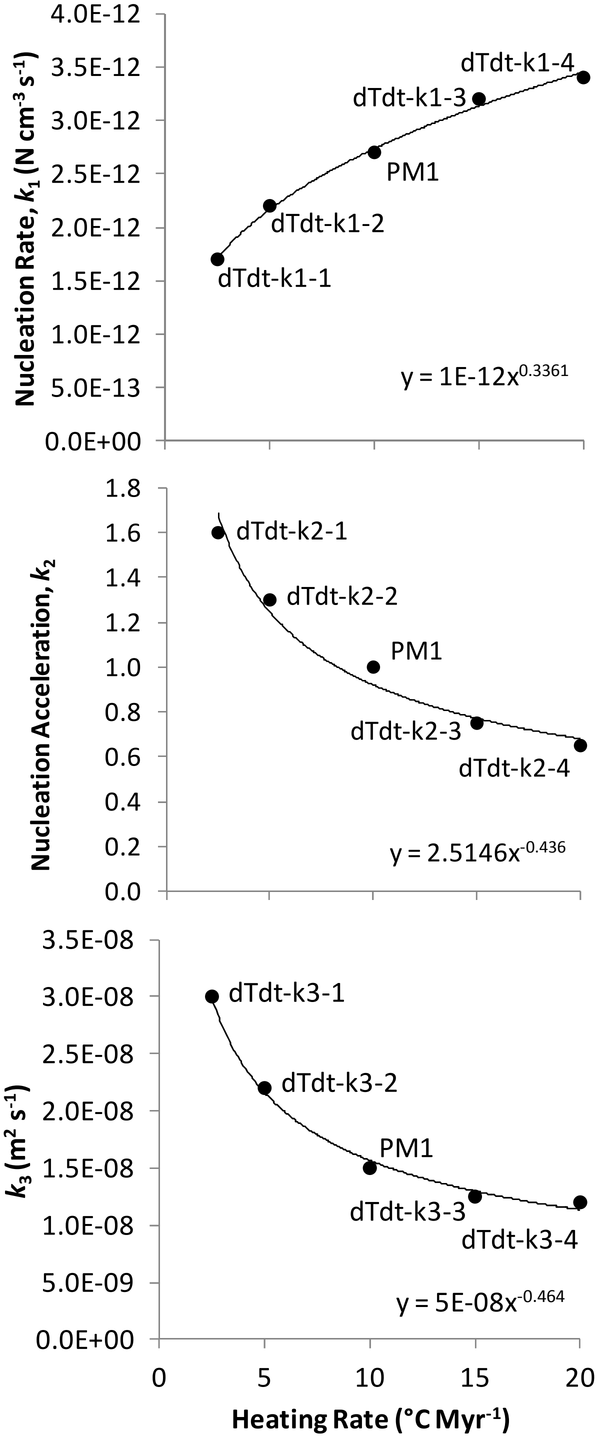

Figure 3.37. Summary of the co-variation of dT/dt and k_1, k_2, and k_3. For a change in dT/dt of roughly one order of magnitude, the nucleation density of the PM1 simulation can be compensated by changes in k_1 of a factor of 2.0, by changes in k_2 by a factor of 2.5, and by changes in k_3 by a factor of 2.5.

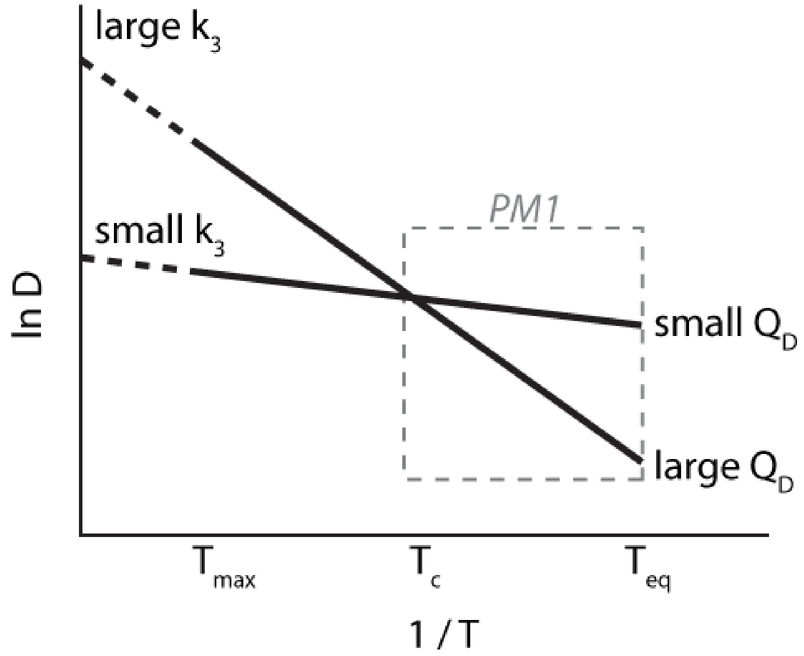

Figure 3-38. Schematic Arrhenius diagram illustrating the effects of changes in Q_D and k_3 on intergranular diffusion with increasing temperature. The integrated diffusional flux can be held constant if Q_D and k_3 are both increased or both decreased. The heating rate for PM1 is isothermal at higher temperature so the diffusional flux approaches a similar value for all conditions of Q_D and k_3.

However, in the simulations for sample PM1, the effect described above is not observed because the bulk of the reaction progress occurs at the point where the diffusional fluxes are practically the same for different values of Q_D and k_3. The range of intergranular diffusion rates differs mostly in the early stages of crystallization, but is very similar in the later stages of crystallization (Figure 3-39). Figures 3-40 through 3-44 show that the nucleation rate curve (nuclei per time step) is virtually unaffected by changes in Q_D and k_3, and the majority of the reaction progress (Al %) occurs after most nucleation has taken place. This demonstrates that many of the locations of the crystal centers were established before the length scales of diffusion were large enough to cause significant changes in nucleation suppression. Furthermore, the isothermal portion of the heating path weighs the integrated flux toward high temperature, which is 530 °C in the case of PM1, so the differences in diffusion rates for each PM1 model follows a pattern that more closely resembles the conditions in the box shown in Figure 3-38. The majority of crystal growth occurs when the diffusion rates are essentially the same (at the crossing point of the two curves), and this causes the textures of the simulations to be nearly the same.

When applied to sample PM1, the model is not sensitive to changes in the diffusive flux, but other rocks may be more strongly influenced. The range of Q_D examined for PM1 (±35 kJ mol^{-1}), spans the uncertainty given by Carlson (2010), and over that range, no significant changes in the simulation were observed. Given a differently shaped heating path for another sample, the effects of Q_D and k_3 may be expressed more strongly.

Fitting procedure

Differences in the sensitivity of the model to its various parameters led to the development of a protocol in which values for the parameters are determined and refined in a particular order. The CSD is highly sensitive to the reactant distribution, as described in the previous chapter, so at first reactants are homogeneously distributed, and any adjustments to reactant distributions are made after the other parameters

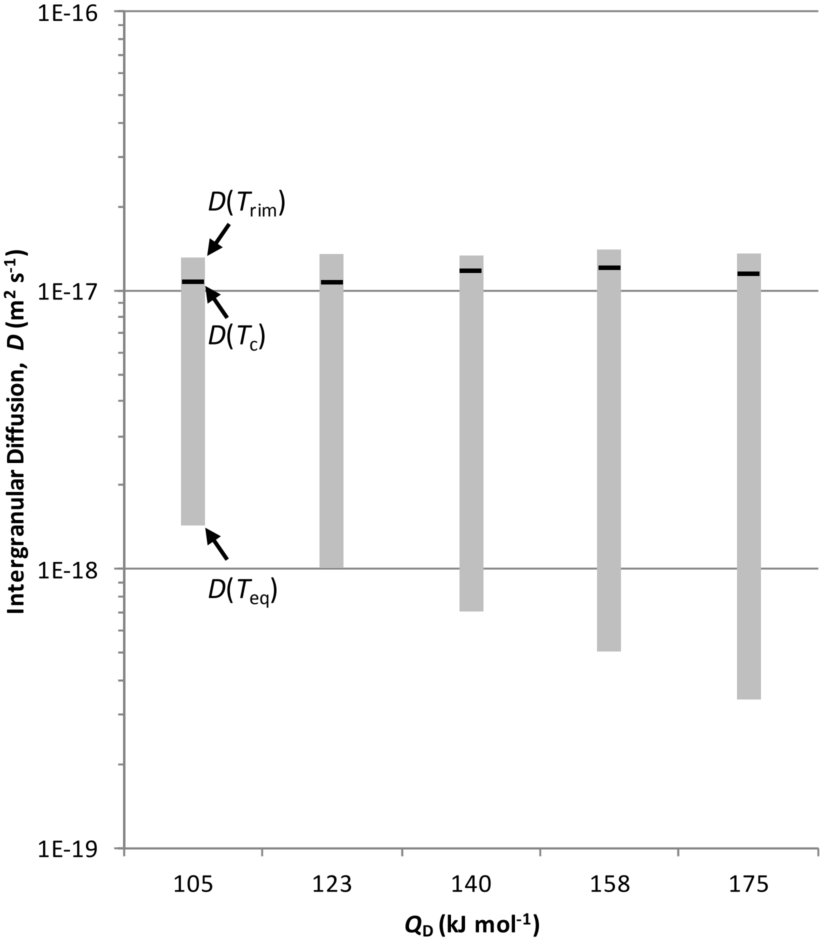

Figure 3-39. Resulting intergranular diffusivities for co-variation of Q_D and k_3. The diffusion rate has a narrower range for values of Q_D that are smaller, but the majority of diffusive flux occurs at the upper temperatures of crystallization, so the range in diffusion rates is insignificant to the texture of the simulation. The reason for the high diffusive flux at higher temperatures is the isothermal portion of the heating path. Because the heating path becomes isothermal at 535 °C, the bulk of the diffusive flux is dependent on diffusion rates near the characteristic temperature, T_c (530 °C for PM1), which is nearly the same for all values of Q_D used in this analysis.

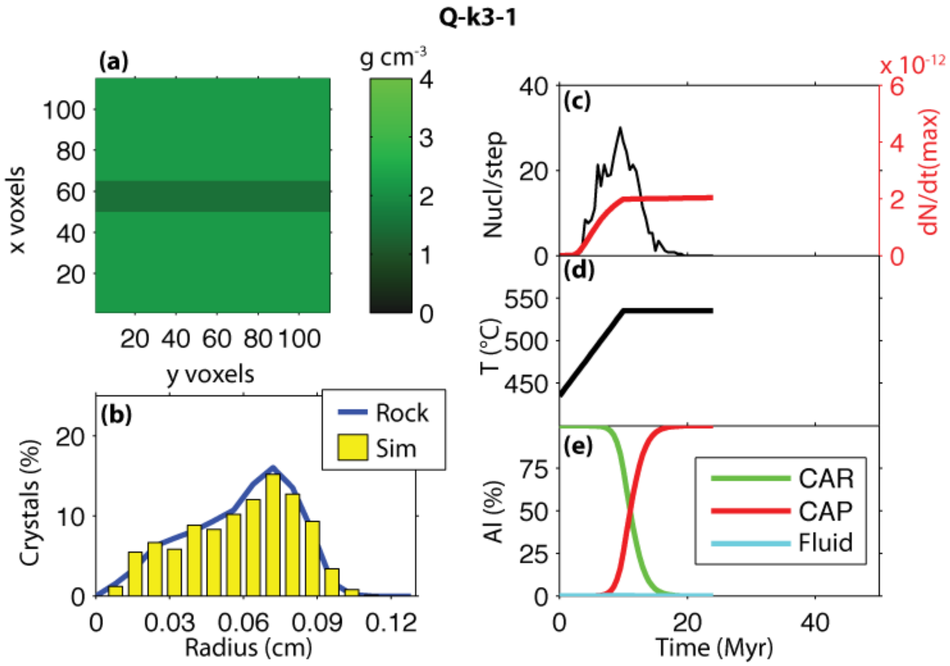

Selected model parameters			
Steady-state nucleation rate	k_1	2.7E-12	nuclei cm^{-3} s^{-1}
Nucleation acceleration	k_2	1.0	
Diffusive flux constant	k_3	8.0E-11	m^2 s^{-1}
Activation energy	Q_D	105	kJ mol^{-1}

Figure 3-40. Results from the sensitivity analysis of the co-variation of Q_D and k_3. (a) Initial distribution of the reactants. In this model, two layers of Al-bearing reactants were used with a layer of Al-poor reactants between. (b) Comparison of the crystal-size distribution between the rock and simulation. (c) Number of nuclei per time step (black curve, nuclei per 0.5 Myr per cm^3) and the maximum nucleation rate (red curve, nuclei cm^{-3} s^{-1}). (d) Extent of the prescribed heating path attained in the simulation. (e) Percentage of Al in the system (mole %) for the reactant assemblage (CAR), the product assemblage (CAP), and the intergranular fluid. The amount of Al in the CAP serves as a proxy for the duration of crystallization when viewing these figures.

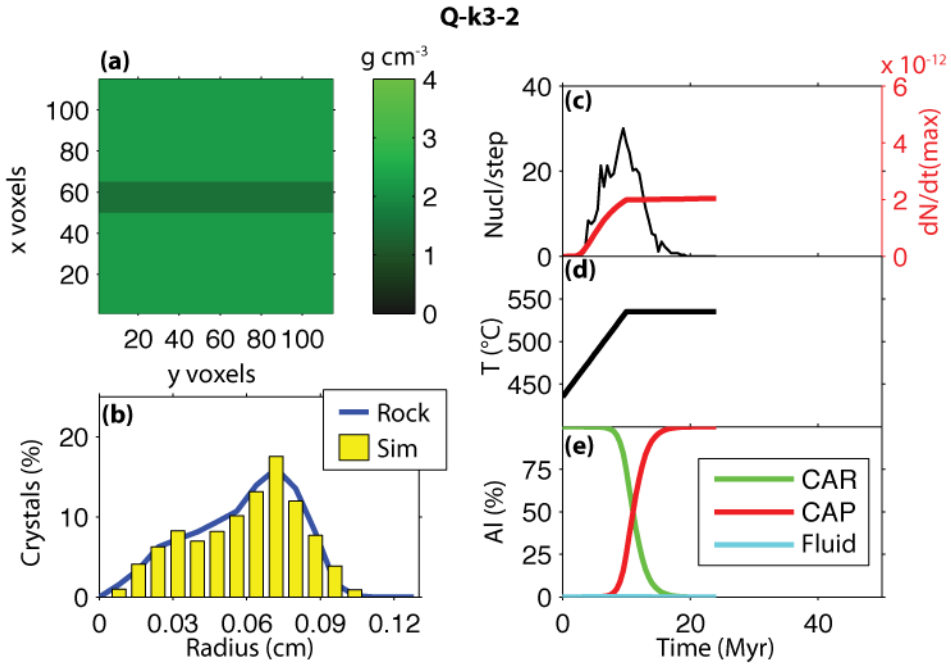

Selected model parameters			
Steady-state nucleation rate	k_1	2.7E-12	nuclei cm^{-3} s^{-1}
Nucleation acceleration	k_2	1.0	
Diffusive flux constant	k_3	1.2E-9	m^2 s^{-1}
Activation energy	Q_D	123	kJ mol^{-1}

Figure 3-41. Results from the sensitivity analysis of the co-variation of Q_D and k_3. (a) Initial distribution of the reactants. In this model, two layers of Al-bearing reactants were used with a layer of Al-poor reactants between. (b) Comparison of the crystal-size distribution between the rock and simulation. (c) Number of nuclei per time step (black curve, nuclei per 0.5 Myr per cm^3) and the maximum nucleation rate (red curve, nuclei cm^{-3} s^{-1}). (d) Extent of the prescribed heating path attained in the simulation. (e) Percentage of Al in the system (mole %) for the reactant assemblage (CAR), the product assemblage (CAP), and the intergranular fluid. The amount of Al in the CAP serves as a proxy for the duration of crystallization when viewing these figures.

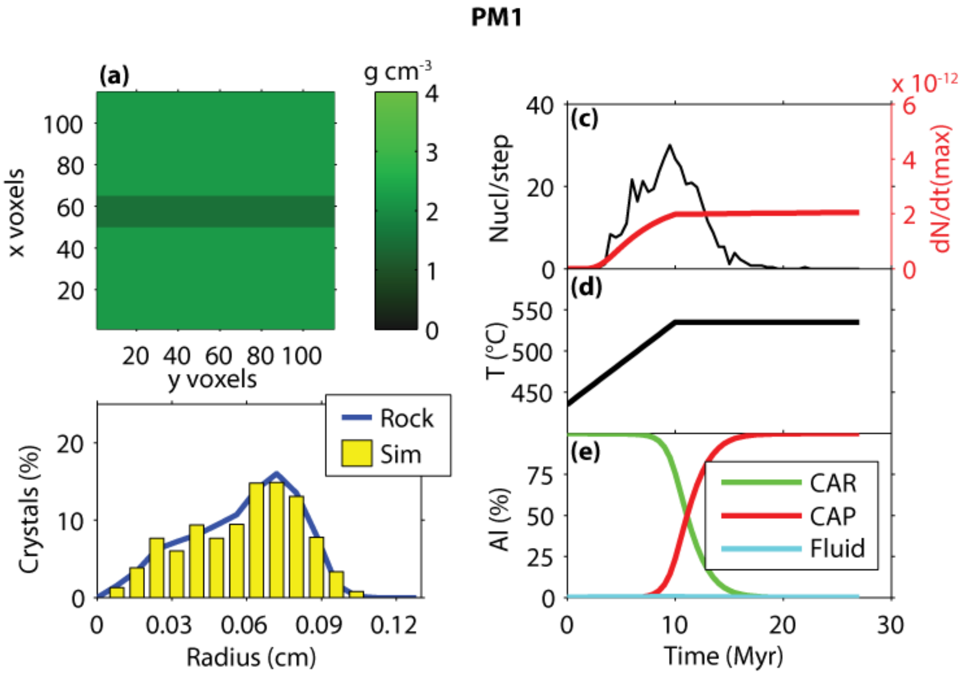

Selected model parameters

Steady-state nucleation rate	k_1	2.7E-12	nuclei cm^{-3} s^{-1}
Nucleation acceleration	k_2	1.0	
Diffusive flux constant	k_3	1.5E-8	m^2 s^{-1}
Activation energy	Q_D	140	kJ mol^{-1}

Figure 3-42. Results from the sensitivity analysis of the co-variation of Q_D and k_3. (a) Initial distribution of the reactants. In this model, two layers of Al-bearing reactants were used with a layer of Al-poor reactants between. (b) Comparison of the crystal-size distribution between the rock and simulation. (c) Number of nuclei per time step (black curve, nuclei per 0.5 Myr per cm^3) and the maximum nucleation rate (red curve, nuclei cm^{-3} s^{-1}). (d) Extent of the prescribed heating path attained in the simulation. (e) Percentage of Al in the system (mole %) for the reactant assemblage (CAR), the product assemblage (CAP), and the intergranular fluid. The amount of Al in the CAP serves as a proxy for the duration of crystallization when viewing these figures.

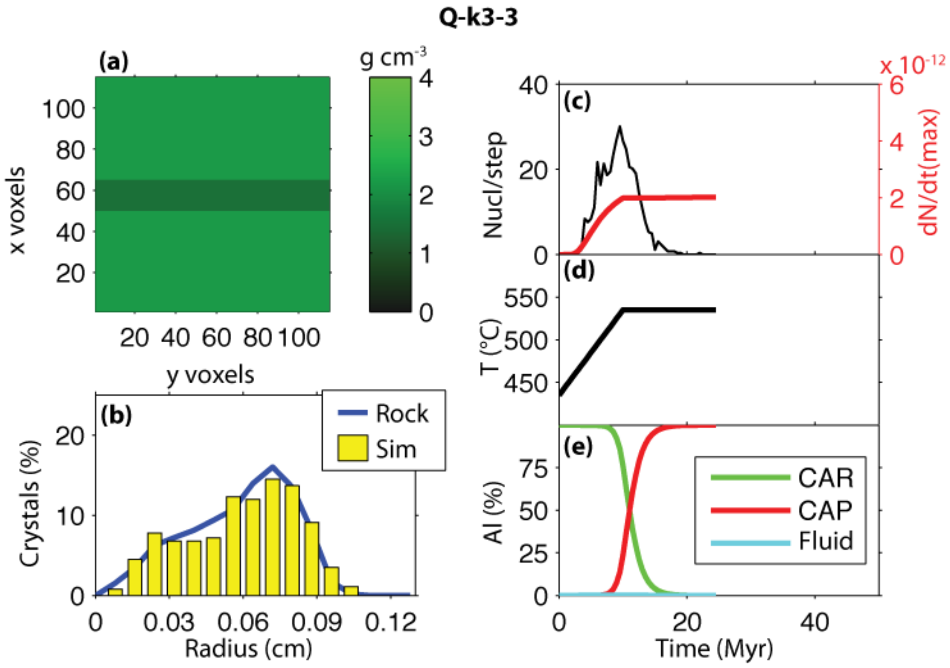

Selected model parameters			
Steady-state nucleation rate	k_1	2.7E-12	nuclei cm^{-3} s^{-1}
Nucleation acceleration	k_2	1.0	
Diffusive flux constant	k_3	2.3 E-7	m^2 s^{-1}
Activation energy	Q_D	158	kJ mol^{-1}

Figure 3-43. Results from the sensitivity analysis of the co-variation of Q_D and k_3. (a) Initial distribution of the reactants. In this model, two layers of Al-bearing reactants were used with a layer of Al-poor reactants between. (b) Comparison of the crystal-size distribution between the rock and simulation. (c) Number of nuclei per time step (black curve, nuclei per 0.5 Myr per cm^3) and the maximum nucleation rate (red curve, nuclei cm^{-3} s^{-1}). (d) Extent of the prescribed heating path attained in the simulation. (e) Percentage of Al in the system (mole %) for the reactant assemblage (CAR), the product assemblage (CAP), and the intergranular fluid. The amount of Al in the CAP serves as a proxy for the duration of crystallization when viewing these figures.

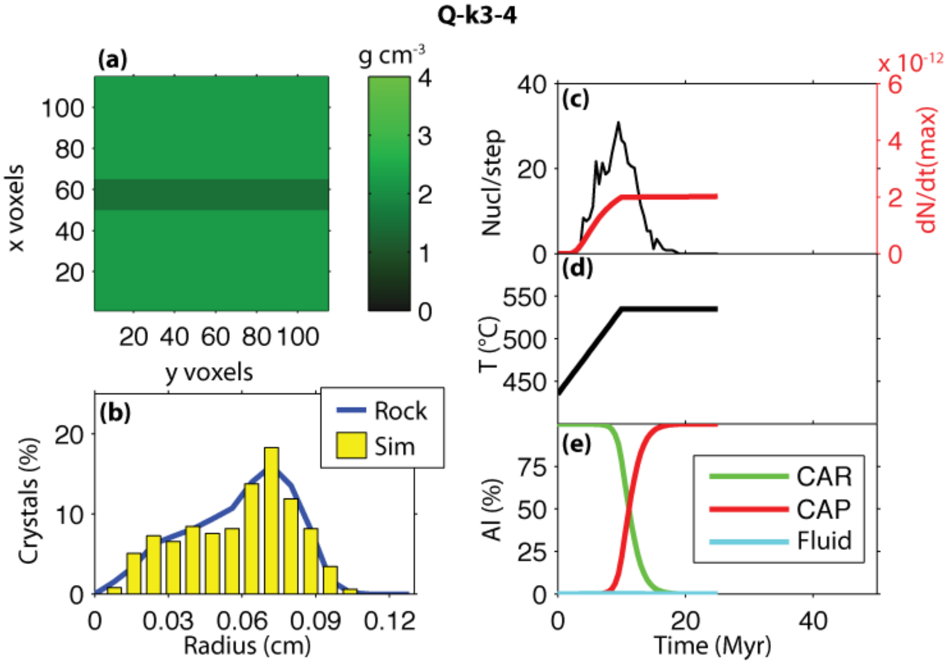

Selected model parameters			
Steady-state nucleation rate	k_1	2.7E-12	nuclei cm^{-3} s^{-1}
Nucleation acceleration	k_2	1.0	
Diffusive flux constant	k_3	2.8E-6	m^2 s^{-1}
Activation energy	Q_D	175	kJ mol^{-1}

Figure 3-44. Results from the sensitivity analysis of the co-variation of Q_D and k_3. (a) Initial distribution of the reactants. In this model, two layers of Al-bearing reactants were used with a layer of Al-poor reactants between. (b) Comparison of the crystal-size distribution between the rock and simulation. (c) Number of nuclei per time step (black curve, nuclei per 0.5 Myr per cm^3) and the maximum nucleation rate (red curve, nuclei cm^{-3} s^{-1}). (d) Extent of the prescribed heating path attained in the simulation. (e) Percentage of Al in the system (mole %) for the reactant assemblage (CAR), the product assemblage (CAP), and the intergranular fluid. The amount of Al in the CAP serves as a proxy for the duration of crystallization when viewing these figures.

approach their final values. Therefore, the following procedure was used to fit the simulations to the natural textures:

1. To begin the fitting procedure, the initial reactant concentration was homogeneously distributed. The initial reactant concentration was adjusted until the mode of the simulation matched the natural sample to within ~10 percent relative.
2. Next, adjustments to the nucleation rate and the diffusive flux were made through k_1 and k_3 to produce a crystal number density that matched the natural texture to within ~10 percent relative, which established a mean crystal size close to the actual mean size in the rock.
3. The parameters k_1 and k_3 were further adjusted in parallel to establish the duration of crystallization (cf. Fig. 2-6).
4. Nucleation acceleration k_2 effectively increases or decreases the sizes of the porphyroblasts, and this shifts the CSD toward larger or smaller crystal radius. At this point in the fitting procedure, k_2 was adjusted to fit the portion of the CSD with the smallest crystals by reducing the small-radius peak that appears in some samples, and by shifting the CSD to larger or smaller sizes to roughly match the radii of the smallest crystals. As k_2 was adjusted, iterative adjustments to k_1 and k_3 were needed to maintain the mean crystal size and the crystallization duration.
5. The next step was to make small adjustments to the reactant distribution while maintaining the total amount of reactant material (to maintain the mode). Changes to the reactant distribution produce portions of the simulation volume with high reactant concentrations that can maintain the maximum Al concentration through a large portion of the crystallization interval, and portions of the simulation volume with low reactant concentrations in which the Al concentration falls below the maximum early in the crystallization interval. In these portions of the simulation volume with low reactant concentrations, the crystal number density will diminish, and Al must diffuse

longer distances between reactants and products, so this results in longer crystallization durations. Increases in k_1 and k_3 can be used to reduce the crystallization duration.

6. The final step was to check the degree of ordering and nucleation suppression, through correlation functions described below, and to increase or decrease the diffusive flux or adjust the reactant distribution to affect their relative length scales.

RESULTS: BEST-FIT SIMULATIONS

Most of the simulations fit the natural samples to a high degree of correspondence. A comparison between the best-fit simulations and the measured textural characteristics appears in Table 3-5, whereas the kinetic parameters extracted from the simulations are given in Table 3-6. Additional comparisons and simulation characteristics are given in Figure 3-45.

Known values

The mode, crystal number density, and mean radius from the simulations fit the characteristics of the natural samples to within 5% relative in most cases, and to within 10% relative with some exceptions like the mode of WR1tp . Comparisons of the CSDs from the simulations with those of the natural samples, especially the locations of the peaks and the minimum and maximum radii, likewise reveal a good fit for most specimens. More sophisticated comparisons are made using a pair-correlation function (PCF) and a mark-correlation function (MCF), described in the previous chapter and briefly reviewed next.

Statistical evidence for nucleation suppression and growth competition can be revealed using functions that determine pair-correlations (PCF) and mark-correlations (MCF) (Raeburn, 1996; Daniel & Spear, 1999; Hirsch *et al.*, 2000; Ketcham *et al.*, 2005). The PCF is designed to determine if the separations of crystal centers are randomly distributed or if there is a more ordered disposition of crystals, which is a result of DCNG. The MCF uses volume for the mark and calculates correlation between

Table 3-5. Comparison of best-fit simulation values with measured and derived crystallization characteristics.

	Mode (volume %)		Crystal Number Density (crystals cm^{-3})		Mean Crystal Radius (cm)		T_{rim} (°C)		Crystallization Duration (Myr)	
Sample	Rock	Sim.	Rock	Sim.	Rock	Sim.	Rock	Sim.	Rock[a]	Sim.
PM1	37.4	38	382	386	0.058	0.059	510-560	535	10	12
PM2	8.3	8.7	112	108	0.047	0.049	510-560	535	10	14
PM4	6.2	6.6	44	43	0.063	0.064	510-560	535	10	13
160A	15.1	15.6	6413	6437	0.017	0.017	510-560	535	10	16
191A	9.5	10.6	31946	31973	0.009	0.009	545-595	570	7.1	13.0
711A	12.4	12.1	3103	3125	0.019	0.019	575-625	600	5	8.5
AG4	9.0	9.2	28	29	0.074	0.078	~600	600	4	14.5
MD	8.8	8.5	7	7	0.121	0.126	630-710	655	20	17
Jen-2-80	28.1	28	239	233	0.046	0.052	~500	500	1.3	8.2
HE-1	29.2	28.7	263	261	0.059	0.060	~550	550	1	5.5
WR1bt	48.3	45.4	193	194	0.077	0.081	610-690	650	7.5	6
WR1tp	39.3	32.2	64	62	0.102	0.100	610-690	650	7.5	9.5
WR3m	23.1	20.6	393	370	0.041	0.044	610-690	650	7.5	10

[a] Crystallization durations for the natural samples were estimated from the heating rates and the thermal history, which are not well constrained.

Table 3-6. Determined parameters

Rock	k_1 (N cm^{-3} s^{-1})	($\mathrm{d}N/\mathrm{d}t)_{\mathrm{max}}$ (N cm^{-3} s^{-1})	k_2	k_3 (m^2 s^{-1})	D_∞ (m^2 s^{-1})	T_c (°C)	$D(T_\mathrm{c})$ (m^2 s^{-1})	D(600 °C) (m^2 s^{-1})
PM1	2.70E-12	2.05E-12	1	1.50E-08	1.50E-03	530	1.18E-12	6.32E-12
PM2	3.50E-13	3.40E-13	0.1	6.00E-09	6.00E-04	530	4.71E-13	2.53E-12
PM4	1.50E-13	1.42E-13	0.2	3.60E-08	3.60E-03	525	2.48E-12	1.52E-11
160A	1.30E-10	2.65E-11	0.5	6.40E-09	1.28E-04	533	1.09E-13	5.40E-13
191A	1.90E-09	1.44E-10	2	2.90E-10	5.80E-06	564	1.07E-14	2.44E-14
711A	3.90E-11	2.32E-11	0.7	8.10E-10	1.62E-05	600	6.83E-14	6.83E-14
AG4	3.00E-13	2.95E-13	0.005	1.00E-08	1.00E-03	600	4.22E-12	4.22E-12
MD	3.00E-14	2.63E-14	0.1	6.00E-09	6.00E-04	630	4.80E-12	2.53E-12
Jen-2-80	1.40E-12	1.40E-12	0.001	5.20E-08	5.20E-03	500	1.81E-12	2.19E-11
HE-1	1.30E-11	2.73E-12	0.5	6.00E-09	6.00E-04	550	7.84E-13	2.53E-12
WR1bt	2.00E-08	3.41E-12	3	4.50E-10	4.50E-04	645	4.88E-12	1.90E-12
WR1tp	2.40E-09	4.09E-13	3	6.40E-10	6.40E-04	645	6.94E-12	2.70E-12
WR3m	1.80E-12	1.75E-12	0.01	3.00E-10	3.00E-04	645	3.25E-12	1.26E-12
Min	3.00E-14	2.63E-14	0.001	2.90E-10	5.80E-06	500	1.07E-14	2.44E-14
Mean	1.88E-09	1.59E-11	0.86	1.08E-08	1.13E-03	577	2.38E-12	4.75E-12
Max	2.00E-08	1.44E-10	3	5.20E-08	5.20E-03	645	6.94E-12	2.19E-11

T_c is the characteristic T (Equation 1-4).

Figure 3-45. Best-fit simulations for all samples. (a) The initial distribution of the reactants. (b) Comparison of the crystal-size distribution between the rock and simulation. (c) Nucleation rate curves expressed as the number of nuclei per time step per unit volume (black curve, nuclei per 0.5 Myr per cm^3) and the maximum nucleation rate (red curve, nuclei cm^{-3} s^{-1}). (d) Extent of the prescribed heating path attained in the simulation. (e) Percentage of Al in the system (mole %) for the reactant assemblage (CAR), the product assemblage (CAP), and the intergranular fluid. The amount of Al in the CAP serves as an indicator of crystallization progress when viewing these figures. (g) Correlation functions for the porphyroblastic texture of the natural dataset. (h) Correlation functions for the porphyroblastic texture of the simulation. The correlation functions are applied by measuring the distances between crystals and the volume of each crystal to look for ordering of crystal centers and decreased volume between neighboring crystals. The test distance is the radial distance of a measurement centered on a single crystal. All crystals in the dataset are measured against all other crystals, but in DCNG, nucleation suppression and growth suppression are influenced almost entirely by neighboring crystals. The yellow area indicates the mean nearest-neighbor distance between crystal centers (± 1σ). The gray area is a 95% confidence envelope for nearly random placements of crystals with the same crystal-size distribution as the analyzed dataset. The pair-correlation function (PCF) indicates either clustering, when the values plot above the envelope, or nucleation suppression, when the values plot below the envelope. The mark-correlation function (MCF) indicates growth suppression when the values plot below the envelope.

PM1

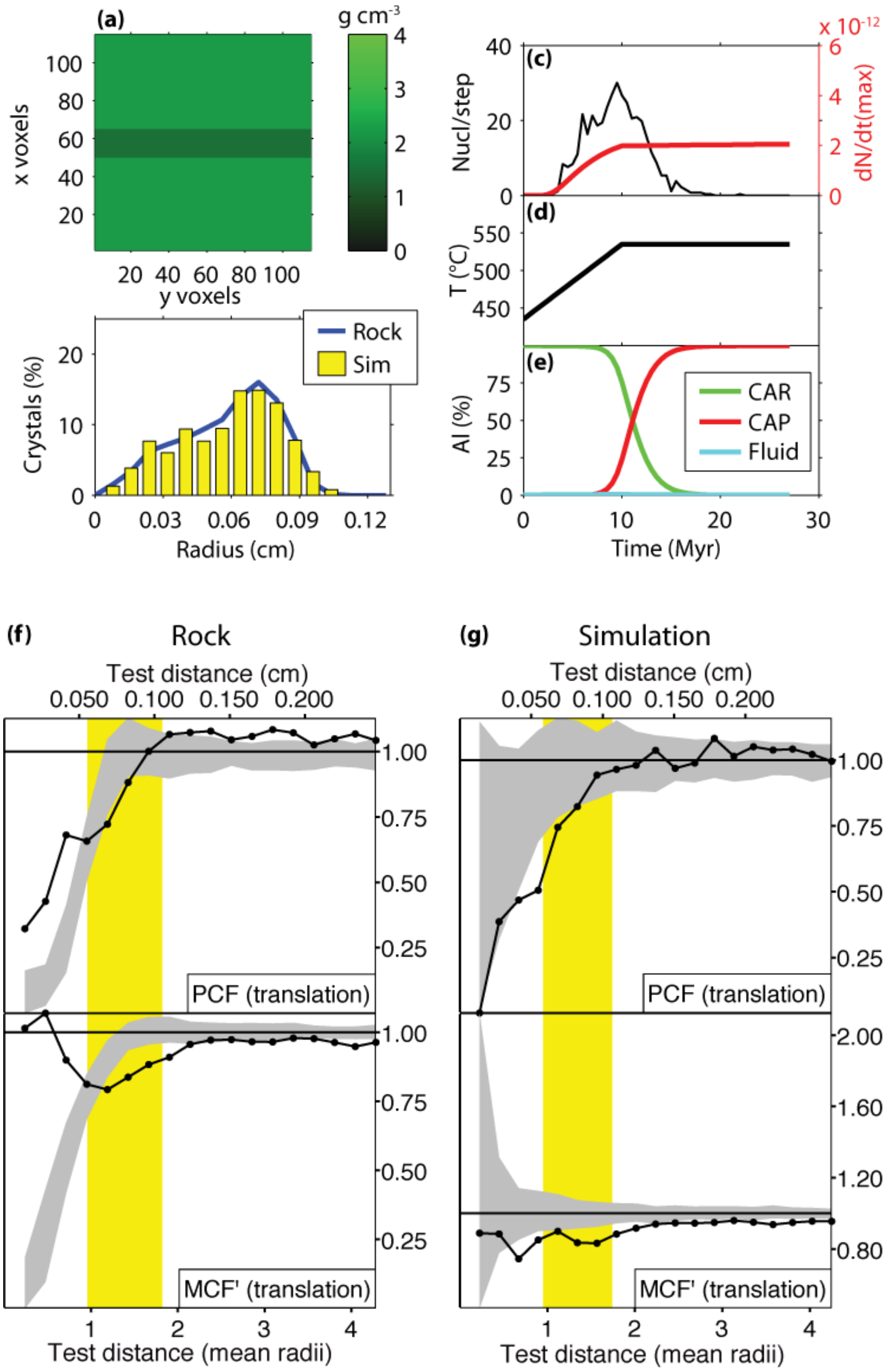
(a)
g cm-3
4
3
2
1
0
100
80
60
40
20
x voxels
20 40 60 80 100
y voxels
Rock
Sim
Crystals (%)
20
10
0
0 0.03 0.06 0.09 0.12
Radius (cm)
(c)
x 10-12
40
20
0
Nucl/step
6
4
2
0
dN/dt(max)
(d)
550
500
450
T (°C)
(e)
75
50
25
0
Al (%)
CAR
CAP
Fluid
0 10 20 30
Time (Myr)
(f)
Rock
Test distance (cm)
0.050 0.100 0.150 0.200
1.00
0.75
0.50
0.25
PCF (translation)
1.00
0.75
0.50
0.25
MCF' (translation)
1 2 3 4
Test distance (mean radii)
(g)
Simulation
Test distance (cm)
0.050 0.100 0.150 0.200
1.00
0.75
0.50
0.25
PCF (translation)
2.00
1.60
1.20
0.80
MCF' (translation)
1 2 3 4
Test distance (mean radii)

PM2

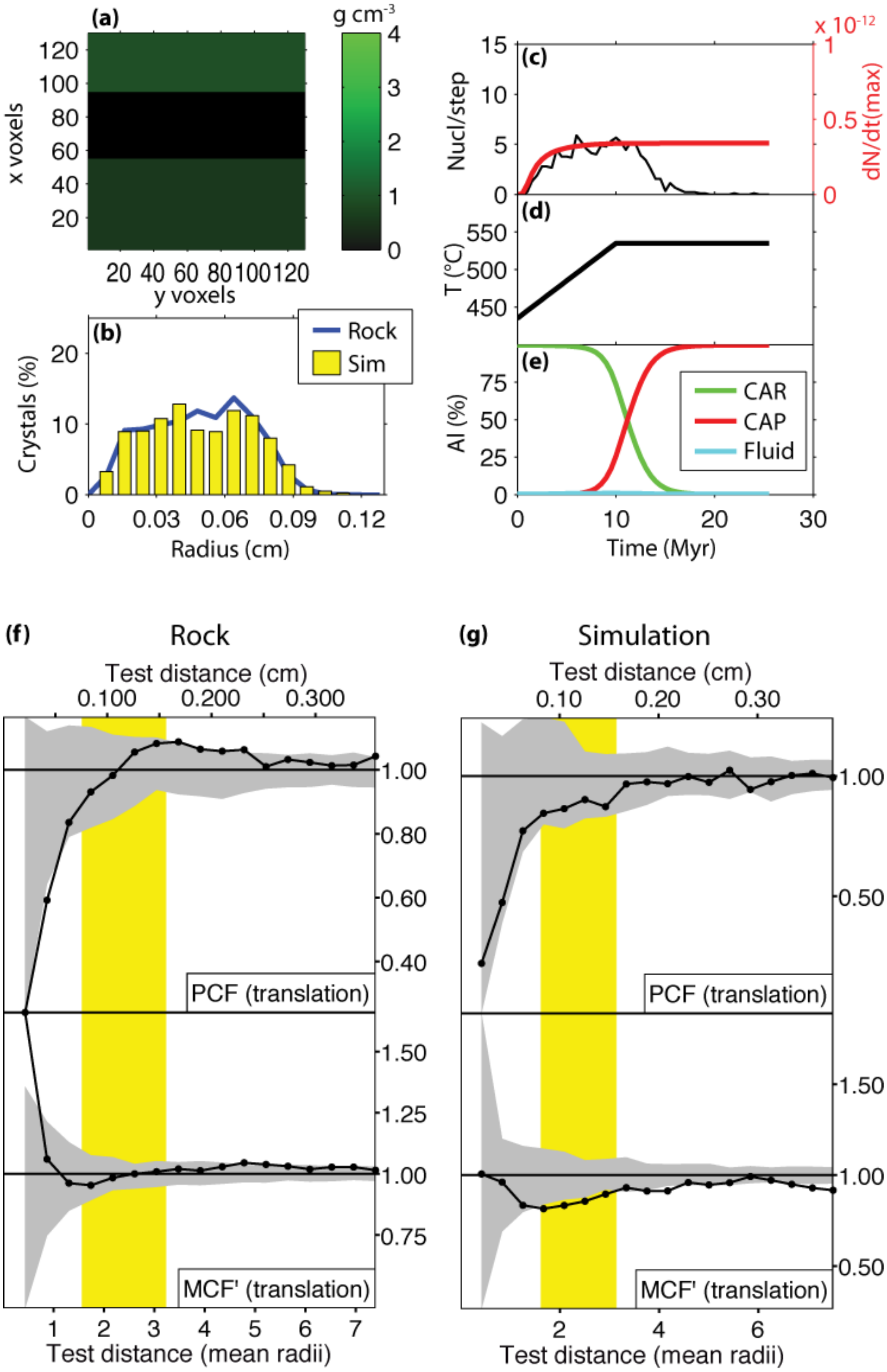

(a)
g cm-3
4
3
2
1
0
120
100
80
60
40
20
x voxels
20 40 60 80 100 120
y voxels
(b)
Rock
Sim
20
10
0
Crystals (%)
0
0.03
0.06
0.09
0.12
Radius (cm)
(c)
x 10-12
15
10
5
0
Nucl/step
1
0.5
0
dN/dt(max)
(d)
550
500
450
T (°C)
(e)
75
50
25
0
Al (%)
CAR
CAP
Fluid
0
10
20
30
Time (Myr)
(f)
Rock
Test distance (cm)
0.100
0.200
0.300
1.00
0.80
0.60
0.40
PCF (translation)
1.50
1.25
1.00
0.75
MCF' (translation)
1
2
3
4
5
6
7
Test distance (mean radii)
(g)
Simulation
Test distance (cm)
0.10
0.20
0.30
1.00
0.50
PCF (translation)
1.50
1.00
0.50
MCF' (translation)
2
4
6
Test distance (mean radii)

PM4

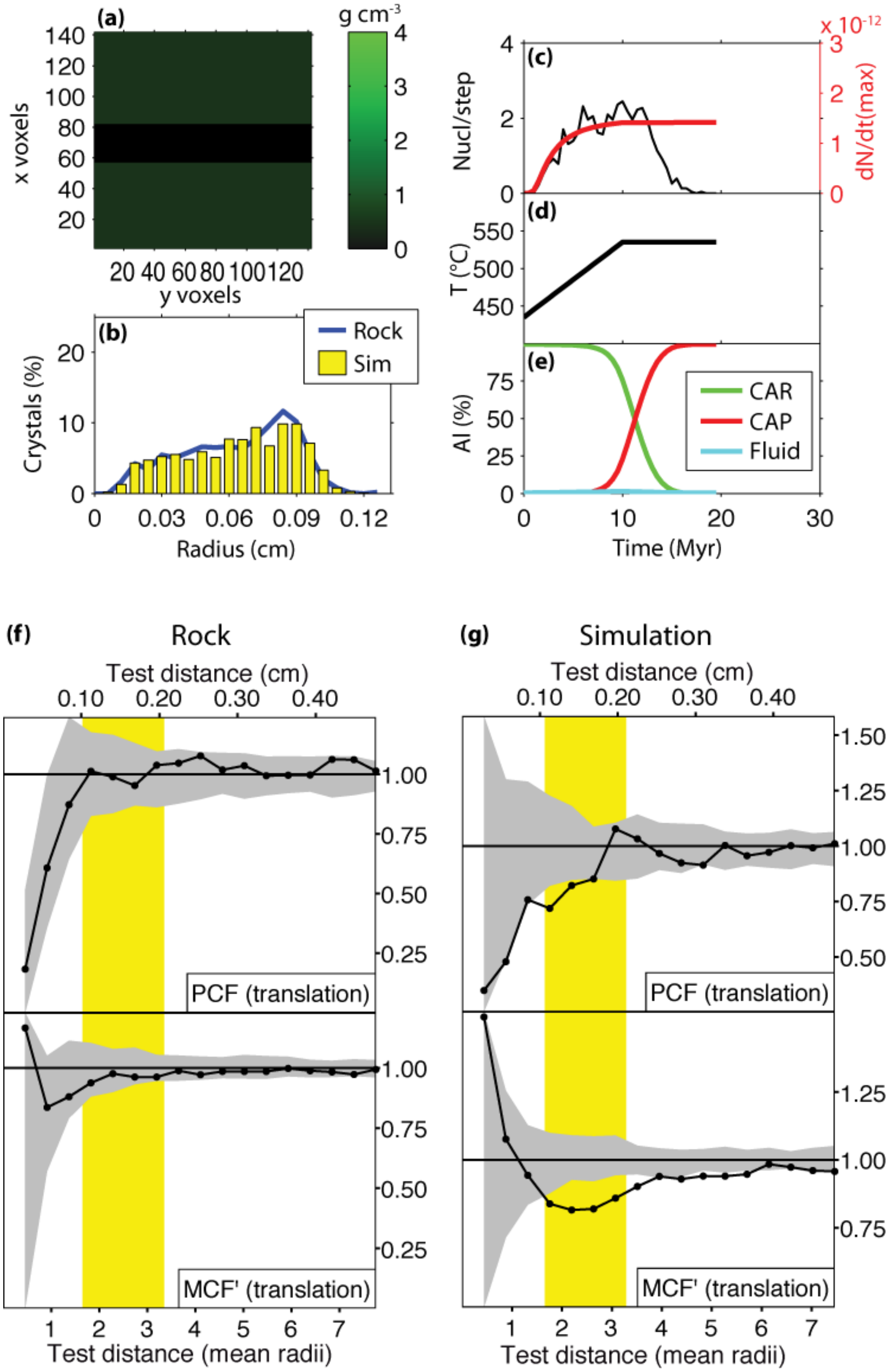
(a)
140
120
100
80
60
40
20
x voxels
20 40 60 80 100 120
y voxels
g cm-3
4
3
2
1
0
(b)
Rock
Sim
20
10
0
Crystals (%)
0 0.03 0.06 0.09 0.12
Radius (cm)
(c)
4
2
0
Nucl/step
x 10-12
3
2
1
0
dN/dt(max)
(d)
550
500
450
T (°C)
(e)
75
50
25
0
Al (%)
CAR
CAP
Fluid
0 10 20 30
Time (Myr)
(f)
Rock
Test distance (cm)
0.10 0.20 0.30 0.40
1.00
0.75
0.50
0.25
PCF (translation)
1.00
0.75
0.50
0.25
MCF' (translation)
1 2 3 4 5 6 7
Test distance (mean radii)
(g)
Simulation
Test distance (cm)
0.10 0.20 0.30 0.40
1.50
1.25
1.00
0.75
0.50
PCF (translation)
1.25
1.00
0.75
MCF' (translation)
1 2 3 4 5 6 7
Test distance (mean radii)

160A

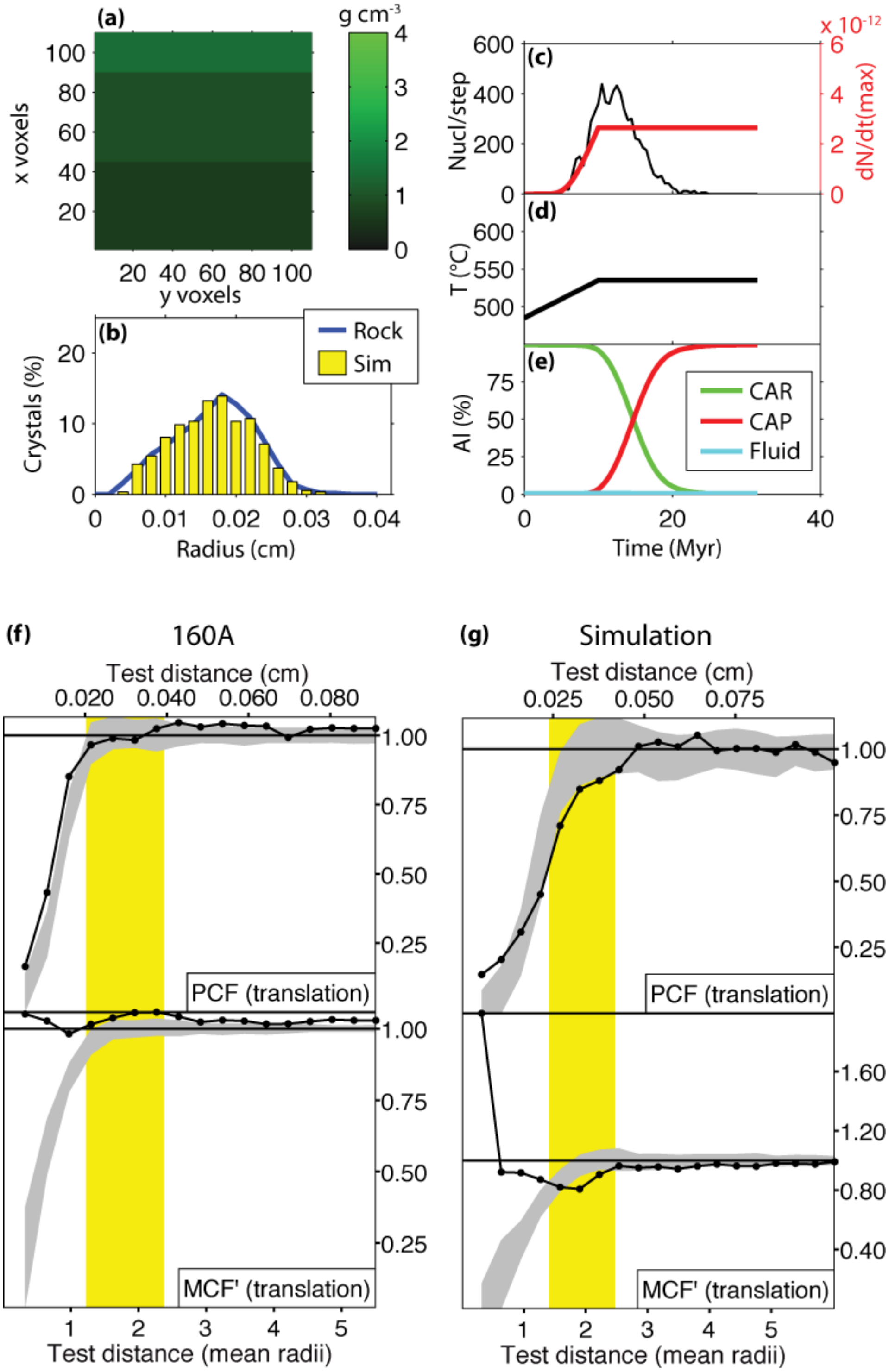
(a)
x voxels
y voxels
g cm-3
(b)
Crystals (%)
Radius (cm)
Rock
Sim
(c)
Nucl/step
x 10-12
dN/dt(max)
(d)
T (°C)
(e)
Al (%)
CAR
CAP
Fluid
Time (Myr)
(f)
160A
(g)
Simulation
Test distance (cm)
PCF (translation)
MCF' (translation)
Test distance (mean radii)

191A

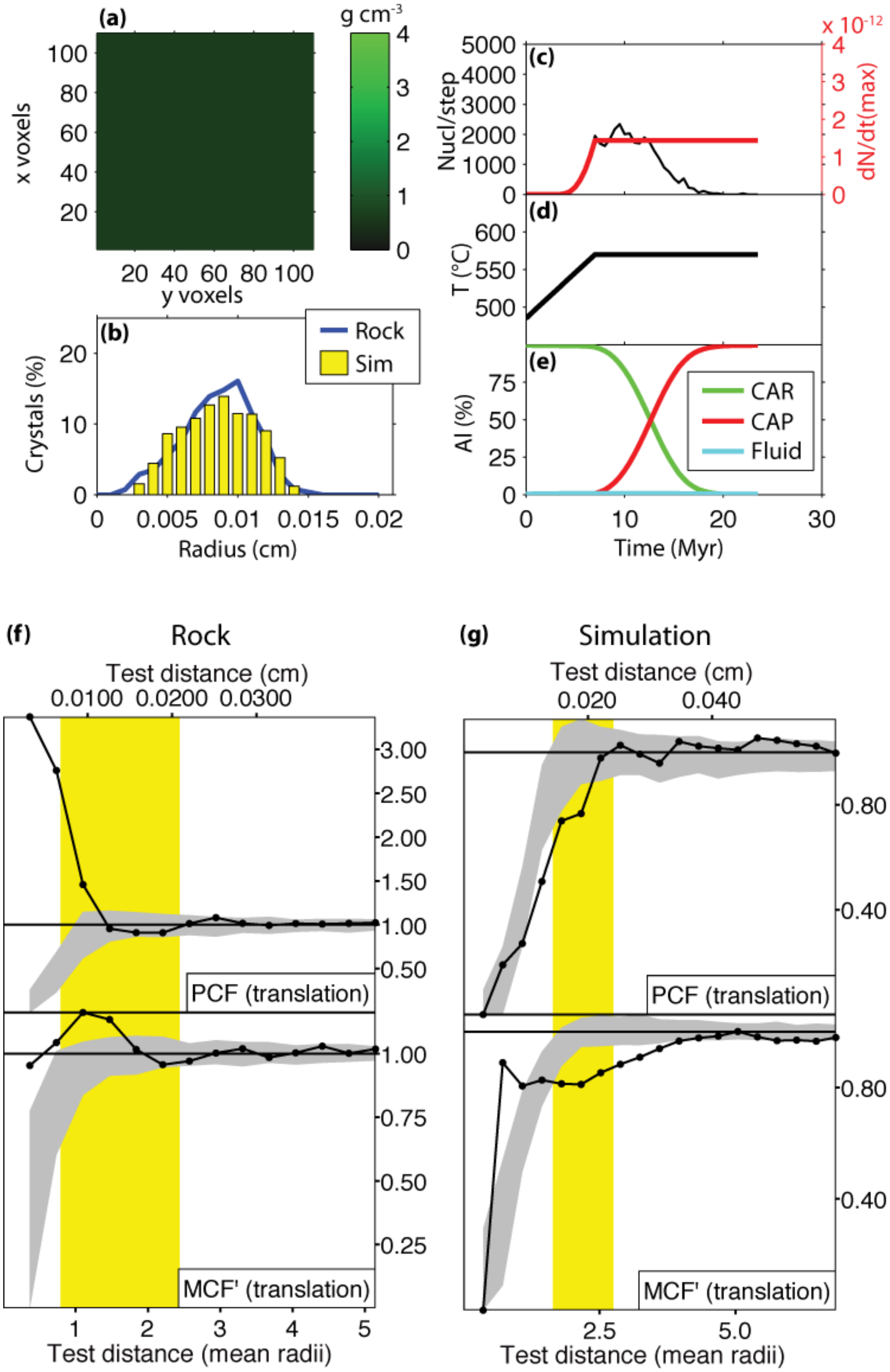
(a)
g cm-3
4
3
2
1
0
100
80
60
40
20
x voxels
20 40 60 80 100
y voxels
(b)
Rock
Sim
Crystals (%)
20
10
0
0 0.005 0.01 0.015 0.02
Radius (cm)
(c)
5000
4000
3000
2000
1000
0
Nucl/step
x 10-12
4
3
2
1
0
dN/dt(max)
(d)
600
550
500
T (°C)
(e)
75
50
25
0
Al (%)
CAR
CAP
Fluid
0 10 20 30
Time (Myr)
(f)
Rock
Test distance (cm)
0.0100 0.0200 0.0300
3.00
2.50
2.00
1.50
1.00
0.50
PCF (translation)
1.00
0.75
0.50
0.25
MCF' (translation)
1 2 3 4 5
Test distance (mean radii)
(g)
Simulation
Test distance (cm)
0.020 0.040
0.80
0.40
PCF (translation)
0.80
0.40
MCF' (translation)
2.5 5.0
Test distance (mean radii)

711A

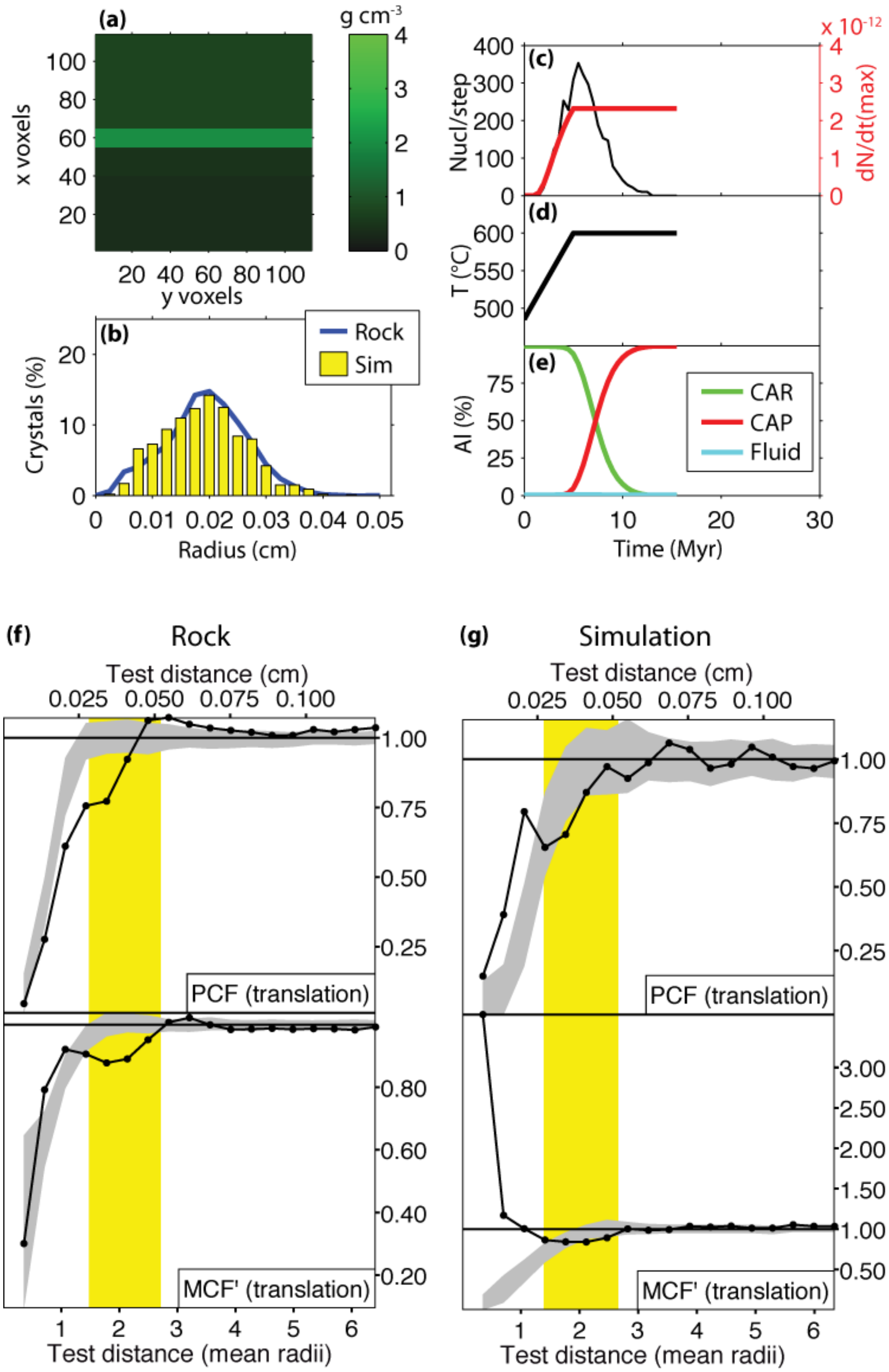
(a)
g cm-3
4
3
2
1
0
100
80
60
40
20
x voxels
20 40 60 80 100
y voxels
(b)
Rock
Sim
Crystals (%)
20
10
0
0 0.01 0.02 0.03 0.04 0.05
Radius (cm)
(c)
x 10-12
400
300
200
100
0
Nucl/step
4
3
2
1
0
dN/dt(max)
(d)
600
550
500
T (°C)
(e)
CAR
CAP
Fluid
75
50
25
0
Al (%)
0 10 20 30
Time (Myr)
(f)
Rock
(g)
Simulation
Test distance (cm)
0.025 0.050 0.075 0.100
1.00
0.75
0.50
0.25
PCF (translation)
0.80
0.60
0.40
0.20
MCF' (translation)
3.00
2.50
2.00
1.50
1.00
0.50
1 2 3 4 5 6
Test distance (mean radii)

AG4

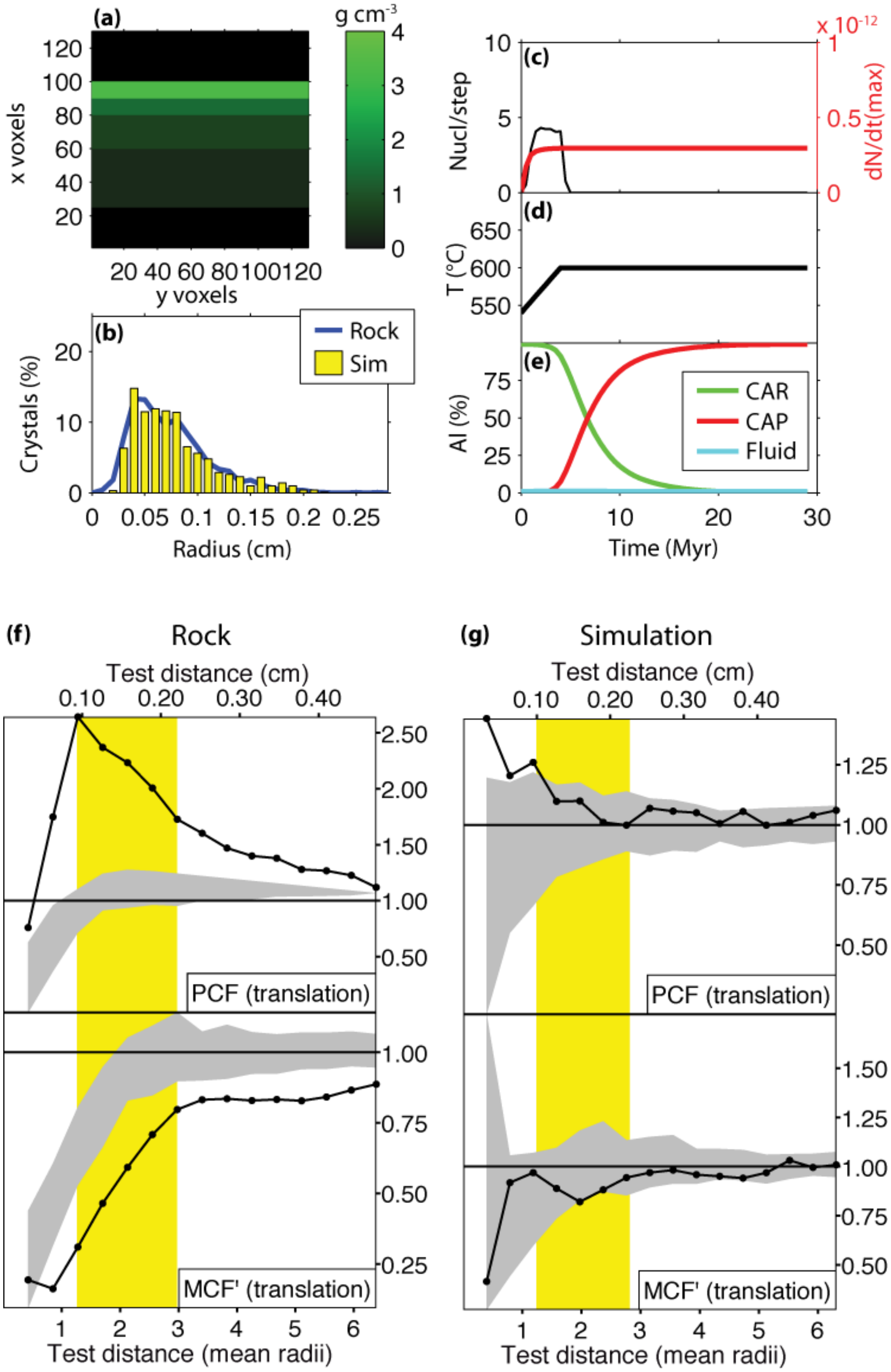
(a)
g cm^{-3}
4
3
2
1
0
120
100
80
60
40
20
x voxels
20 40 60 80 100 120
y voxels
(b)
Rock
Sim
Crystals (%)
20
10
0
0 0.05 0.1 0.15 0.2 0.25
Radius (cm)
(c)
10
5
0
Nucl/step
x 10^{-12}
1
0.5
0
dN/dt(max)
(d)
650
600
550
T (°C)
(e)
75
50
25
0
Al (%)
CAR
CAP
Fluid
0 10 20 30
Time (Myr)
(f)
Rock
Test distance (cm)
0.10 0.20 0.30 0.40
2.50
2.00
1.50
1.00
0.50
PCF (translation)
1.00
0.75
0.50
0.25
MCF' (translation)
1 2 3 4 5 6
Test distance (mean radii)
(g)
Simulation
Test distance (cm)
0.10 0.20 0.30 0.40
1.25
1.00
0.75
0.50
PCF (translation)
1.50
1.25
1.00
0.75
0.50
MCF' (translation)
1 2 3 4 5 6
Test distance (mean radii)

MD

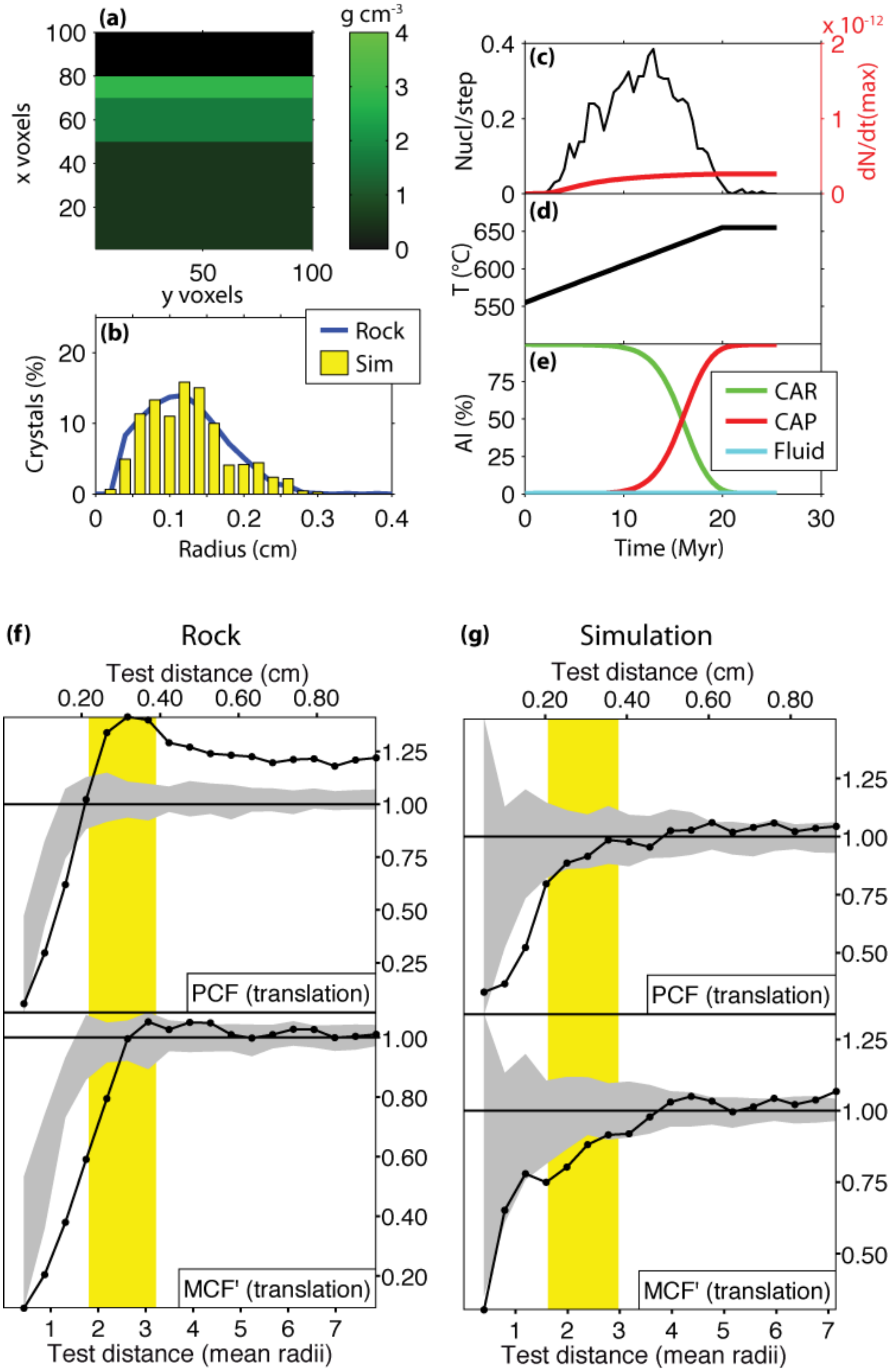
(a)
g cm-3
4
3
2
1
0
100
80
60
40
20
x voxels
50
100
y voxels
(b)
Rock
Sim
Crystals (%)
20
10
0
0
0.1
0.2
0.3
0.4
Radius (cm)
(c)
Nucl/step
0.4
0.2
0
x 10-12
2
1
0
dN/dt(max)
(d)
T (°C)
650
600
550
(e)
Al (%)
75
50
25
0
CAR
CAP
Fluid
0
10
20
30
Time (Myr)
(f)
Rock
Test distance (cm)
0.20
0.40
0.60
0.80
1.25
1.00
0.75
0.50
0.25
PCF (translation)
1.00
0.80
0.60
0.40
0.20
MCF' (translation)
1
2
3
4
5
6
7
Test distance (mean radii)
(g)
Simulation
Test distance (cm)
0.20
0.40
0.60
0.80
1.25
1.00
0.75
0.50
PCF (translation)
1.25
1.00
0.75
0.50
MCF' (translation)
1
2
3
4
5
6
7
Test distance (mean radii)

Jen-2-80

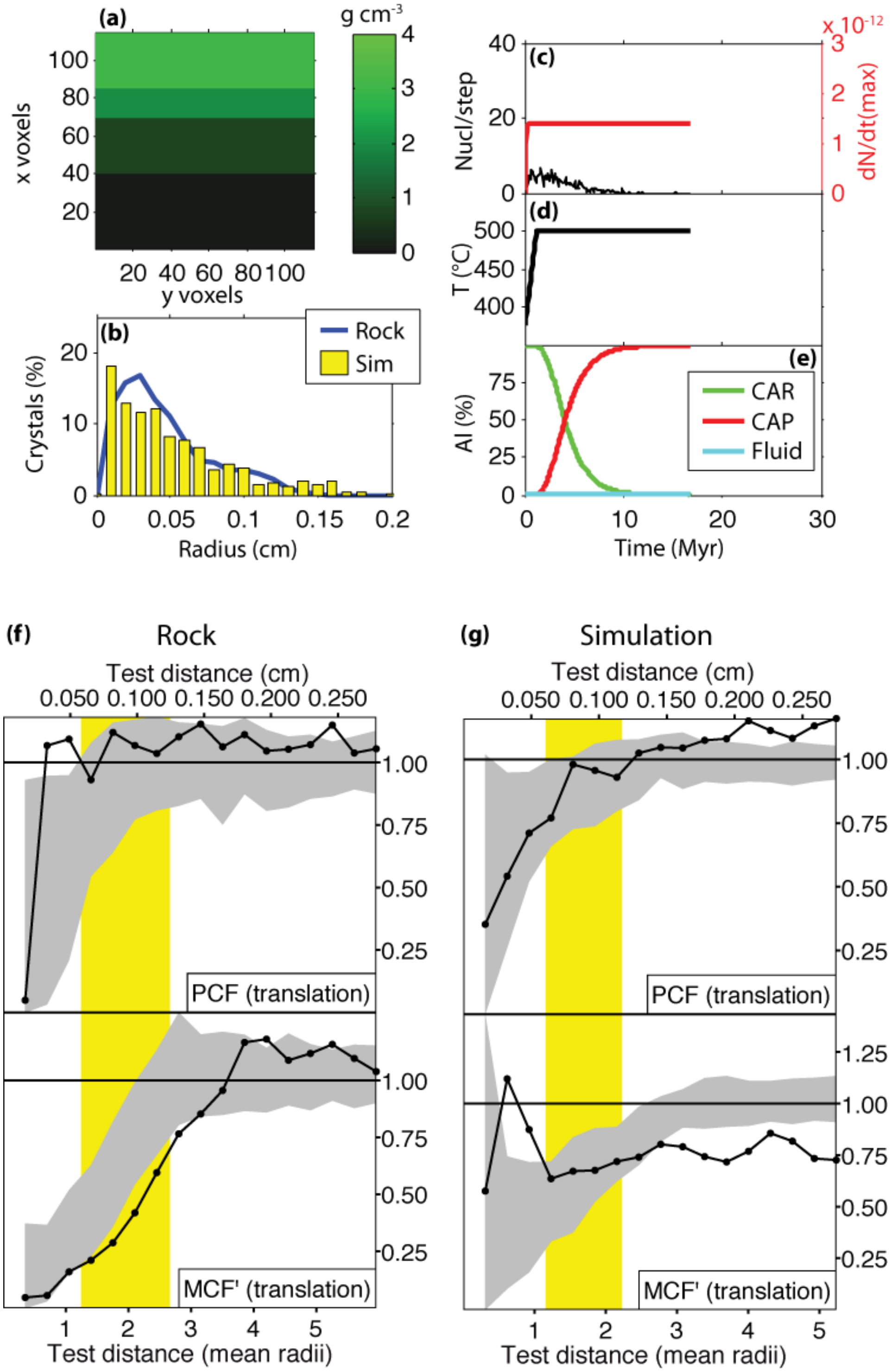
(a)
g cm⁻³
4
3
2
1
0
100
80
60
40
20
x voxels
20 40 60 80 100
y voxels
(b)
Rock
Sim
Crystals (%)
20
10
0
0 0.05 0.1 0.15 0.2
Radius (cm)
(c)
Nucl/step
40
20
0
x 10⁻¹²
3
2
1
0
dN/dt(max)
(d)
T (°C)
500
450
400
(e)
Al (%)
75
50
25
0
CAR
CAP
Fluid
0 10 20 30
Time (Myr)
(f)
Rock
(g)
Simulation
Test distance (cm)
0.050 0.100 0.150 0.200 0.250
1.00
0.75
0.50
0.25
PCF (translation)
1.25
1.00
0.75
0.50
0.25
MCF' (translation)
1 2 3 4 5
Test distance (mean radii)

HE-1

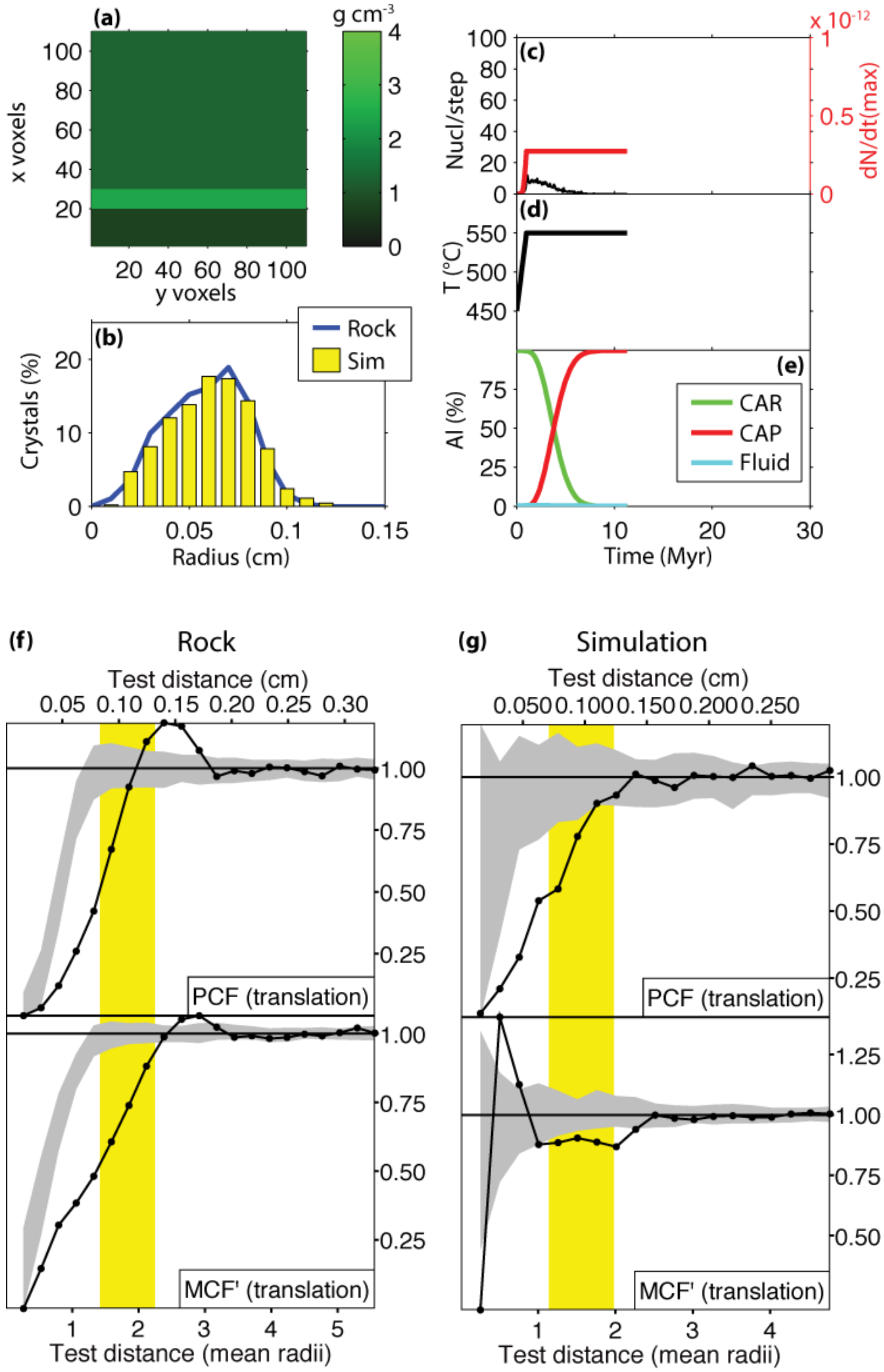

(a)
x voxels
100
80
60
40
20
20 40 60 80 100
y voxels
g cm^{-3}
4
3
2
1
0
(b)
Crystals (%)
20
10
0
0
0.05
0.1
0.15
Radius (cm)
Rock
Sim
(c)
Nucl/step
100
80
60
40
20
0
x 10^{-12}
1
0.5
0
dN/dt(max)
(d)
T (°C)
550
500
450
(e)
Al (%)
75
50
25
0
CAR
CAP
Fluid
0
10
20
30
Time (Myr)
(f)
Rock
Test distance (cm)
0.05 0.10 0.15 0.20 0.25 0.30
1.00
0.75
0.50
0.25
PCF (translation)
1.00
0.75
0.50
0.25
MCF' (translation)
1 2 3 4 5
Test distance (mean radii)
(g)
Simulation
Test distance (cm)
0.050 0.100 0.150 0.200 0.250
1.00
0.75
0.50
0.25
PCF (translation)
1.25
1.00
0.75
0.50
MCF' (translation)
1 2 3 4
Test distance (mean radii)

WR1bt

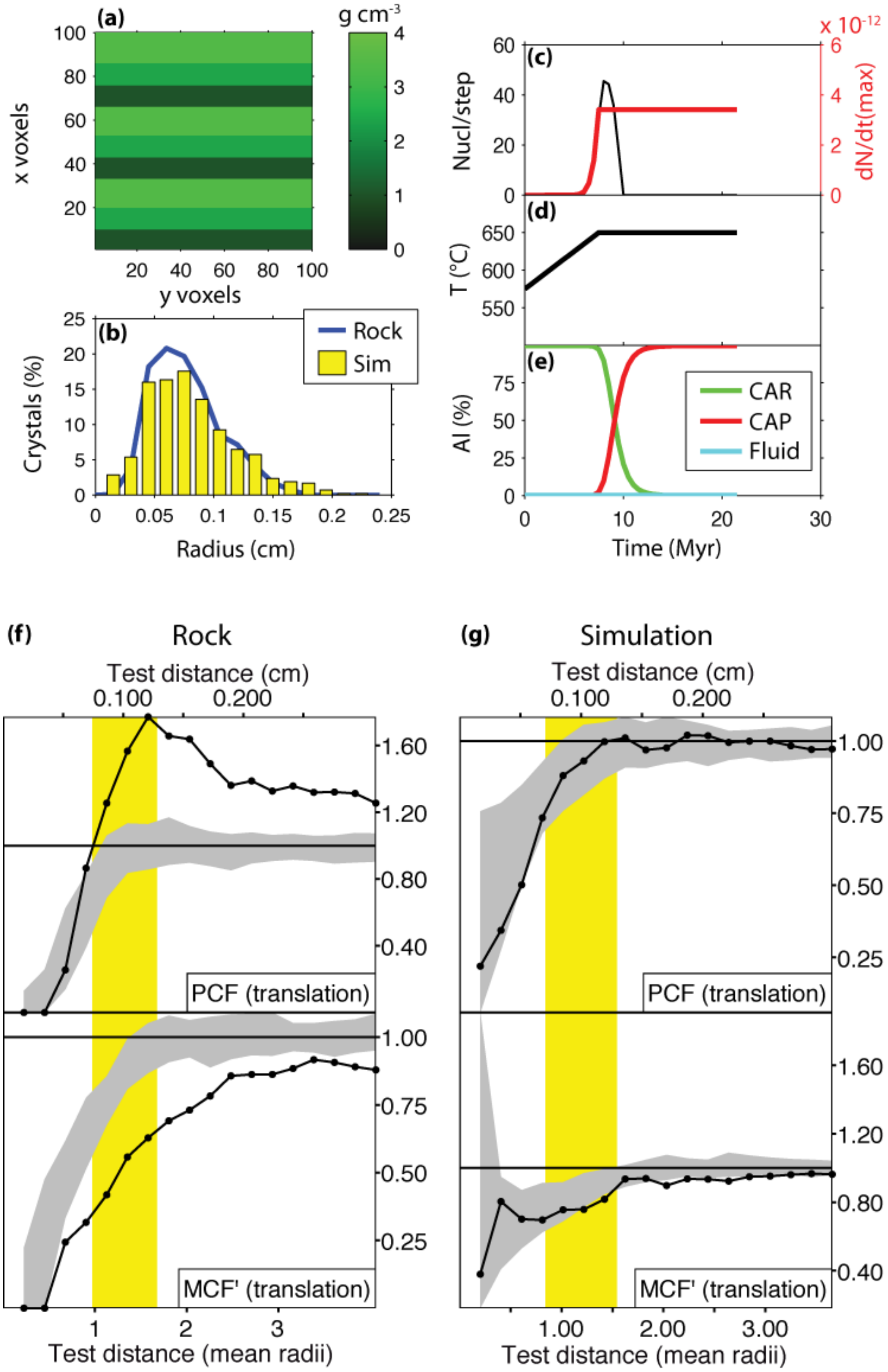

(a)
x voxels
100
80
60
40
20
20 40 60 80 100
y voxels
g cm-3
4
3
2
1
0
(b)
Crystals (%)
25
20
15
10
5
0
0 0.05 0.1 0.15 0.2 0.25
Radius (cm)
Rock
Sim
(c)
Nucl/step
60
40
20
0
x 10-12
6
4
2
0
dN/dt(max)
(d)
T (°C)
650
600
550
(e)
Al (%)
75
50
25
0
CAR
CAP
Fluid
0 10 20 30
Time (Myr)
(f)
Rock
Test distance (cm)
0.100 0.200
1.60
1.20
0.80
0.40
PCF (translation)
1.00
0.75
0.50
0.25
MCF' (translation)
1 2 3
Test distance (mean radii)
(g)
Simulation
Test distance (cm)
0.100 0.200
1.00
0.75
0.50
0.25
PCF (translation)
1.60
1.20
0.80
0.40
MCF' (translation)
1.00 2.00 3.00
Test distance (mean radii)

WR1tp

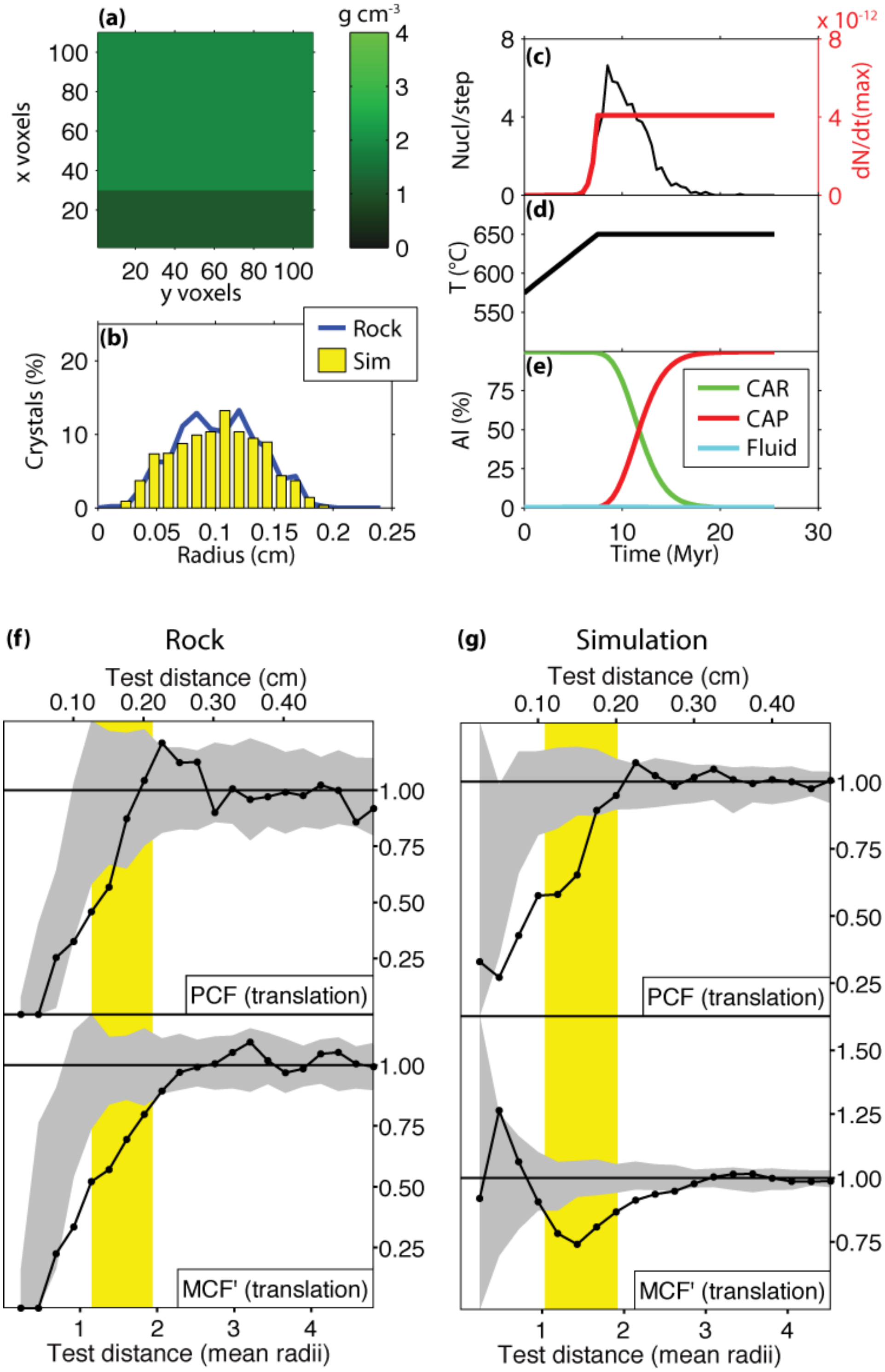

(a)
g cm-3
4
3
2
1
0
100
80
60
40
20
x voxels
20 40 60 80 100
y voxels
(b)
Rock
Sim
Crystals (%)
20
10
0
0 0.05 0.1 0.15 0.2 0.25
Radius (cm)
(c)
x 10-12
8
4
0
Nucl/step
dN/dt(max)
(d)
650
600
550
T (°C)
(e)
CAR
CAP
Fluid
75
50
25
0
Al (%)
0 10 20 30
Time (Myr)
(f)
Rock
Test distance (cm)
0.10 0.20 0.30 0.40
1.00
0.75
0.50
0.25
PCF (translation)
MCF' (translation)
1 2 3 4
Test distance (mean radii)
(g)
Simulation
Test distance (cm)
0.10 0.20 0.30 0.40
1.00
0.75
0.50
0.25
PCF (translation)
1.50
1.25
1.00
0.75
MCF' (translation)
1 2 3 4
Test distance (mean radii)

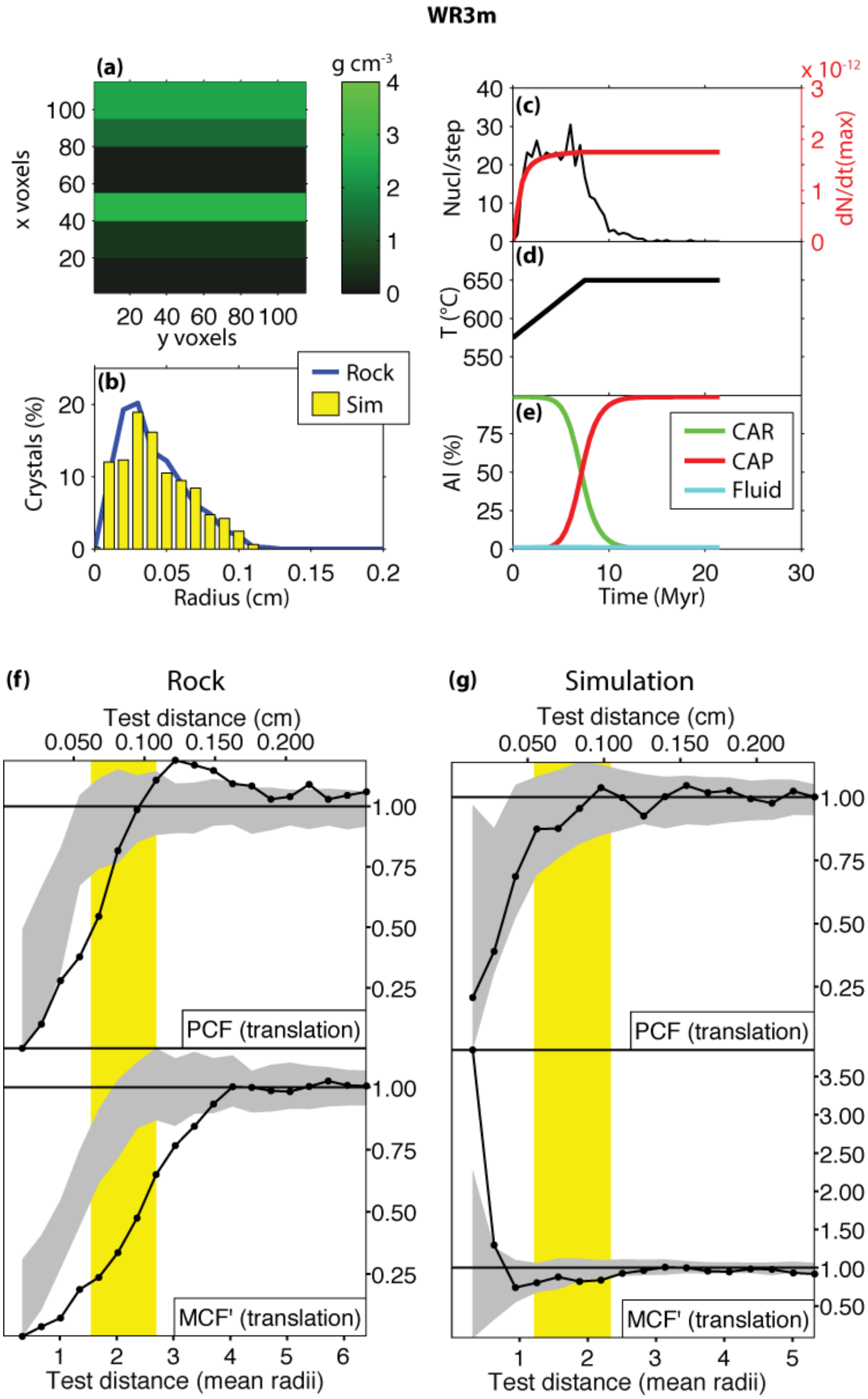

crystal volume and degree of isolation, which essentially determines if crystals with close neighbors are smaller than average. This is also a characteristic of DCNG. In the PCF, values that fall below a 95% confidence envelope for nearly random crystal placements indicate nucleation suppression, interpreted as resulting from reduced reaction affinity surrounding existing crystals (cf. Fig. 1-1), and values that lie above the envelope indicate clustering of crystals, interpreted as nucleation sites located in close proximity to one another due to reactant inhomogeneities. In the MCF, values that fall below the envelope indicate growth suppression, interpreted as nutrient competition between neighboring crystals. These statistical measures bring an added level of robustness to the examination of porphyroblastic textures that result from DCNG by describing features that would otherwise be difficult to see or quantify.

The correlation function results for many of the simulations can be interpreted as showing nucleation and growth suppression, consistent with the natural samples. These measures of nucleation and growth suppression imply a satisfactory determination of the spatial and temporal scales of the Al concentration gradients that are determined by diffusive fluxes and reactant distributions in the natural sample. For example, sample PM1 shows similar signals in both the PCF (nucleation suppression) and the MCF (growth suppression). Several of the plots for the correlation functions are inconclusive and require further evaluation.

Constrained values

The durations of crystallization and the final temperatures are shown in Table 3-5. Crystallization durations, determined from heating rates and core and rim temperatures discussed above, are similar to the estimated values. The modeled T_{rim} was constrained easily within the estimated range of T_{rim} from independent constraints as long as the crystallization interval extended into the isothermal portion of the modeled heating path, which occurred in all cases except 711A in which crystallization finished just before the isothermal portion.

Kinetic parameters

A variety of nucleation rate curves emerge from the results and the values for the kinetic parameters are given in Table 3-6. The steady-state nucleation rate k_1 ranges from $10^{-13.5}$ to $10^{-7.7}$ nuclei cm^{-3} s^{-1}, and the maximum nucleation rate ranges from $10^{-13.6}$ to $10^{-9.8}$, approaching the values of k_1 in models with relatively rapid nucleation (i.e., small k_2). Other estimates of nucleation rates for diffusion-controlled conditions are 10^{-14} to 10^{-12} nuclei cm^{-3} s^{-1} from Carlson et al. (1995), but those rates are considered unreliable, as described in Chapter 1, and the similarity between those values and the values reported here may be fortuitous.

Nucleation acceleration ranges over more than three orders of magnitude (0.001-3) and produces some nucleation curves that rise sharply to the steady-state (e.g., Jen-2-80 and WR3m) and others that gradually climb to their maximum rates (e.g., 191A). These differences are not correlated with heating rates, crystallization temperatures, or specific localities (bulk composition).

In order to evaluate the scales of Al intergranular diffusion (D), the parameters of diffusivity (D_∞ and Q_D; Equation 2-18) must be derived from the extracted model parameters. The diffusive flux (Equation 2-20) is adjusted by changing the diffusion constant k_3 and the Al solubility $c_{\mathrm{Al}}^{\mathrm{Fl_{Grt}}}$. Therefore, to the extent that $c_{\mathrm{Al}}^{\mathrm{Fl_{Grt}}}$ can be determined, k_3 can be determined. The parameter k_3 is the product of ϕ, τ, and D_∞, and consequently, to derive D from the modeling results, D_∞ must be obtained from k_3. This is accomplished by simply dividing k_3 by the values of ϕ and τ for the rock. Therefore, the product of D_∞ and $exp(-Q_D/RT)$ gives D as a function of T. However, this is true only if the values determined for the rock-specific properties (ϕ, τ, and $c_{\mathrm{Al}}^{\mathrm{Fl_{Grt}}}$) are correct for each sample. Under the assumption that the rock-specific properties are correctly specified, and using the derived values for D_∞, a temperature of 873 K (600 °C), and Q_D of 140 kJ mol^{-1}, the values for these samples range from $10^{-13.6}$ to $10^{-10.7}$ m^2 s^{-1}. A range of roughly three orders of magnitude is large considering that D should be a single value for all of these samples at the given temperature.

Previous estimates of Al intergranular diffusivities come from Carlson et al. (1995), as reinterpreted by Carlson (2010), but they are composite diffusivities that incorporate Al solubility and cannot be directly compared with the current results.

CONCLUSIONS

Through numerical modeling of the processes and mechanisms that control nucleation and growth of garnet porphyroblasts in regionally metamorphosed rocks, the first comprehensive dataset for the kinetics of diffusion-controlled nucleation and growth is presented here. The samples used in this work represent a wide range of rock types and metamorphic conditions, including mafic and pelitic compositions, temperatures ranging from 375 to 650 °C, pressures from 0.35 to 2.0 GPa, and tectonic settings that include greenschist- to eclogite-facies metamorphism during orogenesis and metamorphism of blocks in a subduction mélange wedge.

The range of nucleation rates (from $10^{-13.5}$ to $10^{-7.7}$ nuclei cm^{-3} sec^{-1}) and acceleration factors (from 0.001 to 3) extracted from the simulations reflects the complex environments in which nucleation can occur during metamorphism. Some factors that influence this range include the phases present, grain size, and fluid composition, all of which are highly variable in metamorphic rocks. However, the range of Al intergranular diffusivity D (from $10^{-14.0}$ to $10^{-10.4}$ at 600 °C) is large considering that D depends only on T for a given Q_D. Because the diffusive flux depends on both porosity and Al solubility, the determinations of D shown here must include undetermined uncertainties that stem from poorly constrained rock-specific properties, as described in the next chapter.

CHAPTER 4: CRYSTALLIZATION KINETICS DURING REGIONAL METAMORPHISM

ABSTRACT

Through numerical simulations of diffusion-controlled nucleation and growth, the crystallization kinetics during regional metamorphism of rocks from a broad range of localities has been determined using CRYSTALLIZE3D. From the extracted parameters of nucleation and diffusion (k_1, k_2, and k_3), nucleation rates throughout the crystallization interval, interfacial energies of garnet nucleation, and the intrinsic properties of Al intergranular diffusion have been derived. The maximum nucleation rates range from $10^{-13.6}$ to $10^{-9.8}$ nuclei cm^{-3} s^{-1}, and these rates approach the steady-state rates (k_1), which range from $10^{-13.5}$ to $10^{-7.7}$ nuclei cm^{-3} s^{-1}. Nucleation acceleration (k_2) gives interfacial energies that range from 0.004 to 0.14 J m^{-2}, assuming shape factors for the garnet nucleus of 0.1-1.0. The pre-exponential constant for Al intergranular diffusion (D_∞), derived from k_3, gives Al intergranular diffusion (D), assuming Q_D of 140 kJ mol^{-1}, from $10^{-13.6}$ to $10^{-10.7}$ m^2 s^{-1} at 600 °C. The dispersion in D partly arises from large uncertainties in two rock-specific properties, porosity and Al solubility. Normalizing for these properties, and excluding some determinations that exhibit greater complexity than most, yields revised diffusivities ranging from $10^{-12.5}$ to $10^{-11.1}$ m^2 s^{-1} at 600 °C. A new estimate of the activation energy for intergranular diffusion of Al Q_D is 142 ± 53 kJ mol^{-1}, which is similar to previous estimates. Determinations of nucleation kinetics given here show a narrow range of values, but dispersion in D stresses that the input parameters used in the numerical simulations and the constraints used to derive the intrinsic properties of diffusion must be precisely specified for accurate estimates of rates of Al intergranular diffusion.

INTRODUCTION

Metamorphic rocks contain a wealth of chemical and textural information recorded during crystallization deep in the crust that can be extracted to understand a wide range of processes from the micro- to the macro- and tectonic scales. The sizes and locations of porphyroblasts in metamorphic rocks have been used to infer crystallization mechanisms (Kretz, 1969, 1974; Cashman & Ferry, 1988; Carlson, 1989, 1991; Carlson *et al.*, 1995; Raeburn, 1996; Denison & Carlson, 1997; Daniel & Spear, 1999) that are central to understanding and developing models of metamorphism used to infer geologic processes and construct models of geologic history. From porphyroblastic textures, the kinetic processes that control crystallization can be determined.

Kinetic parameters of crystallization in metamorphic rocks are important for determining rates of processes (e.g., reaction rates) and durations of events (e.g., porphyroblast growth). These parameters are difficult to measure experimentally, and evidence of nucleation mechanisms is destroyed as the crystal overgrows the nucleation site, but numerical models that simulate the conditions of crystallization, based on established nucleation and growth theory, can be used to determine them (Carlson, 1989, 1991; Carlson *et al.*, 1995). The compilation of data described in the previous chapter is examined here, first by reviewing the key principles of kinetics processes and the formulation used in CRYSTALLIZE3D, next by deriving values from the constraints of the database, and finally by exploring the implications of the derived values. The nucleation rates and interfacial energies have been determined from the modeling, but large uncertainties in estimates of porosity and Al solubility prevent precise determinations of the intrinsic properties of intergranular diffusivity.

BACKGROUND

The kinetics of DCNG are fundamental to the underlying principles used in numerical simulations of metamorphic crystallization. This section describes the details of crystallization kinetics and the previous models that have been used to apply the theoretical concepts.

Crystallization kinetics

Porphyroblastic nucleation and growth depends on several processes that characterize metamorphic reactions, specifically the dissolution of reactant material, nucleation of the product phases, transport of reactant components to the growing product crystals, and attachment of that material to the product phases (Kretz, 1966; Walther & Wood, 1984). Of these processes, little is understood about nucleation of the product phases (cf. Rubie, 1998) and the rates of diffusion of the reactant components to the products, two processes that are fundamental to our understanding of crystallization during regional metamorphism. Nucleation, furthermore, is dependent on the interfacial energy associated with creation of a cluster of atoms that will become the crystal nucleus, and both interfacial energy and the shape of the atomic cluster are poorly known.

Interfacial energy

Nucleation is a poorly understood process, in part due to the unknown interfacial energies associated with cluster formation on a substrate. Estimates of interfacial energy associated with mineral-mineral and mineral-fluid boundaries are generally 0.1-1 J m^{-2} (Parks, 1984; Ridley & Thompson, 1986; Miyazaki, 1996; Ashworth & Chambers, 2000). For garnet nucleation in a metapelite, interfacial energy was estimated in the range 0.03-0.3 J m^{-2} through numerical modeling of interface-controlled garnet nucleation and growth (Gaidies *et al.*, 2011).

Nucleation Rate

Determining nucleation rates for regionally metamorphosed rocks is difficult, and therefore very few estimates exist. Experimental studies have not produced useful constraints on porphyroblast nucleation rates (Carlson, 2011). However, two end-member natural examples exist that demonstrate that garnet nucleation can be either nearly simultaneous throughout a rock (Meth & Carlson, 2005), or protracted, spanning much of the crystallization interval (Chernoff & Carlson, 1997). Numerical modeling is the most promising approach to quantifying nucleation rates, but, as described in Chapter 1, previous attempts to estimate nucleation rates in diffusional-controlled systems were unsuccessful (Carlson *et al.*, 1995; Hirsch & Carlson, 2006).

Diffusivity

Cations with similar size and charge should diffuse through the intergranular medium at similar rates (Farver & Yund, 1995). In experiments of Si bulk diffusion through a fine-grained quartz aggregate under hydrothermal conditions, Farver and Yund (2000) estimated the activation energy for intergranular diffusion Q_D of Si as 137 ± 18 kJ mol^{-1}. Given the similar size and charge of Si and Al, Q_D for Al should be similar to their results. The effective Al intergranular diffusivities for some of the same samples in this study were estimated from numerical modeling done by Carlson et al. (1995). Using those results and an iterative process to refine the estimate of Q_D, Carlson (2010) derived a value of 136 ± 35 kJ mol^{-1}, which overlaps with the value for Si. This Q_D gives a range of effective diffusivities for Al intergranular diffusion on the order of 10^{-20} to 10^{-19} m^2 s^{-1} at 600 °C (Carlson, 2010).

Complementary and previous models

Of the different processes that can control the rate of porphyroblast nucleation and growth, three have been used as the basis for numerical modeling of porphyroblastic textures: interface-controlled nucleation and growth that is limited by the attachment of material to the surface of the growing porphyroblast (Gaidies *et al.*, 2011); growth that is limited by the dissolution of the reactant material (Schwarz *et al.*, 2011), which might be regarded as a form of interface-controlled nucleation and growth; and diffusion-controlled nucleation and growth (DCNG), in which the reaction rate is limited by the diffusive flux of the components in the intergranular medium from the reactants to the products (Carlson, 1989, 1991; Carlson *et al.*, 1995).

The model in this study builds upon the efforts of Carlson (1989, 1991) and Carlson et al. (1995), and follows the central notion that DCNG is the common, rate-limiting process in regionally metamorphosed rocks (Denison & Carlson, 1997). The Carlson et al. (1995) model was able to simulate porphyroblastic textures through 3-D simulations of DCNG, and produced estimates of kinetic parameters of these processes. The drawbacks to this model included a limited ability to distribute initial reactants; a step function used to approximate nucleation probability, whereas the actual nucleation probability is a smooth function dependent on concentration gradients; an exponentially increasing nucleation rate equation with no limit to the number of porphyroblasts nucleated, which can drive nucleation rates to large values and yield unrealistically large activation energies; and a method of assigning porphyroblast volumes based on the relative size of their diffusional domains, which oversimplifies the process of diffusion-controlled growth and affects nucleation suppression and growth competition.

CRYSTALLIZE3D MODELING

CRYSTALLIZE3D is the current generation of the model (Ketcham & Carlson, in review). It simulates textures with a higher degree of correspondence to natural processes than in previous efforts, by allowing diverse initial reactant distributions, specification of a particular pressure-temperature-time-(free-energy difference) (P-T-t-$\Delta_r G$) path, and more complex reactions (e.g., multiple Al-bearing products and reactants); and it incorporates a nucleation rate equation that is based on classical nucleation theory.

Model description

Descriptions of the modeling concepts appear in Chapters 1 and 2, but a summary of the pertinent details is given here as a necessary background to the determinations of the kinetic parameters.

Reaction affinity

In the numerical simulations, dissolution of reactant phases is governed by thermodynamic calculations of end-member components of a model reaction and the reaction affinity A_r that arises from departures from equilibrium. As the reactants dissolve, the concentrations of the reactant components in the intergranular fluid increase. In a system with a single rate-limiting component (RLC), gradients in concentration are significant only for the RLC because the other gradients are nearly flat and contribute negligibly to the reaction affinity of the system. In such a case, and taking Al as the

RLC, the reaction affinity can be determined from the difference in concentration between fluid in local equilibrium with the reactants (composite aluminous reactant, CAR) and fluid in local equilibrium with the products (composite aluminous product, CAP) from the equation

$$\Delta_r G = RT\ln\left(\frac{c_{Al}^{Fl_{CAP}}}{c_{Al}^{Fl_{CAR}}}\right) \tag{4-1}$$

in which *R* is the ideal gas constant, $c_{Al}^{Fl_{CAR}}$ is the concentration of Al in the intergranular fluid in equilibrium with CAR, and $c_{Al}^{Fl_{CAP}}$ is the concentration of Al in the intergranular fluid in equilibrium with CAP. The reaction affinity drives nucleation rates, and along the concentration gradients, it is highest near the CAR and lowest near the CAP.

Nucleation rate

In Chapter 2, the nucleation rate equation (Equation 2-13) was derived and given as

$$\frac{dN_V}{dt} = k_1 \exp\left(-k_2 \frac{T_{eq}}{T}\frac{(c_{Al}^{Fl_{CAP}})^n}{(\Delta c)^n}\right). \tag{4-2}$$

where k_1 is the steady-state nucleation rate and k_2 is the nucleation acceleration factor defined as

$$k_2 = \frac{s\gamma^3 k_0 \overline{V}_{Grt}^2 n_{Grt}^2}{k_B T_{eq}(c_{Al}^{Fl_{CAP}})^n}\ , \tag{4-3}$$

in which all of the values are known constants except for the shape factor *s* and interfacial energy γ. Rearranging gives

$$\gamma = \left(\frac{k_B T_{eq}(c_{Al}^{Fl_{CAP}})^n k_2}{s k_0 \overline{V}_{Grt}^2 n_{Grt}^2}\right)^{1/3}\ . \tag{4-4}$$

Therefore, extracted values of k_2 from the numerical simulations can be used to estimate interfacial energy with assumed values for *s*.

Diffusive flux

Transport of the RLC depends on the steepness of the concentration gradients from reactants to products, and also on the diffusivity through the interconnected pathways that vary in abundance and shape. The diffusive flux (*J*) is given by a variant of Fick's First Law that accounts for these factors:

$$J = D\nabla c\ \phi\tau\,. \tag{4-5}$$

The first factor is the diffusivity, *D*, of the RLC through the intergranular fluid, which is described in an Arrhenius formulation:

$$D{=}D_\infty \exp\left(\frac{-Q_D}{RT}\right) \tag{4-6}$$

in which D_∞ is the fictive intergranular diffusivity at infinite *T*, and Q_D is the activation energy for intergranular diffusion. Factors that reduce the rate of transport depend on the abundance of pathways (porosity, ϕ), and the shape of the pathways (tortuosity, τ). The expression for *J* is simplified by grouping the constants D_∞, ϕ, and τ into k_3 for implementation in the model:

$$J = k_3 \exp\left(\frac{-Q_D}{RT}\right)\nabla c\,. \tag{4-7}$$

The remaining factor in *J* is the concentration gradient. A simplification of the concentration gradient surrounding a porphyroblast for a fluid buffered by the concentration of the RLC in equilibrium with the reactants and depleted by the porphyroblast is:

$$\nabla c = \frac{\Delta c}{\Delta r} = \frac{c_{Al}^{Fl_{CAP}} - c_{Al}^{Fl_{CAR}}}{\Delta r} = \frac{c_{Al}^{Fl_{CAP}}\left[\exp\left(\frac{-\Delta_r G}{n_{Al}RT}\right) - 1\right]}{\Delta r}\,. \tag{4-8}$$

The radial distance around an isolated porphyroblast is denoted here by *r*. Note that ∇c scales with the concentration of Al in equilibrium with the product assemblage $c_{Al}^{Fl_{CAP}}$, and therefore *J* scales with $c_{Al}^{Fl_{CAP}}$.

Reaction space

The model is composed of discrete volume elements (voxels) that are initially assigned to contain the reactant assemblage in specified concentrations. With progress along a user-specified t-T-$\Delta_r G$ path, the reaction affinity increases and the reactants begin to dissolve. Increasing concentration of Al raises the supersaturation of Al (Δc), and consequently the nucleation rate ($\mathrm{d}N_\mathrm{V}/\mathrm{d}t$) increases. Upon nucleation of a crystal, gradients in Al are established and three zones develop: a zone of voxels that contain the reactants, a zone that contains the products, and a zone between these that contains non-reactive material and phases in excess of the stoichiometry of the reaction. These zones are illustrated in Figure 4-1. Between the reactants and products, Al travels down concentration gradients giving rise to the diffusive fluxes J. The model is fit to the natural sample by specifying the values of the nucleation rate and acceleration (k_1 and k_2), the diffusive flux (k_3, Q_D, and $c_{\mathrm{Al}}^{\mathrm{Fl}_{\mathrm{CAP}}}$), and the initial CAR distribution.

Application of model

As described in Chapter 3, the samples are a collection of porphyroblastic rocks of both pelitic and mafic composition that demonstrate evidence for DCNG (Carlson & Denison, 1992; Denison & Carlson, 1997). The garnets in these samples span syn- to post-deformational growth over a broad range of P-T conditions.

Each rock was simulated by adjusting parameters iteratively until the textural characteristics were within about 10 percent relative of the rock value. The shape of the CSD was fit by eye. The resulting values of the steady-state nucleation rate k_1 range from $10^{-13.5}$ to $10^{-7.7}$ nuclei cm^{-3} s^{-1}; the maximum nucleation rate achieved in each model $(\mathrm{d}N/\mathrm{d}t)_{\max}$ ranges from $10^{-13.6}$ to $10^{-9.8}$ nuclei cm^{-3} s^{-1}; values of k_2 are between 0.001 and 3; and k_3 ranges from $10^{-9.5}$ to $10^{-7.3}$ m^2 s^{-1} (Table 4-1).

KINETIC PARAMETERS OF CRYSTALLIZATION

The kinetic parameters of nucleation and growth constrained by numerical simulations of natural rocks provide estimates of these values that are difficult or impossible

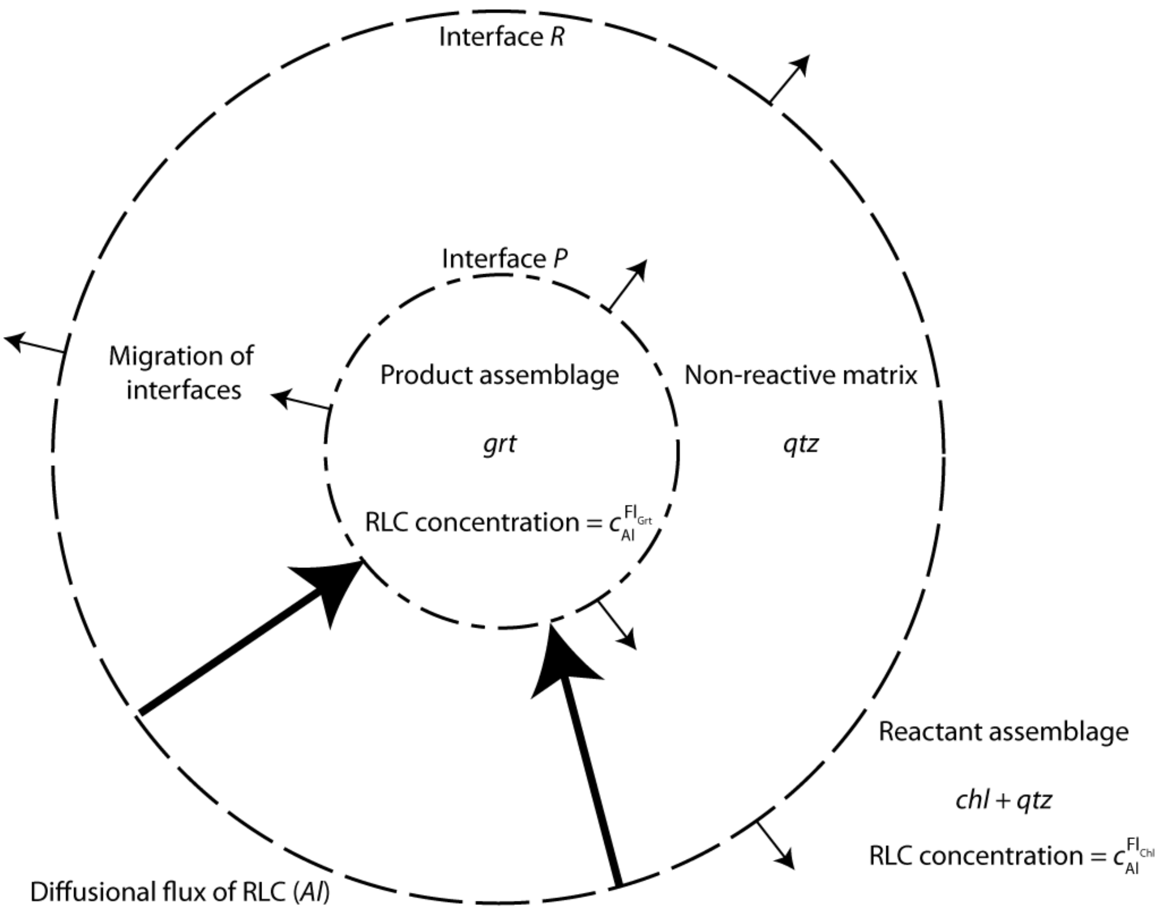

Figure 4-1 Two-dimensional illustration of the reaction space in the CRYSTALLIZE3D model. The reaction space is divided into three types of volumes, those with the reactant assemblage, those with the product assemblage, and those between that are depleted in RLC-bearing reactants but do not include RLC-bearing products. For the example of garnet crystallizing from chlorite and quartz, at interface *R*, Al in the intergranular fluid is in equilibrium with chlorite and at interface *P*, Al in the intergranular fluid is in equilibrium with garnet. The concentration of Al in the intergranular fluid decreases from *R* to *P* and defines diffusional gradients. Both interfaces migrate outward, away from the nucleation site. From Ketcham and Carlson (in review).

Table 4-1. Determined parameters with diffusivity normalized by Al solubility

Rock	k_1 (N cm^{-3} s^{-1})	$(dN/dt)_{max}$ (N cm^{-3} s^{-1})	k_2	k_3 (m^2 s^{-1})	D_∞ (m^2 s^{-1})	T_c (°C)	$D(T_c)_{norm}$ (m^2 s^{-1})	$D(600\ °C)_{norm}$ (m^2 s^{-1})
PM1	2.70E-12	2.05E-12	1	1.50E-08	1.50E-03	530	1.57E-13	8.44E-13
PM2	3.50E-13	3.40E-13	0.1	6.00E-09	6.00E-04	530	6.29E-14	3.38E-13
PM4	1.50E-13	1.42E-13	0.2	3.60E-08	3.60E-03	525	3.31E-13	2.03E-12
160A	1.30E-10	2.65E-11	0.5	6.40E-09	1.28E-04	533	1.30E-14	6.43E-14
191A	1.90E-09	1.44E-10	2	2.90E-10	5.80E-06	564	1.95E-15	4.46E-15
711A	3.90E-11	2.32E-11	0.7	8.10E-10	1.62E-05	600	1.43E-14	1.43E-14
AG4	3.00E-13	2.95E-13	0.005	1.00E-08	1.00E-03	600	1.99E-12	1.99E-12
MD	3.00E-14	2.63E-14	0.1	6.00E-09	6.00E-04	630	6.64E-12	3.50E-12
Jen-2-80	1.40E-12	1.40E-12	0.001	5.20E-08	5.20E-03	500	6.90E-13	8.36E-12
HE-1	1.30E-11	2.73E-12	0.5	6.00E-09	6.00E-04	550	1.03E-12	3.32E-12
WR1bt	2.00E-08	3.41E-12	3	4.50E-10	4.50E-04	645	1.40E-11	5.43E-12
WR1tp	2.40E-09	4.09E-13	3	6.40E-10	6.40E-04	645	1.99E-11	7.72E-12
WR3m	1.80E-12	1.75E-12	0.01	3.00E-10	3.00E-04	645	9.31E-12	3.62E-12
Min	3.00E-14	2.63E-14	0.001	2.90E-10	5.80E-06	500	1.95E-15	4.46E-15
Mean	1.88E-09	1.59E-11	0.86	1.08E-08	1.13E-03	577	4.16E-12	2.86E-12
Max	2.00E-08	1.44E-10	3	5.20E-08	5.20E-03	645	1.99E-11	8.36E-12

T_c is the characteristic temperature (Equation 1-4).
Diffusivity is normalized by Al solubility (Equation 4-9).

to obtain from laboratory experiments. The following section describes the results of the modeling.

Steady-state nucleation rate

The values for k_1 ($10^{-13.5}$ to $10^{-7.7}$ nuclei cm^{-3} s^{-1}) are steady-state nucleation rates in portions of the rock where reactants persist and buffer the reaction affinity to its maximum value; the values of k_1 are approached by the maximum nucleation rate displayed in Figure 3-45c as the red curves in the nucleation-rate diagrams. Near existing porphyroblasts, where reactants have dissolved and the reaction affinity is smaller, the nucleation rate is correspondingly smaller and can go to zero if the Al supersaturation is depleted. The overall nucleation rate in the rock therefore represents the competing effects of (1) the level of supersaturation in reactant-bearing regions, which increases continually until the maximum temperature is reached, and (2) the progressive reduction of supersaturation in the vicinity of growing porphyroblasts, which limits the volume fraction of the rock with high probability of nucleation. Overall nucleation rates are displayed in Figure 3-45c as the black curves in the nucleation-rate diagrams.

An important result of the modeling is the protracted nucleation intervals in all simulations (except for AG4, in which the number of nuclei was manually limited, in keeping with the petrologic evidence in this sample for early site-saturation, discussed immediately below). Nucleation rate depends strongly on the supersaturation of Al in the intergranular fluid, and due to buffering where reactants persist, it will remain at steady-state until the reactants are consumed. As long as reactants remain, nucleation can and should continue until well into the crystallization interval of the rock. This concept is demonstrated by the excellent fits of the simulated textures and the natural samples corresponding with long nucleation intervals in most of the samples (again, the exception is AG4). Petrologic evidence for protracted nucleation in several rocks from the Picuris Mountains (Chernoff & Carlson, 1997), including the samples modeled here, supports the results of the modeling.

In contrast, nucleation in sample AG4 was nearly simultaneous for all crystals (Meth & Carlson, 2005), and to account for this, the number of nucleation events in the simulation was capped at a value that would reproduce this characteristic of the sample. The successful simulation of this sample demonstrates that the model is capable of simulating nearly all crystallization conditions of this special case, which lends credibility to the choices of the nucleation parameters and diffusive flux used for this sample.

Interfacial energy

Estimates of the interfacial energy (γ) are hindered by a lack of knowledge of the shape factor s. Figure 4-2 shows examples of three potential nuclei having the form of truncated spherical clusters with varying shape factors s. Although we have no knowledge of the actual shapes of critical clusters (so there is no reason to believe that they should be spherical caps), and thus no firm estimates of the shape factor, reasonable constraints might be placed on it. It can be argued that values for s greater than ~0.1 are appropriate for garnet nucleation because smaller values would imply that garnet nuclei have a very low energy against whatever substrate localizes them. Although some evidence exists to suggest that garnet nucleation is indeed epitaxial (Spiess *et al.*, 2007), the common occurrence of garnet as a porphyroblast signifies that significant barriers to nucleation exist, which suggests at least modest — and possibly quite large — wetting angles between garnet and substrate. Using the values of k_2 resulting from the model fits and s in the range 0.1-1.0, γ ranges from 0.004 to 0.14 J m^{-2} (Fig. 4-3); if one instead chooses a more restricted range of values for s, say 0.5 to 1.0, the range of γ is only about 0.004 to 0.08 J m^{-2}. Interfacial energies of 0.03-0.3 J m^{-2} determined from numerical simulations of interface-controlled nucleation and growth by Gaidies et al. (2011) are quite similar to these estimates.

The nucleation rate curves from the simulations rise sharply in some cases (e.g., Jen-2-80) and gradually climb to maximum rates in others (e.g., 191A). This behavior is expected from the possible range of interfacial energies associated with the variety of nucleation sites inherent in each rock. For example, nucleation may be favored on a specific phase due to smaller differences in the alignment of atoms between the lattices of the phase and the atomic cluster (epitaxial nucleation). The variability of interfacial energies in natural samples is also expressed in the range of acceleration factors

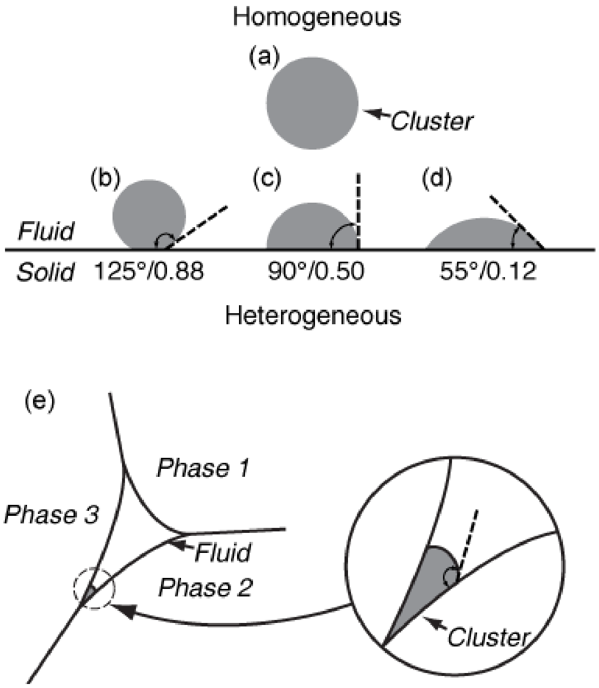

Figure 4-2. Examples of homogeneous and heterogeneous nucleation. Gray shading indicates a cluster of atoms or molecules. (a) Homogeneous nucleation occurs in a fluid. (b-d) Heterogeneous nucleation occurs when a cluster of atoms precipitates onto a solid. Each of the clusters in (b) through (d) is equal in volume. Heterogeneous nucleation is energetically favorable because the surface area is reduced relative to the volume of the cluster. The angles between the solid surface and the surface of the cluster θ are given below each example with their corresponding shape factors *s*. (e) Nucleation is likely to occur in three-grain junctions because the surface area of the cluster is even smaller.

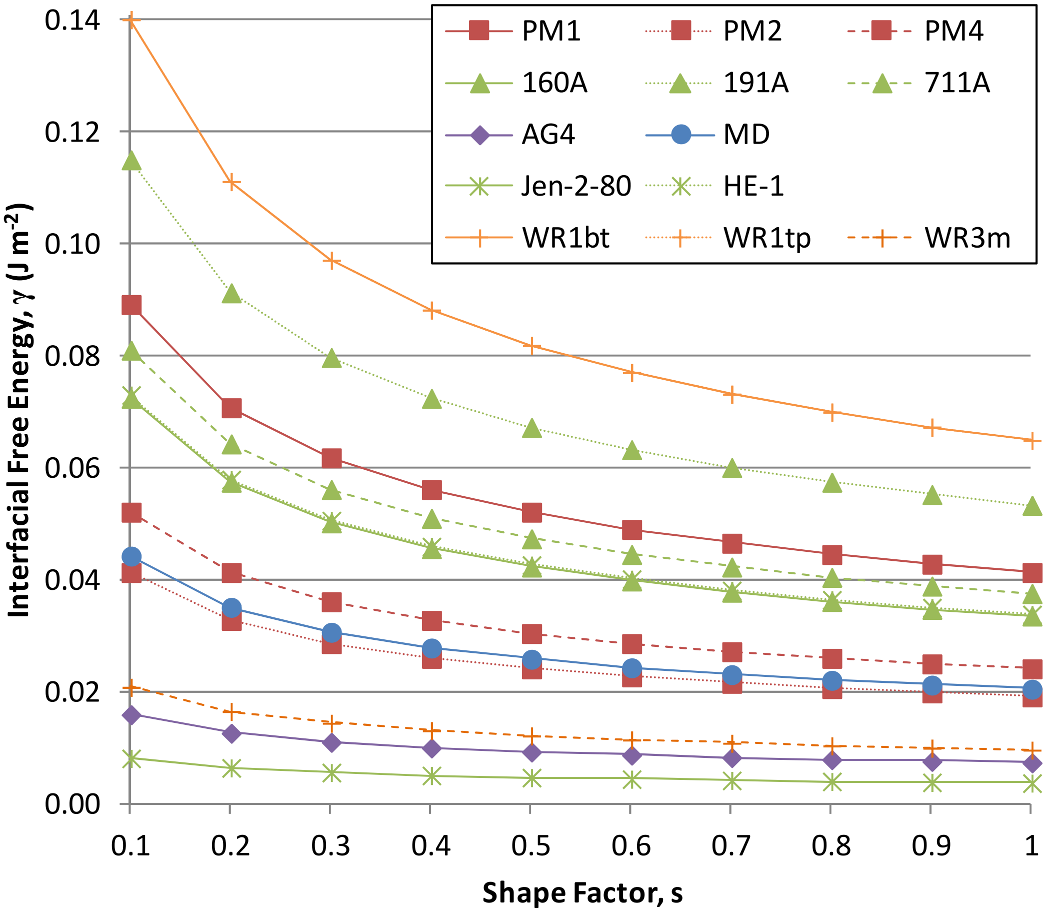

Figure 4-3. Interfacial free energy determinations from the modeled samples for a range of values of the shape factor. The interfacial energy scales with k_2 so large values of k_2 (e.g., 191A, WR1bt, and WR1tp) result in larger values of interfacial energy. Assuming garnet has a shape factor between 0.1 and 1, the corresponding interfacial free energy is 0.004-0.14 J m^{-2}.

(and extracted interfacial energy) within a locality (e.g., k_2 ranges from 0.01 to 3 in the Whitt Ranch rocks). However, there is some evidence from these results that on the sample scale, interfacial energies might be constant. Models of two of the textural data-sets (WR1bt and WR1tp), which were extracted from different parts of the same sample, resulted in the same determination of the nucleation acceleration factor ($k_2 = 3$) suggesting that the interfacial energies throughout the sample were the same, whereas another property, such as diffusivity or the number of nucleation sites, was responsible for the difference in their CSDs.

Aluminum intergranular diffusivity

In this section, an attempt is made to separate and quantify the fundamental properties of Al intergranular diffusion that are universal in all systems, but, as discussed below, the effects of rock-specific properties remain a hindrance to determining precise estimates of these intrinsic diffusion properties.

Intergranular diffusion of Al

A constant, k_3, defined as the mathematical product of D_∞, ϕ, and τ in the diffusivity equation (Equation 4-7), was determined for each sample based on best-fit simulations to the natural samples. The intrinsic properties of Al diffusivity are in the pre-exponential constant (D_∞) and the activation energy for intergranular diffusion (Q_D), which depends on the universal physical properties of the system, in contrast to rock-specific properties ϕ and τ. As described in Chapter 2, if the values determined for the rock-specific properties (ϕ, τ, and $c_{\mathrm{Al}}^{\mathrm{Fl_{Grt}}}$) are correctly specified, values of D_∞ can be extracted from k_3 by simply dividing k_3 by the dimensionless factors ϕ and τ, and the product of D_∞ and *exp*($-Q_D/RT$) gives D as a function of T for a given Q_D. The resulting D_∞ values are given in Table 4-1 and range from $10^{-5.2}$ to $10^{-2.3}$ $\mathrm{m^2 \cdot sec^{-1}}$, and at a temperature of 873 K (600 °C), and Q_D of 140 kJ $\mathrm{mol^{-1}}$, the values of D for these samples range from $10^{-13.6}$ to $10^{-10.7}$ $\mathrm{m^2\ s^{-1}}$. These ranges are substantial, given that D_∞ should have a single value and D varies only with T. The dispersion is attributed to poor estimates of the rock-specific properties.

Normalizing the values of *D* could reduce the effects of the rock-specific properties, so an attempt is made here. Normalization of porosity has already occurred in the determination of *D* when k_3 was divided through by ϕ and τ. Normalization for Al solubility is mathematically more difficult considering that solubility directly affects diffusive flux, and not *D*. To normalize for Al solubility, each solubility value used in the modeling (Table 3-2) was arbitrarily divided by the average solubility for the rock suite and used as a multiplicative factor in the diffusivity determinations:

$$D_i = D_{\infty,i} \exp\left(\frac{-Q_D}{RT}\right)\left(\frac{[c_{Al}^{Fl_{CAP}}]_i}{[c_{Al}^{Fl_{CAP}}]_{ave}}\right). \tag{4-9}$$

In this equation, *i* indicates a value for a specific sample. As an example to help understand the normalization, if $c_{Al}^{Fl_{CAP}}$ is overestimated in the modeling, k_3 will be underestimated and the derived values of D_∞ also will be underestimated. An underestimate of D_∞ will result in an underestimate of *D*, so the normalizing factor will increase *D* by an amount proportional to $c_{Al}^{Fl_{CAP}}$. This method is only intended as a learning exercise and is not a robust method for removing the effects of Al solubility from diffusivity. The resulting diffusivities D_i are listed in Table 4-1 at both the characteristic temperature, for which they are best determined, and at 600 °C, for comparison with each other. At 600 °C, they range from $10^{-14.4}$ to $10^{-11.1}$ m^2 s^{-1}, which demonstrates slightly larger dispersion (3.3 $\log_{10}$ units) than the range given above for *D* (3.0 $\log_{10}$ units).

The dispersion of solubility-normalized intergranular diffusion for all samples (Fig. 4-4) is large and suggests that other factors are contributing to uncertainty in these values. In particular, the samples from Maine and Mica Dam are potentially outliers as suggested by the regression statistics. The samples from Maine have evidence for fluids that may have affected solubility. The fluids should be later than garnet growth, but perhaps that assumption is incorrect, or there were earlier fluids that accompanied garnet growth that reduced Al solubility. Graphite was present in at least two the Maine samples during garnet growth and this could be an indicator of a fluid that suppressed Al solubility. An overestimate of solubility would produce an underestimate of diffusivity. In addition, intrusive heating produced Buchan-type metamorphism that is

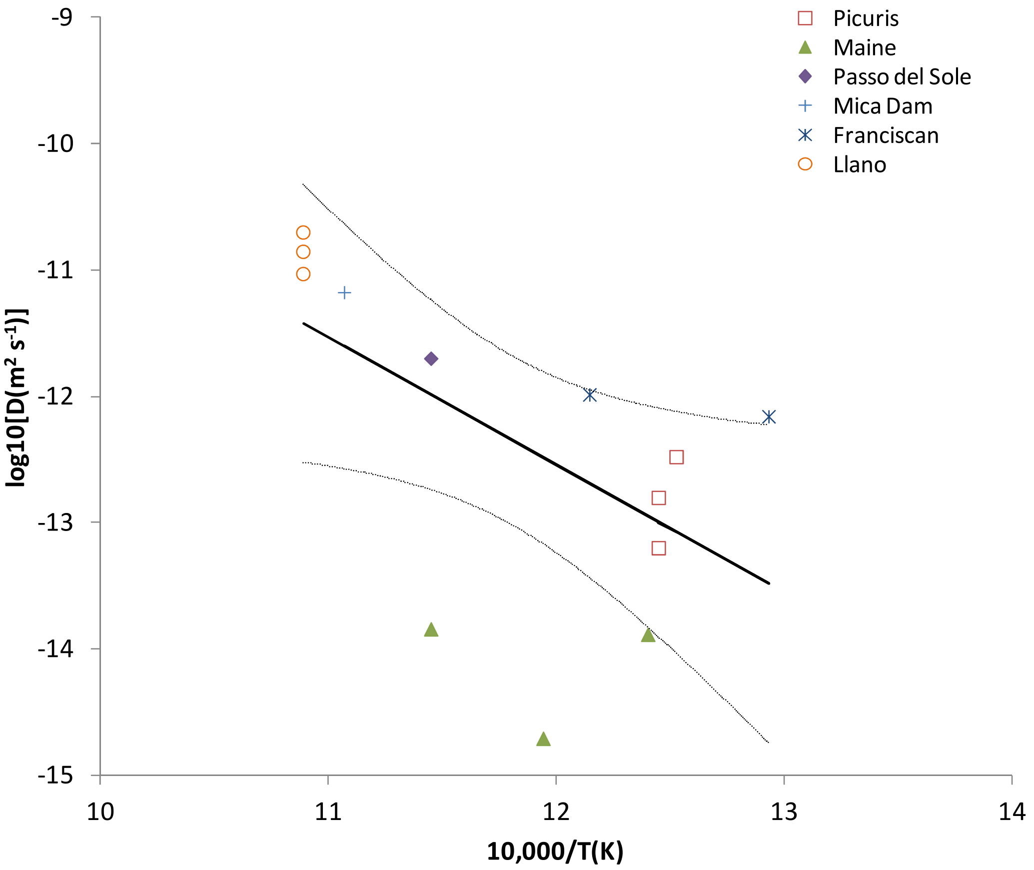

Figure 4-4. Arrhenius diagram showing intergranular diffusion of Al versus inverse T_c for all simulations normalized by Al solubility. Dotted curves represent a 95% confidence interval for the regression. From this regression line, an estimate of the activation energy for intergranular diffusion of Al (Q_D) is 194 ± 83 kJ mol^{-1}.

unique among the localities in this sample suite, and the estimated heating rates could be too fast for the Maine samples. If heating rate is overestimated, diffusivity may be underestimated. The samples from Maine have the largest crystal number densities of the rock suite, and perhaps the small length scales of diffusion needed to transport Al to the closely-spaced crystals in these rocks introduce larger uncertainties that create scatter in the determinations of diffusive flux and therefore diffusivity in these samples. The evidence of the garnet growth conditions is poor but may give reason to question the diffusive fluxes derived in these samples.

Another sample with potentially erroneous determinations of diffusive flux is sample MD. As described in Chapter 3, the garnets in this sample are slightly elongated and their long axes are aligned. Garnets that are not equant are generally the result of growth under limited length scales of diffusion and commonly grow along nutrient-rich materials, such as micaceous schistosity (e.g., Robyr *et al.*, 2009). If the garnets grew in locations with high modal amounts of micas, the pair-correlation function would give a strong clustering signal, which is seen for this sample (Fig. 3-45). If garnets were limited to growth along micaceous layers, the diffusive length scales in the simulations may be overestimated. However, sample AG4 from Passo del Sole has similar characteristics to MD, including synkinematic growth and a strong clustering signal in the PCF, but the diffusive fluxes determined for this sample fall along the regression.

The uncertainties in the growth histories of the samples from Maine and Mica Dam suggest that excluding them from the regression may be appropriate. If the samples (160A, 191A, 711A, and MD) are excluded from the diffusivities determined from Equation 4-9, the range becomes $10^{-12.5}$ to $10^{-11.1}$ m^2 s^{-1} at 600 °C. Although the range given here is more tightly bracketed to 1.4 orders of magnitude, the determinations may be fortuitous.

Activation energy for intergranular diffusion

Despite the complexities introduced by the effects of the rock-specific properties, one of the goals of this study is to determine a new estimate for Q_D. The modeling was performed using a Q_D of 140 kJ mol^{-1}, based on an experimental determination of

Si intergranular diffusivity (Farver & Yund, 2000) and a previous estimate of Al intergranular diffusivity from Carlson (2010). As described in Chapter 1, an estimate of Q_D can be determined by plotting the diffusion results on an Arrhenius diagram of $\log_{10} D$ versus inverse T_c (Equation 1-4) and equating the exponential term of Equation 4-6 with the slope of the best-fit line ($-Q_D/R$) (Fig. 4-5). The values determined for Llano and the Picuris Mountains simulations were averaged to avoid overweighting the points from those localities, and the determinations from Maine and Mica Dam were excluded for the reasons given immediately above. The resulting value for Q_D is 142 ± 53 kJ mol^{-1}. This estimate is similar to that of Carlson (2010), perhaps by chance considering the uncertainties in D, so this determination is questionable.

Challenges from unconstrained parameters

CRYSTALLIZE3D implements individual values of the components that define the diffusive flux of Al between reactants and products, providing a comprehensive framework for determining the fundamental properties of Al intergranular diffusivity (Equation 4-7). However, the lack of precise constraints on the factors that enhance or retard diffusive flux, specifically interconnected porosity and Al solubility, are preventative in determining reliable estimates of intergranular diffusion. The diffusive flux has been constrained by the textures of the natural samples, but the contributions to the flux from each component remains poorly determined.

Estimates of porosity in the literature range over two orders of magnitude (Bickle & Baker, 1990; Ferry & Dipple, 1991; Farver & Yund, 1992), and are essentially averaged values. However, porosity could span a larger range especially considering that it is likely to be a dynamically changing value rather than a constant (e.g., Lyubetskaya & Ague, 2009). As hydrous minerals liberate fluids during prograde reactions, their volume will decrease, increasing porosity. Additional fluids in pore spaces should enhance the dissolution of the dissolving reactants and potentially create more porosity. However, as product phases grow, porosity should decrease. Although a single value for porosity in regionally metamorphosed rocks might be sufficient to model diffusive fluxes, specific values that can be applied to individual rocks are currently unavailable.

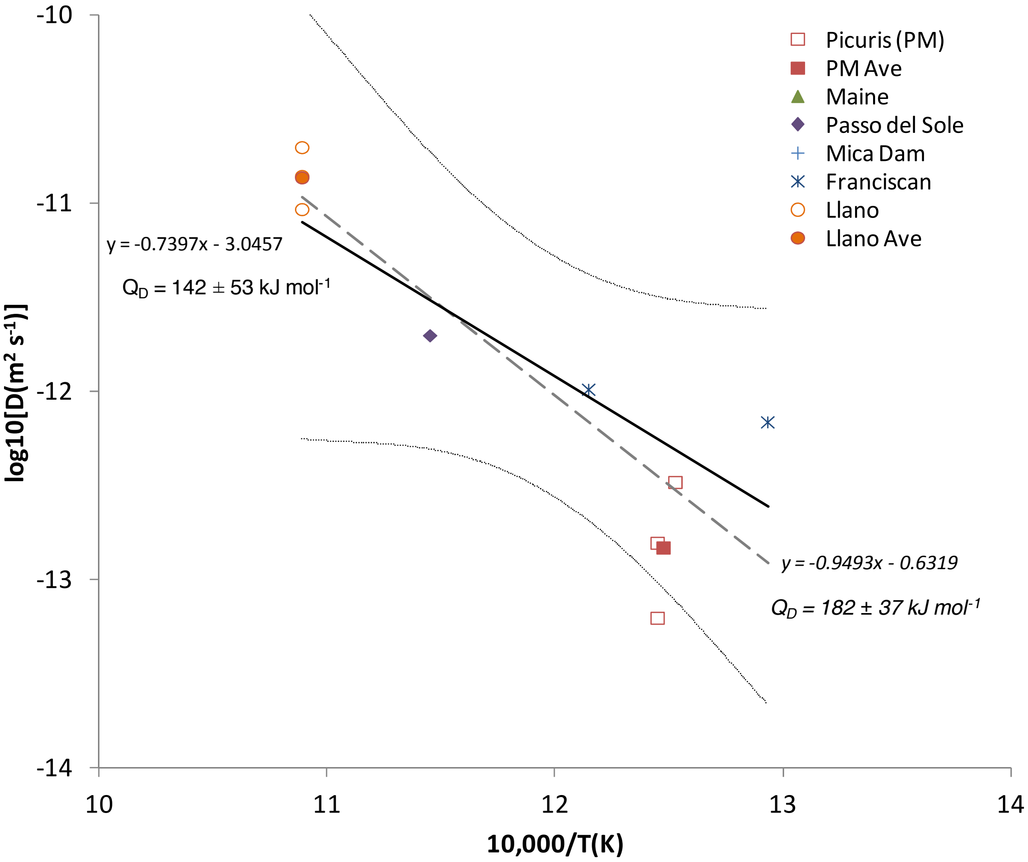

Figure 4-5. Arrhenius diagram showing intergranular diffusion of Al versus inverse T_c for selected simulations normalized by Al solubility. The determinations for samples from Maine and MD have been excluded for reasons described in the text. The filled circles and squares are averaged values of the PM and Llano determinations to avoid overweighing the determinations from those localities. The solid regression line uses the averaged determinations and yields an activation energy for intergranular diffusion of Al (Q_D) of 142 ± 53 kJ mol^{-1}, nearly identical to the determination of Carlson (2010). 95% confidence limits are given by the dotted lines. The dashed regression line uses all samples and gives an estimate of Q_D of 182 ± 37 kJ mol^{-1} but might be overweighed by multiple determinations for the PM and Llano samples.

An additional challenge comes from determining Al solubility in metamorphic fluids, despite recent progress on this subject (e.g., Tropper & Manning, 2007; Beitter et al., 2008; Newton & Manning, 2008). Although solubility estimates made in this study were carefully determined and compared with an independent study, the estimates of solubility were assigned based solely on *P*-*T* conditions and lack further constraints from fluid composition, which will influence Al solubility. In addition, the estimates of solubility used in this work assume that the pH of the fluid is near neutral, which may be the case for pelitic rocks because the fluid should be buffered toward neutrality by K-bearing phases (Beitter *et al.*, 2008). If this is not the case, especially for the mafic samples (Franciscan and Whitt Ranch), the solubility could be higher than estimated here, which would decrease the determined diffusivity for those samples.

The overarching goal of determining the fundamental properties of Al intergranular diffusion is to be able to extract rates of processes that apply to any metamorphic rock. Without precise determinations of each factor that contributes to the diffusive flux, however, the remaining factors cannot be adequately constrained. This shows that determinations of porosity and Al solubility during regional metamorphism are as important a problem as determining the intrinsic properties of diffusivity. Without either one, the overarching goal cannot be achieved.

In CRYSTALLIZE3D, the porphyroblastic textures are simulated by adjustments to the diffusive flux, nucleation rate, and nucleation acceleration. Because the simulations are fit to the natural textures of the rocks, the magnitudes of the diffusive fluxes are robust, and it is only the components that make up the diffusive flux (porosity and Al solubility) that cannot be resolved and specifically estimated. For example, given a diffusive flux, an increase in the Al solubility will increase the amount of Al that can be transported by diffusivity, but a decrease in the diffusivity will slow the rate of transport, and the combined effect produces the same flux.

CONCLUSIONS

The principal determinants of nucleation kinetics and intergranular diffusivities given here are among the first determinations available for regionally metamorphosed rocks. Estimates of interfacial energy for garnet nucleation range from 0.004 to 0.14 J m^{-2} and are very similar to those determined from numerical simulations of interface-controlled nucleation and growth of porphyroblasts (Gaidies *et al.*, 2011). These estimates provide new constraints on interfacial energies needed to simulate garnet nucleation in metamorphic rocks.

Estimates of nucleation kinetics given here describe the magnitude of the maximum and steady-state rates as well as the nature of the nucleation rate through time as crystallization proceeds. The ability of the modeled rates to reproduce the textures of rocks with both protracted and nearly instantaneous nucleation intervals attests to the reliability of the reported nucleation rates.

The estimates of Al intergranular diffusivities span roughly one order of magnitude when the results from Mica Dam and Maine are excluded and a rudimentary normalization is employed to account for variability in Al solubility (-12.1 to -11.1 $\log_{10}$ units at 600 °C). Although the diffusive fluxes in the simulations are well determined when the textures of the simulations are compared with the natural textures, the individual components of the flux remain poorly resolved for some samples, apparently due to lack of adequate knowledge of some parameters such as porosity and Al solubility. This obstacle demonstrates that determinations of porosity and Al solubility, and perhaps other parameters, are just as important to establishing the intrinsic properties of intergranular diffusivity as the diffusion theory itself.

CHAPTER 5: REACTION AFFINITY DURING REGIONAL METAMORPHISM

ABSTRACT

Disequilibrium crystallization during regional metamorphism poses a substantial challenge to interpreting rocks using methods based on the assumption of chemical equilibrium, because the departures from equilibrium add unknown magnitudes of uncertainty and can cause delayed nucleation and metastable phases. Furthermore, disequilibrium commonly goes unrecognized due to cryptic evidence that requires careful analysis of chemical zoning and porphyroblastic textures to reveal it. This study used numerical models of diffusion-controlled nucleation and growth of porphyroblasts to simulate the textures of a range of natural porphyroblastic rocks to quantify disequilibrium in terms of reaction affinity (the negative of the Gibbs free energy change for the reaction). The reaction affinities and corresponding overstepping temperatures (difference between the nucleation temperature and the equilibrium temperature) determined for garnet nucleation in the numerical simulations range from 0.4 to 5.9 kJ mol^{-1} of 12-oxygen garnet (4.0-62.0 °C thermal overstepping) for the earliest garnets to nucleate, to between 5.3 and 29.0 kJ mol^{-1} (450-125 °C thermal overstepping) for garnets that nucleated at the maximum reaction affinity during crystallization (typically at the peak temperature along the *P*-*T* path). These results demonstrate that scales of reaction affinity cause delayed nucleation, but perhaps more importantly, the nucleation intervals of nearly all the rocks extend through the duration of crystallization. Therefore, the potential for delayed reactions during prograde metamorphism is demonstrated, but because the reactions continue to temperatures well beyond the equilibrium temperatures of the reaction, the potential for metastability and disequilibrium mineral compositions and assemblages has also been demonstrated. Using the example of metamorphic isograds along a metamorphic field gradient, these results reinforce the notion that disequilibrium can produce isograds that are offset from their positions predicted from calculations based on equilibrium assumptions, and interpretations of the metamorphic history

may be erroneous or the true crystallization history may be obscured and difficult to decipher.

INTRODUCTION

Equilibrium-based methods of analysis are used to interpret geologic histories, and departures from equilibrium during crystallization can cause spurious results when employing these methods (e.g., Vernon *et al.*, 2008). Disequilibrium has been demonstrated and quantified in contact-metamorphic settings (e.g., Waters & Lovegrove, 2002; Pattison & Tinkham, 2009), and although disequilibrium has received slow recognition as an important obstacle in the study of regionally metamorphosed rocks (e.g., Ridley & Thompson, 1986; Chernoff & Carlson, 1997; Rubie, 1998; Chernoff & Carlson, 1999; Carlson, 2002; Pattison *et al.*, in press), quantitative estimates of departures from equilibrium in this setting only recently have emerged (Wilbur & Ague, 2006; Hetenyi *et al.*, 2007; Padron-Navarta *et al.*, 2008).

One of the challenges in quantifying disequilibrium is that evidence for it can be difficult to recognize and can go unnoticed. Reactions that fail to go to completion provide obvious evidence of disequilibrium, because the reactants are still present in the rock (e.g., corona structures). However, reactions that go to completion, yet lack revealing textures, may nevertheless contain cryptic evidence for disequilibrium in chemically zoned minerals or in the spatial dispositions of porphyroblasts. For example, Chernoff and Carlson (1997) examined chemical zoning in pelitic garnets and found that Ca concentrations do not correlate with garnet size or core compositions of Mn, Mg, and Fe, demonstrating that Ca did not equilibrate rock-wide during garnet growth. In another example, Carlson and Denison (1992) used high-resolution X-ray computed tomography (HRXCT) to examine the sizes and locations of porphyroblastic crystals in four regionally metamorphosed rocks. They found that the porphyroblasts are spatially ordered and concluded that the likely mechanism for the disposition of crystals was slow diffusion. In both of these examples, evidence of disequilibrium crystallization is not apparent without careful examination.

Garnet growth zoning, revealed by electron microprobe analysis, should be concentric when diffusive fluxes of garnet components are large, as in the case of rock-wide chemical equilibrium in which chemical-potential gradients are nearly flat. In garnets with patchy zoning (e.g., Hirsch *et al.*, 2003), the diffusive fluxes were likely small for those elements during crystallization, and the chemical-potential gradients would have been steep. Depending upon the relative rates of intergranular diffusion, chemical-potential gradients between reactants and products can be steep for some elements but virtually flat for others, creating conditions of partial chemical disequilibrium during crystallization.

Differences in chemical potentials of the components $\Delta\mu_i$ between reactants and products sum to the Gibbs free energy change of reaction $\Delta_r G$. During metamorphism, the components that take part in the reaction exist in the intergranular fluid as complexes with other chemical species (e.g., $Al(OH)_3$, AlF_3, etc.). In this text, the components of the reaction are referred to as elements for simplification. In the case of garnet, $\Delta_r G$ is given by the sum of the chemical potentials $\Delta\mu_i$ of the major components:

$$\Delta_r G = \Delta\mu_{Si} + \Delta\mu_{Al} + \Delta\mu_{Mg} + \Delta\mu_{Fe} + \Delta\mu_{Mn} + \Delta\mu_{Ca} . \tag{5-1}$$

As an example of partial disequilibrium, garnet crystallization may occur with Si, Mg, Fe, Mn, and Ca in chemical equilibrium ($\Delta\mu_i = 0$) due to large diffusive fluxes, while the diffusive flux for Al is small (e.g., due to slow intergranular diffusivity) and the result is a gradient between reactants and products ($\Delta\mu_{Al} \neq 0$). In this case, $\Delta_r G$ is dependent only on the $\Delta\mu_{Al}$, and the garnet crystallizes under partial chemical disequilibrium. Reaction affinity A_r is defined as the negative of the Gibbs free energy change of reaction ($-\Delta_r G$) and is used to describe the magnitude of disequilibrium.

During crystallization, Al gradients between reactants and products evolve over time and space. Once nucleation occurs, gradients between reactant and product crystals are established (Figure 5-1). Along these gradients, the reaction affinity varies with Al concentration (Equation 2-5), and nucleation can occur anywhere along the gradients, except near existing porphyroblasts where the reaction affinity falls below a critical value. With increasing temperature and time, the reactants dissolve and more

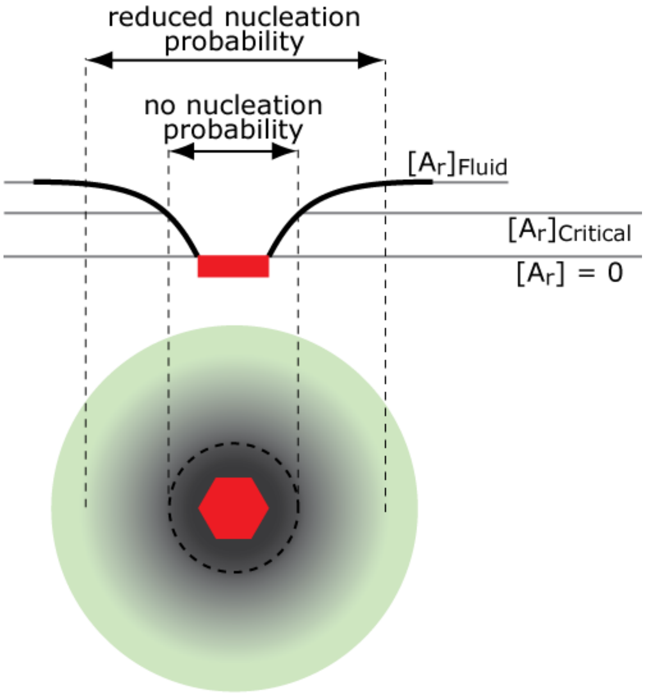

Figure 5-1. Schematic diagram of reduction in reaction affinity due to nutrient depletion around growing porphyroblasts. Nutrient depletion causes reaction affinity (A_r) to decrease with distance toward a growing porphyroblast, and nucleation probability scales with reaction affinity. If reaction affinity falls below a critical value ($[A_r]_{Critical}$), it is more favorable energetically to dissolve a potential nucleus rather than create a nucleus, and therefore, nucleation probability is zero closest to the porphyroblast. After Hirsch et al. (2000).

porphyroblasts nucleate, creating a complex evolution of concentration gradients, and therefore reaction affinity, over the course of crystallization. The values of the reaction affinity reported here are those associated with the time and location of the nucleation of a porphyroblast, and thus the reaction affinity is a dynamic and complex measure that changes throughout crystallization.

To determine the reaction affinity, CRYSTALLIZE3D was used to simulate diffusion-controlled nucleation and growth (DCNG) of porphyroblastic textures that were compared with textures in natural samples. The model tracks changes in Al concentration during porphyroblast crystallization, and thus provides a quantitative link between diffusion-controlled textures and the scales of diffusion and departures from equilibrium that generate these textures. In this chapter, values for the reaction affinity derived from these simulations are examined, and the implications of the magnitudes of disequilibrium are discussed.

PREVIOUS ESTIMATES OF REACTION AFFINITY

Estimates of reaction affinity have been derived primarily from contact metamorphic settings, but some new results from regional metamorphism are available. Disequilibrium crystallization is most easily recognized from textures of incomplete reactions, like corona structures around olivine or garnet (e.g., Johnson & Carlson, 1990; Carlson & Johnson, 1991; Ashworth & Sheplev, 1997). Most studies of disequilibrium crystallization have focused on rocks with textures that clearly indicate incomplete reactions, but more recent work has focused on cryptic examples of disequilibrium and the task of quantifying reaction affinity in these rocks. Several examples of obvious and cryptic disequilibrium are given here.

Ashworth and Sheplev (1997) and Ashworth et al. (1998)

Ashworth and Sheplev (1997) and Ashworth et al. (1998) modeled intracrystalline diffusion across coronal textures from regionally metamorphosed granulite-facies metagabbros and computed chemical potential gradients across the coronas using thermodynamic data. The sum of the chemical potentials across the coronas gives the overall free-energy difference during crystallization of the mineral assemblages. They interpreted the differences in free energy in terms of thermal and baric overstepping of the reactions.

Ashworth and Sheplev (1997) studied a reaction that transformed olivine and plagioclase into amphibole and pyroxene and calculated a reaction affinity of 10 kJ mol^{-1} of 24-oxygen plagioclase, which is ~0.4 kJ mol^{-1} of oxygen in plagioclase. (For comparison with 12-oxygen garnet, reaction affinity of 5 kJ mol^{-1} of garnet translates to ~0.4 kJ mol^{-1} of oxygen in garnet.) This results in ~100 °C of thermal overstepping (ΔT) of the equilibrium T of the reaction (T_{eq}).

Ashworth et al. (1998) determined reaction affinity in a corona where orthopyroxene and plagioclase reacted to garnet, clinopyroxene, and quartz in response to changes in pressure. Their determination yields reaction affinity of ~3.5 kJ mol^{-1} garnet (~0.3 kJ mol^{-1} of oxygen in garnet) with a corresponding baric overstepping of 0.14 ± 0.04 GPa.

Waters and Lovegrove (2002)

Waters and Lovegrove (2002) studied metapelitic rocks from the aureole of the Bushveld Complex in South Africa and found that the textures revealed a different petrogenesis than predicted by equilibrium thermodynamics. Overgrowth and replacement textures clearly indicate the sequence of crystallization in these samples, showing that late nucleation, slow reaction rates, and armoring of some phases caused incomplete reactions and metastable mineral assemblages. For andalusite nucleation, they estimated reaction affinity of 5 kJ mol^{-1} (1 kJ mol^{-1} of oxygen in andalusite) at 40 °C of thermal overstepping.

Wilbur and Ague (2006)

Garnets from the Wepawaug Schist in Connecticut grew during regional metamorphism at amphibolite-facies conditions and exhibit branched and dendritic growth morphologies, revealed by chemical mapping, indicative of interface-controlled growth. Using a Monte Carlo technique, Wilbur and Ague (2006) modeled diffusion of components from a fluid to the surface of garnet, surface attachment kinetics, and diffusion along the garnet surface to simulate the processes that control the development of these crystal morphologies. They estimated the free energy difference between the average composition of the intergranular fluid and the fluid in equilibrium with garnet, yielding values of ~2 kJ mol^{-1} garnet. (Assuming 12-oxygen garnet, this is ~0.16 kJ mol^{-1} of oxygen.)

Hetenyi et al. (2007)

Using Airy-type isostasy gravity modeling to constrain the density of material present beneath the Tibetan Plateau, combined with isochemical diagrams to associate density of mineral assemblages with *P-T* conditions, Hetenyi et al. (2007) determined that eclogitization took place after about 100 °C overstepping of the albite to jadeite reaction. They suggest that overstepping was caused by the absence of a free fluid until the amphibolite protolith began dehydrating. They do not assign an overstepping value in terms of free energy, but in the current study, it was found that 100 °C of thermal overstepping for the amphibolite to eclogite transition requires ~7-10 kJ mol^{-1} garnet (0.6-0.8 kJ mol^{-1} of oxygen in garnet).

Padron-Navarta et al. (2008)

In a study of epitaxial garnet growth in mafic granulites of the Jijal complex in north Pakistan, Padron-Navarta et al. (2008) showed that garnet nucleation was the result of ~5-10 kJ mol^{-1} overstepping of the garnet-forming reaction (0.4-0.8 kJ mol^{-1} oxygen in garnet). Their results are based on the difference in *P-T* conditions of the garnet-forming reaction (zero-mode line) and the *P-T* conditions of the mineral assemblage in equilibrium with garnet as computed in an isochemical phase diagram and constrained by thermal modeling.

Pattison and Tinkham (2009)

In the contact aureole of the Nelson Batholith, British Columbia, Pattison and Tinkham (2009) describe mineral assemblages within metapelitic rocks that do not reflect the sequence of mineral assemblages that are calculated from equilibrium thermodynamics. The reaction affinities for several reactions were determined, and for the garnet-forming reaction, they calculated 4.8 kJ mol^{-1} (~0.4 kJ mol^{-1} of oxygen in garnet), corresponding with ~30 °C of thermal overstepping. The consequences of disequilibrium in this aureole are reflected in the positions of the isograds relative to the equilibrium prediction of their positions (Fig. 5-2), providing a clear example of the shortcomings of applying equilibrium calculations to rocks that have experienced significant degrees of disequilibrium crystallization.

REACTION AFFINITY FROM SIMULATED CRYSTALLIZATION

The techniques used in this study are applied to regionally metamorphosed rocks using the concept of partial disequilibrium under diffusion-controlled conditions. The CRYSTALLIZE3D model numerically simulates DCNG of porphyroblastic crystals in a model space composed of volume elements that track the concentration of Al in the intergranular fluid during dissolution of aluminous reactants and growth of aluminous products, which include garnet. The concentration of Al rises with temperature as the reactants dissolve and this drives nucleation of garnet with the product assemblage; the growing garnet crystals are sinks for Al, and thus gradients are established between the reactant assemblage and the product assemblage. The reaction affinity scales with the intergranular concentration of Al, and thus simulations that produce textures equivalent to natural samples describe, quantitatively, the scales of disequilibrium that were present during DCNG of porphyroblastic rocks. The model was applied to a diverse suite of rocks, which represent a wide variety of crystallization conditions, to explore the range of reaction affinity present during garnet crystallization in common regionally metamorphosed rocks.

As described above, reaction affinity varies in time and space during DCNG of garnet porphyroblasts. Each reaction affinity reported here corresponds with the time and location (temperature and Al concentration) of nucleation of an individual crystal. In portions of the model where the reactant assemblage persists, the reaction affinity is a maximum value for the given reaction and *T*; but nucleation can occur (though with

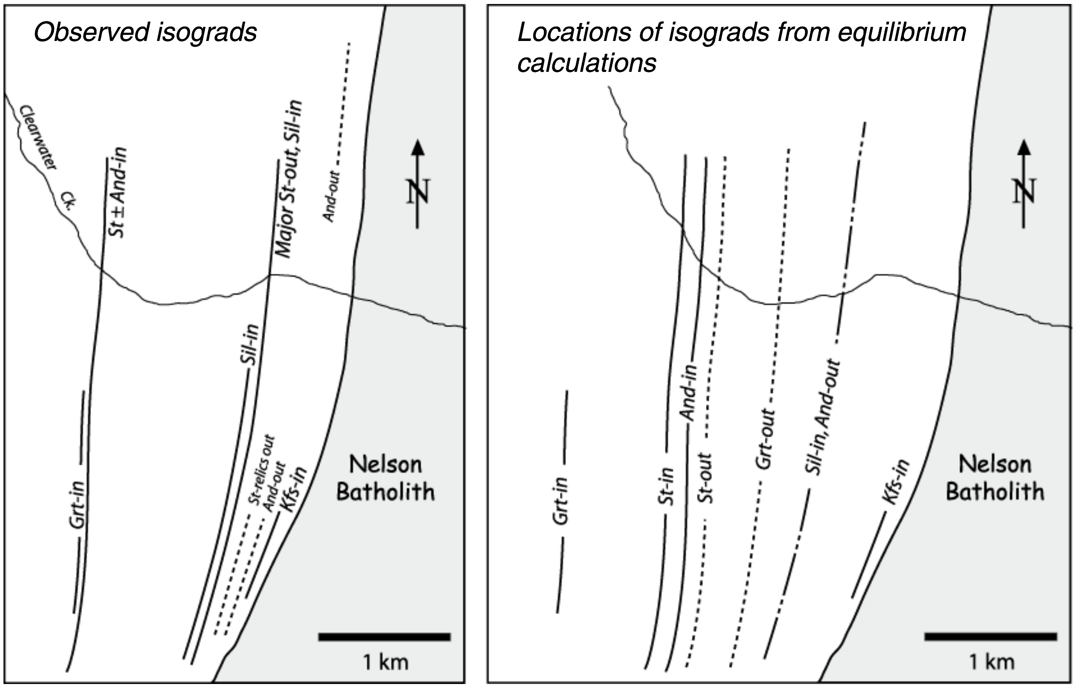

Figure 5-2. Simplified map of a portion of the Nelson Batholith aureole showing observed and calculated isograd locations, modified from Pattison and Tinkham (2009). The observed isograds are given on the *left*. In the equilibrium model (*right*), garnet first nucleates much farther from the contact and the staurolite isograd is approximately the same as observed. The equilibrium model predicts the loss of garnet approaching the contact but this is not observed in the natural samples. Staurolite is predicted to exist over a short interval with distance from the contact, but in the natural samples, staurolite exists over a much larger range in temperatures.

lower probability) in regions along the gradient in reaction affinity between the zones that host reactant and product assemblages.

The following describes the resulting reaction affinity from the simulations as a function of thermal overstepping of the garnet forming reaction. Although reaction affinity has been quantified for the entire crystallization interval, the discussion highlights the reaction affinity at the start of nucleation and growth, which corresponds with the first appearance of garnet along a metamorphic field gradient, and it also highlights the maximum reaction affinities, which corresponds with the highest conditions of garnet stability before a “garnet-out” isograd along a metamorphic field gradient with increasing temperature.

Reaction affinity throughout crystallization

With increasing temperature, T_{eq} is overstepped by a magnitude given by ΔT, and reaction affinity increases (Table 5-1; Fig. 5-3). Plots of reaction affinity versus ΔT during the simulations are characterized by two linear segments. The first has a positive slope that reflects porphyroblast nucleation in portions of the model with maximum reaction affinity as temperature rises. The slope is dependent on the model reaction. The second is a vertical segment that represents porphyroblast nucleation along the isothermal portion of the heating path near the end of crystallization. The points on the plot that fall below the maximum reaction affinity, including the vertical segment, are values for porphyroblasts that nucleated in regions with lower Al concentrations, either near the end of crystallization when reactants were nearly consumed, or in portions of the model in which the concentration of Al was depressed, either in low-reactant-concentration structures, where the concentration of Al is depleted rapidly, or near existing porphyroblasts, where Al has been depleted by local concentration gradients. Therefore, nucleation at reaction affinities below the maximum value are common in simulations that have low concentration layers thicker than the diffusive length scale of the system (PM2, 711A, AG4, MD, and WR3m).

All of the simulated textures require protracted nucleation (except for AG4, for which petrographic evidence exists of early site saturation (Meth & Carlson, 2005)).

Table 5-1. Derived values

Rock	T_{eq} (°C)	k_2	γ for s = 0.75 (J m^{-2})	First Nucl. Overstepping (kJ mol^{-1})	First Nucl. Overstepping (°C)	Max. Nucl. Overstepping (kJ mol^{-1})	Max. Nucl. Overstepping (°C)
PM1	435	1	0.046	5	29	17.7	100
PM2	435	0.1	0.021	1.2	7	17.3	100
PM4	435	0.2	0.027	1.8	11	17.4	100
160A	485	0.5	0.037	2.2	21	5.3	50
191A	485	2	0.059	5.2	49	9	85
711A	485	0.7	0.041	4.1	39	12.3	115
AG4	540	0.005	0.008	0.5	4	6.4	60
MD	555	0.1	0.023	3.4	11	29	95
Jen-2-80	375	0.001	0.004	0.6	10	7.6	125
HE-1	450	0.5	0.037	4.6	62	7.5	100
WR1bt	575	3	0.072	5.7	58	7.3	75
WR1tp	575	3	0.072	5.9	60	7.3	75
WR3m	575	0.01	0.011	0.4	4	7.3	75
Min	375	0.001	0.004	0.4	4	5.3	50
Mean	493	0.86	0.035	3.1	28	12	89
Max	575	3	0.072	5.9	62	29	125

Figure 5-3. Reaction affinity as a function of thermal overstepping for all simulations. Reaction affinity is the value at the time and location of nucleation. Thermal overstepping is the temperature of nucleation above the equilibrium temperature of the reaction. The model reaction number and the nucleation acceleration value (k_2) are given. See text for explanation.

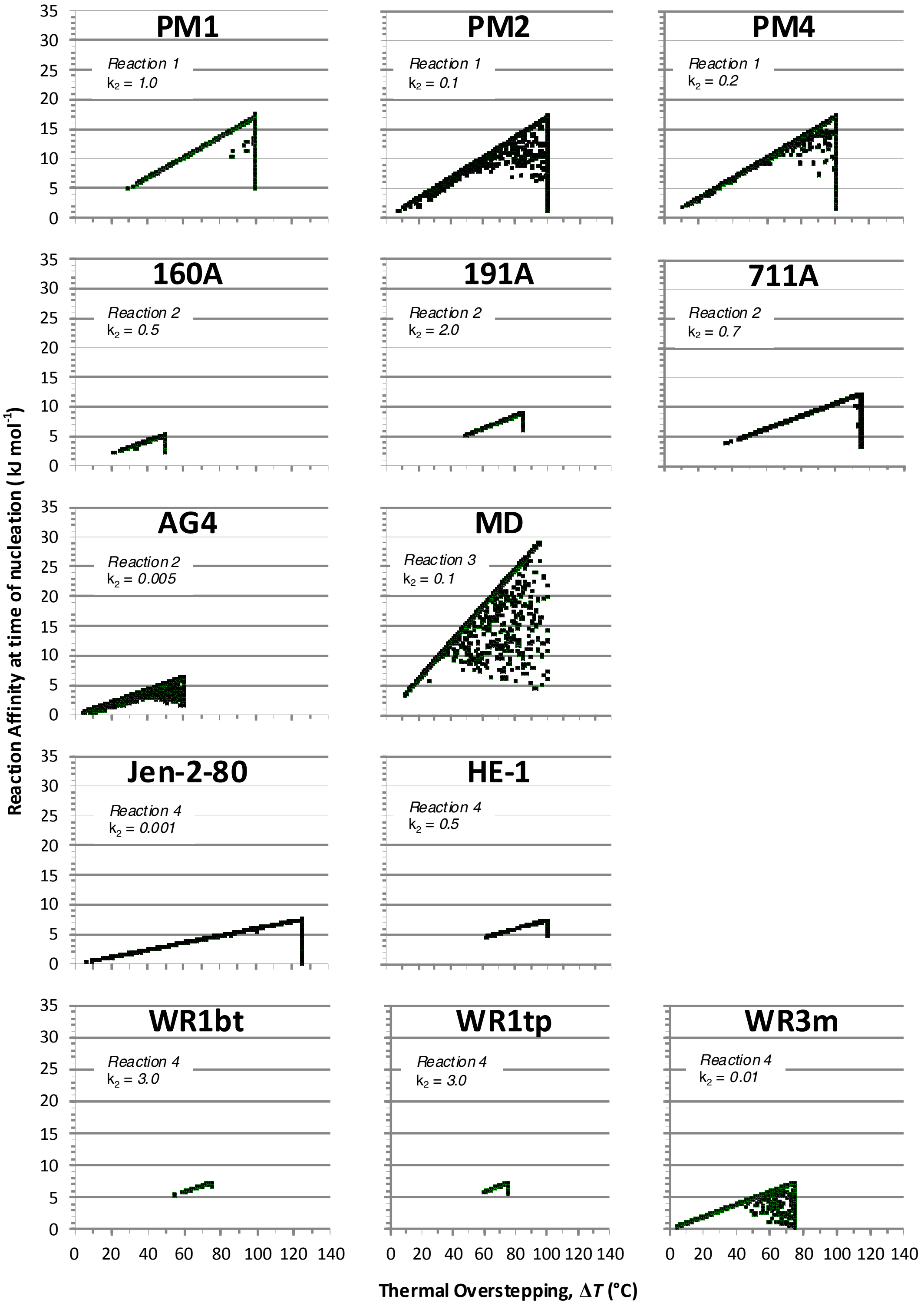
PM1
Reaction 1
k_2 = 1.0
PM2
Reaction 1
k_2 = 0.1
PM4
Reaction 1
k_2 = 0.2
160A
Reaction 2
k_2 = 0.5
191A
Reaction 2
k_2 = 2.0
711A
Reaction 2
k_2 = 0.7
AG4
Reaction 2
k_2 = 0.005
MD
Reaction 3
k_2 = 0.1
Jen-2-80
Reaction 4
k_2 = 0.001
HE-1
Reaction 4
k_2 = 0.5
WR1bt
Reaction 4
k_2 = 3.0
WR1tp
Reaction 4
k_2 = 3.0
WR3m
Reaction 4
k_2 = 0.01
0
5
10
15
20
25
30
35
0
20
40
60
80
100
120
140
Reaction Affinity at time of nucleation (kJ mol^{-1})
Thermal Overstepping, ΔT (°C)

Because nucleation continues throughout crystallization in most simulations, crystals will nucleate at very large magnitudes of disequilibrium near the end of the heating path.

Reaction affinity at first nucleation

Nucleation first becomes possible at the nucleation site after the activation energy for nucleation is exceeded (e.g., ~ 5 kJ mol^{-1} and 29 °C for sample PM1). Within this rock suite, the first crystals to nucleate range in reaction affinity from 0.4 kJ mol^{-1} (4 °C) in sample WR3m to 5.9 kJ mol^{-1} (60 °C) in sample WR1tp. In terms of thermal overstepping, the values range from 4 °C (0.4 kJ mol^{-1}) in sample WR3m to 62 °C (4.6 kJ mol^{-1}) in sample HE-1. Thermal overstepping in this range is predicted from the entropy change of the model reactions as a function of thermal overstepping (e.g., Waters & Lovegrove, 2002; Pattison & Tinkham, 2009), which can be simplified by

$$\mathrm{A_r} = \Delta \mathrm{T}\ \Delta_\mathrm{r}\mathrm{S}. \tag{5-2}$$

In plots of A_r versus ΔT, the slope of the line is $\Delta_\mathrm{r}S$ (Fig. 5-4). Reactions with higher $\Delta_\mathrm{r}S$ require smaller thermal overstepping to produce equivalent reaction affinity and exceed the activation energy of nucleation. The differences in $\Delta_\mathrm{r}S$ for each of the reactions shown here arise dominantly from the magnitude of H_2O released as the reaction progresses (cf. Pattison & Tinkham, 2009). Reaction 2, for example, releases 5 moles of H_2O per mole of garnet, and reaction 3 releases 0.83 moles of H_2O per mole of garnet (Table 3-3).

The relationship between thermal overstepping and entropy suggests that reactions with large entropies would have the smallest thermal overstepping, as was also found by Pattison and Tinkham (2009). However, the simulations shown here do not follow this trend. In Figure 5-3, for example, the simulations for samples Jen-2-80 and HE-1 show drastically different thermal overstepping. The primary difference in these models is the nucleation acceleration factor, which is significantly larger in HE-1 (Table 3-6). Relatively large values of k_2 correspond with relatively large thermal overstepping (e.g., 191A, WR1bt, and WR1tp), and relatively small values of k_2 correspond with smaller thermal overstepping (e.g., Jen-2-80 and WR3m). Nucleation is easier in

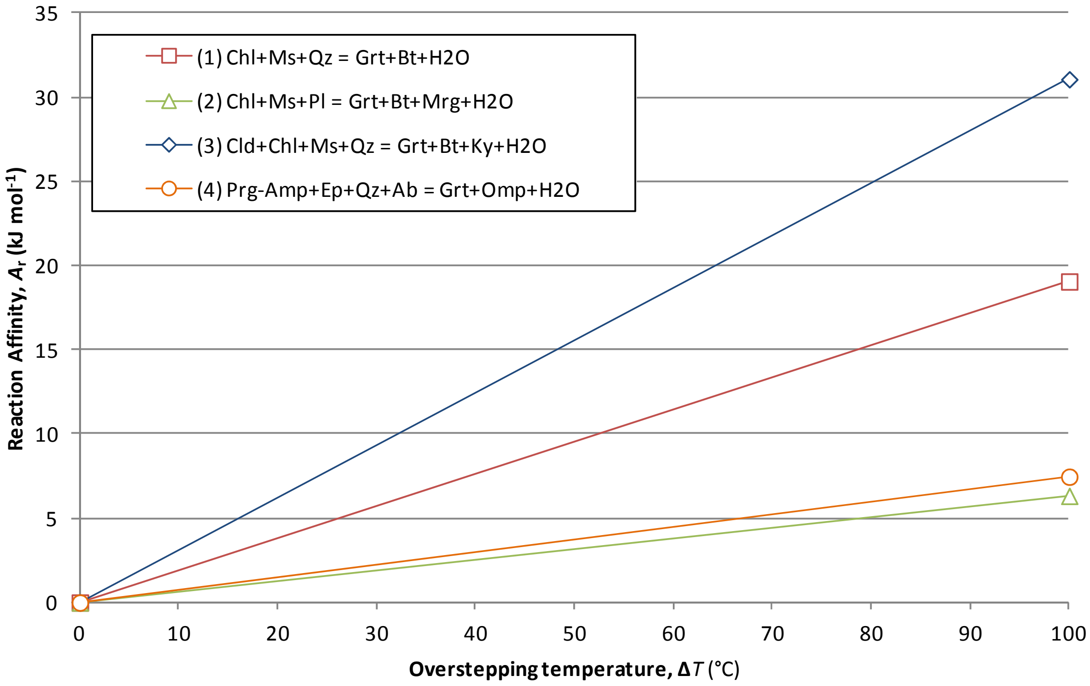

Figure 5-4. Reaction affinity ($-\Delta_r G$) as a function of thermal overstepping for the model reactions. Reactions that liberate larger proportions of H_2O have steeper slopes, reflecting the larger reaction entropies associated with more hydrous reactions, as shown by Pattison and Tinkham (2009).

rocks with conditions that lower the interfacial energy (γ), so the correspondence of the overstepping temperature with k_2 shows that the simulated thermal overstepping reflects the properties of interfacial energy.

Maximum reaction affinity

In the simulations, crystallization along the t-T-Δ_rG path continues until all reactants are consumed, and nucleation in these simulations continues up to the highest temperatures of the heating path. Therefore, the scale of reaction affinity depends only on the Δ_rG of the model reaction and the thermal interval over which nucleation takes place, and the maximum reaction affinity will be Δ_rG at the highest temperature of the heating path as long as nucleation continues to that temperature, which it does for all simulations except for AG4. For example, the samples from Maine (160A, 191A, and 711A) share the same model reaction but have different thermal histories, so the maximum reaction affinity achieved by each simulation is due to the difference in heating paths. Alternatively, both HE-1 and MD experience ~100 °C of thermal overstepping, but the difference in their reactions produces different maximum reaction affinities. The range of maximum reaction affinity attained for all samples is represented by 160A and MD, which have maxima at 5.3 and 29.0 kJ mol^{-1}, respectively.

The maximum affinities are not necessarily associated with the smallest crystals in the rock, as one might expect for crystals that nucleate at large thermal overstepping values. Figure 5-5 shows a general trend of decreasing crystal size with increasing nucleation time, but examination of Figure 5-3 shows that peak reaction affinity does not occur at the last nucleation because the reactants tend to dissolve midway through the crystallization interval (Fig. 5-6) and the last few crystals tend to be small and nucleate at lower reaction affinity.

IMPLICATIONS FOR PETROLOGICAL INVESTIGATIONS

The simulations demonstrate that significant levels of reaction affinity are associated with the first crystals to nucleate and that nucleation continues to large values of reaction affinity and thermal overstepping, which has implications for equilibrium-

Figure 5-5. Final crystal radius as a function of nucleation time. In general, larger crystals nucleate earlier in the crystallization interval. However, the dispersion of the data shows that not all of the largest crystals nucleate first.

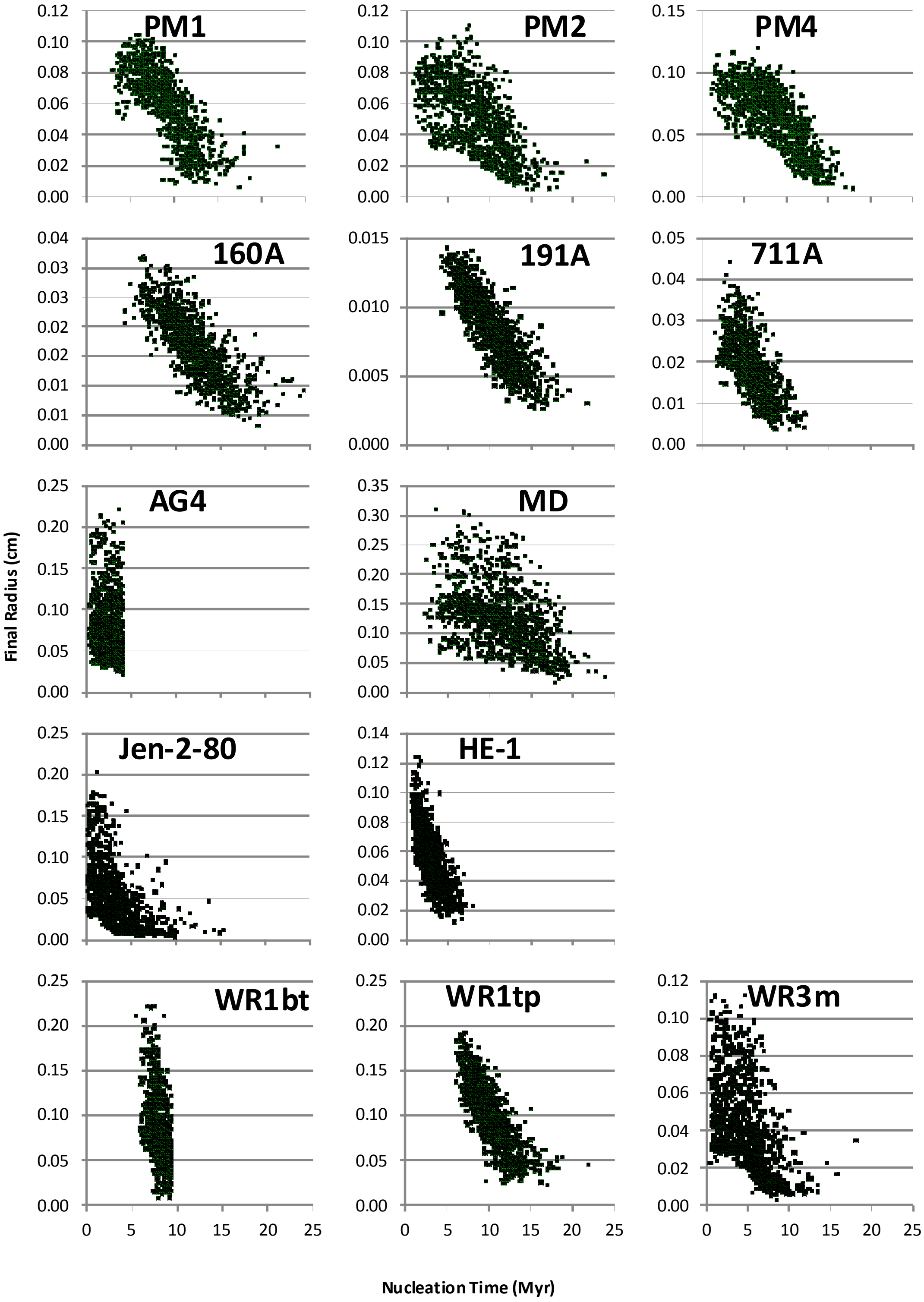
PM1
PM2
PM4
160A
191A
711A
AG4
MD
Jen-2-80
HE-1
WR1bt
WR1tp
WR3m
0.12
0.10
0.08
0.06
0.04
0.02
0.00
0.15
0.05
0.015
0.010
0.005
0.000
0.35
0.30
0.25
0.20
0.14
0.03
0.01
0
5
10
15
20
25
Final Radius (cm)
Nucleation Time (Myr)

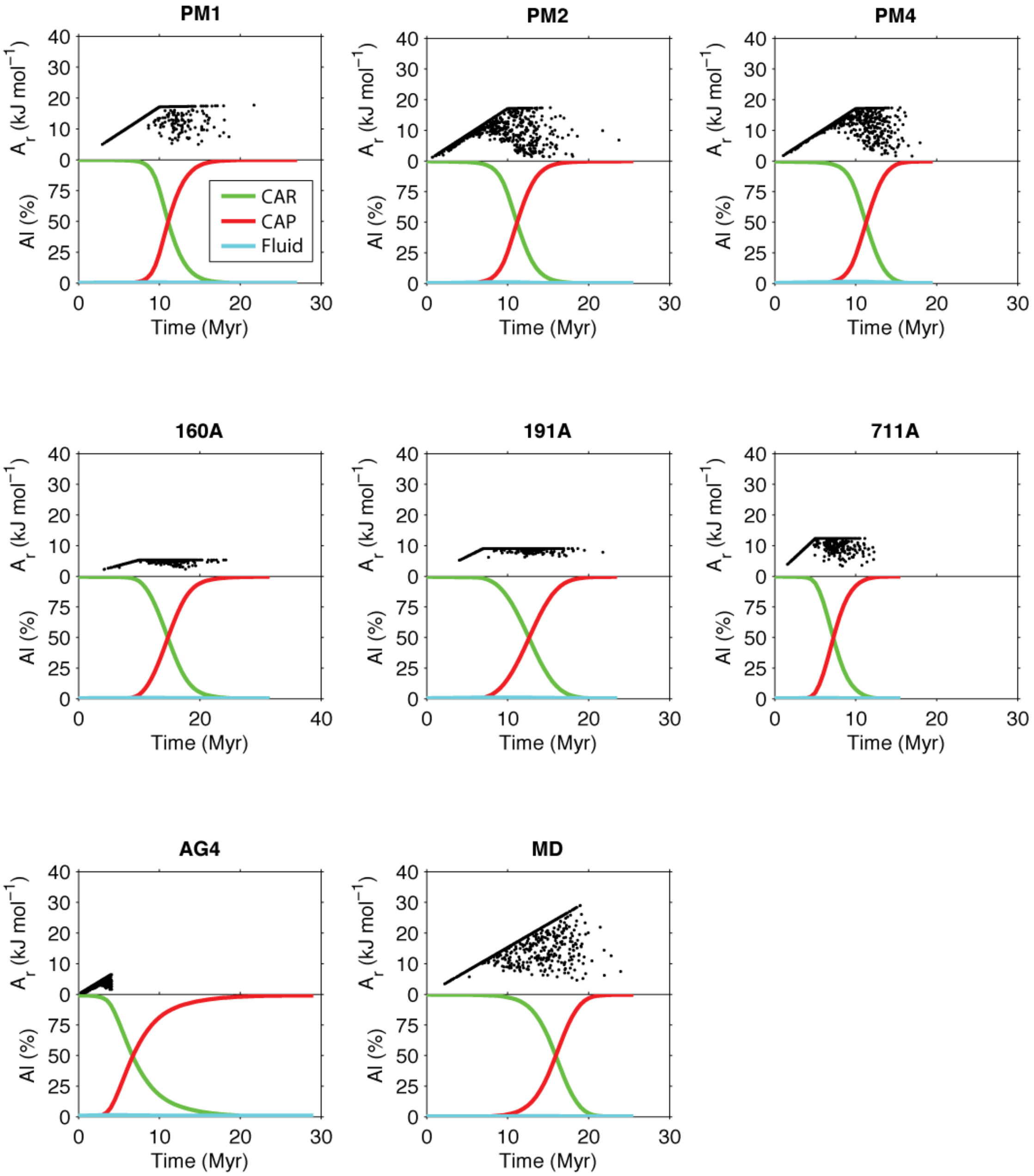

Figure 5-6. Reaction affinity (A_r) as a function of nucleation time compared with the distribution of Al in the reactants (CAR), products (CAP), and intergranular fluid. The lower plots essentially describe the reaction progress; reactants dissolve, releasing Al into the intergranular fluid, and products grow, consuming the Al in the intergranular fluid. As the proportion of Al in the reactants decreases steeply, nucleation occurs more often in portions of the model with reaction affinity below the maximum.

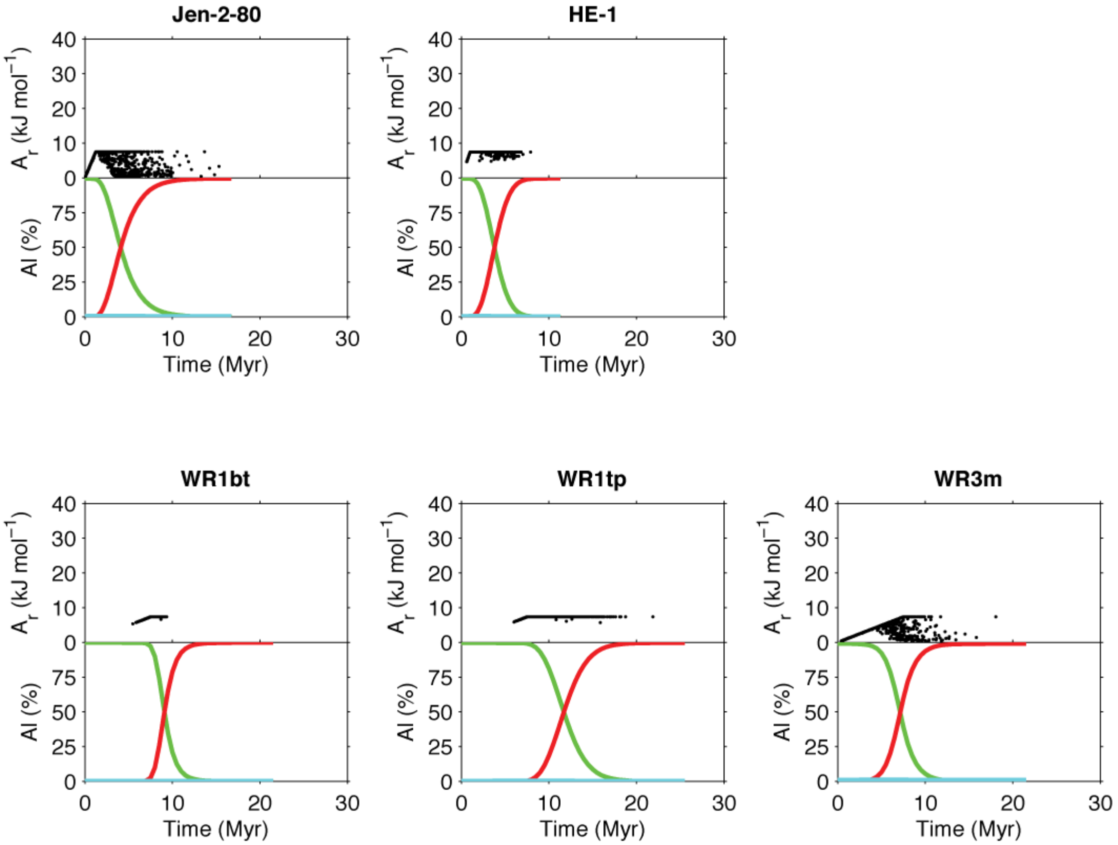

Figure 5-6. (continued)

based techniques applied to mineral assemblages that have experienced large departures from equilibrium, and possibly for geochronology of bulk mineral separates.

Overstepping of reactions

The reaction affinity values for the first crystals to nucleate in the simulations range from 0.4 to 5.9 kJ mol^{-1} of garnet (0.03-0.49 kJ mol^{-1} of oxygen in garnet). These values are similar to those determined in previous work for contact metamorphism: 0.3-1 kJ mol^{-1} of oxygen in the product crystals (Ashworth & Sheplev, 1997; Ashworth *et al.*, 1998; Waters & Lovegrove, 2002; Pattison & Tinkham, 2009), and for regional metamorphism: 0.16-0.8 kJ mol^{-1} of oxygen in the product crystals (Wilbur & Ague, 2006; Hetenyi *et al.*, 2007; Padron-Navarta *et al.*, 2008). The simulations also support the assertion that heating rate does not play a significant role in the magnitude of reaction affinity for the first nucleation in regionally metamorphosed rocks (Ridley & Thompson, 1986; Rubie, 1998; Waters & Lovegrove, 2002). The magnitude of the reaction affinity at the first nucleation can produce erroneous interpretations of metamorphism, especially if the values are as high as ~10 kJ mol^{-1} of garnet. In more practical terms, thermal overstepping associated with this reaction affinity can be large, which would amount to nucleation at ~50 °C above T_{eq} depending on the reaction and the interfacial energy.

Several of the studies cited above focus on the thermal overstepping of the garnet-forming reaction associated with delayed nucleation of the first few crystals to nucleate. However, continued nucleation throughout the crystallization interval, and the corresponding elevated reaction affinities, are concepts that have received less attention. All of the simulations nucleate and grow porphyroblasts throughout the crystallization interval (except for sample AG4, as noted above). The modeling in this study demonstrates that nucleation of porphyroblasts during regional metamorphism that persists up to the highest temperatures of crystallization produces porphyroblastic textures nearly identical to those of natural samples under reasonable constraints of heating rates and crystallization durations, suggesting that protracted nucleation may be common.

The reaction affinity associated with late-nucleating crystals can be large (~60 kJ mol^{-1} of garnet) and represents a significant departure from equilibrium. The reaction affinity in these simulations is based on $\Delta\mu_{Al}$, whereas the other components of the system (e.g., Fe and Mg) are assumed to diffuse rapidly enough to maintain near-equilibrium chemical potentials ($\Delta\mu \approx 0$). This suggests that even at the scales of reaction affinity determined in these samples, Fe-Mg exchange thermometry or other equilibrium-based techniques could be applied successfully to samples that grew under conditions of partial disequilibrium, if the disequilibrium components are identified and avoided.

However, this brings up an additional point about the first crystals that nucleate during crystallization. On isochemical phase diagrams, garnet core isopleths of Mg, Fe, Mn, and Ca commonly do not intersect at the garnet zero-mode line, but instead intersect at higher temperatures (e.g., Stowell & Tinkham, 2003; Tinkham & Ghent, 2005; Zeh *et al.*, 2005). One explanation is that the garnet was not sectioned precisely through the center of the crystal, and the compositions are not of the core but instead are from farther into the rim where garnet compositions would record higher *P-T* conditions. Another explanation, considering that Fe and Mg can diffuse within a garnet crystal for distances between 30 and 50 μm at 600 °C over 2 Myr (Carlson, 2006), is that intracrystalline diffusional relaxation altered the core composition toward the composition just outside of the core. A third explanation is that nucleation of garnet took place above the theoretical equilibrium temperature of the reaction because of slow diffusion of Al, while the divalent cations diffused rapidly enough to minimize their chemical potentials ($\Delta\mu_i \approx 0$). In this last case, the garnet core would record a composition that reflects a temperature above the equilibrium temperature of the reaction, and the *P-T* conditions given by intersecting isopleths are actually the result of partial disequilibrium during garnet growth.

Delayed nucleation also has consequences for *P-T* path construction. Garnet porphyroblasts are commonly used to construct *P-T* paths from chemical zoning, and late-nucleating garnets will record only the latter portions of the *P-T* path. A common assumption is that the largest crystals in a rock nucleated earliest and record nearly the entire *P-T* path. However, the dispersion in the nucleation times of the largest crystals in the simulations (Fig. 5-5) suggests that not all of the largest crystals in a sample will record the entire *P*-*T* path. The protracted nucleation demonstrated for multiple samples in this study suggest that if not enough garnets are chosen to construct a *P*-*T* path, the early portions of the path could be missed entirely.

Another consequence of delayed nucleation is in the use of index minerals and mineral assemblages to determine the metamorphic field gradient of a sequence of rocks. If reaction affinity was large (~50 °C) for initial nucleation of an index mineral, the thermal gradient might appear shallower than it actually was. Protracted crystallization due to delayed nucleation could allow mineral assemblages to exist at temperatures and pressures higher than calculated equilibrium conditions suggest, and thus isograds might be offset along a metamorphic field gradient. These concepts have been described for contact-metamorphic settings (Waters & Lovegrove, 2002; Pattison & Tinkham, 2009). Figure 5-2 shows a comparison from Pattison and Tinkham (2009) of the observed isograds and the expected isograds based on equilibrium calculations. Observations show garnet appearing closer to the contact (higher temperature) than predicted from equilibrium calculations, possibly reflecting delayed nucleation from disequilibrium.

Metastable reactions

Not only can disequilibrium cause minerals to nucleate far from T_{eq}, precursor minerals can also persist metastably into *P*-*T* conditions beyond their expected stability range. If the changes in mineral assemblages do not keep pace with changing *P*-*T* conditions because the garnet-producing reaction has not gone to completion, the predicted equilibrium reactions might not occur, or might be offset to higher *P*-*T* conditions, resulting in metastable minerals and reactions (Foster & Dutrow, 2005). In Figure 5-2, staurolite exists over a wide thermal interval (distance from contact) compared with the interval expected from the equilibrium case, which may reflect metastability due to delayed reactions during disequilibrium crystallization (Pattison & Tinkham, 2009).

Chemical gradients are commonly preserved in garnet, and typically only the rim of the garnet is in equilibrium with the surrounding matrix phases. The sequestration of components within crystals as they grow results in an effective bulk composition for the rock that describes the components that are available to the matrix phases for reaction. If those components are still available because garnet nucleation and growth is delayed, the solubility of the existing phases will be affected. Depending on bulk composition and the *P*-*T* conditions, other reactions might take place, or the same reactions will take place at different *P*-*T* conditions.

Geochronology applied to bulk garnet separates

A basic assumption of geochronology using bulk mineral separates is that the minerals crystallized at the same time and represent a single age within uncertainty. As isotopic analyses become increasingly more precise, the uncertainties applied to ages of mineral separates becomes smaller than the expected duration of crystallization event. For example, if garnet growth spans a range of 10 Myr, an age determined from a bulk garnet separate with uncertainties less than 10 Ma brings into question whether the age is representative of growth of the core, the rim, or somewhere between. Protracted nucleation of garnet porphyroblasts therefore introduces an effect of mixing ages from the beginning to the end of crystallization.

Comparison of nucleation time versus cumulative volume from the model simulations shows that the midpoint of the cumulative garnet volume is commonly in the first half of the growth history (Fig. 5-7). Assuming no biases from separation techniques, differential element uptake, or isotopic fractionation, this implies that bulk garnet separates will give an age that is closer to the beginning of the garnet growth event. However, a more rigorous analysis is required to properly assess this effect considering the large number of possible influences on such ages. As geochronology techniques continue to produce more precise ages and attempt to distinguish between closely timed crystallization events (e.g., Pollington & Baxter, 2010), consideration of crystallization durations will be increasingly important in separating distinct metamorphic events.

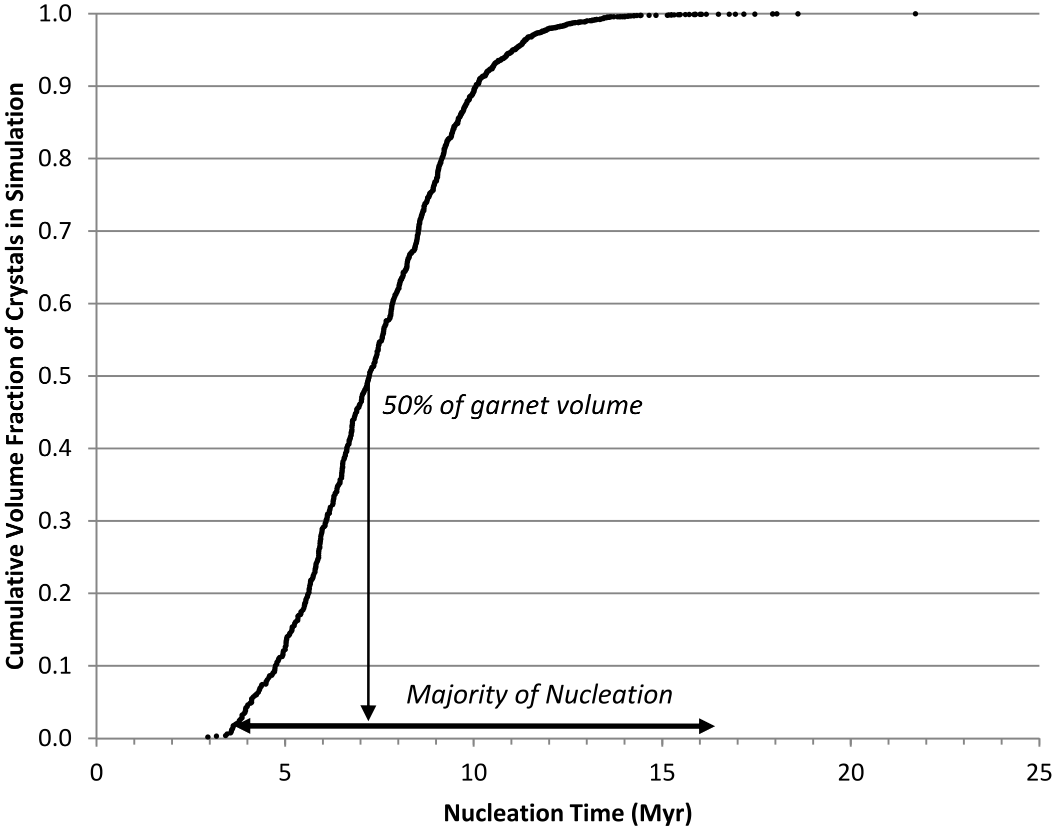

Figure 5-7. Effect of protracted nucleation intervals on geochronology from bulk mineral separates. The plot shows cumulative volume of crystals in a typical simulation (PM1) as a function of nucleation time. Under the assumption of no other biases in the geochronology techniques, the age of a mineral separate would be weighted by the earlier nucleating crystals.

CONCLUSIONS

The determinations of reaction affinity presented here are from a diverse sample suite that spans a wide range of regionally metamorphosed rocks. The full characterization in time and space of reaction affinity through nucleation and growth of all porphyroblasts in a simulation represents the first comprehensive analysis of reaction affinity for regional metamorphism.

The reaction affinities for the first crystals to nucleate in a rock range from modest values (e.g., 1 kJ mol^{-1} garnet) to large values (e.g., 10 kJ mol^{-1} garnet), which can amount to ~50 °C of overstepping beyond the equilibrium conditions of the garnet-forming reaction and greatly alter the geologic interpretation of the onset of reaction in a metamorphic rock.

Continued nucleation at maximum reaction affinity throughout the crystallization interval is an expected consequence of the persistence of reactants to temperatures well in excess of the equilibrium temperature for the reaction, so reactions can be expected to extend to metastable conditions well above the equilibrium conditions of the reaction. If the reactions do not run to completion, as predicted from phase-equilibrium calculations, successive equilibrium mineral assemblages may not appear in natural samples along metamorphic field gradients, and interpretations of the conditions of metamorphism could be erroneous.

The range of reaction affinities determined here suggests that all metamorphic rocks have crystallized under at least a small scale of disequilibrium. However, the general agreement in many localities around the world between natural samples and equilibrium thermodynamic models suggests that reaction affinity for most samples is on a scale that does not appreciably affect the large scale interpretations, but instead may be most important for studies that examine the progressively more precise and intricate details of metamorphism, such as REE zoning in metamorphic minerals used to interpret the crystallization history of a single crystal that is then extrapolated to the tectonic scale. As techniques used to understand metamorphism delve deeper into the recorded history within metamorphic minerals, a complete understanding of the consequences of disequilibrium becomes increasingly important.

PART B: EFFECTS OF GARNET RESORPTION ON LU-HF AGES

CHAPTER 6: IMPLICATIONS OF GARNET RESORPTION FOR THE LU-HF GARNET GEOCHRONOMETER: AN EXAMPLE FROM THE CONTACT AUREOLE OF THE MAKHAVINEKH LAKE PLUTON, LABRADOR

ABSTRACT

In the contact aureole of the Makhavinekh Lake Pluton (MLP), Labrador, garnet resorption caused redistribution of Lu and loss of Hf, creating spuriously young Lu-Hf garnet ages. Garnet grew during granulite-facies regional metamorphism at 1860-1850 Ma. At 1322 Ma, garnet rims were replaced by coronas of cordierite and orthopyroxene during contact metamorphism. Garnet-ilmenite Lu-Hf geochronology using bulk-garnet separates yields apparent ages that young from 1876 ± 21 Ma at 4025 m from the contact to 1396 ± 8 Ma at 450 m from the contact. Toward the contact, garnet crystals are progressively more resorbed. Concentrations of Lu measured by LA-ICPMS along radial traverses on central sections through relict garnets decrease gently away from the cores but rise steeply within 50-200 μm of the edges of the relics. Enrichments of Lu in rims of relict garnets demonstrate strong partitioning of Lu into garnet during resorption and modest intracrystalline diffusion. Hafnium distributions could not be measured, but considering the strong incompatibility of Hf with garnet, it is likely that nearly all Hf in resorbed portions of the garnets was lost from the crystals. Lu-Hf ages in the aureole are thus controlled predominantly by this retention of Lu and loss of Hf during garnet resorption.

This deduction was tested with a simple numerical model in which the partial retention of Lu and loss of Hf is tracked as a population of garnets is resorbed. Assuming a spherical geometry for garnet porphyroblasts, Rayleigh fractionation is used to approximate initial Lu zoning profiles ranging from flat to steeply decreasing toward garnet rims. The model simulates: (1) Lu-Hf decay for a specified period before resorption; (2) instantaneous resorption with retention of Lu and loss of Hf from the resorbed portion of the crystal; and (3) Lu-Hf decay during a specified period after resorption.

Several parameters influence the modeled age, but garnet resorption and Lu retention are the primary factors. When all other parameters are held constant, larger amounts of resorption and higher degrees of Lu retention produce younger apparent ages (false ages). Similarly, flatter initial Lu profiles yield younger apparent ages as a consequence of the larger proportion of Lu and Hf that resides in the outer portions of the porphyroblast. The difference between the apparent and actual ages is greater if the duration of the pre-resorption decay period is large relative to the post-resorption decay period. Larger crystals in a Gaussian crystal-size distribution (CSD) generally dominate the Lu-Hf budget and produce an older apparent age relative to the age of the mean crystal size. Compared to a symmetrical Gaussian CSD, positively skewed CSDs result in reduced resorption of large crystals and produce an older apparent age. Application of the model to the MLP aureole, positing growth at 1850 Ma and resorption at 1320 Ma, yields model ages that young from 1850 Ma to 1374 Ma toward the contact, in good agreement with the apparent ages determined from geochronology.

INTRODUCTION

Lu-Hf garnet geochronology can be an effective tool for linking pressure and temperature conditions with the timing of geological events (e.g., Duchene *et al.*, 1997; Blichert-Toft *et al.*, 1999; Philippot *et al.*, 2001; Anczkiewicz *et al.*, 2007; Kylander-Clark *et al.*, 2007; Lagos *et al.*, 2007). However, Lu-Hf garnet geochronology may be hindered by several obstacles. The factors that can cause the largest differences between the calculated age and the actual age of garnet crystallization are the presence of inherited Hf-bearing inclusions in garnet, uncertainties involved with the Lu-Hf garnet closure temperature, and, as described here, redistribution of Lu and Hf during garnet resorption.

If inclusions that are rich in Hf (e.g., zircon and rutile) and that did not achieve isotopic equilibrium with garnet during crystallization are dissolved with garnet during chemical separation, they will alter the ^{176}Hf/^{177}Hf and ^{176}Lu/^{177}Hf ratios (DeWolf *et al.*, 1996; Scherer *et al.*, 2000; Blichert-Toft & Frei, 2001), unless steps are taken during garnet dissolution to avert such contamination (DeWolf *et al.*, 1996; Connelly, 2006; Lagos *et al.*, 2007).

Analyses of garnets that experienced temperatures characteristic of granulite- and eclogite-facies conditions (>600-700 ºC) must account for cooling rate and closure temperature to place accurate boundaries on the timing of garnet growth. Estimates for the closure temperature of the Lu-Hf system in garnet lie in the range of 540-900 ºC for the slow cooling rates common for regional metamorphism, although consensus is building for a closure temperature in the range of 750-900 ºC (Scherer *et al.*, 2000; Anczkiewicz *et al.*, 2007; Kylander-Clark *et al.*, 2007; Lagos *et al.*, 2007). In fact, the closure temperatures for Lu and Hf in garnet appear to be significantly different from one another, which introduces complications for interpreting ages in slowly cooled terranes (Ganguly *et al.*, 2010).

In this study of garnets from the aureole of the Makhavinekh Lake Pluton (MLP) in Labrador, an additional important effect is apparent, namely the impact on Lu-Hf ages of partial resorption of garnet at high temperature. Such resorption is shown here to produce spuriously young ages, in a pattern that closely mimics the effects expected from partial resetting by heating in the contact aureole. Instead, these young apparent ages (false ages) are attributed to partitioning back into the relict crystal of some of the Lu liberated by resorption, combined with the loss of Hf from resorbed portions of the crystal into the matrix. The relative importance of factors that can influence the apparent age are investigated in a simple numerical model. Application of this model to the rocks of the MLP aureole generates apparent ages that agree well with apparent ages determined from Lu-Hf garnet-ilmenite geochronology.

GEOLOGIC SETTING AND SAMPLE DESCRIPTIONS

In northern Labrador, accretion of the Nain Province to the Rae (Churchill) Province during the Torngat Orogeny (Fig. 6-1) buried graphitic, shaley sandstone to granulite-facies conditions (850 ºC and 0.6-0.9 GPa), producing the Tasiuyak gneiss (Bertrand *et al.*, 1993; Theriault & Ermanovics, 1997). Garnet growth at peak

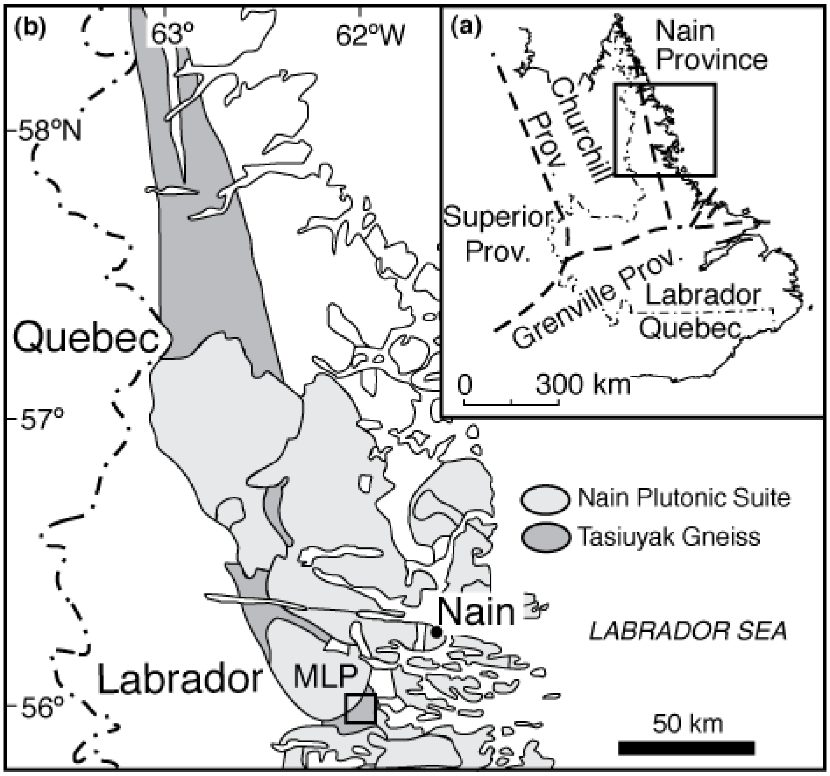

Figure 6-1. Location of the Tasiuyak gneiss and the Makhavinekh Lake Pluton (MLP). (a) The field area is within the Nain Province in northern Labrador. (b) The Tasiuyak gneiss underwent regional metamorphism to granulite-facies conditions during the Torngat Orogeny (1860-1850 Ma) and experienced contact metamorphism in the vicinity of the MLP at 1322 ± 1 Ma (Lee, 1987; Bertrand *et al.*, 1993; McFarlane *et al.*, 2005). The area of Fig. 6-2 is boxed. Modified from McFarlane *et al.* (2003).

temperatures was accompanied by pervasive partial melting at 1860-1850 Ma (Lee, 1987; Bertrand *et al.*, 1993). Movement along the Abloviak shear zone produced a mylonitic fabric starting at about 1844 Ma, and unroofing began at 1794-1786 Ma (Bertrand *et al.*, 1993; Van Kranendonk *et al.*, 1993; Connelly, 2001), suggesting that granulite-facies conditions may have persisted for 50-60 Myr The MLP intruded the Tasiuyak gneiss at 1322 ± 1 Ma (McFarlane *et al.*, 2005) and produced a 5-6 km wide contact aureole (Fig. 6-2) that reached peak temperatures in the range of 700-900 ºC (McFarlane *et al.*, 2003) at ~0.53 GPa (Carlson, 2006).

The Tasiuyak gneiss is composed of alternating melanosomes (garnet + sillimanite + biotite + K-feldspar + quartz + ilmenite + rutile) and leucosomes (quartz + plagioclase + K-feldspar + ilmenite + rutile). In thin section, most garnets are irregular in shape, and outside of the thermal aureole, 5-6 km from the contact with the MLP, garnets are not resorbed (Fig. 6-3). Garnets within the aureole, however, are surrounded by coronas of orthopyroxene + cordierite ± plagioclase ± spinel that are progressively thicker toward the contact, and garnets are completely resorbed within about 450 m of the contact (Fig. 6-4). More complete descriptions of the coronas and the reactions that produced them can be found in McFarlane *et al.* (2003) and in Carlson (2010).

Samples of garnetiferous gneiss were collected by McFarlane *et al*. (2003) along a radial transect perpendicular to the contact with the pluton (Fig. 6-2). For geochronology, five of these samples were chosen that span the range of resorption effects, at distances of 450, 1015, 2025, 3125, and 4025 m from the contact.

LU DISTRIBUTIONS IN RELICT GARNETS

The intracrystalline distribution of Lu within garnet porphyroblasts holds vital clues to understanding the origin of variations in Lu-Hf ages within the MLP aureole. Concentrations of Lu in the interiors of relict garnet crystals in the MLP aureole decrease slightly from the cores outward, but increase steeply across the outermost 50-200 μm of the rims. These rim gradients are attributed to inward intracrystalline

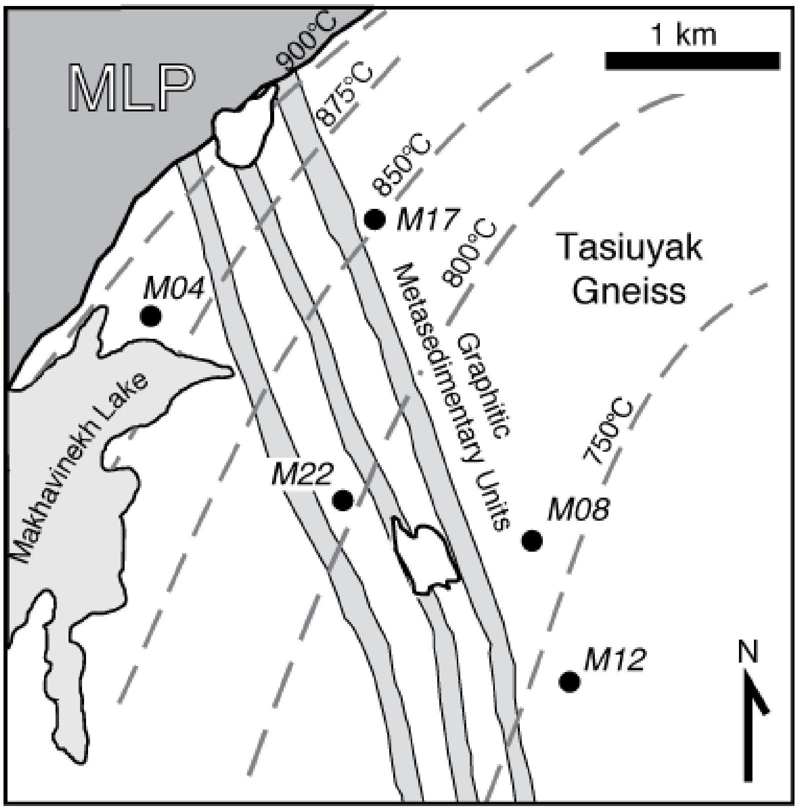

Figure 6-2. Simplified map of the aureole of the MLP at the south-eastern boundary. Sample locations and contours of peak contact-metamorphic temperatures are shown. Graphitic metasedimentary units show the trace of bedding within the aureole. Modified from McFarlane *et al*. (2005).

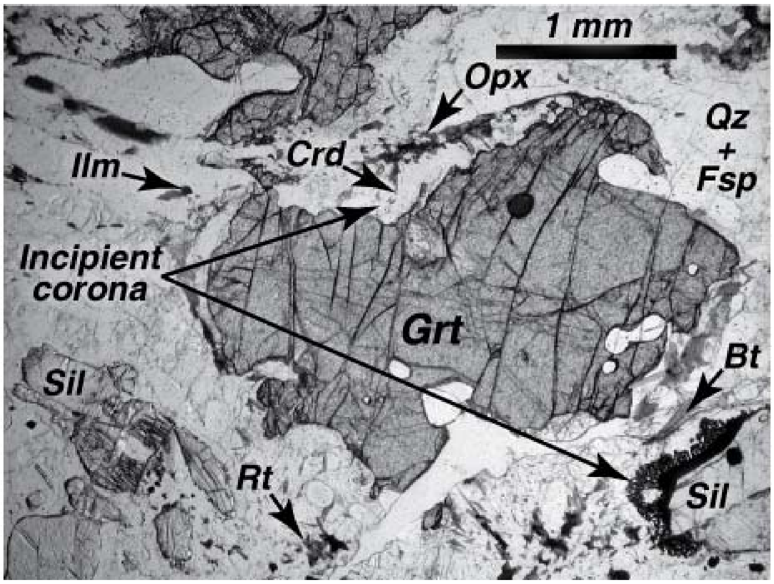

Figure 6-3. Photomicrograph of Tasiuyak gneiss in plane-polarized light. This sample (T03B) was collected 5750 m from the contact and shows incipient corona development on garnet and sillimanite. Garnet is typically irregular in shape in these rocks. Abbreviations after Whitney and Evans (2010).

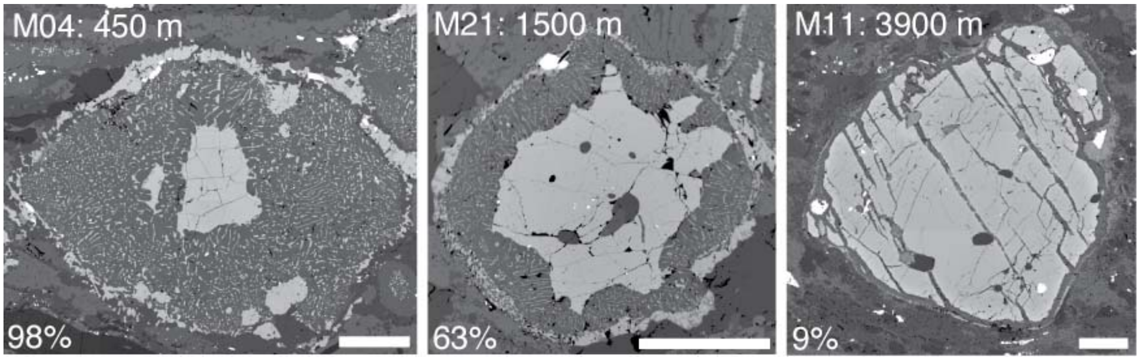

Figure 6-4. Backscattered electron images showing progressive garnet resorption. The distance from the contact with the MLP is given in meters, and the amount of garnet resorption is given in volume percent. Relatively spherical garnets were carefully located by X-ray computed tomography and centrally sectioned for measurements of Lu concentrations and radius. Radial measurements were used to estimate resorption amounts. Scale bars are one millimeter in length.

diffusion of Lu in response to progressive re-partitioning of Lu back into garnet during resorption reactions.

Analytical methods

Concentrations and zoning of rare-earth elements (REEs) in relict garnets were measured by laser-ablation quadrupole inductively-coupled plasma mass spectrometry (LA-ICPMS), on crystals sectioned precisely through their morphological centres as located by 3D imagery from high-resolution X-ray computed tomography. Measurements were made in continuous linear traverses from rim to core to rim, with the specimen translated beneath a stationary laser beam. Similar, but shorter, linear traverses of NIST SRM 612 were used for calibration.

REE analysis employed a 193-nm New Wave FX193 excimer laser system with a low-volume laminar-flow reaction cell (New Wave Supercell^{TM}) to minimize washout times, leading to improved spatial resolution. Ablation products were analyzed with an Agilent 7500ce quadrupole mass spectrometer. A pre-analysis pass using a 50-µm-diameter spot (10 Hz repetition rate, 10% laser power) at a translation rate of 25 $\mu m \cdot s^{-1}$ was followed by an analytical traverse using a 20-µm-diameter spot (15 Hz repetition rate, 40% laser power, irradiance 4.25 $GW \cdot cm^{-2}$, fluence 6.75 $J \cdot cm^{-2}$) at a translation rate of 5 $\mu m \cdot s^{-1}$. Dwell times were 10 ms for ^{157}Gd, ^{163}Dy, ^{166}Er, ^{169}Tm, and ^{172}Yb; 20 ms for ^{147}Sm, ^{159}Tb, ^{165}Ho, and ^{175}Lu; and 100 ms for ^{140}Ce, ^{146}Nd, and ^{153}Eu. In these analyses, ^{29}Si was used as the internal standard for calculation of ablation-volume corrections; ^{90}Zr, ^{137}Ba, and ^{140}Ce were measured to reveal inadvertent ablation of inclusions; and ^{89}Y was determined for verification of the deconvolution procedure described below.

Concentrations of Ce and Eu fell below detection limits for LA-ICPMS and Sm and Nd concentrations were only slightly above detection limits, but all other REEs were present at levels well above detection limits. Concentrations of Lu, the focus of this study, were reliably measured at levels of ~10-200 ppm. An attempt was also made to determine Hf distributions by monitoring the signal for ^{178}Hf, but concentrations were below detection limits.

Significant changes in concentration occur over short distances (50-200 μm) within garnet crystals, and abrupt discontinuities in concentration mark the boundary between garnet crystals and their surrounding matrix. As a result, the original concentration gradients, when measured by LA-ICPMS, are convolved to some degree with effects resulting from the 20-μm spot size, and from particle dispersion during transport from the sample chamber to the plasma. These effects spread the signal in time and distance along the traverse, although the impact is appreciable only at the two positions where sharp curvature is present in the concentration profile: approaching the outermost garnet rim and at the discontinuity represented by the edge of the crystal. A deconvolution procedure based on algorithms devised by Ganguly *et al*. (1988) for electron probe microanalysis (EPMA) removes this convolution artifact (Fig. 6-5). The procedure assumes a Gaussian distribution of the signal intensity as a function of distance from the spot's centre, thus specifying the relationship of the original concentration profile to the convolved measurements. Estimates of the actual concentration profile are convolved with the Gaussian point-spread function, then compared to the measured LA-ICPMS data and adjusted until a good visual fit is achieved that matches the convolved profile to the measurements. The width of the Gaussian function, which is comparable in size to the laser spot diameter, is treated as an adjustable parameter, but it is strongly constrained by how abruptly the signal falls off when the edge of the crystal is traversed. The accuracy of this deconvolution method can be tested, because concentrations of minor elements, such as Y, can be measured by both EPMA and LA-ICPMS. The results of deconvolution of the LA-ICPMS data for Y, for instance, can be compared to the Y measurements made at higher spatial resolution by EPMA, to verify the correctness of the procedure (Fig. 6-5b).

Because concentrations of LREEs were near or below formal detection limits for LA-ICPMS, supplementary data in the form of near-rim profiles for Nd, Sm and Eu were obtained via secondary ion mass spectrometry (SIMS) (Cameca IMS 6f, Arizona State University). A primary ion beam of $^{16}O^{-}$ (current 4-5 nA, nominal beam diameter 20 μm) was accelerated from the duoplasmatron source at -12.5 kV while the sample

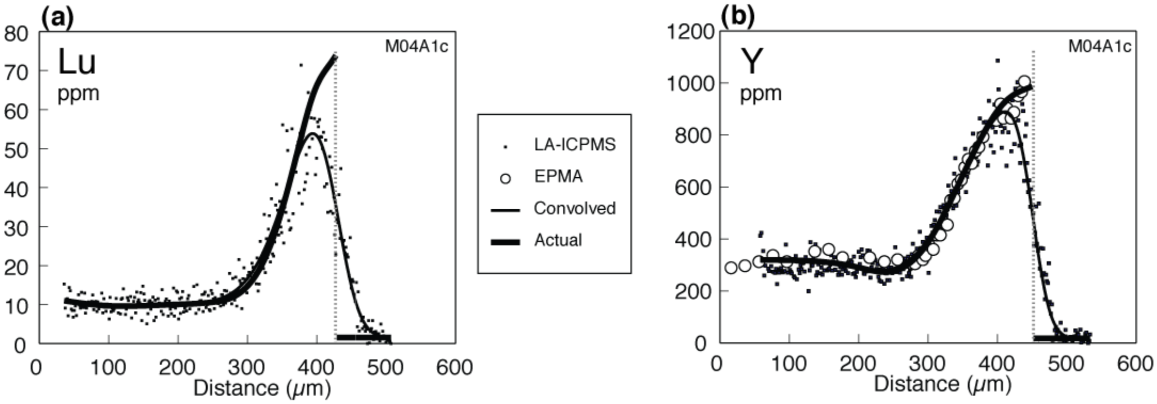

Figure 6-5. Examples of deconvolution procedure. Estimate of actual profile (*heavy line*) is convolved with Gaussian filter to produce convolved curve (*light line*); estimate is adjusted until convolved curve conforms to range of LA-ICPMS measurements (*dots*). Accuracy is verified by comparing results from deconvolution procedure (*heavy line*) with measurements made by EPMA (*open circles* in b) for minor elements (here, Y).

was held at +9 kV. Positive secondary ions were detected using an electron multiplier in pulse-counting mode. The mass spectrometer was operated at low mass resolution (M/ΔM ~300) and energy filtering was used to remove interfering molecular species (Shimizu *et al.*, 1978; Zinner & Crozaz, 1986). Sample voltage was offset by 75V from the peak secondary-ion signal and thus only those ions with 75 ± 20 eV excess kinetic energy entered the mass spectrometer. Each analysis consisted of a pre-sputter time of 420 s followed by 40 measurement cycles for ^{30}Si, ^{89}Y, ^{144}Nd, ^{147}Sm, and ^{151}Eu; analyses of Y were made for comparison with LA-ICPMS data, and all count rates were normalized to that for ^{30}Si. Errors indicated by the integrated signals for the REEs (and Y) were less than 5%. Calibration employed NIST SRM 612. SIMS data provided much higher precision, but were in good agreement with concentrations obtained by LA-ICPMS.

REE zoning in relict garnet

The REEs show only modest gradients in concentration in the interiors of relict garnet crystals: most profiles decrease gently from cores outward. Within 50-200 µm of the edges of relict garnet crystals, however, all REEs show steep gradients in concentration. REEs heavier than Eu (Gd through Lu) increase toward the rims of crystals, with progressively lighter REEs displaying progressively smaller relative increases, whereas REEs lighter than Gd (Eu, Sm, and Nd) decrease toward the rims of the crystals (Fig. 6-6). The distance from the crystal edge at which concentrations begin to increase or decrease sharply (the "penetration distance") is greater for more highly resorbed crystals in hotter portions of the contact aureole, as illustrated by the concentration profiles measured for Lu, shown in Fig. 6-7.

Origin of Lu zoning

The gently decreasing concentration profiles in the interior of relict garnet crystals are interpreted to be the result of preferential partitioning of REEs into garnet during prograde metamorphic growth, followed by strong modification by intracrystalline diffusion during subsequent residence in the deep crust, plus minor effects due to

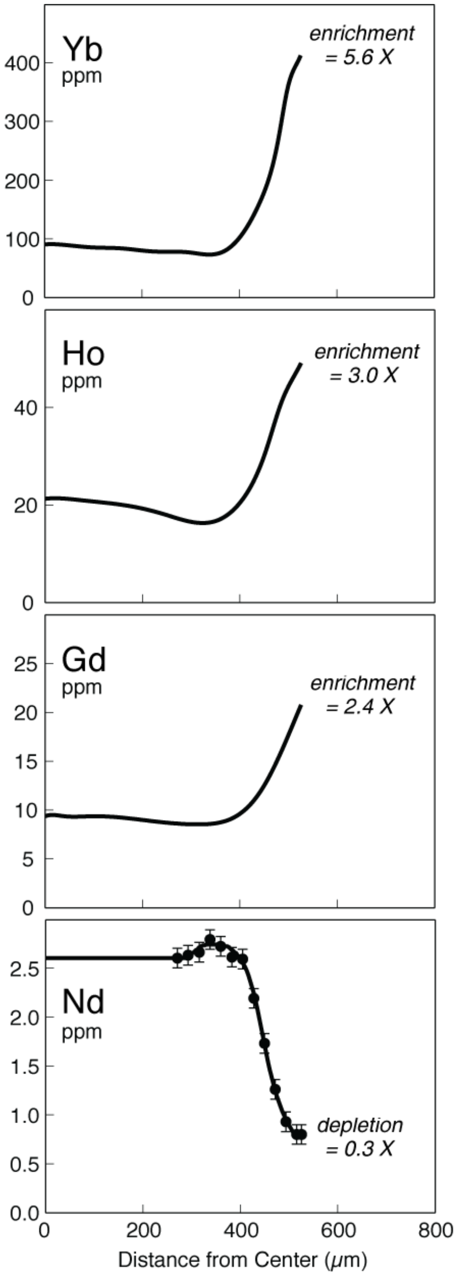

Figure 6-6. Core-to-rim profiles from deconvolution of LA-ICPMS measurements of selected REE in relict garnet in the aureole of the MLP (sample M04A1e, 450 m from contact). Profiles reflect partitioning of REEs between relict garnet and product assemblage of cordierite + orthopyroxene + monazite; thus enrichments at rims are greater for heavier REEs, and slopes reverse to yield decreases at rims for Eu, Sm, and Nd. Enrichments and depletions are given here as ratios of rim values to values at diffusional penetration depth. For Nd, plotted symbols are results of SIMS analyses, overlain on deconvolved LA-ICPMS profile. Note maximum in Nd profile produced by "uphill diffusion" of Nd, the result of appreciable coupling to inward diffusion of Y and HREEs; similar features appear in profiles for Sm and Eu.

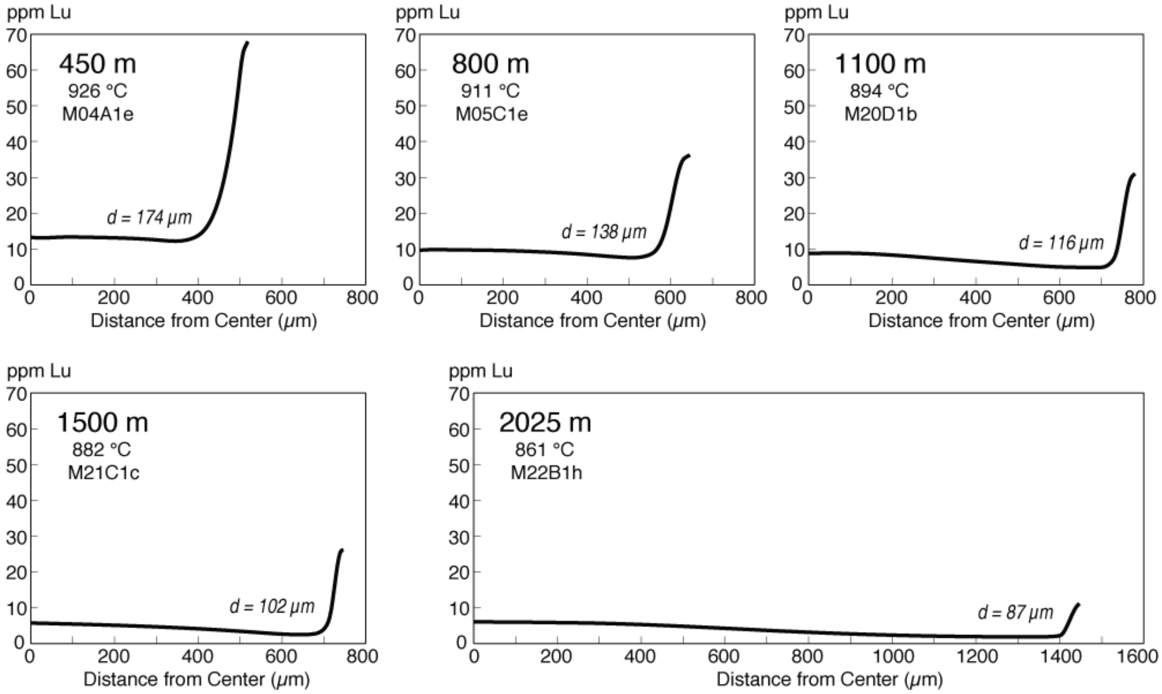

Figure 6-7. Core-to-rim profiles of Lu zoning in five relict garnets from the aureole of the MLP, with distances from contact and corresponding peak temperatures during resorption episode. Scaling is identical for all profiles. The depth *d* to which steep concentration gradients extend into the crystal is defined here as the distance from the rim of the relict crystal to the position of the minimum in the profile; *d* increases with proximity to the contact and with inferred peak temperatures, consistent with the origin of these gradients by inward diffusion of Lu during resorption.

reheating during contact metamorphism in crystals near the contact. REE partitioning among phases during garnet growth commonly results in strongly zoned profiles, with highly elevated core concentrations (Lapen *et al.*, 2003; Skora *et al.*, 2006; Kohn, 2009). These elevated core concentrations result from large partition coefficients between garnet and typical precursor phases: Kohn (2009), for example, estimated a fractionation factor for Lu of about 100 between garnet and whole-rock metapelitic assemblages that include biotite + muscovite + plagioclase + quartz ± kyanite ± rutile ± ilmenite. The strongly zoned Lu profiles typical of most growth zoning are unlike the relatively gentle gradients now present in the interiors of the relict garnets in the MLP aureole. As described above, garnet in the Tasiuyak gneiss formed during a deep-crustal (0.6-0.9 GPa) partial-melting event at temperatures near 850 °C (Lee, 1987), and may not have cooled substantially until uplift began some 65 Myr later (Van Kranendonk *et al.*, 1993). This protracted residence at very high temperature would have made possible the flattening of originally steep REE concentration profiles by intracrystalline diffusion. This interpretation is supported by the observation that interior gradients tend to be shallower in smaller crystals, the expected result of partial homogenization by diffusion, as illustrated for major elements at lower temperatures by Carlson and Schwarze (1997). (The Lu profiles in Fig. 6-7 show an apparently systematic decrease in core concentration for crystals progressively more distant from the contact, but this is merely coincidental; core concentrations depend on bulk-rock abundances and on the sizes of the crystals, as homogenization of larger crystals leads to greater dilution of initial core concentrations.).

The steep profiles for Lu near the edges of relict crystals (Fig. 6-7) are interpreted to be the result of strong preferential re-partitioning of Lu into the outermost rims of the crystals during resorption, accompanied by appreciable but limited inward diffusion. Uptake of Lu into garnet during resorption is expected on the basis of large partition coefficients relative to cordierite + orthopyroxene + accessory monazite, the coronal minerals that are the products of resorption. For garnet vs. cordierite, extrapolation of the data of Otamendi *et al*. (2002) on measured partition coefficients as a function of ionic radius implies a value of 300-400; those data (Table 6-1) are for Dy, Y, Er, and Yb in garnet vs. cordierite + plagioclase + quartz. For garnet vs. orthopyroxene, the partitioning measured by Carlson *et al.* (2007) at comparable temperatures but higher pressures implies a value close to 100 (cf. Burgess & Harte, 2004). In this respect, Lu is behaving similarly to Y and Mn — two other elements with a strong affinity for garnet — that commonly develop annuli of high concentrations in the rims of relict crystals: these compatible elements, when freed from portions of the crystal that are consumed, back-diffuse into the relict garnet (Lanzirotti, 1995; Pyle & Spear, 1999; Carlson, 2002; Kohn & Malloy, 2004; Kohn, 2009). A similar interpretation for the high-Lu rims in garnets of the MLP aureole is supported by: (1) the pattern of more pronounced increases at rims for heavier REEs, coupled with the reversal of profile slopes to yield decreases at rims for REEs lighter than Gd, demonstrating the role of partitioning of REEs between the reacting garnet and the product cordierite + orthopyroxene + monazite (Fig. 6-6); (2) the greater penetration distances observed for crystals in hotter portions of the aureole, demonstrating the role of diffusion in redistributing Lu inward toward the interior portions of the garnet crystals (Fig. 6-7); and (3) the ability of numerical models of intracrystalline diffusion to replicate the shapes of the profiles (Fig. 6-8).

Material-balance calculations

Important to interpretation of Lu-Hf ages in the MLP aureole are estimates of the amounts of Lu retained within garnet crystals versus the amounts lost to the surrounding matrix during partial resorption. The fraction of Lu that is retained will depend on several factors. Two of the most influential factors are the equilibrium partition coefficients for Lu between garnet and cordierite and between garnet and orthopyroxene, which are large at the temperatures of resorption, as described above. Such large values would imply a high degree of Lu retention in garnet if equilibrium were to be achieved, but the material re-partitioning into the garnet at its outer surface can only be retained to the extent that it is able to diffuse into the interior of the crystal, which limits the degree to which the actual bulk distribution approaches equilibrium partitioning. Consequently, the temperature at which resorption occurs becomes a third

Table 6-1. Effective ionic radius and partition coefficients for elements in garnet.

Element	[a]Effective Ionic Radius in VIII-fold Coordination (Å)	Charge	[b]$\beta^{Grt/matrix}$
Hf	0.830	4+	-
Mg	0.890	2+	-
Lu	0.977	3+	-
Yb	0.985	3+	265
Er	1.004	3+	146
Y	1.019	3+	80
Dy	1.027	3+	54
Ca	1.120	2+	-

[a] Shannon (1976)

[b] Otamendi *et al*. (2002)

matrix = quartz + plagioclase + cordierite

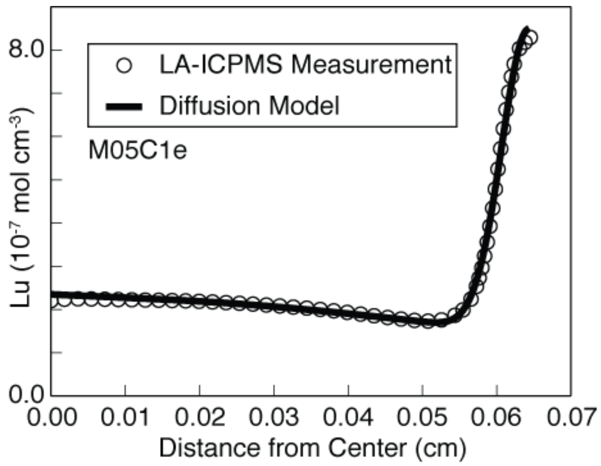

Figure 6-8. Comparison of measured Lu concentrations (*open circles*) with calculated diffusion profile (*solid line*), generated using the modelling approach and thermal histories described in Carlson (2006). Close correspondence supports interpretation of Lu retention due to re-partitioning and inward intracrystalline diffusion of Lu into garnet during resorption reactions.

important factor, because it controls the distance within the relict crystal over which Lu can diffuse.

An attempt was made to determine the proportions of Lu retained during resorption reactions in the MLP aureole from a simple material balance that compares the total amount of Lu found in the relict crystal with an estimate of the amount originally present in the crystal before resorption. The Lu initially present can be estimated by assuming spherical symmetry and extrapolating the gently sloping Lu profiles present in the interiors of relict crystals out to the radii of the original crystals, which lie at a position in each corona nearly coincident with the boundary between the inner cordierite + orthopyroxene layer and the outer orthopyroxene ± plagioclase layer (Carlson, 2010). The results of these calculations, however, turned out to be subject to very large uncertainties because the estimates of prior concentrations in now-vanished garnet, based on outward extrapolations of interior compositions, cannot be adequately constrained.

LU-HF GARNET GEOCHRONOLOGY

Mineral separates used in this work were derived from the study reported in McFarlane *et al.* (2006), in which minerals were separated by standard techniques (Wilfley table, sieving, Franz magnetic separator, and heavy liquids). Garnet, ilmenite, and rutile fractions were handpicked to a purity of >99% using a binocular microscope. Garnet separates sealed in evacuated silica glass ampoules were annealed in a furnace at 1000 °C for 48 hours prior to dissolution in HCl plus a minor amount of HF, to minimize or eliminate the incorporation of Hf from zircon inclusions within the garnet porphyroblasts, according to methods outlined by Connelly (2006). Purification of Lu and Hf from garnet, ilmenite, and rutile utilized a first-stage cation column and a second-stage TODGA (Eichrom Industries) following the methods outlined in Connelly *et al.* (2006). Lutetium and Hf were analyzed using two different multi-collector inductively coupled plasma mass spectrometers: garnet was analyzed on an Axiom at Copenhagen University, whereas ilmenite and rutile were analyzed on a Micromass Isoprobe at The University of Texas at Austin. Data were reduced using in-house programs according to the protocol outlined in Connelly *et al*. (2006). The results of running standards BHVO-1 and BCR-2 at Copenhagen University and The University of Texas at Austin during the course of this study are summarized in Connelly *et al*. (2006). We use the reproducibility of these standards as an estimate of the errors for the ^{176}Lu/^{177}Hf analyses in this study because of the dependence of this variable on unquantified weighing errors of our unmixed spike. These errors, combined with internal errors from the Hf isotopic analyses, provide uncertainties for the ages (Table 6-2).

Both ilmenite and rutile crystallized with garnet during the regional metamorphic event, but the contact event promoted additional ilmenite growth. All samples contain abundant ilmenite, but only three samples contain rutile in sufficient quantities for isotopic analysis. Therefore, we processed the three rutile separates along with the ilmenite separates to monitor the influence of the second ilmenite growth event on the overall ilmenite isotopic ratios. The differences between the ilmenite and rutile are within the stated errors and thus insignificant in the age determinations, especially in the context of this study. As ilmenite was present in all samples, the ages discussed below were determined from garnet-ilmenite pairs. Using the decay constant of Söderlund *et al*. (2004), the ages range from 1876 ± 21 Ma to 1396 ± 8 Ma toward the pluton (Table 6-2). The trend of decreasing ages toward the pluton is illustrated by the trend of decreasing slopes of the two-point “isochrons” (Fig. 6-9).

REDISTRIBUTION OF LU AND HF DURING GARNET RESORPTION

It is tempting to ascribe the age progression within the MLP aureole documented above to partial resetting caused by heating during contact metamorphism. However, resetting can be complicated, especially in the Lu-Hf system where the diffusivity of Lu is one to two orders of magnitude higher than that of Hf at the temperatures of the MLP aureole (Kohn, 2009; Ganguly *et al.*, 2010). As described above, the garnets from the MLP aureole show evidence for significant Lu intracrystalline diffusion. In contrast, much slower Hf intracrystalline diffusion, owing to its high charge, combined with the rapid initial cooling rates in the aureole (>10 °C Myr^{-1}) (Carlson, 2006) would not

Table 6-2. Apparent ages from Lu-Hf geochronology.

Sample/ Mineral	Lu (ppm)	Hf (ppm)	Weight (g)	$^{176}Lu/^{177}Hf$	Error (%)	$^{176}Hf/^{177}Hf$	Error (%)	Age (Ma)
M04: 450 m								
garnet	14.480	0.680	0.0538	3.00469	0.33	0.360426	0.0120	
ilmenite	0.899	8.938	0.0151	0.01429	0.50	0.281470	0.0040	1396 ± 8
M17: 1015 m								
garnet	2.674	0.872	0.0600	0.43526	0.33	0.295767	0.0019	
ilmenite	0.095	21.904	0.0110	0.00061	0.50	0.281419	0.0080	1740 ± 29
M22: 2025 m								
garnet	3.129	0.901	0.0930	0.49218	0.33	0.297668	0.0022	
rutile	0.011	98.038	0.0147	0.000016	0.50	0.281022	0.0021	1782 ± 9
ilmenite	0.132	26.289	0.0099	0.00071	0.50	0.281213	0.0018	1764 ± 25
M08: 3125 m								
garnet	2.766	0.786	0.0650	0.49985	0.33	0.298113	0.0024	
rutile	0.020	92.188	0.0161	0.000031	0.50	0.281041	0.0060	1799 ± 10
ilmenite	0.110	26.106	0.0085	0.00060	0.50	0.281311	0.0016	1773 ± 25
M12: 4025 m								
garnet	3.810	0.823	0.0560	0.65765	0.33	0.304707	0.0030	
rutile	0.035	89.554	0.0052	0.000055	0.50	0.281315	0.0025	1872 ± 9
ilmenite	0.094	50.088	0.0068	0.00027	0.50	0.281275	0.0016	1876 ± 21

$^{176}Hf/^{177}Hf$ errors are internal and $^{176}Lu/^{177}Hf$ errors are estimated from standard reproducibility.
Errors are two standard deviations.
Ages were calculated using the decay constant of Söderlund *et al*. (2004).

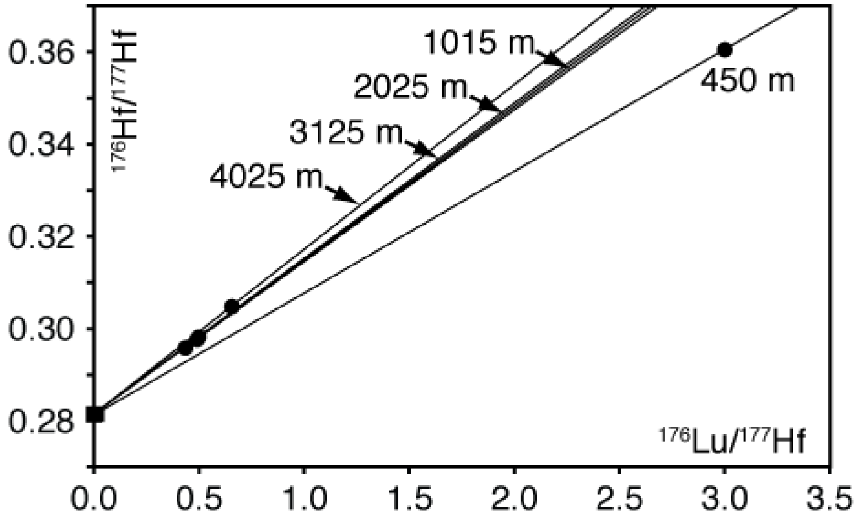

Figure 6-9. Garnet-ilmenite two-point Lu-Hf "isochrons" for the MLP samples. Labels are sampling distances from the contact with the pluton. Circles represent ratios determined from garnet, and squares represent ratios determined from ilmenite.

permit significant Hf diffusion at these temperatures (Ganguly *et al.*, 2010). In addition to differences in closure temperature, resetting is complicated by the different partitioning behaviors of Lu and Hf between garnet and matrix phases.

As already noted, Lu partitions strongly into relict garnet during resorption, rather than into product cordierite and orthopyroxene. At the temperatures that affected the MLP aureole, the diffusivity of Lu in garnet is sufficient to convey appreciable amounts of Lu from the surface of the garnet crystals into their outer rims, at a rate faster than the rate of garnet dissolution, resulting in partial retention of Lu during resorption (Fig. 6-7).

In strong contrast, Hf overwhelmingly prefers zircon over garnet, as demonstrated by Rubatto (2002), who measured HREE concentrations in zircon and garnet equilibrated at *P-T* conditions similar to those in the current study, and calculated garnet/zircon Hf partition coefficients that fall in the range $10^{-6} – 10^{-5}$. In our samples from the MLP aureole, thin overgrowths of new zircon on earlier crystals lie within the symplectitic coronal rims of garnets (McFarlane *et al.*, 2006, p. 141), demonstrating the availability of a local sink for Hf liberated along with Zr during garnet resorption. This incompatibility of Hf in garnet, especially in the presence of zircon, combined with the expectation of extremely slow intracrystalline diffusion of Hf, suggests that Hf should not back-diffuse into relict garnet to an appreciable extent during resorption.

The net effect of these two very different behaviors for Lu and Hf is to produce a strong fractionation between the parent ^{176}Lu and the daughter ^{176}Hf during garnet resorption as predicted by Kohn (2009, p. 176) and illustrated in Fig. 6-10. The effect on Lu-Hf ages of this redistribution can be evaluated by numerical modelling of the isotopic evolution of a Lu-Hf system in which normal decay processes are interrupted by an episode of garnet resorption.

RESORPTION MODELING

To produce deeper understanding of the geochronological effects of Lu-Hf partitioning during garnet resorption, a simple numerical model of the process was

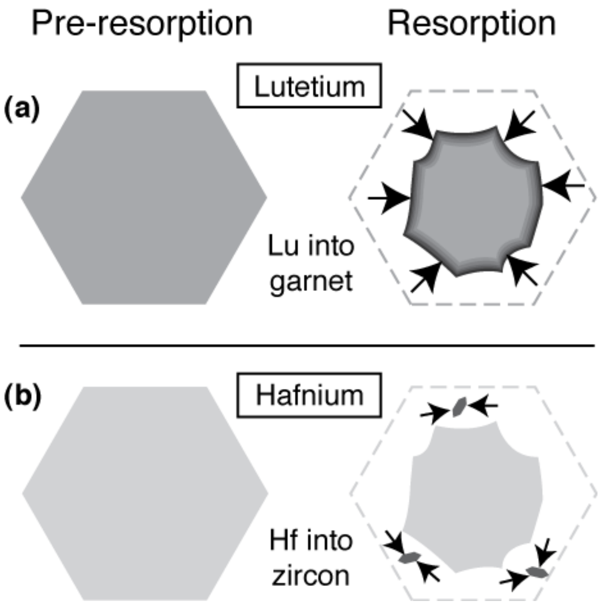

Figure 6-10. Illustration of Lu and Hf redistribution during garnet resorption. Darker shading indicates higher relative concentration. Partitioning of Lu into garnet retains some Lu (a), but Hf is lost because of strong partitioning into matrix phases like zircon (b). The net effect is an increase in the ^{176}Lu/^{177}Hf ratio in the relict garnet. The ^{176}Hf/^{177}Hf ratio in the relict garnet is unchanged.

developed to assess the relative importance of factors that impact the apparent ages. The model assumes a spherical geometry for the garnet porphyroblasts, and their initial Lu concentration profiles are specified using a Rayleigh fractionation scheme (Hollister, 1966) in which

$$\mathrm{C^{Grt}} = \beta\left(\mathrm{C^{Rock}}\right)\left(1 - \frac{\mathrm{W^{Grt}}}{\mathrm{W^{Rock}}}\right)^{\beta-1}, \tag{6-1}$$

where C is concentration, β is the fractionation factor, W^{Grt} is the mass of crystallized garnet, and W^{Rock} is the mass of the original rock. Adjustment of β produces profiles that range from flat to steeply zoned with decreasing concentrations toward the garnet rim (bell shaped). Production of daughter ^{176}Hf from the initial concentration of ^{176}Lu is calculated from the standard exponential decay relation

$$^{176}\mathrm{Hf} = {}^{176}\mathrm{Lu}\left(1 - \mathrm{e}^{-\lambda t}\right) \tag{6-2}$$

in which λ = 1.867e-11 year^{-1} for ^{176}Lu decay (Söderlund *et al.*, 2004), and t is time. The model simulates the evolution of the Lu-Hf isotopic system subjected to garnet resorption in a series of three steps (Fig. 6-11): (1) Over an interval of duration t_1, between crystallization (regional metamorphism) and resorption (contact metamorphism), ^{176}Lu decays to ^{176}Hf and both remain in the garnet. (2) The garnet rim is instantaneously resorbed and a fraction of the ^{176}Lu liberated from the resorbed portion of the crystal is retained by partitioning into the rim of the relict garnet, while ^{176}Hf liberated from the resorbed portion of the crystal is incorporated into matrix phases. (3) The remaining ^{176}Lu in the relict garnet decays from the time of resorption until the present, over an interval of duration t_2.

The effects of such an evolution on the apparent age of the garnet population are illustrated in a schematic isochron plot that follows the progression of the Lu-Hf system in the relict portion of a garnet (Fig. 6-12). In the first period of isotopic decay (1), the slope of the isochron increases normally as ^{176}Lu decays to ^{176}Hf, decreasing the ^{176}Lu/^{177}Hf ratio and increasing the ^{176}Hf/^{177}Hf ratio. Resorption (2) causes an increase in ^{176}Lu/^{177}Hf in the relict garnet, as Lu is partially retained. The amount of Lu retained is variable, depending upon the strength of the partitioning and effectiveness of

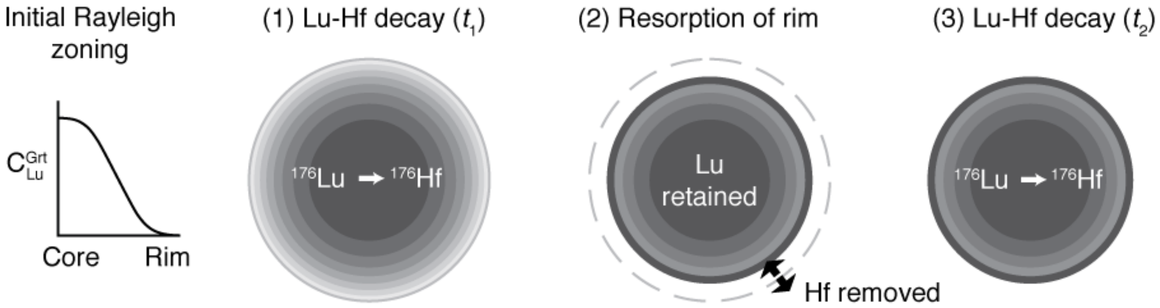

Figure 6-11. Illustration of numerical model. Darker shading indicates higher relative concentration. The model assumes a spherical geometry for garnet and tracks the quantities of Lu and Hf in discrete shells of equal volume. The initial distribution of Lu in garnet can be uniform or concentrated in the core using a Rayleigh fractionation expression. (1) The initial ^{176}Lu decays to ^{176}Hf for a specified duration (t_1). (2) A specified proportion of the garnet rim is instantaneously resorbed, and a fraction of the Lu from the resorbed portion is partitioned into the relict garnet (retention). All Hf from the resorbed rim is removed. (3) The remaining ^{176}Lu in the relict garnet plus the ^{176}Lu retained decays to ^{176}Hf for a specified duration (t_2).

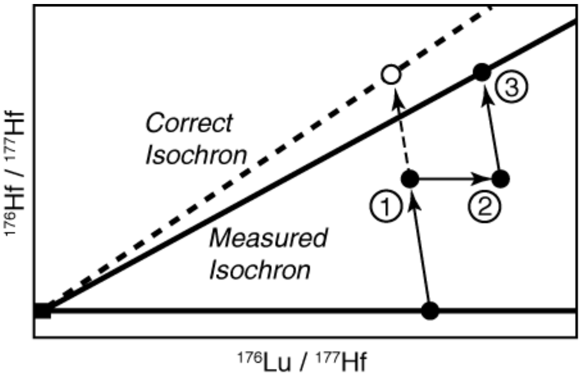

Figure 6-12. Schematic isochron plot illustrating the evolution of the measured isochron. For an unresorbed garnet, the correct isochron would result from decay following the dashed arrow. In the relict portion of a resorbed garnet from the MLP aureole, the measured isochron is the result of (1) isotopic decay before resorption; (2) resorption producing an increase in ^{176}Lu by retaining some of the Lu from the resorbed rim; and (3) further decay after resorption. The measured isochron has a shallower slope than the isochron for an undisturbed system (correct isochron), and produces an apparent age younger than the actual age.

intracrystalline diffusion, as described above. All Hf is presumed to leave the resorbed portion of the garnet, and the ^{176}Hf/^{177}Hf ratio in the relict portion of the garnet is unaffected. After resorption, continued isotopic decay (3) produces a steeper slope for the model isochron. The resulting measured isochron has a shallower slope than the correct isochron, so the apparent age is younger than the actual age.

Sensitivity analysis

To determine how each of the factors identified above influences the apparent age of a population of partially resorbed garnets, simulations were run that examined the impacts of variations in each of them, holding the others fixed. The reference state to which all comparisons are made is the case of a population of garnets with a uniform size, with initially homogeneous (unzoned) distributions of Lu, in which 100% of the Lu released by resorption is retained in the relict crystal, and for which the pre-resorption decay period is half the length of the post-resorption decay period. Each of the following factors was varied in turn: (1) the volume percent of garnet resorption; (2) the degree of retention of Lu; (3) the initial Lu zoning pattern; (4) the relative magnitudes of the isotopic decay periods before and after resorption; and (5) crystal size.

Case 1: Variable amount of resorption

Resorption of garnet is the fundamental reason for changes in the Lu/Hf ratio in this model, because it causes excess Lu to accumulate in the relict garnet while Hf from the resorbed rim is lost to the matrix. Figure 6-13 illustrates the effect of resorption on apparent age. The fractional age (defined as the ratio of the actual age to the measured apparent age) is calculated as a function of the volume percent of resorption, and is contoured to show the effect of varying the amount of Lu retained from the resorbed garnet. In Case 1, the discussion focuses on the case in which all Lu is retained, the contour labeled "Retention factor = 1.0".

As the crystals undergo progressively greater resorption, the Lu/Hf ratio in the relict garnet is driven to values progressively higher than the ratio produced during the pre-resorption decay period (t_1), increasing the difference between the actual age and

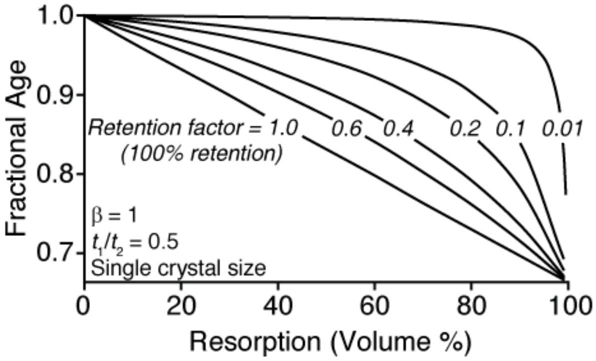

Figure 6-13. Effect of variable Lu retention on fractional age. Retention is the fraction of Lu partitioned into the relict garnet from the resorbed rim. Fractional age is defined as the ratio of the apparent age to the actual age. If all Lu and Hf is lost to the matrix from the resorbed rim, there will be no change in the ^{176}Lu/^{176}Hf ratio in the relict garnet. If some Lu is retained in the relict garnet, the ^{176}Lu/^{176}Hf ratio increases and the apparent age will become younger. Modeled contours of retention during garnet resorption demonstrate that more efficient retention of Lu in the relict garnet produces larger differences in the actual and apparent ages.

the apparent age. If all Lu is retained, the fractional age changes linearly with the volume fraction of resorption and approaches the age t_2. At the very latest stages of reaction (>99% resorption), when the crystal size becomes too small to house Lu and Hf, the age is meaningless.

If one considers the condition of 100% resorption, it might seem that the apparent age of the sample should approach zero as the resorption amount approaches 100%, but in fact, the age approaches t_2. Assuming only that the relict crystal is large enough to house the small amount of Lu retained from the resorbed rim, even for values of resorption approaching 100%, ^{176}Lu in the relict garnet will decay after resorption producing a ^{176}Lu/^{176}Hf ratio representative of the period t_2. Resorption removes from the garnet crystal the ^{176}Hf produced during t_1, so the apparent age of the sample approaches t_2 when resorption is very extensive.

Case 2: Variable retention of Lu

The effect of variable magnitudes of Lu retention on the apparent age, at all scales of resorption, is illustrated by the contours of retention in Fig. 6-13. A retention factor of 1.0 partitions 100% of the Lu from the resorbed portion of the crystal into the relict garnet; a value of 0.4 partitions only 40% into the relict garnet, and so forth. As noted above, the amount of Lu that is retained during resorption depends upon the extent of fractionation between garnet and the minerals that replace it (which determines the magnitude of the increase in concentration at the relict garnet rim), and upon the temperature at which resorption occurs (which determines the efficacy with which the Lu accumulated in the rim can be conveyed into the interior of the relict crystal). If appreciable amounts of Lu are to be retained in the relict garnet, the fractionation into the garnet must be great enough to produce a significant increase in the Lu concentration at the rim, and temperature must be high enough to ensure that the rate of intracrystalline diffusion of Lu into the garnet interior is greater than the rate at which garnet is consumed.

With smaller values of retention, less Lu is incorporated into the relict garnet and larger amounts of resorption are required to produce the same change in the apparent age. More efficient retention increases the Lu/Hf ratio and produces a younger apparent age for a given amount of resorption.

Case 3: Initial Lu zoning

In the model, variable fractionation of Lu into garnet during its original growth is governed by the value of β in Equation 1, as shown in Figs. 14a and 14b. If, as in Fig. 6-14a, the fractionation factor is small (e.g., $\beta = 1$), the initial profile is flat, so a large amount of Lu and Hf will be redistributed during resorption because a high proportion of these elements resides in the outermost rim. If, as in Fig. 6-14b, the fractionation factor is large (e.g., $\beta = 40$), the initial profile is steep, and the apparent age, after a given amount of resorption, is closer to the actual age because a smaller proportion of the Lu is redistributed and a smaller proportion of the Hf is lost from the garnet during resorption.

Figure 6-14c shows β contours illustrating the effect of initial growth zoning on apparent age for all levels of resorption. Flatter initial Lu profiles produce larger differences between the apparent and actual ages. More steeply zoned garnets require larger amounts of resorption to produce the same apparent age than more homogeneous garnets.

Case 4: Relative magnitudes of decay periods

The relative magnitudes of the pre-resorption decay period t_1 and the post-resorption decay period t_2 affect the apparent age because resorption modifies only the Lu/Hf ratio produced during t_1. If t_1 is large relative to t_2 (e.g., $t_1/t_2 = 2$), the contribution to the Lu/Hf ratio from the initial decay period is relatively large and resorption will more strongly influence the apparent age. In other words, if the resorption event occurs long after crystallization of garnet, the age is strongly affected. If the resorption event occurs shortly after crystallization of garnet, the age is weakly affected. Figure 6-15 shows decreasing fractional age for increasing values of t_1/t_2 at all levels of resorption.

Figure 6-14. Effect of initial Lu zoning on fractional age. The initial distribution of Lu in garnet and the effects of back-diffusion caused by resorption are illustrated for initially flat (a) and steep (b) Lu concentration profiles in garnet. Three Lu concentration profiles are shown in each plot: an initial profile (0% resorption) and two profiles demonstrating progressively larger amounts of resorption and back-diffusion into the relict garnet (20% and 80%). The shaded areas highlight the resorbed portions of the rims at 20% and 80% resorption, and the corresponding amount of Lu redistributed is indicated. For example, in the crystal with an initially flat Lu profile (a) that is resorbed by 20%, the amount of Lu redistributed from the resorbed rim is 20%. In the crystal with an initially steep Lu profile (b) that is resorbed by 20%, the amount of Lu redistributed from the resorbed rim is only 0.5%. Therefore, weak initial zoning can result in large redistributions of Lu even for small amounts of resorption, and in strongly zoned crystals, larger amounts of resorption are required to redistribute a significant amount of Lu. (c) Fractional age as a function of resorption amount, contoured for variable degrees of initial zoning (β), showing that crystals with flatter initial profiles yield larger differences between the actual and apparent ages.

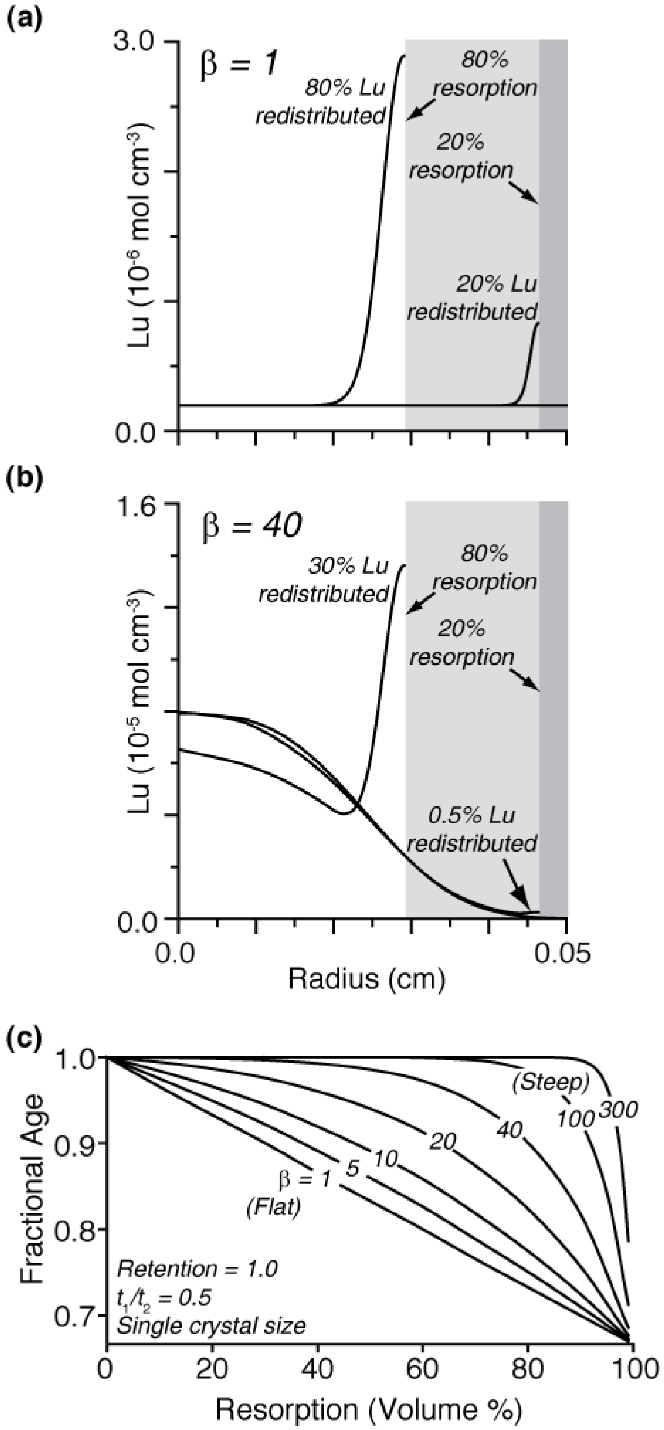
(a)
3.0
β = 1
80% Lu redistributed
80% resorption
20% resorption
20% Lu redistributed
Lu (10^{-6} mol cm^{-3})
0.0
(b)
1.6
β = 40
30% Lu redistributed
80% resorption
20% resorption
0.5% Lu redistributed
Lu (10^{-5} mol cm^{-3})
0.0
0.0
0.05
Radius (cm)
(c)
1.0
0.9
0.8
0.7
Fractional Age
(Steep)
100
300
40
20
10
5
β = 1
(Flat)
Retention = 1.0
t_1/t_2 = 0.5
Single crystal size
0
20
40
60
80
100
Resorption (Volume %)

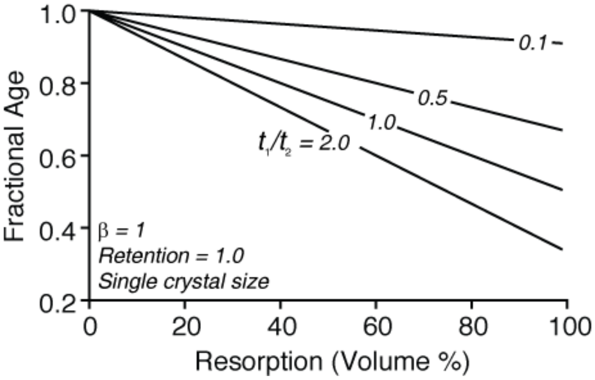

Figure 6-15. Effect of relative magnitudes of decay periods on fractional age. The change in fractional age as a function of resorption amount is contoured for the ratio of pre-resorption decay time to post-resorption decay time (t_1/t_2). Resorption changes the ^{176}Lu/^{176}Hf ratio generated during the first period of decay (t_1), so larger t_1/t_2 ratios result in larger differences between the apparent age and the actual age.

Case 5: Crystal size

Mechanisms limited by rates of intergranular diffusion typify many garnet-resorption reactions (e.g., Carlson, 2002), including those in the aureole of the MLP (McFarlane *et al.*, 2003; Carlson, 2010). When such diffusional controls operate, a garnet-consuming event will resorb an equal volume (or mass) from each garnet crystal, which means that small garnets will experience a greater *percentage* of volume reduction than larger crystals. Thus crystal size, and crystal size distributions (CSDs), will have an impact on the apparent age of a partially resorbed garnet population. In this section, the effects of crystal size are considered by examining the changes in apparent age for populations of garnets of uniform size, populations of garnets with Gaussian CSDs of variable dispersion that are symmetrical about their mean size, and populations of garnets whose CSDs are near-Gaussian, but asymmetrical (skewed).

If two populations of garnet crystals, each with a single uniform size but one larger than the other, are subjected to the same garnet-consuming event, the percentage of resorption for each crystal will be greater in the population with the smaller size. Consequently, as already illustrated above in Fig. 6-13, the effect on apparent age will be more pronounced in the smaller population.

Extending this idea to populations that contain crystals of variable size, smaller crystals would undergo a greater percentage of volume reduction than larger ones, so the effects on ages (from unbiased bulk-garnet separates) of a resorption event will depend upon the details of the population's CSD. Figure 6-16 compares — in parts a-c — three symmetrical CSDs, ranging in dispersion from wide to narrow, and — in parts d-f — one symmetrical and two asymmetrical CSDs, one with positive skewness and one with negative skewness, all with a wide dispersion of sizes. In the widely dispersed CSDs, the largest crystals are about twice the mean crystal size, which is common in natural samples (Carlson, 1999). Each population contains the same initial total volume of garnet and has been resorbed by similar amounts (43-50% of the total garnet volume) by removing an equal volume from each crystal within a population; the volume percent resorbed for each category of crystal size is indicated in the inset. Smaller crystals are

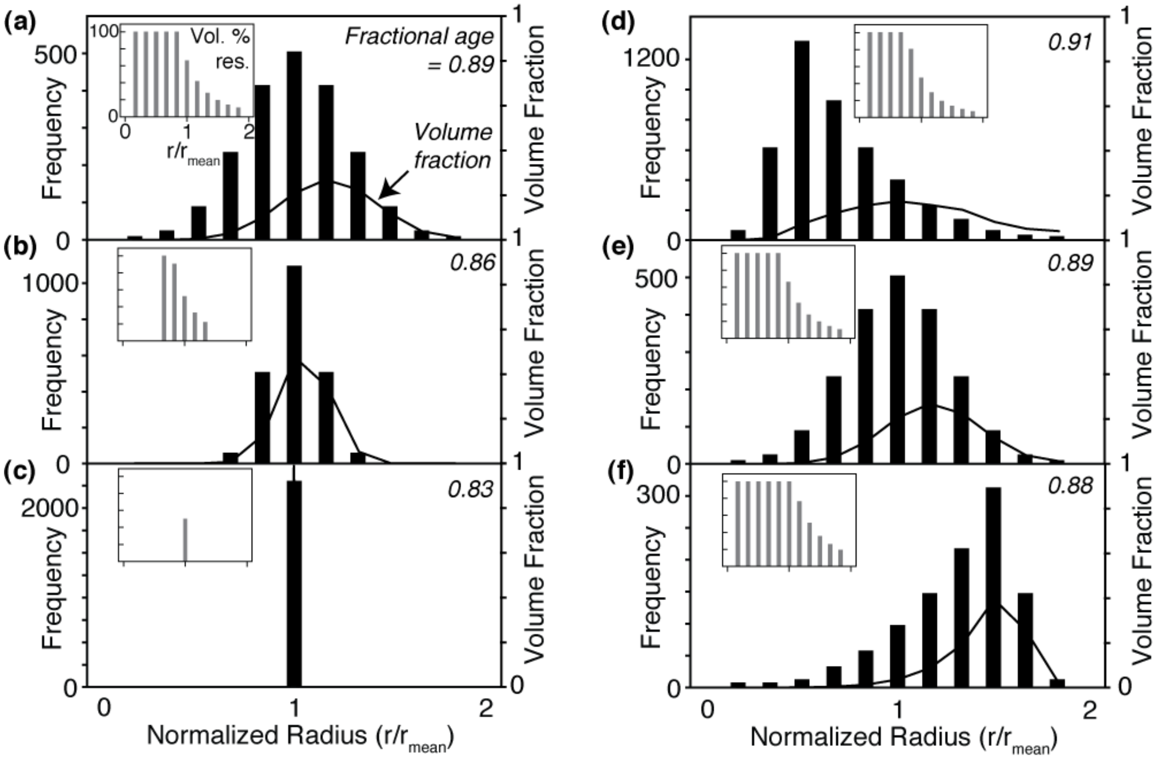

Figure 6-16. Effects of CSDs on fractional age. Fractional ages are shown in top right corner of each panel. Histograms are CSDs before resorption occurs in each population. Continuous black curves show volume fraction of garnet in the population. Insets show resorption amount for each crystal size. The resorption amount for the crystals in each population was adjusted to maintain a nearly constant total volume decrease for the resorption event. Because of their small volume, the smallest crystals are commonly resorbed entirely when the total amount of resorption is as high as that shown here (43-50% by volume). (a-c) Gaussian distributions of variable width showing decreasing apparent age with decreasing distribution width. The age of a population of garnets is strongly influenced by the crystal sizes that account for the bulk of the population, so a population with a wider CSD has an apparent age that is older because of larger crystals that were less resorbed. (d-f) Variable skewness showing decreasing age with shift toward negative skewness. As the skewness changes from positive (d) to negative (f), the volume-percent resorption of the larger crystals increases, and the number of smaller crystal sizes that are completely resorbed increases. This shift toward mostly large crystals that are increasingly resorbed decreases the apparent age of the population.

commonly completely resorbed, so resulting ages depend largely on the resorption of the larger crystals.

Comparison of Fig. 6-16a-c shows the effect on apparent ages of dispersion in a symmetrical CSD (Gaussian in this instance). The continuous curves in each panel indicate the relative distribution of volume: the largest volume fraction of garnet is represented by crystals with radii slightly larger than the mean radius, and this effect is more pronounced for wider CSDs. Because larger crystals undergo a lower percentage volume reduction and represent a larger volume fraction of the population, they shift the result toward an older apparent age. This comparison illustrates that wider CSDs produce apparent ages closer to the actual age of the crystals.

Figure 6-16d-f compares CSDs with positive and negative skewness to a symmetrical CSD. As indicated by the continuous curves in each panel, the size class making up the largest fraction of the total volume migrates toward larger radius as the CSDs become more negatively skewed, yet the apparent age is seen to decrease — a result that may seem somewhat counter-intuitive, considering the higher proportion of large crystals in the negatively skewed CSD. This is explained by the fact that negatively skewed distributions contain fewer small crystals; because most of these small crystals are completely consumed, the larger crystals must account for the bulk of the resorption. Thus, as the skewness shifts from positive to negative, the volume percent resorption of the larger crystals increases (as shown by the insets), which causes the apparent age to decrease.

The changes in apparent age shown in these CSDs are reflected in all levels of resorption (Fig. 6-17). Wide CSDs and CSDs with positive skewness produce ages that are older and closer to the actual age of garnet crystallization.

Summary of sensitivity analysis

The dominant factors governing changes in the apparent age of a population of garnets are the amount of garnet resorption and the degree of Lu retention. Other factors, however, can modify their effects. First, even for small amounts of resorption, flat initial Lu zoning will cause a significant percentage of Lu to be redistributed from the

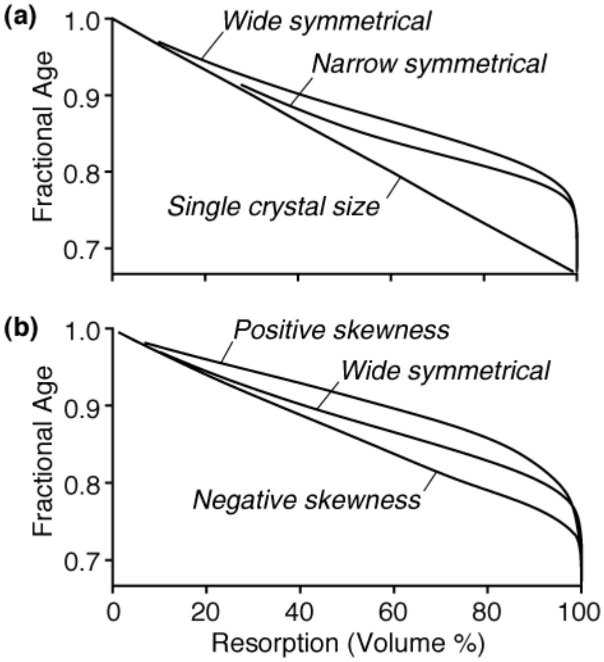

Figure 6-17. Effect of CSDs on fractional age, as a function of percentage resorption. These CSDs are the same as shown in Fig. 6-16. (a) Relative to a single crystal size (equal to the mean of the Gaussian distribution), a Gaussian distribution produces apparent ages that are closer to the actual age of crystallization. (b) Relative to a Gaussian distribution, positive skewness produces apparent ages closer to the actual age of crystallization, and negative skewness produces apparent ages further from the actual age of crystallization.

resorbed portion of the garnet to the relict portion. Second, only the Lu/Hf ratio produced during the decay period before resorption (t_1) is susceptible to redistribution of Lu and Hf, so the apparent age is more sensitive to larger values of t_1/t_2. Third, the shape of the CSD affects the total amount of redistribution of Lu and Hf, but the consequent variability in apparent age is relatively small unless the garnets experience large amounts of resorption (>40-60%).

TASIUYAK GNEISS GARNETS

It is apparent from the foregoing sensitivity analysis that any effort to predict or to replicate quantitatively the Lu-Hf ages in a sample suite in which garnet resorption has occurred would require detailed knowledge for each sample of extents of resorption, partitioning of Lu between garnet and the products of the resorption reaction, rates of intracrystalline diffusion of Lu as a function of temperature, initial Lu zoning, the timing of crystallization and resorption, and crystal size distributions. We will not make such an attempt here. However, it is worth considering whether reasonable estimates of the key parameters controlling apparent ages in the MLP aureole yield results consistent with observation; in essence, we seek simply to compare the trend of decreasing apparent age in the MLP aureole with the trends expected on the basis of the resorption modelling.

The basis of the comparison is the relationship between apparent age and the amount of resorption in each of the natural samples, which correlates with distance from the contact with the intrusion. Note that samples were separated by hundreds of meters during garnet crystallization, so they are not expected to have had identical initial ^{176}Lu/^{176}Hf ratios. Each sample would have experienced Lu-Hf decay that follows a path like that shown in Fig. 6-12. However, because the initial ^{176}Lu/^{176}Hf ratio is unique to each sample, and not necessarily dependent on distance from the contact, and because the samples are progressively more resorbed toward the contact, the ages from the measured ^{176}Lu/^{176}Hf ratios are expected to correlate with the extent of resorption, not with the ratios themselves.

Estimating resorption in these samples is challenging, considering the wide variety of crystal sizes and CSDs, and the irregular shape of the original and relict garnet crystals. Fortunately, however, in a previous study of the kinetics of the resorption reaction (Carlson, 2010), precise measurements of the amount of resorption were made on fifteen garnets from eight samples using crystals that were carefully selected for being equant, relatively free of internal fractures along which reaction had occurred, and isolated from other crystals. These measurements, combined with the observation that virtually no resorption was evident in a sample collected 5750 m from the contact, provide constraints on the extent of resorption as a function of distance from the contact. The resorption vs. distance function interpolated from the measurements (Fig. 6-18) was used to assign representative degrees of resorption to each of the samples used for geochronology, leading to the relationships between apparent age and resorption amount diagrammed in Fig. 6-19a.

For comparison, model predictions were computed for a case in which: (a) pre- and post-resorption intervals were 530 Myr and 1320 Myr, respectively, to match the known timing of events in the MLP aureole; (b) a small fractionation factor ($\beta = 4$) was used to approximate the slightly decreasing Lu concentrations toward the rims of the relict garnets, as seen in Fig. 6-7; and (c) a retention factor of 0.2 was arbitrarily chosen. The distribution of apparent ages as a function of the resorption amount was then calculated for a set of four possible CSDs. The results, shown in Fig. 6-19b, define trends that correspond well with the trend observed in rocks of the MLP aureole.

CONCLUSION

Resorption of garnet at temperatures high enough to produce significant amounts of intracrystalline Lu diffusion can redistribute Lu and Hf, and thus produce apparent Lu-Hf ages that are markedly younger than the actual ages of garnet crystallization. As the modelling shows, the degree to which apparent ages depart from actual ages depends on many factors, but a key indicator of potentially significant effects is the

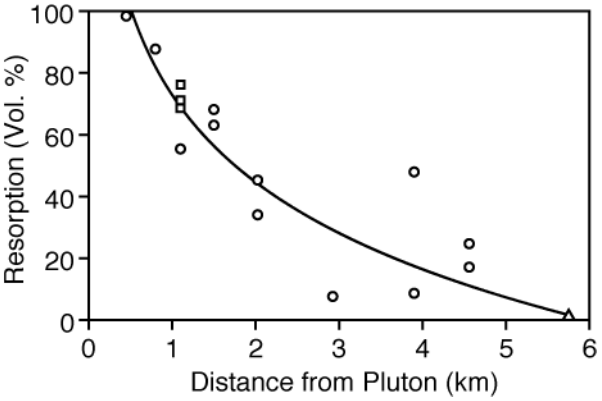

Figure 6-18. Measured volume-percent resorption for garnets in the MLP aureole as a function of distance from the intrusive contact. A logarithmic curve was fit through resorption determinations from garnets at various distances from the pluton. Most determinations (*circles*) were obtained from precisely-measured central sections. The curve was constrained to fit through especially well-determined resorption measurements in two samples: three crystals (*squares*) in one sample were examined using very high-resolution X-ray computed tomography in conjunction with volume calculations using image-analysis software, and one sample (*triangle*) has garnets with nearly zero resorption.

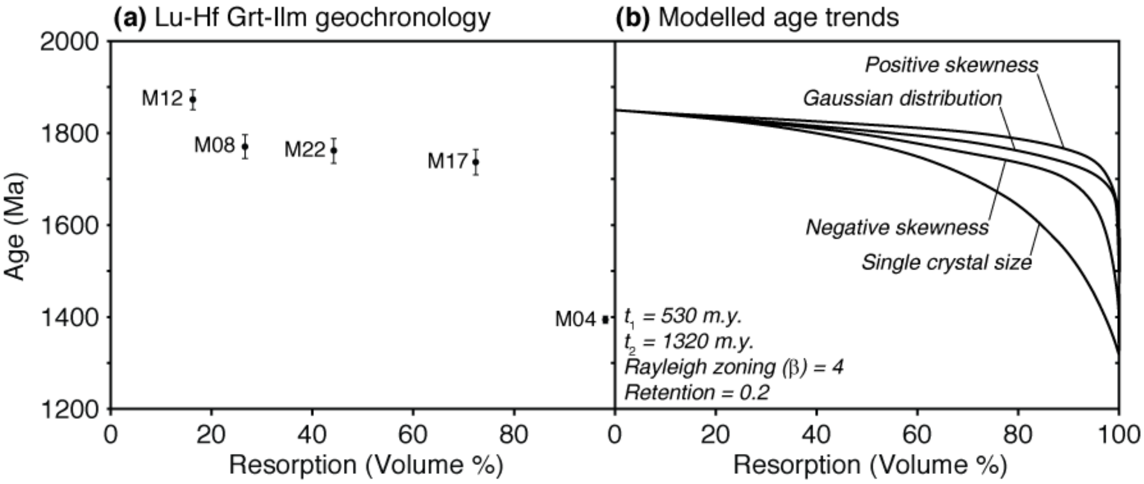

Figure 6-19. Comparison of geochronology and modeled ages. (a) Apparent ages from Lu-Hf garnet-ilmenite geochronology. (b) Models of age progression with increasing resorption corresponding to likely conditions in the MLP aureole. Models based on variable CSDs are shown to represent the possible size distribution of each sample.

presence of stranded diffusion profiles for Lu at the rims of relict crystals. Proper interpretation of Lu-Hf ages using partially resorbed garnets therefore requires careful determination and evaluation of the internal distribution of Lu within the crystals.

APPENDICES

APPENDIX A: ROCK AND SIMULATION NAMES

Most of the rocks in this collection have other names, so those names are listed in the first table. In the second table, the model names (or filenames) used in this study are given.

Rock	Alias
PM1	Pic
PM2	Portia
PM4	Pearl
160A	Paul
191A	George
711A	John
AG4	
MD	DC-1
Jen-2-80	Glowy
HE-1	Theo
WR1	21
WR3	Vito, cdj?

Simulation Name Used in Text	Simulation Name Used in Modeling (filename)
PM1	PM1_110927_0801
PM2	PM2_110927_0822
PM4	PM4_110927_0824
160A	160A_111006_0908
191A	191A_110927_0811
711A	711A_110828_0947
AG4	AG4_110920_1501
MD	MD_110816_1842
Jen-2-80	Jen_111031_0837
HE-1	HE1_111026_1912
WR1bt	WR1bt_110710_1415
WR1tp	WR1tp_110706_1541
WR3m	WR3m_110708_1437
k1-k2-3	PM1_110927_0801_SAk2-03
k1-k2-4	PM1_110927_0801_SAk2-04
k1-k2-5	PM1_110927_0801_SAk2-05
k1-k2-6	PM1_110927_0801_SAk2-06
k1-k2-7	PM1_110927_0801_SAk2-07c
k1-k3-6	PM1_110927_0801_SAk1-06
k1-k3-7	PM1_110927_0801_SAk1-07
dTdt-k1-1	PM1_110927_0801_dTdtk1-01a
dTdt-k1-2	PM1_110927_0801_dTdtk1-02a
dTdt-k1-3	PM1_110927_0801_dTdtk1-03b
dTdt-k1-4	PM1_110927_0801_dTdtk1-04b
dTdt-k2-1	PM1_110927_0801_dTdtk2-01d
dTdt-k2-2	PM1_110927_0801_dTdtk2-02d
dTdt-k2-3	PM1_110927_0801_dTdtk2-03c
dTdt-k2-4	PM1_110927_0801_dTdtk2-04c
dTdt-k3-1	PM1_110927_0801_dTdtk3-01c
dTdt-k3-2	PM1_110927_0801_dTdtk3-02d
dTdt-k3-3	PM1_110927_0801_dTdtk3-03b
dTdt-k3-4	PM1_110927_0801_dTdtk3-04b
Q-k3-1	PM1_110927_0801_Qk3-01c
Q-k3-2	PM1_110927_0801_Qk3-02d
Q-k3-3	PM1_110927_0801_Qk3-03e
Q-k3-4	PM1_110927_0801_Qk3-04f

APPENDIX B: FREE-ENERGY PATH CALCULATIONS

Free-energy differences between product phases and reactant phases in the model reactions ($\Delta_r G$) were calculated at each point along a *P-T* path using thermodynamic data for endmember phases following Holland and Powell (1998), with supplemental data and methods from Holland and Powell (1990) as noted.

The free-energy change of a reaction is expressed as the difference between the free-energy of the product phases and the reactant phases:

$$\Delta_r G = \sum G_{\text{products}} - \sum G_{\text{reactants}} \ . \qquad \text{(B1)}$$

The molar free-energy of each phase at temperature *T* and pressure *P* is given by

$$\overline{G}_{(T,P)} = \overline{G}_{(T_{ref},P_{ref})} + \int_{T_{ref}}^{T} \left(\frac{\partial \overline{G}}{\partial T} \right)_{P_{ref}} dT + \int_{P_{ref}}^{P} \left(\frac{\partial \overline{G}}{\partial P} \right)_{T} dP \ . \qquad \text{(B2)}$$

The first term accounts for the free-energy of the system at the reference temperature and pressure (T_{ref}, P_{ref}), and is expressed by the relation

$$\overline{G}_{(T_{ref},P_{ref})} = \Delta_f \overline{H} - T_{ref} \overline{S} \ , \qquad \text{(B3)}$$

where the molar enthalpy of formation ($\Delta_f \overline{H}$) and molar entropy ($\overline{S}$) are derived from experimental determinations (Holland & Powell, 1998). The second term in B2 describes the change in free-energy due to temperature, and thus entropy. The change in entropy is approximated by using a polynomial that describes the dependence of heat capacity on temperature (Holland & Powell, 1998):

$$\begin{aligned} \int_{T_{ref}}^{T} \left(\frac{\partial \overline{G}}{\partial T} \right)_{P} dT = & -\left[\overline{S} - a \ln T_{ref} - bT_{ref} + 0.5cT_{ref}^{-2} + 2dT_{ref}^{-1/2} \right] (T - T_{ref}) \\ & - \left[\begin{array}{l} a\left((T \ln T - T) - (T_{ref} \ln T_{ref} - T_{ref}) \right) \\ + 0.5b\left(T^{2} - T_{ref}^{2}\right) + 0.5c\left(T^{-1} - T_{ref}^{-1}\right) - 4d\left(T^{1/2} - T_{ref}^{1/2}\right) \end{array} \right] . \end{aligned} \qquad \text{(B4)}$$

The third term in B2 describes the change in free-energy due to pressure. For solid phases, volume changes are approximated using the Murnaghan equation of state (Holland & Powell, 1998):

$$\int_{P_{ref}}^{P}\left(\frac{\partial\overline{G}}{\partial P}\right)_T dP = \frac{\overline{V}_{P_{ref},T}\,\kappa_T}{3}\left(\left(1+\frac{4P}{\kappa_T}\right)^{3/4}-1\right), \qquad \text{(B5)}$$

in which the molar volume, at a reference pressure (1 bar) and a given temperature, is given by

$$V_{P_{ref},T} = V_{P_{ref},T_{ref}}\left(1+a^{\circ}(T-T_{ref})-20a^{\circ}\left(T^{1/2}-T_{ref}^{1/2}\right)\right), \qquad \text{(B6)}$$

where *a*° is a limiting parameter for thermal expansion (Holland & Powell, 1998), and the bulk modulus (κ_T) is expressed as

$$\kappa_T = \kappa_{T_{ref}}\left(1-1.5\times10^{-4}(T-T_{ref})\right). \qquad \text{(B7)}$$

Here, T_{ref} is 298.15 K. Volume changes in fluid phases are approximated from a polynomial function given by (Holland & Powell, 1990):

$$\int_{P_{ref}}^{P}\left(\frac{\partial\overline{G}}{\partial P}\right)_T dP = RT\ln f = a + bT + cT^2, \qquad \text{(B8)}$$

in which *a*, *b*, and *c* are polynomials defined as

$$a = a_1 + a_2P + a_3P^2 + a_4P^{-1} + a_5P^{-2}, \qquad \text{(B9)}$$

$$b = b_1 + b_2P + b_3P^{-1} + b_4P^{-2} + b_5P^{-1/2} + b_6P^{-3}, \text{ and} \qquad \text{(B10)}$$

$$c = c_1 + c_2P + c_3P^{-2} + c_4P^{-1/2} + c_5P^{-1} + c_6P^{-3} \qquad \text{(B11)}$$

for a_i, b_i, and c_i derived from fits to experimental determinations and listed in Holland and Powell (1990). All of the values used in the thermodynamic modeling are compiled in the following table.

Thermodynamic properties from Holland and Powell (1990, 1998)

Phase:	QTZ	ALM	PRP	GRS	DPH	CCHL	PRG	Fe-GLN	ANN	PHL	MS	MRG
Thermal expansion and compressibility												
a^o	6.50E-06	4.03E-05	4.36E-05	3.93E-05	3.98E-05	3.98E-05	5.34E-05	5.30E-05	0.0000579	5.79E-05	0.0000596	4.87E-05
κ_{Tref}	750	1690	1737	1680	472	472	912	890	513	512	490	1300
κ_T	693.2382	1562.0967	1605.5396	1552.8535	436.2779	436.2779	842.9776	822.6426	474.1749	473.2506	452.9156	1201.6128
$V_{Pref,T}$	2.2732	11.6424	11.4578	12.6745	21.5806	21.3278	27.6013	26.9892	15.6851	15.2094	14.3207	13.1428

End-member properties													
$\Delta_f H$	kJ	-910.88	-5263.65	-6284.23	-6644.07	-7153.99	-8929.86	-12719.6	-10890.01	-5143.44	-6219.44	-5984.12	-6241.19
S	kJ·K^{-1}	0.0415	0.34	0.2663	0.255	0.545	0.4105	0.601	0.624	0.428	0.328	0.292	0.267
V	kJ·kbar^{-1}	2.269	11.511	11.318	12.535	21.34	21.09	27.19	26.59	15.432	14.964	14.083	12.964
a	kJ·K^{-1}	0.1107	0.6773	0.6335	0.626	1.2374	1.1618	1.2802	1.7629	0.8157	0.7703	0.7564	0.7444
b	kJ·K^{-2}	-0.000005189	0	0.00E+00	0.00E+00	0.000013594	1.01E-05	2.30E-05	1.19E-04	-0.000034861	-3.69E-05	-0.00001984	-1.68E-05
c	kJ·K	0	-3772.7	-5196.1	-5779.2	-3743	-7657.3	-12359.5	9423.7	19.8	-2328.9	-2170	-2074.4
d	kJ·K$^{-0.5}$	-1.1283	-5.044	-4.3152	-4.0029	-11.25	-9.6909	-8.0658	-20.2071	-7.4667	-6.5316	-6.9792	-6.7832

Phase:	AB	AN	KY	CLD	EP (ordered)	JD	WO	EN	H_2O
Thermal expansion and compressibility									
a^o	4.56E-05	0.0000238	0.0000404	5.42E-05	5.05E-05	4.66E-05	4.60E-05	5.05E-05	
κ_{Tref}	593	919	1590	1465	1233	1284	795	1070	
κ_T	548.1203	849.4478	1469.6649	1354.1252	1139.6836	1186.8237	734.8325	989.0198	
$V_{Pref,T}$	10.1352	10.1469	4.4645	7.0872	14.1090	6.1197	4.0450	6.3516	

End-member properties										
$\Delta_f H$	kJ	-3934.6	-4233.48	-2593.13	-3209.17	-6463.2	-3027.83	-1634.04	-3090.26	-241.81
S	kJ·K^{-1}	0.2101	0.2	0.0835	0.1620	0.328	0.1335	0.0825	0.1325	0.1888
V	kJ·kbar^{-1}	10.006	10.079	4.414	6.98	13.91	6.04	3.993	6.262	
a	kJ·K^{-1}	0.452	0.3716	0.2794	0.4846	0.5446	0.3011	0.1593	0.3562	0.0401
b	kJ·K^{-2}	-1.34E-05	0.000012615	-0.000007124	-1.38E-05	2.48E-05	1.01E-05	0.00E+00	-2.99E-06	0.000008656
c	kJ·K	-1275.9	-4110.2	-2055.6	-198.9	-11230	-2239.3	-967.3	-596.9	487.5
d	kJ·K$^{-0.5}$	-3.9536	-2.0384	-2.2894	-4.7622	-1.1921	-2.0551	-1.0754	-3.1853	-0.2512

For H_2O fugacity:

	a	b	c
1	-40.338	0.117372	-7.37E-06
2	1.6474	0	1.10E-07
3	-0.0062115	0	-9.88E-07
4	2.0068	-0.0004671	-2.48E-05
5	0.0562929	0	8.29E-06
6		0	8.34E-06

The results of the thermodynamic modeling are shown in the tables below. The reactions used for approximating the free-energy changes along the *P*-*T* path are model reactions that use endmember phases. Therefore, their equilibrium *P*-*T* conditions are not the same as those of the reactions in the natural samples. The dominant influence on free-energy changes come from the changes in pressure and temperature, not necessarily the absolute pressure and temperature. Therefore, in the thermodynamic modeling, the equilibrium *P*-*T* conditions were found for each reaction, and the changes in pressure and temperature were imposed to determine the change in free-energy with changes in *P*-*T* conditions. Reactions 1-3 are strongly temperature dependent, so the equilibrium temperature was determined by minimizing $\Delta_r G$ using Solver in Microsoft EXCEL 2007 at the estimated equilibrium pressure. Reaction 4 is strongly pressure dependent so the equilibrium pressure was determined by minimizing $\Delta_r G$ using Solver in Microsoft EXCEL 2007 at the estimated equilibrium temperature.

Thermodynamic modeling results used to calculate t-T-P-$\Delta_r G$ paths

Reaction 1: **-(3/4)*dph-(1/4)*ms-(3/4)*qtz+alm+(1/4)*ann+3*h2o**

Picuris Mountains

Rock and Simulation		Thermodynamic model				
T (°C)	P (kbar)	T (°C)	P (kbar)	ΔT	ΔP	Δ_rG
435	4	529.55	4	0	0	0.0000
535	5	629.55	5	100	1	-19.0582
535	4	629.55	4	100	0	-20.1369

Reaction 2: **-(0.6)*dph-(0.2)*ms-an+(0.8)*alm+(0.2)*grs+(0.2)*ann+(0.4)*mrg+(2)*h2o**

Maine: 160A

Rock and Simulation		Thermodynamic model				
T (°C)	P (kbar)	T (°C)	P (kbar)	ΔT	ΔP	Δ_rG
485	3.5	611.99	3.5	0	0	0.0000
535	3.5	661.99	3.5	50	0	-5.5645

Maine: 191A

Rock and Simulation		Thermodynamic model				
T (°C)	P (kbar)	T (°C)	P (kbar)	ΔT	ΔP	Δ_rG
485	3.5	611.99	3.5	0	0	0.0000
570	3.5	696.99	3.5	85	0	-9.4929

Maine: 711A

Rock and Simulation		Thermodynamic model				
T (°C)	P (kbar)	T (°C)	P (kbar)	ΔT	ΔP	$\Delta_r G$
485	3.5	611.99	3.5	0	0	0.0000
600	3.5	726.99	3.5	115	0	-12.8826

Passo del Sole

Note: The minimum free-energy was mistakenly determined using a pressure of 5 kbar instead of 4 kbar.

Used in Crystallize3D modeling

Rock and Simulation		Thermodynamic model				
T (°C)	P (kbar)	T (°C)	P (kbar)	ΔT	ΔP	$\Delta_r G$
540	*4*	*597.57*	*5*	*0*	*0*	*0.0000*
600	*5*	*657.57*	*5*	*60*	*0*	*-6.3299*

Corrected

540	4	607.95	4	0	0	0.0000
600	5	667.95	5	60	0	-7.4311

Reaction 3: -cld-dph-ms-qtz+alm+ann+(2)*ky+(5)*h2o

Mica Dam

Rock and Simulation		Thermodynamic model				
T (°C)	P (kbar)	T (°C)	P (kbar)	ΔT	ΔP	$\Delta_r G$
555	7.5	570.12	7.5	0	0	0.0000
655	7.5	670.12	7.5	100	0	-31.0630

Reaction 4: -(1/6)*fgln-(1/3)*prg-(2/3)*ep-(1/3)*qtz-(1/6)*ab +(5/6)*jd+(1)*wo+(1/4)*en+(7/18)*alm+(5/18)*prp+(1/3)*grs+(5/6)*h2o

Jenner

Rock and Simulation		Thermodynamic model				
T (°C)	P (kbar)	T (°C)	P (kbar)	ΔT	ΔP	$\Delta_r G$
375	8	375	93.92	0	0	0.0000
500	13	500	98.92	125	5	-7.5501

Healdsburg

Rock and Simulation		Thermodynamic model				
T (°C)	P (kbar)	T (°C)	P (kbar)	ΔT	ΔP	$\Delta_r G$
450	15	450	94.31	0	0	0.0000
550	20	550	99.31	100	5	-7.4687

Whitt Ranch

Rock and Simulation		Thermodynamic model				
T (°C)	P (kbar)	T (°C)	P (kbar)	ΔT	ΔP	$\Delta_r G$
575	9	575.00	95.34	0	0	0.0000
650	14	650	100.34	75	5	-7.3434

APPENDIX C: BEST-FIT SIMULATIONS

The following simulations are illustrated using PLOTSIM, a program written by the author in MATLAB for reading the CRYSTALLIZE3D output files and summarizing the modeling results. The files read by PLOTSIM are the *.int.txt, *.run.txt, *.xl.txt, and params*.txt file for the given simulation.

Most plots and values are calculated from data in the run file, so the resolution of the data is subject to the reporting interval used in the simulation. Thus, the data points are accurately retrieved from the CRYSTALLIZE3D output to within one reporting interval (500,000 years here). The thermal overstepping value is taken from the xl file and is accurately retrieved from the CRYSTALLIZE3D data to within one degree Celsius.

The number of crystals reported for the rock is not necessarily the same as reported from REDUCE3D (Hirsch, 2011). The values reported here are taken from a compilation of BLOB3D (Ketcham, 2005a) "integrate" files and are only used for comparison of the crystal-size distribution between the natural sample and the simulation.

The crystal number density, radii measurements, and mode for each simulation were taken from REDUCE3D 2.58 output calculated in previous studies.

The version of CRYSTALLIZE3D used for all simulations in this dissertation is 1.3 (last modified March 4, 2011 at 13:47).

The version of REDUCE3D (Hirsch, 2011) used for all PCF and MCF calculations in this dissertation is 3.30.

PM1

Simulation: PM1_110927_0801

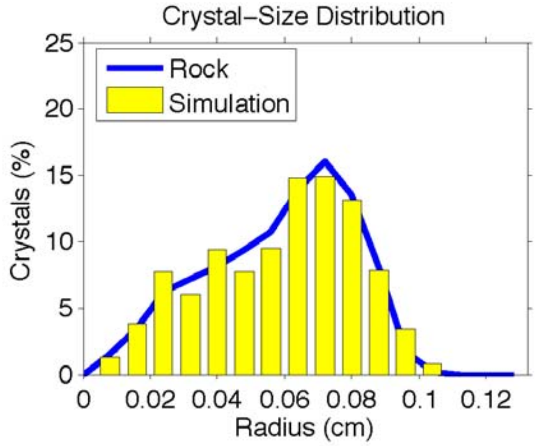

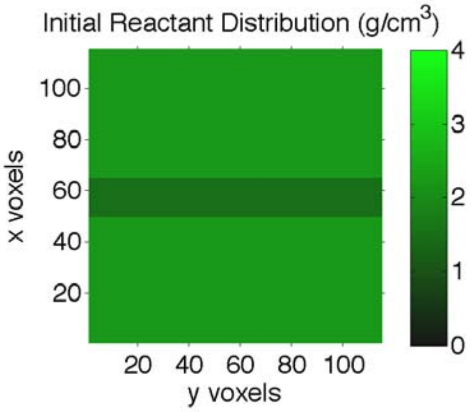

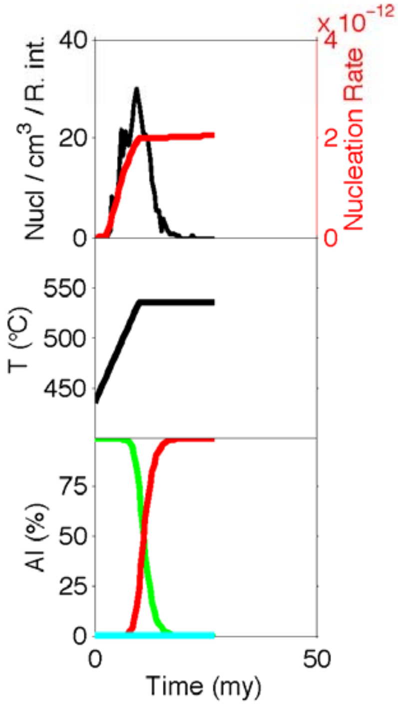

	Rock	Simulation
Total crystals:	1748	1015
Xtl Num Density (xtls/cm^3):	382	386
Crystallization duration (my):	10	12.0[a]
Equil T of rxn (°C):	unknown	435
Thermal overstepping (°C):		29
T at 95% Al in products (°C):	535	535[a]
Min radius (cm):	0.006	0.006
Mean radius (cm):	0.058	0.059
Max radius (cm):	0.104	0.104
Mode (vol%):	37.4	38.0
D_{inf} (cm^2/s):		5.00e-006
$[Al]_{fl}$ in eq w/products (mol/cm^3):		5.60e-007
Porosity, ϕ:		3.00e+001
Tortuosity, τ:		1.00e+000
Q_D (kJ/mol):		140
$D = D_{inf} \phi \tau e^{(-Q_D/RT)}$ (m^2/s): (at characteristic T, 530°C or 9.5 my)[a]		1.18e-017[a]
$(dN/dt)_{steady-state}, k_1$ (nucl/cm^3/s):		2.70e-012
$(dN/dt)_{max}$ (nucl/cm^3/s):		2.05e-012
Nucleation acceleration, k_2:		1.00e+000
Time step (y):		200
Reporting interval (y):		5.00e+005

[a] Determined at nearest reporting interval

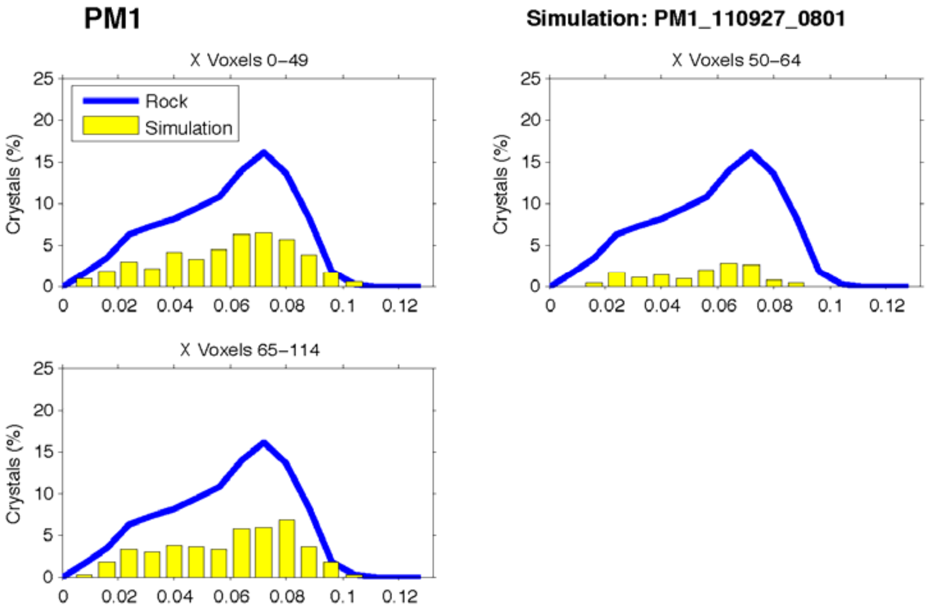
PM1
Simulation: PM1_110927_0801
X Voxels 0–49
X Voxels 50–64
X Voxels 65–114
Rock
Simulation
Crystals (%)
25
20
15
10
5
0
0
0.02
0.04
0.06
0.08
0.1
0.12

Parameters File

```
Crystallize 1.3
Run name:                                                           PM1_110927_0801
Result file directory:                                              runsPM1\PM1_110927_0801
Reporting interval (years):                                         5.00E+05
Fractional porosity (0-1):                                          3.00E+01
Tortuosity (0-1):                                                   1.0
Activation energy for diffusion (kJ/mol):                           140
Dinf (cm^2/s):                                                      5.00E-06
Al concentration in fluid in eq with CAP (moles/cm^3):              5.60E-07
Nucleation acceleration (dimensionless):                            1.00E-00
Nucleation rate at infinite overstepping (nuclei/s/cm^3):           2.70E-12
Nucleation proportional to CAR amount in voxel (0=no,1=yes):        0
Maximum number of porphyroblasts (0=unlimited):                     0
Maximum modal amount of product (0=limited by reactant amount):     0
Al content of CAR (moles Al/moles CAR):                             2.25
Avg. formula weight of CAR (g CAR / mol CAR):                       634.7072
Al content of CAP (moles Al/moles CAP):                             2.25
Avg. formula weight of CAP (g CAP / mol CAP):                       625.7249
Density of CAP (g/cm^3):                                            4.07
Voxel edge length (cm):                                             0.012
Time step (yr):                                                     200
Number of voxels in X:                                              115
Number of voxels in Y:                                              115
Number of voxels in Z:                                              115
Dimensions:                                                         3
Default CAR amount (g/cm^3 rock):                                   2.20
**** Reactant distribution: One header line, then one line per layer ****
Number of structures (0=homogeneous):                               1
Layer (see format codes)                                            1       50      64      1.50
FD approximation source/sink parameter (dimensionless):             200
Subvoxel growth acceleration factor (dimensionless, 0=none):        2.8284
Random seed (0=generate new):                                       -1717
Volume fraction of porphyroblast in CAP assemblage (fv):            0.7490
Number of moles of porphyroblast in reaction equation (moles):      1.0
Concentration to delGrxn conversion power-law factor n:             1.4165
Free energy specification mode (0=thermo, 1=delGrxn path):          1
Equilibrium temperature used for G-C conversion (°C):               528
Number of Time-Temp-DelGrxn triplets:                               3
DelGrxn path (Myr after start,°C,kJ/mol): (0.0,435.0,-0.0001)    (10.0,535.0,-19.0582)    (30.0,535.0,-20.1369)
```

PM2

Simulation: PM2_110927_0822

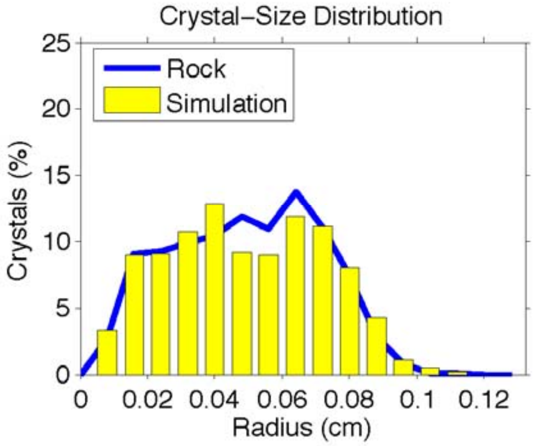

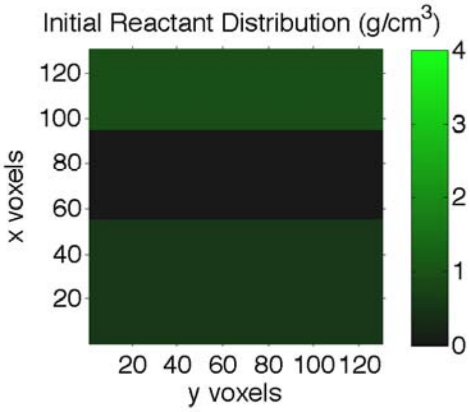

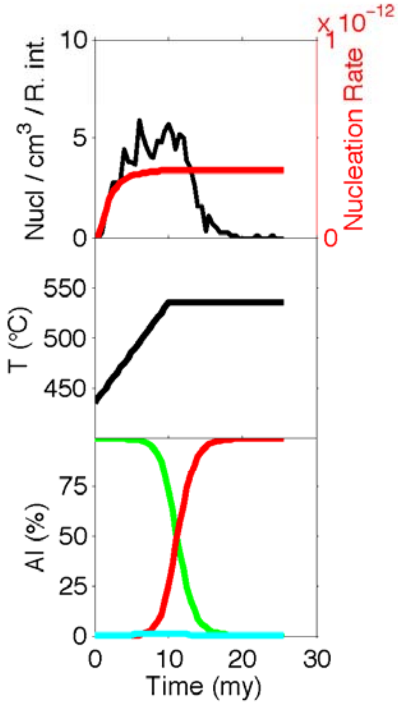

	Rock	Simulation
Total crystals:	2298	975
Xtl Num Density (xtls/cm^3):	112	108
Crystallization duration (my):	10	14.0[a]
Equil T of rxn (°C):	unknown	435
Thermal overstepping (°C):		7
T at 95% Al in products (°C):	535	535[a]
Min radius (cm):	0.008	0.005
Mean radius (cm):	0.049	0.049
Max radius (cm):	0.108	0.111
Mode (vol%):	8.3	8.7
D_{inf} (cm^2/s):		2.00e-005
$[Al]_{fl}$ in eq w/products (mol/cm^3):		5.60e-007
Porosity, ϕ:		1.20e+001
Tortuosity, τ:		1.00e+000
Q_D (kJ/mol):		140
$D = D_{inf} \phi \tau e^{(-Q_D/RT)}$ (m^2/s):		1.88e-017[a]
(at characteristic T, 530°C or 9.5 my)[a]		
$(dN/dt)_{steady-state}, k_1$ (nucl/cm^3/s):		3.50e-013
$(dN/dt)_{max}$ (nucl/cm^3/s):		3.40e-013
Nucleation acceleration, k_2:		1.00e-001
Time step (y):		200
Reporting interval (y):		5.00e+005

[a] Determined at nearest reporting interval

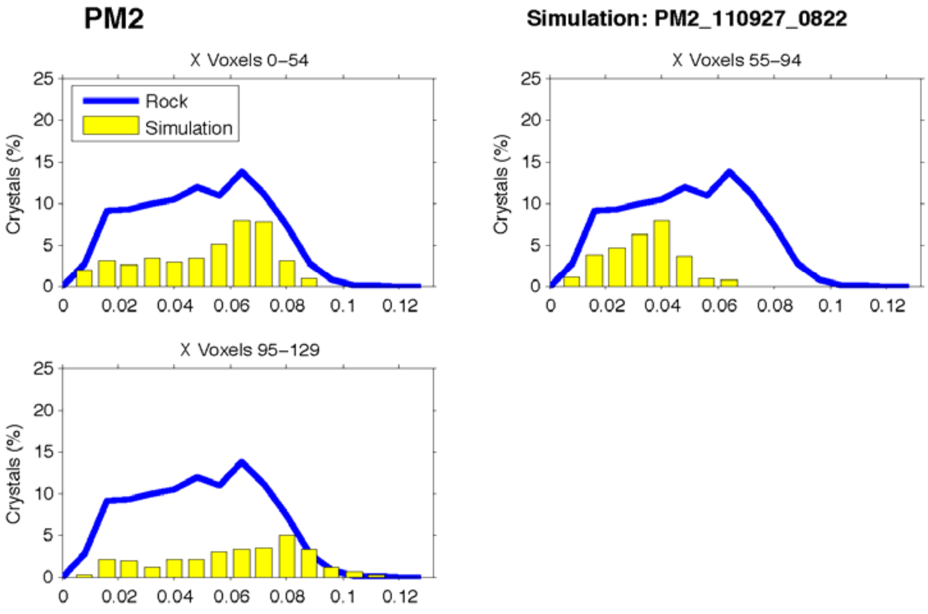
PM2
Simulation: PM2_110927_0822
X Voxels 0–54
X Voxels 55–94
X Voxels 95–129
Rock
Simulation
Crystals (%)
0
5
10
15
20
25
0
0.02
0.04
0.06
0.08
0.1
0.12

Parameters File

```
Crystallize 1.3
Run name:                                                           PM2_110927_0822
Result file directory:                                              runsPM2\PM2_110927_0822
Reporting interval (years):                                         5.00E+05
Fractional porosity (0-1):                                          1.20E+01
Tortuosity (0-1):                                                   1.0
Activation energy for diffusion (kJ/mol):                           140
Dinf (cm^2/s):                                                      2.00E-05
Al concentration in fluid in eq with CAP (moles/cm^3):              5.60E-07
Nucleation acceleration (dimensionless):                            1.00E-01
Nucleation rate at infinite overstepping (nuclei/s/cm^3):           3.50E-13
Nucleation proportional to CAR amount in voxel (0=no,1=yes):        0
Maximum number of porphyroblasts (0=unlimited):                     0
Maximum modal amount of product (0=limited by reactant amount):     0
Al content of CAR (moles Al/moles CAR):                             2.25
Avg. formula weight of CAR (g CAR / mol CAR):                       634.7072
Al content of CAP (moles Al/moles CAP):                             2.25
Avg. formula weight of CAP (g CAP / mol CAP):                       625.7249
Density of CAP (g/cm^3):                                            4.07
Voxel edge length (cm):                                             0.016
Time step (yr):                                                     200
Number of voxels in X:                                              130
Number of voxels in Y:                                              130
Number of voxels in Z:                                              130
Dimensions:                                                         3
Default CAR amount (g/cm^3 rock):                                   0.0
**** Reactant distribution: One header line, then one line per layer ****
Number of structures (0=homogeneous):                               2
Layer (see format codes)                                            1       0       54      0.55
Layer (see format codes)                                            1       95      129     0.95
FD approximation source/sink parameter (dimensionless):             200
Subvoxel growth acceleration factor (dimensionless, 0=none):        2.8284
Random seed (0=generate new):                                       -1717
Volume fraction of porphyroblast in CAP assemblage (fv):            0.7490
Number of moles of porphyroblast in reaction equation (moles):      1.0
Concentration to delGrxn conversion power-law factor n:             1.4165
Free energy specification mode (0=thermo, 1=delGrxn path):          1
Equilibrium temperature used for G-C conversion (°C):               528
Number of Time-Temp-DelGrxn triplets:                               3
DelGrxn path (Myr after start,°C,kJ/mol): (0.0,435.0,-0.0001)    (10.0,535.0,-19.0582)    (30.0,535.0,-20.1369)
```

PM4

Simulation: PM4_110927_0824

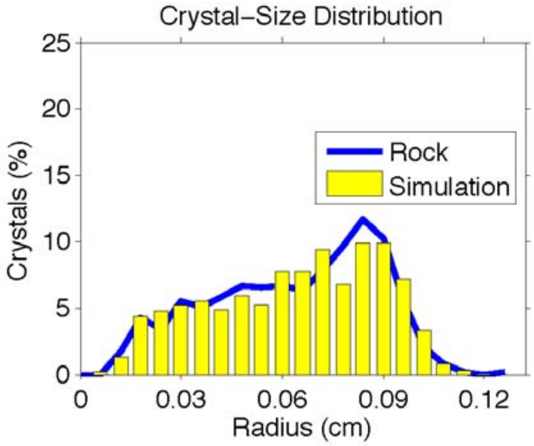

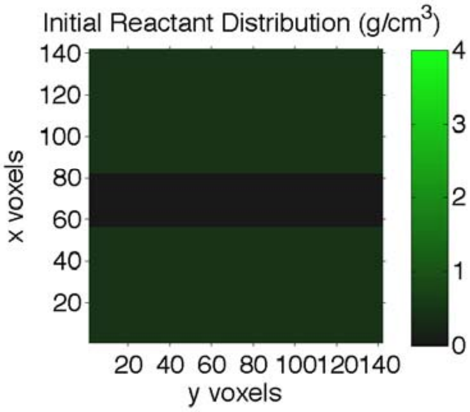

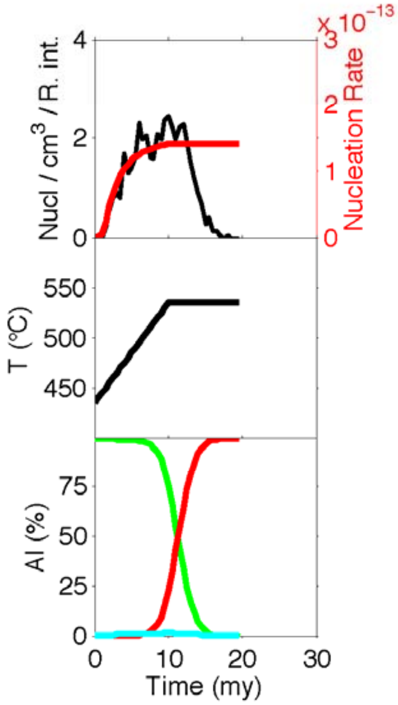

	Rock	Simulation
Total crystals:	1630	995
Xtl Num Density (xtls/cm^3):	44	43
Crystallization duration (my):	10	13.0[a]
Equil T of rxn (°C):	unknown	435
Thermal overstepping (°C):		11
T at 95% Al in products (°C):	535	535[a]
Min radius (cm):	0.010	0.007
Mean radius (cm):	0.063	0.064
Max radius (cm):	0.130	0.120
Mode (vol%):	6.2	6.6
D_{inf} (cm^2/s):		3.00e-005
$[Al]_{fl}$ in eq w/products (mol/cm^3):		5.60e-007
Porosity, ϕ:		1.20e+001
Tortuosity, τ:		1.00e+000
Q_D (kJ/mol):		140
$D = D_{inf}\,\phi\,\tau\,e^{(-Q_D/RT)}$ (m^2/s): (at characteristic T, 525°C or 9.0 my)[a]		2.48e-017[a]
$(dN/dt)_{steady-state}, k_1$ (nucl/cm^3/s):		1.50e-013
$(dN/dt)_{max}$ (nucl/cm^3/s):		1.42e-013
Nucleation acceleration, k_2:		2.00e-001
Time step (y):		200
Reporting interval (y):		5.00e+005

[a] Determined at nearest reporting interval

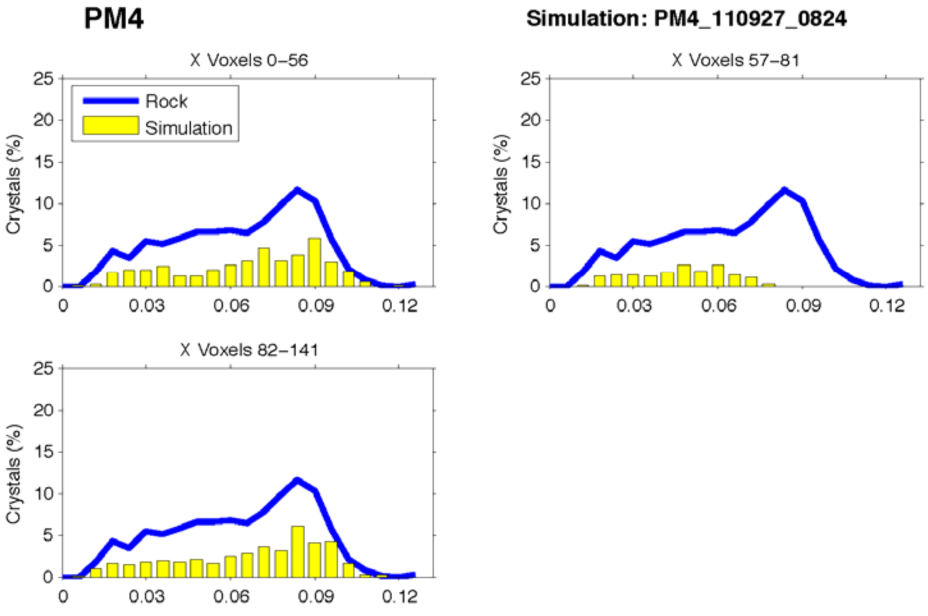
PM4
Simulation: PM4_110927_0824
X Voxels 0–56
X Voxels 57–81
X Voxels 82–141
Rock
Simulation
Crystals (%)
0
5
10
15
20
25
0
0.03
0.06
0.09
0.12

Parameters File

```
Crystallize 1.3
Run name:                                                        PM4_110927_0824
Result file directory:                                           runsPM4\PM4_110927_0824
Reporting interval (years):                                      5.00E+05
Fractional porosity (0-1):                                       1.20E+01
Tortuosity (0-1):                                                1.0
Activation energy for diffusion (kJ/mol):                        140
Dinf (cm^2/s):                                                   3.00E-05
Al concentration in fluid in eq with CAP (moles/cm^3):           5.60E-07
Nucleation acceleration (dimensionless):                         2.00E-01
Nucleation rate at infinite overstepping (nuclei/s/cm^3):        1.50E-13
Nucleation proportional to CAR amount in voxel (0=no,1=yes):     0
Maximum number of porphyroblasts (0=unlimited):                  0
Maximum modal amount of product (0=limited by reactant amount):  0
Al content of CAR (moles Al/moles CAR):                          2.25
Avg. formula weight of CAR (g CAR / mol CAR):                    634.7072
Al content of CAP (moles Al/moles CAP):                          2.25
Avg. formula weight of CAP (g CAP / mol CAP):                    625.7249
Density of CAP (g/cm^3):                                         4.07
Voxel edge length (cm):                                          0.020
Time step (yr):                                                  200
Number of voxels in X:                                           142
Number of voxels in Y:                                           142
Number of voxels in Z:                                           142
Dimensions:                                                      3
Default CAR amount (g/cm^3 rock):                                0.45
**** Reactant distribution: One header line, then one line per layer ****
Number of structures (0=homogeneous):                            1
Layer (see format codes)                                         1       57      81      0.00
FD approximation source/sink parameter (dimensionless):          200
Subvoxel growth acceleration factor (dimensionless, 0=none):     2.8284
Random seed (0=generate new):                                    -1717
Volume fraction of porphyroblast in CAP assemblage (fv):         0.7490
Number of moles of porphyroblast in reaction equation (moles):   1.0
Concentration to delGrxn conversion power-law factor n:          1.4165
Free energy specification mode (0=thermo, 1=delGrxn path):       1
Equilibrium temperature used for G-C conversion (°C):            528
Number of Time-Temp-DelGrxn triplets:                            3
DelGrxn path (Myr after start,°C,kJ/mol): (0.0,435.0,-0.0001)    (10.0,535.0,-19.0582)    (30.0,535.0,-20.1369)
```

160A

Simulation: 160A_111006_0908

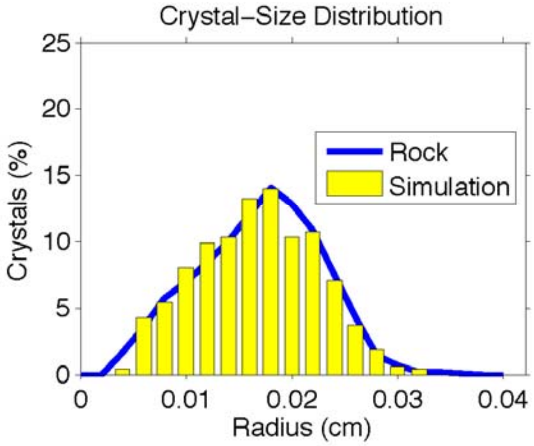

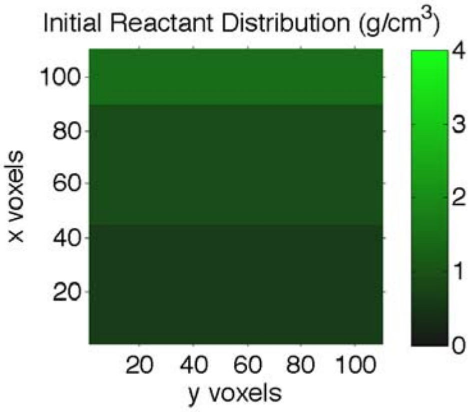

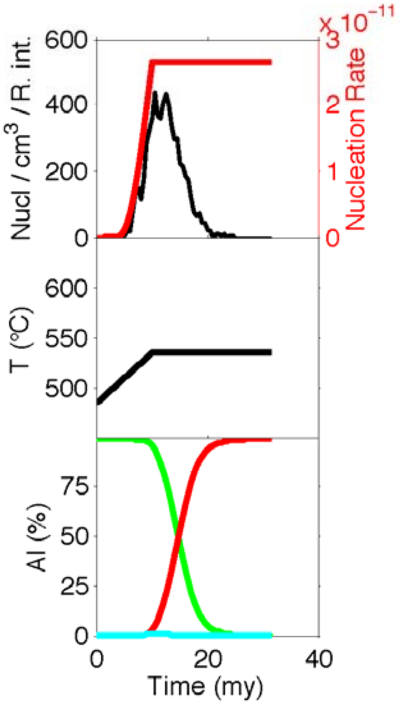

	Rock	Simulation
Total crystals:	5992	1056
Xtl Num Density (xtls/cm^3):	6413	6347
Crystallization duration (my):	10	16.0[a]
Equil T of rxn (°C):	485	485
Thermal overstepping (°C):		21
T at 95% Al in products (°C):	535	535[a]
Min radius (cm):	0.003	0.003
Mean radius (cm):	0.017	0.017
Max radius (cm):	0.035	0.032
Mode (vol%):	15.1	15.6
D_{inf} (cm^2/s):		2.00e-006
$[Al]_{fl}$ in eq w/products (mol/cm^3):		5.00e-007
Porosity, ϕ:		3.20e+001
Tortuosity, τ:		1.00e+000
Q_D (kJ/mol):		140
$D = D_{inf}\phi\tau e^{(-Q_D/RT)}$ (m^2/s):		5.36e-018[a]
(at characteristic T, 533°C or 9.5 my)[a]		
$(dN/dt)_{steady-state}, k_1$ (nucl/cm^3/s):		1.30e-010
$(dN/dt)_{max}$ (nucl/cm^3/s):		2.65e-011
Nucleation acceleration, k_2:		5.00e-001
Time step (y):		200
Reporting interval (y):		5.00e+005

[a]Determined at nearest reporting interval

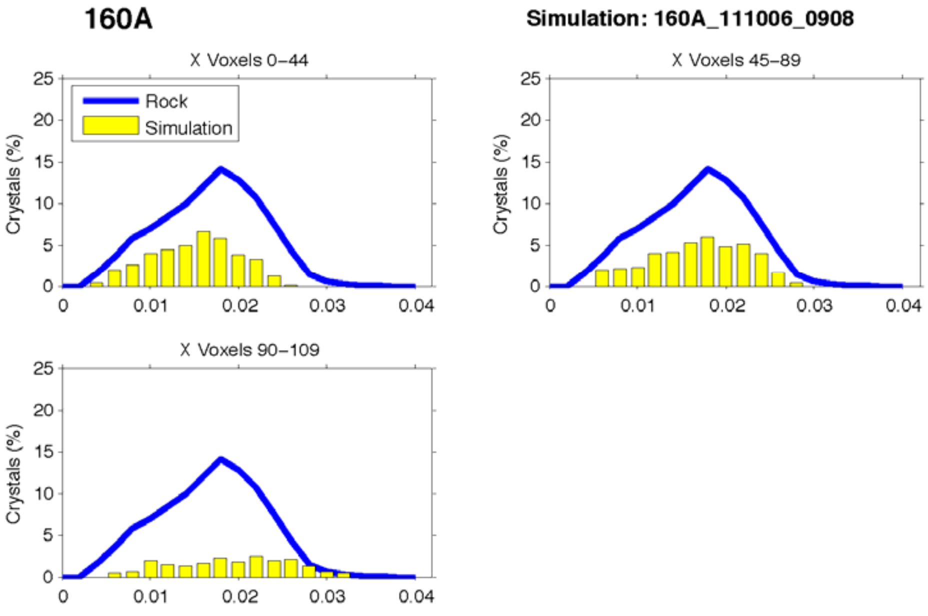
160A
Simulation: 160A_111006_0908
X Voxels 0–44
X Voxels 45–89
X Voxels 90–109
Rock
Simulation
Crystals (%)
0
5
10
15
20
25
0
0.01
0.02
0.03
0.04

Parameters File

```
Crystallize 1.3
Run name:                                                              160A_111006_0908
Result file directory:                                                 runs160A\160A_111006_0908
Reporting interval (years):                                            5.00E+05
Fractional porosity (0-1):                                             3.20E+01
Tortuosity (0-1):                                                      1.0
Activation energy for diffusion (kJ/mol):                              140
Dinf (cm^2/s):                                                         2.00E-06
Al concentration in fluid in eq with CAP (moles/cm^3):                 5.00E-07
Nucleation acceleration (dimensionless):                               5.00E-01
Nucleation rate at infinite overstepping (nuclei/s/cm^3):              1.30E-10
Nucleation proportional to CAR amount in voxel (0=no,1=yes):           0
Maximum number of porphyroblasts (0=unlimited):                        0
Maximum modal amount of product (0=limited by reactant amount):        0
Al content of CAR (moles Al/moles CAR):                                2.25
Avg. formula weight of CAR (g CAR / mol CAR):                          634.7072
Al content of CAP (moles Al/moles CAP):                                2.25
Avg. formula weight of CAP (g CAP / mol CAP):                          625.7249
Density of CAP (g/cm^3):                                               4.07
Voxel edge length (cm):                                                0.005
Time step (yr):                                                        200
Number of voxels in X:                                                 110
Number of voxels in Y:                                                 110
Number of voxels in Z:                                                 110
Dimensions:                                                            3
Default CAR amount (g/cm^3 rock):                                      0.0
**** Reactant distribution: One header line, then one line per layer ****
Number of structures (0=homogeneous):                                  3
Layer (see format codes)                                               1       0       44      0.60
Layer (see format codes)                                               1       45      89      0.90
Layer (see format codes)                                               1       90      109     1.45
FD approximation source/sink parameter (dimensionless):                200
Subvoxel growth acceleration factor (dimensionless, 0=none):           2.8284
Random seed (0=generate new):                                          -1717
Volume fraction of porphyroblast in CAP assemblage (fv):               0.7490
Number of moles of porphyroblast in reaction equation (moles):         1.0
Concentration to delGrxn conversion power-law factor n:                1.4009
Free energy specification mode (0=thermo, 1=delGrxn path):             1
Equilibrium temperature used for G-C conversion (°C):                  528
Number of Time-Temp-DelGrxn triplets:                                  3
DelGrxn path (Myr after start,°C,kJ/mol): (0.0,485.0,-0.0001)     (10.0,535.0,-5.5645)     (40.0,535.0,-5.5645)
```

191A

Simulation: 191A_110927_0811

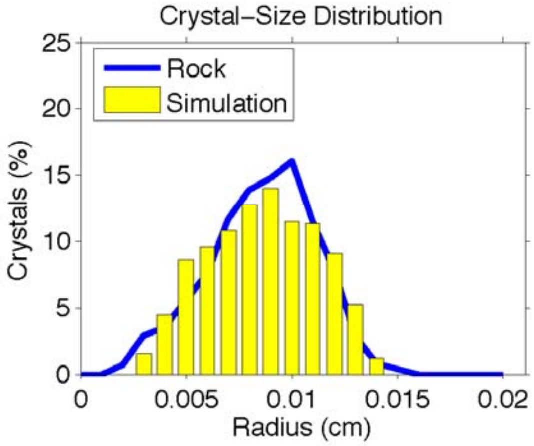

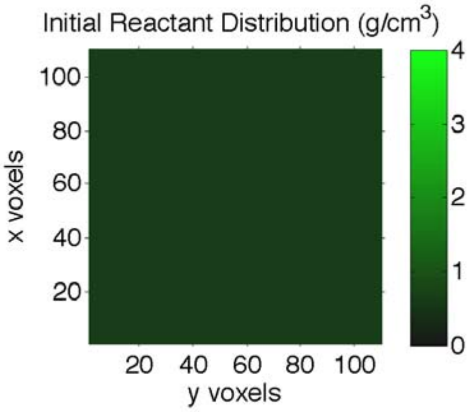

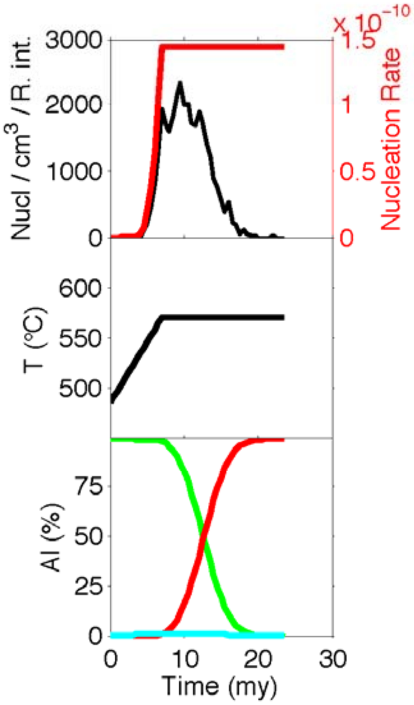

	Rock	Simulation
Total crystals:	1424	1149
Xtl Num Density (xtls/cm^3):	31946	31973
Crystallization duration (my):	7	13.0[a]
Equil T of rxn (°C):	485	485
Thermal overstepping (°C):		49
T at 95% Al in products (°C):	570	570[a]
Min radius (cm):	0.002	0.003
Mean radius (cm):	0.009	0.009
Max radius (cm):	0.015	0.014
Mode (vol%):	9.5	10.6
D_{inf} (cm^2/s):		2.00e-007
$[Al]_{fl}$ in eq w/products (mol/cm^3):		7.70e-007
Porosity, ϕ:		1.45e+001
Tortuosity, τ:		1.00e+000
Q_D (kJ/mol):		140
$D = D_{inf} \phi \tau e^{(-Q_D/RT)}$ (m^2/s):		5.33e-019[a]
(at characteristic T, 564°C or 6.5 my)[a]		
$(dN/dt)_{steady-state}, k_1$ (nucl/cm^3/s):		1.90e-009
$(dN/dt)_{max}$ (nucl/cm^3/s):		1.44e-010
Nucleation acceleration, k_2:		2.00e+000
Time step (y):		200
Reporting interval (y):		5.00e+005

[a] Determined at nearest reporting interval

Parameters File

```
Crystallize 1.3
Run name:                                                              191A_110927_0811
Result file directory:                                                 runs191A\191A_110927_0811
Reporting interval (years):                                            5.00E+05
Fractional porosity (0-1):                                             1.45E+01
Tortuosity (0-1):                                                      1.0
Activation energy for diffusion (kJ/mol):                              140
Dinf (cm^2/s):                                                         2.00E-07
Al concentration in fluid in eq with CAP (moles/cm^3):                 7.70E-07
Nucleation acceleration (dimensionless):                               2.00E+00
Nucleation rate at infinite overstepping (nuclei/s/cm^3):              1.90E-09
Nucleation proportional to CAR amount in voxel (0=no,1=yes):           0
Maximum number of porphyroblasts (0=unlimited):                        0
Maximum modal amount of product (0=limited by reactant amount):        0
Al content of CAR (moles Al/moles CAR):                                2.25
Avg. formula weight of CAR (g CAR / mol CAR):                          634.7072
Al content of CAP (moles Al/moles CAP):                                2.25
Avg. formula weight of CAP (g CAP / mol CAP):                          625.7249
Density of CAP (g/cm^3):                                               4.07
Voxel edge length (cm):                                                0.003
Time step (yr):                                                        200
Number of voxels in X:                                                 110
Number of voxels in Y:                                                 110
Number of voxels in Z:                                                 110
Dimensions:                                                            3
Default CAR amount (g/cm^3 rock):                                      0.60
**** Reactant distribution: One header line, then one line per layer ****
Number of structures (0=homogeneous):                                  1
Layer (see format codes)                                               1       0       109     0.60
FD approximation source/sink parameter (dimensionless):                200
Subvoxel growth acceleration factor (dimensionless, 0=none):           2.8284
Random seed (0=generate new):                                          -1717
Volume fraction of porphyroblast in CAP assemblage (fv):               0.7490
Number of moles of porphyroblast in reaction equation (moles):         1.0
Concentration to delGrxn conversion power-law factor n:                1.4009
Free energy specification mode (0=thermo, 1=delGrxn path):             1
Equilibrium temperature used for G-C conversion (°C):                  528
Number of Time-Temp-DelGrxn triplets:                                  3
DelGrxn path (Myr after start,°C,kJ/mol): (0.0,485.0,-0.0001)    (7.0,570.0,-9.4929)      (30.0,570.0,-9.4929)
```

711A

Simulation: 711A_110828_0947

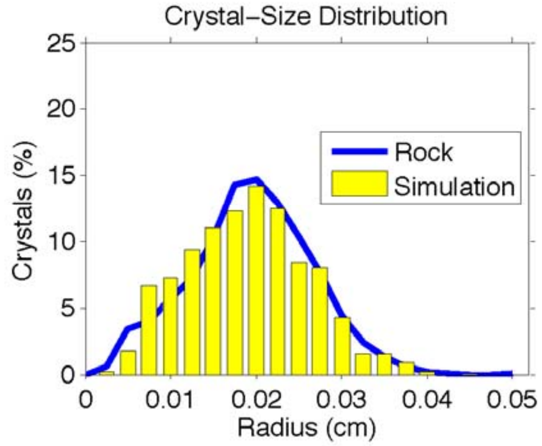

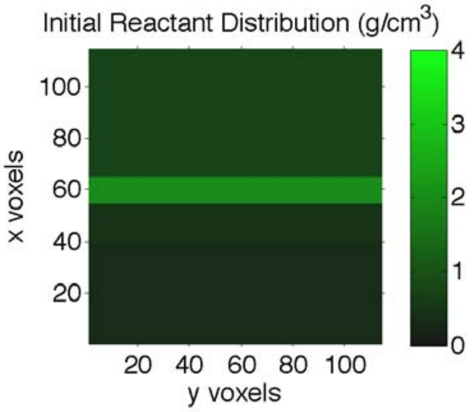

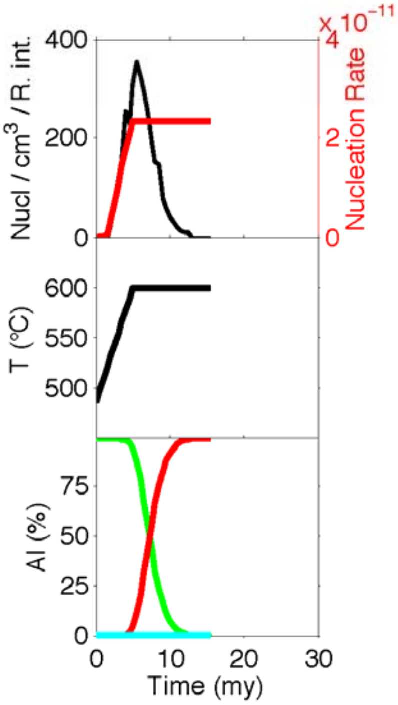

	Rock	Simulation
Total crystals:	6293	1000
Xtl Num Density (xtls/cm^3):	3103	3125
Crystallization duration (my):	5	8.5[a]
Equil T of rxn (°C):	485	485
Thermal overstepping (°C):		36
T at 95% Al in products (°C):	600	600[a]
Min radius (cm):	0.003	0.004
Mean radius (cm):	0.019	0.019
Max radius (cm):	0.050	0.044
Mode (vol%):	12.4	12.1
D_{inf} (cm^2/s):		9.00e-007
$[Al]_{fl}$ in eq w/products (mol/cm^3):		8.80e-007
Porosity, ϕ:		9.00e+000
Tortuosity, τ:		1.00e+000
Q_D (kJ/mol):		140
$D = D_{inf}\,\phi\,\tau\,e^{(-Q_D/RT)}$ (m^2/s):		3.41e-018[a]
(at characteristic T, 600°C or 5.0 my)[a]		
$(dN/dt)_{steady-state}, k_1$ (nucl/cm^3/s):		3.90e-011
$(dN/dt)_{max}$ (nucl/cm^3/s):		2.32e-011
Nucleation acceleration, k_2:		7.00e-001
Time step (y):		200
Reporting interval (y):		5.00e+005

[a] Determined at nearest reporting interval

711A **Simulation: 711A_110828_0947**

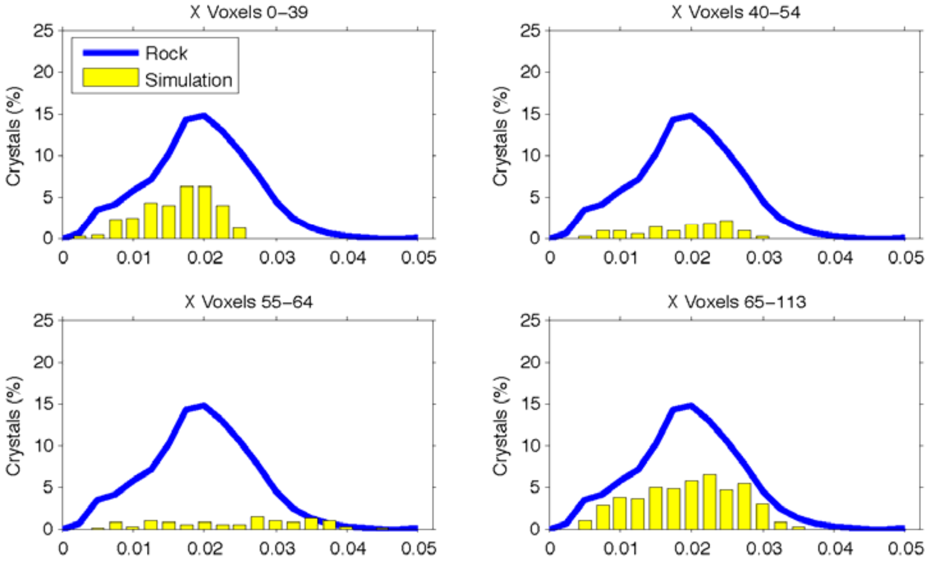

Parameters File

```
Crystallize 1.3
Run name:                                                          711A_110828_0947
Result file directory:                                             runs711A\711A_110828_0947
Reporting interval (years):                                        5.00E+05
Fractional porosity (0-1):                                         9.00E+00
Tortuosity (0-1):                                                  1.0
Activation energy for diffusion (kJ/mol):                          140
Dinf (cm^2/s):                                                     9.00E-07
Al concentration in fluid in eq with CAP (moles/cm^3):             8.80E-07
Nucleation acceleration (dimensionless):                           7.00E-01
Nucleation rate at infinite overstepping (nuclei/s/cm^3):          3.90E-11
Nucleation proportional to CAR amount in voxel (0=no,1=yes):       0
Maximum number of porphyroblasts (0=unlimited):                    0
Maximum modal amount of product (0=limited by reactant amount):    0
Al content of CAR (moles Al/moles CAR):                            2.25
Avg. formula weight of CAR (g CAR / mol CAR):                      634.7072
Al content of CAP (moles Al/moles CAP):                            2.25
Avg. formula weight of CAP (g CAP / mol CAP):                      625.7249
Density of CAP (g/cm^3):                                           4.07
Voxel edge length (cm):                                            0.006
Time step (yr):                                                    200
Number of voxels in X:                                             114
Number of voxels in Y:                                             114
Number of voxels in Z:                                             114
Dimensions:                                                        3
Default CAR amount (g/cm^3 rock):                                  0.0
**** Reactant distribution: One header line, then one line per layer ****
Number of structures (0=homogeneous):                              4
Layer (see format codes)                                           1      0      39     0.35
Layer (see format codes)                                           1      40     54     0.45
Layer (see format codes)                                           1      55     64     2.00
Layer (see format codes)                                           1      65     113    0.75
FD approximation source/sink parameter (dimensionless):            200
Subvoxel growth acceleration factor (dimensionless, 0=none):       2.8284
Random seed (0=generate new):                                      -1717
Volume fraction of porphyroblast in CAP assemblage (fv):           0.7490
Number of moles of porphyroblast in reaction equation (moles):     1.0
Concentration to delGrxn conversion power-law factor n:            1.4009
Free energy specification mode (0=thermo, 1=delGrxn path):         1
Equilibrium temperature used for G-C conversion (°C):              528
Number of Time-Temp-DelGrxn triplets:                              3
DelGrxn path (Myr after start,°C,kJ/mol): (0.0,485.0,-0.0001)    (5.0,600.0,-12.8826)    (30.0,600.0,-12.8826)
```

AG4

Simulation: AG4_110920_1501

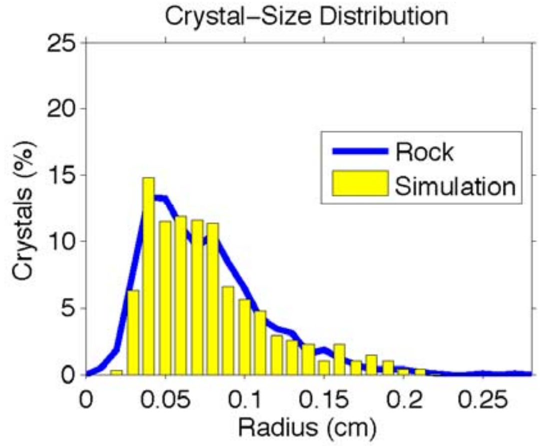

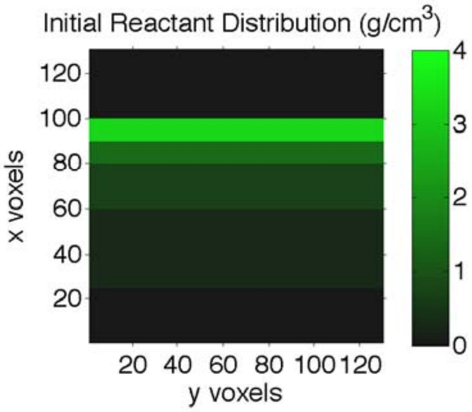

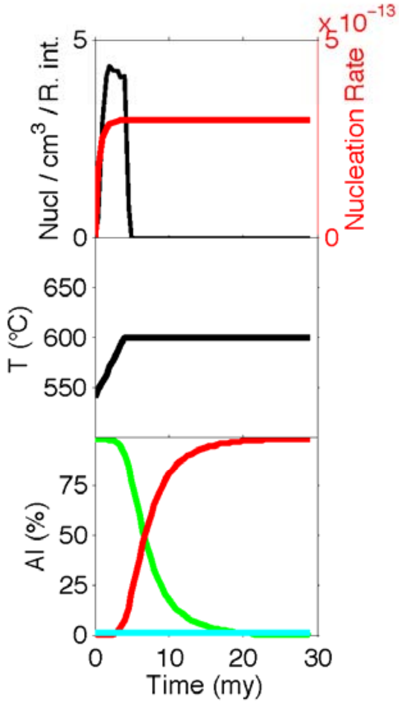

	Rock	Simulation
Total crystals:	1429	1000
Xtl Num Density (xtls/cm^3):	28	29
Crystallization duration (my):	>4	14.5[a]
Equil T of rxn (°C):	540	540
Thermal overstepping (°C):		4
T at 95% Al in products (°C):	600	600[a]
Min radius (cm):	0.012	0.021
Mean radius (cm):	0.074	0.078
Max radius (cm):	0.271	0.221
Mode (vol%):	9.0	9.2
D_{inf} (cm^2/s):		1.00e-005
$[Al]_{fl}$ in eq w/products (mol/cm^3):		1.80e-006
Porosity, ϕ:		1.00e+001
Tortuosity, τ:		1.00e+000
Q_D (kJ/mol):		140
$D = D_{inf} \phi \tau e^{(-Q_D/RT)}$ (m^2/s):		4.22e-017[a]
(at characteristic T, 600°C or 4.0 my)[a]		
$(dN/dt)_{steady-state}, k_1$ (nucl/cm^3/s):		3.00e-013
$(dN/dt)_{max}$ (nucl/cm^3/s):		2.95e-013
Nucleation acceleration, k_2:		5.00e-003
Time step (y):		200
Reporting interval (y):		5.00e+005

[a] Determined at nearest reporting interval

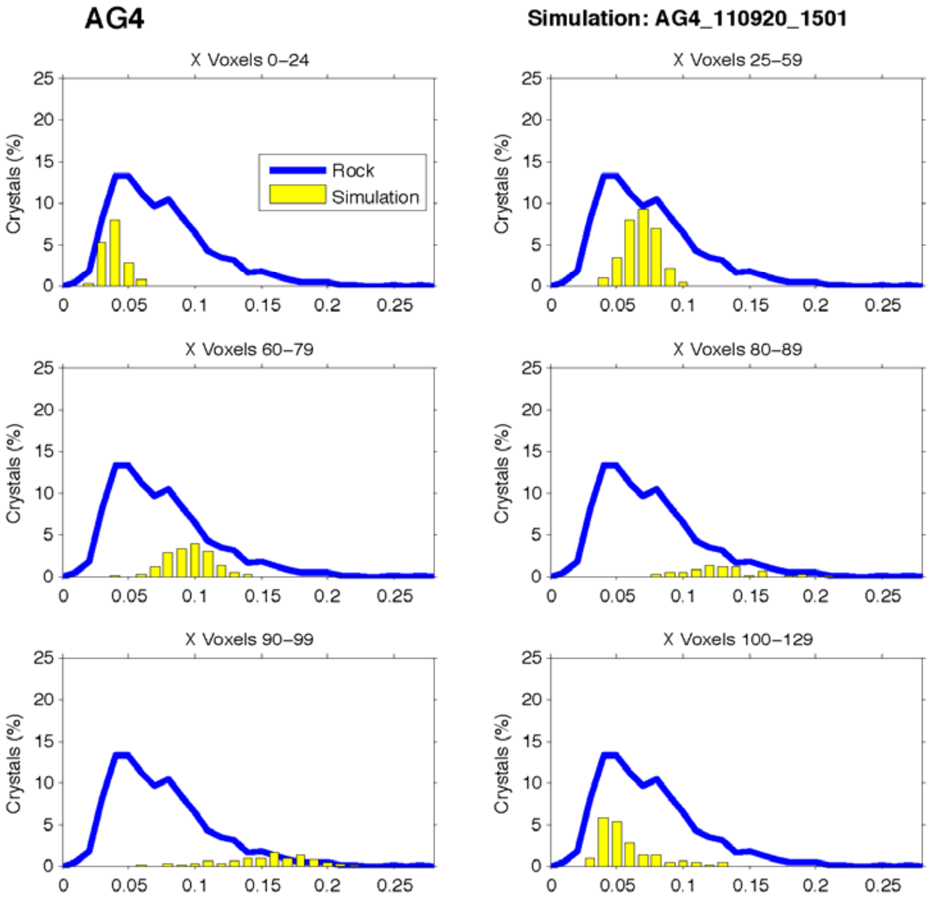
AG4
Simulation: AG4_110920_1501
X Voxels 0–24
X Voxels 25–59
X Voxels 60–79
X Voxels 80–89
X Voxels 90–99
X Voxels 100–129
Crystals (%)
0
5
10
15
20
25
0
0.05
0.1
0.15
0.2
0.25
Rock
Simulation

Parameters File

```
Crystallize 1.3
Run name:                                                             AG4_110920_1501
Result file directory:                                                runsAG4\AG4_110920_1501
Reporting interval (years):                                           5.00E+05
Fractional porosity (0-1):                                            1.00E+01
Tortuosity (0-1):                                                     1.0
Activation energy for diffusion (kJ/mol):                             140
Dinf (cm^2/s):                                                        1.00E-05
Al concentration in fluid in eq with CAP (moles/cm^3):                1.80E-06
Nucleation acceleration (dimensionless):                              5.00E-03
Nucleation rate at infinite overstepping (nuclei/s/cm^3):             3.00E-13
Nucleation proportional to CAR amount in voxel (0=no,1=yes):          0
Maximum number of porphyroblasts (0=unlimited):                       1000
Maximum modal amount of product (0=limited by reactant amount):       0
Al content of CAR (moles Al/moles CAR):                               2.25
Avg. formula weight of CAR (g CAR / mol CAR):                         679.770
Al content of CAP (moles Al/moles CAP):                               2.25
Avg. formula weight of CAP (g CAP / mol CAP):                         625.725
Density of CAP (g/cm^3):                                              4.07
Voxel edge length (cm):                                               0.025
Time step (yr):                                                       200
Number of voxels in X:                                                130
Number of voxels in Y:                                                130
Number of voxels in Z:                                                130
Dimensions:                                                           3
Default CAR amount (g/cm^3 rock):                                     0.0
**** Reactant distribution: One header line, then one line per layer ****
Number of structures (0=homogeneous):                                 4
Layer (see format codes)                                              1      25      59      0.30
Layer (see format codes)                                              1      60      79      0.70
Layer (see format codes)                                              1      80      89      1.40
Layer (see format codes)                                              1      90      99      3.30
FD approximation source/sink parameter (dimensionless):               200
Subvoxel growth acceleration factor (dimensionless, 0=none):          2.8284
Random seed (0=generate new):                                         -1717
Volume fraction of porphyroblast in CAP assemblage (fv):              0.7490
Number of moles of porphyroblast in reaction equation (moles):        1.0
Concentration to delGrxn conversion power-law factor n:               1.6201
Free energy specification mode (0=thermo, 1=delGrxn path):            1
Equilibrium temperature used for G-C conversion (°C):                 530
Number of Time-Temp-DelGrxn triplets:                                 3
DelGrxn path (Myr after start,°C,kJ/mol): (0.0,540.0,-0.0001)    (4.0,600.0,-6.3299)    (30.0,600.0,-6.3299)
```

MD

Simulation: MD_110816_1842

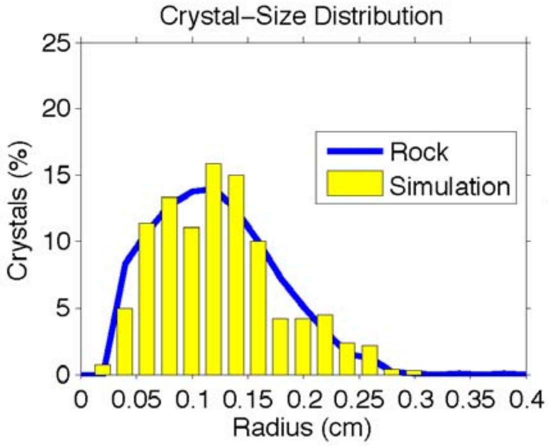

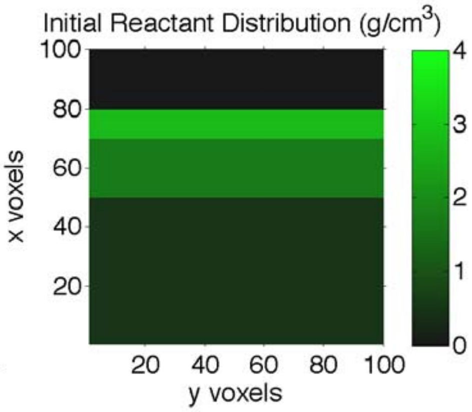

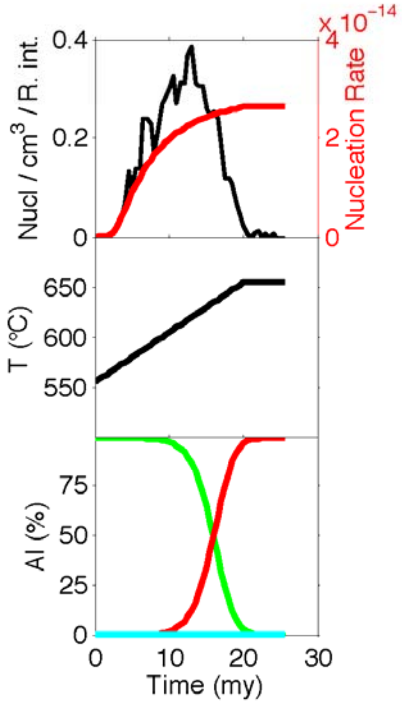

	Rock	Simulation
Total crystals:	1698	1199
Xtl Num Density (xtls/cm^3):	7	7
Crystallization duration (my):	20	17.0[a]
Equil T of rxn (°C):	555	555
Thermal overstepping (°C):		11
T at 95% Al in products (°C):	630–710	653[a]
Min radius (cm):	0.035	0.018
Mean radius (cm):	0.121	0.126
Max radius (cm):	0.388	0.310
Mode (vol%):	8.8	8.5
D_{inf} (cm^2/s):		2.00e-005
$[Al]_{fl}$ in eq w/products (mol/cm^3):		5.80e-006
Porosity, ϕ:		3.00e+000
Tortuosity, τ:		1.00e+000
Q_D (kJ/mol):		140
$D = D_{inf}\,\phi\,\tau\,e^{(-Q_D/RT)}$ (m^2/s): (at characteristic T, 630°C or 15.0 my)[a]		4.80e-017[a]
$(dN/dt)_{steady-state}, k_1$ (nucl/cm^3/s):		3.00e-014
$(dN/dt)_{max}$ (nucl/cm^3/s):		2.63e-014
Nucleation acceleration, k_2:		1.00e-001
Time step (y):		200
Reporting interval (y):		5.00e+005

[a] Determined at nearest reporting interval

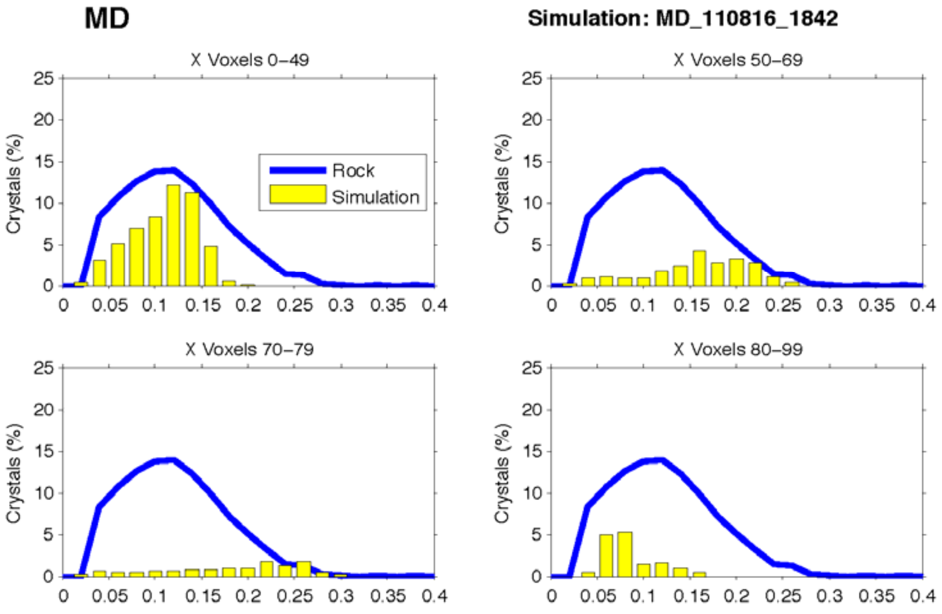
MD
Simulation: MD_110816_1842
X Voxels 0–49
X Voxels 50–69
X Voxels 70–79
X Voxels 80–99
Crystals (%)
25
20
15
10
5
0
0
0.05
0.1
0.15
0.2
0.25
0.3
0.35
0.4
Rock
Simulation

Parameters File

```
Crystallize 1.3
Run name:                                                        MD_110816_1842
Result file directory:                                           runsMD\MD_110816_1842
Reporting interval (years):                                      5.00E+05
Fractional porosity (0-1):                                       3.00E+00
Tortuosity (0-1):                                                1.0
Activation energy for diffusion (kJ/mol):                        140
Dinf (cm^2/s):                                                   2.00E-05
Al concentration in fluid in eq with CAP (moles/cm^3):           5.80E-06
Nucleation acceleration (dimensionless):                         1.00E-01
Nucleation rate at infinite overstepping (nuclei/s/cm^3):        3.00E-14
Nucleation proportional to CAR amount in voxel (0=no,1=yes):     0
Maximum number of porphyroblasts (0=unlimited):                  0
Maximum modal amount of product (0=limited by reactant amount):  0
Al content of CAR (moles Al/moles CAR):                          7.0
Avg. formula weight of CAR (g CAR / mol CAR):                    1423.810
Al content of CAP (moles Al/moles CAP):                          7.0
Avg. formula weight of CAP (g CAP / mol CAP):                    1333.730
Density of CAP (g/cm^3):                                         3.73
Voxel edge length (cm):                                          0.055
Time step (yr):                                                  200
Number of voxels in X:                                           100
Number of voxels in Y:                                           100
Number of voxels in Z:                                           100
Dimensions:                                                      3
Default CAR amount (g/cm^3 rock):                                0.00
**** Reactant distribution: One header line, then one line per layer ****
Number of structures (0=homogeneous):                            4
Layer (see format codes)                                         1      0      49     0.50
Layer (see format codes)                                         1      50     69     1.70
Layer (see format codes)                                         1      70     79     2.80
Layer (see format codes)                                         1      80     99     0.01
FD approximation source/sink parameter (dimensionless):          200
Subvoxel growth acceleration factor (dimensionless, 0=none):     2.8284
Random seed (0=generate new):                                    -1717
Volume fraction of porphyroblast in CAP assemblage (fv):         0.40
Number of moles of porphyroblast in reaction equation (moles):   1.0
Concentration to delGrxn conversion power-law factor n:          1.4035
Free energy specification mode (0=thermo, 1=delGrxn path):       1
Equilibrium temperature used for G-C conversion (°C):            570
Number of Time-Temp-DelGrxn triplets:                            3
DelGrxn path (Myr after start,°C,kJ/mol): (0.0,555.0,-0.0001)    (20.0,655.0,-31.0630)    (30.0,655.0,-31.0630)
```

Jen

Simulation: Jen_111031_0837

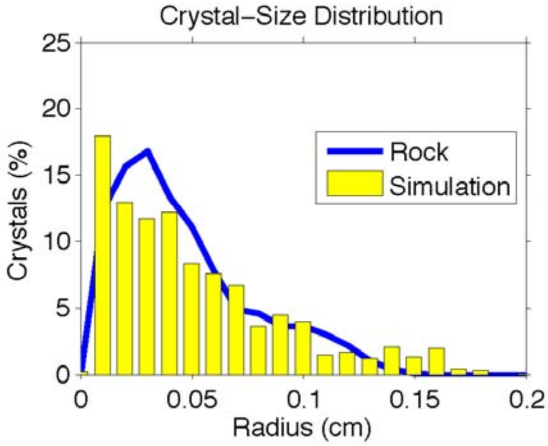

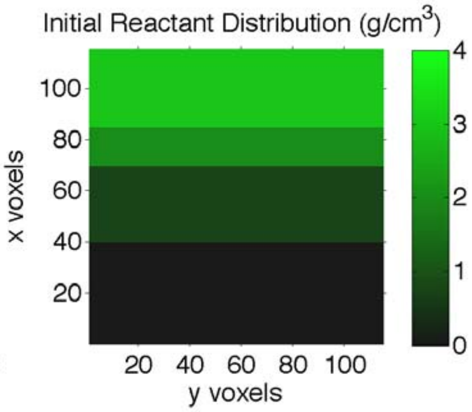

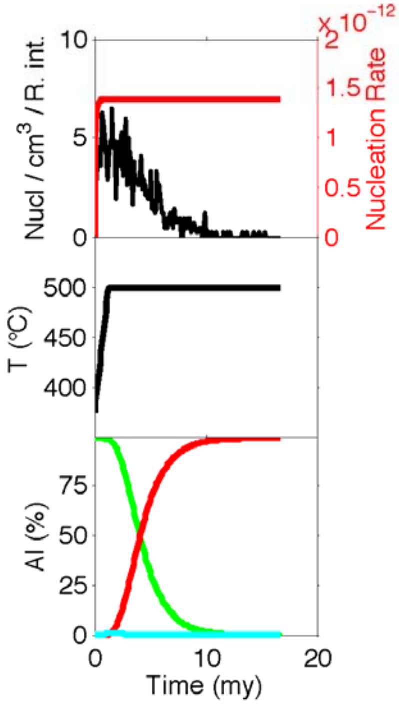

	Rock	Simulation
Total crystals:	1570	973
Xtl Num Density (xtls/cm^3):	239	233
Crystallization duration (my):	1.25	8.2[a]
Equil T of rxn (°C):	375	375
Thermal overstepping (°C):		6
T at 95% Al in products (°C):	500	500[a]
Min radius (cm):	0.006	0.004
Mean radius (cm):	0.046	0.052
Max radius (cm):	0.150	0.204
Mode (vol%):	28.1	28.0
D_{inf} (cm^2/s):		4.00e-005
$[Al]_{fl}$ in eq w/products (mol/cm^3):		1.60e-006
Porosity, ϕ:		1.30e+001
Tortuosity, τ:		1.00e+000
Q_D (kJ/mol):		140
$D = D_{inf} \phi \tau e^{(-Q_D/RT)}$ (m^2/s):		1.81e-017[a]
(at characteristic T, 500°C or 1.3 my)[a]		
$(dN/dt)_{steady-state}, k_1$ (nucl/cm^3/s):		1.40e-012
$(dN/dt)_{max}$ (nucl/cm^3/s):		1.40e-012
Nucleation acceleration, k_2:		1.00e-003
Time step (y):		300
Reporting interval (y):		1.00e+005

[a] Determined at nearest reporting interval

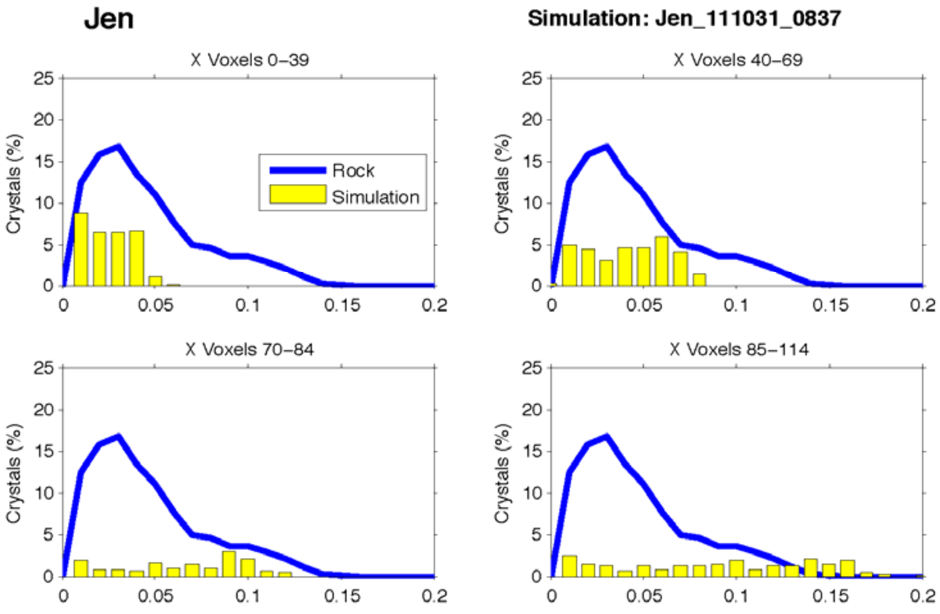

Jen

Simulation: Jen_111031_0837

X Voxels 0–39

X Voxels 40–69

X Voxels 70–84

X Voxels 85–114

Parameters File

```
Crystallize 1.3
Run name:                                                            Jen_111031_0837
Result file directory:                                               runsJen\Jen_111031_0837
Reporting interval (years):                                          1.00E+05
Fractional porosity (0-1):                                           1.30E+01
Tortuosity (0-1):                                                    1.0
Activation energy for diffusion (kJ/mol):                            140
Dinf (cm^2/s):                                                       4.00E-05
Al concentration in fluid in eq with CAP (moles/cm^3):               1.60E-06
Nucleation acceleration (dimensionless):                             1.00E-03
Nucleation rate at infinite overstepping (nuclei/s/cm^3):            1.40E-12
Nucleation proportional to CAR amount in voxel (0=no,1=yes):         0
Maximum number of porphyroblasts (0=unlimited):                      0
Maximum modal amount of product (0=limited by reactant amount):      0
Al content of CAR (moles Al/moles CAR):                              2.6667
Avg. formula weight of CAR (g CAR / mol CAR):                        777.164
Al content of CAP (moles Al/moles CAP):                              2.6667
Avg. formula weight of CAP (g CAP / mol CAP):                        756.819
Density of CAP (g/cm^3):                                             3.51
Voxel edge length (cm):                                              0.014
Time step (yr):                                                      300
Number of voxels in X:                                               115
Number of voxels in Y:                                               115
Number of voxels in Z:                                               115
Dimensions:                                                          3
Default CAR amount (g/cm^3 rock):                                    0.00
**** Reactant distribution: One header line, then one line per layer ****
Number of structures (0=homogeneous):                                4
Layer (see format codes)                                             1      0      39     0.05
Layer (see format codes)                                             1      40     69     0.75
Layer (see format codes)                                             1      70     84     2.00
Layer (see format codes)                                             1      85     114    3.00
FD approximation source/sink parameter (dimensionless):              200
Subvoxel growth acceleration factor (dimensionless, 0=none):         2.8284
Random seed (0=generate new):                                        -1717
Volume fraction of porphyroblast in CAP assemblage (fv):             0.81
Number of moles of porphyroblast in reaction equation (moles):       1.0
Concentration to delGrxn conversion power-law factor n:              1.8483
Free energy specification mode (0=thermo, 1=delGrxn path):           1
Equilibrium temperature used for G-C conversion (°C):                375
Number of Time-Temp-DelGrxn triplets:                                3
DelGrxn path (Myr after start,°C,kJ/mol): (0.0,375.0,-0.0001)    (1.25,500.0,-7.5501)    (30.0,500.0,-7.5501)
```

HE1

Simulation: HE1_111026_1912

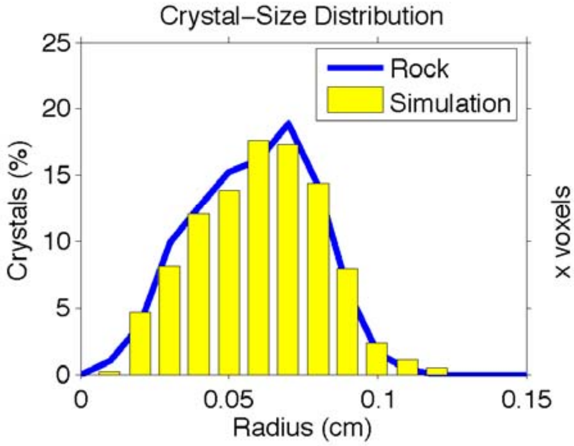

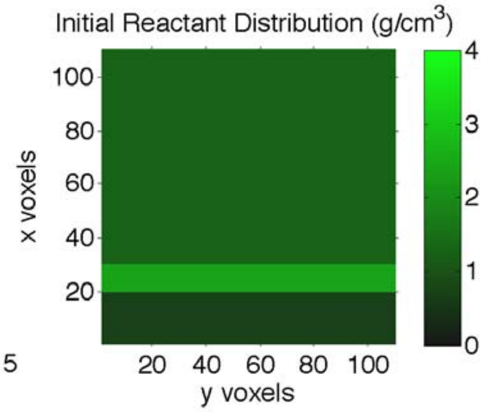

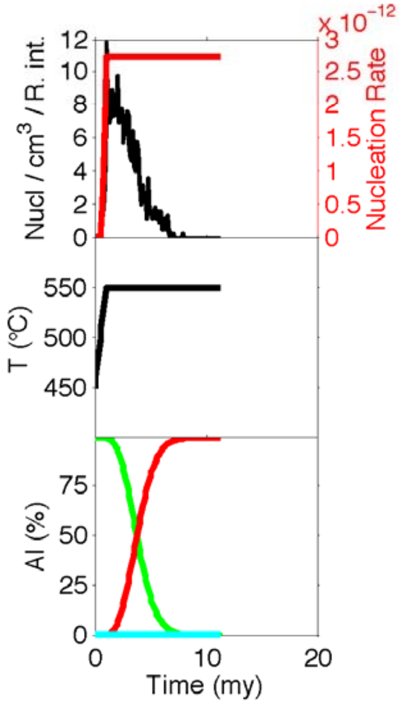

	Rock	Simulation
Total crystals:	2306	1171
Xtl Num Density (xtls/cm^3):	263	261
Crystallization duration (my):	1	5.5[a]
Equil T of rxn (°C):	450	450
Thermal overstepping (°C):		62
T at 95% Al in products (°C):	550	550[a]
Min radius (cm):	0.008	0.012
Mean radius (cm):	0.059	0.060
Max radius (cm):	0.113	0.124
Mode (vol%):	29.2	28.7
D_{inf} (cm^2/s):		2.00e-005
$[Al]_{fl}$ in eq w/products (mol/cm^3):		5.50e-006
Porosity, ϕ:		3.00e+000
Tortuosity, τ:		1.00e+000
Q_D (kJ/mol):		140
$D = D_{inf}\,\phi\,\tau\,e^{(-Q_D/RT)}$ (m^2/s): (at characteristic T, 550°C or 1.0 my)[a]		7.84e-018[a]
$(dN/dt)_{steady-state}, k_1$ (nucl/cm^3/s):		1.30e-011
$(dN/dt)_{max}$ (nucl/cm^3/s):		2.73e-012
Nucleation acceleration, k_2:		5.00e-001
Time step (y):		200
Reporting interval (y):		1.00e+005

[a] Determined at nearest reporting interval

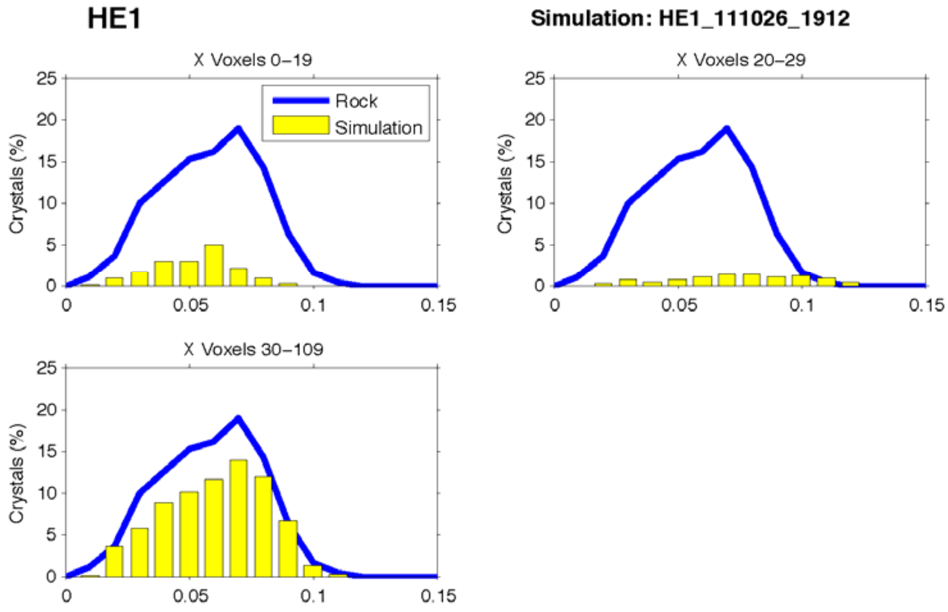
HE1
Simulation: HE1_111026_1912
X Voxels 0–19
X Voxels 20–29
X Voxels 30–109
Rock
Simulation
Crystals (%)
0
5
10
15
20
25
0
0.05
0.1
0.15

Parameters File

```
Crystallize 1.3
Run name:                                                           HE1_111026_1912
Result file directory:                                              runsHE1\HE1_111026_1912
Reporting interval (years):                                         1.00E+05
Fractional porosity (0-1):                                          3.00E+00
Tortuosity (0-1):                                                   1.0
Activation energy for diffusion (kJ/mol):                           140
Dinf (cm^2/s):                                                      2.00E-05
Al concentration in fluid in eq with CAP (moles/cm^3):              5.50E-06
Nucleation acceleration (dimensionless):                            5.00E-01
Nucleation rate at infinite overstepping (nuclei/s/cm^3):           1.30E-11
Nucleation proportional to CAR amount in voxel (0=no,1=yes):        0
Maximum number of porphyroblasts (0=unlimited):                     0
Maximum modal amount of product (0=limited by reactant amount):     0
Al content of CAR (moles Al/moles CAR):                             2.6667
Avg. formula weight of CAR (g CAR / mol CAR):                       777.164
Al content of CAP (moles Al/moles CAP):                             2.6667
Avg. formula weight of CAP (g CAP / mol CAP):                       756.819
Density of CAP (g/cm^3):                                            3.51
Voxel edge length (cm):                                             0.015
Time step (yr):                                                     200
Number of voxels in X:                                              110
Number of voxels in Y:                                              110
Number of voxels in Z:                                              110
Dimensions:                                                         3
Default CAR amount (g/cm^3 rock):                                   0
**** Reactant distribution: One header line, then one line per layer ****
Number of structures (0=homogeneous):                               3
Layer (see format codes)                                            1      0      19     0.70
Layer (see format codes)                                            1      20     29     2.40
Layer (see format codes)                                            1      30     109    1.30
FD approximation source/sink parameter (dimensionless):             200
Subvoxel growth acceleration factor (dimensionless, 0=none):        2.8284
Random seed (0=generate new):                                       -1717
Volume fraction of porphyroblast in CAP assemblage (fv):            0.81
Number of moles of porphyroblast in reaction equation (moles):      1.0
Concentration to delGrxn conversion power-law factor n:             1.8593
Free energy specification mode (0=thermo, 1=delGrxn path):          1
Equilibrium temperature used for G-C conversion (°C):               450
Number of Time-Temp-DelGrxn triplets:                               3
DelGrxn path (Myr after start,°C,kJ/mol): (0.0,450.0,-0.0001)   (1.0,550.0,-7.4687)     (30.0,550.0,-7.4687)
```

WR1bt

Simulation: WR1bt_110710_1415

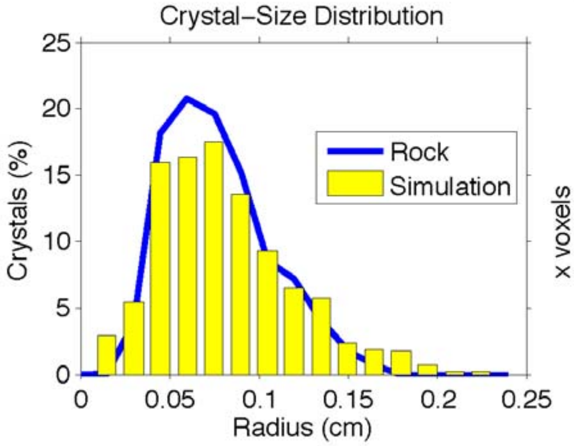

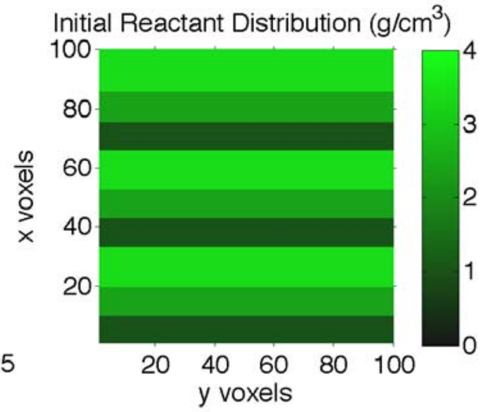

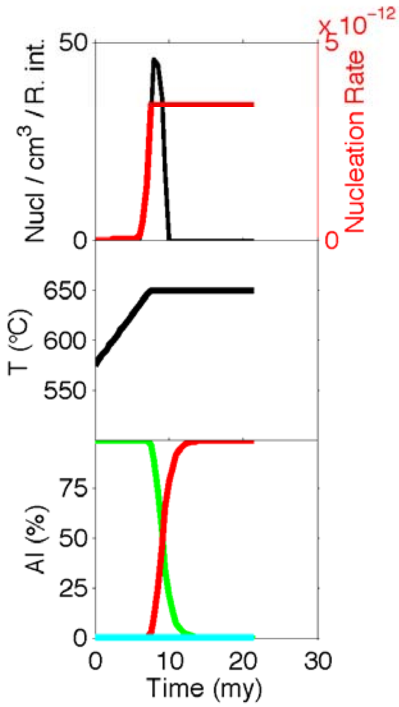

	Rock	Simulation
Total crystals:	1150	1550
Xtl Num Density (xtls/cm^3):	193	194
Crystallization duration (my):	7.5	6.0[a]
Equil T of rxn (°C):	575	575
Thermal overstepping (°C):		55
T at 95% Al in products (°C):	610−690	650[a]
Min radius (cm):	0.017	0.008
Mean radius (cm):	0.077	0.081
Max radius (cm):	0.172	0.222
Mode (vol%):	48.3	45.4
D_{inf} (cm^2/s):		3.00e−006
$[Al]_{fl}$ in eq w/products (mol/cm^3):		1.20e−005
Porosity, ϕ:		1.50e+000
Tortuosity, τ:		1.00e+000
Q_D (kJ/mol):		140
$D = D_{inf} \phi \tau e^{(-Q_D/RT)}$ (m^2/s):		4.88e−018[a]
(at characteristic T, 645°C or 7.0 my)[a]		
$(dN/dt)_{steady-state}, k_1$ (nucl/cm^3/s):		2.00e−008
$(dN/dt)_{max}$ (nucl/cm^3/s):		3.41e−012
Nucleation acceleration, k_2:		3.00e+000
Time step (y):		200
Reporting interval (y):		5.00e+005

[a] Determined at nearest reporting interval

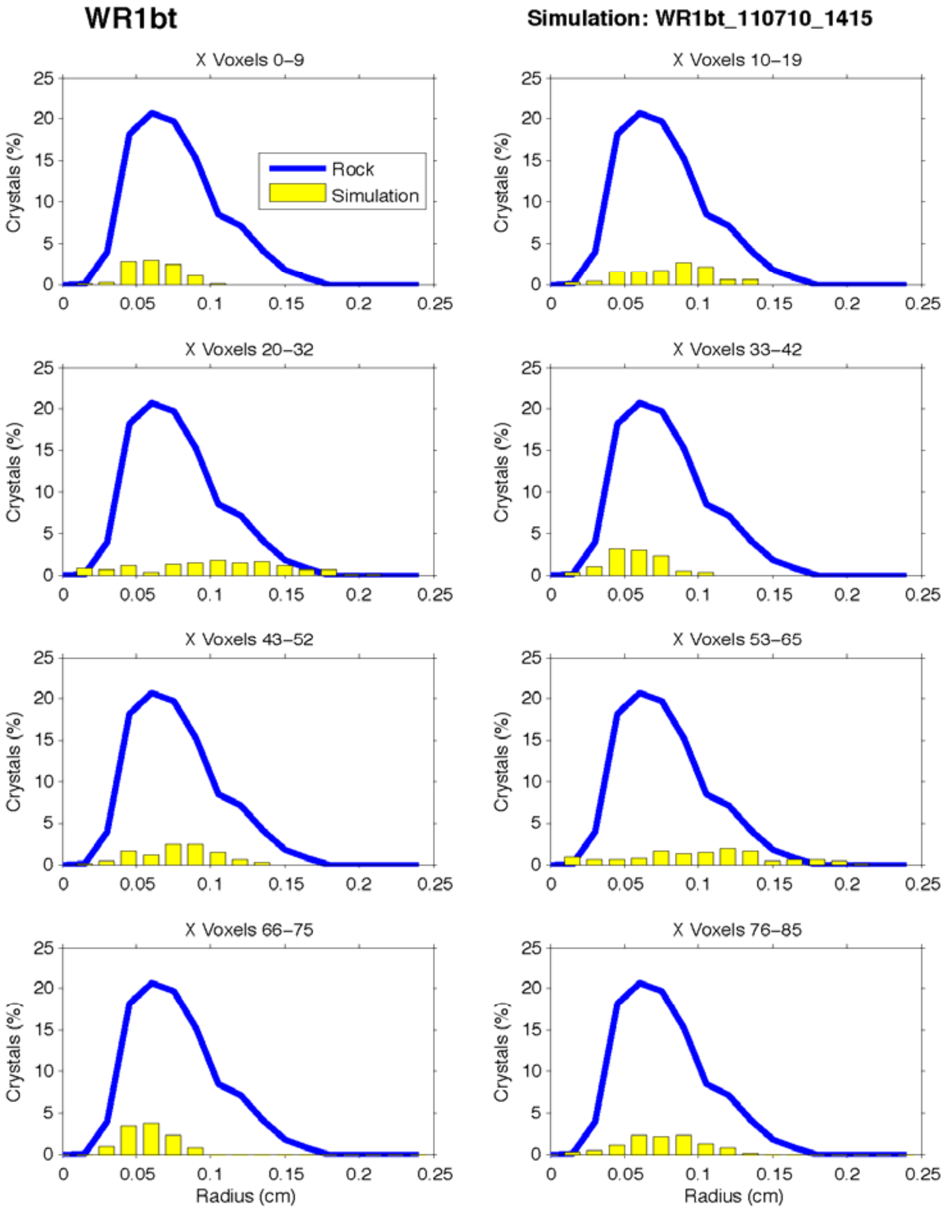
WR1bt

Simulation: WR1bt_110710_1415

X Voxels 0–9

X Voxels 10–19

X Voxels 20–32

X Voxels 33–42

X Voxels 43–52

X Voxels 53–65

X Voxels 66–75

X Voxels 76–85

Parameters File

```
Crystallize 1.3
Run name:                                                         WR1bt_110710_1415
Result file directory:                                            runsWR1bt\WR1bt_110710_1415
Reporting interval (years):                                       5.00E+05
Fractional porosity (0-1):                                        1.50E+00
Tortuosity (0-1):                                                 1.0
Activation energy for diffusion (kJ/mol):                         140
Dinf (cm^2/s):                                                    3.00E-06
Al concentration in fluid in eq with CAP (moles/cm^3):            1.20E-05
Nucleation acceleration (dimensionless):                          3.00E+00
Nucleation rate at infinite overstepping (nuclei/s/cm^3):         2.00E-08
Nucleation proportional to CAR amount in voxel (0=no,1=yes):      0
Maximum number of porphyroblasts (0=unlimited):                   1550
Maximum modal amount of product (0=limited by reactant amount):   0
Al content of CAR (moles Al/moles CAR):                           2.8333
Avg. formula weight of CAR (g CAR / mol CAR):                     810.854
Al content of CAP (moles Al/moles CAP):                           2.8333
Avg. formula weight of CAP (g CAP / mol CAP):                     790.508
Density of CAP (g/cm^3):                                          3.49
Voxel edge length (cm):                                           0.020
Time step (yr):                                                   200
Number of voxels in X:                                            100
Number of voxels in Y:                                            100
Number of voxels in Z:                                            100
Dimensions:                                                       3
Default CAR amount (g/cm^3 rock):                                 1.0
**** Reactant distribution: One header line, then one line per layer ****
Number of structures (0=homogeneous):                             6
Layer (see format codes)                                          1      10     19     2.40
Layer (see format codes)                                          1      20     32     3.40
Layer (see format codes)                                          1      43     52     2.40
Layer (see format codes)                                          1      53     65     3.40
Layer (see format codes)                                          1      76     85     2.40
Layer (see format codes)                                          1      86     99     3.40
FD approximation source/sink parameter (dimensionless):           200
Subvoxel growth acceleration factor (dimensionless, 0=none):      2.8284
Random seed (0=generate new):                                     -1717
Volume fraction of porphyroblast in CAP assemblage (fv):          0.69
Number of moles of porphyroblast in reaction equation (moles):    1.0
Concentration to delGrxn conversion power-law factor n:           1.2574
Free energy specification mode (0=thermo, 1=delGrxn path):        1
Equilibrium temperature used for G-C conversion (°C):             575
Number of Time-Temp-DelGrxn triplets:                             3
DelGrxn path (Myr after start,°C,kJ/mol): (0.0,575.0,-0.0001)   (7.5,650.0,-7.3434)   (30.0,650.0,-7.3434)
```

WR1tp

Simulation: WR1tp_110706_1541

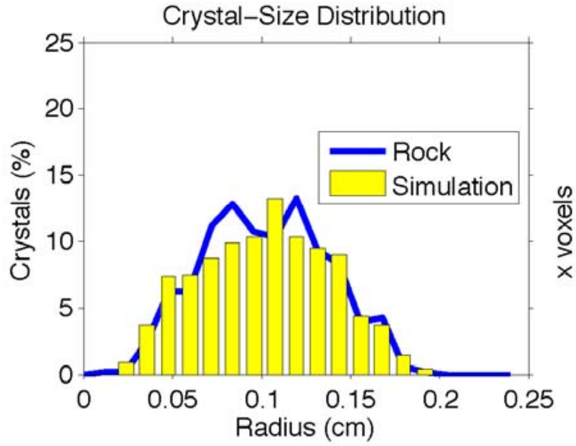

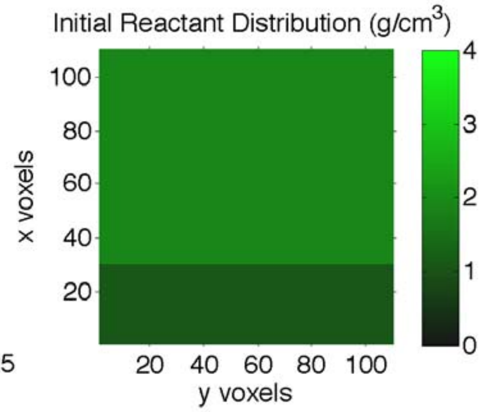

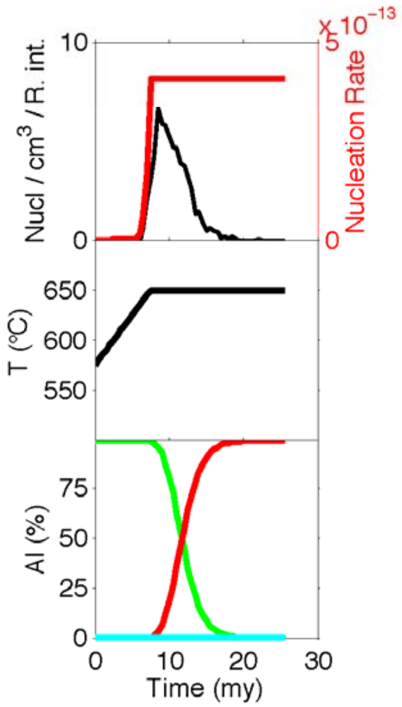

	Rock	Simulation
Total crystals:	514	1143
Xtl Num Density (xtls/cm^3):	64	62
Crystallization duration (my):	7.5	9.5[a]
Equil T of rxn (°C):	575	575
Thermal overstepping (°C):		60
T at 95% Al in products (°C):	610–690	650[a]
Min radius (cm):	0.012	0.022
Mean radius (cm):	0.102	0.102
Max radius (cm):	0.197	0.193
Mode (vol%):	39.3	32.2
D_{inf} (cm^2/s):		4.00e-006
$[Al]_{fl}$ in eq w/products (mol/cm^3):		1.20e-005
Porosity, ϕ:		1.60e+000
Tortuosity, τ:		1.00e+000
Q_D (kJ/mol):		140
$D = D_{inf}\,\phi\,\tau\, e^{(-Q_D/RT)}$ (m^2/s): (at characteristic T, 645°C or 7.0 my)[a]		6.94e-018[a]
$(dN/dt)_{steady-state}, k_1$ (nucl/cm^3/s):		2.40e-009
$(dN/dt)_{max}$ (nucl/cm^3/s):		4.09e-013
Nucleation acceleration, k_2:		3.00e+000
Time step (y):		200
Reporting interval (y):		5.00e+005

[a] Determined at nearest reporting interval

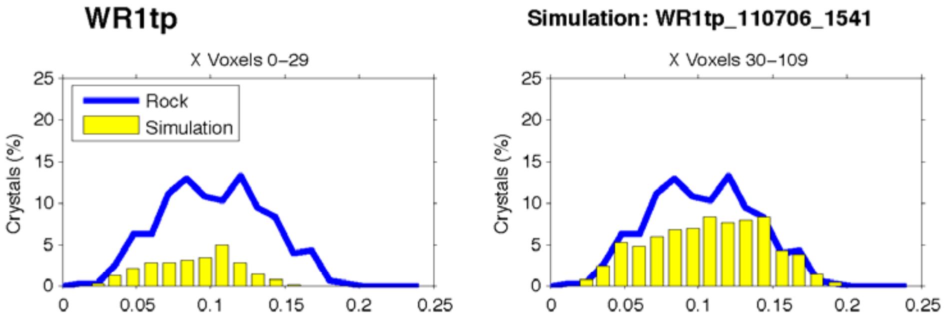
WR1tp
Simulation: WR1tp_110706_1541
X Voxels 0−29
X Voxels 30−109
Rock
Simulation
Crystals (%)
25
20
15
10
5
0
0
0.05
0.1
0.15
0.2
0.25

Parameters File

```
Crystallize 1.3
Run name:                                                          WR1tp_110706_1541
Result file directory:                                             runsWR1tp\WR1tp_110706_1541
Reporting interval (years):                                        5.00E+05
Fractional porosity (0-1):                                         1.60E+00
Tortuosity (0-1):                                                  1.0
Activation energy for diffusion (kJ/mol):                          140
Dinf (cm^2/s):                                                     4.00E-06
Al concentration in fluid in eq with CAP (moles/cm^3):             1.20E-05
Nucleation acceleration (dimensionless):                           3.00E-00
Nucleation rate at infinite overstepping (nuclei/s/cm^3):          2.40E-09
Nucleation proportional to CAR amount in voxel (0=no,1=yes):       0
Maximum number of porphyroblasts (0=unlimited):                    0
Maximum modal amount of product (0=limited by reactant amount):    0
Al content of CAR (moles Al/moles CAR):                            2.8333
Avg. formula weight of CAR (g CAR / mol CAR):                      810.854
Al content of CAP (moles Al/moles CAP):                            2.8333
Avg. formula weight of CAP (g CAP / mol CAP):                      790.508
Density of CAP (g/cm^3):                                           3.49
Voxel edge length (cm):                                            0.024
Time step (yr):                                                    200
Number of voxels in X:                                             110
Number of voxels in Y:                                             110
Number of voxels in Z:                                             110
Dimensions:                                                        3
Default CAR amount (g/cm^3 rock):                                  0.0
**** Reactant distribution: One header line, then one line per layer ****
Number of structures (0=homogeneous):                              2
Layer (see format codes)                                           1      0      29     1.10
Layer (see format codes)                                           1      30     109    1.90
FD approximation source/sink parameter (dimensionless):            200
Subvoxel growth acceleration factor (dimensionless, 0=none):       2.8284
Random seed (0=generate new):                                      -1717
Volume fraction of porphyroblast in CAP assemblage (fv):           0.69
Number of moles of porphyroblast in reaction equation (moles):     1.0
Concentration to delGrxn conversion power-law factor n:            1.2574
Free energy specification mode (0=thermo, 1=delGrxn path):         1
Equilibrium temperature used for G-C conversion (°C):              575
Number of Time-Temp-DelGrxn triplets:                              3
DelGrxn path (Myr after start,°C,kJ/mol): (0.0,575.0,-0.0001)    (7.5,650.0,-7.3434)      (30.0,650.0,-7.3434)
```

WR3m

Simulation: WR3m_110708_1437

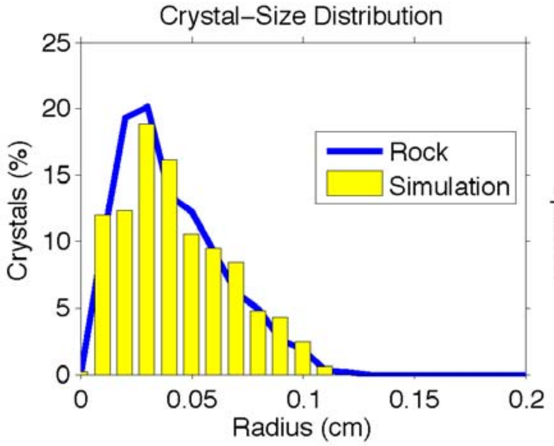

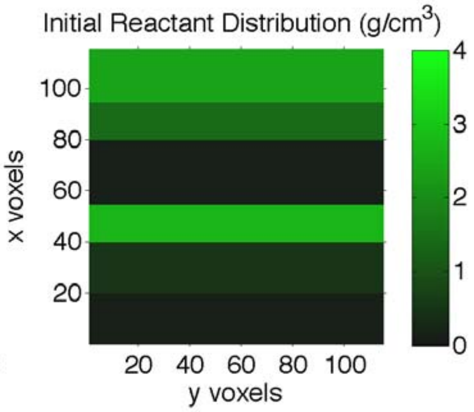

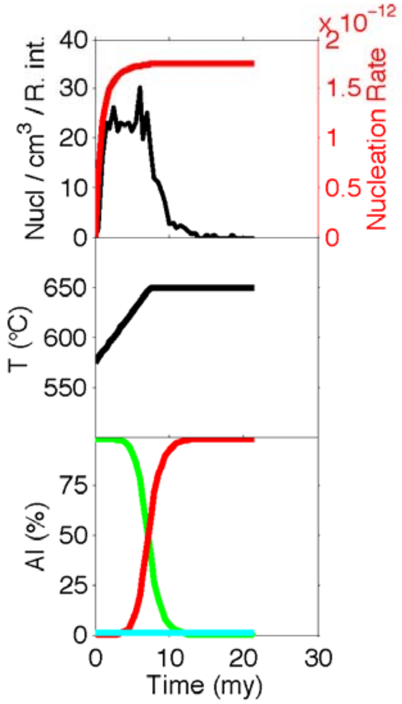

	Rock	Simulation
Total crystals:	986	973
Xtl Num Density (xtls/cm^3):	393	370
Crystallization duration (my):	7.5	10.0[a]
Equil T of rxn (°C):	575	575
Thermal overstepping (°C):		4
T at 95% Al in products (°C):	610–690	650[a]
Min radius (cm):	0.006	0.003
Mean radius (cm):	0.041	0.044
Max radius (cm):	0.123	0.112
Mode (vol%):	23.1	20.6
D_{inf} (cm^2/s):		1.00e–006
$[Al]_{fl}$ in eq w/products (mol/cm^3):		1.20e–005
Porosity, ϕ:		3.00e+000
Tortuosity, τ:		1.00e+000
Q_D (kJ/mol):		140
$D = D_{inf}\,\phi\,\tau\,e^{(-Q_D/RT)}$ (m^2/s):		3.25e–018[a]
(at characteristic T, 645°C or 7.0 my)[a]		
$(dN/dt)_{steady-state}$, k_1 (nucl/cm^3/s):		1.80e–012
$(dN/dt)_{max}$ (nucl/cm^3/s):		1.75e–012
Nucleation acceleration, k_2:		1.00e–002
Time step (y):		200
Reporting interval (y):		5.00e+005

[a] Determined at nearest reporting interval

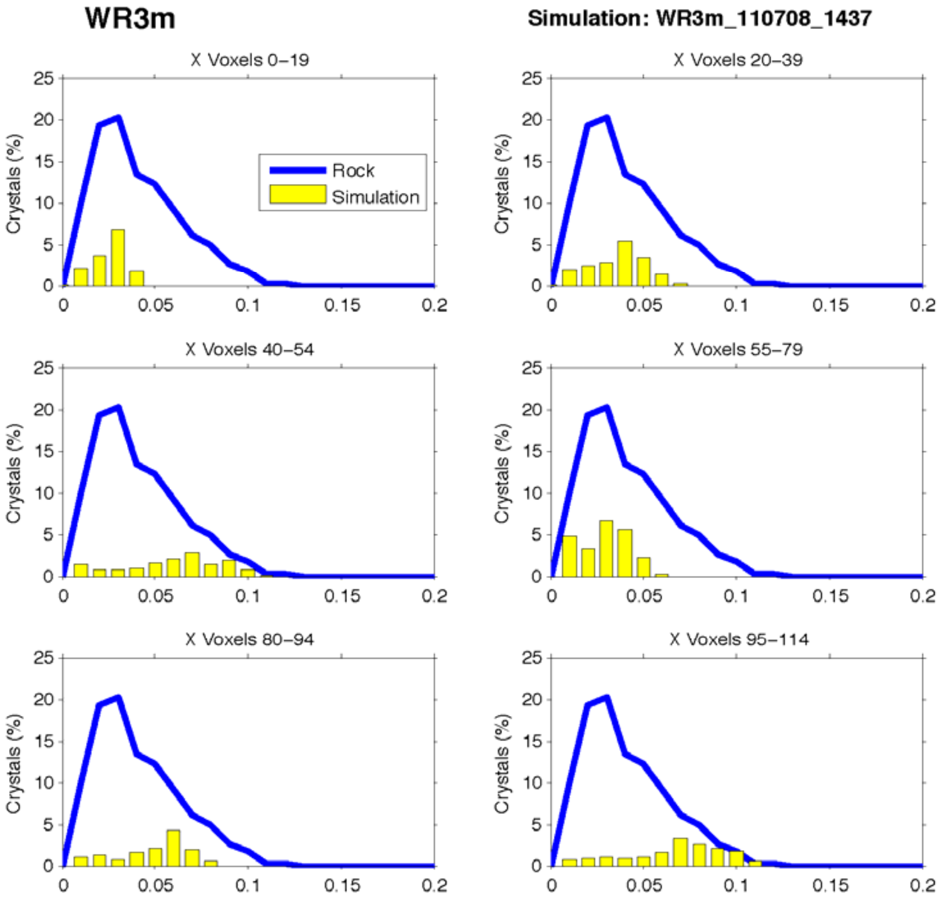
WR3m
Simulation: WR3m_110708_1437
X Voxels 0–19
X Voxels 20–39
X Voxels 40–54
X Voxels 55–79
X Voxels 80–94
X Voxels 95–114
Crystals (%)
0
5
10
15
20
25
0
0.05
0.1
0.15
0.2
Rock
Simulation

Parameters File

```
Crystallize 1.3
Run name:                                                         WR3m_110708_1437
Result file directory:                                            runsWR3m\WR3m_110708_1437
Reporting interval (years):                                       5.00E+05
Fractional porosity (0-1):                                        3.00E+00
Tortuosity (0-1):                                                 1.0
Activation energy for diffusion (kJ/mol):                         140
Dinf (cm^2/s):                                                    1.00E-06
Al concentration in fluid in eq with CAP (moles/cm^3):            1.20E-05
Nucleation acceleration (dimensionless):                          1.00E-02
Nucleation rate at infinite overstepping (nuclei/s/cm^3):         1.80E-12
Nucleation proportional to CAR amount in voxel (0=no,1=yes):      0
Maximum number of porphyroblasts (0=unlimited):                   0
Maximum modal amount of product (0=limited by reactant amount):   0
Al content of CAR (moles Al/moles CAR):                           2.8333
Avg. formula weight of CAR (g CAR / mol CAR):                     810.854
Al content of CAP (moles Al/moles CAP):                           2.8333
Avg. formula weight of CAP (g CAP / mol CAP):                     790.508
Density of CAP (g/cm^3):                                          3.49
Voxel edge length (cm):                                           0.012
Time step (yr):                                                   200
Number of voxels in X:                                            115
Number of voxels in Y:                                            115
Number of voxels in Z:                                            115
Dimensions:                                                       3
Default CAR amount (g/cm^3 rock):                                 0.0
**** Reactant distribution: One header line, then one line per layer ****
Number of structures (0=homogeneous):                             6
Layer (see format codes)                                          1      0      19     0.10
Layer (see format codes)                                          1      20     39     0.50
Layer (see format codes)                                          1      40     54     2.70
Layer (see format codes)                                          1      55     79     0.10
Layer (see format codes)                                          1      80     94     1.40
Layer (see format codes)                                          1      95     114    2.40
FD approximation source/sink parameter (dimensionless):           200
Subvoxel growth acceleration factor (dimensionless, 0=none):      2.8284
Random seed (0=generate new):                                     -1717
Volume fraction of porphyroblast in CAP assemblage (fv):          0.69
Number of moles of porphyroblast in reaction equation (moles):    1.0
Concentration to delGrxn conversion power-law factor n:           1.2574
Free energy specification mode (0=thermo, 1=delGrxn path):        1
Equilibrium temperature used for G-C conversion (°C):             575
Number of Time-Temp-DelGrxn triplets:                             3
DelGrxn path (Myr after start,°C,kJ/mol): (0.0,575.0,-0.0001)    (7.5,650.0,-7.3434)    (30.0,650.0,-7.3434)
```

APPENDIX D: SIMULATIONS FOR SENSITIVITY ANALYSIS

The following simulations are illustrated using PLOTSIM, a program written by the author in MATLAB for reading the CRYSTALLIZE3D output files and summarizing the modeling results. The files read by PLOTSIM are the *.int.txt, *.run.txt, *.xl.txt, and params*.txt file for the given simulation.

Most plots and values are calculated from data in the run file, so the resolution of the data is subject to the reporting interval used in the simulation. Thus, the data points are accurately retrieved from the CRYSTALLIZE3D output to within one reporting interval (500,000 years here). The thermal overstepping value is taken from the xl file and is accurately retrieved from the CRYSTALLIZE3D data to within one degree Celsius.

The number of crystals reported for the rock is not necessarily the same as reported from REDUCE3D (Hirsch, 2011). The values reported here are taken from a compilation of BLOB3D (Ketcham, 2005a) “integrate” files and are only used for comparison of the crystal-size distribution between the natural sample and the simulation.

The crystal number density, radii measurements, and mode for each simulation were taken from REDUCE3D 2.58 output calculated in previous studies.

The version of CRYSTALLIZE3D used for all simulations in this dissertation is 1.3 (last modified March 4, 2011 at 13:47).

The version of REDUCE3D (Hirsch, 2011) used for all PCF and MCF calculations in this dissertation is 3.30.

PM1

Simulation: PM1_110927_0801_SAk1–06

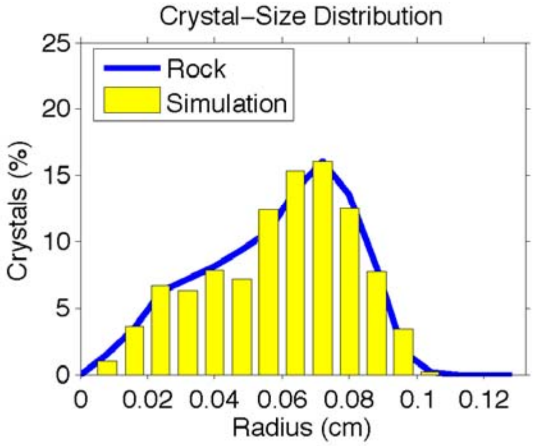

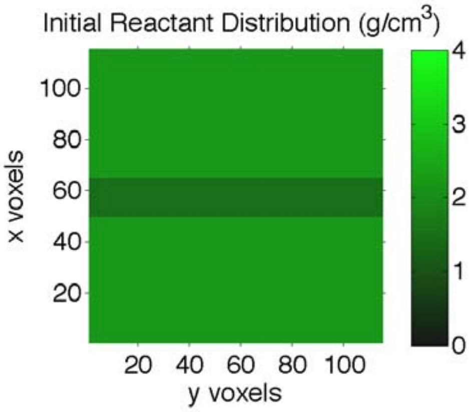

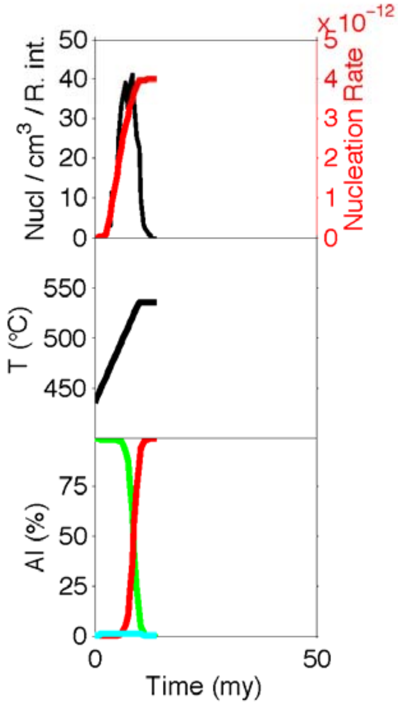

	Rock	Simulation
Total crystals:	1748	1020
Xtl Num Density (xtls/cm^3):	382	388
Crystallization duration (my):	10	8.0[a]
Equil T of rxn (°C):	unknown	435
Thermal overstepping (°C):		23
T at 95% Al in products (°C):	535	535[a]
Min radius (cm):	0.006	0.009
Mean radius (cm):	0.058	0.059
Max radius (cm):	0.104	0.101
Mode (vol%):	37.4	38.0
D_{inf} (cm^2/s):		5.00e-006
$[Al]_{fl}$ in eq w/products (mol/cm^3):		5.60e-007
Porosity, ϕ:		8.00e+001
Tortuosity, τ:		1.00e+000
Q_D (kJ/mol):		140
$D = D_{inf}\,\phi\,\tau\,e^{(-Q_D/RT)}$ (m^2/s):		2.11e-017[a]
(at characteristic T, 515°C or 8.0 my)[a]		
$(dN/dt)_{steady\text{-}state}$, k_1 (nucl/cm^3/s):		5.40e-012
$(dN/dt)_{max}$ (nucl/cm^3/s):		4.01e-012
Nucleation acceleration, k_2:		1.00e+000
Time step (y):		200
Reporting interval (y):		5.00e+005

[a] Determined at nearest reporting interval

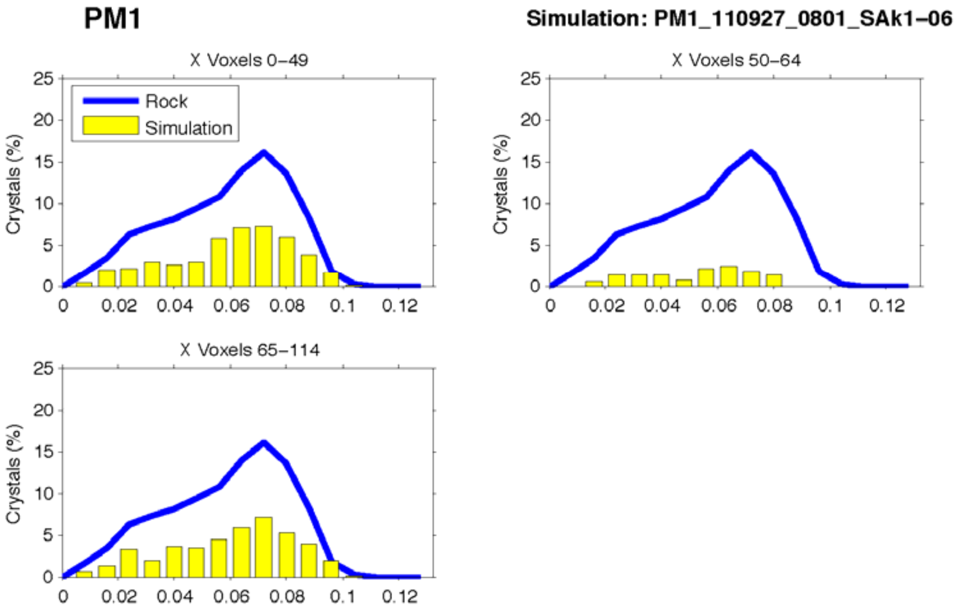

PM1

Simulation: PM1_110927_0801_SAk1–06

Parameters File

```
Crystallize 1.3
Run name:                                                        PM1_110927_0801_SAk1-06
Result file directory:                                           runsPM1\PM1_110927_0801_SAk1-06
Reporting interval (years):                                      5.00E+05
Fractional porosity (0-1):                                       8.00E+01
Tortuosity (0-1):                                                1.0
Activation energy for diffusion (kJ/mol):                        140
Dinf (cm^2/s):                                                   5.00E-06
Al concentration in fluid in eq with CAP (moles/cm^3):           5.60E-07
Nucleation acceleration (dimensionless):                         1.00E-00
Nucleation rate at infinite overstepping (nuclei/s/cm^3):        5.40E-12
Nucleation proportional to CAR amount in voxel (0=no,1=yes):     0
Maximum number of porphyroblasts (0=unlimited):                  0
Maximum modal amount of product (0=limited by reactant amount):  0
Al content of CAR (moles Al/moles CAR):                          2.25
Avg. formula weight of CAR (g CAR / mol CAR):                    634.7072
Al content of CAP (moles Al/moles CAP):                          2.25
Avg. formula weight of CAP (g CAP / mol CAP):                    625.7249
Density of CAP (g/cm^3):                                         4.07
Voxel edge length (cm):                                          0.012
Time step (yr):                                                  200
Number of voxels in X:                                           115
Number of voxels in Y:                                           115
Number of voxels in Z:                                           115
Dimensions:                                                      3
Default CAR amount (g/cm^3 rock):                                2.20
**** Reactant distribution: One header line, then one line per layer ****
Number of structures (0=homogeneous):                            1
Layer (see format codes)                                         1       50      64      1.50
FD approximation source/sink parameter (dimensionless):          200
Subvoxel growth acceleration factor (dimensionless, 0=none):     2.8284
Random seed (0=generate new):                                    -1717
Volume fraction of porphyroblast in CAP assemblage (fv):         0.7490
Number of moles of porphyroblast in reaction equation (moles):   1.0
Concentration to delGrxn conversion power-law factor n:          1.4165
Free energy specification mode (0=thermo, 1=delGrxn path):       1
Equilibrium temperature used for G-C conversion (°C):            528
Number of Time-Temp-DelGrxn triplets:                            3
DelGrxn path (Myr after start,°C,kJ/mol): (0.0,435.0,-0.0001)    (10.0,535.0,-19.0582)    (30.0,535.0,-20.1369)
```

PM1

Simulation: PM1_110927_0801_SAk1–07

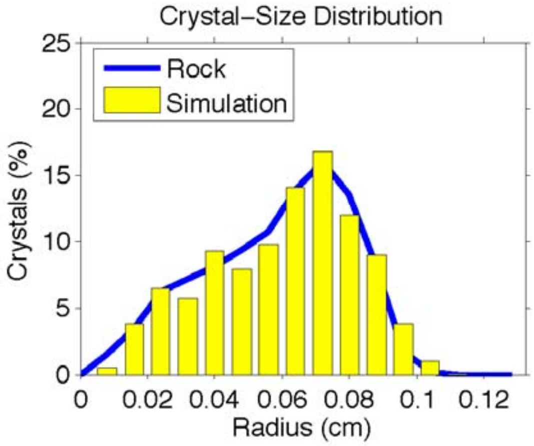

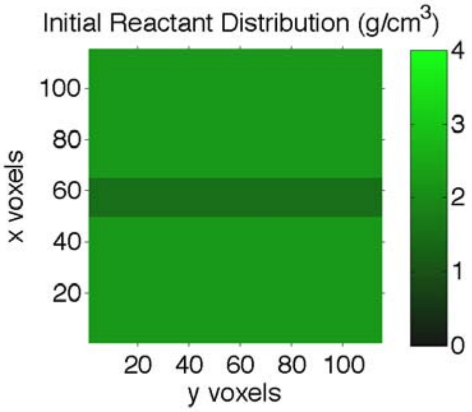

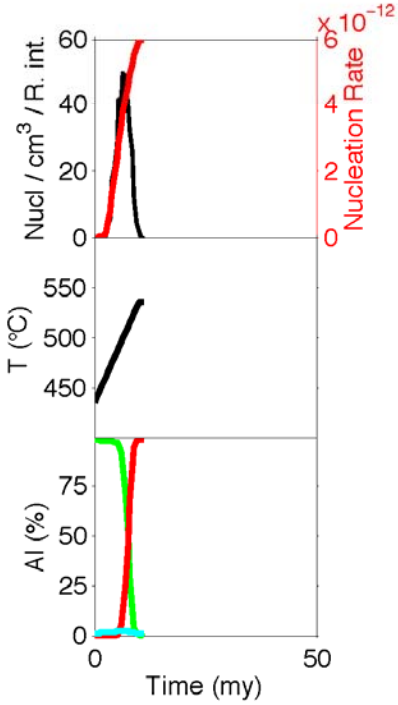

	Rock	Simulation
Total crystals:	1748	981
Xtl Num Density (xtls/cm^3):	382	373
Crystallization duration (my):	10	6.5[a]
Equil T of rxn (°C):	unknown	435
Thermal overstepping (°C):		23
T at 95% Al in products (°C):	535	525[a]
Min radius (cm):	0.006	0.010
Mean radius (cm):	0.058	0.060
Max radius (cm):	0.104	0.114
Mode (vol%):	37.4	38.0
D_{inf} (cm^2/s):		5.00e-006
$[Al]_{fl}$ in eq w/products (mol/cm^3):		5.60e-007
Porosity, ϕ:		1.60e+002
Tortuosity, τ:		1.00e+000
Q_D (kJ/mol):		140
$D = D_{inf}\,\phi\,\tau\,e^{(-Q_D/RT)}$ (m^2/s): (at characteristic T, 510°C or 7.5 my)[a]		3.68e-017[a]
$(dN/dt)_{steady-state}$, k_1 (nucl/cm^3/s):		8.10e-012
$(dN/dt)_{max}$ (nucl/cm^3/s):		5.97e-012
Nucleation acceleration, k_2:		1.00e+000
Time step (y):		200
Reporting interval (y):		5.00e+005

[a] Determined at nearest reporting interval

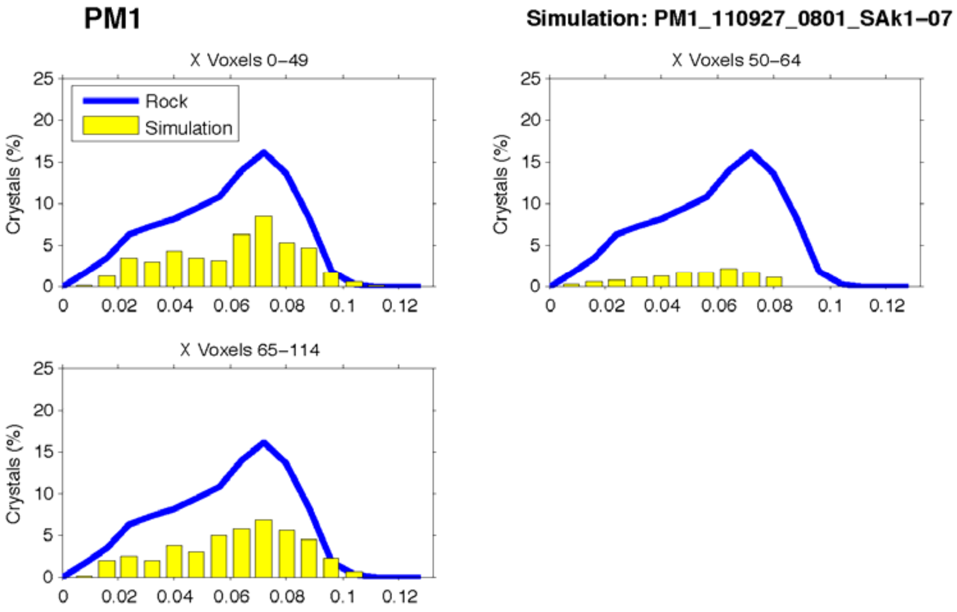
PM1
Simulation: PM1_110927_0801_SAk1-07
X Voxels 0-49
X Voxels 50-64
X Voxels 65-114
Rock
Simulation
Crystals (%)
25
20
15
10
5
0
0
0.02
0.04
0.06
0.08
0.1
0.12

Parameters File

```
Crystallize 1.3
Run name:                                                        PM1_110927_0801_SAk1-07
Result file directory:                                           runsPM1\PM1_110927_0801_SAk1-07
Reporting interval (years):                                      5.00E+05
Fractional porosity (0-1):                                       1.60E+02
Tortuosity (0-1):                                                1.0
Activation energy for diffusion (kJ/mol):                        140
Dinf (cm^2/s):                                                   5.00E-06
Al concentration in fluid in eq with CAP (moles/cm^3):           5.60E-07
Nucleation acceleration (dimensionless):                         1.00E-00
Nucleation rate at infinite overstepping (nuclei/s/cm^3):        8.10E-12
Nucleation proportional to CAR amount in voxel (0=no,1=yes):     0
Maximum number of porphyroblasts (0=unlimited):                  0
Maximum modal amount of product (0=limited by reactant amount):  0
Al content of CAR (moles Al/moles CAR):                          2.25
Avg. formula weight of CAR (g CAR / mol CAR):                    634.7072
Al content of CAP (moles Al/moles CAP):                          2.25
Avg. formula weight of CAP (g CAP / mol CAP):                    625.7249
Density of CAP (g/cm^3):                                         4.07
Voxel edge length (cm):                                          0.012
Time step (yr):                                                  200
Number of voxels in X:                                           115
Number of voxels in Y:                                           115
Number of voxels in Z:                                           115
Dimensions:                                                      3
Default CAR amount (g/cm^3 rock):                                2.20
**** Reactant distribution: One header line, then one line per layer ****
Number of structures (0=homogeneous):                            1
Layer (see format codes)                                         1       50      64      1.50
FD approximation source/sink parameter (dimensionless):          200
Subvoxel growth acceleration factor (dimensionless, 0=none):     2.8284
Random seed (0=generate new):                                    -1717
Volume fraction of porphyroblast in CAP assemblage (fv):         0.7490
Number of moles of porphyroblast in reaction equation (moles):   1.0
Concentration to delGrxn conversion power-law factor n:          1.4165
Free energy specification mode (0=thermo, 1=delGrxn path):       1
Equilibrium temperature used for G-C conversion (°C):            528
Number of Time-Temp-DelGrxn triplets:                            3
DelGrxn path (Myr after start,°C,kJ/mol): (0.0,435.0,-0.0001)    (10.0,535.0,-19.0582)    (30.0,535.0,-20.1369)
```

PM1

Simulation: PM1_110927_0801_SAk2–03

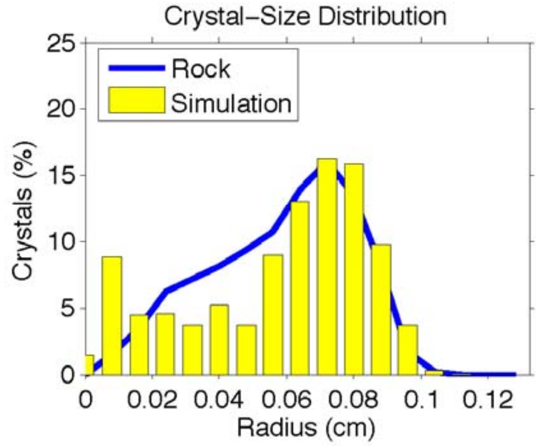

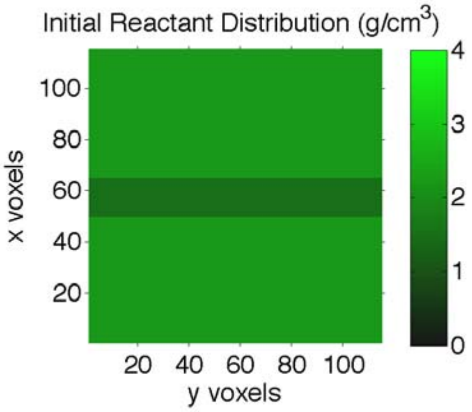

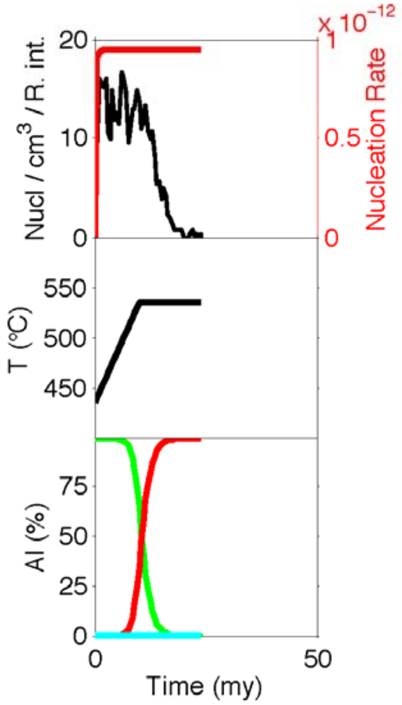

	Rock	Simulation
Total crystals:	1748	983
Xtl Num Density (xtls/cm^3):	382	374
Crystallization duration (my):	10	14.0[a]
Equil T of rxn (°C):	unknown	435
Thermal overstepping (°C):		1
T at 95% Al in products (°C):	535	535[a]
Min radius (cm):	0.006	0.002
Mean radius (cm):	0.058	0.058
Max radius (cm):	0.104	0.113
Mode (vol%):	37.4	38.1
D_{inf} (cm^2/s):		5.00e-006
$[Al]_{fl}$ in eq w/products (mol/cm^3):		5.60e-007
Porosity, ϕ:		3.00e+001
Tortuosity, τ:		1.00e+000
Q_D (kJ/mol):		140
$D = D_{inf}\,\phi\,\tau\,e^{(-Q_D/RT)}$ (m^2/s):		1.03e-017[a]
(at characteristic T, 525°C or 9.0 my)[a]		
$(dN/dt)_{steady-state}$, k_1 (nucl/cm^3/s):		9.50e-013
$(dN/dt)_{max}$ (nucl/cm^3/s):		9.50e-013
Nucleation acceleration, k_2:		1.00e-003
Time step (y):		200
Reporting interval (y):		5.00e+005

[a] Determined at nearest reporting interval

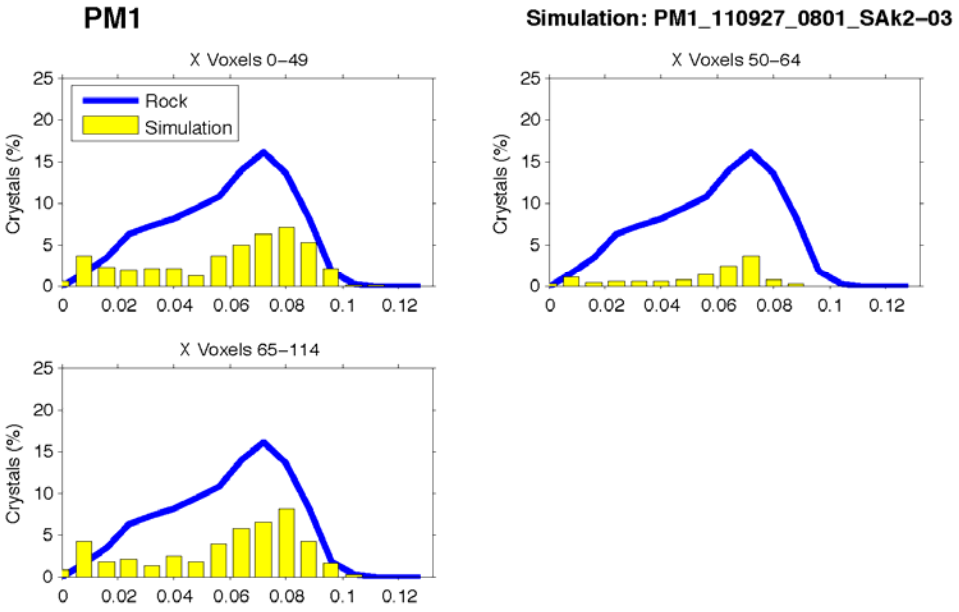

PM1

Simulation: PM1_110927_0801_SAk2–03

X Voxels 0–49

X Voxels 50–64

X Voxels 65–114

Parameters File

```
Crystallize 1.3
Run name:                                                          PM1_110927_0801_SAk2-03
Result file directory:                                             runsPM1\PM1_110927_0801_SAk2-03
Reporting interval (years):                                        5.00E+05
Fractional porosity (0-1):                                         3.00E+01
Tortuosity (0-1):                                                  1.0
Activation energy for diffusion (kJ/mol):                          140
Dinf (cm^2/s):                                                     5.00E-06
Al concentration in fluid in eq with CAP (moles/cm^3):             5.60E-07
Nucleation acceleration (dimensionless):                           1.00E-03
Nucleation rate at infinite overstepping (nuclei/s/cm^3):          9.50E-13
Nucleation proportional to CAR amount in voxel (0=no,1=yes):       0
Maximum number of porphyroblasts (0=unlimited):                    0
Maximum modal amount of product (0=limited by reactant amount):    0
Al content of CAR (moles Al/moles CAR):                            2.25
Avg. formula weight of CAR (g CAR / mol CAR):                      634.7072
Al content of CAP (moles Al/moles CAP):                            2.25
Avg. formula weight of CAP (g CAP / mol CAP):                      625.7249
Density of CAP (g/cm^3):                                           4.07
Voxel edge length (cm):                                            0.012
Time step (yr):                                                    200
Number of voxels in X:                                             115
Number of voxels in Y:                                             115
Number of voxels in Z:                                             115
Dimensions:                                                        3
Default CAR amount (g/cm^3 rock):                                  2.20
**** Reactant distribution: One header line, then one line per layer ****
Number of structures (0=homogeneous):                              1
Layer (see format codes)                                           1      50      64      1.50
FD approximation source/sink parameter (dimensionless):            200
Subvoxel growth acceleration factor (dimensionless, 0=none):       2.8284
Random seed (0=generate new):                                      -1717
Volume fraction of porphyroblast in CAP assemblage (fv):           0.7490
Number of moles of porphyroblast in reaction equation (moles):     1.0
Concentration to delGrxn conversion power-law factor n:            1.4165
Free energy specification mode (0=thermo, 1=delGrxn path):         1
Equilibrium temperature used for G-C conversion (°C):              528
Number of Time-Temp-DelGrxn triplets:                              3
DelGrxn path (Myr after start,°C,kJ/mol): (0.0,435.0,-0.0001)    (10.0,535.0,-19.0582)    (30.0,535.0,-20.1369)
```

PM1

Simulation: PM1_110927_0801_SAk2–04

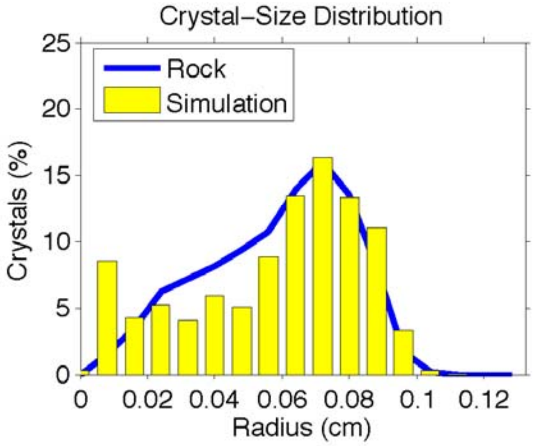

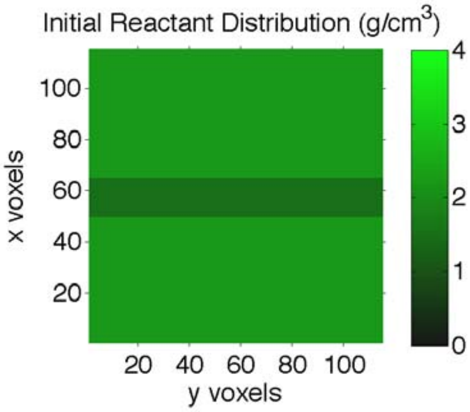

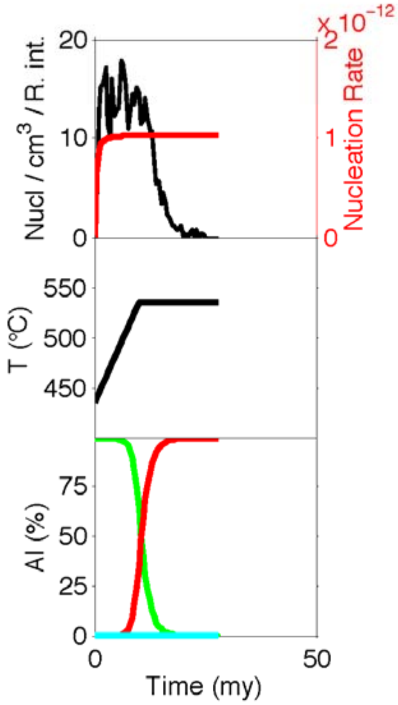

	Rock	Simulation
Total crystals:	1748	1006
Xtl Num Density (xtls/cm^3):	382	383
Crystallization duration (my):	10	14.0[a]
Equil T of rxn (°C):	unknown	435
Thermal overstepping (°C):		3
T at 95% Al in products (°C):	535	535[a]
Min radius (cm):	0.006	0.003
Mean radius (cm):	0.058	0.058
Max radius (cm):	0.104	0.109
Mode (vol%):	37.4	38.0
D_{inf} (cm^2/s):		5.00e-006
$[Al]_{fl}$ in eq w/products (mol/cm^3):		5.60e-007
Porosity, ϕ:		3.00e+001
Tortuosity, τ:		1.00e+000
Q_D (kJ/mol):		140
$D = D_{inf}\phi\tau e^{(-Q_D/RT)}$ (m^2/s):		1.18e-017[a]
(at characteristic T, 530°C or 9.5 my)[a]		
$(dN/dt)_{steady-state}, k_1$ (nucl/cm^3/s):		1.03e-012
$(dN/dt)_{max}$ (nucl/cm^3/s):		1.03e-012
Nucleation acceleration, k_2:		1.00e-002
Time step (y):		200
Reporting interval (y):		5.00e+005

[a] Determined at nearest reporting interval

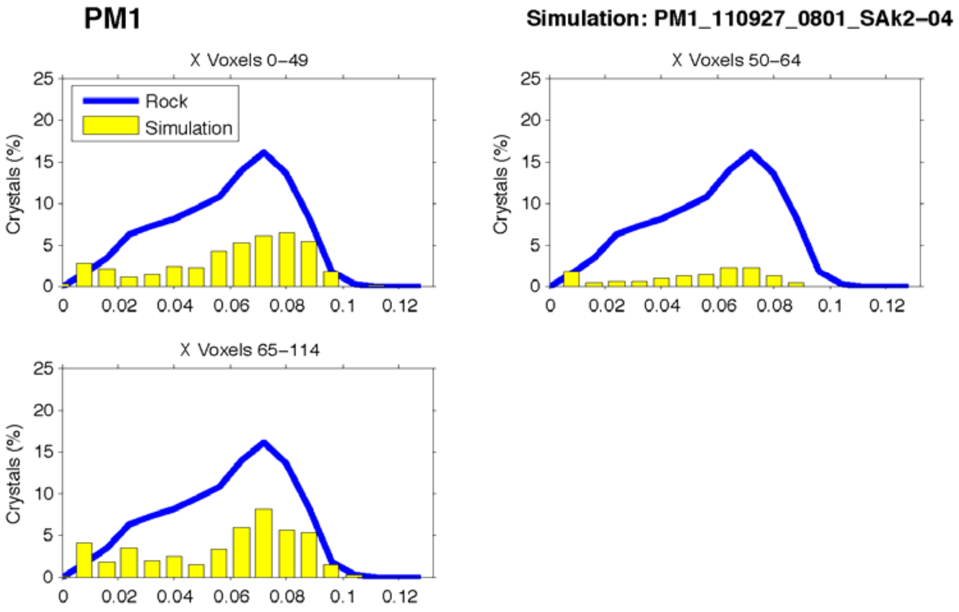
PM1
Simulation: PM1_110927_0801_SAk2–04
X Voxels 0–49
X Voxels 50–64
X Voxels 65–114
Rock
Simulation
Crystals (%)
0
5
10
15
20
25
0
0.02
0.04
0.06
0.08
0.1
0.12

Parameters File

```
Crystallize 1.3
Run name:                                                         PM1_110927_0801_SAk2-04
Result file directory:                                            runsPM1\PM1_110927_0801_SAk2-04
Reporting interval (years):                                       5.00E+05
Fractional porosity (0-1):                                        3.00E+01
Tortuosity (0-1):                                                 1.0
Activation energy for diffusion (kJ/mol):                         140
Dinf (cm^2/s):                                                    5.00E-06
Al concentration in fluid in eq with CAP (moles/cm^3):            5.60E-07
Nucleation acceleration (dimensionless):                          1.00E-02
Nucleation rate at infinite overstepping (nuclei/s/cm^3):         1.03E-12
Nucleation proportional to CAR amount in voxel (0=no,1=yes):      0
Maximum number of porphyroblasts (0=unlimited):                   0
Maximum modal amount of product (0=limited by reactant amount):   0
Al content of CAR (moles Al/moles CAR):                           2.25
Avg. formula weight of CAR (g CAR / mol CAR):                     634.7072
Al content of CAP (moles Al/moles CAP):                           2.25
Avg. formula weight of CAP (g CAP / mol CAP):                     625.7249
Density of CAP (g/cm^3):                                          4.07
Voxel edge length (cm):                                           0.012
Time step (yr):                                                   200
Number of voxels in X:                                            115
Number of voxels in Y:                                            115
Number of voxels in Z:                                            115
Dimensions:                                                       3
Default CAR amount (g/cm^3 rock):                                 2.20
**** Reactant distribution: One header line, then one line per layer ****
Number of structures (0=homogeneous):                             1
Layer (see format codes)                                          1      50      64      1.50
FD approximation source/sink parameter (dimensionless):           200
Subvoxel growth acceleration factor (dimensionless, 0=none):      2.8284
Random seed (0=generate new):                                     -1717
Volume fraction of porphyroblast in CAP assemblage (fv):          0.7490
Number of moles of porphyroblast in reaction equation (moles):    1.0
Concentration to delGrxn conversion power-law factor n:           1.4165
Free energy specification mode (0=thermo, 1=delGrxn path):        1
Equilibrium temperature used for G-C conversion (°C):             528
Number of Time-Temp-DelGrxn triplets:                             3
DelGrxn path (Myr after start,°C,kJ/mol): (0.0,435.0,-0.0001)    (10.0,535.0,-19.0582)    (30.0,535.0,-20.1369)
```

PM1

Simulation: PM1_110927_0801_SAk2–05

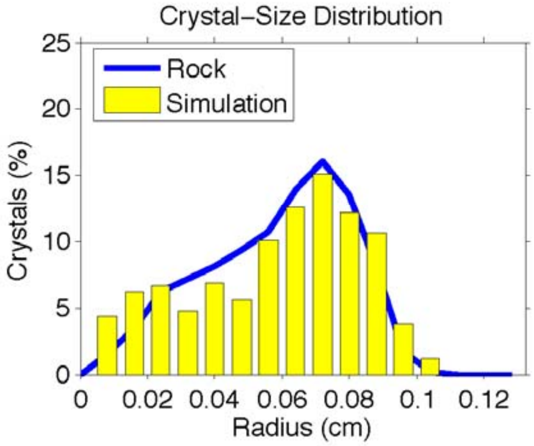

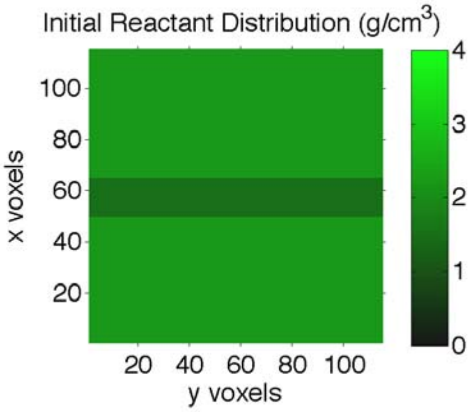

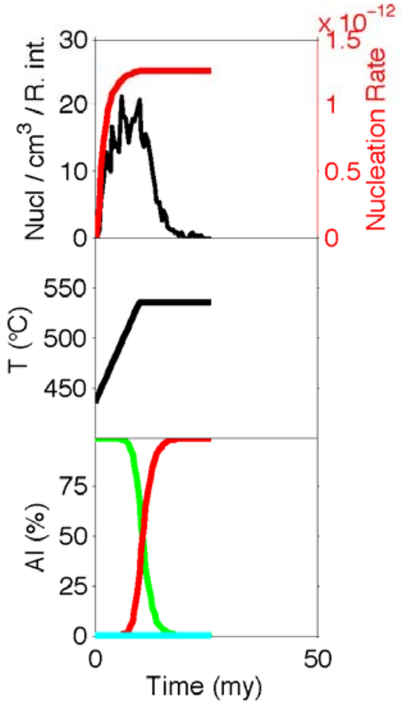

	Rock	Simulation
Total crystals:	1748	1019
Xtl Num Density (xtls/cm^3):	382	388
Crystallization duration (my):	10	14.0[a]
Equil T of rxn (°C):	unknown	435
Thermal overstepping (°C):		7
T at 95% Al in products (°C):	535	535[a]
Min radius (cm):	0.006	0.006
Mean radius (cm):	0.058	0.058
Max radius (cm):	0.104	0.107
Mode (vol%):	37.4	38.0
D_{inf} (cm^2/s):		5.00e-006
$[Al]_{fl}$ in eq w/products (mol/cm^3):		5.60e-007
Porosity, ϕ:		3.00e+001
Tortuosity, τ:		1.00e+000
Q_D (kJ/mol):		140
$D = D_{inf}\phi\tau e^{(-Q_D/RT)}$ (m^2/s):		1.18e-017[a]
(at characteristic T, 530°C or 9.5 my)[a]		
$(dN/dt)_{steady-state}$, k_1 (nucl/cm^3/s):		1.30e-012
$(dN/dt)_{max}$ (nucl/cm^3/s):		1.26e-012
Nucleation acceleration, k_2:		1.00e-001
Time step (y):		200
Reporting interval (y):		5.00e+005

[a] Determined at nearest reporting interval

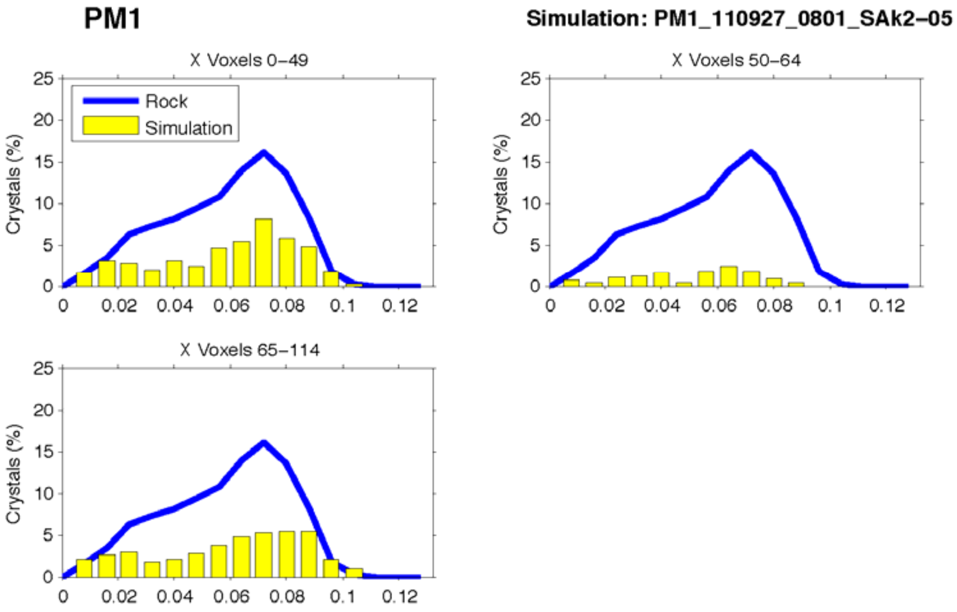
PM1
Simulation: PM1_110927_0801_SAk2–05
X Voxels 0–49
X Voxels 50–64
X Voxels 65–114
Rock
Simulation
Crystals (%)
25
20
15
10
5
0
0
0.02
0.04
0.06
0.08
0.1
0.12

Parameters File

```
Crystallize 1.3
Run name:                                                          PM1_110927_0801_SAk2-05
Result file directory:                                             runsPM1\PM1_110927_0801_SAk2-05
Reporting interval (years):                                        5.00E+05
Fractional porosity (0-1):                                         3.00E+01
Tortuosity (0-1):                                                  1.0
Activation energy for diffusion (kJ/mol):                          140
Dinf (cm^2/s):                                                     5.00E-06
Al concentration in fluid in eq with CAP (moles/cm^3):             5.60E-07
Nucleation acceleration (dimensionless):                           1.00E-01
Nucleation rate at infinite overstepping (nuclei/s/cm^3):          1.30E-12
Nucleation proportional to CAR amount in voxel (0=no,1=yes):       0
Maximum number of porphyroblasts (0=unlimited):                    0
Maximum modal amount of product (0=limited by reactant amount):    0
Al content of CAR (moles Al/moles CAR):                            2.25
Avg. formula weight of CAR (g CAR / mol CAR):                      634.7072
Al content of CAP (moles Al/moles CAP):                            2.25
Avg. formula weight of CAP (g CAP / mol CAP):                      625.7249
Density of CAP (g/cm^3):                                           4.07
Voxel edge length (cm):                                            0.012
Time step (yr):                                                    200
Number of voxels in X:                                             115
Number of voxels in Y:                                             115
Number of voxels in Z:                                             115
Dimensions:                                                        3
Default CAR amount (g/cm^3 rock):                                  2.20
**** Reactant distribution: One header line, then one line per layer ****
Number of structures (0=homogeneous):                              1
Layer (see format codes)                                           1      50      64      1.50
FD approximation source/sink parameter (dimensionless):            200
Subvoxel growth acceleration factor (dimensionless, 0=none):       2.8284
Random seed (0=generate new):                                      -1717
Volume fraction of porphyroblast in CAP assemblage (fv):           0.7490
Number of moles of porphyroblast in reaction equation (moles):     1.0
Concentration to delGrxn conversion power-law factor n:            1.4165
Free energy specification mode (0=thermo, 1=delGrxn path):         1
Equilibrium temperature used for G-C conversion (°C):              528
Number of Time-Temp-DelGrxn triplets:                              3
DelGrxn path (Myr after start,°C,kJ/mol): (0.0,435.0,-0.0001)   (10.0,535.0,-19.0582)   (30.0,535.0,-20.1369)
```

PM1

Simulation: PM1_110927_0801_SAk2–06

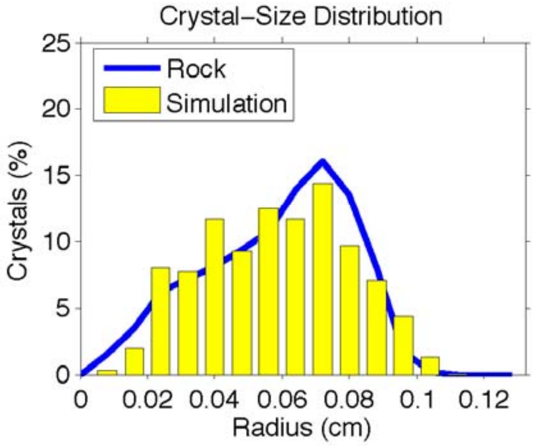

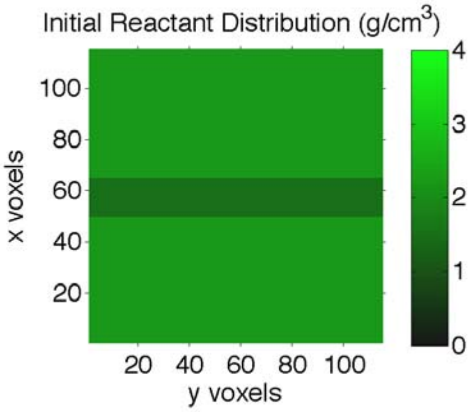

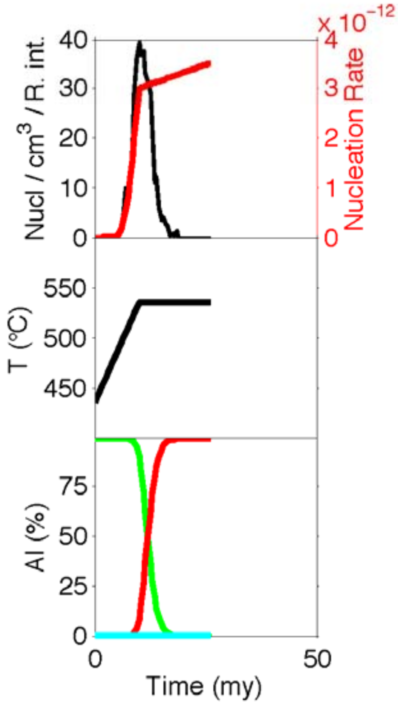

	Rock	Simulation
Total crystals:	1748	1034
Xtl Num Density (xtls/cm^3):	382	393
Crystallization duration (my):	10	10.0[a]
Equil T of rxn (°C):	unknown	435
Thermal overstepping (°C):		55
T at 95% Al in products (°C):	535	535[a]
Min radius (cm):	0.006	0.010
Mean radius (cm):	0.058	0.058
Max radius (cm):	0.104	0.115
Mode (vol%):	37.4	38.0
D_{inf} (cm^2/s):		5.00e-006
$[Al]_{fl}$ in eq w/products (mol/cm^3):		5.60e-007
Porosity, ϕ:		3.00e+001
Tortuosity, τ:		1.00e+000
Q_D (kJ/mol):		140
$D = D_{inf} \phi \tau e^{(-Q_D/RT)}$ (m^2/s): (at characteristic T, 530°C or 9.5 my)[a]		1.18e-017[a]
$(dN/dt)_{steady-state}$, k_1 (nucl/cm^3/s):		1.40e-011
$(dN/dt)_{max}$ (nucl/cm^3/s):		3.52e-012
Nucleation acceleration, k_2:		5.00e+000
Time step (y):		200
Reporting interval (y):		5.00e+005

[a] Determined at nearest reporting interval

PM1 **Simulation: PM1_110927_0801_SAk2–06**

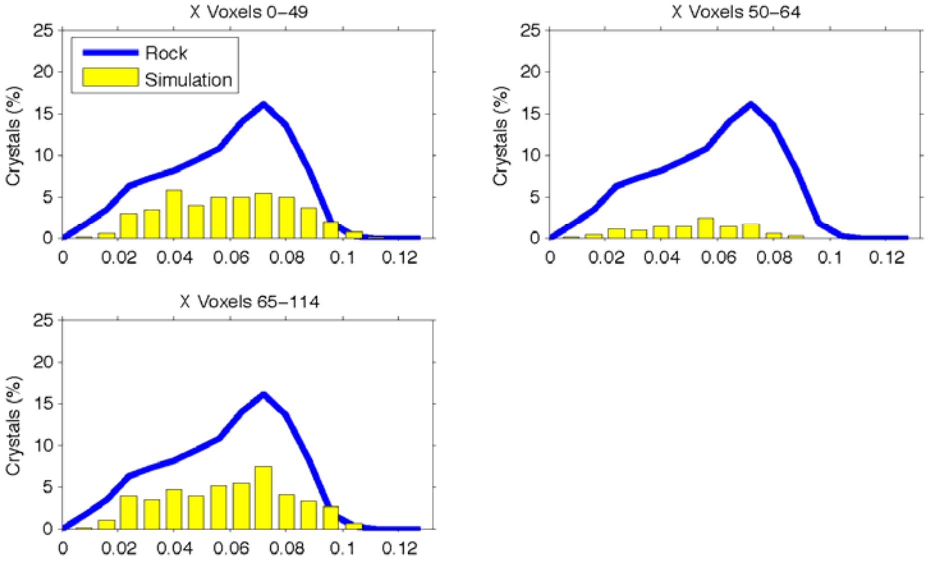

Parameters File

```
Crystallize 1.3
Run name:                                                            PM1_110927_0801_SAk2-06
Result file directory:                                               runsPM1\PM1_110927_0801_SAk2-06
Reporting interval (years):                                          5.00E+05
Fractional porosity (0-1):                                           3.00E+01
Tortuosity (0-1):                                                    1.0
Activation energy for diffusion (kJ/mol):                            140
Dinf (cm^2/s):                                                       5.00E-06
Al concentration in fluid in eq with CAP (moles/cm^3):               5.60E-07
Nucleation acceleration (dimensionless):                             5.00E-00
Nucleation rate at infinite overstepping (nuclei/s/cm^3):            1.40E-11
Nucleation proportional to CAR amount in voxel (0=no,1=yes):         0
Maximum number of porphyroblasts (0=unlimited):                      0
Maximum modal amount of product (0=limited by reactant amount):      0
Al content of CAR (moles Al/moles CAR):                              2.25
Avg. formula weight of CAR (g CAR / mol CAR):                        634.7072
Al content of CAP (moles Al/moles CAP):                              2.25
Avg. formula weight of CAP (g CAP / mol CAP):                        625.7249
Density of CAP (g/cm^3):                                             4.07
Voxel edge length (cm):                                              0.012
Time step (yr):                                                      200
Number of voxels in X:                                               115
Number of voxels in Y:                                               115
Number of voxels in Z:                                               115
Dimensions:                                                          3
Default CAR amount (g/cm^3 rock):                                    2.20
**** Reactant distribution: One header line, then one line per layer ****
Number of structures (0=homogeneous):                                1
Layer (see format codes)                                             1        50        64        1.50
FD approximation source/sink parameter (dimensionless):              200
Subvoxel growth acceleration factor (dimensionless, 0=none):         2.8284
Random seed (0=generate new):                                        -1717
Volume fraction of porphyroblast in CAP assemblage (fv):             0.7490
Number of moles of porphyroblast in reaction equation (moles):       1.0
Concentration to delGrxn conversion power-law factor n:              1.4165
Free energy specification mode (0=thermo, 1=delGrxn path):           1
Equilibrium temperature used for G-C conversion (°C):                528
Number of Time-Temp-DelGrxn triplets:                                3
DelGrxn path (Myr after start,°C,kJ/mol):   (0.0,435.0,-0.0001)   (10.0,535.0,-19.0582)    (30.0,535.0,-20.1369)
```

PM1

Simulation: PM1_110927_0801_SAk2–07c

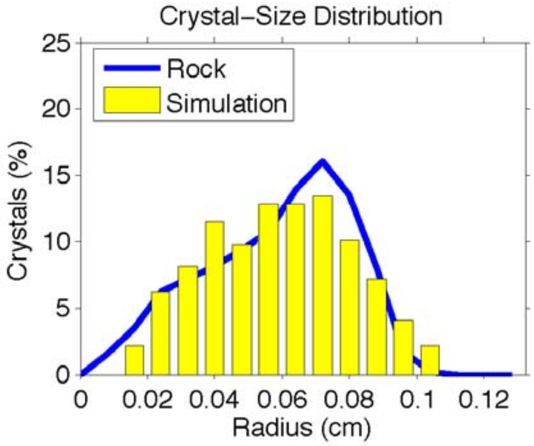

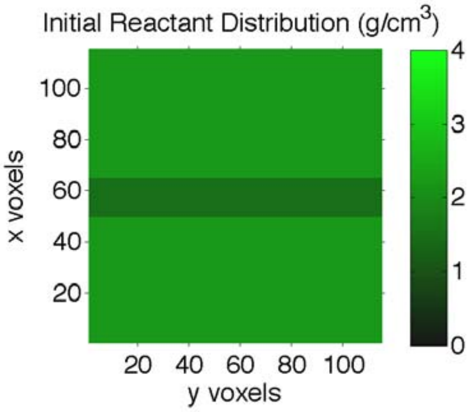

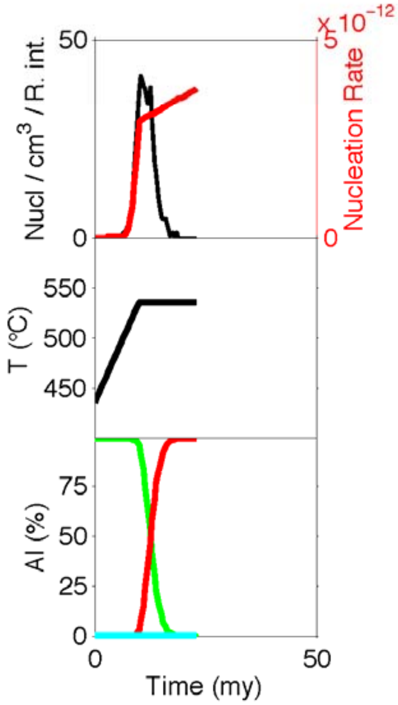

	Rock	Simulation
Total crystals:	1748	1002
Xtl Num Density (xtls/cm^3):	382	381
Crystallization duration (my):	10	9.5[a]
Equil T of rxn (°C):	unknown	435
Thermal overstepping (°C):		62
T at 95% Al in products (°C):	535	535[a]
Min radius (cm):	0.006	0.013
Mean radius (cm):	0.058	0.059
Max radius (cm):	0.104	0.107
Mode (vol%):	37.4	38.0
D_{inf} (cm^2/s):		5.00e-006
$[Al]_{fl}$ in eq w/products (mol/cm^3):		5.60e-007
Porosity, ϕ:		3.00e+001
Tortuosity, τ:		1.00e+000
Q_D (kJ/mol):		140
$D = D_{inf}\,\phi\,\tau\,e^{(-Q_D/RT)}$ (m^2/s): (at characteristic T, 525°C or 9.0 my)[a]		1.03e-017[a]
$(dN/dt)_{steady-state}$, k_1 (nucl/cm^3/s):		6.30e-011
$(dN/dt)_{max}$ (nucl/cm^3/s):		3.77e-012
Nucleation acceleration, k_2:		1.00e+001
Time step (y):		200
Reporting interval (y):		5.00e+005

[a] Determined at nearest reporting interval

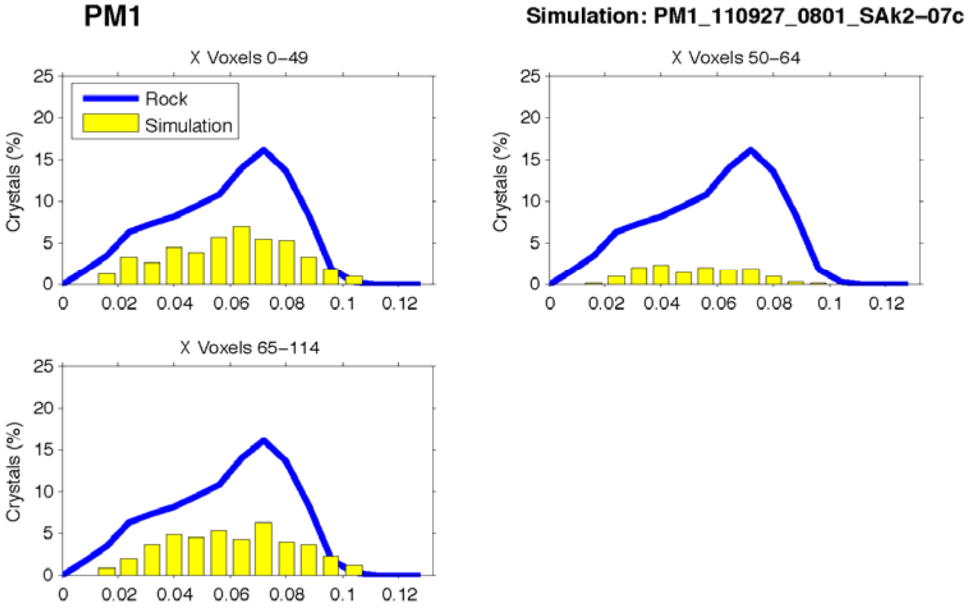
PM1
Simulation: PM1_110927_0801_SAk2–07c
X Voxels 0–49
X Voxels 50–64
X Voxels 65–114
Rock
Simulation
Crystals (%)
0
5
10
15
20
25
0
0.02
0.04
0.06
0.08
0.1
0.12

Parameters File

```
Crystallize 1.3
Run name:                                                        PM1_110927_0801_SAk2-07c
Result file directory:                                           runsPM1\PM1_110927_0801_SAk2-07c
Reporting interval (years):                                      5.00E+05
Fractional porosity (0-1):                                       3.00E+01
Tortuosity (0-1):                                                1.0
Activation energy for diffusion (kJ/mol):                        140
Dinf (cm^2/s):                                                   5.00E-06
Al concentration in fluid in eq with CAP (moles/cm^3):           5.60E-07
Nucleation acceleration (dimensionless):                         1.00E+01
Nucleation rate at infinite overstepping (nuclei/s/cm^3):        6.30E-11
Nucleation proportional to CAR amount in voxel (0=no,1=yes):     0
Maximum number of porphyroblasts (0=unlimited):                  0
Maximum modal amount of product (0=limited by reactant amount):  0
Al content of CAR (moles Al/moles CAR):                          2.25
Avg. formula weight of CAR (g CAR / mol CAR):                    634.7072
Al content of CAP (moles Al/moles CAP):                          2.25
Avg. formula weight of CAP (g CAP / mol CAP):                    625.7249
Density of CAP (g/cm^3):                                         4.07
Voxel edge length (cm):                                          0.012
Time step (yr):                                                  200
Number of voxels in X:                                           115
Number of voxels in Y:                                           115
Number of voxels in Z:                                           115
Dimensions:                                                      3
Default CAR amount (g/cm^3 rock):                                2.20
**** Reactant distribution: One header line, then one line per layer ****
Number of structures (0=homogeneous):                            1
Layer (see format codes)                                         1      50      64      1.50
FD approximation source/sink parameter (dimensionless):          200
Subvoxel growth acceleration factor (dimensionless, 0=none):     2.8284
Random seed (0=generate new):                                    -1717
Volume fraction of porphyroblast in CAP assemblage (fv):         0.7490
Number of moles of porphyroblast in reaction equation (moles):   1.0
Concentration to delGrxn conversion power-law factor n:          1.4165
Free energy specification mode (0=thermo, 1=delGrxn path):       1
Equilibrium temperature used for G-C conversion (°C):            528
Number of Time-Temp-DelGrxn triplets:                            3
DelGrxn path (Myr after start,°C,kJ/mol): (0.0,435.0,-0.0001)   (10.0,535.0,-19.0582)   (30.0,535.0,-20.1369)
```

PM1

Simulation: PM1_110927_0801_dTdtk1–01a

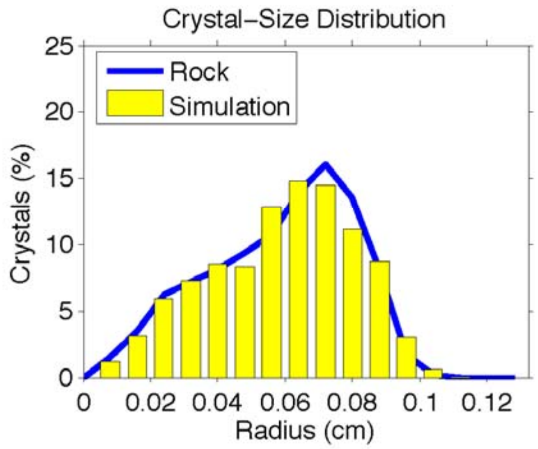

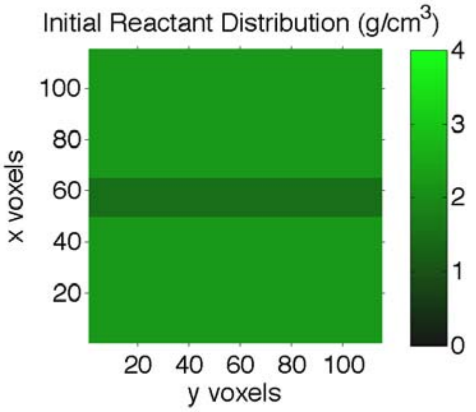

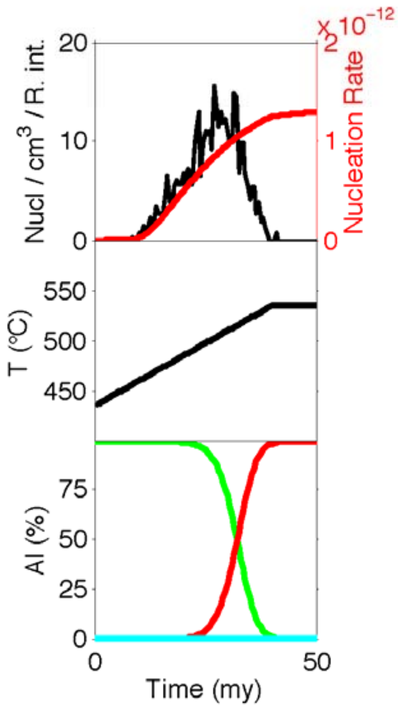

	Rock	Simulation
Total crystals:	1748	1031
Xtl Num Density (xtls/cm^3):	382	392
Crystallization duration (my):	10	29.5[a]
Equil T of rxn (°C):	unknown	435
Thermal overstepping (°C):		21
T at 95% Al in products (°C):	535	530[a]
Min radius (cm):	0.006	0.008
Mean radius (cm):	0.058	0.059
Max radius (cm):	0.104	0.109
Mode (vol%):	37.4	38.0
D_{inf} (cm^2/s):		5.00e-006
$[Al]_{fl}$ in eq w/products (mol/cm^3):		5.60e-007
Porosity, ϕ:		3.00e+001
Tortuosity, τ:		1.00e+000
Q_D (kJ/mol):		140
$D = D_{inf}\,\phi\,\tau\,e^{(-Q_D/RT)}$ (m^2/s):		6.44e-018[a]
(at characteristic T, 508°C or 29.0 my)[a]		
$(dN/dt)_{steady-state}$, k_1 (nucl/cm^3/s):		1.70e-012
$(dN/dt)_{max}$ (nucl/cm^3/s):		1.30e-012
Nucleation acceleration, k_2:		1.00e+000
Time step (y):		200
Reporting interval (y):		5.00e+005

[a] Determined at nearest reporting interval

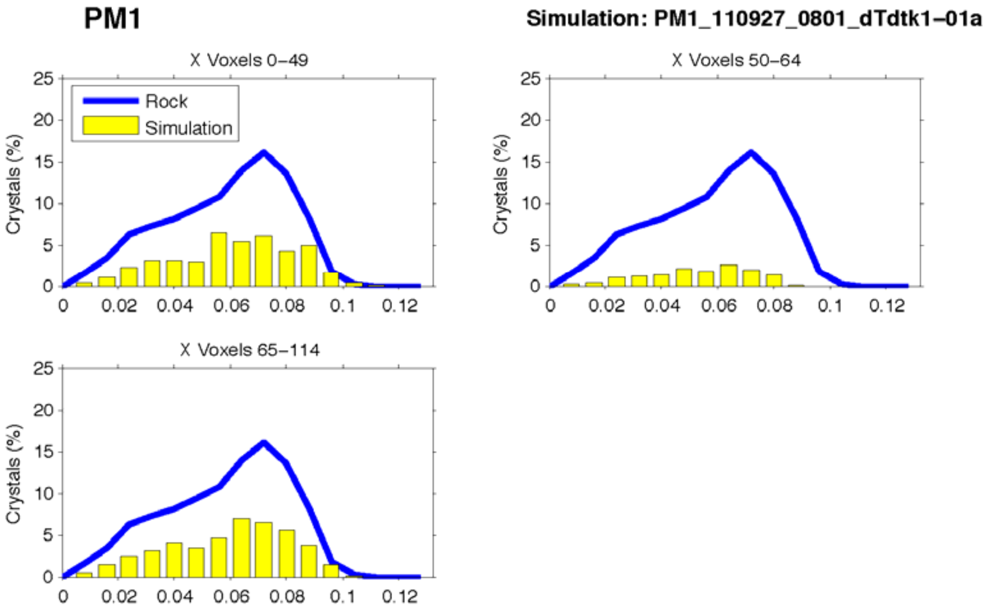
PM1
Simulation: PM1_110927_0801_dTdtk1–01a
X Voxels 0–49
X Voxels 50–64
X Voxels 65–114
Rock
Simulation
Crystals (%)
0
5
10
15
20
25
0
0.02
0.04
0.06
0.08
0.1
0.12

Parameters File

```
Crystallize 1.3
Run name:                                                        PM1_110927_0801_dTdtk1-01a
Result file directory:                                           runsPM1\PM1_110927_0801_dTdtk1-01a
Reporting interval (years):                                      5.00E+05
Fractional porosity (0-1):                                       3.00E+01
Tortuosity (0-1):                                                1.0
Activation energy for diffusion (kJ/mol):                        140
Dinf (cm^2/s):                                                   5.00E-06
Al concentration in fluid in eq with CAP (moles/cm^3):           5.60E-07
Nucleation acceleration (dimensionless):                         1.00E-00
Nucleation rate at infinite overstepping (nuclei/s/cm^3):        1.70E-12
Nucleation proportional to CAR amount in voxel (0=no,1=yes):     0
Maximum number of porphyroblasts (0=unlimited):                  0
Maximum modal amount of product (0=limited by reactant amount):  0
Al content of CAR (moles Al/moles CAR):                          2.25
Avg. formula weight of CAR (g CAR / mol CAR):                    634.7072
Al content of CAP (moles Al/moles CAP):                          2.25
Avg. formula weight of CAP (g CAP / mol CAP):                    625.7249
Density of CAP (g/cm^3):                                         4.07
Voxel edge length (cm):                                          0.012
Time step (yr):                                                  200
Number of voxels in X:                                           115
Number of voxels in Y:                                           115
Number of voxels in Z:                                           115
Dimensions:                                                      3
Default CAR amount (g/cm^3 rock):                                2.20
**** Reactant distribution: One header line, then one line per layer ****
Number of structures (0=homogeneous):                            1
Layer (see format codes)                                         1      50      64      1.50
FD approximation source/sink parameter (dimensionless):          200
Subvoxel growth acceleration factor (dimensionless, 0=none):     2.8284
Random seed (0=generate new):                                    -1717
Volume fraction of porphyroblast in CAP assemblage (fv):         0.7490
Number of moles of porphyroblast in reaction equation (moles):   1.0
Concentration to delGrxn conversion power-law factor n:          1.4165
Free energy specification mode (0=thermo, 1=delGrxn path):       1
Equilibrium temperature used for G-C conversion (°C):            528
Number of Time-Temp-DelGrxn triplets:                            3
DelGrxn path (Myr after start,°C,kJ/mol): (0.0,435.0,-0.0001)    (40.0,535.0,-19.0582)    (50.0,535.0,-20.1369)
```

PM1

Simulation: PM1_110927_0801_dTdtk1–02a

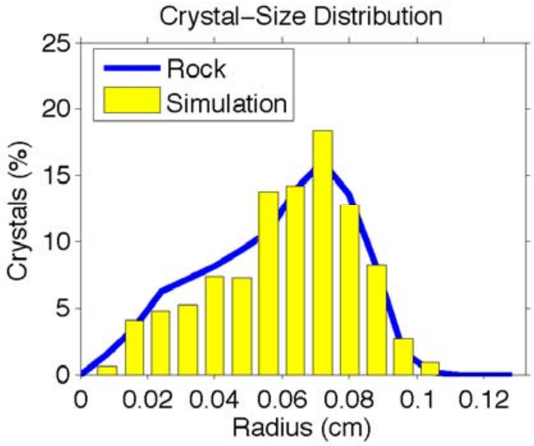

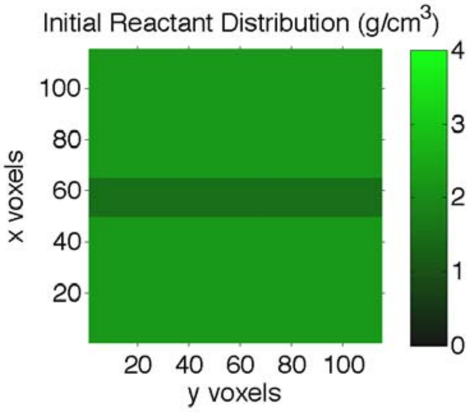

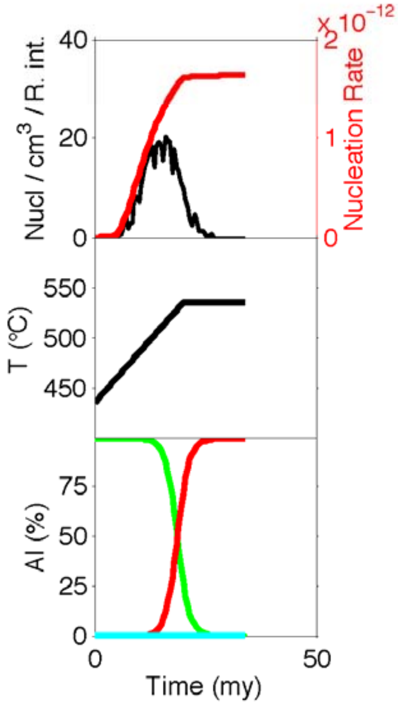

	Rock	Simulation
Total crystals:	1748	1012
Xtl Num Density (xtls/cm^3):	382	385
Crystallization duration (my):	10	18.5[a]
Equil T of rxn (°C):	unknown	435
Thermal overstepping (°C):		21
T at 95% Al in products (°C):	535	535[a]
Min radius (cm):	0.006	0.009
Mean radius (cm):	0.058	0.061
Max radius (cm):	0.104	0.107
Mode (vol%):	37.4	38.0
D_{inf} (cm^2/s):		5.00e-006
$[Al]_{fl}$ in eq w/products (mol/cm^3):		5.60e-007
Porosity, ϕ:		3.00e+001
Tortuosity, τ:		1.00e+000
Q_D (kJ/mol):		140
$D = D_{inf}\,\phi\,\tau\,e^{(-Q_D/RT)}$ (m^2/s): (at characteristic T, 520°C or 17.0 my)[a]		9.04e-018[a]
$(dN/dt)_{steady-state}, k_1$ (nucl/cm^3/s):		2.20e-012
$(dN/dt)_{max}$ (nucl/cm^3/s):		1.65e-012
Nucleation acceleration, k_2:		1.00e+000
Time step (y):		200
Reporting interval (y):		5.00e+005

[a] Determined at nearest reporting interval

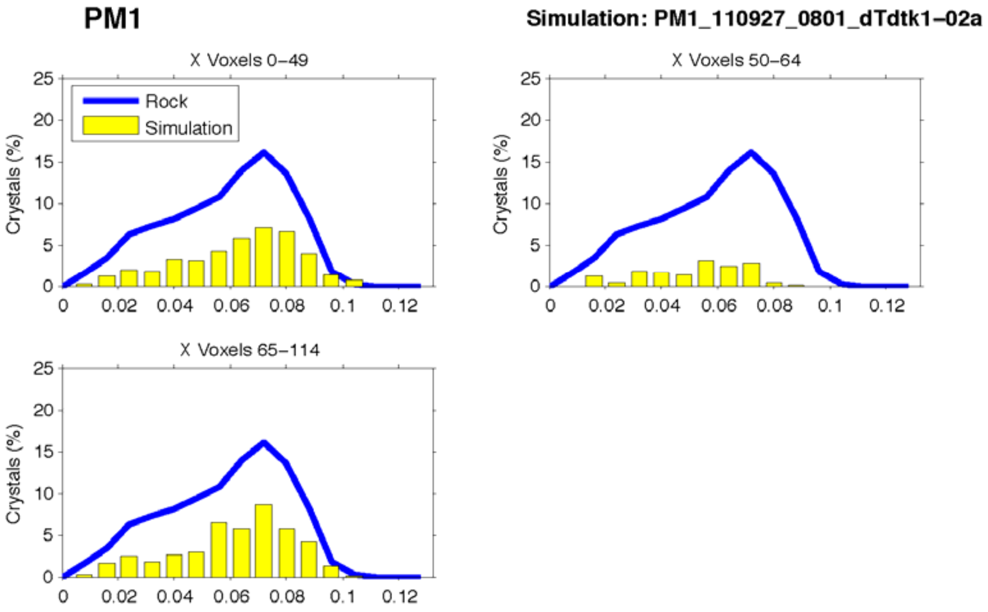
PM1
Simulation: PM1_110927_0801_dTdtk1−02a
X Voxels 0−49
X Voxels 50−64
X Voxels 65−114
Rock
Simulation
Crystals (%)
0
5
10
15
20
25
0
0.02
0.04
0.06
0.08
0.1
0.12

Parameters File

```
Crystallize 1.3
Run name:                                                          PM1_110927_0801_dTdtk1-02a
Result file directory:                                             runsPM1\PM1_110927_0801_dTdtk1-02a
Reporting interval (years):                                        5.00E+05
Fractional porosity (0-1):                                         3.00E+01
Tortuosity (0-1):                                                  1.0
Activation energy for diffusion (kJ/mol):                          140
Dinf (cm^2/s):                                                     5.00E-06
Al concentration in fluid in eq with CAP (moles/cm^3):             5.60E-07
Nucleation acceleration (dimensionless):                           1.00E-00
Nucleation rate at infinite overstepping (nuclei/s/cm^3):          2.20E-12
Nucleation proportional to CAR amount in voxel (0=no,1=yes):       0
Maximum number of porphyroblasts (0=unlimited):                    0
Maximum modal amount of product (0=limited by reactant amount):    0
Al content of CAR (moles Al/moles CAR):                            2.25
Avg. formula weight of CAR (g CAR / mol CAR):                      634.7072
Al content of CAP (moles Al/moles CAP):                            2.25
Avg. formula weight of CAP (g CAP / mol CAP):                      625.7249
Density of CAP (g/cm^3):                                           4.07
Voxel edge length (cm):                                            0.012
Time step (yr):                                                    200
Number of voxels in X:                                             115
Number of voxels in Y:                                             115
Number of voxels in Z:                                             115
Dimensions:                                                        3
Default CAR amount (g/cm^3 rock):                                  2.20
**** Reactant distribution: One header line, then one line per layer ****
Number of structures (0=homogeneous):                              1
Layer (see format codes)                                           1       50      64      1.50
FD approximation source/sink parameter (dimensionless):            200
Subvoxel growth acceleration factor (dimensionless, 0=none):       2.8284
Random seed (0=generate new):                                      -1717
Volume fraction of porphyroblast in CAP assemblage (fv):           0.7490
Number of moles of porphyroblast in reaction equation (moles):     1.0
Concentration to delGrxn conversion power-law factor n:            1.4165
Free energy specification mode (0=thermo, 1=delGrxn path):         1
Equilibrium temperature used for G-C conversion (°C):              528
Number of Time-Temp-DelGrxn triplets:                              3
DelGrxn path (Myr after start,°C,kJ/mol): (0.0,435.0,-0.0001)    (20.0,535.0,-19.0582)    (50.0,535.0,-20.1369)
```

PM1

Simulation: PM1_110927_0801_dTdtk1–03b

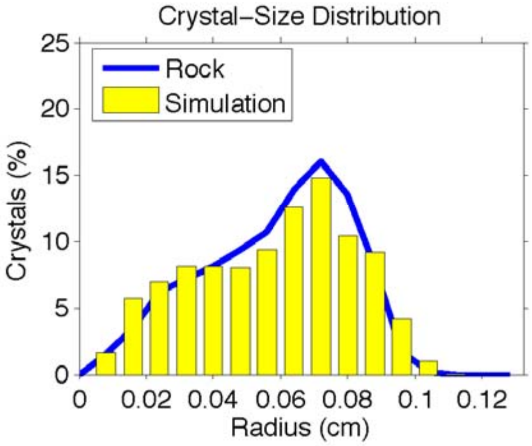

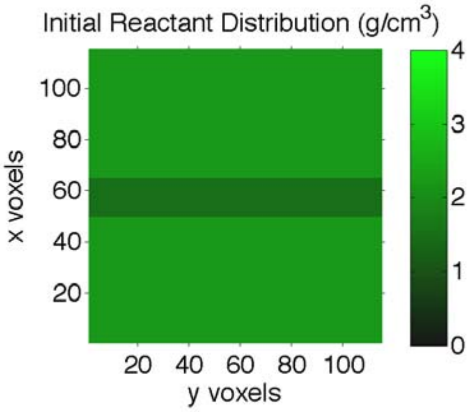

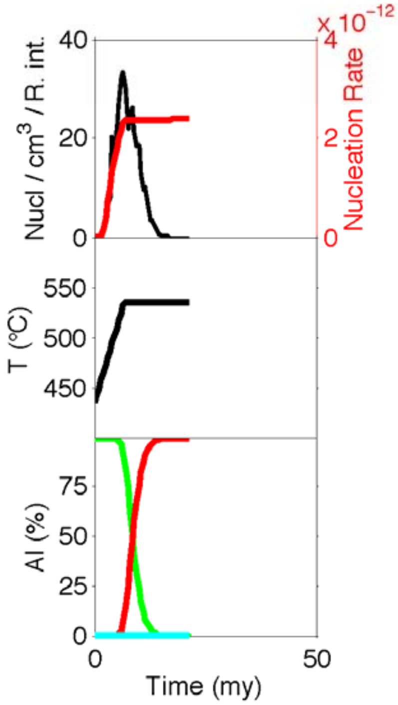

	Rock	Simulation
Total crystals:	1748	1018
Xtl Num Density (xtls/cm^3):	382	387
Crystallization duration (my):	10	10.5[a]
Equil T of rxn (°C):	unknown	435
Thermal overstepping (°C):		24
T at 95% Al in products (°C):	535	535[a]
Min radius (cm):	0.006	0.008
Mean radius (cm):	0.058	0.058
Max radius (cm):	0.104	0.115
Mode (vol%):	37.4	38.0
D_{inf} (cm^2/s):		5.00e-006
$[Al]_{fl}$ in eq w/products (mol/cm^3):		5.60e-007
Porosity, ϕ:		3.00e+001
Tortuosity, τ:		1.00e+000
Q_D (kJ/mol):		140
$D = D_{inf}\,\phi\,\tau\,e^{(-Q_D/RT)}$ (m^2/s):		1.24e-017[a]
(at characteristic T, 532°C or 6.5 my)[a]		
$(dN/dt)_{steady-state}, k_1$ (nucl/cm^3/s):		3.20e-012
$(dN/dt)_{max}$ (nucl/cm^3/s):		2.39e-012
Nucleation acceleration, k_2:		1.00e+000
Time step (y):		200
Reporting interval (y):		5.00e+005

[a] Determined at nearest reporting interval

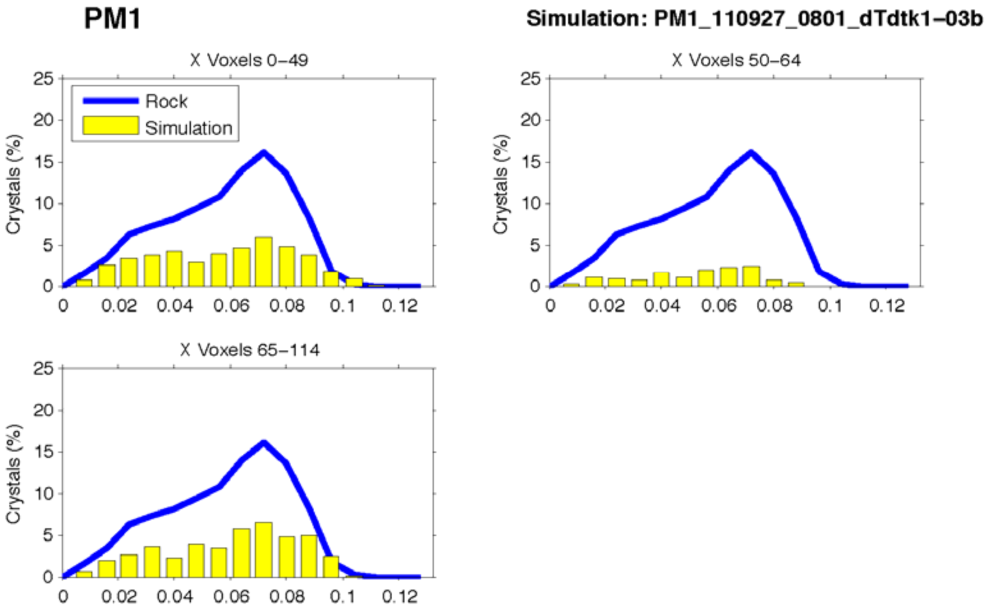
PM1
Simulation: PM1_110927_0801_dTdtk1−03b
X Voxels 0−49
X Voxels 50−64
X Voxels 65−114
Rock
Simulation
Crystals (%)
0
5
10
15
20
25
0
0.02
0.04
0.06
0.08
0.1
0.12

Parameters File

```
Crystallize 1.3
Run name:                                                        PM1_110927_0801_dTdtk1-03b
Result file directory:                                           runsPM1\PM1_110927_0801_dTdtk1-03b
Reporting interval (years):                                      5.00E+05
Fractional porosity (0-1):                                       3.00E+01
Tortuosity (0-1):                                                1.0
Activation energy for diffusion (kJ/mol):                        140
Dinf (cm^2/s):                                                   5.00E-06
Al concentration in fluid in eq with CAP (moles/cm^3):           5.60E-07
Nucleation acceleration (dimensionless):                         1.00E-00
Nucleation rate at infinite overstepping (nuclei/s/cm^3):        3.20E-12
Nucleation proportional to CAR amount in voxel (0=no,1=yes):     0
Maximum number of porphyroblasts (0=unlimited):                  0
Maximum modal amount of product (0=limited by reactant amount):  0
Al content of CAR (moles Al/moles CAR):                          2.25
Avg. formula weight of CAR (g CAR / mol CAR):                    634.7072
Al content of CAP (moles Al/moles CAP):                          2.25
Avg. formula weight of CAP (g CAP / mol CAP):                    625.7249
Density of CAP (g/cm^3):                                         4.07
Voxel edge length (cm):                                          0.012
Time step (yr):                                                  200
Number of voxels in X:                                           115
Number of voxels in Y:                                           115
Number of voxels in Z:                                           115
Dimensions:                                                      3
Default CAR amount (g/cm^3 rock):                                2.20
**** Reactant distribution: One header line, then one line per layer ****
Number of structures (0=homogeneous):                            1
Layer (see format codes)                                         1        50        64        1.50
FD approximation source/sink parameter (dimensionless):          200
Subvoxel growth acceleration factor (dimensionless, 0=none):     2.8284
Random seed (0=generate new):                                    -1717
Volume fraction of porphyroblast in CAP assemblage (fv):         0.7490
Number of moles of porphyroblast in reaction equation (moles):   1.0
Concentration to delGrxn conversion power-law factor n:          1.4165
Free energy specification mode (0=thermo, 1=delGrxn path):       1
Equilibrium temperature used for G-C conversion (°C):            528
Number of Time-Temp-DelGrxn triplets:                            3
DelGrxn path (Myr after start,°C,kJ/mol): (0.0,435.0,-0.0001)    (6.7,535.0,-19.0582)    (50.0,535.0,-20.1369)
```

PM1

Simulation: PM1_110927_0801_dTdtk1–04b

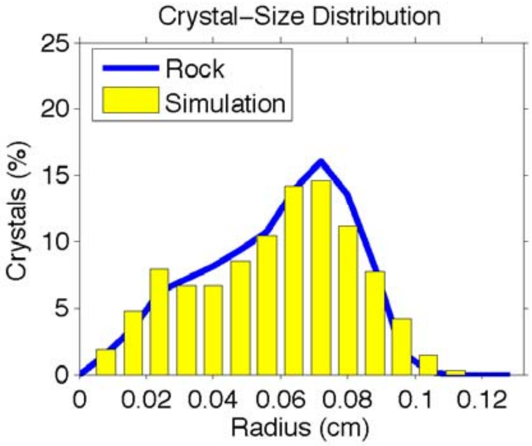

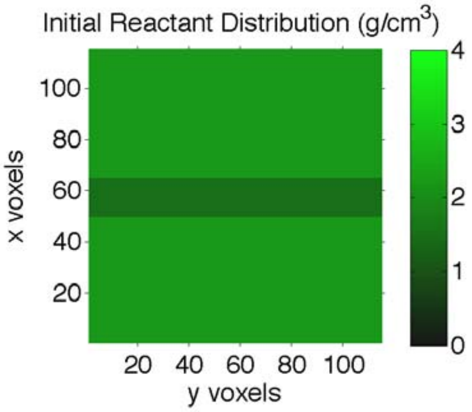

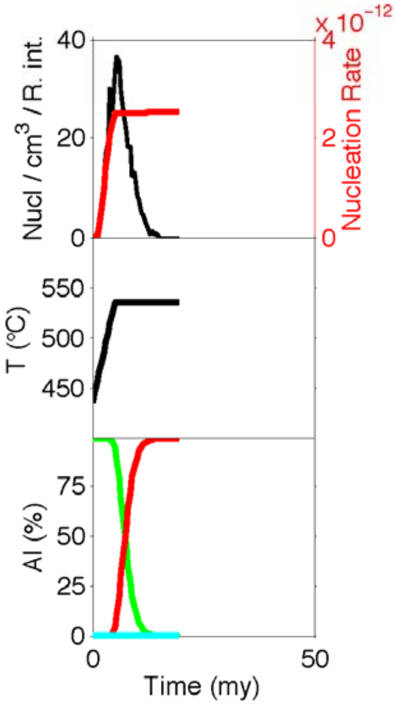

	Rock	Simulation
Total crystals:	1748	1016
Xtl Num Density (xtls/cm^3):	382	387
Crystallization duration (my):	10	9.5[a]
Equil T of rxn (°C):	unknown	435
Thermal overstepping (°C):		30
T at 95% Al in products (°C):	535	535[a]
Min radius (cm):	0.006	0.008
Mean radius (cm):	0.058	0.058
Max radius (cm):	0.104	0.114
Mode (vol%):	37.4	38.0
D_{inf} (cm^2/s):		5.00e-006
$[Al]_{fl}$ in eq w/products (mol/cm^3):		5.60e-007
Porosity, ϕ:		3.00e+001
Tortuosity, τ:		1.00e+000
Q_D (kJ/mol):		140
$D = D_{inf} \phi \tau e^{(-Q_D/RT)}$ (m^2/s): (at characteristic T, 535°C or 5.0 my)[a]		1.34e-017[a]
$(dN/dt)_{steady-state}, k_1$ (nucl/cm^3/s):		3.40e-012
$(dN/dt)_{max}$ (nucl/cm^3/s):		2.53e-012
Nucleation acceleration, k_2:		1.00e+000
Time step (y):		200
Reporting interval (y):		5.00e+005

[a] Determined at nearest reporting interval

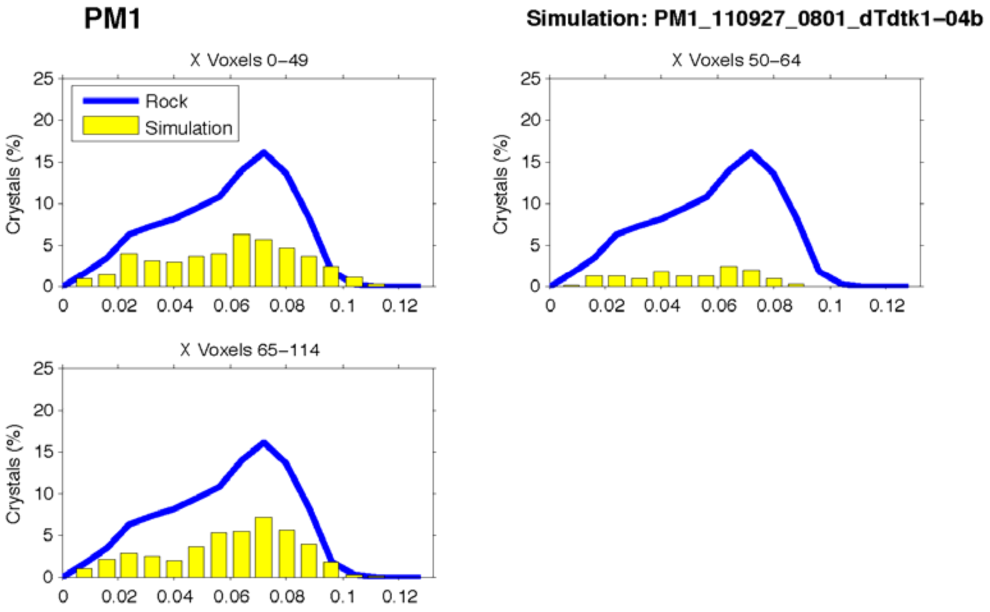
PM1
Simulation: PM1_110927_0801_dTdtk1−04b
X Voxels 0−49
X Voxels 50−64
X Voxels 65−114
Rock
Simulation
Crystals (%)
0
5
10
15
20
25
0
0.02
0.04
0.06
0.08
0.1
0.12

Parameters File

```
Crystallize 1.3
Run name:                                                         PM1_110927_0801_dTdtk1-04b
Result file directory:                                            runsPM1\PM1_110927_0801_dTdtk1-04b
Reporting interval (years):                                       5.00E+05
Fractional porosity (0-1):                                        3.00E+01
Tortuosity (0-1):                                                 1.0
Activation energy for diffusion (kJ/mol):                         140
Dinf (cm^2/s):                                                    5.00E-06
Al concentration in fluid in eq with CAP (moles/cm^3):            5.60E-07
Nucleation acceleration (dimensionless):                          1.00E-00
Nucleation rate at infinite overstepping (nuclei/s/cm^3):         3.40E-12
Nucleation proportional to CAR amount in voxel (0=no,1=yes):      0
Maximum number of porphyroblasts (0=unlimited):                   0
Maximum modal amount of product (0=limited by reactant amount):   0
Al content of CAR (moles Al/moles CAR):                           2.25
Avg. formula weight of CAR (g CAR / mol CAR):                     634.7072
Al content of CAP (moles Al/moles CAP):                           2.25
Avg. formula weight of CAP (g CAP / mol CAP):                     625.7249
Density of CAP (g/cm^3):                                          4.07
Voxel edge length (cm):                                           0.012
Time step (yr):                                                   200
Number of voxels in X:                                            115
Number of voxels in Y:                                            115
Number of voxels in Z:                                            115
Dimensions:                                                       3
Default CAR amount (g/cm^3 rock):                                 2.20
**** Reactant distribution: One header line, then one line per layer ****
Number of structures (0=homogeneous):                             1
Layer (see format codes)                                          1      50      64      1.50
FD approximation source/sink parameter (dimensionless):           200
Subvoxel growth acceleration factor (dimensionless, 0=none):      2.8284
Random seed (0=generate new):                                     -1717
Volume fraction of porphyroblast in CAP assemblage (fv):          0.7490
Number of moles of porphyroblast in reaction equation (moles):    1.0
Concentration to delGrxn conversion power-law factor n:           1.4165
Free energy specification mode (0=thermo, 1=delGrxn path):        1
Equilibrium temperature used for G-C conversion (°C):             528
Number of Time-Temp-DelGrxn triplets:                             3
DelGrxn path (Myr after start,°C,kJ/mol): (0.0,435.0,-0.0001)   (5.0,535.0,-19.0582)   (50.0,535.0,-20.1369)
```

PM1

Simulation: PM1_110927_0801_dTdtk2–01d

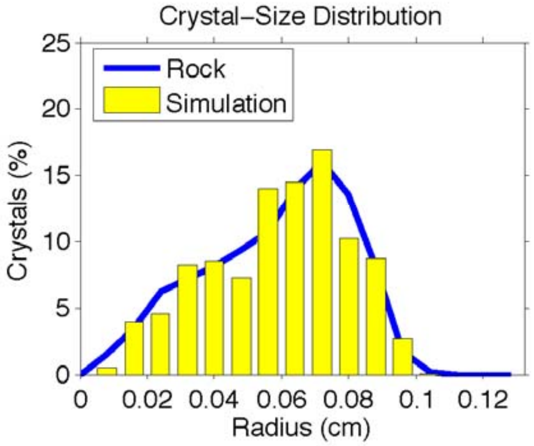

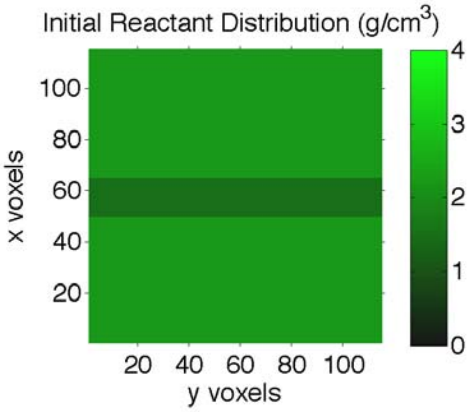

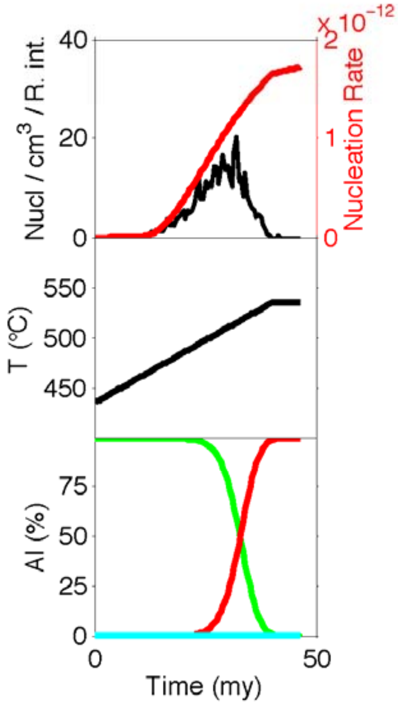

	Rock	Simulation
Total crystals:	1748	1034
Xtl Num Density (xtls/cm^3):	382	393
Crystallization duration (my):	10	28.0[a]
Equil T of rxn (°C):	unknown	435
Thermal overstepping (°C):		25
T at 95% Al in products (°C):	535	531[a]
Min radius (cm):	0.006	0.009
Mean radius (cm):	0.058	0.059
Max radius (cm):	0.104	0.102
Mode (vol%):	37.4	38.0
D_{inf} (cm^2/s):		5.00e-006
$[Al]_{fl}$ in eq w/products (mol/cm^3):		5.60e-007
Porosity, ϕ:		3.00e+001
Tortuosity, τ:		1.00e+000
Q_D (kJ/mol):		140
$D = D_{inf} \phi \tau e^{(-Q_D/RT)}$ (m^2/s):		6.22e-018[a]
(at characteristic T, 506°C or 28.5 my)[a]		
$(dN/dt)_{steady-state}$, k_1 (nucl/cm^3/s):		2.70e-012
$(dN/dt)_{max}$ (nucl/cm^3/s):		1.72e-012
Nucleation acceleration, k_2:		1.60e+000
Time step (y):		200
Reporting interval (y):		5.00e+005

[a] Determined at nearest reporting interval

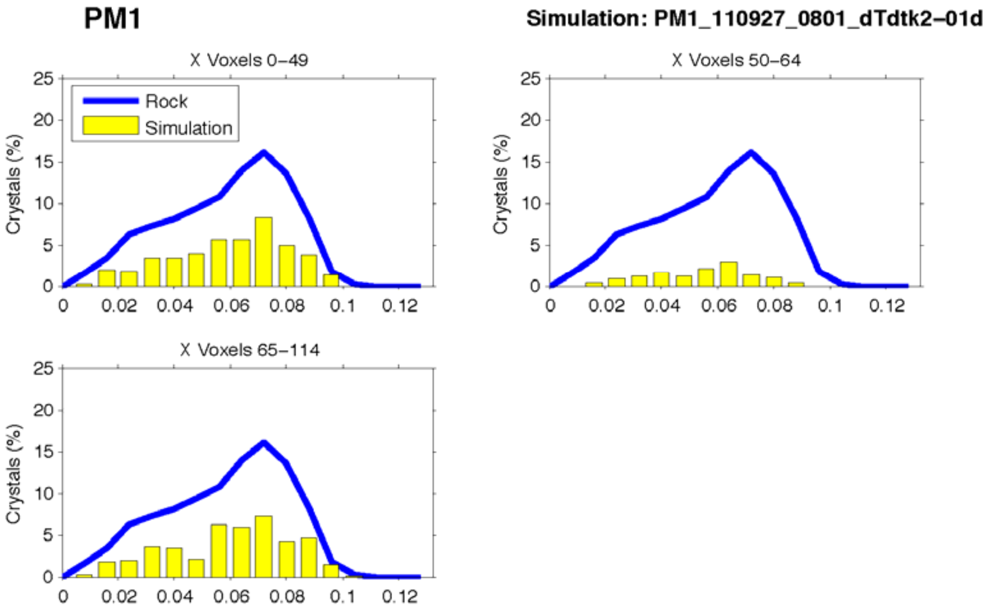
PM1
Simulation: PM1_110927_0801_dTdtk2–01d
X Voxels 0–49
X Voxels 50–64
X Voxels 65–114
Rock
Simulation
Crystals (%)
0
5
10
15
20
25
0
0.02
0.04
0.06
0.08
0.1
0.12

Parameters File

```
Crystallize 1.3
Run name:                                                       PM1_110927_0801_dTdtk2-01d
Result file directory:                                          runsPM1\PM1_110927_0801_dTdtk2-01d
Reporting interval (years):                                     5.00E+05
Fractional porosity (0-1):                                      3.00E+01
Tortuosity (0-1):                                               1.0
Activation energy for diffusion (kJ/mol):                       140
Dinf (cm^2/s):                                                  5.00E-06
Al concentration in fluid in eq with CAP (moles/cm^3):          5.60E-07
Nucleation acceleration (dimensionless):                        1.60E-00
Nucleation rate at infinite overstepping (nuclei/s/cm^3):       2.70E-12
Nucleation proportional to CAR amount in voxel (0=no,1=yes):    0
Maximum number of porphyroblasts (0=unlimited):                 0
Maximum modal amount of product (0=limited by reactant amount): 0
Al content of CAR (moles Al/moles CAR):                         2.25
Avg. formula weight of CAR (g CAR / mol CAR):                   634.7072
Al content of CAP (moles Al/moles CAP):                         2.25
Avg. formula weight of CAP (g CAP / mol CAP):                   625.7249
Density of CAP (g/cm^3):                                        4.07
Voxel edge length (cm):                                         0.012
Time step (yr):                                                 200
Number of voxels in X:                                          115
Number of voxels in Y:                                          115
Number of voxels in Z:                                          115
Dimensions:                                                     3
Default CAR amount (g/cm^3 rock):                               2.20
**** Reactant distribution: One header line, then one line per layer ****
Number of structures (0=homogeneous):                           1
Layer (see format codes)                                        1      50      64      1.50
FD approximation source/sink parameter (dimensionless):         200
Subvoxel growth acceleration factor (dimensionless, 0=none):    2.8284
Random seed (0=generate new):                                   -1717
Volume fraction of porphyroblast in CAP assemblage (fv):        0.7490
Number of moles of porphyroblast in reaction equation (moles):  1.0
Concentration to delGrxn conversion power-law factor n:         1.4165
Free energy specification mode (0=thermo, 1=delGrxn path):      1
Equilibrium temperature used for G-C conversion (°C):           528
Number of Time-Temp-DelGrxn triplets:                           3
DelGrxn path (Myr after start,°C,kJ/mol): (0.0,435.0,-0.0001)   (40.0,535.0,-19.0582)   (50.0,535.0,-20.1369)
```

PM1

Simulation: PM1_110927_0801_dTdtk2–02d

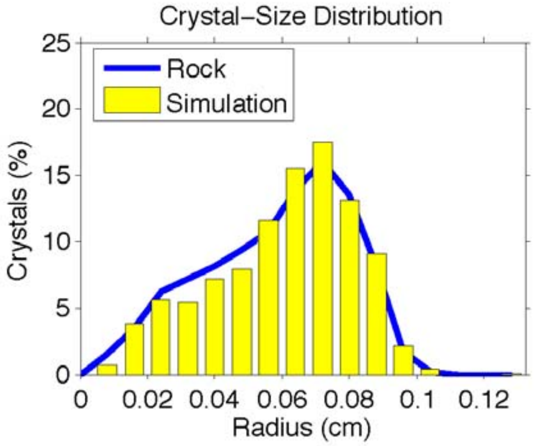

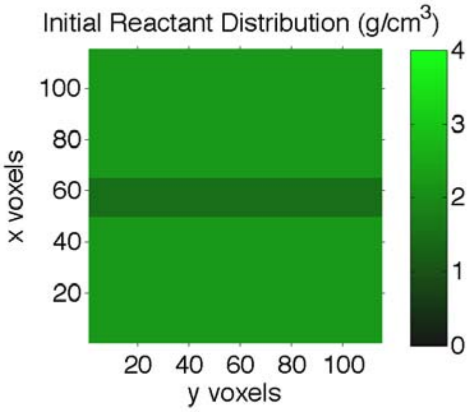

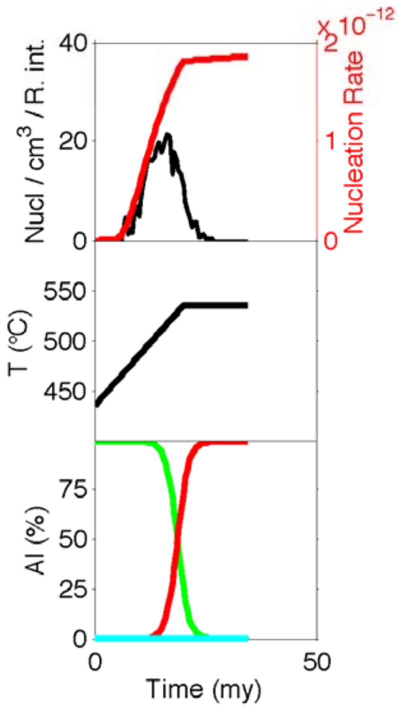

	Rock	Simulation
Total crystals:	1748	1001
Xtl Num Density (xtls/cm^3):	382	381
Crystallization duration (my):	10	16.0[a]
Equil T of rxn (°C):	unknown	435
Thermal overstepping (°C):		30
T at 95% Al in products (°C):	535	535[a]
Min radius (cm):	0.006	0.010
Mean radius (cm):	0.058	0.060
Max radius (cm):	0.104	0.151
Mode (vol%):	37.4	38.0
D_{inf} (cm^2/s):		5.00e-006
$[Al]_{fl}$ in eq w/products (mol/cm^3):		5.60e-007
Porosity, ϕ:		3.00e+001
Tortuosity, τ:		1.00e+000
Q_D (kJ/mol):		140
$D = D_{inf}\phi\tau e^{(-Q_D/RT)}$ (m^2/s):		9.04e-018[a]
(at characteristic T, 520°C or 17.0 my)[a]		
$(dN/dt)_{steady-state}, k_1$ (nucl/cm^3/s):		2.70e-012
$(dN/dt)_{max}$ (nucl/cm^3/s):		1.86e-012
Nucleation acceleration, k_2:		1.30e+000
Time step (y):		200
Reporting interval (y):		5.00e+005

[a]Determined at nearest reporting interval

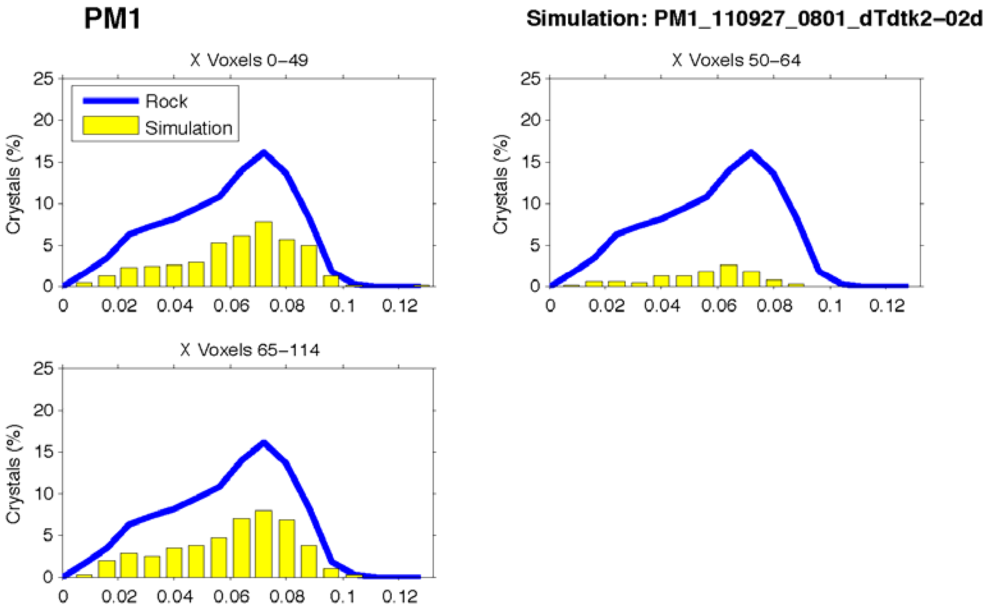
PM1
Simulation: PM1_110927_0801_dTdtk2–02d
X Voxels 0–49
X Voxels 50–64
X Voxels 65–114
Rock
Simulation
Crystals (%)
0
5
10
15
20
25
0
0.02
0.04
0.06
0.08
0.1
0.12

Parameters File

```
Crystallize 1.3
Run name:                                                          PM1_110927_0801_dTdtk2-02d
Result file directory:                                             runsPM1\PM1_110927_0801_dTdtk2-02d
Reporting interval (years):                                        5.00E+05
Fractional porosity (0-1):                                         3.00E+01
Tortuosity (0-1):                                                  1.0
Activation energy for diffusion (kJ/mol):                          140
Dinf (cm^2/s):                                                     5.00E-06
Al concentration in fluid in eq with CAP (moles/cm^3):             5.60E-07
Nucleation acceleration (dimensionless):                           1.30E-00
Nucleation rate at infinite overstepping (nuclei/s/cm^3):          2.70E-12
Nucleation proportional to CAR amount in voxel (0=no,1=yes):       0
Maximum number of porphyroblasts (0=unlimited):                    0
Maximum modal amount of product (0=limited by reactant amount):    0
Al content of CAR (moles Al/moles CAR):                            2.25
Avg. formula weight of CAR (g CAR / mol CAR):                      634.7072
Al content of CAP (moles Al/moles CAP):                            2.25
Avg. formula weight of CAP (g CAP / mol CAP):                      625.7249
Density of CAP (g/cm^3):                                           4.07
Voxel edge length (cm):                                            0.012
Time step (yr):                                                    200
Number of voxels in X:                                             115
Number of voxels in Y:                                             115
Number of voxels in Z:                                             115
Dimensions:                                                        3
Default CAR amount (g/cm^3 rock):                                  2.20
**** Reactant distribution: One header line, then one line per layer ****
Number of structures (0=homogeneous):                              1
Layer (see format codes)                                           1        50        64        1.50
FD approximation source/sink parameter (dimensionless):            200
Subvoxel growth acceleration factor (dimensionless, 0=none):       2.8284
Random seed (0=generate new):                                      -1717
Volume fraction of porphyroblast in CAP assemblage (fv):           0.7490
Number of moles of porphyroblast in reaction equation (moles):     1.0
Concentration to delGrxn conversion power-law factor n:            1.4165
Free energy specification mode (0=thermo, 1=delGrxn path):         1
Equilibrium temperature used for G-C conversion (°C):              528
Number of Time-Temp-DelGrxn triplets:                              3
DelGrxn path (Myr after start,°C,kJ/mol): (0.0,435.0,-0.0001)   (20.0,535.0,-19.0582)   (50.0,535.0,-20.1369)
```

PM1

Simulation: PM1_110927_0801_dTdtk2–03c

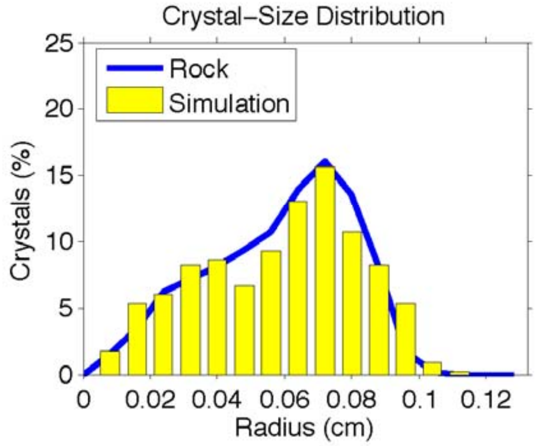

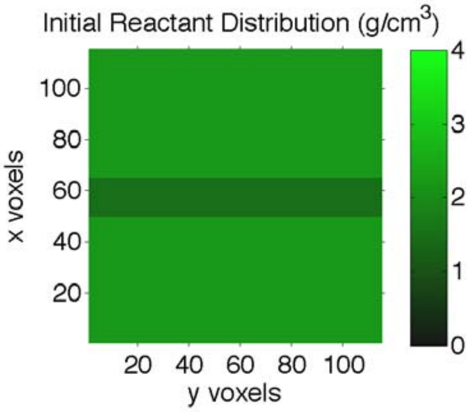

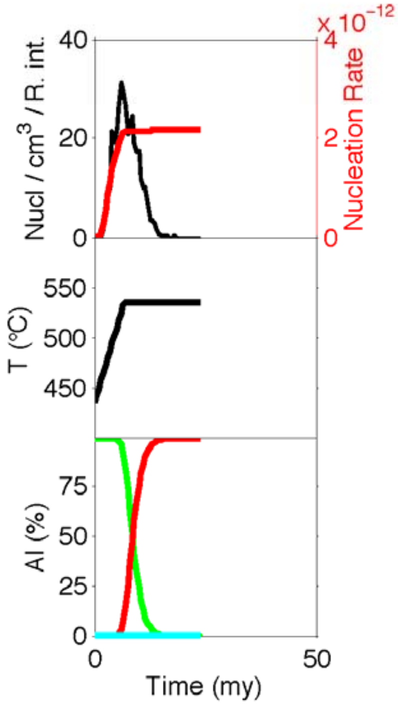

	Rock	Simulation
Total crystals:	1748	995
Xtl Num Density (xtls/cm^3):	382	379
Crystallization duration (my):	10	10.5[a]
Equil T of rxn (°C):	unknown	435
Thermal overstepping (°C):		24
T at 95% Al in products (°C):	535	535[a]
Min radius (cm):	0.006	0.008
Mean radius (cm):	0.058	0.059
Max radius (cm):	0.104	0.115
Mode (vol%):	37.4	38.0
D_{inf} (cm^2/s):		5.00e-006
$[Al]_{fl}$ in eq w/products (mol/cm^3):		5.60e-007
Porosity, ϕ:		3.00e+001
Tortuosity, τ:		1.00e+000
Q_D (kJ/mol):		140
$D = D_{inf}\phi\tau e^{(-Q_D/RT)}$ (m^2/s):		1.24e-017[a]
(at characteristic T, 532°C or 6.5 my)[a]		
$(dN/dt)_{steady-state}, k_1$ (nucl/cm^3/s):		2.70e-012
$(dN/dt)_{max}$ (nucl/cm^3/s):		2.17e-012
Nucleation acceleration, k_2:		7.50e-001
Time step (y):		200
Reporting interval (y):		5.00e+005

[a] Determined at nearest reporting interval

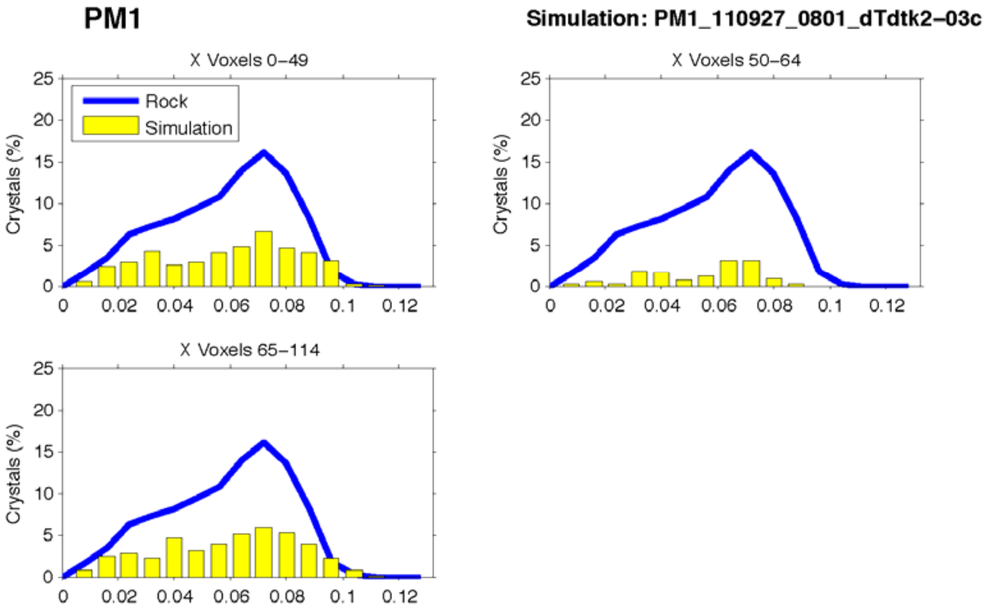
PM1
Simulation: PM1_110927_0801_dTdtk2–03c
X Voxels 0–49
Rock
Simulation
Crystals (%)
25
20
15
10
5
0
0
0.02
0.04
0.06
0.08
0.1
0.12
X Voxels 50–64
Crystals (%)
X Voxels 65–114
Crystals (%)

Parameters File

```
Crystallize 1.3
Run name:                                                        PM1_110927_0801_dTdtk2-03c
Result file directory:                                           runsPM1\PM1_110927_0801_dTdtk2-03c
Reporting interval (years):                                      5.00E+05
Fractional porosity (0-1):                                       3.00E+01
Tortuosity (0-1):                                                1.0
Activation energy for diffusion (kJ/mol):                        140
Dinf (cm^2/s):                                                   5.00E-06
Al concentration in fluid in eq with CAP (moles/cm^3):           5.60E-07
Nucleation acceleration (dimensionless):                         7.50E-01
Nucleation rate at infinite overstepping (nuclei/s/cm^3):        2.70E-12
Nucleation proportional to CAR amount in voxel (0=no,1=yes):     0
Maximum number of porphyroblasts (0=unlimited):                  0
Maximum modal amount of product (0=limited by reactant amount):  0
Al content of CAR (moles Al/moles CAR):                          2.25
Avg. formula weight of CAR (g CAR / mol CAR):                    634.7072
Al content of CAP (moles Al/moles CAP):                          2.25
Avg. formula weight of CAP (g CAP / mol CAP):                    625.7249
Density of CAP (g/cm^3):                                         4.07
Voxel edge length (cm):                                          0.012
Time step (yr):                                                  200
Number of voxels in X:                                           115
Number of voxels in Y:                                           115
Number of voxels in Z:                                           115
Dimensions:                                                      3
Default CAR amount (g/cm^3 rock):                                2.20
**** Reactant distribution: One header line, then one line per layer ****
Number of structures (0=homogeneous):                            1
Layer (see format codes)                                         1       50      64      1.50
FD approximation source/sink parameter (dimensionless):          200
Subvoxel growth acceleration factor (dimensionless, 0=none):     2.8284
Random seed (0=generate new):                                    -1717
Volume fraction of porphyroblast in CAP assemblage (fv):         0.7490
Number of moles of porphyroblast in reaction equation (moles):   1.0
Concentration to delGrxn conversion power-law factor n:          1.4165
Free energy specification mode (0=thermo, 1=delGrxn path):       1
Equilibrium temperature used for G-C conversion (°C):            528
Number of Time-Temp-DelGrxn triplets:                            3
DelGrxn path (Myr after start,°C,kJ/mol): (0.0,435.0,-0.0001)  (6.7,535.0,-19.0582)   (50.0,535.0,-20.1369)
```

PM1

Simulation: PM1_110927_0801_dTdtk2–04c

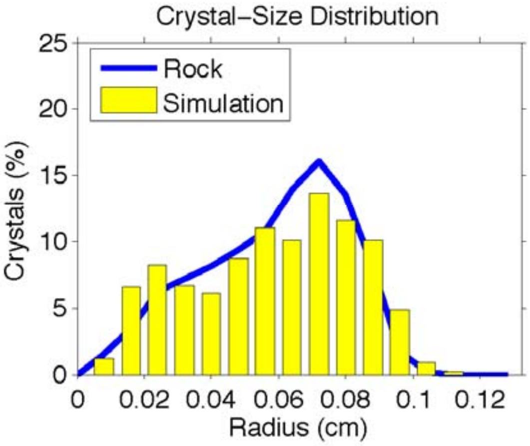

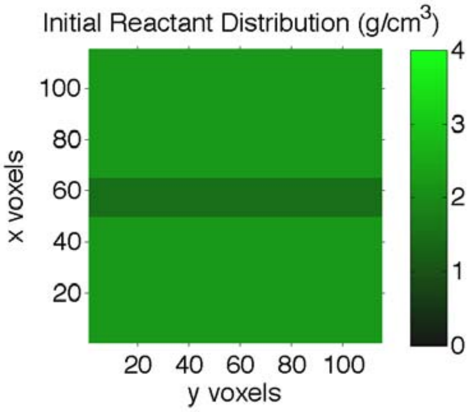

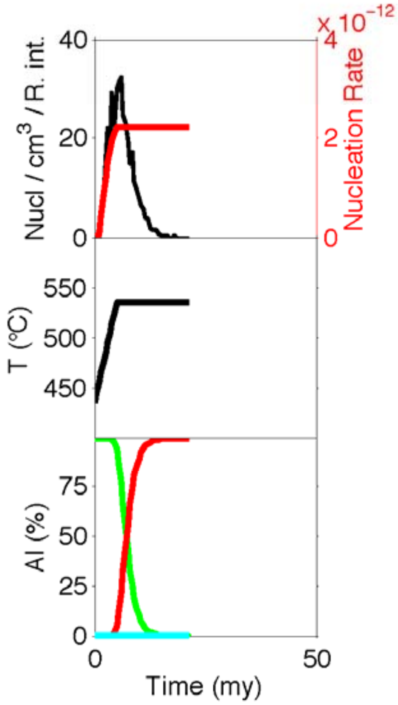

	Rock	Simulation
Total crystals:	1748	976
Xtl Num Density (xtls/cm^3):	382	371
Crystallization duration (my):	10	10.0[a]
Equil T of rxn (°C):	unknown	435
Thermal overstepping (°C):		20
T at 95% Al in products (°C):	535	535[a]
Min radius (cm):	0.006	0.007
Mean radius (cm):	0.058	0.058
Max radius (cm):	0.104	0.114
Mode (vol%):	37.4	38.0
D_{inf} (cm^2/s):		5.00e-006
$[Al]_{fl}$ in eq w/products (mol/cm^3):		5.60e-007
Porosity, ϕ:		3.00e+001
Tortuosity, τ:		1.00e+000
Q_D (kJ/mol):		140
$D = D_{inf} \phi \tau e^{(-Q_D/RT)}$ (m^2/s):		1.34e-017[a]
(at characteristic T, 535°C or 5.0 my)[a]		
$(dN/dt)_{steady-state}, k_1$ (nucl/cm^3/s):		2.70e-012
$(dN/dt)_{max}$ (nucl/cm^3/s):		2.23e-012
Nucleation acceleration, k_2:		6.50e-001
Time step (y):		200
Reporting interval (y):		5.00e+005

[a] Determined at nearest reporting interval

PM1 **Simulation: PM1_110927_0801_dTdtk2–04c**

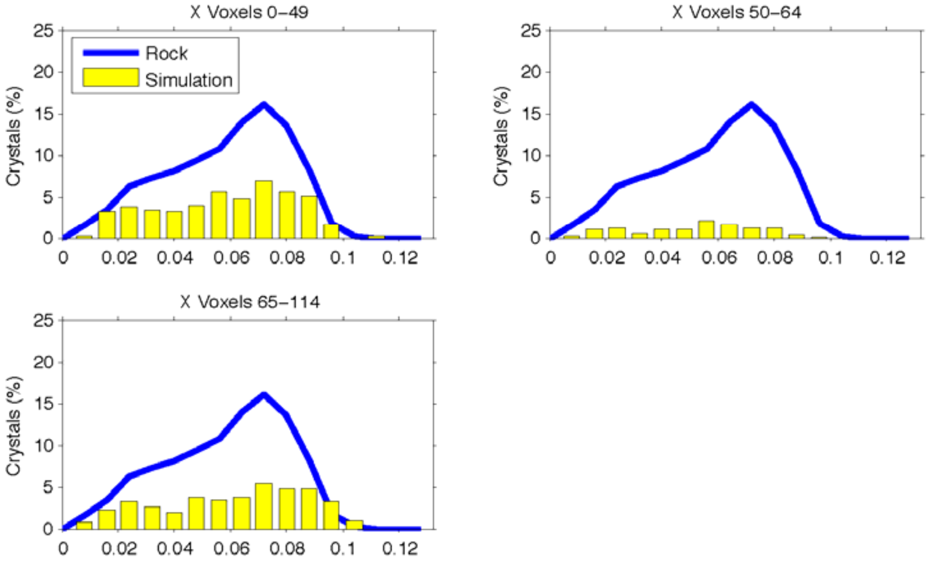
X Voxels 0–49

X Voxels 50–64

X Voxels 65–114

Parameters File

```
Crystallize 1.3
Run name:                                                       PM1_110927_0801_dTdtk2-04c
Result file directory:                                          runsPM1\PM1_110927_0801_dTdtk2-04c
Reporting interval (years):                                     5.00E+05
Fractional porosity (0-1):                                      3.00E+01
Tortuosity (0-1):                                               1.0
Activation energy for diffusion (kJ/mol):                       140
Dinf (cm^2/s):                                                  5.00E-06
Al concentration in fluid in eq with CAP (moles/cm^3):          5.60E-07
Nucleation acceleration (dimensionless):                        6.50E-01
Nucleation rate at infinite overstepping (nuclei/s/cm^3):       2.70E-12
Nucleation proportional to CAR amount in voxel (0=no,1=yes):    0
Maximum number of porphyroblasts (0=unlimited):                 0
Maximum modal amount of product (0=limited by reactant amount): 0
Al content of CAR (moles Al/moles CAR):                         2.25
Avg. formula weight of CAR (g CAR / mol CAR):                   634.7072
Al content of CAP (moles Al/moles CAP):                         2.25
Avg. formula weight of CAP (g CAP / mol CAP):                   625.7249
Density of CAP (g/cm^3):                                        4.07
Voxel edge length (cm):                                         0.012
Time step (yr):                                                 200
Number of voxels in X:                                          115
Number of voxels in Y:                                          115
Number of voxels in Z:                                          115
Dimensions:                                                     3
Default CAR amount (g/cm^3 rock):                               2.20
**** Reactant distribution: One header line, then one line per layer ****
Number of structures (0=homogeneous):                           1
Layer (see format codes)                                        1       50      64      1.50
FD approximation source/sink parameter (dimensionless):         200
Subvoxel growth acceleration factor (dimensionless, 0=none):    2.8284
Random seed (0=generate new):                                   -1717
Volume fraction of porphyroblast in CAP assemblage (fv):        0.7490
Number of moles of porphyroblast in reaction equation (moles):  1.0
Concentration to delGrxn conversion power-law factor n:         1.4165
Free energy specification mode (0=thermo, 1=delGrxn path):      1
Equilibrium temperature used for G-C conversion (°C):           528
Number of Time-Temp-DelGrxn triplets:                           3
DelGrxn path (Myr after start,°C,kJ/mol): (0.0,435.0,-0.0001)  (5.0,535.0,-19.0582)   (50.0,535.0,-20.1369)
```

PM1

Simulation: PM1_110927_0801_dTdtk3–01c

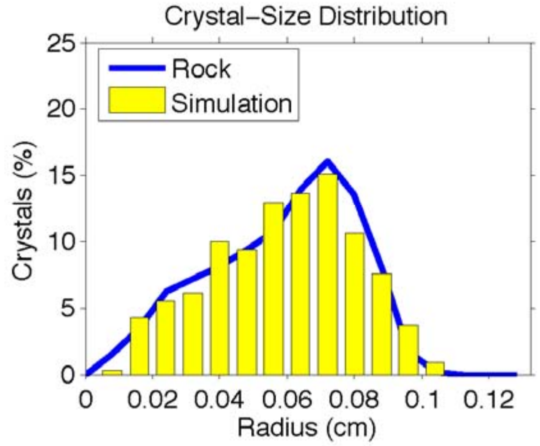

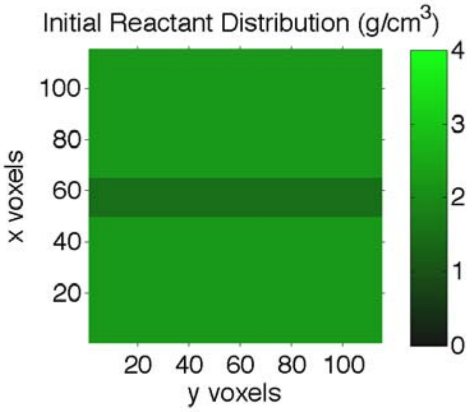

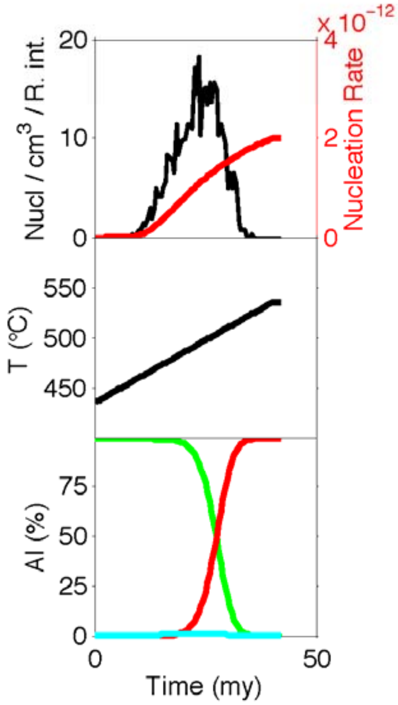

	Rock	Simulation
Total crystals:	1748	1024
Xtl Num Density (xtls/cm^3):	382	390
Crystallization duration (my):	10	24.0[a]
Equil T of rxn (°C):	unknown	435
Thermal overstepping (°C):		21
T at 95% Al in products (°C):	535	516[a]
Min radius (cm):	0.006	0.008
Mean radius (cm):	0.058	0.059
Max radius (cm):	0.104	0.105
Mode (vol%):	37.4	38.0
D_{inf} (cm^2/s):		5.00e-006
$[Al]_{fl}$ in eq w/products (mol/cm^3):		5.60e-007
Porosity, ϕ:		6.00e+001
Tortuosity, τ:		1.00e+000
Q_D (kJ/mol):		140
$D = D_{inf} \phi \tau e^{(-Q_D/RT)}$ (m^2/s):		1.08e-017[a]
(at characteristic T, 501 °C or 26.5 my)[a]		
$(dN/dt)_{steady-state}, k_1$ (nucl/cm^3/s):		2.70e-012
$(dN/dt)_{max}$ (nucl/cm^3/s):		2.00e-012
Nucleation acceleration, k_2:		1.00e+000
Time step (y):		200
Reporting interval (y):		5.00e+005

[a] Determined at nearest reporting interval

PM1 **Simulation: PM1_110927_0801_dTdtk3-01c**

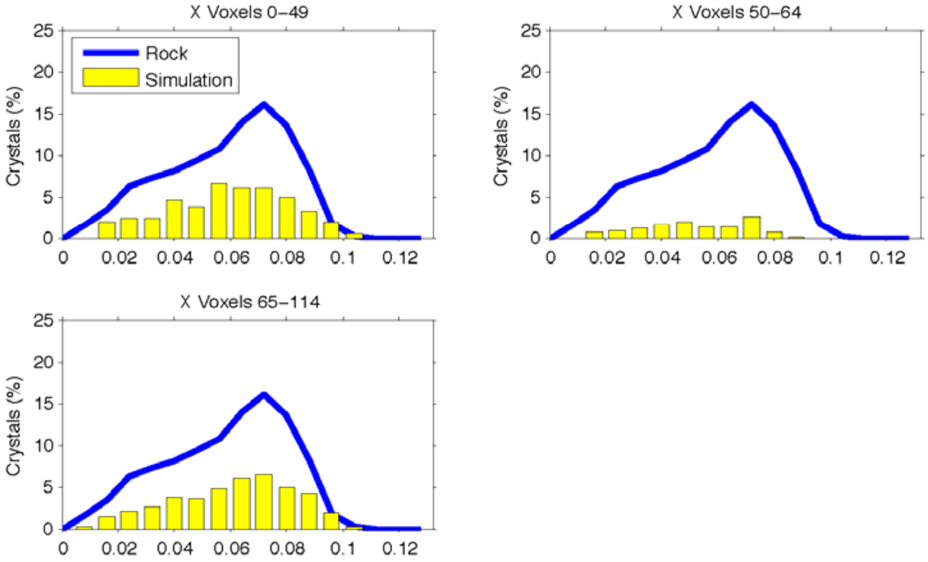

Parameters File

```
Crystallize 1.3
Run name:                                                          PM1_110927_0801_dTdtk3-01c
Result file directory:                                             runsPM1\PM1_110927_0801_dTdtk3-01c
Reporting interval (years):                                        5.00E+05
Fractional porosity (0-1):                                         6.00E+01
Tortuosity (0-1):                                                  1.0
Activation energy for diffusion (kJ/mol):                          140
Dinf (cm^2/s):                                                     5.00E-06
Al concentration in fluid in eq with CAP (moles/cm^3):             5.60E-07
Nucleation acceleration (dimensionless):                           1.00E-00
Nucleation rate at infinite overstepping (nuclei/s/cm^3):          2.70E-12
Nucleation proportional to CAR amount in voxel (0=no,1=yes):       0
Maximum number of porphyroblasts (0=unlimited):                    0
Maximum modal amount of product (0=limited by reactant amount):    0
Al content of CAR (moles Al/moles CAR):                            2.25
Avg. formula weight of CAR (g CAR / mol CAR):                      634.7072
Al content of CAP (moles Al/moles CAP):                            2.25
Avg. formula weight of CAP (g CAP / mol CAP):                      625.7249
Density of CAP (g/cm^3):                                           4.07
Voxel edge length (cm):                                            0.012
Time step (yr):                                                    200
Number of voxels in X:                                             115
Number of voxels in Y:                                             115
Number of voxels in Z:                                             115
Dimensions:                                                        3
Default CAR amount (g/cm^3 rock):                                  2.20
**** Reactant distribution: One header line, then one line per layer ****
Number of structures (0=homogeneous):                              1
Layer (see format codes)                                           1        50        64        1.50
FD approximation source/sink parameter (dimensionless):            200
Subvoxel growth acceleration factor (dimensionless, 0=none):       2.8284
Random seed (0=generate new):                                      -1717
Volume fraction of porphyroblast in CAP assemblage (fv):           0.7490
Number of moles of porphyroblast in reaction equation (moles):     1.0
Concentration to delGrxn conversion power-law factor n:            1.4165
Free energy specification mode (0=thermo, 1=delGrxn path):         1
Equilibrium temperature used for G-C conversion (°C):              528
Number of Time-Temp-DelGrxn triplets:                              3
DelGrxn path (Myr after start,°C,kJ/mol): (0.0,435.0,-0.0001)     (40.0,535.0,-19.0582)     (50.0,535.0,-20.1369)
```

PM1

Simulation: PM1_110927_0801_dTdtk3–02d

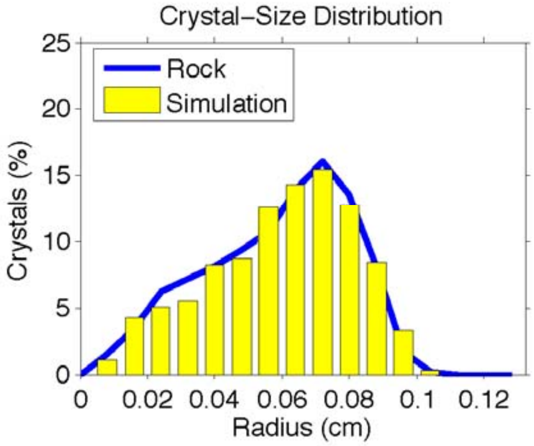

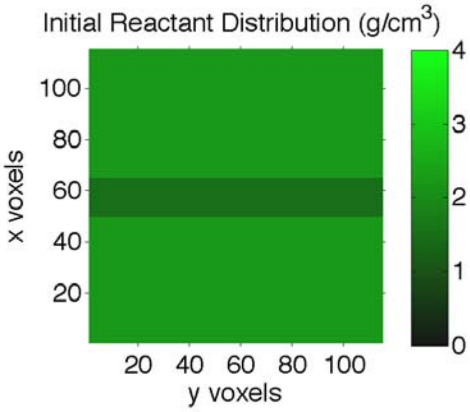

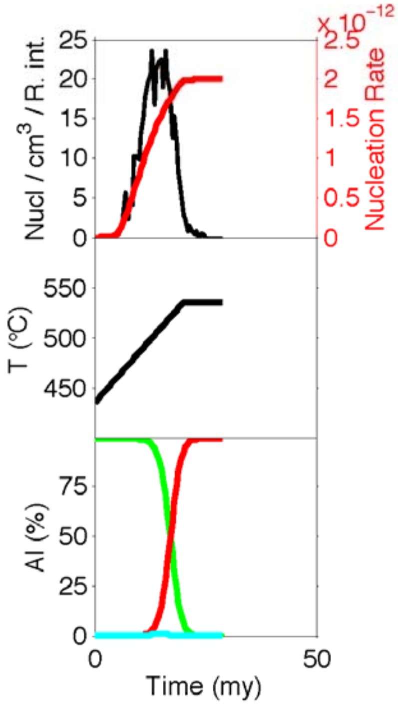

	Rock	Simulation
Total crystals:	1748	1021
Xtl Num Density (xtls/cm^3):	382	388
Crystallization duration (my):	10	16.0[a]
Equil T of rxn (°C):	unknown	435
Thermal overstepping (°C):		21
T at 95% Al in products (°C):	535	535[a]
Min radius (cm):	0.006	0.010
Mean radius (cm):	0.058	0.060
Max radius (cm):	0.104	0.102
Mode (vol%):	37.4	38.0
D_{inf} (cm^2/s):		5.00e-006
$[Al]_{fl}$ in eq w/products (mol/cm^3):		5.60e-007
Porosity, ϕ:		4.40e+001
Tortuosity, τ:		1.00e+000
Q_D (kJ/mol):		140
$D = D_{inf} \phi \tau e^{(-Q_D/RT)}$ (m^2/s):		1.16e-017[a]
(at characteristic T, 515°C or 16.0 my)[a]		
$(dN/dt)_{steady-state}, k_1$ (nucl/cm^3/s):		2.70e-012
$(dN/dt)_{max}$ (nucl/cm^3/s):		2.01e-012
Nucleation acceleration, k_2:		1.00e+000
Time step (y):		200
Reporting interval (y):		5.00e+005

[a] Determined at nearest reporting interval

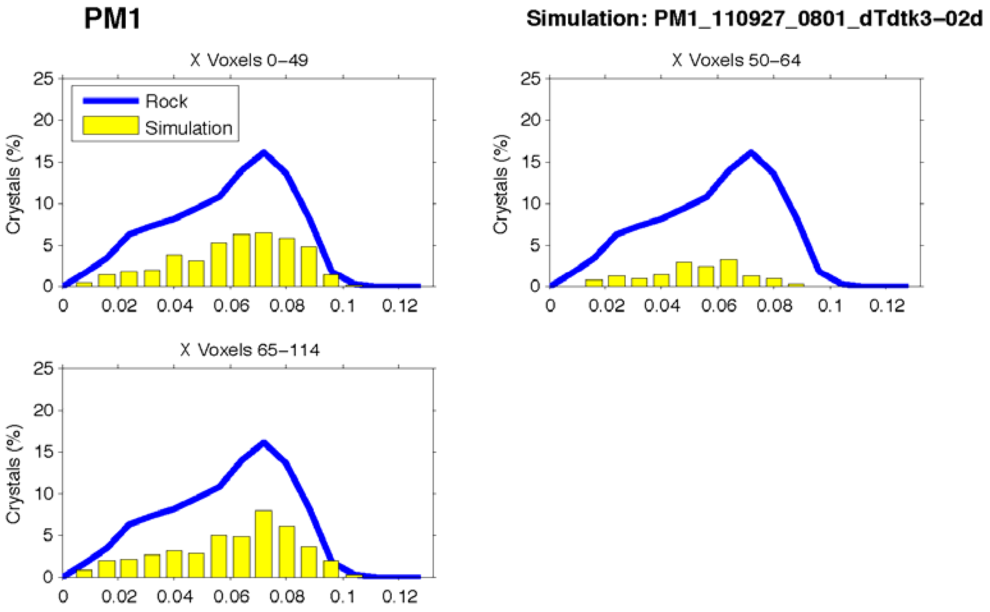
PM1
Simulation: PM1_110927_0801_dTdtk3−02d
X Voxels 0−49
X Voxels 50−64
X Voxels 65−114
Rock
Simulation
Crystals (%)
0
5
10
15
20
25
0
0.02
0.04
0.06
0.08
0.1
0.12

Parameters File

```
Crystallize 1.3
Run name:                                                      PM1_110927_0801_dTdtk3-02d
Result file directory:                                         runsPM1\PM1_110927_0801_dTdtk3-02d
Reporting interval (years):                                    5.00E+05
Fractional porosity (0-1):                                     4.40E+01
Tortuosity (0-1):                                              1.0
Activation energy for diffusion (kJ/mol):                      140
Dinf (cm^2/s):                                                 5.00E-06
Al concentration in fluid in eq with CAP (moles/cm^3):         5.60E-07
Nucleation acceleration (dimensionless):                       1.00E-00
Nucleation rate at infinite overstepping (nuclei/s/cm^3):      2.70E-12
Nucleation proportional to CAR amount in voxel (0=no,1=yes):   0
Maximum number of porphyroblasts (0=unlimited):                0
Maximum modal amount of product (0=limited by reactant amount): 0
Al content of CAR (moles Al/moles CAR):                        2.25
Avg. formula weight of CAR (g CAR / mol CAR):                  634.7072
Al content of CAP (moles Al/moles CAP):                        2.25
Avg. formula weight of CAP (g CAP / mol CAP):                  625.7249
Density of CAP (g/cm^3):                                       4.07
Voxel edge length (cm):                                        0.012
Time step (yr):                                                200
Number of voxels in X:                                         115
Number of voxels in Y:                                         115
Number of voxels in Z:                                         115
Dimensions:                                                    3
Default CAR amount (g/cm^3 rock):                              2.20
**** Reactant distribution: One header line, then one line per layer ****
Number of structures (0=homogeneous):                          1
Layer (see format codes)                                       1     50     64     1.50
FD approximation source/sink parameter (dimensionless):        200
Subvoxel growth acceleration factor (dimensionless, 0=none):   2.8284
Random seed (0=generate new):                                  -1717
Volume fraction of porphyroblast in CAP assemblage (fv):       0.7490
Number of moles of porphyroblast in reaction equation (moles): 1.0
Concentration to delGrxn conversion power-law factor n:        1.4165
Free energy specification mode (0=thermo, 1=delGrxn path):     1
Equilibrium temperature used for G-C conversion (°C):          528
Number of Time-Temp-DelGrxn triplets:                          3
DelGrxn path (Myr after start,°C,kJ/mol): (0.0,435.0,-0.0001)   (20.0,535.0,-19.0582)   (50.0,535.0,-20.1369)
```

PM1

Simulation: PM1_110927_0801_dTdtk3–03b

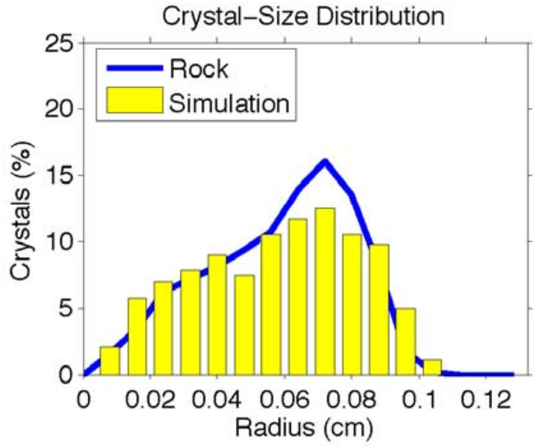
Crystal–Size Distribution

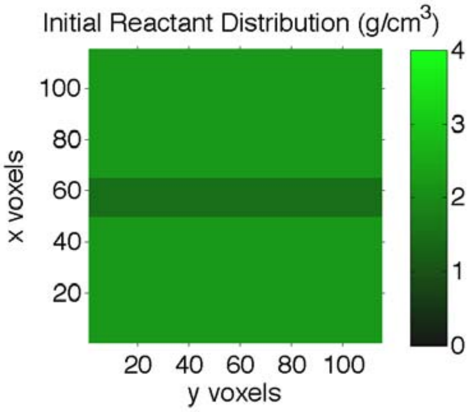
Initial Reactant Distribution (g/cm^3)

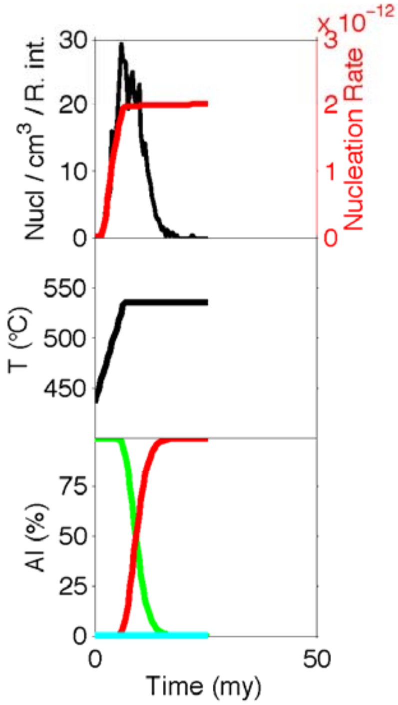

	Rock	Simulation
Total crystals:	1748	1013
Xtl Num Density (xtls/cm^3):	382	385
Crystallization duration (my):	10	12.0[a]
Equil T of rxn (°C):	unknown	435
Thermal overstepping (°C):		24
T at 95% Al in products (°C):	535	535[a]
Min radius (cm):	0.006	0.007
Mean radius (cm):	0.058	0.057
Max radius (cm):	0.104	0.106
Mode (vol%):	37.4	38.0
D_{inf} (cm^2/s):		5.00e-006
$[Al]_{fl}$ in eq w/products (mol/cm^3):		5.60e-007
Porosity, ϕ:		2.50e+001
Tortuosity, τ:		1.00e+000
Q_D (kJ/mol):		140
$D = D_{inf} \phi \tau e^{(-Q_D/RT)}$ (m^2/s):		1.03e-017[a]
(at characteristic T, 532°C or 6.5 my)[a]		
$(dN/dt)_{steady-state}, k_1$ (nucl/cm^3/s):		2.70e-012
$(dN/dt)_{max}$ (nucl/cm^3/s):		2.02e-012
Nucleation acceleration, k_2:		1.00e+000
Time step (y):		200
Reporting interval (y):		5.00e+005

[a] Determined at nearest reporting interval

PM1 **Simulation: PM1_110927_0801_dTdtk3–03b**

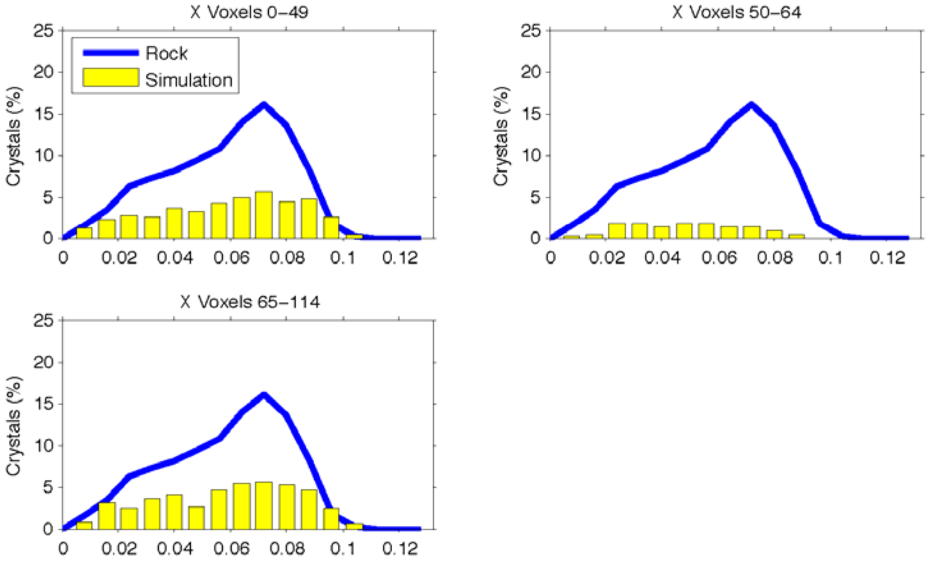

Parameters File

```
Crystallize 1.3
Run name:                                                          PM1_110927_0801_dTdtk3-03b
Result file directory:                                             runsPM1\PM1_110927_0801_dTdtk3-03b
Reporting interval (years):                                        5.00E+05
Fractional porosity (0-1):                                         2.50E+01
Tortuosity (0-1):                                                  1.0
Activation energy for diffusion (kJ/mol):                          140
Dinf (cm^2/s):                                                     5.00E-06
Al concentration in fluid in eq with CAP (moles/cm^3):             5.60E-07
Nucleation acceleration (dimensionless):                           1.00E-00
Nucleation rate at infinite overstepping (nuclei/s/cm^3):          2.70E-12
Nucleation proportional to CAR amount in voxel (0=no,1=yes):       0
Maximum number of porphyroblasts (0=unlimited):                    0
Maximum modal amount of product (0=limited by reactant amount):    0
Al content of CAR (moles Al/moles CAR):                            2.25
Avg. formula weight of CAR (g CAR / mol CAR):                      634.7072
Al content of CAP (moles Al/moles CAP):                            2.25
Avg. formula weight of CAP (g CAP / mol CAP):                      625.7249
Density of CAP (g/cm^3):                                           4.07
Voxel edge length (cm):                                            0.012
Time step (yr):                                                    200
Number of voxels in X:                                             115
Number of voxels in Y:                                             115
Number of voxels in Z:                                             115
Dimensions:                                                        3
Default CAR amount (g/cm^3 rock):                                  2.20
**** Reactant distribution: One header line, then one line per layer ****
Number of structures (0=homogeneous):                              1
Layer (see format codes)                                           1       50      64      1.50
FD approximation source/sink parameter (dimensionless):            200
Subvoxel growth acceleration factor (dimensionless, 0=none):       2.8284
Random seed (0=generate new):                                      -1717
Volume fraction of porphyroblast in CAP assemblage (fv):           0.7490
Number of moles of porphyroblast in reaction equation (moles):     1.0
Concentration to delGrxn conversion power-law factor n:            1.4165
Free energy specification mode (0=thermo, 1=delGrxn path):         1
Equilibrium temperature used for G-C conversion (°C):              528
Number of Time-Temp-DelGrxn triplets:                              3
DelGrxn path (Myr after start,°C,kJ/mol): (0.0,435.0,-0.0001)    (6.7,535.0,-19.0582)    (50.0,535.0,-20.1369)
```

PM1

Simulation: PM1_110927_0801_dTdtk3–04b

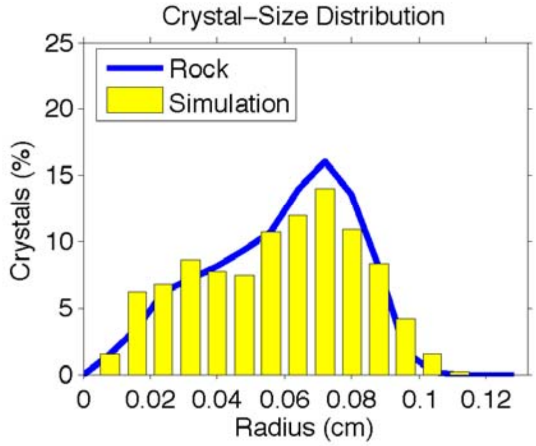

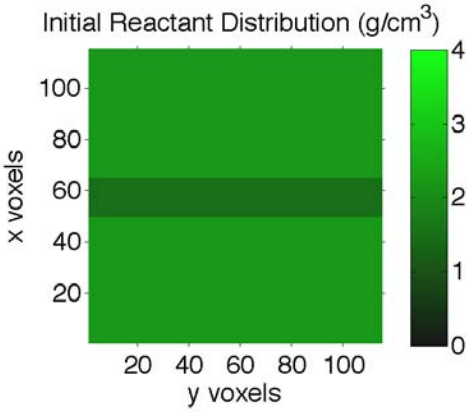

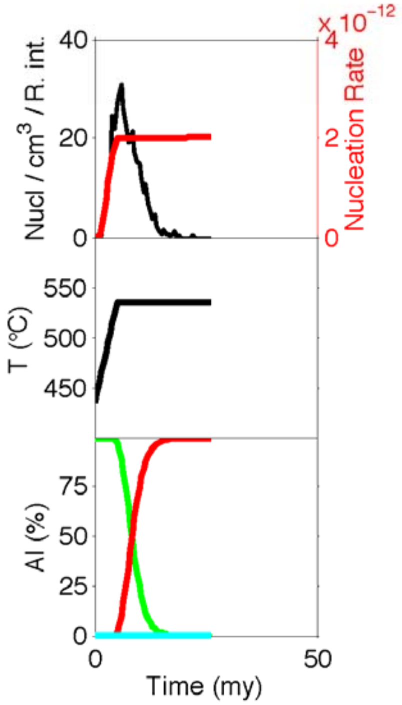

	Rock	Simulation
Total crystals:	1748	1021
Xtl Num Density (xtls/cm^3):	382	388
Crystallization duration (my):	10	11.0[a]
Equil T of rxn (°C):	unknown	435
Thermal overstepping (°C):		30
T at 95% Al in products (°C):	535	535[a]
Min radius (cm):	0.006	0.007
Mean radius (cm):	0.058	0.058
Max radius (cm):	0.104	0.111
Mode (vol%):	37.4	38.0
D_{inf} (cm^2/s):		5.00e-006
$[Al]_{fl}$ in eq w/products (mol/cm^3):		5.60e-007
Porosity, ϕ:		2.40e+001
Tortuosity, τ:		1.00e+000
Q_D (kJ/mol):		140
$D = D_{inf}\,\phi\,\tau\,e^{(-Q_D/RT)}$ (m^2/s):		1.07e-017[a]
(at characteristic T, 535°C or 5.0 my)[a]		
$(dN/dt)_{steady\text{-}state}, k_1$ (nucl/cm^3/s):		2.70e-012
$(dN/dt)_{max}$ (nucl/cm^3/s):		2.02e-012
Nucleation acceleration, k_2:		1.00e+000
Time step (y):		200
Reporting interval (y):		5.00e+005

[a] Determined at nearest reporting interval

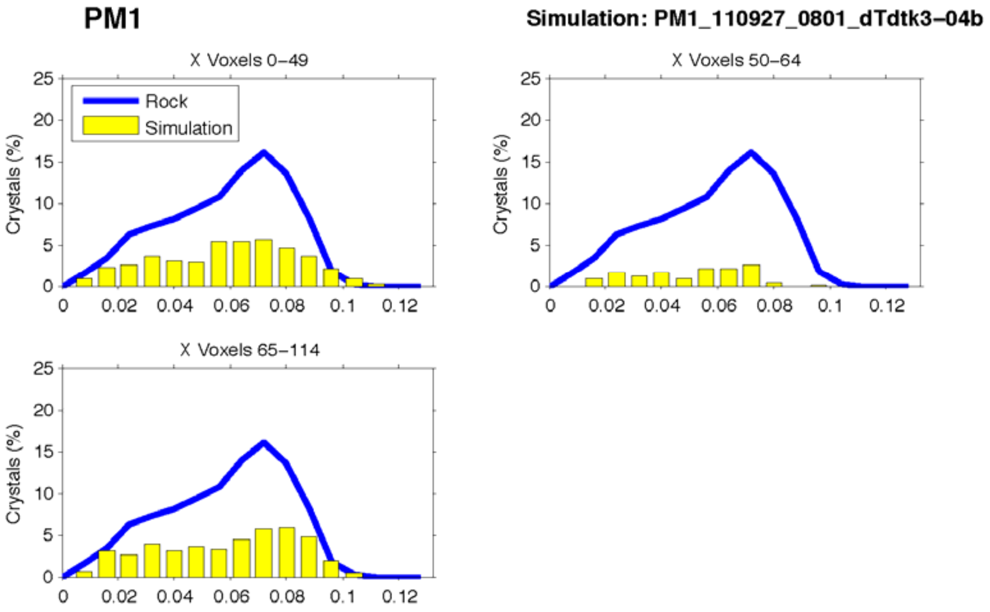
PM1
Simulation: PM1_110927_0801_dTdtk3−04b
X Voxels 0−49
X Voxels 50−64
X Voxels 65−114
Rock
Simulation
Crystals (%)
0
5
10
15
20
25
0
0.02
0.04
0.06
0.08
0.1
0.12

Parameters File

```
Crystallize 1.3
Run name:                                                        PM1_110927_0801_dTdtk3-04b
Result file directory:                                           runsPM1\PM1_110927_0801_dTdtk3-04b
Reporting interval (years):                                      5.00E+05
Fractional porosity (0-1):                                       2.40E+01
Tortuosity (0-1):                                                1.0
Activation energy for diffusion (kJ/mol):                        140
Dinf (cm^2/s):                                                   5.00E-06
Al concentration in fluid in eq with CAP (moles/cm^3):           5.60E-07
Nucleation acceleration (dimensionless):                         1.00E-00
Nucleation rate at infinite overstepping (nuclei/s/cm^3):        2.70E-12
Nucleation proportional to CAR amount in voxel (0=no,1=yes):     0
Maximum number of porphyroblasts (0=unlimited):                  0
Maximum modal amount of product (0=limited by reactant amount):  0
Al content of CAR (moles Al/moles CAR):                          2.25
Avg. formula weight of CAR (g CAR / mol CAR):                    634.7072
Al content of CAP (moles Al/moles CAP):                          2.25
Avg. formula weight of CAP (g CAP / mol CAP):                    625.7249
Density of CAP (g/cm^3):                                         4.07
Voxel edge length (cm):                                          0.012
Time step (yr):                                                  200
Number of voxels in X:                                           115
Number of voxels in Y:                                           115
Number of voxels in Z:                                           115
Dimensions:                                                      3
Default CAR amount (g/cm^3 rock):                                2.20
**** Reactant distribution: One header line, then one line per layer ****
Number of structures (0=homogeneous):                            1
Layer (see format codes)                                         1       50      64      1.50
FD approximation source/sink parameter (dimensionless):          200
Subvoxel growth acceleration factor (dimensionless, 0=none):     2.8284
Random seed (0=generate new):                                    -1717
Volume fraction of porphyroblast in CAP assemblage (fv):         0.7490
Number of moles of porphyroblast in reaction equation (moles):   1.0
Concentration to delGrxn conversion power-law factor n:          1.4165
Free energy specification mode (0=thermo, 1=delGrxn path):       1
Equilibrium temperature used for G-C conversion (°C):            528
Number of Time-Temp-DelGrxn triplets:                            3
DelGrxn path (Myr after start,°C,kJ/mol): (0.0,435.0,-0.0001)   (5.0,535.0,-19.0582)    (50.0,535.0,-20.1369)
```

PM1

Simulation: PM1_110927_0801_Qk3–01c

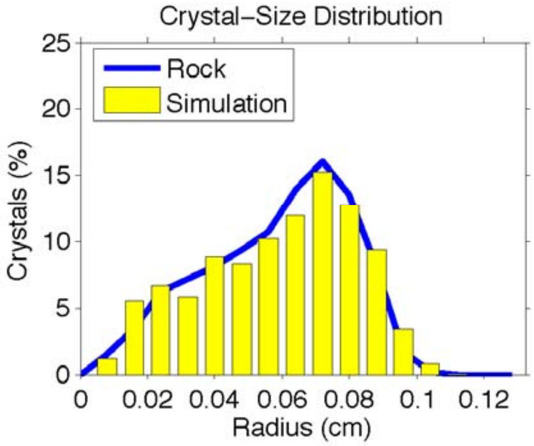

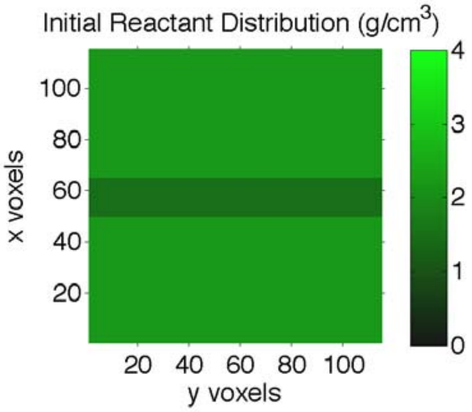

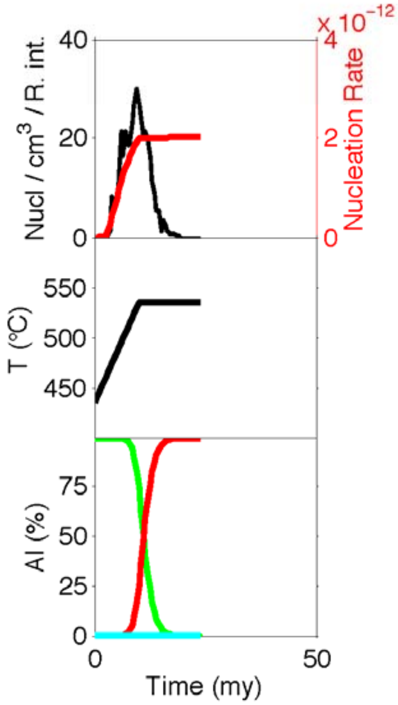

	Rock	Simulation
Total crystals:	1748	1008
Xtl Num Density (xtls/cm^3):	382	384
Crystallization duration (my):	10	12.0[a]
Equil T of rxn (°C):	unknown	435
Thermal overstepping (°C):		29
T at 95% Al in products (°C):	535	535[a]
Min radius (cm):	0.006	0.009
Mean radius (cm):	0.058	0.059
Max radius (cm):	0.104	0.113
Mode (vol%):	37.4	38.0
D_{inf} (cm^2/s):		1.00e-007
$[Al]_{fl}$ in eq w/products (mol/cm^3):		5.60e-007
Porosity, ϕ:		8.00e+000
Tortuosity, τ:		1.00e+000
Q_D (kJ/mol):		105
$D = D_{inf}\phi\tau e^{(-Q_D/RT)}$ (m^2/s): (at characteristic T, 525°C or 9.0 my)[a]		1.08e-017[a]
$(dN/dt)_{steady-state}, k_1$ (nucl/cm^3/s):		2.70e-012
$(dN/dt)_{max}$ (nucl/cm^3/s):		2.04e-012
Nucleation acceleration, k_2:		1.00e+000
Time step (y):		200
Reporting interval (y):		5.00e+005

[a] Determined at nearest reporting interval

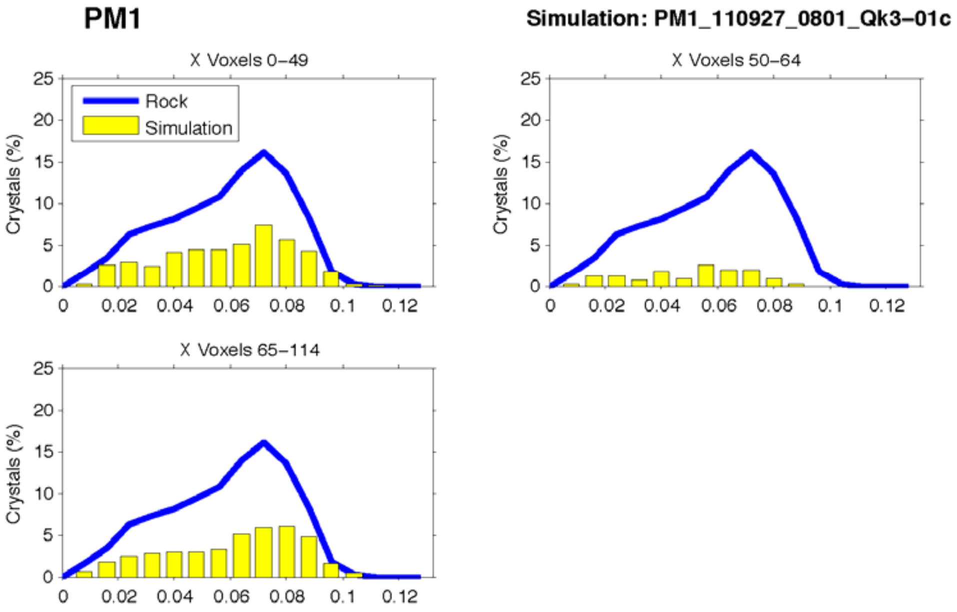
PM1
Simulation: PM1_110927_0801_Qk3−01c
X Voxels 0−49
Rock
Simulation
Crystals (%)
0
5
10
15
20
25
0
0.02
0.04
0.06
0.08
0.1
0.12
X Voxels 50−64
Crystals (%)
X Voxels 65−114
Crystals (%)

Parameters File

```
Crystallize 1.3
Run name:                                                        PM1_110927_0801_Qk3-01c
Result file directory:                                           runsPM1\PM1_110927_0801_Qk3-01c
Reporting interval (years):                                      5.00E+05
Fractional porosity (0-1):                                       8.00E+00
Tortuosity (0-1):                                                1.0
Activation energy for diffusion (kJ/mol):                        105
Dinf (cm^2/s):                                                   1.00E-07
Al concentration in fluid in eq with CAP (moles/cm^3):           5.60E-07
Nucleation acceleration (dimensionless):                         1.00E-00
Nucleation rate at infinite overstepping (nuclei/s/cm^3):        2.70E-12
Nucleation proportional to CAR amount in voxel (0=no,1=yes):     0
Maximum number of porphyroblasts (0=unlimited):                  0
Maximum modal amount of product (0=limited by reactant amount):  0
Al content of CAR (moles Al/moles CAR):                          2.25
Avg. formula weight of CAR (g CAR / mol CAR):                    634.7072
Al content of CAP (moles Al/moles CAP):                          2.25
Avg. formula weight of CAP (g CAP / mol CAP):                    625.7249
Density of CAP (g/cm^3):                                         4.07
Voxel edge length (cm):                                          0.012
Time step (yr):                                                  200
Number of voxels in X:                                           115
Number of voxels in Y:                                           115
Number of voxels in Z:                                           115
Dimensions:                                                      3
Default CAR amount (g/cm^3 rock):                                2.20
**** Reactant distribution: One header line, then one line per layer ****
Number of structures (0=homogeneous):                            1
Layer (see format codes)                                         1        50        64        1.50
FD approximation source/sink parameter (dimensionless):          200
Subvoxel growth acceleration factor (dimensionless, 0=none):     2.8284
Random seed (0=generate new):                                    -1717
Volume fraction of porphyroblast in CAP assemblage (fv):         0.7490
Number of moles of porphyroblast in reaction equation (moles):   1.0
Concentration to delGrxn conversion power-law factor n:          1.4165
Free energy specification mode (0=thermo, 1=delGrxn path):       1
Equilibrium temperature used for G-C conversion (°C):            528
Number of Time-Temp-DelGrxn triplets:                            3
DelGrxn path (Myr after start,°C,kJ/mol): (0.0,435.0,-0.0001)    (10.0,535.0,-19.0582)    (30.0,535.0,-20.1369)
```

PM1

Simulation: PM1_110927_0801_Qk3-02d

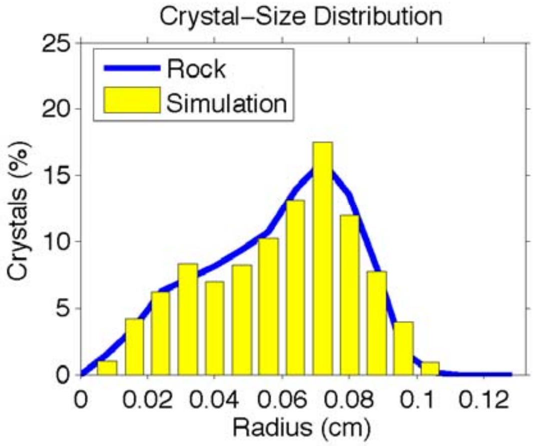

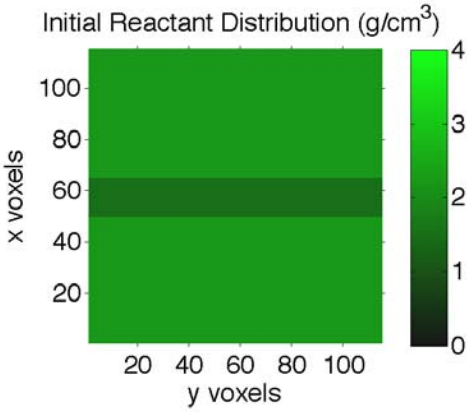

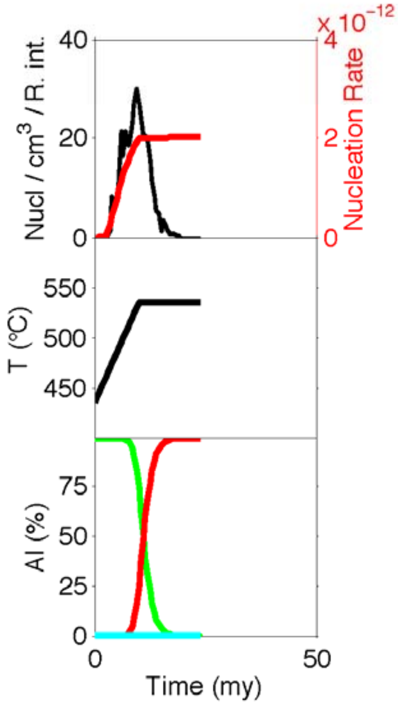

	Rock	Simulation
Total crystals:	1748	1004
Xtl Num Density (xtls/cm^3):	382	382
Crystallization duration (my):	10	12.0[a]
Equil T of rxn (°C):	unknown	435
Thermal overstepping (°C):		29
T at 95% Al in products (°C):	535	535[a]
Min radius (cm):	0.006	0.009
Mean radius (cm):	0.058	0.059
Max radius (cm):	0.104	0.106
Mode (vol%):	37.4	38.0
D_{inf} (cm^2/s):		1.00e-006
$[Al]_{fl}$ in eq w/products (mol/cm^3):		5.60e-007
Porosity, ϕ:		1.20e+001
Tortuosity, τ:		1.00e+000
Q_D (kJ/mol):		123
$D = D_{inf} \phi \tau e^{(-Q_D/RT)}$ (m^2/s): (at characteristic T, 525°C or 9.0 my)[a]		1.07e-017[a]
$(dN/dt)_{steady-state}$, k_1 (nucl/cm^3/s):		2.70e-012
$(dN/dt)_{max}$ (nucl/cm^3/s):		2.04e-012
Nucleation acceleration, k_2:		1.00e+000
Time step (y):		200
Reporting interval (y):		5.00e+005

[a] Determined at nearest reporting interval

PM1 **Simulation: PM1_110927_0801_Qk3−02d**

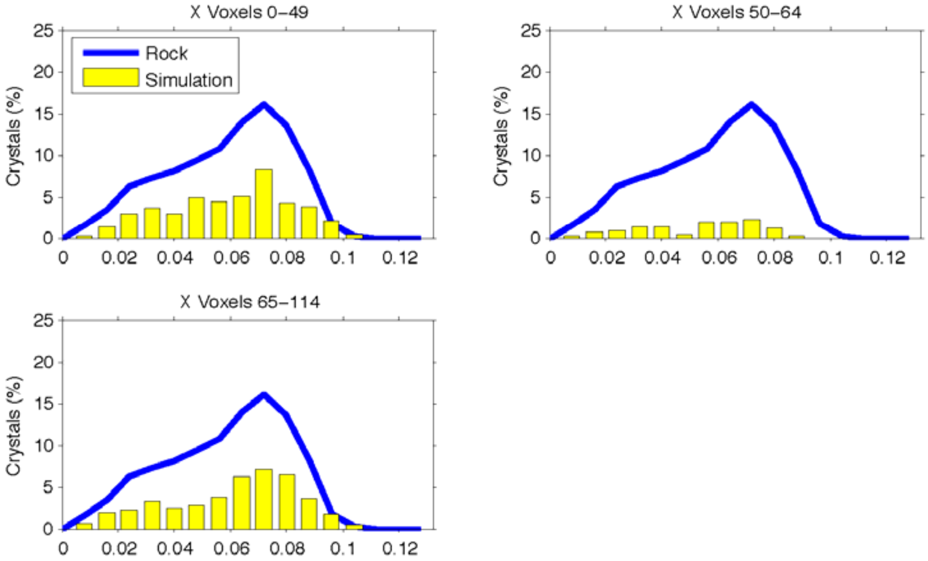

Parameters File

```
Crystallize 1.3
Run name:                                                        PM1_110927_0801_Qk3-02d
Result file directory:                                           runsPM1\PM1_110927_0801_Qk3-02d
Reporting interval (years):                                      5.00E+05
Fractional porosity (0-1):                                       1.20E+01
Tortuosity (0-1):                                                1.0
Activation energy for diffusion (kJ/mol):                        123
Dinf (cm^2/s):                                                   1.00E-06
Al concentration in fluid in eq with CAP (moles/cm^3):           5.60E-07
Nucleation acceleration (dimensionless):                         1.00E-00
Nucleation rate at infinite overstepping (nuclei/s/cm^3):        2.70E-12
Nucleation proportional to CAR amount in voxel (0=no,1=yes):     0
Maximum number of porphyroblasts (0=unlimited):                  0
Maximum modal amount of product (0=limited by reactant amount):  0
Al content of CAR (moles Al/moles CAR):                          2.25
Avg. formula weight of CAR (g CAR / mol CAR):                    634.7072
Al content of CAP (moles Al/moles CAP):                          2.25
Avg. formula weight of CAP (g CAP / mol CAP):                    625.7249
Density of CAP (g/cm^3):                                         4.07
Voxel edge length (cm):                                          0.012
Time step (yr):                                                  200
Number of voxels in X:                                           115
Number of voxels in Y:                                           115
Number of voxels in Z:                                           115
Dimensions:                                                      3
Default CAR amount (g/cm^3 rock):                                2.20
**** Reactant distribution: One header line, then one line per layer ****
Number of structures (0=homogeneous):                            1
Layer (see format codes)                                         1      50      64      1.50
FD approximation source/sink parameter (dimensionless):          200
Subvoxel growth acceleration factor (dimensionless, 0=none):     2.8284
Random seed (0=generate new):                                    -1717
Volume fraction of porphyroblast in CAP assemblage (fv):         0.7490
Number of moles of porphyroblast in reaction equation (moles):   1.0
Concentration to delGrxn conversion power-law factor n:          1.4165
Free energy specification mode (0=thermo, 1=delGrxn path):       1
Equilibrium temperature used for G-C conversion (°C):            528
Number of Time-Temp-DelGrxn triplets:                            3
DelGrxn path (Myr after start,°C,kJ/mol): (0.0,435.0,-0.0001)   (10.0,535.0,-19.0582)   (30.0,535.0,-20.1369)
```

PM1

Simulation: PM1_110927_0801_Qk3–03e

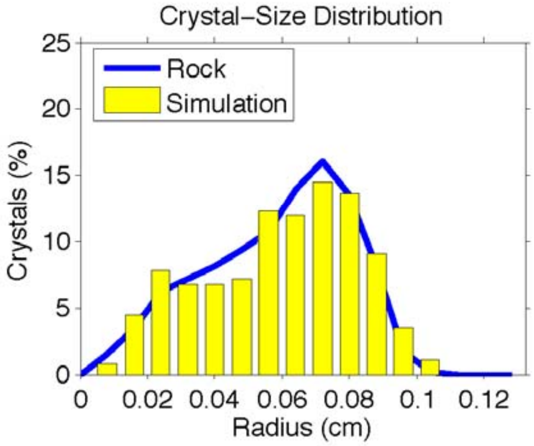

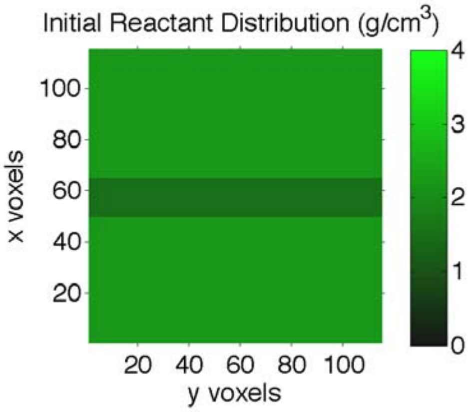

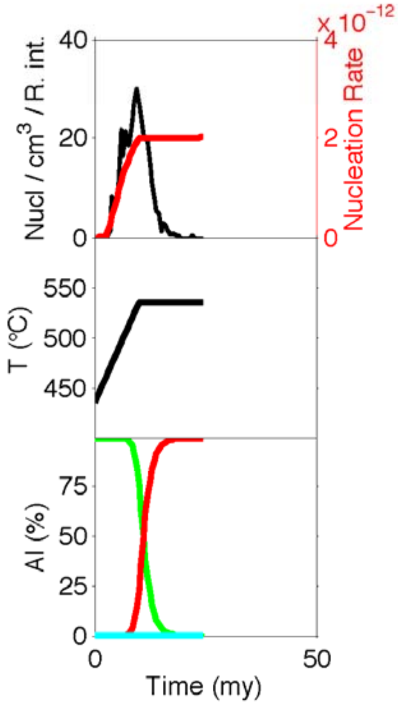

	Rock	Simulation
Total crystals:	1748	1001
Xtl Num Density (xtls/cm^3):	382	381
Crystallization duration (my):	10	12.0[a]
Equil T of rxn (°C):	unknown	435
Thermal overstepping (°C):		29
T at 95% Al in products (°C):	535	535[a]
Min radius (cm):	0.006	0.008
Mean radius (cm):	0.058	0.059
Max radius (cm):	0.104	0.107
Mode (vol%):	37.4	38.0
D_{inf} (cm^2/s):		1.90e-004
$[Al]_{fl}$ in eq w/products (mol/cm^3):		5.60e-007
Porosity, ϕ:		1.20e+001
Tortuosity, τ:		1.00e+000
Q_D (kJ/mol):		158
$D = D_{inf} \phi \tau e^{(-Q_D/RT)}$ (m^2/s): (at characteristic T, 530°C or 9.5 my)[a]		1.21e-017[a]
$(dN/dt)_{steady-state}$, k_1 (nucl/cm^3/s):		2.70e-012
$(dN/dt)_{max}$ (nucl/cm^3/s):		2.02e-012
Nucleation acceleration, k_2:		1.00e+000
Time step (y):		200
Reporting interval (y):		5.00e+005

[a] Determined at nearest reporting interval

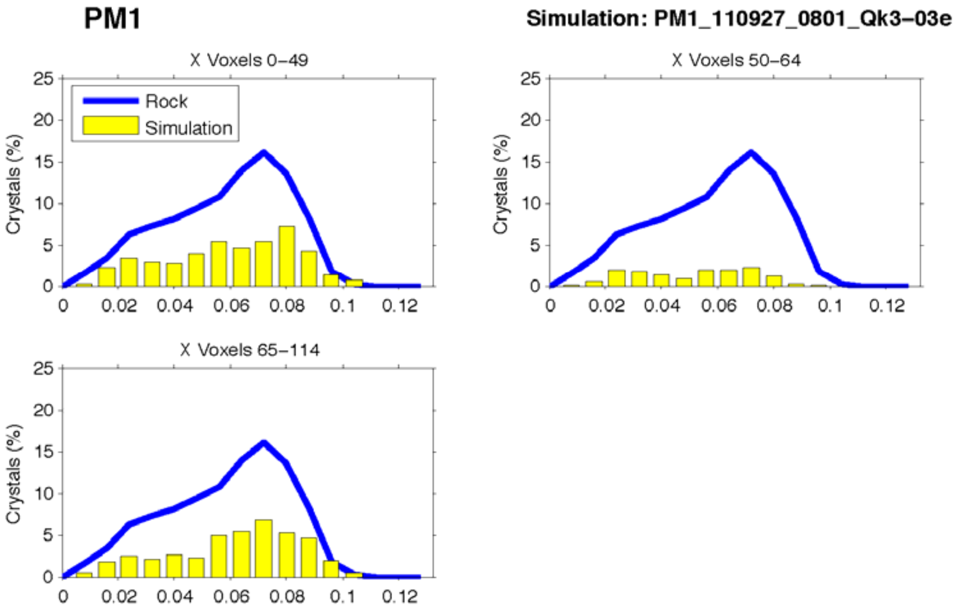
PM1
Simulation: PM1_110927_0801_Qk3-03e
X Voxels 0–49
X Voxels 50–64
X Voxels 65–114
Rock
Simulation
Crystals (%)
0
5
10
15
20
25
0
0.02
0.04
0.06
0.08
0.1
0.12

Parameters File

```
Crystallize 1.3
Run name:                                                        PM1_110927_0801_Qk3-03e
Result file directory:                                           runsPM1\PM1_110927_0801_Qk3-03e
Reporting interval (years):                                      5.00E+05
Fractional porosity (0-1):                                       1.20E+01
Tortuosity (0-1):                                                1.0
Activation energy for diffusion (kJ/mol):                        158
Dinf (cm^2/s):                                                   1.90E-04
Al concentration in fluid in eq with CAP (moles/cm^3):           5.60E-07
Nucleation acceleration (dimensionless):                         1.00E-00
Nucleation rate at infinite overstepping (nuclei/s/cm^3):        2.70E-12
Nucleation proportional to CAR amount in voxel (0=no,1=yes):     0
Maximum number of porphyroblasts (0=unlimited):                  0
Maximum modal amount of product (0=limited by reactant amount):  0
Al content of CAR (moles Al/moles CAR):                          2.25
Avg. formula weight of CAR (g CAR / mol CAR):                    634.7072
Al content of CAP (moles Al/moles CAP):                          2.25
Avg. formula weight of CAP (g CAP / mol CAP):                    625.7249
Density of CAP (g/cm^3):                                         4.07
Voxel edge length (cm):                                          0.012
Time step (yr):                                                  200
Number of voxels in X:                                           115
Number of voxels in Y:                                           115
Number of voxels in Z:                                           115
Dimensions:                                                      3
Default CAR amount (g/cm^3 rock):                                2.20
**** Reactant distribution: One header line, then one line per layer ****
Number of structures (0=homogeneous):                            1
Layer (see format codes)                                         1      50      64      1.50
FD approximation source/sink parameter (dimensionless):          200
Subvoxel growth acceleration factor (dimensionless, 0=none):     2.8284
Random seed (0=generate new):                                    -1717
Volume fraction of porphyroblast in CAP assemblage (fv):         0.7490
Number of moles of porphyroblast in reaction equation (moles):   1.0
Concentration to delGrxn conversion power-law factor n:          1.4165
Free energy specification mode (0=thermo, 1=delGrxn path):       1
Equilibrium temperature used for G-C conversion (°C):            528
Number of Time-Temp-DelGrxn triplets:                            3
DelGrxn path (Myr after start,°C,kJ/mol): (0.0,435.0,-0.0001)   (10.0,535.0,-19.0582)   (50.0,535.0,-20.1369)
```

PM1

Simulation: PM1_110927_0801_Qk3–04f

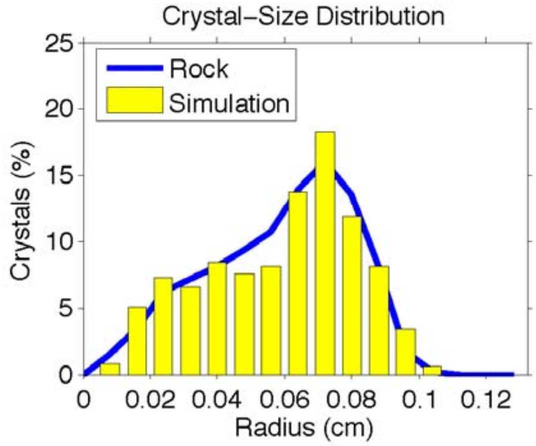

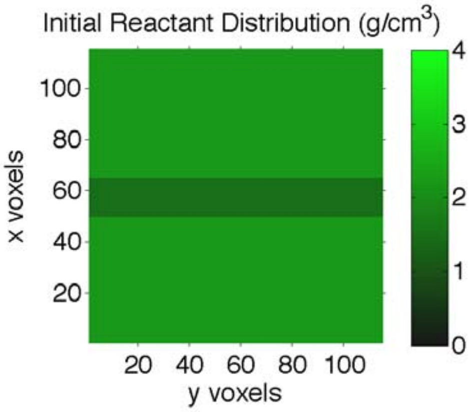

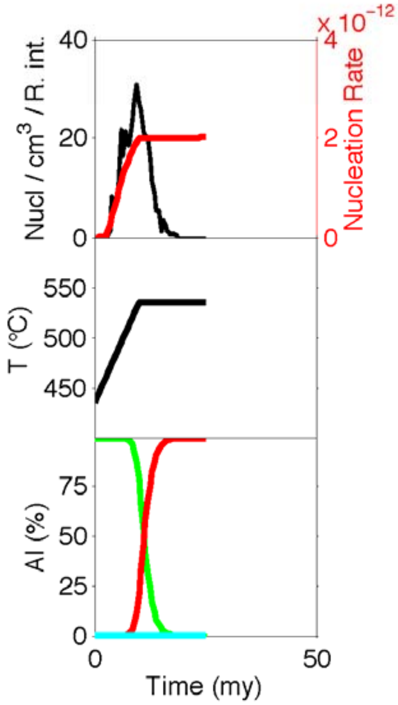

	Rock	Simulation
Total crystals:	1748	1018
Xtl Num Density (xtls/cm^3):	382	387
Crystallization duration (my):	10	12.0[a]
Equil T of rxn (°C):	unknown	435
Thermal overstepping (°C):		29
T at 95% Al in products (°C):	535	535[a]
Min radius (cm):	0.006	0.009
Mean radius (cm):	0.058	0.059
Max radius (cm):	0.104	0.106
Mode (vol%):	37.4	38.0
D_{inf} (cm^2/s):		2.30e-003
$[Al]_{fl}$ in eq w/products (mol/cm^3):		5.60e-007
Porosity, ϕ:		1.20e+001
Tortuosity, τ:		1.00e+000
Q_D (kJ/mol):		175
$D = D_{inf}\,\phi\,\tau\, e^{(-Q_D/RT)}$ (m^2/s): (at characteristic T, 530°C or 9.5 my)[a]		1.15e-017[a]
$(dN/dt)_{steady\text{-}state}, k_1$ (nucl/cm^3/s):		2.70e-012
$(dN/dt)_{max}$ (nucl/cm^3/s):		2.02e-012
Nucleation acceleration, k_2:		1.00e+000
Time step (y):		200
Reporting interval (y):		5.00e+005

[a] Determined at nearest reporting interval

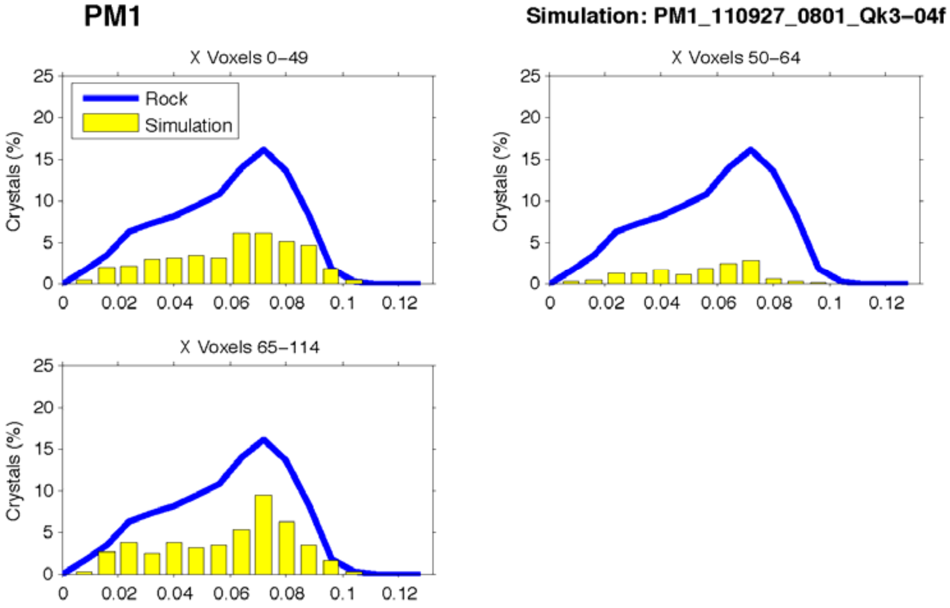
PM1
Simulation: PM1_110927_0801_Qk3−04f
X Voxels 0−49
X Voxels 50−64
X Voxels 65−114
Rock
Simulation
Crystals (%)
25
20
15
10
5
0
0
0.02
0.04
0.06
0.08
0.1
0.12

Parameters File

```
Crystallize 1.3
Run name:                                                          PM1_110927_0801_Qk3-04f
Result file directory:                                             runsPM1\PM1_110927_0801_Qk3-04f
Reporting interval (years):                                        5.00E+05
Fractional porosity (0-1):                                         1.20E+01
Tortuosity (0-1):                                                  1.0
Activation energy for diffusion (kJ/mol):                          175
Dinf (cm^2/s):                                                     2.30E-03
Al concentration in fluid in eq with CAP (moles/cm^3):             5.60E-07
Nucleation acceleration (dimensionless):                           1.00E-00
Nucleation rate at infinite overstepping (nuclei/s/cm^3):          2.70E-12
Nucleation proportional to CAR amount in voxel (0=no,1=yes):       0
Maximum number of porphyroblasts (0=unlimited):                    0
Maximum modal amount of product (0=limited by reactant amount):    0
Al content of CAR (moles Al/moles CAR):                            2.25
Avg. formula weight of CAR (g CAR / mol CAR):                      634.7072
Al content of CAP (moles Al/moles CAP):                            2.25
Avg. formula weight of CAP (g CAP / mol CAP):                      625.7249
Density of CAP (g/cm^3):                                           4.07
Voxel edge length (cm):                                            0.012
Time step (yr):                                                    200
Number of voxels in X:                                             115
Number of voxels in Y:                                             115
Number of voxels in Z:                                             115
Dimensions:                                                        3
Default CAR amount (g/cm^3 rock):                                  2.20
**** Reactant distribution: One header line, then one line per layer ****
Number of structures (0=homogeneous):                              1
Layer (see format codes)                                           1      50      64      1.50
FD approximation source/sink parameter (dimensionless):            200
Subvoxel growth acceleration factor (dimensionless, 0=none):       2.8284
Random seed (0=generate new):                                      -1717
Volume fraction of porphyroblast in CAP assemblage (fv):           0.7490
Number of moles of porphyroblast in reaction equation (moles):     1.0
Concentration to delGrxn conversion power-law factor n:            1.4165
Free energy specification mode (0=thermo, 1=delGrxn path):         1
Equilibrium temperature used for G-C conversion (°C):              528
Number of Time-Temp-DelGrxn triplets:                              3
DelGrxn path (Myr after start,°C,kJ/mol): (0.0,435.0,-0.0001)    (10.0,535.0,-19.0582)    (50.0,535.0,-20.1369)
```

REFERENCES

Adams, H.G., Cohen, L.H. & Rosenfeld, J.L., 1975. Solid Inclusion piezothermometry II: Geometric basis, calibration for the association quartz-garnet, and application to some pelitic schists. *American Mineralogist*, **60**, 584-598.

Anczkiewicz, R., Szczepanski, J., Mazur, S., Storey, C.D., Crowley, Q., Villa, I.M., Thirlwall, M.F. & Jeffries, T.E., 2007. Lu-Hf geochronology and trace element distribution in garnet; implications for uplift and exhumation of ultra-high pressure granulites in the Sudetes, SW Poland. *Lithos*, **95**, 363-380.

Ashworth, J.R. & Chambers, A.D., 2000. Symplectic reaction in olivine and the controls of intergrowth spacing in symplectites. *Journal of Petrology*, **41**, 285-304.

Ashworth, J.R. & Sheplev, V.S., 1997. Diffusion modelling of metamorphic layered coronas with stability criterion and consideration of affinity. *Geochimica et Cosmochimica Acta*, **61**, 3671-3689.

Ashworth, J.R., Sheplev, V.S., Bryxina, N.A., Kolobov, V.Y. & Reverdatto, V.V., 1998. Diffusion-controlled corona reaction and overstepping of equilibrium in a garnet granulite, Yenisey Ridge, Siberia. *Journal of Metamorphic Geology*, **16**, 231-246.

Barker, D.S., 1961. *Hallowell granite and associated rocks, South-Central Maine*. Unpublished Ph.D. Thesis, Princeton University, 240 pp.

Barnett, A., 1999. *Quantitative textural analysis used to determine garnet porphyroblast nucleation and growth mechanisms on a blueschist from the Franciscan complex, Jenner, california*. Unpublished Senior Honors Thesis, University of Texas, Austin, # pp.

Bear, J., 1988. *Dynamics of fluids in porous media*, 764 pp. Dover, New York.

Beitter, T., Wagner, T. & Markl, G., 2008. Formation of kyanite-quartz veins of the Alpe Sponda, Central Alps, Switzerland; implications for Al transport during regional metamorphism. *Contributions to Mineralogy and Petrology*, **156**, 689-707.

Berg, C.A., 2007. *Strain rates and constraints on chemical homogeneity and length scales of equilibriation during alpine metamorphism at Passo del Sole, central Swiss Alps*. Unpublished Ph.D. Thesis, University of Texas, Austin, 357 pp.

Bertrand, J.-M., Roddick, J.C., Van Kranendonk, M.J. & Ermanovics, I., 1993. U-Pb geochronology of deformation and metamorphism across a central transect of the early Proterozoic Torngat Orogen, North River map area, Labrador. *Canadian Journal of Earth Sciences*, **30**, 1470-1489.

Bickle, M.J. & Baker, J., 1990. Advective-diffusive transport of isotopic fronts: an example from Naxos, Greece. *Earth and Planetary Science Letters*, **97**, 78-93.

Blichert-Toft, J., Albarede, F. & Kornprobst, J., 1999. Lu-Hf isotope systematics of garnet pyroxenites from Beni Bousera, Morocco; implications for basalt origin. *Science*, **283**, 1303-1306.

Blichert-Toft, J. & Frei, R., 2001. Complex Sm-Nd and Lu-Hf isotope systematics in metamorphic garnets from the Isua supracrustal belt, West Greenland. *Geochimica et Cosmochimica Acta*, **65**, 3177-3189.

Brady, J.B., 1983. Intergranular diffusion in metamorphic rocks. *American Journal of Science*, **283-A**, 181-200.

Burgess, S.R. & Harte, B., 2004. Tracing lithosphere evolution through the analysis of heterogeneous G9-G10 garnets in peridotite xenoliths, II: REE chemistry. *Journal of Petrology*, **45**, 609-634.

Carlson, W. & Schwarze, E., 1997. Petrological significance of prograde homogenization of growth zoning in garnet: an example from the Llano Uplift. *Journal of Metamorphic Geology*, **15**, 631-644.

Carlson, W.D., 1989. The significance of intergranular diffusion to the mechanism and kinetics of porphyroblast crystallization. *Contributions to Mineralogy and Petrology*, **103**, 1-24.

Carlson, W.D., 1991. Competitive diffusion-controlled growth of porphyroblasts. *Mineralogical Magazine*, **55**, 317-330.

Carlson, W.D., 1999. The case against Ostwald ripening of porphyroblasts. *Canadian Mineralogist*, **37**, 403-413.

Carlson, W.D., 2002. Scales of disequilibrium and rates of equilibration during metamorphism. *American Mineralogist*, **87**, 185-204.

Carlson, W.D., 2006. Rates of Fe, Mg, Mn, and Ca diffusion in garnet. *American Mineralogist*, **91**, 1-11.

Carlson, W.D., 2010. Dependence of reaction kinetics on H_2O activity as inferred from rates of intergranular diffusion of aluminium. *Journal of Metamorphic Geology*, **28**, 735-752.

Carlson, W.D., 2011. Porphyroblast crystallization: Linking mechanisms, kinetics, and microstructures. *International Geology Review*, **53**, 406-445.

Carlson, W.D., Anderson, S.D., Mosher, S., Davidow, J.S., Crawford, W.D. & Lane, E.D., 2007. High-pressure metamorphism in the Texas Grenville Orogen: Mesoproterozoic subduction of the Southern Laurentian continental margin. *International Geology Review*, **49**, 99-119.

Carlson, W.D. & Denison, C., 1992. Mechanisms of porphyroblast crystallization; results from high-resolution computed X-ray tomography. *Science*, **257**, 1236-1239.

Carlson, W.D., Denison, C. & Ketcham, R.A., 1995. Controls on the nucleation and growth of porphyroblasts; kinetics from natural textures and numerical models. *Geological Journal*, **30**, 207-225.

Carlson, W.D. & Gordon, C.L., 2004. Effects of matrix grain size on the kinetics of intergranular diffusion. *Journal of Metamorphic Geology*, **22**, 733-742.

Carlson, W.D. & Johnson, C.D., 1991. Coronal reaction textures in garnet amphibolites of the Llano Uplift. *American Mineralogist*, **76**, 756-772.

Cashman, K.V. & Ferry, J.M., 1988. Crystal size distribution (CSD) in rocks and the kinetics and dynamics of crystallization III. Metamorphic crystallization. *Contributions to Mineralogy and Petrology*, **99**, 401-415.

Catlos, E.J. & Sorensen, S.S., 2003. Phengite-based chronology of K- and Ba-rich fluid flow in two paleosubduction zones. *Science*, **299**, 92-95.

Chernoff, C.B. & Carlson, W.D., 1997. Disequilibrium for Ca during growth of pelitic garnet. *Journal of Metamorphic Geology*, **15**, 421-438.

Chernoff, C.B. & Carlson, W.D., 1999. Trace element zoning as a record of chemical disequilibrium during garnet growth. *Geology*, **27**, 555-558.

Cloos, M., 1982. Flow melanges: Numerical modeling and geologic constraints on their origin in the Franciscan subduction complex, California. *Geological Society of America Bulletin*, **93**, 330.

Cloos, M., 1985. Thermal evolution of convergent plate margins; thermal modeling and reevaluation of isotopic Ar-ages for blueschists in the Franciscan Complex of California. *Tectonics*, **4**, 421-433.

Connelly, J.N., 2001. Constraining the Timing of Metamorphism: U-Pb and Sm-Nd Ages from a Transect across the Northern Torngat Orogen, Labrador, Canada. *The Journal of Geology*, **109**, 57-77.

Connelly, J.N., 2006. Improved dissolution and chemical separation methods for Lu-Hf garnet chronometry. *Geochemistry, Geophysics, Geosystems - G^3*, **7**, 1-9.

Connelly, J.N., Ulfbeck, D.G., Thrane, K., Bizzarro, M. & Housh, T., 2006. A method for purifying Lu and Hf for analyses by MC-ICP-MS using TODGA resin. *Chemical Geology*, **233**, 126-136.

Crowley, J.L., Ghent, E.D., Carr, S.D., Simony, P.S. & Hamilton, M.A., 2000. Multiple thermotectonic events in a continuous metamorphic sequence, Mica Creek area, southeastern Canadian Cordillera. *Geological Materials Research*, **2**, 1-45.

Dallmeyer, R.D., 1979. Chronology of igneous and metamorphic activity in south-central Maine. In: *The caledonides in the U.S.A.: geological excursions in the northeast Appalacians* (eds Skehan, S. J. & Osberg, P. H.), pp. 63-71, Weston Observatory, Department of Geology and Geophysics, Weston, MA.

Daniel, C.G. & Pyle, D.M., 2006. Monazite-xenotime thermochronometry and Al_2SiO_5 reaction textures in the Picuris Range, northern New Mexico, USA: New evidence for a 1450-1400 Ma orogenic event. *Journal of Petrology*, **47**, 97-118.

Daniel, C.G. & Spear, F.S., 1999. The clustered nucleation and growth processes of garnet in regional metamorphic rocks from North-west Connecticut, USA. *Journal of Metamorphic Geology*, **17**, 503-520.

de Yoreo, J.J., Lux, D.R., Decker, E.R. & Osberg, P.H., 1989. The Acadian thermal history of western Maine. *Journal of Metamorphic Geology*, **7**, 169-190.

Denison, C. & Carlson, W.D., 1997. Three-dimensional quantitative textural analysis of metamorphic rocks using high-resolution computed X-ray tomography; Part II, Application to natural samples. *Journal of Metamorphic Geology*, **15**, 45-57.

Denison, C., Carlson, W.D. & Ketcham, R.A., 1997. Three-dimensional quantitative textural analysis of metamorphic rocks using high-resolution computed X-ray tomography; Part I, Methods and techniques. *Journal of Metamorphic Geology*, **15**, 29-44.

DeWolf, C.P., Zeissler, C.J., Halliday, A.N., Mezger, K. & Essene, E.J., 1996. The role of inclusions in U-Pb and Sm-Nd garnet geochronology; stepwise dissolution experiments and trace uranium mapping by fission track analysis. *Geochimica et Cosmochimica Acta*, **60**, 121-134.

Duchene, S., Blichert-Toft, J., Luais, B., Telouk, P., Lardeaux, J.M. & Albarede, F., 1997. The Lu-Hf dating of garnets and the ages of the Alpine high-pressure metamorphism. *Nature*, **387**, 586-589.

England, P.C. & Thompson, A.B., 1984. Pressure-temperature-time paths of regional metamorphism I. heat transfer during the evolution of regions of thickened continental crust. *Journal of Petrology*, **25** 894 -928

Farver, J.R. & Yund, R.A., 1992. Oxygen diffusion in a fine-grained quartz aggregate with wetted and nonwetted microstructures. *Journal of Geophysical Research*, **97**, 14,017-14,029.

Farver, J.R. & Yund, R.A., 1995. Grain boundary diffusion of oxygen, potassium and calcium in natural and hot-pressed feldspar aggregates. *Contributions to Mineralogy and Petrology*, **118**, 340-355.

Farver, J.R. & Yund, R.A., 2000. Silicon diffusion in a natural quartz aggregate: constraints on solution-transfer diffusion creep. *Tectonophysics*, **325**, 193-205.

Ferry, J.M., 1978. Fluid interaction between granite and sediment during metamorphism, South-central Maine. *American Journal of Science*, **278**, 1025-1056.

Ferry, J.M., 1980. A comparative study of geothermometers and geobarometers in pelitic schists from south-central Maine. *American Mineralogist*, **65**, 720-732.

Ferry, J.M., 1981. Petrology of graphitic sulfide-rich schists from south-central Maine: an example of desulfidation during prograde regional metamorphism. *American Mineralogist*, **66**, 908-930.

Ferry, J.M. & Dipple, G.M., 1991. Fluid flow, mineral reactions, and metasomatism. *Geology*, **19**, 211-214.

Foster, C.T. & Dutrow, B.L., 2005. Local reaction affinities and their effect on nucleation patterns in metamorphic rocks. *Geological Society of America Abstracts with Programs*, **37**, 53.

Foster, G., Parrish, R.R., Horstwood, M.S.A., Chenery, S., Pyle, J. & Gibson, H.D., 2004. The generation of prograde P-T-t points and paths; a textural, compositional, and chronological study of metamorphic monazite. *Earth and Planetary Science Letters*, **228**, 125-142.

Frey, M., Trommsdorff, V. & Wenk, E., 1980. Excursion No. VI; Alpine metamorphism of the Central Alps. In: *Geology of Switzerland; a guide-book* (eds Aubert, D., Ayrton, S., Badoux, H., Bearth, P., Bernoulli, D., Boriani, A., Bugnon, P., Burri, M., Caron, C., Dietrich, V., Dolivo, E., Escher, A., Frank, E., Frey, M., Gabus, J., Herb, R., Homewood, P., Laubscher, H., Masson, H., Matter, A., Metzeltin, S., Rigassi, D., Schaer, J. P., Schlaeppi, E., Steck, A., van Stuijvenberg, J., Trommsdorff, V., Truempy, R., Weidmann, M., Wenk, E., Winkler, W. & Zingg, A.), pp. 296-316, Wepf & Co. : Basel, Switzerland, Switzerland.

Gaidies, F., Pattison, D.R.M. & de Capitani, C., 2011. Toward a quantitative model of metamorphic nucleation and growth. *Contributions to Mineralogy and Petrology*, **in press**.

Ganguly, J., Bhattacharya, R.N. & Chakraborty, S., 1988. Convolution Effect in the Determination of Compositional Profiles and Diffusion-Coefficients by Microprobe Step Scans. *American Mineralogist*, **73**, 901-909.

Ganguly, J., Bloch, E. & Ito, M., 2010. Experimental diffusion kinetics of geochronological systems and interpretations of mineral ages in terrestrial rocks and meteorites. *Geological Society of America Abstracts with Programs*, **42**, 340.

Gibson, H.D., Brown, R.L. & Parrish, R.R., 1999. Deformation-induced inverted metamorphic field gradients: an example from the southeastern Canadian Cordillera. *Journal of Structural Geology*, **21**, 751-767.

Hetenyi, G., Cattin, R., Brunet, F., Bollinger, L., Vergne, J., Nabelek, J.L. & Diament, M., 2007. Density distribution of the India plate beneath the Tibetan plateau: geophysical and petrological constraints on the kinetics of lower-crustal eclogitization. *Earth and Planetary Science Letters*, **264**, 226-244.

Hirsch, D.M., 2008. Controls on porphyroblast size along a regional metamorphic field gradient. *Contributions to Mineralogy and Petrology*, **155**, 401-415.

Hirsch, D.M., 2011. Reduce3D: A tool for three-dimensional spatial statistical analysis of crystals. *Geosphere*, **7**, 724-732.

Hirsch, D.M. & Carlson, W.D., 2006. Variations in rates of nucleation and growth of biotite porphyroblasts. *Journal of Metamorphic Geology*, **24**, 763-777.

Hirsch, D.M., Ketcham, R.A. & Carlson, W.D., 2000. An evaluation of spatial correlation functions in textural analysis of metamorphic rocks. *Geological Materials Research*, **2**, 1.

Hirsch, D.M., Prior, D.J. & Carlson, W.D., 2003. An overgrowth model to explain multiple, dispersed high-Mn regions in the cores of garnet porphyroblasts. *American Mineralogist*, **88**, 131-141.

Hoisch, T.D., Wells, M.L. & Grove, M., 2008. Age trends in garnet-hosted monazite inclusions from upper amphibolite facies schist in the northern Grouse Creek Mountains, Utah. *Geochimica et Cosmochimica Acta*, **72**, 5505-5520.

Holdaway, M.J., 1978. Significance of chloritoid-bearing and staurolite-bearing rocks in the Picuris Range, New-Mexico. *Geological Society of America Bulletin*, **89**, 1404-1414.

Holdaway, M.J., 2000. Application of new experimental and garnet Margules data to the garnet-biotite geothermometer. *American Mineralogist*, **85**, 881-892.

Holdaway, M.J., Mukhopadhyay, B., Dyar, M.D., Guidotti, C.V. & Dutrow, B.L., 1997. Garnet-biotite geothermometry revised; new Margules parameters and a natural specimen data set from Maine. *American Mineralogist*, **82**, 582-595.

Holland, T.J.B. & Powell, R., 1990. An enlarged and updated internally consistent thermodynamic dataset with uncertainties and correlations; the system K (sub 2) O-Na (sub 2) O-CaO-MgO-MnO-FeO-Fe (sub 2) O (sub 3) -Al (sub 2) O (sub 3) -TiO (sub 2) -SiO (sub 2) -C-H (sub 2). *Journal of Metamorphic Geology*, **8**, 89-124.

Holland, T.J.B. & Powell, R., 1998. An internally consistent thermodynamic data set for phases of petrological interest. *Journal of Metamorphic Geology*, **16**, 309-343.

Hollister, L.S., 1966. Garnet zoning; an interpretation based on the Rayleigh fractionation model *Science* **154**, 1647-1651.

Hopson, C.A., Mattinson, J.M., Pessagno, E.A., Jr. & Luyendyk, B.P., 2008. California Coast Range Ophiolite; composite Middle and Late Jurassic oceanic lithosphere. *Geological Society of America Special Paper*, **438**, 1-102.

Hsu, L.C., 1968. Selected phase relationships in the system Al-Mn-Fe-Si-O-H: A model for garnet equilibria. *Journal of Petrology*, **9**, 40-83.

Janots, E., Engi, M., Rubatto, D., Berger, A., Gregory, C. & Rahn, M., 2009. Metamorphic rates in collisional orogeny from in situ allanite and monazite dating. *Geology*, **37**, 11-14.

Johnson, C.D. & Carlson, W.D., 1990. The origin of olivine-plagioclase coronas in metagabbros from the Adirondack Mountains, New York. *Journal of Metamorphic Geology*, **8**, 697-717.

Ketcham, R.A., 2005a. Computational methods for quantitative analysis of three-dimensional features in geological specimens. *Geosphere*, **1**, 32-41.

Ketcham, R.A., 2005b. Three-dimensional grain fabric measurements using high-resolution X-ray computed tomography. *Journal of Structural Geology*, **27**, 1217-1228.

Ketcham, R.A. & Carlson, W.D., in review. Numerical simulation of diffusion-controlled nucleation and growth of porphyroblasts. *Journal of Metamorphic Geology*.

Ketcham, R.A., Meth, C., Hirsch, D.M. & Carlson, W.D., 2005. Improved methods for quantitative analysis of three-dimensional porphyroblastic textures. *Geosphere*, **1**, 42-59.

Kohn, M.J., 2009. Models of garnet differential geochronology. *Geochimica et Cosmochimica Acta*, **73**, 170-182.

Kohn, M.J. & Malloy, M.A., 2004. Formation of monazite via prograde metamorphic reactions among common silicates; implications for age determinations. *Geochimica et Cosmochimica Acta*, **68**, 101-113.

Kretz, R., 1966. Grain-size distribution for certain metamorphic minerals in relation to nucleation and growth. *Journal of Geology*, **74**, 147-173.

Kretz, R., 1969. On the spatial distribution of crystals in rocks. *Lithos*, **2**, 39-65.

Kretz, R., 1973. Kinetics of the crystallization of garnet at two localities near Yellowknife. *Canadian Mineralogist*, **12, Part 1**, 1-20.

Kretz, R., 1974. The rate of crystallization of minerals in rocks. *Canadian Mineralogist*, **12, Part 6**, 430.

Krogh, E.J., 1988. The garnet-clinopyroxene Fe-Mg geothermometery - a reinterpretation of existing experimental data. *Contributions to Mineralogy and Petrology*, **99**, 44-48.

Krogh, E.J., Oh, C.W. & Liou, J.G., 1994. Polyphase and anticlockwise P-T evolution for Franciscan eclogites and blueschists from Jenner, California, USA. *Journal of Metamorphic Geology*, **12**, 121-134.

Krogh Ravna, E.J. & Terry, M.P., 2004. Geothermobarometry of UHP and HP eclogites and schists: an evaluation of equilibria among garnet-clinopyroxene-kyanite-phengite-coesite/quartz. *Journal of Metamorphic Geology*, **22**, 579-592.

Kylander-Clark, A.R.C., Hacker, B.R., Johnson, C.M., Beard, B.L., Mahlen, N.J. & Lapen, T.J., 2007. Coupled Lu/Hf and Sm/Nd geochronology constrains prograde and exhumation histories of high- and ultrahigh pressure eclogites from western Norway. *Chemical Geology*, **242**, 137-154.

Lagos, M., Scherer, E.E., Tomaschek, F., Muenker, C., Keiter, M., Berndt, J. & Ballhaus, C., 2007. High-precision Lu/Hf geochronology of Eocene eclogite-facies rocks from Syros, Cyclades, Greece. *Chemical Geology*, **243**, 16-35.

Lanzirotti, A., 1995. Yttrium zoning in metamorphic garnets. *Geochimica et Cosmochimica Acta*, **59**, 4105-4110.

Lapen, T.J., Johnson, C.M., Baumgartner, L.P., Mahlen, N.J., Beard, B.L. & Amato, J.M., 2003. Burial rates during prograde metamorphism of an ultra-high-pressure terrane; an example from Lago di Cignana, Western Alps, Italy. *Earth and Planetary Science Letters*, **215**, 57-72.

Lee, D.V., 1987. *Geothermobarometry and petrologic history of a contact metamorphosed section of the Tasiuyak Gneiss, west of Nain, Labrador*. Unpublished Bachelor of Science (Honors) Thesis, Memorial University of Newfoundland, St John's, Newfoundland, 111 pp.

Lindquist, W.B., Lee, S.-M., Coker, D.A., Jones, K.W. & Spanne, P., 1996. Medial axis analysis of void structure in three-dimensional tomographic images of porous media. *Journal of Geophysical Research*, **101**, 8297-8310.

Lyubetskaya, T. & Ague, J.J., 2009. Modeling the magnitudes and directions of regional metamorphic fluid flow in collisional orogens. *Journal of Petrology*, **50**, 1505-1531.

Marshall, W.L. & Franck, E.U., 1981. Ion product of water substance, 0-1000 °C, 1-10,000 bars; New international formulation and its background. *Journal of Physical and Chemical Reference Data*, **10**, 295-304.

McFarlane, C.R.M., Carlson, W.D. & Connelly, J.N., 2003. Prograde, peak, and retrograde P-T paths from aluminium in orthopyroxene; high-temperature contact metamorphism in the aureole of the Makhavinekh Lake Pluton, Nain Plutonic Suite, Labrador. *Journal of Metamorphic Geology*, **21**, 405-423.

McFarlane, C.R.M., Connelly, J.N. & Carlson, W.D., 2005. Intracrystalline redistribution of Pb in zircon during high temperature contact metamorphism. *Chemical Geology*, **217**, 1-28.

McFarlane, C.R.M., Connelly, J.N. & Carlson, W.D., 2006. Contrasting response of monazite and zircon to a high-T thermal overprint. *Lithos*, **88**, 135-149.

Meth, C.E. & Carlson, W.D., 2005. Diffusion-controlled synkinematic growth of garnet from a heterogeneous precursor at Passo del Sole, Switzerland. *Canadian Mineralogist*, **43**, 157-182.

Miyazaki, K., 1996. A numerical simulation of textural evolution due to Ostwald ripening in metamorphic rocks: a case for small amount of volume of dispersed crystals. *Geochimica et Cosmochimica Acta*, **60**, 277-290.

Mosher, S., 1998. Tectonic evolution of the southern Laurentian Grenville orogenic belt. *Geological Society of America Bulletin*, **110**, 1357-1375.

Mosher, S., Levine, J.S.F. & Carlson, W.D., 2008. Mesoproterozoic plate tectonics; a collisional model for the Grenville-aged orogenic belt in the Llano Uplift, central Texas. *Geology*, **36**, 55-58.

Newton, R. & Manning, C., 2008. Solubility of corundum in the system Al2O3–SiO2–H2O–NaCl at 800 °C and 10 kbar. *Chemical Geology*, **249**, 250-261.

Nielsen, A.E., 1959. The kinetics of crystal growth in Barium Sulfate. *Acta Chemica Scandinavica*, **13**, 784-802.

O'Brien, P.J., 1999. Asymmetric zoning profiles in garnet from HP-HT granulite and implications for volume and grain-boundary diffusion. *Mineralogical Magazine*, **63**, 227-238.

Osberg, P.H., 1971. An equilibrium model for Buchan-type metamorphic rocks, south-central Maine. *American Mineralogist*, **56**, 570-586.

Otamendi, J.E., de la Rosa, J.D., Patino Douce, A.E. & Castro, A., 2002. Rayleigh fractionation of heavy rare earths and yttrium during metamorphic garnet growth. *Geology*, **30**, 159-162.

Padron-Navarta, J.A., Garrido, C.J., Sanchez-Navas, A., Tommasi, A., Lopez Sanchez-Vizcaino, V., Gomez-Pugnaire, M.T. & Hussain, S.S., 2008. Oriented growth of garnet by topotactic reactions and epitaxy in high-pressure, mafic garnet granulite formed by dehydration melting of metastable hornblende-gabbronorite (Jijal Complex, Kohistan Complex, north Pakistan). *Journal of Metamorphic Geology*, **26**, 855-870.

Page, F.Z., Armstrong, L.S., Essene, E.J. & Mukasa, S.B., 2007. Prograde and retrograde history of the junction school eclogite, California, and an evaluation of garnet-phengite-clinopyroxene thermobarometry. *Contributions to Mineralogy and Petrology*, **153**, 533-555.

Parks, G.A., 1984. Surface and interfacial free energy of quartz. *Journal of Geophysical Research*, **89**, 3997-4008.

Pattison, D.R.M., 1992. Stability of andalusite and sillimanite and the Al_2SiO_5 triple point: constraints from the Ballachulish Aureole, Scotland. *Journal of Geology*, **100**, 423-446.

Pattison, D.R.M., De Capitani, C. & Gaidies, F., in press. Petrological consequences of variations in metamorphic reaction affinity. *Journal of Metamorphic Geology*.

Pattison, D.R.M. & Tinkham, D.K., 2009. Interplay between equilibrium and kinetics in prograde metamorphism of pelites: an example from the Nelson aureole, British Columbia. *Journal of Metamorphic Geology*, **27**, 249-279.

Philippot, P., Blichert-Toft, J., Perchuk, A., Costa, S. & Gerasimov, V., 2001. Lu-Hf and Ar-Ar chronometry supports extreme rate of subduction zone metamorphism deduced from geospeedometry. *Tectonophysics*, **342**, 23-38.

Poli, S., 1993. The amphibolite-eclogite transformation; an experimental study on basalt. *American Journal of Science*, **293**, 1061-1107.

Pollington, A.D. & Baxter, E.F., 2010. High resolution Sm–Nd garnet geochronology reveals the uneven pace of tectonometamorphic processes. *Earth and Planetary Science Letters*, **293**, 63-71.

Porter, D.A. & Easterling, K.E., 1992. *Phase transformations in metals and alloys*, 514 pp. Chapman and Hall, London.

Pyle, J.M. & Spear, F.S., 1999. Yttrium zoning in garnet; coupling of major and accessory phases during metamorphic reactions. *Geological Materials Research*, **1**, 1-49.

Raeburn, S.P., 1996. *New methods in quantitative metamorphic petrology; 1, In situ determination of iron valence in minerals; 2, The application of 3-D textural analysis to the study of crystallization kinetics*. Unpublished Doctoral Thesis, Pennsylvania State University at University Park, University Park, PA, 279 pp.

Ridley, J. & Thompson, A.B., 1986. The role of mineral kinetics in the development of metamorphic microtextures. In: *Fluid-rock interactions during metamorphism* (eds Walther, J. V. & Wood, B. J.), pp. 154-193, Springer-Verlag, New York.

Robyr, M., Carlson, W.D., Passchier, C. & Vonlanthen, P., 2009. Microstructural, chemical and textural records during growth of snowball garnet. *Journal of Metamorphic Geology*, **27**, 423-437.

Rubatto, D., 2002. Zircon trace element geochemistry; partitioning with garnet and the link between U-Pb ages and metamorphism. *Chemical Geology*, **184**, 123-138.

Rubie, D.C., 1998. Disequilibrium during metamorphism; the role of nucleation kinetics. In: *What Drives Metamorphism and Metamorphic Reactions? Special Publication 138* (eds Treloar, P. J. & Obrien, P. J.), pp. 199-214, Geological Society, London.

Scherer, E.E., Cameron, K.L. & Blichert-Toft, J., 2000. Lu-Hf garnet geochronology; closure temperature relative to the Sm-Nd system and the effects of trace mineral inclusions. *Geochimica et Cosmochimica Acta*, **64**, 3413-3432.

Schneider, R., 1999. *3-D textural analysis of a garnet-amphibole rock from the Franciscan complex of california: nucleation and growth mechanism of porphyroblastic crystals using high-resolution x-ray compound tomography*. Unpublished Senior Honors Thesis, University of Texas, Austin, # pp.

Schwarz, J.O., Engi, M. & Berger, A., 2011. Porphyroblast crystallization kinetics: the role of the nutrient production rate. *Journal of Metamorphic Geology*, no-no.

Shannon, R.D., 1976. Revised effective ionic radii and systematic studies of interatomic distances in halides and chalcogenides. *Acta Crystallographica*, **A32**, 751-767.

Shewmon, P.G., 1969. *Transformations in metals*, 394 pp. McGraw-Hill, New York.

Shimizu, N., Semet, M.P. & Allègre, C.J., 1978. Geochemical applications of quantitative ion-microprobe analysis. *Geochimica et Cosmochimica Acta*, **42**, 1321-1334.

Simony, P.S., Ghent, E.D., Craw, D. & Mitchell, W., 1980. Structural and metamorphic evolution of the northeast flank of the Shuswap Complex, southern Canoe River area, British Columbia. *Geological Society of America Memoir*, **153**, 445-461.

Skora, S., Baumgartner, L.P., Mahlen, N.J., Johnson, C.M., Pilet, S. & Hellebrand, E., 2006. Diffusion-limited REE uptake by eclogite garnets and its consequences for Lu/Hf and Sm/Nd geochronology. *Contributions to Mineralogy and Petrology*, **152**, 703-720.

Skora, S., Lapen, T.J., Baumgartner, L.P., Johnson, C.M., Hellebrand, E. & Mahlen, N.J., 2009. The duration of prograde garnet crystallization in the UHP eclogites at Lago di Cignana, Italy. *Earth and Planetary Science Letters*, **287**, 402-411.

Söderlund, U., Patchett, P.J., Vervoort, J.D. & Isachsen, C.E., 2004. The ^{176}Lu decay constant determined by Lu–Hf and U–Pb isotope systematics of Precambrian mafic intrusions. *Earth and Planetary Science Letters*, **219**, 311-324.

Spear, F.S., 1995. Metamorphic phase equilibria and pressure-temperature-time paths *Monograph 1*, pp. 799, Mineralogical Society of America, Washington, D.C.

Spiess, R., Groppo, C. & Compagnoni, R., 2007. When epitaxy controls garnet growth. *Journal of Metamorphic Geology*, **25**, 439-450.

Stowell, H.H. & Tinkham, D.K., 2003. Integration of phase equilibria modelling and garnet Sm-Nd chronology for construction of P-T-t paths: examples from the Cordilleran Coast Plutonic Complex, USA. *Geological Society, London, Special Publications*, **220**, 119-145.

Theriault, R.J. & Ermanovics, I., 1997. Sm-Nd isotopic and geochemical characterisation of Paleoproterozoic Torngat Orogen, Labrador, Canada. *Precambrian Research*, **81**, 15-35.

Tinkham, D.K. & Ghent, E.D., 2005. Estimating P-T conditions of garnet growth with isochemical phase diagram sections and the problem of effective bulk composition. *Canadian Mineralogist*, **43, Part 1**, 35-50.

Todd, C.S. & Engi, M., 1997. Metamorphic field gradients in the Central Alps. *Journal of Metamorphic Geology*, **15**, 513-530.

Tropper, P. & Manning, C., 2007. The solubility of corundum in H2O at high pressure and temperature and its implications for Al mobility in the deep crust and upper mantle. *Chemical Geology*, **240**, 54-60.

Van Kranendonk, M.J., St-Onge, M.R. & Henderson, J.R., 1993. Paleoproterozoic tectonic assembly of Northeast Laurentia through multiple indentations. *Precambrian Research*, **63**, 325-347.

Vance, D. & O'Nions, R.K., 1990. Isotopic chronometry of zoned garnets: growth kinetics and metamorphic histories. *Earth and Planetary Science Letters*, **97**, 227-240.

Vance, D. & O'Nions, R.K., 1992. Prograde and retrograde thermal histories from the Central Swiss Alps. *Earth and Planetary Science Letters*, **114**, 113-129.

Vernon, R.H., White, R.W. & Clarke, G.L., 2008. False metamorphic events inferred from misinterpretation of microstructural evidence and P-T data. *Journal of Metamorphic Geology*, **26**, 437-449.

Wakabayashi, J., 1990. Counterclockwise P-T-t paths from amphibolites, Franciscan Complex, California; relics from the early stages of subduction zone metamorphism. *Journal of Geology*, **98**, 657-680.

Wakabayashi, J. & Dumitru, T.A., 2007. ^{40}Ar/^{39}Ar ages from coherent, high-pressure metamorphic rocks of the Franciscan Complex, California; revisiting the timing of metamorphism of the world's type subduction complex. *International Geology Review*, **49**, 873-906.

Walther, J.V. & Wood, B.J., 1984. Rate and mechanism in prograde metamorphism. *Contributions to Mineralogy and Petrology*, **88**, 246-259.

Waters, D.J. & Lovegrove, D.P., 2002. Assessing the extent of disequilibrium and overstepping of prograde metamorphic reactions in metapelites from the Bushveld Complex aureole, South Africa. *Journal of Metamorphic Geology*, **20**, 135-149.

Whitney, D.L. & Evans, B.W., 2010. Abbreviations for names of rock-forming minerals. *American Mineralogist*, **95**, 185-187.

Wilbur, D.E. & Ague, J.J., 2006. Chemical disequilibrium during garnet growth: Monte Carlo simulations of natural crystal morphologies. *Geology*, **34**, 689.

Wohlers, A. & Manning, C.E., 2009. Solubility of corundum in aqueous KOH solutions at 700 °C and 1 GPa. *Chemical Geology*, **262**, 310-317.

Zeh, A., Klemd, R. & Barton, J.M., 2005. Petrological evolution in the roof of the high-grade metamorphic Central Zone of the Limpopo Belt, South Africa. *Geological Magazine*, **142**, 229-240.

Zinner, E. & Crozaz, G., 1986. A method for the quantitative measurement of rare earth elements in the ion microprobe. *International Journal of Mass Spectrometry and Ion Processes*, **69**, 17-38.

VITA

Eric David Kelly grew up in Portola Valley, California on the San Andreas Fault. He attended Woodside High School and later enrolled at Foothill College to explore the sciences. Before committing to a degree in Geology, Eric worked for SRI International as a mechanic at the Sondrestrom Radar Project Office in Kellyville, Greenland. Upon his return to the United States, he finalized courses at Foothill College and transferred to The University of California at Davis where he worked with Howard Day in metamorphic petrology and Eric Larsen in fluvial geomorphology. He earned the degree of Bachelor of Science in Geology in September, 2000. Eric continued working in metamorphic petrology with Thomas Hoisch at Northern Arizona University, and he earned the degree of Master of Science in August, 2004. Eric's interest in disequilibrium problems led him to pursue a doctorate with William Carlson at The University of Texas at Austin. During Eric's final semester in Austin, he was a Lecturer at The University of Texas at San Antonio.

Permanent address: 12748 The Hollow, Grass Valley, California 95945
Eric.Kelly@utexas.edu

This dissertation was typed by the author.